Kinetic Effects in Magnetic Reconnection

Homam Betar

UNIVERSITÉ DE LORRAINE

École doctorale: C2MP

Kinetic Effects in Magnetic Reconnection

THÈSE

présentée et soutenue publiquement le 12 Février 2021

pour l'obtention du

Doctorat de l'Université de Lorraine

(Spécialité doctorale "Physique des Plasmas")

par

Homam BETAR

Composition du jury

Présidente :	**Mme. Caterina RICONDA**,	Professeur, Université Paris VI
Rapporteurs :	**M. Jean-Marcel RAX**, **M. Oliver AGULLO**,	Professeur, Université de Paris-Saclay Maitre de Conférences, Université d'Aix-Marseille
Examinateur :	**Mme. Chiara MARCHETTO**,	Chercheuse au CNR Italien
Invités :	**M. Maurizio OTTAVIANI**,	Senior Scientist of the European Commission, IRFM (CEA)
Directeur:	**M. Alain GHIZZO**,	Professeur, Université de Lorraine
Co-directeur:	**M. Daniele DEL SARTO**,	Maitre de Conférences, Université de Lorraine

Institut Jean Lamour, UMR 7198 CNRS—Université de Lorraine, F-54000 Nancy, France

Mis en page avec la classe thesul.

Remerciements

Le processus de la compréhension et de l'apprentissage ne se représente pas par une fonction échelon mais par une fonction d'activation non linéaire où les résultats sont obtenus grace au travail de nos professeurs.

Tout d'abord, je tiens à remercier mes directeurs Daniele Del SARTO et Alain GHIZZO qui m'ont accompagné tout au long de mon périple d'apprentissage durant ces trois dernières années. Ils se sont montrés patients. Et grâce aux discussions indispensables à la compréhension et aux précieuses explications, ils ont éclairci des sujets qui m'étaient inaccessibles, participant ainsi intensément à la réalisation de ce travail de recherche. Ils m'ont aidé à explorer de nombreux sujets en physique des plasmas, en mathématiques, en méthodes numériques mais également d'autres sujets scientifiques.

J'aimerais remercier Alain de m'avoir offert cette opportunité, de s'être investi dans mon travail, d'avoir partagé avec moi ses connaissances si riches en matière de simulation numérique, méthodes numériques, programmation parallèle et, bien sûr, de toutes les questions de physique évoquées dans ce mémoire de recherche. Je voudrais également le remercier pour son suivi et son investissement lors des derniers travaux de recherche réalisés malgré les nombreuses pressions car il a su se rendre disponible afin de répondre à toutes mes questions et m'apporter les explications nécessaires quand je ne pouvais plus avancer seul.

Je ne sais pas, en toute honnêteté, ce que je devrais dire à Daniele, tous mes mots de remerciement aussi humbles et sincères soient-ils ne pourraient exprimer ma reconnaissance envers lui. Daniele m'a apporté un soutien primordial non seulement en ce qui concerne les sujets scientifiques traités dans mon travail de recherche mais aussi lors des difficultés que j'ai rencontrées. Il est d'une grande ouverture d'esprit et nous pouvons discuter de n'importe quel sujet avec lui. Nos discussions et conversations ont dépassé les sujets scientifiques auxquels nous nous sommes intéressés, et nous avons discuté de tout : politique, philosophie, histoire, littérature et même cuisine. C'est quelqu'un de très positif et patient, il possède une culture très riche et sait comment vous donner l'impression d'avoir accompli une belle réalisation alors que vous n'êtes pas satisfait de ce que vous venez d'accomplir. Il ne tolère jamais les erreurs scientifiques mais son attitude positive et optimiste envers les personnes qu'il encadre les propulse continuellement en avant et leur procure, grâce à ses explications d'une grande qualité scientifique, un plaisir intense quand ils comprennent mieux ce qu'ils avaient mal compris auparavant.

De même, je tiens à remercier M. Maurizio OTTAVIANI d'avoir mis à mon profit sa longue et importante expérience scientifique lors de notre collaboration. Ses questionnements sur le travail de recherche que je mène, ses commentaires et ses corrections ont été d'une grande importance dans la réalisation de ce travail. Et je le remercie d'avoir accepté invitation d'assister à la soutenance de ma thèse.

Je souhaite pareillement remercier M. Jean-Marcel RAX et M. Oliver AGULLO d'avoir bien voulu être les rapporteurs de mon mémoire de thèse et j'espère que mon travail sera à la hauteur de leurs attentes. Mes remerciements vont également à Mme. Caterina RICONDA et Mme. Chiara MARCHETTO d'avoir été mes examinateurs.

Je tiens aussi à remercier chaleureusement M. Etienne GRAVIER qui m'a aidé d'effectuer mon master, malgré la longue interruption de mes études imposée par la situation actuelle de mon pays d'origine, son aide m'a été particulièrement précieuse. Je remercie Erwan DERIAZ qui a sans hésitation fait de son mieux pour répondre à mes questions et m'aider lors de mes années de master et doctorat.

J'aimerais remercier aussi M. Simone LANDI, M. Emanuele PAPINI de répondre à toutes mes questions et m'apporter les explications scientifiques durant ma participation à la conférence

Arcetri sur l'astrophysique du plasma (Florence - 2019).

Merci, bien sûr, à tous les membres de l'équipe de Physique des Plasmas Chauds(107), y compris mes amis Lili, kyungtak, Julien, Fatima et Jordan.

Je voudrais adresser un immense remerciement à mes amis Main, Rim, Charif et Nadim qui m'ont aidé depuis mon arrivée en France jusqu'à présent et ont ainsi participé à la réalisation de ce travail, sans oublier ma chère amie Houda pour son soutien. Je remercie aussi Mariana, Youssef, Fadi et aussi Yasmine pour son aide.

Enfin, je remercie ma mère, mon père et mes frères et sœurs pour leur soutien infaillible et permanent, et bien sûr je profondément remercie soukaina, qui est la plus belle âme que j'aie jamais rencontrée, et qui m'a soutenu dans toutes les difficultés que j'ai rencontrées.

Table of Contents

"Nature uses only the longest threads to weave her patterns, so that each small piece of her fabric reveals the organization of the entire tapestry."

Richard FEYNMAN, The Character of Physical Law

Summary

In plasmas, gaseous collective systems of charged particles, magnetic lines acquire at macroscopic scales what can be said a "topological identity", that is, when embedded in the plasma, they evolve as dragged by the particle flow without intersecting nor breaking. This, however, is true only in certain regimes, namely at the so-called "magnetohydrodynamic" (MHD) scales. When some microscopic effects, otherwise negligible, becomes locally important, such a lagrangian invariance is lost. Magnetic reconnection is the physical process by which this occurs: magnetic field lines can thus break and reconnect in some points in the space. This re-arrangement of the field topology drives the conversion of the magnetic energy stored in field lines into kinetic energy, and thermal energy. Magnetic reconnection is ubiquitous in laboratory and natural plasmas: in the former, it can be responsible of the loss of magnetic confinement, which, for example, is detrimental for the achievement of burning conditions in thermonuclear fusion experiments (e.g. in tokamaks like ITER). In the latter, it is responsible of a range of massively energy releasing phenomena, ranging from coronal mass ejections and solar flares on the Sun, to magnetic substorms in planetary magnetospheres (which can lead to the spectacular polar lights but also interfering with the functioning of electronic and communication devices on the Earth), to ultra-intense electromagnetic emissions in neutron stars and other magnetized astrophysical objects.

Despite its occurrence, which makes it relevant to several research sub-fields, magnetic reconnection is a complex phenomenon since it involves several physical parameters and conditions, which in turn implies that a realistic study of this phenomenon by means of a single, complete model, is practically not possible. This is surely true from the analytical point of view, but also from the numerical point of view, because of the intrinsic multi-scale nature of the reconnection phenomenon. However, thanks to its multi-scale nature, several complementary models can be tailored in order to analyze different regimes. For example, when the bulk velocities of ions and electrons are equal and can be approximated, at the leading order, with the electromagnetic drift velocity, several "reduced magnetohydrdynamic models" can be devised so to investigate magnetic reconnection in this regime. In these models, microscopic effects related to both ion and electron dynamics can be included as ordered small with respect to some expansion parameter. However, even so the parameter space remains large, and further physical approximations and modifications can be necessary. In some cases, these modifications can be self-consistently motivated by the underlying physics. In other cases, they are motivated by the need to simplify analytically or numerically the problem in order to get insight into the fundamental physics behind it. These models include the one-fluid model, two-fluid models, or different "extensions" of the one-fluid model in which different strategies are pursued in order to incorporate the kinetic and two-fluid effects. We have in particular addressed the linear study of reconnecting MHD instabilities in presence of more than one "non-ideal" kinetic effect at a time.

A particular example of "reduced" models, in which the study of magnetic reconnection is somehow simplified, is provided by those models in which the dynamics of the electromagnetic fields in the plasma is coupled to that of the electrons, alone. These models, in which ions just form a static neutralizing background, are justified by the large electron-to-ion mass ratio, and by the restriction to fast time scales, and short spatial lengths compared to those of ions: ions decouple indeed from the magnetic field at larges scales than electrons, so that a range of scales exists, in which magnetic lines are still dragged by the electron flow, while they loose their "topological

invariance" with respect to the ion flow. When using a fluid description, which accounts for the fast time scales and short spatial lengths of the electrons, while ions are assumed immobile, one is then led to consider the so-called "electron-MHD" (EMHD) regime. A first model, suitable for describing the reconnection dynamics when non-relativistic phase-velocities are considered, is the incompressible EMHD, which is suitable to explore the dynamics of weakly magnetized plasma. However, when effects related to the compressibility of the electron flow become relevant, an extension of this model to include both the pressure tensor, and displacement current becomes interesting. Studying the role of the full electron pressure tensor in reconnecting instabilities in an extended, non-relativistic EMHD model, is another topic addressed in the present dissertation. Although such a study is meant as a primary step to the inclusion of kinetic temperature effects of this kind in more complete two-fluid or even full-kinetic models of reconnection, we will show it to provide a very complex problem in itself.

Due to its macroscopic interpretation as the violation of the Lagrangian invariance of magnetic lines dragged by the particle bulk flow, magnetic reconnection finds a natural description in fluid-type models. However, the fact that it is triggered by microscopic effects, leads to an equally natural description by means of full-kinetic models, namely of Vlasov-Maxwell (VM) type. Kinetic models, although more "complete", are of course more complex and demanding, both from an analytical and from a numerical point of view. In this dissertation we have then addressed the numerical study of magnetic reconnection in a kinetic description in which the dynamics of electrons alone is retained (i.e., a sort of "kinetic counterpart" of EMHD fluid models). In particular, since many other instabilities can co-exist, compete, or even initiate and seed magnetic reconnection, we have chosen to investigate the occurrence of reconnection phenomena that are coupled to some beam-plasma instabilities, which are of relevance to both laser-plasma interaction experiments and to some astrophysical processes. To this purpose, in this dissertation, we have studied the nonlinear evolution of initial plasma configurations in which reconnection can co-exist with Weibel-type instabilities. The latter involves a somehow opposite mechanism to that involved in magnetic reconnection: the conversion of thermal and kinetic energy of the particles into electromagnetic energy, which leads to the amplification of background magnetic fluctuations. We address this problem by numerically solving the (VM) using two types of numerical models. The first one relies on the particle-in-cell (PIC) method: in particular, we have used SMILEI, an open-source, relativistic, parallel PIC code. The second one is the parallel code VLEM which uses the semi-Lagrangian method in order to numerically integrate the relativistic VM system.

This dissertation is organized as follows:

* A general introduction presents the concept of magnetic reconnection and briefly reviews its history.

* Chapter 1 discusses magnetic reconnection and its different, relevant features in a more formal way: a simplified model is presented and linearized to obtain the scaling laws. We thus present the concept of instability parameter, and we discuss its "limits" with respect to the wavelength of the perturbation for reconnecting instabilities in a two-dimensional, rectangular current sheet. Finally, we briefly review the notion of "ideal" tearing, recently introduced in literature.

* Chapter 2 is devoted to a general review of the plasma models used in studying magnetic reconnection: we start with a general discussion of kinetic-type models. We then explicitly address the derivation of fluid models from the VM system and the related closure problem.

Finally, we end the chapter by providing a detailed derivation of the one-fluid model, with a primary focus on the generalized Ohm law.

* Chapter 3 addresses the methods for the numerical solution of the VM system. In this chapter, we provide an in-depth review of the mathematical principles which are required to build a parallel semi-Lagrangian solver or a PIC solver, and the way these two complementary types of solvers are derived.

* Chapter 4 is devoted to the discussion of the adaptive multi-precision eigensolver we developed to solve generalized eigenvalue problems resulting from the linear analysis of magnetic reconnection in different regimes. The main difficulty addressed and solved by this code is the ill-conditioning of finite-difference stencils, which arise due to the non-uniformity of the underlying grid.

* Chapter 5 is devoted to a detailed discussion of the derivation of different two-field reduced MHD models. By linearizing a quite general reduced reconnection model that includes several non-ideal effects at a time, we derive a generalized eigenvalue problem. This can be used to investigate the scaling laws of magnetic reconnection that occurs as a primary instability inside a current sheet formed by an equilibrium magnetic shear field. Nevertheless, the devised eigenvalue problem can also be applied to study other instabilities. For example, it can be applied to explore Kelvin-Helmholtz instability occurring due to the presence of a background shear velocity, or the secondary tearing modes growing on an elongated current sheet developing on the shoulder of a primary reconnection event. We have also formulated and discussed the linear problem for Hall-MHD modes in presence of a finite electron inertia. Finally, we derived a reduced MHD model in toroidal geometry, which simultaneously accounts for the resistivity, the finite inertia of electrons and for the possible presence of an arbitrary density profile.

* Chapter 6 discusses the Electron-MHD regime. First, we derive the incompressible model, which neglects density fluctuations and relativistic effects. Then, we extend it to account for the effects of a strong background guide field and of charge separation effects. After that, we address the consequences of including an electron full pressure tensor (FPT) in the problem. Finally, we linearize the problem for two cases. The first one includes a strong guide field, while, in the second, the guide field is absent. This model is important to explain and understand the results of kinetic simulations, and also to investigate the roles played by different components of the pressure tensor in the onset and the development of magnetic reconnection. Again, due to the complexity of the analytical eigen-value problem which we have formulated, the implementation of a numerical solver, based on the algorithm discussed in Chapters 4-5 and attempt to solve it, is post-poned to future research work.

* Chapter 7 presents the results of the study of tearing modes in thin current sheets in different reconnection regimes, in which more than one non-ideal effect at a time is included. Although, in most of the regimes addressed, analytical estimates for the growth rates (and eigenmodes) had been already provided in literature, it is worth noticing that such estimates had never been systematically verified with a numerical solver, before. The numerical solver developed and discussed in Chapters 4 and 5 has allowed us to verify these analytical estimates but also to provide new insights in the physics of reconnecting instabilities of "tearing-type".

* Chapter 8, which is the last chapter, is devoted to the kinetic study of the linear and nonlinear evolution of some plasma configurations, which are unstable to Weibel-type instabilities, and possibly to reconnecting modes. To this end, we have performed several numerical experiments using the `PIC` code (`SMILEI`) and the semi-Lagrangian code (`VLEM`).

Finally, we end this dissertation with the conclusions, in which we summarize the main results of this thesis and we outline the future works, by also mentioning a few subsidiary research subjects that we have developed during this PhD research but which we have chosen not to discuss explicitly in this dissertation. Several appendices follow, in which all the calculations, performed in this manuscript, have been written.

Résumé

Dans les plasmas, systèmes collectifs gazeux de particules chargées, les lignes magnétiques acquièrent à des échelles macroscopiques ce que l'on peut dire d'une «identité topologique», c'est-à-dire, lorsqu'elles sont noyées dans le plasma, elles évoluent comme entraînées par le flux de particules sans se croiser ni se rompre.

Ceci n'est cependant vrai que dans certains régimes, à savoir aux échelles dites "magnétohydrodynamiques" (MHD). Lorsque certains effets microscopiques, autrement négligeables, deviennent localement importants, cette invariance lagrangienne est perdue. La reconnexion magnétique est le processus physique par lequel cela se produit: les lignes de champ magnétique peuvent ainsi se rompre et se reconnecter en certains points de l'espace. Ce réarrangement de la topologie du champ entraîne la conversion de l'énergie magnétique stockée dans les lignes de champ en énergie cinétique et en énergie thermique.

La reconnexion magnétique est omniprésente dans les plasmas de laboratoire et naturels: dans les premiers, elle peut être responsable de la perte de confinement magnétique, ce qui, par exemple, est préjudiciable à l'atteinte des conditions de combustion dans les expériences de fusion thermonucléaire (par exemple dans les tokamaks comme ITER). Dans ce dernier, il est responsable d'une gamme de phénomènes massivement libérant de l'énergie, allant des éjections de masse coronale et des éruptions solaires sur le Soleil, aux sous-tempêtes magnétiques dans les magnétosphères planétaires (qui peuvent conduire à des aurore boréales spectaculaires mais aussi interférer avec le fonctionnement des appareils électroniques et de communication sur la Terre), aux émissions électromagnétiques ultra-intenses dans les étoiles à neutrons et autres objets astrophysiques magnétisés.

Malgré son occurrence, qui la rend pertinente pour plusieurs sous-domaines de recherche, la reconnexion magnétique est un phénomène complexe car elle implique plusieurs paramètres et conditions physiques, ce qui implique à son tour qu'une étude réaliste de ce phénomène par un modèle unique et complet, n'est pratiquement pas possible.

Ceci est sûrement vrai du point de vue analytique, mais aussi du point de vue numérique, en raison de la nature intrinsèque multi-échelles du phénomène de reconnexion. Cependant, grâce à sa nature multi-échelles, plusieurs modèles complémentaires peuvent être adaptés afin d'analyser différents régimes. Par exemple, lorsque les vitesses globales des ions et des électrons sont égales et peuvent être approximées, à l'ordre principal, avec la vitesse de dérive électromagnétique, plusieurs «modèles magnétohydrdynamiques réduits» peuvent être conçus afin d'étudier la reconnexion magnétique.

Dans ces modèles, les effets microscopiques liés à la fois à la dynamique des ions et des électrons peuvent être inclus comme étant classés petits par rapport à certains paramètres d'expansion. Cependant, même ainsi, l'espace des paramètres reste grand, donc d'autres approximations et modifications physiques peuvent être nécessaires.

Dans certains cas, ces modifications peuvent être motivées par la physique sous-jacente. Dans d'autres cas, ils sont motivés par la nécessité de simplifier analytiquement ou numériquement le problème afin d'avoir un aperçu de la physique fondamentale qui le sous-tend. Ces modèles comprennent le modèle à un fluide, les modèles à deux fluides ou différentes "extensions" du modèle à un fluide dans lequel différentes stratégies sont poursuivies afin d'incorporer les effets cinétiques et deux-fluides. Nous avons en particulier abordé l'étude linéaire des instabilités de reconnexion MHD en présence de plus d'un effet cinétique "non idéal".

Un exemple particulier de modèles «réduits», dans lesquels l'étude de la reconnexion magnétique est en quelque sorte simplifiée, est fourni par ces modèles dans lesquels la dynamique des champs électromagnétiques dans le plasma est couplée à celle des électrons.

Ces modèles, dans lesquels les ions ne forment qu'un fond neutralisant statique, sont justifiés par le grand rapport de masse électron-ion, et par la restriction à des échelles de temps rapides, et des longueurs spatiales petites par rapport à celles des ions: les ions se découplent en effet du champ magnétique à de plus grandes échelles que les électrons, de sorte qu'il existe une gamme d'échelles, dans laquelle les lignes magnétiques sont encore porté par le flux d'électrons, alors qu'elles perdent leur «invariance topologique» par rapport au flux ionique.

Lorsqu'on utilise une description fluide, qui tient compte des échelles de temps rapides et des courtes longueurs spatiales des électrons, alors que les ions sont supposés immobiles, on est alors amené à considérer le soi-disant "électron- `MHD`" (`EMHD`). Un premier modèle, adapté pour décrire la dynamique de reconnexion lorsque des vitesses de phase non relativistes sont considérées, est l'incompressible `EMHD`, qui convient pour explorer la dynamique d'un plasma faiblement magnétisé.

Cependant, lorsque les effets liés à la compressibilité du flux d'électrons deviennent pertinents, une extension de ce modèle pour inclure à la fois le tenseur de pression et le courant de déplacement devient intéressante. L'étude du rôle du tenseur de pression électronique dans les instabilités de reconnexion dans un modèle `EMHD` étendu et non relativiste est un autre sujet abordé dans la présente thèse. Bien qu'une telle étude soit censée être une étape principale vers l'inclusion des effets cinétiques dans des modèles de reconnexion plus complets à deux fluides ou même à cinétique, nous montrerons qu'elle fournit un problème très complexe en soi.

En raison de son interprétation macroscopique comme la violation de l'invariance lagrangienne des lignes magnétiques porté par le flux des particules, la reconnexion magnétique trouve une description naturelle dans les modèles fluide. Cependant, le fait qu'il soit déclenché par des effets microscopiques, conduit à une description tout aussi naturelle au moyen des modèles cinétiques: Vlasov-Maxwell (`VM`). Les modèles cinétiques, bien que plus «complets», sont bien sûr plus complexes, tant d'un point de vue analytique que numérique.

Dans cette thèse, nous avons abordé l'étude numérique de la reconnexion magnétique dans une description cinétique dans laquelle seule la dynamique des électrons est retenue (c'est-à-dire une sorte de «contrepartie cinétique» des modèles fluide `EMHD`).

En particulier, étant donné que de nombreuses autres instabilités peuvent coexister, ou même initier la reconnexion magnétique, nous avons choisi d'étudier l'occurrence de phénomènes de reconnexion qui sont couplés à certaines instabilités faisceau-plasma.

Pour cela, nous avons étudié l'évolution non-linéaire des configurations initiales de plasma dans lesquelles la reconnexion peut coexister avec des instabilités de type Weibel. Ce dernier implique un mécanisme quelque peu opposé à celui impliqué dans la reconnexion magnétique: la conversion de l'énergie thermique et cinétique des particules en énergie électromagnétique, qui conduit à l'amplification des fluctuations magnétiques de fond.

Nous abordons ce problème en résolvant numériquement le (`VM`) en utilisant deux types de modèles numériques. Le premier s'appuie sur la méthode particule-dans-cellule (`PIC`): en particulier, nous avons utilisé `SMILEI`, un code PIC parallèle open-source, relativiste. Le second est le code parallèle `VLEM` qui utilise la méthode semi-lagrangienne pour intégrer numériquement le système relativiste `VM`.

Cette thèse est organisée comme suit:

* Une introduction générale présente le concept de reconnexion magnétique et passe brièvement en revue son histoire.

* Le chapitre 1 traite de la reconnexion magnétique et de ses différentes aspects pertinentes

d'une manière plus formelle: un modèle simplifié est présenté et linéarisé pour obtenir les lois d'échelle.

Nous présentons ainsi le concept de paramètre d'instabilité, qui détermine le spectre des nombres d'onde instables pour un équilibre donné. Le spectre resultant est divisé en trois régimes distincts: une limite de longueur d'onde longue, connue aussi sous le nom de mode kink interne, une limite de longueur d'onde courte connue sous le nom de mode de déchirement (tearing mode) ou constante - ψ limite, et la région de mode à la croissance la plus rapide . Les trois limites distinctes définies ici restent valables pour tous les régimes de reconnexion.

Après, nous discutons ses «limites» par rapport à la longueur d'onde de la perturbation pour les instabilités dans une nappe de courant (current sheet) rectangulaire bidimensionnelle. Enfin, nous passons brièvement en revue la notion de "ideal tearing", récemment introduite dans la littérature.

* Le chapitre 2 est consacré à une revue générale des modèles de plasma utilisés dans l'étude de la reconnexion magnétique. Nous commençons par une discussion générale des modèles cinétiques. Nous abordons ensuite explicitement la dérivation des modèles fluides à partir du système `VM`. Après, on discute en détails le problème de fermeture ("closure problem").

  Enfin, nous terminons le chapitre en fournissant une dérivation détaillée du modèle à un fluide, avec un accent principal sur la loi d'Ohm généralisée.

* Le chapitre 3 traite des méthodes de résolution numérique du système `VM`. On commence par discuter la méthode de Yee pour résoudre les équations de Maxwell. Cette méthode est basée sur une méthode de domaine temporel à différence finie (`FDTD`) pour résoudre les équations de Maxwell en utlisant des schémas de différences finies centrales du second ordre.

  Après, nous passons en revue en profondeur les principes mathématiques nécessaires pour construire un solveur semi-lagrangien parallèle ou un solveur `PIC`, et la façon dont ces deux solveurs sont dérivés.

* Le chapitre 4 est consacré à la discussion de l'eigensolver multi-précision adaptatif que nous avons développé pour résoudre des problèmes généralisés de valeurs propres résultant de l'analyse linéaire de la reconnexion magnétique dans différents régimes.

  La principale difficulté abordée et résolue par ce code est le "ill-conditioning" de matrices de différences finies, qui surviennent en raison de la non-uniformité de la grille sous-jacente.

* Le chapitre 5 est consacré à une discussion détaillée de la dérivation de différents modèles `MHD` réduits à deux champs . Après, en linéarisant un modèle réduite général qui inclut plusieurs effets non idéaux, nous dérivons un problème de valeurs propres généralisé.

  Cela peut être utilisé pour étudier les lois d'échelle de la reconnexion magnétique qui se produit comme une instabilité primaire à l'intérieur d'une feuille de courant formée par un champ de cisaillement magnétique d'équilibre.

Néanmoins, le modèle drivé peut également être appliqué pour étudier d'autres instabilités. Par exemple, il peut être appliqué pour explorer l'instabilité de Kelvin-Helmholtz survenant en raison de la présence d'une vitesse de cisaillement, ou les modes de déchirement secondaires se développant sur une feuille de courant se développant sur l'épaule d'un événement de reconnexion primaire.

Nous avons également formulé et discuté le problème linéaire pour les modes Hall-`MHD` en présence d'inertie électronique finie. Enfin, nous avons dérivé un modèle `MHD` réduit en géométrie toroïdale, qui tient compte simultanément de la résistivité, de l'inertie finie des électrons et de la présence d'un profil de densité arbitraire.

* Le chapitre 6 traite le régime Electron-`MHD`. Tout d'abord, nous dérivons le modèle incompressible, qui néglige les fluctuations de densité et les effets relativistes. Ensuite, nous l'étendons pour tenir compte des effets d'un champ magnatique fort et des effets de séparation de charge. Après, nous abordons les conséquences de l'inclusion le tenseur de pression d'électrons (`FPT`) dans le problème.

  Enfin, nous linéarisons le problème pour deux cas. Le premier comprend un champ fort (guide field), tandis que, dans le second, le champ de guidage est absent. Ce modèle est important pour expliquer et comprendre les résultats des simulations cinétiques, mais aussi pour étudier les rôles joués par les différents composants du tenseur de pression dans l'apparition et le développement de la reconnexion magnétique.

  Encore, en raison de la complexité du problème analytique des valeurs propres que nous avons formulé, l'implémentation d'un solveur numérique, basé sur l'algorithme discuté dans les chapitres 4 -5, est reporté à de futurs travaux de recherche.

* Le chapitre 7 présente les résultats de l'étude des modes de déchirement dans différents régimes de reconnexion, dans lesquels plusieurs effets non idéaux à la fois sont inclus.

  Bien que, dans la plupart des régimes abordés, des estimations analytiques des taux de croissance (et des modes propres) aient déjà été fournies dans la littérature, il convient de noter que ces estimations n'avaient jamais été systématiquement vérifiées par un solveur numérique.

  Le solveur numérique développé et discuté dans les chapitres 4 et 5 nous a permis de vérifier ces estimations analytiques et aussi de fournir de nouvelles connaissances en physique des instabilités de type "tearing".

* Dans le chapitre 8, nous étudions, en utilisant des simulations cinétiques non-linéaires, la compétition de reconnexion magnétique avec des instabilités de type Weibel. Nous présentons des simulations réalisées à l'aide du code `VLEM`, détaillé dans le chapitre 3. De plus, nous montrons également des simulations `PIC` effectuées avec `SMILEI` code [1].

Le code VLEM a été largement utilisé pour étudier l'instabilité CFI, les instabilités de type Weibel [2], et plus récemment, les modes obliques [3]. Dans ce chapitre, nous nous intéressons à l'étude cinétique de l'évolution linéaire et non-linéaire de certaines configurations de plasma, constituées de deux faisceaux contra-propagatifs. Ces configurations sont instables aux instabilités de type Weibel, et éventuellement aux modes de reconnexion.

Nous commençons le chapitre en introduisant les instabilités de type Weibel, puis en présentant les résultats. Nous avons abordé en particulier deux types de problèmes, pour lesquels nous avons réalisé deux séries "d'expériences numériques" liées aux modes de Weibel pour deux faisceaux d'électrons contra-propagatifs.

Dans le premier ensemble de simulations, nous avons considéré l'instabilité CFI de deux faisceaux d'électrons contra-propagatifs ayant une largeur radiale finie [4, 5]. Dans le deuxième ensemble de simulations, nous avons abordé, bien qu'avec une étude préliminaire, la concurrence entre CFI et la reconnexion magnétique dominée par l'anisotropie de pression liée à la dynamique primaire de CFI.

Enfin, nous terminons cette thèse par les conclusions, dans lesquelles nous résumons les principaux résultats de ce travail et nous esquissons les travaux futurs, en mentionnant également quelques sujets de recherche subsidiaires que nous avons développés au cours de cette recherche doctorale mais que nous avons choisi de ne pas discuter explicitement dans cette thèse. Plusieurs annexes suivent, dans lesquelles tous les calculs, effectués dans ce manuscrit, ont été écrits.

Magnetic Reconnection

The constituents of matter in our universe interact with each other through different kinds of forces. For example, gravitational attraction works on clustering the matter and might lead to the formation of stars, whose stability and life cycle depend on the balance between the pressure and the gravitational forces of their ingredients (the star hydrostatic equilibrium). However, 99% of the ordinary matter in the universe is in a plasma state, considered now to be the fourth fundamental state of matter. Irving Langmuir [6] first described it to consist of ions (atoms which lose all, or a part of their electrons) and free electrons. Electromagnetic forces play a key role in the mutual interactions of these particles. Strictly speaking, their motion generates a magnetic field whose energy is stored in the field lines: this is why the notion of "magnetic topology" is so important in magnetized plasmas, in which the configuration of magnetic lines can be related to a "potential magnetic energy".

The known forces feed the dynamics in the universe on different spatial and time scales. Hence, it is entirely plausible to expect in some systems (regions with distinct spatial and time scales) the release of energy from one form into another that drives a new dynamic in the system. For example, a mechanism allowing the conversion of kinetic into magnetic energy is known as Weibel instability [7, 8] and is responsible for the amplification of small amplitude magnetic fluctuations. This amplification occurs due to the conversion of the particle kinetic energy into magnetic energy, while the anisotropy in particle temperature (different temperatures along different velocity directions) is removed.

Another example involves the opposite mechanism: converting magnetic energy into kinetic energy. This process might drive explosive events, such as "magnetospheric storms" in the near-earth environment, flares on stars like our Sun, and other phenomena occurring in the solar winds, disc accretions, supernovae, and magnetars (neutron stars with large magnetic fields). The mechanism behind the conversion from magnetic to kinetic energy (ordered, i.e. beams and currents, or thermal) of charged particles is known as "magnetic reconnection".

This process is essential also on Earth. On the one hand, understanding it is important in order to prevent or control some effects in thermonuclear fusion devices that are detrimental for the magnetic confinement, such as tearing modes and disruptions in tokamaks [9, 10, 11]. Therefore, a satisfactory modelling of reconnecting instability will take us a further step toward harnessing the energy of nuclear fusion and converting it into electric power using thermonuclear devices, such as tokamaks, stellarators, or RFP (reverse field pinch). On the other hand, particles released when this process occurs on the Sun can be dangerous for astronautics, when they come close to the Earth, and, in general, can damage spacecraft. Also, when the solar wind collides with the Earth's magnetic field, the electromagnetic phenomena they induce (e.g., magnetic substorms and particle penetration on the Earth radiation belts [1]) can lead to severe consequences on the

[1] They are also known as Van Allen belts, a zone of energetic charged particles captured by and held around Earth by its magnetic field [12, 13]. Most of these particles are thought to come from solar wind and other particles by cosmic rays.

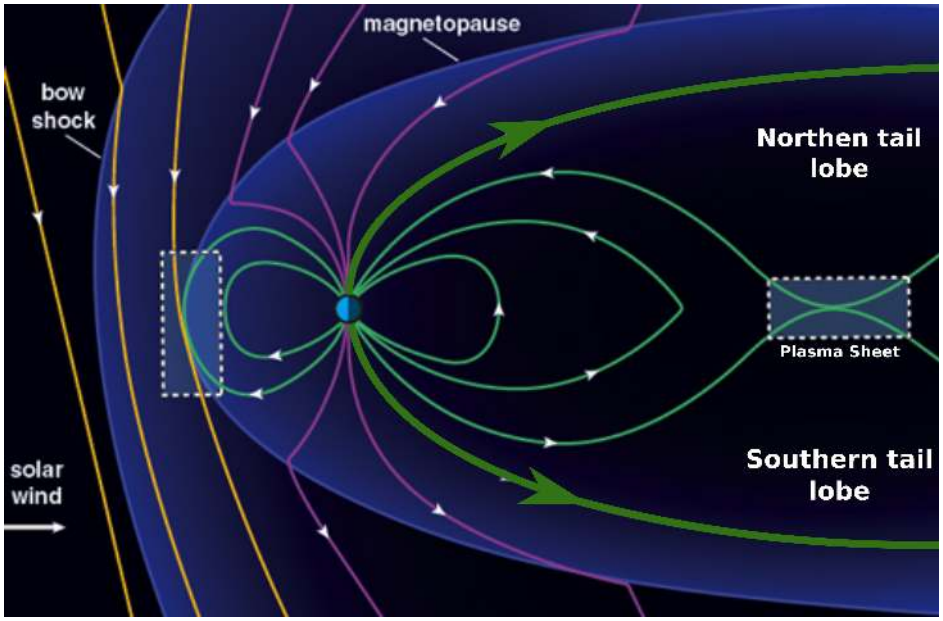

Figure 1: Two reconnection events are shown here. The first is the reconnection between the solar wind's magnetic field (yellow lines) and geomagnetic field lines of the Earth (green lines) on the day-side of the magnetosphere. The second reconnection occurs on the night-side between the open field lines of our planet carried downstream by the solar wind. Credit Burch [14]. The original figure has been adapted.

communication technologies, satellites and also cause disruptions on power plants and generally damage electronic devices on Earth. These consequences, potentially dangerous for the human environment have recently led to the birth of the new sub-discipline of "Space-Weather Research".

Therefore, answering the questions of how magnetic reconnection occurs, and what are the time and spatial scales involved in the process is very important. An intuitive picture of the reconnection phenomenon is when two oppositely oriented magnetic field lines (i.e., a sheared magnetic field) come close in space, inside the plasma: their intersection is permitted only by some microscopic effects which induce a release of magnetic energy, which heats and accelerates charged particles in the surrounding. An example of this phenomenon is shown in Fig.1 for reconnection events in the near-Earth environment. Another example is shown in Fig.2 which displays a reconnecting event on a Sunspot that has been detected by SDO [1] and RHESSI [2] NASA spacecraft. In the reconnection region, an `X`-like structure forms, which is called a null magnetic field point, or `X-` point.

A quantitative answer about the modelling of reconnecting instabilities is however much more complex than what this picture would suggest. To start with, the rates at which magnetic energy is converted into kinetic energy, i.e., the "reconnection rates", by different models fail to account for the experimental evidence. For example, according to some "standard" models, some thousands of years would be required to release the magnetic energy which, during solar flares, is measured to be relieved in a few hundreds of seconds [14].

[1] SDO is a NASA mission which has been observing the Sun since 2010, and it is part of the Living With a Star (LWS) program. [15]

[2] RHESSI is a NASA solar flare observatory designed to image solar flares in energetic photons from soft X-rays (∼3 keV) to gamma rays (up to ∼20 MeV) and to provide high-resolution spectroscopy up to gamma-ray energies.[16]

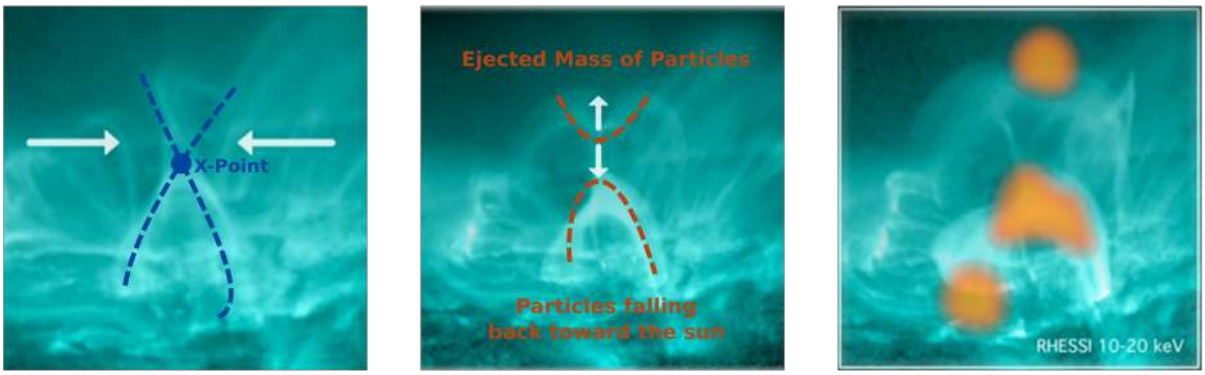

Figure 2: This figure shows a series of images taken by Solar Dynamics Observatory (SDO) on August 17, 2011. Two bundles of field lines move toward each other, meet briefly to form what appears to be an X-point (left), and then reconnect. As a consequence, they release plasma particles in the space, while part of the plasma falls back towards the Sun surface (middle frame). The right frame shows the spectrograms which prove the presence of hot solar materials forming above and below the X-point: this is a signature of magnetic reconnection (yellow spots in the right frame). These spectrograms were collected by Reuven Ramaty High Energy Solar Spectroscopic Imager (RHESSI) [17]. The two figures on the left have been adapted to highlight the formation of X-point and the mass ejections. Credit: NASA.

According to the electrodynamic theory, the magnetic field is a divergence-free vector field, meaning the field lines either "extend to infinity" or close on themselves [18].

In magnetized plasma, although it always follows the Gauss-Maxwell equation, the dynamic of field lines changes considerably. Here, the magnetic field interacts with the charged particles, and the particles of lightest species of the plasma carry the field lines. Unless ion and electron bulk velocities are the same (e.g. when, at large magnetohydrodynamic scales, their fluid motion is given at the leading order by the $\boldsymbol{E}\times\boldsymbol{B}$-drift speed), the field lines are co-moving with electrons.

On the one hand, this co-motion prevents charged particles, when diffusion-like regions don't exist, from moving across field lines (frozen flux theorem -Alfvén theorem). Therefore, we can assign different labels (identities) to distinct field lines which preserve their identity. On the other hand, under some conditions such as the presence of a region with a strong shear magnetic field and a small resistivity, charged particles can slip across field lines along which they were spiralling and in this way they can move between regions of plasma that, before, were not "connected" by a given magnetic line; hence the term magnetic reconnection which was first introduced by Dungey in 1958 [19]. Clearly, this local process makes the magnetic lines lose their "topological identity".

Historically speaking, magnetic reconnection owes its origin to the study of the Sun. We can trace the idea of magnetic reconnection back to the work of Giovanelli which aimed to understand the heating of the solar corona and the tremendous amount of energy associated with solar flares [20, 21, 22]. Giovanelli observed that these solar flares occur in locations above the sunspots where the magnetic field have a complex structure and vanishes at neutral points (X-points). Therefore, he suggested that the high energy particles of the solar flares, occurring near the sunspots are accelerated into the space inside narrow regions where oppositely-directed fields annihilate each other [23]. This destruction of the field was first suggested to be a result of the Ohmic diffusion of field lines when a finite, but very small resistivity of the plasma is taken into

account. However as mentioned before, a simple estimation of the resistive decay of the field lines gives a very long period compared to the observed one[2] (see chapter 1 for details). Later, Hoyle [25] suggested that a similar picture might apply to the Earth, and it can be responsible of polar lights. [3].

In his PhD thesis, Dungey (1950), following a suggestion of his supervisor, Hoyle, studied in details the conditions and the behaviour of the plasma near X-points and concluded that the field lines could be subjected to an instability that leads to the magnetic reconnection and the growth of the current density inside the current layers formed in correspondence of the magnetic shear [26]. However, the term magnetic reconnection was not introduced until 1958 [19, 27, 23]. In his PhD thesis, Dungey also proposed the open model of the Earth's magnetosphere [28, 29], which has been confirmed later by Coleman et al. (1960) after studying the data from Pioneer 5 space mission [30].

In 1958, Sweet [31] suggested that an electric current density concentrated inside the current layers could release energy at an increased rate. He showed that Ohmic diffusion is not the main contribution to the conversion of magnetic energy into kinetic energy. This model was independently proposed by Parker in 1963 [32], and now it is known as the Sweet-Parker model. Although this model leads to a larger dissipation rate of the magnetic energy, once compared to that expected from resistive decay, it remains too slow to account for the observed values in the solar flares (the reconnection rate R_r scales as $R_r \sim S^{-1/2}$, which is much larger than that Ohmic diffusion time, which scales like $\sim S^{-1}$). The derivation of reconnection rate in this model starts from the fluid description of the plasma, in which the dynamic is governed by the steady-state Navier-Stokes equation coupled with Maxwell equations. Therefore, it does not account for the occurrence of spontaneous reconnecting instabilities. The reconnection rate is calculated by balancing the plasma inflow flux toward X- point with its outflow after the onset of the reconnection [4], and the main reason responsible for establishing a diffusion region for the field lines is the finite resistivity of the plasma (see Refs [34, 35, 36, 37] for detailed reviews on the subject).

As already mentioned, reconnection does not concern only the Sun, in the near-space: it is relevant also to the interaction between the solar winds and the planet's geomagnetic field leading to the formation of a magnetotail and a plasma sheet on the night side. This magnetotail is composed of two regions, referred to as the northern and the southern lobes. These two lobes, shown in Fig.1, are separated by a plasma sheet, where the magnetic field becomes weaker, and the charged particles density is larger. The magnetotail represents another "natural laboratory" for the study of magnetic reconnection in the environment in the immediate proximity of our planet (see the review by Ness [38] for early works on this subject). Piddington (1960) [39] was among the first scientists who suggested the formation of this tail on the night-side. But such a tail was considered as a temporary phenomenon since the solar wind was not regarded as a continuous flux of charged particles flowing past the Earth. However, at the same time, Johnson

[2] The scaling of reconnection time in this model is $\tau_{Rec} \sim S$, where S the Lundquist number. S can be very large $10^{11} - 10^{15}$ on the low corona, and 10^{11} in ITER thermonuclear device [24]. Therefore, the estimated time is much order of magnitude larger than the observed one.

[3] According Britannica Encyclopaedia, "aurora, luminous phenomenon of Earth's upper atmosphere that occurs primarily in high latitudes of both hemispheres; auroras in the Northern Hemisphere are called aurora borealis, aurora Polaris, or northern lights, and in the Southern Hemisphere aurora australis, or southern lights. They are caused by the interaction of energetic particles (electrons and protons) of the solar wind with atoms of the upper atmosphere."

[4] In fact, $R_r \sim \frac{u_{in}}{u_{out}} \sim S^{-1/2}$. Taking $S = 10^{10}$, one finds $u_{in} = 10^{-5} u_{out}$, where u_{in} is the inflow velocity of the plasma toward the $X-$point, and u_{out} is the outflow velocity. This value is very small to account for reconnection rate associated with solar flares, coronal mass ejections, and thermonuclear experiments [33].

(1960) [40] studied the effects of a possible steady flow of the solar wind, as it had been indicated by Parker[41, 42], and he suggested that the generated tail won't extend out to the infinity. The extension of this tail was then the subject of extensive studies by many scientists [43, 44, 45] and space missions, including Pioneer 5 [30, 46], Explorer 6 [47, 48], Explorer 10 [49, 50], Explorer 12 [51], and Explorer 14 [52, 53]. These missions contributed significantly to the confirmation of the existence of the magnetotail, whose full structure was later observed by Singer et al. (1965) [54] using the data from the Vela satellite.

Based on these experimental results, two models have been suggested for the magnetotail: one by Dessler and Juday (1965) [55], and another by Axford et al. (1965) [56] which is suitable for studying magnetotail reconnection. In the first model by Dessler and Juday (1965) [55], the merging of the field lines was considered negligible due to the high conductivity of the plasma. However, in the second one, proposed by Axford et al.[56], a plasma sheet will form with merging magnetic field lines at the neutral line, whose existence had been already predicted by Dungey (1961) [28]. This neutral sheet, shown in Fig. 1, is unstable to reconnecting modes, whose existence in a slab geometry has been first studied by Furth, Kileen and Rosenbluth (1963) [57]. In the very long and thin current sheet in the magnetotail, one can expect an almost continuous spectrum of wave-lengths to become potentially unstable. In this case, the fastest-growing mode will dominate the dynamic. The scaling of the fastest growing mode was numerically addressed in a series of papers by Cross and Van Hoven (1971-1973) [58, 59, 60, 61].

In the same period of this great observational and modelling efforts for space and solar plasmas, the study of magnetic reconnection processes attracted attention also for their occurrence in magnetic confinement devices for laboratory plasmas. Here, the occurrence of spontaneous reconnecting instabilities was first devised. The theoretical efforts for establishing a model of spontaneous reconnection started with the seminal work of Furth et al. in 1963 [57], where they first formulated the theory of resistive instabilities: the so-called "tearing modes". They showed that a sheared magnetic field could be unstable to small perturbations, which tear and then reconnect the field lines, as shown in Fig. 3. Hence the name tearing modes. However, in that work, the reconnection was due to the resistivity of the plasma, i.e. to inter-species collisions between charged particles. The restriction to small-wavelength perturbations allowed the authors, with some additional approximations (and the use of a boundary layer theory to solve the involved differential equations), to find an analytical solution to the problem.

In a series of papers, Furth (1963) [62], and Coppi (1964) [63, 64] devised the possibility of these tearing mode to occur in a collisionless plasma, namely because of finite electron inertia. A non-negligible collisionality of the plasma implies that the width of the reconnecting layer [5] is much larger than the mean free path of the charged particles[6], which makes the reconnection resistive and accessible to fluid-like treatments (one-fluid or two-fluid models). However, most astrophysical and space plasmas, and thermonuclear fusion plasmas, as well, are subjected to collisionless reconnection processes. Thus, the width of the reconnecting layer in collisionless plasma is typically dependent on the electron inertia[7], but is still smaller than the mean free path of charged particles, as shown in Fig. 3. The resulting reconnection rates in low-collision plasmas are much faster than their counterparts in the resistive models. Later on, a full kinetic treatment has been considered in further works (Laval et al. (1966) [65] , Coppi et al. (1966)

[5] It is the region inside which the field lines break and reconnect. Inside this layer, the magnetic energy, stored in the field lines, is released as kinetic energy and thermal energy of the particles.

[6] The mean free path is the average distance travelled by a moving particle between successive impacts, which modifies its direction or energy or other particle properties.

[7] The characteristic length that accounts for the importance of the electron inertia is the electron skin depth d_e, defined as the depth in a plasma to which electromagnetic radiation can penetrate.

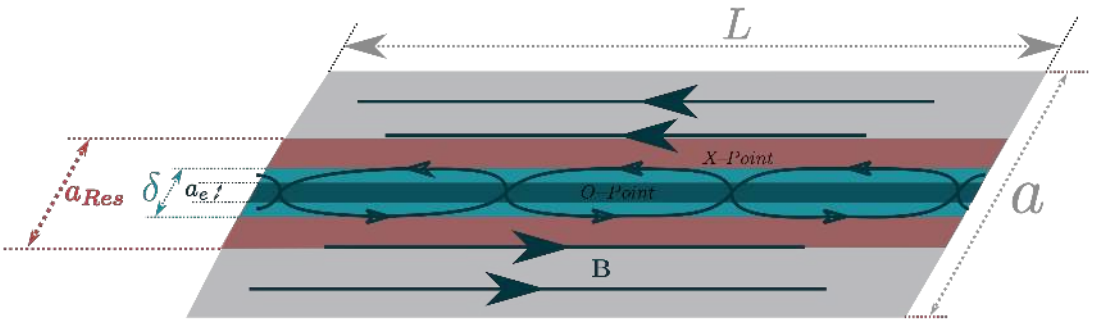

Figure 3: A collisionless current sheet of width a, and length L with shear field $\mathbf{B}$. As shown here, the width of the reconnection layer δ is larger than the electron inertia characteristic length (dubbed here as a_e, which is of the order of the electron skin depth d_e), but is still smaller than the resistive layer's width a_{Res} which is of the order of the mean free path of charged particles. Therefore, we expect the reconnection on this current layer to be due to non-collisional effects (such as electron inertia). The $X-$ and $O-$ points are also shown in the figure.

[66], Drake et al. (1977) [67], and Daughton (1999)[68]).

It is also important to mention that in the sixties of the last century, Petschek [69] proposed another steady model for magnetic reconnection, in which the reconnection rates are larger than those estimated using the Sweet-Parker model. He introduced the idea of slow shocks emerging near the `X`-point, which lead to much faster reconnection rates that can be compatible with the observations. Numerical studies have then been performed to investigate this model. Some of them, like those performed by Ugai et al. (1977) [70, 71] and Sato et al. (1977) [72], included a resistivity with spatial dependence and strong gradient near the $X-$point: this has been shown [73] to be a required ingredient for Petschek's model. Biskamp (1986) [74] on the other hand, investigated numerically both Petscheck and Sweet-Parker models using a constant resistivity, and obtained results consistent with the Sweet-Parker reconnection model, as long as a steady configuration was initially prepared with an aspect ratio not too large (see the reviews by Pontin [75], and Zweibel and Yamada [35] for a more detailed discussion on the subject).

Saying that the study of Biskamp was in the eighties of the last century, we also mention that many reduced models, as we are going to see in details in a later chapter, were formulated to study the reconnection as a `2D` problem. These reduced models started with the seminal works of Strauss (1977) [76, 77], Rosenbluth (1973) [78], and Kadomtsev (1976) [79]. These works relied on the resistivity as a dissipative parameter and neglected the electron inertia and all other effects, such as those resulting from including a finite electron or ion temperatures. These effects were later included in many extended models, such as those derived by Pegoraro and Schep [80, 81, 82, 83], Hazeltine [84] and Porcelli [85] (see the introduction of chapter 5 for a brief review of reduced models).

In the previously discussed models, except when we mentioned the full kinetic description, the plasma is considered as fluid, carried mainly by the ions (one-fluid model -see chapter 2 for detailed review). Some of these models involve effects resulting from considering the dynamics of the two species: electrons and ions, as we are going to see in details in chapter 5. But these models are mainly 2D. Nevertheless, 3D effects can also appear and be very important.

When the width of the reconnecting layer is smaller than the mean free paths of both electrons and ions, it will be reasonable to assume that this width could be comparable to the ion skin

depth value. If the ion Larmor radius [8] is larger than its skin depth, ions can be considered unmagnetized at spatial scales of the order of their skin depth. Therefore, in a reconnecting region with a width of that order, or smaller, ions follow their inertia.

This, on the one hand, means that the ions' dynamic decouples from that of electrons. On the other hand, the electrons remain in a co-motion with the magnetic field until they reach the X-point (we prove this in section 2.4.4). Sonnerup (1979) [86] was probably the first who recognized the importance of this motion decoupling. As the electron continue their flow toward the X-point, an opposite current density appears and, hence, generates a magnetic field perpendicular to the reconnection plane, which introduces 3D effects and might considerably change the dynamic of the reconnection process (see section 5.5 for details).

Another regime of relevant importance to the turbulence and plasma-laser physics where the fast collisionless reconnection is expected to occur is the so-called electron magnetohydrodynamic (EMHD) [87]. This model is adequate to study magnetic reconnection events in high-frequency regimes where the usual magnetohydrodynamic is no longer valid [88, 89, 90]. Electron magnetohydrodynamic can be employed to investigate phenomena occurring on a faster time, and shorter length scales compared to those of ions. At these scales, the ions are considered immobile and form a neutralizing background. Kingsep et al. [91] first proposed this model and showed that it arises when the Hall term becomes larger than the convective term in the generalized Ohm law (see chapter 6). Later, Bulanov et al. [89], Ebra and Pegoraro [92], Attico, Pegoraro and Califano [93] employed this model to obtain the linear growth rates of tearing-type modes, both for resistive and collisionless (i.e., inertia-driven) magnetic reconnection. EMHD reconnection clearly occurs with much larger growth rates than Alfvénic reconnection at the MHD scale, since whistler waves propagate the energy in EMHD.

It must be noted that a transition of reconnection from a regime dominated by Alfvén waves to a regime dominated by Hall-term can also spontaneously occur: it is the so-called "whistler mediated reconnection" [94]. While this regime has been numerically confirmed by several studies (see Biskamp [95] for a review on the subject) and has become one of the most accredited candidate for the "fast reconnection" in space plasmas (cf. the "GEM challenge" [96]), it should be noted that the analytical estimates it relies upon are essentially based on heuristic estimates, differently from those of tearing modes in reduced MHD or EMHD.

Magnetic reconnection also plays a fundamental role in plasma turbulence, where it is thought to provide one of the chief mechanisms for the "heating" of magnetized plasmas. On the one hand, reconnection can be initiated by the turbulent dynamics of the plasma, which might lead to the formation of current sheets that could be unstable to the reconnecting modes [97, 98, 99]. On the other hand, reconnection itself will have effects on the dynamic of turbulence [100, 101] where it has been suggested that the dissipation of magnetic energy through the reconnection process plays a crucial role in heating and accelerating the particles, and therefore feeding the dynamics on kinetic scales (see the review by Matthaeus and Velli [102], and Schekochihin [103]).

After this brief survey, it is not surprising to note that magnetic reconnection is nowadays actively studied in dedicated laboratory experiments (see the review by Yamada et al. [36]) and has been the main purpose of spacecraft missions such as MMS (Magnetospheric Multiscale [9]) launched on 13 March 2015, with the primary aim to study the microphysics of magnetic reconnection, energetic particle acceleration, and turbulence. Also, Parker Solar Probe, which is

[8] Larmor radius or gyroradius is the radius of the circular motion of the charged particle in the presence of a magnetic filed B_0. It is given by $\rho_s = \frac{m_s v}{q_s B_0}$, where m_s and q_s are the mass and the charge of the particle, while v is its velocity.

[9] You can find an overview about the mission on its official website: *https://www.nasa.gov/mission_pages/mms/overview/index.html*

another NASA mission, was launched on 12 August 2018, aiming to find answers to the question of how energy and heat move through the solar corona and to explore the mechanisms behind the extremely effective heating of the solar wind, whose raise in temperature from about $6000K$ on the chromosphere to about 10^6K just at one solar radius above it, is believed to be mostly due to turbulent reconnection processes.

Finally, magnetic reconnection is thought to be the main mechanism behind extreme electromagnetic emissions in astrophysical objects (such as neutron stars), thanks to the acceleration it can provide to charged particles. In these environments, it can occur at "extreme" regimes, in which also relativistic effects are important. Similar processes are nowadays investigated, although, of course, in a re-scaled setup, in the so-called "laboratory astrophysics" experiments: several laser facilities such as the Extreme Light Infrastructure (ELI, $https://www.eli-beams.eu$) or the laser facility APOLLON ($https://apollonlaserfacility.cnrs.fr$) have these kinds of studies among their goals. In laser-plasma interactions, magnetic reconnection often occurs secondary to Weibel-type instabilities or other dynamic effects that first generate and-or amplify magnetic perturbations.

Investigating the interplay between certain beam-plasma instabilities and magnetic reconnection, on the one hand, and spontaneous reconnecting instabilities in magnetized plasmas, with a special focus on tearing-type modes occurring in tokamaks and possibly in turbulent, magnetized plasmas such as the solar wind, is one of the main subjects of this dissertation.

1

Introduction to Magnetic Reconnection

Contents

1.1 Introduction

In this chapter, we are going to introduce the basic mechanisms behind magnetic reconnection phenomenon using a simplified picture. To do so, we will look at the problem in the one fluid description, in which the plasma dynamics coincide, at the leading order in the electron-to-ion mass ratio, with that of ions. This model accounts for the dynamics of electrons through Ohm law which describes the evolution of the current density. In the context of a perfectly conducting plasma (expressed in terms of ideal Ohm law), the topology of field lines remains conserved with time. Therefore phenomena, that violate this conservation, such as reconnection, are not allowed. We call this model ideal `MHD`. Hence, to explain such phenomena, new effects, that allow for the breaking of the field topology, are incorporated into the "ideal" Ohm law, which is therefore dubbed "generalized Ohm's law". We start this chapter by introducing, without derivation (which will be detailed in section 2.4.3), Ohm law and its ideal version. Then, we illustrate the implication of the latter for the field topology. Finally, we present a simple model of magnetic reconnection, based on the one-fluid description.

As mentioned in the introduction, magnetic reconnection is a phenomenon in which the topology of field lines changes and the energy stored in it converts into thermal and kinetic energy. Therefore, to describe reconnection with a simplified picture, we need an equation that describes the dynamics of the magnetic field: to this purpose, Faraday equation can be combined

with (the curl of) Ohm's law. These equations read,

$$mn\frac{\partial \mathbf{u}}{\partial t} + mn\mathbf{u}\cdot\nabla\mathbf{u} = -\nabla p + \mathbf{J}\times\mathbf{B}, \tag{1.1}$$

$$\frac{\partial \mathbf{B}}{\partial t} = -\nabla\times\mathbf{E}, \quad \mathbf{J} = \frac{1}{\mu_0}\nabla\times\mathbf{B}, \tag{1.2}$$

$$\mathbf{E} + \mathbf{u}\times\mathbf{B} = \eta\mathbf{J}, \tag{1.3}$$

where η is the resistivity of the plasma, $\mathbf{u}$ its velocity, $\mathbf{J}$ is the current density, n is the plasma density, p is the scalar pressure, $\mathbf{E}$ and $\mathbf{B}$ are the electric and magnetic fields, respectively. The applicability of these equations is, of course, limited to a plasma in which resistivity is the dominant non-ideal effect, the current displacement in Ampere's law can be neglected (restriction to non-relativistic regimes), and the flow is essentially incompressible (we have neglected the continuity equation for the density evolution).

1.2 Consequences of Ideal Ohm Law on the Magnetic Field Topology

The main consequence of the ideal Ohm law is that the plasma and the field lines exist in an on-going co-motion, and therefore charged particles cannot jump between different magnetic lines. This co-motion, in turn, means that the field lines, in the context of ideal MHD, retain their identities for all times. Because of effects such as those resulting from including the plasma resistivity, break this identity preserving, and it is no longer possible to assign distinct identities to different lines. In simple words, particles can slip across different lines.

1.2.1 Frozen Flux Theorem

In the ideal `MHD` regime, the magnetic field lines behave as if they move with the plasma (*Alfvén flux theorem* [104]). We are going to prove that in this section. Consider a surface $\mathcal{S}$ enclosed by a curve $\mathcal{C}$, as shown in Fig.1.1, whose points move with the local fluid velocity of the plasma ($\mathbf{u}$). Then the magnetic flux through $\mathcal{S}$ reads

$$\Psi = \int_{\mathcal{S}} \mathbf{B}\cdot d\mathcal{S}, \tag{1.4}$$

As can be shown in the Fig.1.1, the variation of the magnetic flux with time is composed of two parts. The first contribution comes from the time dependence of the magnetic field, while the second is a result of the magnetic flux swept out by the curve $\mathcal{C}$ due to its motion with the plasma. Therefore,

$$\frac{d\Psi}{dt} = \int_{\mathcal{S}} \frac{\partial \mathbf{B}}{\partial t}\cdot d\mathcal{S} + \oint_{\mathcal{C}} \mathbf{B}\cdot\mathbf{u}\times d\mathbf{l} = -\int_{\mathcal{S}} \nabla\times\mathbf{E}\cdot d\mathcal{S} - \oint_{\mathcal{C}} \mathbf{u}\times\mathbf{B}\cdot d\mathbf{l} = -\oint_{\mathcal{C}} (\mathbf{E}+\mathbf{u}\times\mathbf{B})\cdot d\mathbf{l}, \tag{1.5}$$

In the ideal MHD limit,

$$\mathbf{E} + \mathbf{u}\times\mathbf{B} = 0. \tag{1.6}$$

Eq.(1.5) vanishes. Hence, the frozen flux theorem follows, when infinitesimally thin flux tubes are considered [104, 33]:

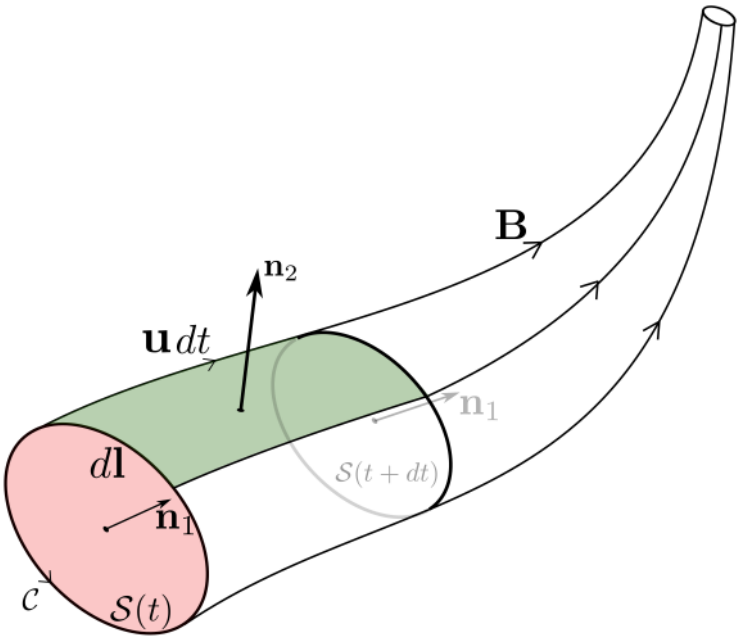

Figure 1.1: A moving surface ($\mathcal{S}$) with plasma velocity $\mathbf{u}$. The curve $\mathcal{C}$ which encloses $\mathcal{S}$ sweeps out a lateral area $d\mathbf{a} = dt\mathbf{u} \times \mathbf{dl}$. $\mathcal{S}$ becomes smaller as the field lines compressed following the frozen-in condition (constant magnetic flux).

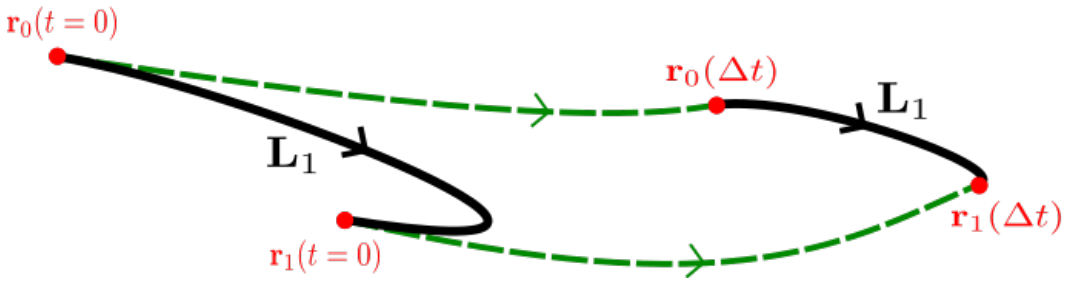

Figure 1.2: Integrating Eq.(1.7) at time $t = 0$ starting from $\mathbf{r}_0(t = 0)$ for distance l maps this point to $\mathbf{r}_1(t = 0)$ (field line $\mathbf{L}_1$ to the left). The plasma advects these points, with velocity $\mathbf{u}$, to the new positions $\mathbf{r}_0(\Delta t)$ and $\mathbf{r}_1(\Delta t)$, respectively. However, if we again integrate Eq.(1.7) starting from $\mathbf{r}_0(\Delta t)$, the resulting line must also pass through $\mathbf{r}_1(\Delta t)$, which means that $\mathbf{L}_1$ retains its identity.

In ideal MHD, the magnetic flux through any surface element dragged by the fluid remains constant in time.

It is the violation of this principle which allows the plasma to flow across the magnetic field lines due to diffusive effects emerging from some terms in generalized Ohm law. This process changes the topology of field lines and permits converting the magnetic energy stored in field topology into kinetic and thermal energy (magnetic reconnection).

We said before that in ideal MHD we could assign different labels (identities) to separate lines of the field, and these distinct labels will be preserved for all times, which can be understood by looking at the equation of field lines which are tangent to the magnetic field. Consequently one has $\mathbf{B} \times d\mathbf{l} = 0$, where $d\mathbf{l}$ is the element length. Hence, the parametrized equations of field line are given by,

$$\frac{dx}{B_x} = \frac{dy}{B_y} = \frac{dz}{B_z}, \tag{1.7}$$

If we integrate, starting from a point $\mathbf{r}_0(t = 0)$, the previous equation for distance l, one ends at the point $\mathbf{r}_1(t = 0)$. After time Δt and according to frozen flux theorem, these two points move with plasma velocity $\mathbf{u}$, and each of them ends on the new position $\mathbf{r}_0(\Delta t)$, and $\mathbf{r}_1(\Delta t)$. The identity conservation of magnetic field lines implies that if after a time Δt, we again integrate Eq.(1.7), starting from $\mathbf{r}_0(\Delta t)$, the field lines must pass through the fluid element at $\mathbf{r}_1(\Delta t)$, which means that the field lines only moved and swirled around but kept on being distinct one from another (they might be stretched or compressed, but a line with label $\mathbf{L}_1$ remains with the same label at any time in ideal MHD as shown in Fig.1.2).

The latter statement can be mathematically expressed by another topological theorem, which is sometimes referred to as "linking theorem", and which we do not discuss further, here (see Lundquist (1951) [105], Newcomb (1958) [106], Pegoraro et al. (2004) [107]). It can be however noted that, from a more formal point of view, the rewriting of ideal Ohm's law combined with Faraday's equation by means of a well-known vector identity,

$$\frac{\partial}{\partial t}\boldsymbol{B} + \boldsymbol{u} \cdot \boldsymbol{\nabla B} - \boldsymbol{B} \cdot \boldsymbol{\nabla u} + \boldsymbol{B\nabla} \cdot \boldsymbol{u} = 0, \tag{1.8}$$

is sufficient by itself to state that magnetic lines are dragged by the fluid flow, when it is incompressible (or that $\boldsymbol{B}/n$ is dragged by the fluid flow, when $\boldsymbol{\nabla} \cdot \boldsymbol{u} \neq 0$ - see Del Sarto et al.(2006) [108]). In these cases Eq.(1.8) expresses indeed the "Lie-derivative[10]" of the corresponding vector field $\boldsymbol{B}$ or $\boldsymbol{B}/n$ with respect to the velocity field $\boldsymbol{u}$. This is the same property which is behind the conservation of vorticity lines in classical hydrodynamics, which has been extensively discussed in Ref.[109].

1.2.2 Magnetic Helicity

A magnetized plasma, when considered as a conducting fluid described by the MHD model, exhibits a wide range of complicated 3D structures depending on its configuration, boundary conditions, and forces driving its dynamics. Therefore, the existence of a global quantity which is conserved at the MHD scales and that accounts for the complexity of the plasma structure is useful to both model and understand several nonlinear phenomena: it is the case of the "magnetic helicity", which we discuss in this section.

[10] Lie derivative is a measure of the change of a field (scalar field, vector field, or in general a tensor field) along the flow defined by another field. The Lie derivative of vector field $\mathbf{B}$ with respect to $\mathbf{u}$ is $\mathcal{L}_{\mathbf{u}}\mathbf{B} = [\mathbf{u}, \mathbf{B}] = \mathbf{u} \cdot \nabla\mathbf{B} - \mathbf{B} \cdot \nabla\mathbf{u}$.

Electric and magnetic fields are essential components to be studied in plasma physics. The Maxwell equations govern the evolution and dynamics of these quantities. As shown in the previous section, the plasma and the magnetic field lines are co-moving together, and hence a charged particle cannot jump between different field lines when the plasma is perfectly conducting. Also, Maxwell-Thomson equation (i.e., $\boldsymbol{\nabla} \cdot \boldsymbol{B} = 0$), implying a divergence-free magnetic field, says that magnetic induction lines can either fill the space ergodically, or they can close on themselves after a finite number of twisting and bending and wrapping around one another, inside a finite volume (e.g., tokamaks, or stellarators under conditions of magnetic stability). Therefore, one may suggest using quantities that account for the topology of field lines and measure its structural complexity. Here comes the idea of the magnetic helicity (a second-order topological invariant which encompasses the topological features of the field lines) and of higher-order topological invariants. As we are going to see next, the magnetic helicity is conserved in ideal MHD, and this is almost true when localized magnetic reconnection occurs. However, while the reconnection event destroys all other topological invariants, magnetic helicity can survive as a sort of "adiabatic invariant", as shown by Taylor in his model of "MHD relaxation" ([110, 111]). Elsasser was the first who observed that the quantity $(\mathbf{A} \cdot \mathbf{B})$ is, like the field lines, frozen into the plasma in ideal MHD [112]. Though in 1958, Woltjer [113] considered an integral quantity (henceforth named Woltjer's invariant, and then magnetic helicity [114])

$$K_w = \int_V \mathbf{A} \cdot \mathbf{B} dV, \tag{1.9}$$

and he proved that, under a suitable choice of the gauge of the vector potential $\mathbf{A}$, this quantity is conserved in ideal MHD. Its topological meaning, as a measure of the linkage between field lines that fill the volume V, was first introduced by Moffatt in 1969 [114, 115, 116] (see also [117]).

The interpretation of the magnetic helicity naturally leads us to relate this concept to the Gauss linking number [118], which in turns makes that interpretation as a measure of the topological complexities evident and easy to understand. Hence,

Magnetic helicity is a second-order topological invariant, associated with a volume of magnetized plasma, measuring the total linkage (complexity of the field topology) of the flux tubes.

Before going further on discussing the conservation of this quantity in ideal MHD, it is tempting to shed some light on the concept of linking number. Gauss first introduced this notion in a half-page paper [118] (see Fig.1.3) where he suggested a formula to count the number of times a closed curve ($\mathbf{r_1}$) encircles a second curve ($\mathbf{r_2}$) as shown in the Fig.(1.4). However, Gauss never provided or mentioned a derivation of that formula. Nevertheless, it always has been thought that his work on terrestrial magnetism [120] inspired the formula [121, 122]. This concept was later rediscovered by Maxwell [119], who was undoubtedly unaware of the work of Gauss, to other works of whom he devoted many sections in his treatise [123].

The Gauss linking number between two curves, as shown in Fig.(1.4), and defined in Fig.(1.3), can be easily cast in the following form [124]

$$L_{g,12} = \frac{1}{4\pi} \int_0^{2\pi} \int_0^{2\pi} \frac{d\mathbf{r}_1(\sigma)}{d\sigma} \times \frac{\mathbf{r}_0}{r_0^3} \cdot \frac{d\mathbf{r}_2(\tau)}{d\tau} d\sigma d\tau, \tag{1.10}$$

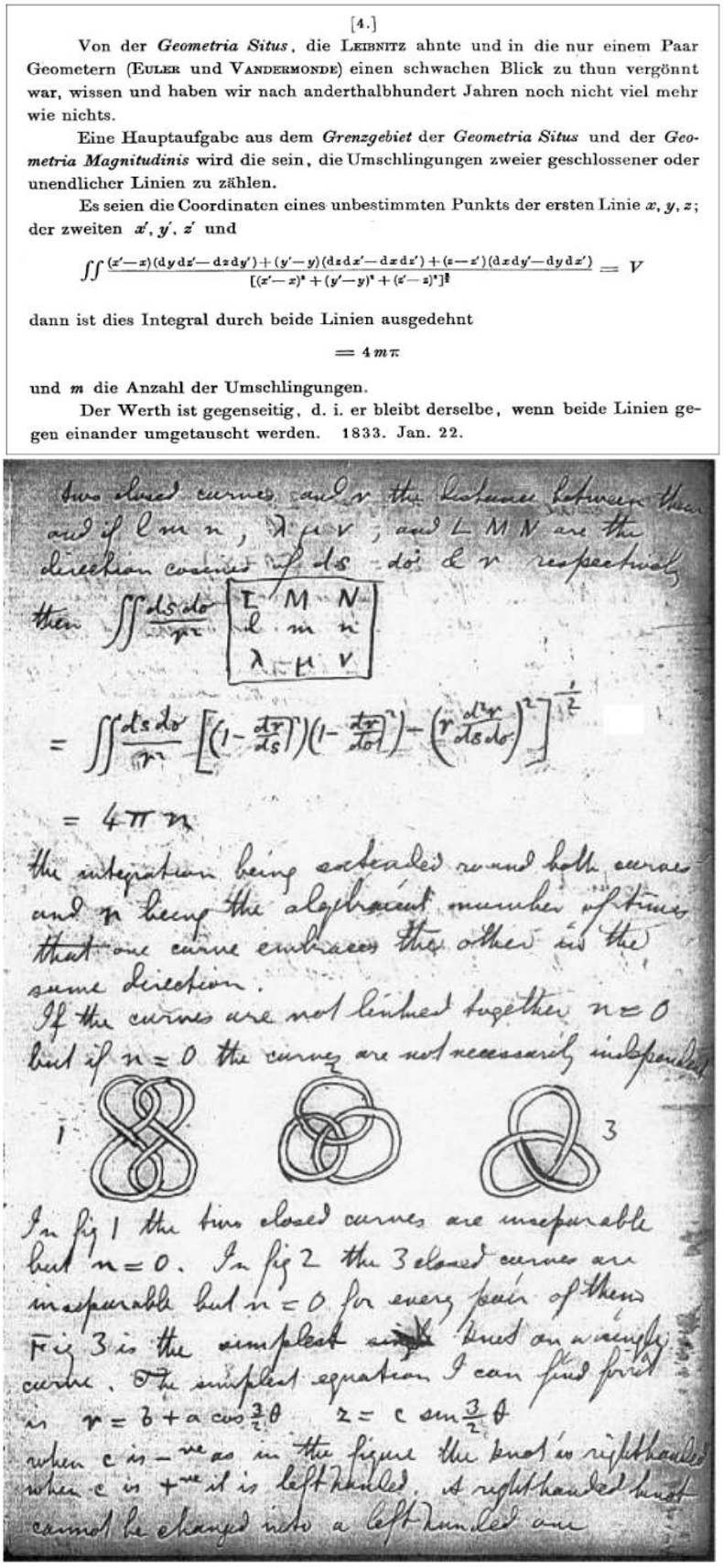

[4.]

Von der *Geometria Situs*, die LEIBNITZ ahnte und in die nur einem Paar Geometern (EULER und VANDERMONDE) einen schwachen Blick zu thun vergönnt war, wissen und haben wir nach anderthalbhundert Jahren noch nicht viel mehr wie nichts.

Eine Hauptaufgabe aus dem *Grenzgebiet* der *Geometria Situs* und der *Geometria Magnitudinis* wird die sein, die Umschlingungen zweier geschlossener oder unendlicher Linien zu zählen.

Es seien die Coordinaten eines unbestimmten Punkts der ersten Linie x, y, z; der zweiten x', y', z' und

$$\iint \frac{(x'-x)(dy\,dz'-dz\,dy')+(y'-y)(dz\,dx'-dx\,dz')+(z-z')(dx\,dy'-dy\,dx')}{[(x'-x)^2+(y'-y)^2+(z'-z)^2]^{\frac{3}{2}}} = V$$

dann ist dies Integral durch beide Linien ausgedehnt

$$= 4m\pi$$

und m die Anzahl der Umschlingungen.

Der Werth ist gegenseitig, d. i. er bleibt derselbe, wenn beide Linien gegen einander umgetauscht werden. 1833. Jan. 22.

two closed curves, and r the distance between them and if l m n, λ μ ν, and L M N are the direction cosines of ds, dσ & r respectively

then $\iint \frac{ds\,d\sigma}{r^2} \begin{vmatrix} L & M & N \\ l & m & n \\ \lambda & \mu & \nu \end{vmatrix}$

$= \iint \frac{ds\,d\sigma}{r^2} \left[\left(1-\frac{dx}{ds}\right)\left(1-\frac{dx}{d\sigma}\right)-\left(r\frac{d^2r}{ds\,d\sigma}\right)^2\right]^{\frac{1}{2}}$

$= 4\pi n$

the integration being extended round both curves and n being the algebraical number of times that one curve embraces the other in the same direction.

If the curves are not linked together $n = 0$ but if $n = 0$ the curves are not necessarily independent

1 3

In fig 1 the two closed curves are inseparable but $n = 0$. In fig 2 the 3 closed curves are inseparable but $n = 0$ for every pair of them Fig 3 is the simplest knot on a cylindric curve. The simplest equation I can find for it is $r = b + a\cos\frac{3}{2}\theta \quad z = c\sin\frac{3}{2}\theta$

when c is −ve as in the figure the knot is right handed when c is +ve it is left handed. A right handed knot cannot be changed into a left handed one

Figure 1.3: Excerpt from the "Nachlass zur Electrodynamik" (top) [118], published in the Gauss'Werke (1867). In this note Gauss introduces the concept of linking number. In the bottom frame, a letter by Maxwell sent to Tait, dated December 4, 1867, in which he calculates the linking number [119].

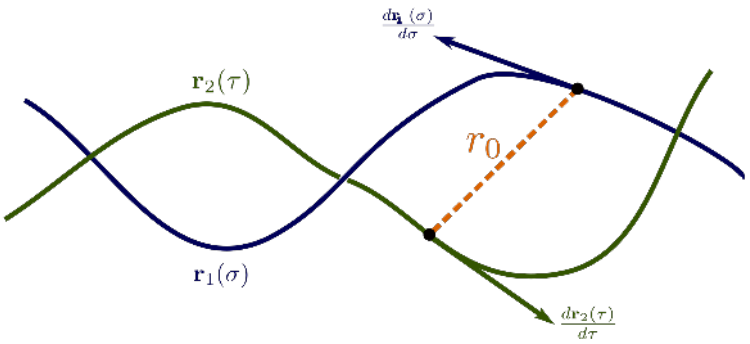

Figure 1.4: Two interlocked curves.

where $\mathbf{r}_1$ and $\mathbf{r}_2$ represent the curves parameterized by σ and τ, respectively. $\mathbf{r}_0 = \mathbf{r}_2 - \mathbf{r}_1$, and $r_0 = |\mathbf{r}_0|$. Now, given two flux tubes, that enclose the magnetic fields $\mathbf{B}_1$ and $\mathbf{B}_2$, the vector potential $\mathbf{A}$, at a point $\mathbf{r}$, can be calculated using Biot-Savart law. That is,

$$\mathbf{A}(\mathbf{r}) = \frac{1}{4\pi}\int_V \mathbf{B}(\mathbf{r}') \times \frac{\mathbf{r}-\mathbf{r}'}{|\mathbf{r}-\mathbf{r}'|^3} dV, \tag{1.11}$$

where V is the volume of all the space. Therefore, the magnetic helicity of the total field ($\mathbf{B} = \mathbf{B}_1 + \mathbf{B}_2$) becomes

$$H(\mathbf{B}) = \frac{2}{4\pi}\int_{V_1}\int_{V_2} \mathbf{B}(\mathbf{r}_2) \times \frac{\mathbf{r}-\mathbf{r}'}{|\mathbf{r}-\mathbf{r}'|^3} \cdot \mathbf{B}(\mathbf{r}_1) dV_1 dV_2, \tag{1.12}$$

where V_1 and V_2 are the volume of the two flux tubes, respectively. Now, knowing that $\Phi_i = \mathbf{B}\cdot\mathbf{n}_i S_i$, where Φ_i is the flux associated with i^{th} tube, we identify S_i as the surface crossed by $\boldsymbol{B}$ and $\mathbf{n}_i$ as the normal to S_i. After substituting this relationship into the previous equation, one easily finds,

$$H(\mathbf{B}) = 2\Phi_1\Phi_2 \frac{1}{4\pi}\int_0^{2\pi}\int_0^{2\pi} \frac{d\mathbf{r}_1(\sigma)}{d\sigma} \times \frac{\mathbf{r}-\mathbf{r}'}{|\mathbf{r}-\mathbf{r}'|^3} \cdot \frac{d\mathbf{r}_2(\tau)}{d\tau} d\sigma d\tau = 2\Phi_1\Phi_2 L_{g,12}, \tag{1.13}$$

This is the results obtained by Moffatt, and later generalized by Arnold to include open field lines [125, 126]. In our previous discussion, we defined the magnetic helicity using an integral form that depends on the vector potential and on the magnetic field. We also made an additional assumption: the flux tubes are closed. Since the vector potential depends on the choice of the gauge, a well-defined magnetic helicity must be gauge invariant. To explain this idea, let us perform the transformation $\mathbf{A}' = \mathbf{A} + \nabla\chi$, where χ is a scalar potential. Substituting this into Eq.(1.9), one finds

$$H'(\mathbf{B}) = \int_V \mathbf{A}'\cdot\mathbf{B} dV = H(\mathbf{B}) + \oiint_S \chi \mathbf{B}\cdot\mathbf{n} dS, \tag{1.14}$$

where S is the surface that encloses the volume of the plasma V. Hence, it is evident that a well-defined helicity implies a vanishing surface integral. The condition $\mathbf{B}\cdot\mathbf{n} = 0$ is relevant to many practical cases, such as plasma with perfectly conducting boundaries or periodic boundary conditions. Nevertheless, it does not work for other cases with complicated geometries and open field lines. Therefore, a gauge-invariant definition is preferable. A general definition of

a *"generalized magnetic helicity"* which is independent of the gauge was proposed in 1984 (see Berger and Field [127], Jensen and Chu [128], Finn and Antonsen [129], and Berger [124]), which reads

$$H(\mathbf{B}) = \int_V (\mathbf{A} + \mathbf{A}_0) \cdot (\mathbf{B} - \mathbf{B}_0) dV, \tag{1.15}$$

where $\mathbf{B}_0 = \nabla \times \mathbf{A}_0$ is a reference field to be defined so that it allows a well-defined helicity (performing the same analysis in Eq.(1.14), we find that if we choose $\mathbf{B}_0$ such that $\mathbf{B}\cdot\mathbf{n} = \mathbf{B}_0\cdot\mathbf{n}$, the helicity will be gauge invariant [33]). Now, taking the time derivative of Eq.(1.15), one finds

$$\frac{dH}{dt} = -2\int_V (\mathbf{E}\cdot\mathbf{B} - \mathbf{E}_0\cdot\mathbf{B}_0) dV, \tag{1.16}$$

where $\mathbf{E}_0 = -\frac{\partial \mathbf{A}_0}{\partial t}$. Therefore, if $\mathbf{E} = -\mathbf{u}\times\mathbf{B}$ and $\mathbf{E}_0 = \mathbf{u}\times\mathbf{B}_0$, as it is the case in ideal MHD, the generalized magnetic helicity is conserved.

After understanding the geometrical interpretation of the helicity, one critical question arises: what are the effects of reconnection, initiated in some diffusive regions, on the magnetic helicity? In the resistive MHD regime, the plasma has non-vanishing resistivity leading, when some conditions are met to the development of reconnection regions inside of which the topology of field lines changes. This question was first addressed by Taylor [110] , who argued that the turbulent environment leads to magnetic reconnection events in localised regions, and their overall effect on helicity is negligible. Then in 1984, Berger [130] derived a condition which sets an upper limit to the magnetic helicity dissipation, which reads

$$\left|\frac{\Delta H}{H}\right| \leq \sqrt{\frac{\Delta t}{\tau_d}}, \tag{1.17}$$

where $\tau_d = \frac{L^2}{\eta}$ is the diffusivity time, and Δt is the estimated duration of reconnection. This relation shows that, indeed, in a typical reconnection scenario ($\Delta t \ll \tau_d$), the change of magnetic helicity is negligible.

Lastly, We mention the fact that the magnetic helicity fails to detect all forms of interlocking between field lines (e.g. Whitehead link [131, 132] and Borromean rings [133, 134]), so higher-order topological invariants, sensitive to these forms of linkage, can be defined. When a small non-vanishing resistivity is included in the model, reconnection destroys all higher-order topological invariants while only creates fluctuations in the helicity, which remains almost conserved (see Ruzmaikin and Akhmetiev [135] and references therein for an excellent and detailed study of topological invariants and the effect of reconnections). In simple words,

Magnetic helicity is almost conserved during reconnection events, while these events destroy all higher-order invariants. In ideal MHD, magnetic helicity is precisely conserved.

1.3 Magnetic Reconnection: A Simple Description

Magnetic reconnection is a process leading to the breaking and reconnecting of magnetic field lines. As a result of this change and re-arrangement of the topology, magnetic energy is converted to kinetic energy, thermal energy, and particle acceleration. This event involves oppositely-directed field lines that reconnect in a narrow region (hereafter, *"inner (reconnecting) layer"*) localized inside a region defined by an equilibrium profile (hereafter, the *"current sheet"*). The

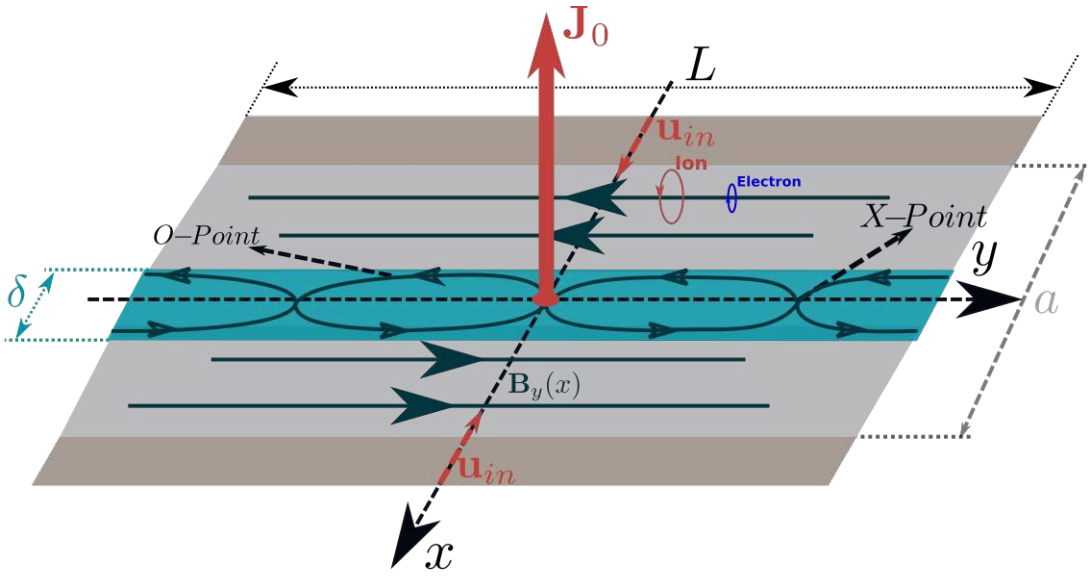

Figure 1.5: Two oppositely-directed magnetic field plasmas flowing, due to some external mechanisms, toward a narrow region (current sheet) inside which the field lines break and reconnect at points with null magnetic fields (X-point).

current sheet, bounded by an ideal MHD *"outer region"*, is characterized by its aspect ratio (the ratio between its length and width $\epsilon_a = L/a$). As shown in Fig.(1.5), two plasma configurations, with different directions, are pushed together with some external means with velocity u_{in}, and therefore a current sheet is formed. The dynamics behind the formation of these current sheets can be due to some external forcing mechanisms, like those which are seen in the evolution of solar flares [20, 136, 32, 137], of coronal mass ejections (CMEs), in the interaction between the solar winds and the earth's magnetosphere, and in the so-called "Ellerman bombs" [138, 139], and in the process of star formation [140, 141, 142, 143]. It also can naturally occur in turbulent plasmas [97, 144], or as self-organization process in current-carrying fusion plasmas. This is observed in tearing and kink modes and in disruption processes in tokamaks [9, 10, 11, 145, 146], and in relaxation processes in reversed field pinch (RFP) and spheromaks [111, 147].

To understand the magnetic reconnection, let us look at the configuration in Fig.(1.5). In this figure, two plasma fluid elements, embedded in oppositely directed magnetic fields, approach each other inside the current sheet. In this picture, we consider a 2D configuration where x is the variable of shear of the magnetic field. The inhomogeneous component of the magnetic field ($B_s = B_y(x)$) is known as the shear field, which becomes zero at the central line (neutral line). We know from the frozen flux theorem that in ideal MHD, the plasma and field lines are co-moving together, which is the case in the ideal MHD region in the figure. However, thanks to the local non-negligibility of non-ideal effects such as resistivity, when two field lines with opposite directions cross each other due to some perturbation, an intersection point with a null magnetic field (X-point) will be generated, and an island is formed ($O-$point). This implies that the magnetic energy does not simply disappear, but is converted into another form of energy. As we are going to see next, this breaking and reconnection of field lines is not allowed in ideal MHD because it leads to unphysical singularities (singular surface with infinite out-flow velocity). Therefore, to resolve this singularity, the ideal MHD model (strictly speaking, its ideal Ohm equation) must be modified to allow the generation of an $x-$ component of the field,

which in turn will let the particles to slip across different lines and thus have a well-defined $y-$component of the velocity in the out-flow direction. A first suggestion would be, therefore, a term that allows the diffusion of field lines inside the reconnecting layer. This is what the resistive term does ($\eta\mathbf{J}$ in Eq.1.3). However, for this resistive reconnection to occur, the width of the reconnecting layer must be larger than the mean free path between the electron and ion collisions. Otherwise, different mechanisms of reconnection must be considered, such as collisionless magnetic reconnection due to finite electron inertia effects [63, 64, 62, 148], or due to an anisotropic electron pressure tensor, EMHD reconnection [93, 89], or to other intrinsically kinetic effects such as Landau damping, that must be addressed in the framework of a full kinetic (i.e. Vlasov-based) study of reconnection [65, 66, 149], which we are going to discuss and study in details in other chapters (e.g., chapter 5).

Sticking here to the resistive case, let us assume a configuration in which we are in a reference frame moving with the plasma velocity (e.g. the equilibrium velocity vanishes $\mathbf{u}_0 = 0$), and that the equilibrium magnetic field shown in Fig.(1.5) reads,

$$\mathbf{B}_0 = B_y(x)\mathbf{e}_y + B_{z,0}\mathbf{e}_z, \tag{1.18}$$

Again we name $B_s = B_y(x)$ for clarity of notation. B_s is the inhomogeneous shear field that vanishes at $x = 0$, and $B_{z,0}$ is a uniform guide field along $z-$direction. The problem we are studying here is $2D$, and it is independent of the z coordinate. The current density resulting from this field, can be estimated using Ampere equation given by Eq.(1.2):

$$\mathbf{J}_0 = J_{z,0}\mathbf{e}_z = \frac{B_s^{'}}{\mu_0}\mathbf{e}_z, \tag{1.19}$$

where the "$'$" refers to the derivative with respect to x. This configuration gives a Lorentz force $\mathbf{J}_0 \times \mathbf{B}_0 = -\frac{B_s^{'}B_s}{\mu_0}\mathbf{e}_x$. In this figure, a denotes the width of the current sheet which is defined by the equilibrium magnetic field, L is its length, and δ is the width of the inner layer. Therefore, to sustain this equilibrium ($\frac{d}{dt} = 0$), Eq.(1.1) shows that an $x-$component of the pressure gradient must exist. For simplicity, we assume in this introductory chapter that the pressure is isotropic, and thus it is a scalar quantity. Otherwise, an equation that describes the evolution of full pressure tensor is needed, as we are going to show in a later chapter. For the sake of the analysis, we also assume that this sheet extends infinitely along $y-$ direction, and it is bounded by perfectly conducting walls in the $x-$ direction (dark brown parallelograms in the Fig.1.5).

Now, assuming periodic perturbations along the $y-$direction (that is, the perturbed quantities have sinusoidal shape along this direction $\sim e^{iky}$), we perform a linear stability analysis of the system, by focusing on its dynamics before it enters a fully developed nonlinear stage. This study can be performed by means of Fourier analysis, where we decompose each quantity Q, in the following form

$$Q = Q_0 + Q_1 = Q_0 + \tilde{Q}(x)e^{\gamma t}e^{iky}, \tag{1.20}$$

where Q_0 is the equilibrium quantity, γ is the growth rate of any possible instability. Therefore, the perturbations are growing (instability occurs), damped, or even oscillating depending on γ being a positive real number, negative real number, or complex number with a non-null imaginary part; respectively. k is the wave-number in $y-$direction, and it is related to the number of islands that will be generated in the current sheet ($k = \frac{2\pi m}{L}$, where m is the number of modes). Now, substituting Eq.(1.2) and Eq.(1.3) into Faraday equation, it is easy to find

$$\frac{\partial \mathbf{B}}{\partial t} = \nabla \times (\mathbf{u} \times \mathbf{B}) + \frac{\eta}{\mu_0}\nabla^2\mathbf{B}, \tag{1.21}$$

where we have used Eq.(B.21), and Thomson-Maxwell equation. Linearizing this equation using Eq.(1.20), we obtain

$$\frac{\partial \mathbf{B}_1}{\partial t} = \nabla \times (\mathbf{u}_1 \times \mathbf{B}_0) + \frac{\eta}{\mu_0}\nabla^2 \mathbf{B}_1, \tag{1.22}$$

Where we only keep the zeroth and first order quantities. We also have $\frac{\partial}{\partial t} = \gamma$, $\frac{\partial}{\partial y} = ik$, while non-uniform perturbed quantities are allowed in $x-$direction. With this in hand, the $x-$component of Eq.(1.22) becomes,

$$\gamma B_x = ikB_s u_x + \frac{\eta}{\mu_0}(\frac{d^2}{dx^2} - k^2)B_x, \tag{1.23}$$

where we omitted $\sim$ from the perturbed quantities to simplify the notation. Now, let us assume for a moment that the last term in the previous equation vanishes (ideal `MHD`). This is a relevant approximation in the outer, "ideal" region, where the weak spatial in-homogeneity does not make the current density compensate the smallness of the resistivity. Therefore, the velocity becomes

$$u_x = -\frac{i\gamma B_x}{kB_s}, \tag{1.24}$$

This means that if $kB_s(x) = 0$, as it is the case in the Fig.(1.5), either $u_x \to \infty$ which is an unphysical result to be disregarded, or $\gamma = 0$. Thus, the configuration is stable in ideal `MHD`. However, a solution with a non-vanishing u_x is also admitted in the presence of an arbitrarily small but not vanishing resistivity: a finite u_x, although small, would imply the divergence of the current density at $x = 0$, due to the piling up of the magnetic lines, but this makes the last right-hand side term of Eq.(1.23) not negligible. Its presence allows the removal of the singularity in the current density. To see this we consider then Eq.(1.23) written as

$$ikB_s u_x = \Big[\gamma - \frac{\eta}{\mu_0}(\frac{d^2}{dx^2} - k^2)\Big]B_x, \tag{1.25}$$

The contribution of the left hand side can be neglected in the inner region, so we write

$$\gamma B_x = \frac{\eta}{\mu_0}(\frac{d^2}{dx^2} - k^2)B_x \tag{1.26}$$

We have thus obtained an eigenvalue problem, where the growth rate γ is the eigenvalue and B_x is the eigenvector. Neglecting the velocity term in the previous equation can be justified by the fact that the time scales are much longer than Alfvén time which characterizes the time scales at which the effects of inertia become important. However, in this simplified model, it is clear that by balancing the term on `LHS` with the first one on `RHS` (we are going to call this dimensional analysis, which depends on balancing different terms to find the scaling laws in a way that must be verified a posteriori, "heuristic approach"), we obtain

$$\gamma \sim \frac{\eta}{\mu_0 a^2} \sim \frac{\eta}{\mu_0 a v_A}\frac{v_A}{a} = \frac{1}{S\tau_A}, \quad S = \frac{a^2\mu_0}{\eta}\frac{v_A}{a} = \frac{\tau_d}{\tau_A} \implies \gamma\tau_A \sim S^{-1}, \tag{1.27}$$

In the second expression of Eq.(1.27) we have introduced the Lundquist number S, which measures the resistive diffusion time τ_d in units of the time (i.e., the Alfvèn time τ_A) that an Alfvèn wave takes to cross the current layer width, a. For most cases of plasma, $S \gg 1$ (in tokamaks $S \sim 10^{7-10}$, and S can reach 10^{14} in astrophysical plasma), this implies that $\gamma \sim 0$ when $S \to \infty$. The estimate of γ in Eq.(1.27) does not account for the observed rates in real plasmas. One might

suggest that a scaling corresponding to a larger growth rate can be obtained if we keep only the resistivity into the equation, and let $\gamma\tau_A \sim S^{-\alpha}$, where $0 \leq \alpha \leq 1$. We will show that this assumption makes sense, and there are indeed formal solutions to the tearing equations, that fulfil it. This is what we are going to call in this thesis the *purely resistive regime* of spontaneous reconnecting instabilities. In order to obtain this kind of solution, we must no longer neglect the velocity term in Eq.(1.25). Therefore, to close the system, we take the $z-$ component of the curl of Eq.(1.1), which allows us to eliminate the pressure gradient term ($\nabla \times \nabla p = 0$). The linear version of this equation reads,

$$mn\frac{\partial \mathbf{u}_1}{\partial t} = -\nabla p_1 + \mathbf{J}_0 \times \mathbf{B}_1 + \mathbf{J}_1 \times \mathbf{B}_0, \tag{1.28}$$

where the contribution of the convective term is neglected because it is of second order $\mathbf{u}\cdot\nabla\mathbf{u} \sim \mathbf{u}_1 \cdot \nabla\mathbf{u}_1$. Now, taking the curl of the previous equation gives,

$$\begin{aligned}
&\mathbf{J}_0 \times \mathbf{B}_1 = -J_{z,0}B_{y,1}\mathbf{e}_x + J_{z,0}B_{x,1}\mathbf{e}_y,\ \nabla \times (\mathbf{J}_0 \times \mathbf{B}_1) = \frac{\partial j_{z,0}}{\partial x}B_{x,1}\mathbf{e}_z = \frac{B_s''}{\mu_0}B_{x,1}\mathbf{e}_z,\\
&\mathbf{J}_1 \times \mathbf{B}_0 = (B_{z,0}J_{y,1} - B_s J_{z,1})\mathbf{e}_x - B_{z,0}J_{x,1}\mathbf{e}_y + B_s J_{x,1}\mathbf{e}_z,\\
&\nabla \times (\mathbf{J}_1 \times \mathbf{B}_0) = B_s\frac{\partial J_{x,1}}{\partial y}\mathbf{e}_x - (B_s' J_{x,1} + B_s\frac{\partial J_{x,1}}{\partial x})\mathbf{e}_y - \frac{B_s}{\mu_0}\nabla^2 B_{x,1}\mathbf{e}_z,\\
&\mathbf{J}_1 = \frac{1}{\mu_0}\frac{\partial B_{z,1}}{\partial y}\mathbf{e}_x - \frac{1}{\mu_0}\frac{\partial B_{z,1}}{\partial x}\mathbf{e}_y + \frac{1}{\mu_0}(\frac{\partial B_{y,1}}{\partial x} - \frac{\partial B_{x,1}}{\partial y})\mathbf{e}_z,\\
&\nabla \times \mathbf{u}_1 = \frac{\partial u_{z,1}}{\partial y}\mathbf{e}_x - \frac{\partial u_{z,1}}{\partial x}\mathbf{e}_y + (\frac{\partial u_{y,1}}{\partial x} - \frac{\partial u_{x,1}}{\partial y})\mathbf{e}_z,
\end{aligned} \tag{1.29}$$

where we have used $\nabla \cdot \mathbf{B} = 0$, Ampere equation, and the translation invariance along z, that is $\frac{\partial}{\partial z} = 0$. Now, substituting these equation int the curl of Eq.(1.28), the $z-$component of the resulting equation reads,

$$mn\frac{\partial}{\partial t}\Big[\frac{\partial u_{y,1}}{\partial x} - \frac{\partial u_{x,1}}{\partial y}\Big] = -\frac{B_s}{\mu_0}\nabla^2 B_{x,1} + \frac{B_s'}{\mu_0}B_{x,1}, \tag{1.30}$$

which gives, after taking its Fourier transform and using the incompressibility condition ($\nabla\cdot\mathbf{u} = 0,\ \Longrightarrow\ u_y = \frac{i}{k}\frac{\partial u_{x,1}}{\partial x}$), the following equation

$$\frac{imn\gamma}{k}\Big[\frac{\partial^2}{\partial x^2} - k^2\Big]u_x = -\frac{B_s}{\mu_0}\Big[\frac{\partial^2}{\partial x^2} - k^2\Big]B_x + \frac{B_s''}{\mu_0}B_x, \tag{1.31}$$

Here we have omitted again $\sim$ in perturbed quantities. The previous equation coupled with Eq.(1.25) represents a closed generalized eigenvalue problem, where γ is the eigenvalue to be found, and $V = [B_x, u_x]^T$ is the eigenvector. Also, the quantities in these equations are dimensional: it is after normalization that we will be able to compare the result to the estimate of Eq.(1.27). The main objective of the linear analysis is to solve this problem and find the scaling laws of the growth rate; that is the power-law dependence of γ on the different non-ideal parameters entering in Ohm law (here, only η). Even if it is not always easy or possible to find an analytical solution to the eigenvalue problem resulting from the linear analysis of reconnection, these solutions are available under certain conditions using a boundary layer approach. The notion of the boundary layer is what we are going to introduce in the next section, although in the framework of heuristic analysis. Its applications to the approximated solution of the linear differential equations will be reconsidered later in Chapter 7.

1.3.1 Instability Parameter Δ' and the Outer Region

The most important question to be asked now is what are the conditions, if they do exist, for the occurrence of a positive-real growth rate; that is for the occurrence of a growing reconnecting mode. To answer this question, we go back to an idea explained before. We mentioned that for the configuration in Fig.(1.5), the system is divided into two distinct regions. One is the outer region in which we entirely neglect the non-ideal parameters. The second one is the inner region where we take into account the non-ideal effects, and we ignore all the terms proportional to k^2 because perturbations along $y-$direction are negligible compared to those along x, inside this region. Splitting the domain in two sub-domains according to this scale separation, which allows the search of two separate solutions of the differential problem to be matched in an overlapping "boundary", is known as "boundary layer approach". Therefore, the outer region equations read,

$$\gamma B_{x,out} = ikB_s u_{x,out}, \tag{1.32}$$

$$\Big[\frac{d^2}{dx^2} - k^2\Big]B_{x,out} - \frac{B_s''}{B_s}B_{x,out} = 0, \tag{1.33}$$

where the subscript "out" refers to the outer region solution. It is obvious that an analytical solution $B_{x,out}$ exists, which just depend on the given equilibrium B_s (see table 7.1 in chapter 7). The only remaining question is: does any solution $B_{x,out}$ implies the occurrence of a growing reconnecting mode? If the answer is no, then what is the interval of k that allows a growing mode ($\gamma \in \mathbb{R}^*$)?

The example of resistive reconnection considered here can help to answer this question. After all, magnetic reconnection is a process in which the magnetic energy stored in the ideal MHD region converts into kinetic energy (E_k) of the charged particles inside the reconnecting layer. Hence, for the instability to occur, the kinetic energy inside the inner layer must increase with time (the total power generated by MHD (hereafter, P) must be positive $P > 0$). Therefore, we first calculate the force operator in ideal MHD region ($\mathbf{F} = \mathbf{J} \times \mathbf{B} - \nabla p$), next we estimate the total power using the definition of power ($P = \int_V dV \mathbf{u} \cdot \mathbf{F}$), then we exploit the fact that the contribution to the growth rate will only come from the inner layer. Finally, by requiring a positive power $P > 0 \implies \frac{dE_k}{dt} > 0$, we obtain the condition for the instability to occur. Due to the incompressibility assumption ($\nabla \cdot \mathbf{u} = 0$), we write $\mathbf{u} = \nabla \times \mathbf{\Phi} = \nabla \times (\Phi \mathbf{e}_z)$. Then the power P reads,

$$P = \int_V dV \nabla \times \mathbf{\Phi} \cdot \mathbf{F} = \int_V dV \mathbf{\Phi} \cdot \nabla \times \mathbf{F}, \tag{1.34}$$

where we have used Eq.(B.27), and the fact that the solution is well-behaved at infinity, therefore the surface integral will vanish. The $z-$ component of the force operator of ideal MHD region reads,

$$\mathbf{e}_z \cdot \nabla \times \mathbf{F} = \mathbf{e}_z \cdot \Big[\nabla \times (\mathbf{J}_0 \times \mathbf{B}_1) + \nabla \times (\mathbf{J}_1 \times \mathbf{B}_0)\Big] = -\frac{B_s}{\mu_0}\Big[\frac{\partial^2}{\partial x^2} - k^2\Big]B_x + \frac{B_s''}{\mu_0}B_x \tag{1.35}$$

where we have used Eq.(1.29). Now, using the definition of $\mathbf{u}$ in terms of $\mathbf{\Phi}$, the power becomes

$$P = \int_{-\infty}^{+\infty} dx \frac{\gamma B_x}{\mu_0 k^2}\Big[\frac{d^2 B_x}{dx^2} - (k^2 + \frac{B_s''}{B_s})B_x\Big] = \int_{-\delta}^{+\delta} dx \frac{\gamma B_x}{\mu_0 k^2}\Big[\frac{d^2 B_x}{dx^2} - (k^2 + \frac{B_s''}{B_s})B_x\Big], \tag{1.36}$$

In the previous equation, we used the fact that $\Phi = -\frac{iu_x}{k} = -\frac{\gamma}{k^2 B_s}B_x$. The limits of the previous integral were changed to $\pm\delta$ because all the power will be generated inside the reconnecting layer. Now, neglecting the k^2-terms and assuming $B_x \approx B_x(0) = const$, which is known as constant-ψ approximation [57], the previous integral becomes

$$P \approx \frac{\gamma B_x(0)}{\mu_0 k^2} \int_{-\delta}^{+\delta} dx \frac{d^2 B_x}{dx^2} = \frac{\gamma B_x(0)}{\mu_0 k^2} \left[\frac{dB_{x,out}}{dx}\Big|_{+\delta} - \frac{dB_{x,out}}{dx}\Big|_{0\delta} \right] = \frac{\gamma B_x(0)^2}{\mu_0 k^2} \Delta^{'}, \tag{1.37}$$

where $\Delta^{'}$ is known as the instability parameter [57], and is given by

$$\Delta^{'} = \frac{1}{B_x(0)} \left[\frac{dB_{x,out}}{dx}\Big|_{+\delta} - \frac{dB_{x,out}}{dx}\Big|_{-\delta} \right] = \frac{1}{B_x(0)} \left[\frac{dB_{x,out}}{dx} \right]_{-\delta}^{+\delta}, \tag{1.38}$$

By looking at equation Eq.(1.37), we obtain the condition for a growing instability is ($P > 0$),

$$\Delta^{'} > 0, \tag{1.39}$$

$\Delta^{'}$ gives a measure of the free energy available in the magnetic configuration, that can be released by the reconnecting mode. $\Delta^{'}$ depends only on the outer solution, which in turn is strongly related to the choice of the equilibrium, and on the wavenumber (k). In our previous discussion, we assumed that the field is approximately constant in the neighbourhood of $x = 0$. This assumption is consistent with the case in which the wavelengths are small. This is equivalent to Δ' being small ($\Delta'\delta \ll 1$), or what is known as "*tearing mode*". We can summarize the key points about the instability parameter, which we will discuss in detail in the next subsection, with the following statement:

The instability parameter $\Delta^{'} = \Delta^{'}(k, a)$ determines the spectrum of unstable wave-numbers ($[k_{min}, k_{max}]$) for a given equilibrium profile corresponding to a current sheet with a characteristic width a and an "infinite" elongation. The spectrum is divided into three distinct regimes: a long wavelength limit, known also as internal-kink mode ($\Delta^{'}\delta \gg 1$), a short wavelength limit known as tearing mode or constant-ψ limit ($\Delta^{'}\delta \ll 1$), and a fastest-growing mode region ($\Delta^{'}\delta \sim 1$). Since, $\Delta^{'}$ depends only on the outer solution, this makes it universal in the sense that it does not rely on the reconnection mechanism. Therefore, the three distinct limits defined here remain valid for all reconnection regimes, as shown in Fig.(1.6).

1.3.2 Scaling Laws and the Inner Region

In the previous section, we obtained a criterion allowing to determine whether a configuration is stable or not. A fundamental conclusion was drawn: the stability of any magnetized plasma to the reconnecting modes is entirely determined by the available free energy in the ideal MHD region measured by the instability parameter (see Fig. 1.5). The conversion mechanism between magnetic energy and kinetic one, when the regime is purely resistive, involves the diffusion of field lines inside the inner layer where one can no longer neglect the resistive term in generalized Ohm law. As mentioned above, in this layer, we can ignore k^2-terms. Therefore, Eqs.[1.25, 1.31] become

$$\gamma B_{x,in} = ikB_s u_{x,in} + \frac{\eta}{\mu_0} B^{''}_{x,in}, \tag{1.40}$$

$$\frac{imn\gamma}{k} u^{''}_{x,in} = -\frac{B_s}{\mu_0} B^{''}_{x,in} + \frac{B^{''}_s}{\mu_0} B_{x,in}, \tag{1.41}$$

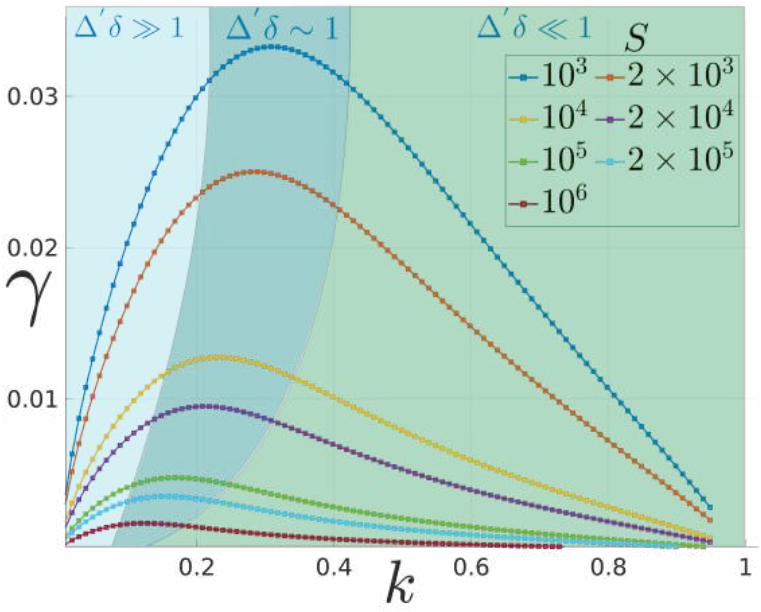

Figure 1.6: A spectrum of unstable modes for the purely resistive case when $B_s = \sin(x)$ and the current sheet aspect ratio is large. Three distinct regions are shown: large wavelength limit (left), the fastest growing mode region (middle), and the small wavelength limit (right). The configuration is unstable to reconnecting modes as long as $k \in [0, 1]$.

These equations consist of a generalized eigenvalue problem composed of two partial differential equations. An exact analytical solution to this eigenvalue problem does not generally exist in a closed form although it has been provided in the approximated form in Ref.[150]. Specific solutions, still relying on the approximation of the boundary layer analysis, have been separately obtained in constant$-\psi$ [57], and internal kink regimes [150, 151]. To characterize quantitatively the idea behind boundary layer approach, we are going to solve these equations in the constant$-\psi$ limit (tearing mode), and approximating the shear field as $B_s \sim xB_s^{'}(0)$ in the vicinity of the neutral line. Therefore, all the higher derivatives vanish. Solving the equations in the outer region, that is Eqs[1.32, 1.33] gives the following value of $\Delta^{'}$ [152] (see also [153] for details),

$$\Delta^{'} = \frac{1}{B_x(0)}\left[\frac{dB_{x,out}}{dx}\right]_{-\delta}^{+\delta} = 2\sqrt{1-(ka)^2}\tan\left(\frac{\pi}{2}\sqrt{1-(ka)^2}\right), \tag{1.42}$$

Following the constant$-\psi$ approximation , Eqs[1.40, 1.41] become

$$\gamma B_{x,in}(0) = ikxB_s^{'}(0)u_{x,in} + \frac{\eta}{\mu_0}B_{x,in}^{''}, \tag{1.43}$$

$$\gamma u_{x,in}^{''} = \frac{ikB_s^{'}(0)}{mn\mu_0}xB_{x,in}^{''}, \tag{1.44}$$

Now, substituting Eq.(1.44) into Eq.(1.43), one obtains,

$$au_{x,in}^{''} - bx^2u_{x,in} = cx, \tag{1.45}$$

where $a = \frac{imn\eta\gamma}{kB_s^{'}(0)}$, $b = ikB_s^{'}(0)$, and $c = -\gamma B_{x,in}(0)$. We then make the following change of variables,

$$x = \delta X, \quad u_{x,in} = \chi U, \tag{1.46}$$

Eq.(1.45) becomes

$$U'' - \frac{b\delta^4}{a}X^2U = \frac{c\delta^3}{\chi a}X, \implies U'' - X^2U = X, \tag{1.47}$$

where we required $\frac{c\delta^3}{\chi a} = 1$, and $\frac{b\delta^4}{a} = 1$. The previous equation can be solved by means of Hermite expansion, and has a solution of the following integral form (see Ref.[154] for details about solving equations of this type),

$$U(X) = -\frac{X}{2}\int_0^{\pi/2} e^{-\frac{X^2}{2}\cos\theta}\sqrt{\sin\theta}d\theta, \tag{1.48}$$

with

$$\delta = \frac{(mn\eta\gamma)^{\frac{1}{4}}}{k^{\frac{1}{2}}B_s'(0)^{\frac{1}{2}}}, \quad \chi = \frac{iB_{x,in}(0)\gamma}{(mn\eta\gamma)^{\frac{1}{4}}(kB_s'(0))^{\frac{1}{2}}}, \tag{1.49}$$

with this solution in hand, we have now a solution ($B_{x,out}$) in the outer region (by solving Eqs[1.32, 1.33]), and another one ($B_{x,in}$) in the inner region after solving Eqs[1.44, 1.43], and therefore obtaining Eq.(1.48). In order to have a well-behaved solution for the problem, the outer and the inner solutions must match each others at some boundaries. The inner layer can be assumed to extend up to a distance δ from the neutral line as shown in Fig.(1.5). That is,

$$\lim_{x\to\pm\infty} B_{x,in} = \lim_{x\to\pm 0} B_{x,out}, \tag{1.50}$$

which also applies to their derivatives, $\lim_{x\to\pm\infty}\frac{dB_{x,in}}{dx} = \lim_{x\to\pm 0}\frac{dB_{x,out}}{dx}$. Substituting Eq.(1.46), and Eq.(1.49) into Eq.(1.43), one easily finds after integrating once,

$$\begin{aligned}\left[\frac{dB_{x,in}}{dx}\right]_{-\delta}^{+\delta} = \left[\frac{dB_{x,out}}{dx}\right]_{-\delta}^{+\delta} = \frac{1}{B_{x,in}(0)}\Delta' = \frac{\mu_0 B_{x,in}(0)\delta\gamma}{\eta}\int_{-\infty}^{+\infty}(1+XU)dX \\ = \sqrt{2}\Gamma^2(\frac{3}{4})\frac{\mu_0 B_{x,in}(0)\delta\gamma}{\eta},\end{aligned} \tag{1.51}$$

where

$$\int_{-\infty}^{+\infty}(1+XU)dX = \sqrt{2}\Gamma^2(\frac{3}{4}), \tag{1.52}$$

where Γ is the known gamma function, and we have used the definition of the instability parameter given by Eq.(1.38). Now, substituting the definition of δ into Eq.(1.51), we obtain the well known scaling law for the purely resistive regime [57], which reads [see chapter 7 for a detailed analysis of the linear theory],

$$\gamma_{SD} \sim k^{2/5}\Delta'^{4/5}\eta^{3/5}, \text{or in term of S,} \gamma_{SD} \sim k^{2/5}\Delta'^{4/5}S^{-3/5}. \tag{1.53}$$

where the subscript SD refers to the "Small Δ' limit". In the opposite limit (large wavelength limit, discussed in detail in chapter 7), the scaling law of the growth rate reads,

$$\gamma_{LD} \sim k^{2/3}S^{-1/3} \tag{1.54}$$

Even with this large gain in the growth rate compared, for $S \gg 1$, to the $\sim S^{-1}$ scaling discussed before, this growth rate does not alone account for the fast reconnection events we observe in nature or laboratory. Therefore, other effects should be accounted for, in spontaneous reconnecting instabilities. Promising candidates are further non-ideal terms, such as Finite Larmor Radius effects or the Hall-term in the generalized Ohm's law, or other kinetic effects that should be better described in a fully kinetic description (see chapter 7).

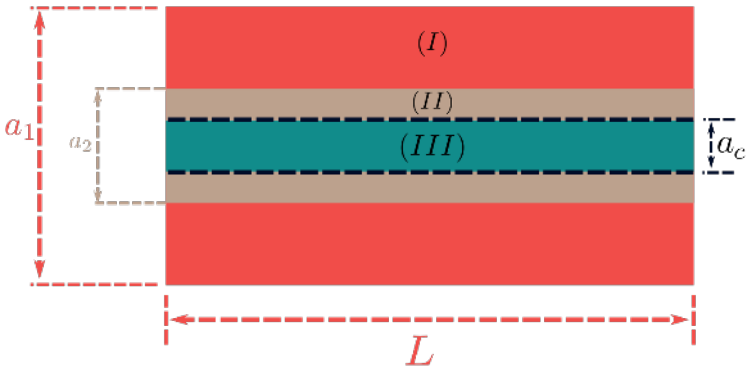

Figure 1.7: Classification of reconnection regimes for $B_0 \sim B_s$, when varying the width a at fixed length of the current sheet L. The first region (light red) is the slow modes region (with aspect ratio $L/a \ll (L/a)_{cr} = (L/a_c)$, where $a_2 \leq a \leq a_1$). The second (light brown) is the fast modes' region with $a_c \leq a \leq a_2$. The third (light green) is the violently unstable modes' region ($a \leq a_c$) which is accessible due to the un-realizability of the formation of the corresponding current sheet. See Del Sarto et al [155] for more details.

1.4 Fastest Growing Mode and the "Ideal" Limit

The existence of the fastest growing mode, when a continuous spectrum of wavelengths is destabilized, had been evidenced in the original paper by Furth et al [57]. Assuming a Harris type equilibrium [156], and the width of the current sheet a as a reference length, they showed by numerical solution of the resistive tearing equations that the scaling laws of the fastest growing mode read,

$$\gamma_M \sim S^{-1/2}, \quad k_M \sim S^{-1/4}, \tag{1.55}$$

Where the subscript M refers to the maximum growth rate in a continuum spectrum of unstable wavenumbers. The fastest growing mode, in a $B_s(x) \sim \cos(mx)$ equilibrium, had been studied numerically by Van Hoven and Cross [60]. Later in 1989, Velli and Hood [157] performed thorough numerical analysis of the single-tearing dominant mode in a Harris-type slab configuration, showing that the fastest growing mode can be destabilized in a current sheet with a sufficiently large aspect ratio, which can be numerically assumed to be as small as ~ 20.

For a long time the study of tearing mode has been focusing on the two distinct limits ($\Delta'\delta \gg 1$, and $\Delta'\delta \ll 1$) because the attention was mostly oriented to tokamak physics, where the reconnecting modes (tearing and internal kink instabilities) occur on resonant surfaces with a defined wavelength. In that case, the aspect ratio of the current layer ($\epsilon_a = L/a$) is of the order of unity ($L \sim a \sim r$, where r is the small radius of the tokamak, and L is the current sheet length) and periodic boundary conditions hold at the extremities of the current sheet. Therefore, the current layer width a appears as the only natural reference length in the problem. However, this is not the case in astrophysics, where long sheets can exist and form due to the underlying dynamics and non-linear processes involved in the system. In this case, another reference length must considered, namely the length of the current sheet L.

As shown in Fig.1.6, the fact that the wavelength of the fastest growing mode sets in between the tearing and internal kink limits, suggests that the scaling of the maximum growth rate can be estimated by matching those of tearing and internal kink modes (Eq.1.53 and Eq.1.54) [158, 159, 24]. When doing so, Δ' can be approximated as k^{-p} , which is consistent with the large wavelength limit ($k \to 0$). The power p depends on the chosen equilibrium. For example,

$p = 1$ for Harris type equilibrium (see chapter 7 for detailed discussion). Taking this into account and requiring $\gamma_{SD} \sim \gamma_{LD}$, one then easily obtains Eq.(1.55).

The space-depending variables in all scaling laws, obtained in the previous discussions, are normalized with respect to the current sheet width (a). The existence of another characteristic length (L) in the problem suggests that the scaling laws change when rescaled with respect to it [11].

Depending on the studied regime, the microscopic quantities which depend on space and/or time are normalized to the characteristic length and time of the problem (in our introductory case: a and Alfvén time $\tau_A = a/v_A$). Hence, the non-ideal parameter h, that can be the resistivity, viscosity, electron skin depth, or another non-ideal parameter involved in the problem, has a power-law dependence on a and τ_A, which can be written as

$$h \sim \left(\frac{1}{a}\right)^m \left(\frac{a}{B_0}\right)^n, \tag{1.56}$$

Where $\tau_A \sim a/B_0$, and B_0 is a reference magnetic field assumed to be equal to the shear field B_s in our case. When rescaling h with respect to L, one finds

$$h \sim \left(\frac{L}{a}\right)^{m-n} h^*, \tag{1.57}$$

Where the superscript "*" refers to quantities normalized to L (e.g, $h^* \sim (1/L)^m (L/B_0)^n$). When, $h = S^{-1}$, Eq.(1.27) gives $m = 2$ and $n = 1$. Now, by rescaling γ_M with respect to L ($\gamma_M \sim \gamma^*(a/L)$), and substituting the rescaled Lundquist number in Eq.(1.55), one finds,

$$\gamma_M^* \sim \left(\frac{L}{a}\right)^{\frac{3}{2}} S^{*-\frac{1}{2}} \tag{1.58}$$

It was shown [157, 153] that an aspect ratio $L/a \geq 20$ is sufficient to destabilize a mode whose growth rate is well approximmated by Eq.(1.55). In this case, the value of $(\frac{L}{a})^{3/2}$ can compensate the smallness of $S^{-*1/2}$ leading to spontaneous reconnecting modes whose time scale is of the order of the $L-$normalized Alfvén time ($\gamma_M^* \sim 1 \implies \tilde{\gamma}_M \sim \tau_A^{*-1}$, where $\sim$ refers to dimensional quantities).

This conclusion was first found and discussed by Pucci and Velli [161], and led them to introduce the notion of "ideal tearing" regime in resistive MHD. The main idea here is that a $\Delta'\delta \sim 1$ tearing mode, with macroscopic Alfvénic growth rate $\gamma^* \sim 1$ independent of the non-ideal parameter (whence the name "ideal tearing") allowing the reconnection (S^{*-1} in our case), can develop if a critical aspect ratio is reached. From Eq.(1.58), this critical aspect ratio reads,

$$\left(\frac{L}{a}\right)_{cr} \sim S^{*\frac{1}{3}}, \tag{1.59}$$

This geometrical threshold allowed the distinction between modes classified as slow (i.e., those with growth rates much smaller than the ideal limit), fast (i.e., those with growth rates of the order of the ideal limit), and violently unstable where diverging growth rates had been obtained

[11] This rescaling argument applies not only to the space-depending variables in the problem but also to the time. Since the reference time in many regimes depends on the magnetic field, one, or more characteristic magnetic fields appear in the problem. In general, the shear field in the outer region is considered as the reference field. When quantities are referred to as a magnetic field component which is largely different from the guide field, a rescaling of quantities (notably time scales) must be performed with respect to it, too. In that case, the asymptotic ratio between the guide field and such a magnetic field can be accounted for in the re-normalized scalings. This can have important implications for secondary modes to resistive instabilities (see Del Sarto et al [155] and Del Sarto and Ottaviani [160] for a detailed discussion).

(see Fig.1.7). It also allowed [161] to explain the paradox of the diverging growth rate obtained for the plasmoid instability [162, 163] to be as a result of the impossibility of the formation of the Sweet-Parker steady configuration since its aspect ratio ($(L/a) \sim S^{*1/2}$) is larger than the critical one given by Eq.(1.59). These results have been then shown in Ref. [24] to be in principle generalizable to any reconnecting regime (resistive, collisionless or kinetic), regardless of the equilibrium profile (see also Pucci et al.([164]) and Betar et al. [153] for more details).

Moreover, this growth rate threshold, although requiring a formally diverging aspect ratio, in the asymptotic limit, is of practical relevance for natural and laboratory plasma since numerical analysis shows that the fastest growing mode approaches the growth rate of the "ideal tearing" limit already for realistic values of the non-ideal parameters involved (see, e.g. Pucci et al. [161] and Del Sarto et al. [24] for a discussion). Moreover, it can provide the estimate of the longest stable aspect ratio of a current sheet that evolves in time, for example, in a turbulent plasma [153].

1.5 Conclusions

In this chapter, we have discussed a simplified model of the magnetic reconnection phenomenon: spontaneous instabilities in the purely resistive regime. Magnetic reconnection is a process occurring in highly conducting plasma in which the magnetic topology of the field breaks and reconnects at null field spots, known as `X-` points. The magnetic energy, stored in the field lines, is so converted into kinetic energy, thermal energy, and acceleration of the particles.

In Ideal `MHD`, such a phenomenon is impossible since the plasma and the field lines are co-moving together, and hence the charged particles cannot slip across field lines. Thus to interpret and understand this process, a more general version of Ohm law must be considered. This generalized Ohm's law should involve terms, such as the resistivity in this chapter, allowing the formation of diffusion-like regions (current sheets) which in turn allow releasing the magnetic energy stored in the filed lines.

Thanks to the large scale separation, the domain in which resistive reconnection occurs can be divided into two distinct regions: outer, ideal MHD layer, and an inner reconnecting layer. The instability of the current sheet is completely controlled by the free energy available in the outer region, which is measured by the instability parameter that must be positive for the unstable modes to exist. The equations of the two layers are separately solved, and then using the boundary layer approach the outer and inner solutions must match each other in an intermediate layer. This leads us to obtain the scaling of the growth rate, and the eigenfunctions of the reconnecting modes. However, as we add more terms in generalized Ohm law, solving the differential equations with boundary layer approach becomes more and more challenging since more than one inner layer might form now (see chapter 7).

In general, the universality of the instability parameter as defined with respect to the outer layer, which depends only on the equilibrium profile and on the wavenumber of the perturbation, allows us to distinguish three regimes in the unstable spectrum. The first one is the long wavelength limit (internal kink instability, for which $\Delta'\delta \gg 1$), the second one is the short wavelength limit (tearing modes, for which $\Delta'\delta \ll 1$), and then there is the fastest growing mode with $\Delta'\delta \sim 1$.

The existence of more than one length and/or time scales of the equilibrium suggests that the scaling laws of the maximum growth rate might change when re-scaling the variables to different characteristic lengths and/or times. This appears to be true for the situations in which long current sheets form. In that case, a fast reconnecting mode, with a growth rate of the order

of the macroscopic Alfvénic time, can develop, if some criterion on the aspect ratio amplitude is met, depending on the magnitude of the non-ideal parameters at play. Above such a critical aspect ratio, stable current sheets are not likely to be observed, since fast reconnecting modes would disrupt them.

2

General Review of Plasma Models for Magnetic Reconnection

Contents

Magnetic reconnection is a complex physical process, which involves a wide range of parameters. These parameters are essential to account for realistic situations. A part of this complexity is in the multiscale nature of reconnection problem. In its simplest picture, the purely resistive regime, described in chapter 1 adopting a fluid model, a single parameter fixes the scale length of the reconnecting layer. The representative of this regime is the resistive term in Ohm law resulting from including the collisions between ions and electrons. This term is responsible of the formation of a field lines' diffusion region and allows the reconnection of magnetic field lines at null `X`-points. Resistive reconnection can play a major role in some magnetised laboratory plasmas (see the review by Yamada et al. [36]), as well as in the solar chromosphere and accretion

disks around compact astrophysical objects [165]. Depending on the reconnection model chosen, the mechanism responsible for reconnection may completely change (for example, reconnection becomes collisionless, e.g. thanks to the inclusion of kinetic effects through the full pressure tensor). As a consequence, the scaling laws of the growth rate and inner layer width, but also the nonlinear dynamics as well, can vary when including kinetic, or two-fluid effects. Some of these effects, such as viscosity or finite electron and ion temperatures, cannot break the field topology, but can affect the dynamics and the growth rate.

All this motivates us to review some different plasma models applied to reconnection. Hence, we begin this chapter by exploring the kinetic description of the plasma, which gives models such as the Vlasov-Maxwell description. For example, the Vlasov model can be employed to study reconnecting events occurring on fast time scales of electrons, whose dynamics decouple from that of ions. Then, we derive multi-fluid models and discuss the closure problem, which also leads to different regimes depending on the studied case or on the kinetic effects kept in the model. Finally, we conclude the chapter with a detailed discussion of the one-fluid model widely adopted to study reconnection. This can be "extended" so to incorporate many aspects of kinetic description, as we are going to see in this and next chapters.

2.1 Kinetic Description of the Plasma

The vast parameter space and richness of the plasma physics at both microscopic and macroscopic levels, beside of complexities associated with geometry and homogeneity of physical quantities lead inevitably to the derivation of several models which are tailored to address specific phenomena. The range of validity and physical phenomena described by these models are incorporated at the very first step in their derivation -strictly speaking, in the initial hypotheses which constitute the building blocks of the model. Due to the large number of particles involved, a single-particle description is out of the question, so the most complete and detailed description of the plasma behaviour is the one based on statistical physics. Statistical models contain all the microscopic and macroscopic information about plasma. These models can study and investigate physical phenomena that occur at the level of gyro-motion of the charged particles around the magnetic field lines -among the smallest length and shortest time scales in magnetized plasmas– but can precisely describe also the macroscopic dynamics at large scales.

In order to introduce a statistical, kinetic description we should better start from a more complete model (although of no practical use in plasma because of the too large number of degrees of freedom), from which the former can be derived: actually, two equivalent models are likely to provide such a "complete" description. One is the Klimontovih approach [166], defined in the $6D$-phase space for each single particle and the other one is the Liouville approach, based on the description of the N-particle dynamics in the $6N$-dimensional phase space (cf. Fig.2.1).

Let us first consider the Klimontovich approach[166] which is based on the particle density function of α-species in a 6-dimensional phase space. This density reads,

$$N_\alpha^K = \sum_i \delta[\mathbf{r} - \mathbf{R}_i(t)]\delta[\mathbf{v} - \mathbf{V}_i(t)] \tag{2.1}$$

where $\mathbf{R}_i(t)$ and $\mathbf{V}_i(t)$ represents the Lagrangian coordinates -the location and velocity of the i^{th} particle at time t. The time evolution of such a distribution of particles is described by the so-called Klimontovich equation,

$$\frac{\partial N_\alpha^K}{\partial t} + \mathbf{v}\cdot\nabla_{\mathbf{r}} N_\alpha^K + \frac{e_\alpha}{m_\alpha}\Big[\mathbf{E}^m(\mathbf{r},t) + \mathbf{v}\times\mathbf{B}^m(\mathbf{r},t)\Big]\cdot\nabla_{\mathbf{v}} N_\alpha^K = 0, \tag{2.2}$$

where e_α and m_α are the electric charge and the mass of α-species particle, respectively. $\mathbf{E}^m(\mathbf{r},t)$ is the total electric field, and $\mathbf{B}^m(\mathbf{r},t)$ is the total magnetic field. $\mathbf{r}$, and $\mathbf{v}$ are the Eulerian coordinates. The previous equation can be obtained by calculating the partial time derivative ($\frac{\partial}{\partial t}$) of Eq.(2.1). [12]

Solving this equation, analytically but even numerically is practically impossible due to its complexity. This difficulty is due to the fact that the equation requires information about the entire electromagnetic fields (external fields, and the self-consistent fields generated by all particles except the one we calculate the density function at its location).Thus, some kind of averaging over a small volume in the phase space will result in a significant simplification of the Klimontovich equation and indeed it is this operation that leads us to kinetic equation. This averaging procedure leads to the definition of a one-particle distribution function $f_\alpha(\mathbf{r},\mathbf{v},t)$ that represents the number of the α-species particles in the unit volume of the phase space. This averaging must have some trade-off between the physical phenomena we are interested in, and the Dirac-functional nature of the particle distribution function N_α^K. On the one hand, the volume in phase space must not be too large so to avoid losing important physics ingredients due to the lack of phase-space resolution. On the other hand, it should not be too small in order to eliminate the sharp variation in N_α^K between neighbouring volumes which would break the smooth property of the averaging process that aims to describe the plasma with a continuous distribution function [167, 168, 169]. The kinetic equation is given by

$$\frac{\partial f_\alpha(\mathbf{r},\mathbf{v},t)}{\partial t} + \mathbf{v}\cdot\nabla_{\mathbf{r}} f_\alpha(\mathbf{r},\mathbf{v},t) + \frac{e_\alpha}{m_\alpha}\Big[\mathbf{E}+\mathbf{v}\times\mathbf{B}\Big]\cdot\nabla_{\mathbf{v}} f_\alpha(\mathbf{r},\mathbf{v},t) = \Big[\frac{\partial f_\alpha(\mathbf{r},\mathbf{v},t)}{\partial t}\Big]_{coll} \tag{2.3}$$

Here $\mathbf{E}(\mathbf{r},\mathbf{t})$ and $\mathbf{B}(\mathbf{r},t)$ are the averaged fields, and $C_B = \Big[\frac{\partial f_\alpha(\mathbf{r},\mathbf{v},t)}{\partial t}\Big]_{coll}$ [13] is the Boltzmann collision term which is given in this approach by

$$C_B = -\frac{e_\alpha}{m_\alpha}\Big\langle(\delta\mathbf{E}^m + \mathbf{v}\times\delta\mathbf{B}^m)\cdot\nabla_{\mathbf{v}}\delta\bar{N}_\alpha^K\Big\rangle \tag{2.4}$$

C_B also gives the variation of the distribution function due to collisions. In the previous averaging procedure, we divided each of $\mathbf{E}^m$, $\mathbf{B}^m$, and N_α^K in two parts. The first is an averaged value ($\mathbf{E}$, $\mathbf{B}$), while the second is a perturbation that results from collisions ($\mathbf{E}^m = \mathbf{E} + \delta\mathbf{E}^m$ and $\mathbf{B}^m = \mathbf{B} + \delta\mathbf{B}^m$, meaning $< \delta\mathbf{E}^m >=< \delta\mathbf{B}^m >= 0$). Even though this equation for C_B is symbolically correct, Klimontovich approach does not provide any explicit formula to estimate the collision term. A formula for C_B, Eq.(2.3), and the Maxwell equations given by Eqs.(2.5) would provide a closed system of equations,

$$\nabla\cdot\mathbf{E} = \frac{\rho_c}{\epsilon_0} \tag{2.5}$$

$$\nabla\cdot\mathbf{B} = 0 \tag{2.6}$$

$$\nabla\times\mathbf{E} = -\frac{\partial\mathbf{B}}{\partial t} \tag{2.7}$$

$$\nabla\times\mathbf{B} = \mu_0\mathbf{J} + \frac{1}{c^2}\frac{\partial\mathbf{E}}{\partial t} \tag{2.8}$$

[12] For example, $\frac{\partial}{\partial t}\delta(\mathbf{r}-\mathbf{R}_i(t)) = \frac{\partial\mathbf{R}_i(t)}{\partial t}\cdot\frac{\partial}{\partial\mathbf{R}_i}\delta(\mathbf{r}-\mathbf{R}_i(t)) = -\mathbf{V}_i(t)\cdot\frac{\partial}{\partial\mathbf{r}}\delta(\mathbf{r}-\mathbf{R}_i(t))$. Since delta function implies that these derivatives will be estimated only in locations where there are particles, then $\mathbf{V}_i(t) = \mathbf{v}$. Therefore, $\frac{\partial}{\partial t}\delta(\mathbf{r}-\mathbf{R}_i(t)) = -\mathbf{v}\cdot\frac{\partial}{\partial\mathbf{r}}\delta(\mathbf{r}-\mathbf{R}_i(t)) = -\mathbf{v}\cdot\nabla_{\mathbf{r}}\delta(\mathbf{r}-\mathbf{R}_i(t))$. The same argument applies to the derivative $\frac{\partial}{\partial t}\delta(\mathbf{v}-\mathbf{V}_i(t))$, which leads to the third term in Eq.(2.2).

[13] It is important here to mention that collision term in the context of plasma physics is completely different from that derived by Boltzmann. The latter was aiming to study the collisions between neutral particles which lead in general to large-angle scattering.

with,

$$\mathbf{J} = \sum_{\alpha} e_{\alpha} \int \mathbf{v} f_{\alpha}(\mathbf{r}, t) d^3 v \tag{2.9}$$

$$\rho_c = \sum_{\alpha} e_{\alpha} \int f_{\alpha}(\mathbf{r}, t) d^3 v \tag{2.10}$$

Let us now consider the second "complete" approach, which is based on the idea of the description of a plasma, composed of N_α particle, in $6N_\alpha$-dimensional phase space. Here, a single point in this space determines the state of the plasma system entirely, and therefore its time evolution. The density function in this approach is given by

$$N_{\alpha}^{L} = \prod_{i=1}^{N_\alpha} \delta[\mathbf{r}_i - \mathbf{R}_i(t)] \delta[\mathbf{v}_i - \mathbf{V}_i(t)] \tag{2.11}$$

where the superscript L refers to *"Liouville"* so to distinguish it from K that stands for *"Klimontovich"*, in the approach previously described. The meaning of this density function is logically different from N_α^K. The former has a Dirac-functional nature, while the latter is the number of particles in 6−dimensional phase space. At time t, it is either $N_\alpha^L = 1$ if the system, composed of N_α particles, exists at the point $(\mathbf{r}_1, \mathbf{v}_1, \mathbf{r}_2, \mathbf{v}_2, ..., \mathbf{r}_{N_\alpha}, \mathbf{v}_{N_\alpha})$, or, otherwise $N_\alpha^L = 0$. After taking the partial time derivative of Eq.(2.11), one obtains the famous Liouville equation [170] given by

$$\frac{\partial N_{\alpha}^{L}}{\partial t} + \sum_{i=1}^{N_\alpha} \mathbf{v}_i \cdot \nabla_{\mathbf{r}_i} N_{\alpha}^{L} + \sum_{i=1}^{N_\alpha} \frac{\mathbf{F}_i^m}{m_\alpha} \cdot \nabla_{\mathbf{v}_i} N_{\alpha}^{L} = 0 \tag{2.12}$$

where $\mathbf{F}_i^m$ is the microscopic force resulting from external fields, and from all particles except the one at which we calculate the force. Eq.(2.12) is the Liouville equation of the system density function N_α^L. Theoretically speaking, this equation coupled with Maxwell equations Eqs.(2.5) give an accurate description of the plasma, and also predicts precisely its evolution. However, solving this $(6N_\alpha+1)$−dimensional equation is very far from being an easy task -both, numerically and analytically. Therefore, a further simplification is needed , here too, in order to reduce the complexities inherited in this equation, and we can achieve that through introducing a new distribution function which deals with an ensemble of systems of particles. This density distribution function, denoted by $f_{N_\alpha}(\mathbf{r}_1, \mathbf{v}_1, \mathbf{r}_2, \mathbf{v}_2, ..., \mathbf{r}_{N_\alpha}, \mathbf{v}_{N_\alpha}, t)$, gives the probability of finding a system in a unit element volume in the $6N_\alpha$−dimensional phase space. The time evolution of this distribution function is given by the following equation,

$$\frac{\partial f_{N_\alpha}}{\partial t} + \sum_{i=1}^{N_\alpha} \mathbf{v}_i \cdot \nabla_{\mathbf{r}_i} f_{N\alpha} + \sum_{i=1}^{N_\alpha} \frac{\mathbf{F}_i^m}{m_\alpha} \cdot \nabla_{\mathbf{v}_i} f_{N_\alpha} = 0 \tag{2.13}$$

Eq.(2.13) is the Liouville equation of the system probability density function. The difference between Eq.(2.12) and Eq.(2.13) is that the later shows how the probability density of an ensemble of systems evolves with time in the phase space through the $6N_\alpha$−dimensional distribution function (f_{N_α}) that represents an ensemble of N_α−particle systems, while the former describes the evolution of one single system which exists initially at $(\mathbf{r}_1, \mathbf{v}_1, ..., \mathbf{r}_{N_\alpha}, \mathbf{v}_{N_\alpha})$. In other words, N_α^L is the density function of one system, while f_{N_α} is a joint probability density function. A quick look at Eq.(2.13) indicates that it has the same dimensions of the Liouville equation. But another careful glance shows the main idea that leads to a significant simplification of the

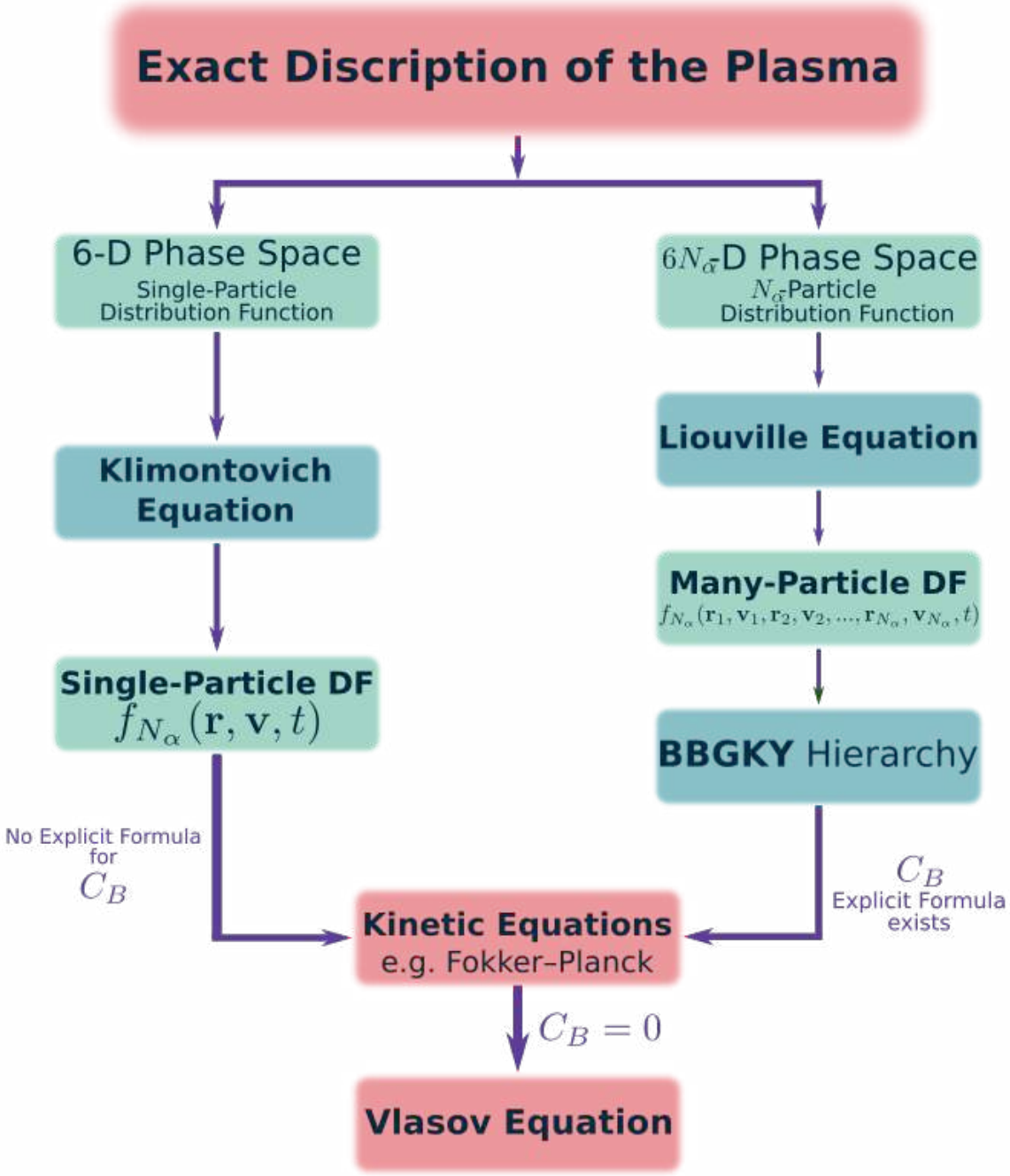

Figure 2.1: A flowchart shows the steps followed starting from an exact description of the plasma along the toward the derivation of Vlasov (collisionless Boltzmann) equation. *DF* stands for distribution function and C_B for Boltzmann collision terms (see section 2.1).

problem: lowering the dimensions of the phase space is possible by introducing the reduced distribution function defined by

$$f_\alpha^l = V^{l-N_\alpha} \int f_\alpha^{N_\alpha} d\mathbf{r}_{l+1} d\mathbf{v}_{l+1} d\mathbf{r}_{l+2} d\mathbf{v}_{l+2} \cdots \cdot d\mathbf{r}_{N_\alpha} d\mathbf{v}_{N_\alpha} \tag{2.14}$$

where f_α^l is the reduced distribution function of an ensemble of systems, each of them composed of l particles. This distribution gives the probability of finding a system of N_α particles inside the volume $d\mathbf{r}_1 d\mathbf{v}_1 d\mathbf{r}_2 d\mathbf{v}_2 \cdots \cdot d\mathbf{r}_l d\mathbf{v}_l$ in the reduced $l-$dimensional phase space, irrespective of the positions and velocities of the remaining $(N_\alpha - l)$ particles.

We notice that multiplying Eq.(2.13) by $d\mathbf{r}_{N_\alpha} \cdot d\mathbf{v}_{N_\alpha}$, and integrating the resulting formula over these components of the original phase space reduces its dimensions by 6, and gives a new equation of the same form with an additional term that involves the effects of inter-particle interactions, via all existing forces, with the particle $(\mathbf{r}_{N_\alpha}, \mathbf{v}_{N_\alpha})$. Therefore, the obtained equation describes the evolution of the reduced function $f_\alpha^{N_\alpha - 1}$, and it still provides an exact representation of the plasma. By repeating this reduction procedure, it is not difficult to show that we obtain the following set of equations (**BBGKY** hierarchy)[171, 172, 173, 174, 175],

$$\frac{\partial f_\alpha^l}{\partial t} + \sum_{i=1}^{l} \left(\mathbf{v}_i \cdot \nabla_{\mathbf{r}_i} f_\alpha^l + \sum_{j \neq i}^{l} \frac{\mathbf{F}_{ij}}{m_\alpha} \cdot \nabla_{\mathbf{v}_i} f_\alpha^l + \frac{N_\alpha - l}{V} \int d\mathbf{r}_{l+1} d\mathbf{v}_{l+1} \frac{\mathbf{F}_{i,l+1}}{m_\alpha} \cdot \nabla_{\mathbf{v}_i} f_\alpha^l \right) = 0 \tag{2.15}$$

The previous equation leads to lowering the dimensions of phase space by $6(N_\alpha - l)$. Taking $l = 1$, one obtains the following equation for the one-particle distribution function

$$\frac{\partial f_\alpha(\mathbf{r}_1, \mathbf{v}_1, t)}{\partial t} + \mathbf{v}_1 \cdot \nabla_{\mathbf{r}_1} f_\alpha(\mathbf{r}_1, \mathbf{v}_1, t) + \frac{N_\alpha - 1}{V} \int d\mathbf{r}_2 d\mathbf{v}_2 \frac{\mathbf{F}_{12}}{m_\alpha} \cdot \nabla_{\mathbf{v}_1} f_\alpha^2(\mathbf{r}_1, \mathbf{v}_1, \mathbf{r}_2, \mathbf{v}_2, t) = 0, \tag{2.16}$$

where f_α^2 is the two-body distribution function -note that the superscript is not a power here. f_α^2 represents the joint probability of finding the first particle at the location $(d\mathbf{r}_1, d\mathbf{v}_1)$ and the second one at $(d\mathbf{r}_2, d\mathbf{v}_2)$ in the $12-$dimensional phase space. To close the system of equations that determines the plasma evolution (Maxwell equations and Eq.(2.16)), we need an additional equation for f_α^2 which in turns leads, after substituting $l = 2$ in Eq.(2.15), to a joint probability density function (hereafter, joint PDF), namely the three-body joint PDF f_α^3. So, at some point, it is necessary to truncate the process to close the system. This closure means that we allow losing information concerning the correlation between a number of particles larger than $l + 1$ at truncation level l. This closure depends strongly on understanding the meaning of the joint PDF. For example, the two-body joint PDF $f_\alpha^2(\mathbf{r}_1, \mathbf{v}_1, \mathbf{r}_2, \mathbf{v}_2, t)$ can be decomposed into two components. The first one is the zeroth-order one $f_\alpha(\mathbf{r}_1, \mathbf{v}_1, t) f_\alpha(\mathbf{r}_1, \mathbf{v}_1, t)$, which assumes that there is no correlation between the two particles, and then means that they behave independently. In essence, the position of the first particle is completely independent of that of the second one. The second component is the two-body correlation function $g_\alpha^2(\mathbf{r}_1, \mathbf{v}_1, \mathbf{r}_2, \mathbf{v}_2, t)$ that takes into account the "collision", or, generally speaking, the interaction between two particles. Then,

$$f_\alpha^2(\mathbf{r}_1, \mathbf{v}_1, \mathbf{r}_2, \mathbf{v}_2, t) = f_\alpha(\mathbf{r}_1, \mathbf{v}_1, t) f_\alpha(\mathbf{r}_2, \mathbf{v}_2, t) + g_\alpha^2(\mathbf{r}_1, \mathbf{v}_1, \mathbf{r}_2, \mathbf{v}_2, t) \tag{2.17}$$

Now, by taking $l = 2$ in Eq.(2.15) and neglecting the three-body (and above) correlations, we obtain an equation for g_α^2 which together with Eqs.(2.17,2.16, 2.10, 2.9) and Maxwell equations, constitute a closed system. The most impressing advantage of this reduction is that we obtain the 6-dimensional kinetic equation (2.3) for f_α. Nevertheless, this is a delicate point because

this explicit relationship depends on solving an equation for g_α^2 in $12-$dimensional phase space coupled with Eq.(2.3) in a phase space of six dimensions. Therefore, these two equations are complicated to solve, and further approximations are required to find a good formula to C_B. This again requires a deep understanding of the studied plasma, and of the investigated phenomena. For example, an approximation of C_B, which takes into account only the binary collisions, is suitable for some cases, such as a weakly ionized plasma where the binary collisions dominate. Another approximation which is the Fokker-Planck equation is possible. Here, the collective behaviour of the plasma and the long-range Columb force between particles, are considered through approximation of the large-angle scattering as series of small-angle binary collisions[176]. Last but not least, we can write a collisionless approximation for kinetic equation by neglecting the collision term. This equation is known as the Vlasov equation [177] and is given by

$$V(f) = \frac{\partial f_\alpha(\mathbf{r},\mathbf{v},t)}{\partial t} + \mathbf{v}\cdot\nabla_{\mathbf{r}} f_\alpha(\mathbf{r},\mathbf{v},t) + \frac{e_\alpha}{m_\alpha}\Big[\mathbf{E}+\mathbf{v}\times\mathbf{B}\Big]\cdot\nabla_{\mathbf{v}} f_\alpha(\mathbf{r},\mathbf{v},t) = 0, \tag{2.18}$$

Vlasov equation, along with Maxwell equations, constitutes a closed system of equations. Fig.2.1 shows a flowchart that summarizes the different kinetic descriptions of the plasma, starting from the exact one and ending with the collisionless approximation: Vlasov equation.

2.2 Extended Fluid Models of Plasma

In the previous section, we reviewed the microscopic statistical models of plasma physics. Some of them give an exact representation of the plasma (Klimontovich and Liouville equations). Others give very accurate approximations for the collisional case (kinetic equation), and collisionless case (Vlasov equation). These models, with different degrees, are based on the detailed knowledge of the examined system, and hence cover the broadest possible range of phenomena including microscopic and macroscopic processes. However, there are several points which motivate considering different models based on macroscopic quantities. These quantities result from averaging over velocity domain in phase space, which lowers the dimensions from 6 to the three dimensions of the physical space. In the following, we list some of those points that motivate considering macroscopic models (fluid models):

1. **Complexity:** Statistical equations are highly complex. Exact equations like Klimontovich and Liouville are of little practical use due to complexities related to their phase spaces and the huge number of equations to be solved -$6N_\alpha$ equations. Those complexities still exist for approximated models (kinetic and Vlasov equations), but they are much less difficult now because we have one equation to be solved in $6d-$dimensional phase space. In fact, the main code used in this thesis is dedicated to solve the Vlasov-Maxwell system in this $6d-$phase space.

2. **Information:** The particle density function in Eq.(2.2), and the system density function in Eq.(2.12) contain all the details about the plasma. Moreover, the distribution functions in Eq.(2.3) and Eq.(2.18) involve a great amount of information about the plasma. Nevertheless, it turns out that we can understand a wide range of phenomena which occur inside the plasma without the need for this detailed knowledge of the statistical functions. This is, for example, true for understanding macroscopic equilibrium and instabilities that play crucial roles in designing thermonuclear devices.

3. **Computation:** The simulations of kinetic equations, based on numerical methods, require substantial computational resources and are very time-consuming. Therefore, one advantage of using a macroscopic description is saving time and resources, and thus understanding some physics more quickly. However, this occurs at the expense of the physical description: in order to mimic a complete Vlasov description, one should solve an infinite number of moments of the distribution function.

4. **Physical Insight** This is a no-nonsense point. Despite the fact that macroscopic quantities, such as particle density $n_\alpha(\mathbf{r}, t)$, hold less information compared to distribution function, they are more intuitive to understand compared to microscopic quantities. It is, therefore, reasonable to start with an attempt to understand the essence of a physical process using fluid models. Then, by extending the model to a kinetic one -if necessary-, we can improve our knowledge, or discover other aspects of the same process.

Still, it is not always possible to rely on fluid models, and a kinetic description of the plasma becomes unavoidable in many cases. Fluid models of the plasma, as said above, depend on averaging over eulerian velocity components in phase space. Consequently, they do not take into account the details of the velocity distribution. The idea behind these models is to divide the plasma into a large number of small fluid elements which contain plasma particles. The evolution of these fluid elements is determined by the time evolution of some macroscopic quantities. Furthermore, the size of the fluid element must be chosen carefully. On the one hand, it must not be too large to avoid losing the necessary spatial resolution to study the plasma. On the other hand, it cannot be too small in order to ensure the validity of the averaging procedure from a statistical point of view. As mentioned above, fluid models are obtained by averaging the kinetic equation over velocity space (moments of distribution function). We are going to see that the evolution equation of the i^{th} moment involves the divergence of a moment of a higher order. One of the main problems in the fluid description is knowing how many moments must be kept in the model to obtain a good description of the reality: this is the "Closure Problem".

However, if the plasma is not collisionless, the right-hand side of the kinetic equation will survive. Hence, it will be inevitable to find explicit formulae for terms resulting from collisions (transport coefficients) [178, 179, 170]. The way to proceed is by first taking a local expansion of the distribution function, then to write it in terms of the macroscopic quantities, which leads after matching with fluid equations to the correct expressions for transport coefficients and macroscopic quantities which involves collisions, such as the viscous pressure tensor. Nevertheless, the calculations quickly become overcomplicated when the plasma consists of more than one species, or if a magnetic field is present [170].

2.2.1 Moments of Kinetic Equation

To obtain fluid models, we take the moments of the kinetic equation (2.3) by multiplying it with the desired quantity $\chi(\mathbf{v})$, and then by averaging over velocity phase space. This approach will produce an open system of equations which has to be truncated at some point, which is the closure problem discussed above. The l^{th} moment of Eq.(2.3) generates a new physical quantity with $(3l)$ components, which necessitates either taking a new moment to derive its evolution equation, or closing the system at this level by relating it with lower moments. However, this truncation is a trade-off between the "simplicity" of the model and the correct physics it describes. Multiplying kinetic equation by $\chi(\mathbf{v})$, and integrating over velocity space, we obtain

$$I^1 + I^2 + I^E + I^B = I^C \tag{2.19}$$

where,

$$I^1 = \int \chi(\mathbf{v}) \frac{\partial f_\alpha}{\partial t} d\mathbf{v} = \frac{\partial}{\partial t} \int \chi(\mathbf{v}) f_\alpha d\mathbf{v} = \frac{\partial}{\partial t} \Big\langle n_\alpha(\mathbf{r}, t) \chi(\mathbf{v}) \Big\rangle_\alpha \tag{2.20}$$

$$I^2 = \int \chi(\mathbf{v}) \mathbf{v} \cdot \nabla_{\mathbf{r}} f_\alpha d\mathbf{v} = \nabla \int \chi(\mathbf{v}) \mathbf{v} f_\alpha d\mathbf{v} = \frac{\partial}{\partial \mathbf{r}} \Big\langle n_\alpha(\mathbf{r}, t) \mathbf{v} \chi(\mathbf{v}) \Big\rangle_\alpha \tag{2.21}$$

$$\begin{aligned} I^E = \frac{e_\alpha}{m_\alpha} \int \chi(\mathbf{v}) \mathbf{E} \cdot \nabla_{\mathbf{v}} f_\alpha d\mathbf{v} = \frac{e_\alpha}{m_\alpha} E_i \underbrace{\int \frac{\partial(\chi(\mathbf{v}) f_\alpha)}{\partial v_i} d\mathbf{v}}_{=0,\ \text{boundend DF}} - \frac{e_\alpha}{m_\alpha} E_i \int f_\alpha \frac{\partial \chi(\mathbf{v})}{\partial v_i} d\mathbf{v} = \\ - \frac{e_\alpha}{m_\alpha} E_i n_\alpha(\mathbf{r}, t) \Big\langle \frac{\partial \chi(\mathbf{v})}{\partial v_i} \Big\rangle_\alpha \end{aligned} \tag{2.22}$$

$$\begin{aligned} I^B = \frac{e_\alpha}{m_\alpha} \int \chi(\mathbf{v}) (\mathbf{v} \times \mathbf{B}) \cdot \frac{\partial f_\alpha}{\partial \mathbf{v}} = \frac{e_\alpha}{m_\alpha} \int \chi(\mathbf{v}) \varepsilon_{ijk} B_k v_j \frac{\partial f_\alpha}{\partial v_i} = \frac{e_\alpha}{m_\alpha} \varepsilon_{ijk} B_k \int \Big\{ \underbrace{\frac{\partial(\chi(\mathbf{v}) v_j f_\alpha)}{\partial v_i}}_{\substack{0 \text{ contribution: bounded DF}}} \\ - f_\alpha \frac{\partial}{\partial v_i} (\chi(\mathbf{v}) v_j) \Big\} d\mathbf{v} = - \frac{e_\alpha}{m_\alpha} \varepsilon_{ijk} B_k n_\alpha(\mathbf{r}, t) \Big\langle \frac{\partial}{\partial v_i} (\chi(\mathbf{v}) v_j) \Big\rangle_\alpha \end{aligned} \tag{2.23}$$

$$I^c = \int \chi(\mathbf{v}) C_B d\mathbf{v} \tag{2.24}$$

where χ depends only on the velocity, and the fields are functions of the position and time: $\mathbf{E}(\mathbf{r}, t)$, and $\mathbf{B}(\mathbf{r}, t)$. The average bracket of a quantity χ with respect to the distribution function of the species α is given by

$$< \chi(\mathbf{v}) >_\alpha = \frac{1}{n_\alpha(\mathbf{r}, t)} \int \chi(\mathbf{v}) f_\alpha(\mathbf{r}, \mathbf{v}, t) d\mathbf{v}, \tag{2.25}$$

Now by taking different values of $\chi(\mathbf{v})$, we generate new macroscopic variables, such as density, averaged velocity, pressure, temperature, and other transport quantities, which depend on $\mathbf{r}$ and t.

2.2.2 Continuity Equation

By substituting $\chi = 1$ into equations Eqs.(2.20-2.25), one easily obtain the continuity equation (**CE**) given by

$$\frac{\partial n_\alpha}{\partial t} + \nabla \cdot \Big(n_\alpha \mathbf{u}_\alpha \Big) = 0, \quad \frac{dn_\alpha}{dt} + n \nabla \cdot \mathbf{u}_\alpha = 0, \tag{2.26}$$

The first form is the conservative form of the equation, while the second one is the Lagrangian form. For example, if the fluid is incompressible ($\nabla \cdot \mathbf{u}_\alpha = 0$), then the particle density is constant along the trajectories of fluid elements (look at Lagrangian form). This incompressibility, or the term $\nabla \cdot (n_\alpha \mathbf{u}_\alpha)$, are very important when constructing stream functions, which will be the starting point in the derivations of reduced models, such as Reduced MHD (hereafter, *RMHD*) with Strauss density profile (constant density)[180], or an extended `RMHD` model with an arbitrary density profile.

2.2.3 Momentum Equation

Eq.(2.26) is a scalar equation which relates the density of the particles with the averaged velocity of the α-species. Therefore, to close the system, we need another equation that describes the time evolution of the macroscopic quantity $\mathbf{u}_\alpha$: momentum equation. To derive this equation, we substitute $\chi = \mathbf{v}$ into Eqs.(2.20-2.25). Then, one obtains

$$\mathbf{I}^1 = \frac{\partial}{\partial t}\Big\langle \mathbf{v} \Big\rangle_\alpha = \frac{\partial}{\partial t}\Big(n_\alpha \mathbf{u}_\alpha\Big) \tag{2.27}$$

Before going further to obtain I^2, we introduce a new quantity: the random velocity $\mathbf{s}_\alpha$. Then the total velocity can be decomposed into two components: averaged velocity and random one,

$$\mathbf{v} = \mathbf{u}_\alpha + \mathbf{s}_\alpha \tag{2.28}$$

where we have $< \mathbf{v} >_\alpha = \mathbf{u}_\alpha \implies < \mathbf{s}_\alpha >_\alpha = 0$. By using the fact that $< \mathbf{s}_\alpha >= 0$, we have

$$\begin{aligned} \{< \mathbf{v} \otimes \mathbf{v} >_\alpha\}_{ij} &=< (u_{\alpha,i} + s_{\alpha,i})(u_{\alpha,j} + s_{\alpha,j}) >= u_{\alpha,i}u_{\alpha,j} + < s_{\alpha,i}s_{\alpha,j} >_\alpha \\ &= u_{\alpha,i}u_{\alpha,j} + \frac{1}{m_\alpha n_\alpha}\mathcal{P}_{\alpha,ij} \end{aligned} \tag{2.29}$$

The symbol $\otimes$ refers to the tensor product [14]. Substituting the previous relation into Eq.(2.21), one obtains in vector notation,

$$\mathbf{I}^2 = \nabla \cdot (n_\alpha \mathbf{u}_\alpha \otimes \mathbf{u}_\alpha) + \frac{1}{m_\alpha}\nabla \cdot \mathcal{P}_\alpha \tag{2.30}$$

where we define the pressure tensor by,

$$\mathcal{P}_\alpha = m_\alpha n_\alpha < \mathbf{s}_\alpha \otimes \mathbf{s}_\alpha >_\alpha \tag{2.31}$$

As explained in section 2.2.1 about the closure problem, pressure tensor results here from taking the first moment of kinetic equation, and it has 9 components. From Eq.(2.31), $\mathcal{P}$ is a symmetric tensor, hence there are only six independent components to be found. The transport equation for the pressure tensor will also generate a new variable -heat flux triad $\mathcal{Q}$.

The pressure tensor can be decomposed into two parts. The first is the scalar isotropic pressure, denoted by p_α, which represents the thermodynamic pressure that results from the isotropic thermal, un-magnetized motion in the phase space. The second which is the anisotropic part given by,

$$\Pi_\alpha = \mathcal{P} - p_\alpha \mathcal{I}, \tag{2.32}$$

Now, the contributions of I^E and I^B are

$$I_i^E = -\frac{e_\alpha n_\alpha}{m_\alpha}E_j < \frac{\partial v_i}{\partial v_j} >_\alpha = -\frac{e_\alpha n_\alpha}{m_\alpha}E_j < \delta_{ij} >_\alpha = -\frac{e_\alpha n_\alpha}{m_\alpha}E_i, \implies \mathbf{I}^E = -\frac{e_\alpha n_\alpha}{m_\alpha}\mathbf{E} \tag{2.33}$$

$$\begin{aligned} I_i^B &= -\frac{e_\alpha n_\alpha}{m_\alpha}\varepsilon_{ljk}B_k < \frac{\partial(v_j v_i)}{\partial v_l} >_\alpha = -\frac{e_\alpha n_\alpha}{m_\alpha}\varepsilon_{ljk}B_k < \underbrace{\delta_{jl}v_i}_{\varepsilon_{llk}=0} + \underbrace{\delta_{il}v_j}_{i=l} >_\alpha \\ &= -\frac{e_\alpha n_\alpha}{m_\alpha}\varepsilon_{ijk}B_k < v_j >_\alpha, \implies \mathbf{I}^B = -\frac{e_\alpha n_\alpha}{m_\alpha}\mathbf{u}_\alpha \times \mathbf{B}, \end{aligned} \tag{2.34}$$

[14] The direct tensor product of two vector spaces $\mathcal{V}$ and $\mathcal{W}$ of dimensions n and m, respectively, is a tensor space of higher rank, and nm-dimensional. For example, for the case of the particles' velocities (the velocity vector is a tensor of first rank and dimension $n = 3$), their tensor product $\mathbf{v} \otimes \mathbf{v}$ gives a matrix $\mathcal{A}$ (it is a tensor of second rank and dimensions $nm = 9$, where $\mathcal{A}_{ij} = v_i v_j$).

By substituting the various contributions into Eq.(2.19), we obtain the momentum equation

$$\frac{\partial}{\partial t}\Big(m_\alpha n_\alpha \mathbf{u}_\alpha\Big) + \nabla\cdot\Big(m_\alpha n_\alpha \mathbf{u}_\alpha \otimes \mathbf{u}_\alpha\Big) = -\nabla\cdot\mathcal{P}_\alpha + e_\alpha n_\alpha\Big(\mathbf{E}+\mathbf{u}_\alpha\times\mathbf{B}\Big) + \Upsilon^{\alpha,\mathcal{M}}, \tag{2.35}$$

Differentiating the first and second terms in the previous equation, and using continuity equation, one easily obtains the convective form (**ME**),

$$\begin{aligned}\frac{\partial \mathbf{u}_\alpha}{\partial t} + \mathbf{u}_\alpha\cdot\nabla\mathbf{u}_\alpha &= -\frac{1}{m_\alpha n_\alpha}\nabla\cdot\mathcal{P}_\alpha + \frac{e_\alpha}{m_\alpha}\Big(\mathbf{E}+\mathbf{u}_\alpha\times\mathbf{B}\Big) + I_\alpha^C \\ &= -\frac{1}{m_\alpha n_\alpha}\nabla p_\alpha - \frac{1}{m_\alpha n_\alpha}\nabla\cdot\Pi_\alpha + \frac{e_\alpha}{m_\alpha}\Big(\mathbf{E}+\mathbf{u}_\alpha\times\mathbf{B}\Big) + \frac{\Upsilon^{\alpha,\mathcal{M}}}{m_\alpha},\end{aligned} \tag{2.36}$$

where $\Upsilon^{\alpha,\mathcal{M}} = m_\alpha I_\alpha^C$ represents the change in the distribution function of $\alpha-$particles due to momentum transfer from other particles $I_\alpha^C = \sum_\beta I_{\alpha\beta}^C$, with a general property $I_{\alpha,\alpha}^C = 0$, and

$$\Upsilon^{\alpha,\mathcal{M}} = \sum_\beta \int m_\alpha \mathbf{v} C_B(f_\alpha, f_\beta) d\mathbf{v} \tag{2.37}$$

To close the system of equations, composed of Eq.(2.26) and Eq.(2.36), six additional equations are required for $\mathcal{P}_\alpha$. So, either we use results from transport theory [181, 170] which leads, in the relevant regimes of applicability, to an equation for Π_α of the form $\Pi_\alpha = g(\nu, \mathbf{u}_\alpha)$, or it is also possible to take the second moment of the kinetic equation so to obtain evolution equation for pressure tensor. Closure at any step depends on the physics we are studying. For example, full pressure tensor may play a key role in some physical processes like Weibel-type instabilities and collisionless reconnection. In contrast, in many cases, it might completely be neglected, or retaining its effects via the viscosity parameter ν.

2.2.4 Full Pressure Tensor Equation

Following the same procedure as above, we now take $\chi(\mathbf{v}) = \mathbf{v}\otimes\mathbf{v}$. Then the different terms in Eq.(2.19) are

$$I_{ij}^1 = \frac{\partial}{\partial t}(n_\alpha < v_i v_j >_\alpha) = u_{\alpha,i}u_{\alpha,j}\frac{\partial n_\alpha}{\partial t} + n_\alpha u_{\alpha,i}\frac{\partial u_{\alpha,j}}{\partial t} + n_\alpha u_{\alpha,j}\frac{u_{\alpha,i}}{\partial t} + \frac{1}{m_\alpha}\frac{\partial \mathcal{P}_{\alpha,ij}}{\partial t}, \tag{2.38}$$

In the previous relation, we used Eq.(2.29), and we decomposed that term in order to substitute the continuity and momentum equations so to obtain the pressure tensor equation. Before going further, we calculate the following triad,

$$\begin{aligned}< v_i v_j v_k >_\alpha =& < (u_{\alpha,i}+s_{\alpha,i})(u_{\alpha,j}+s_{\alpha,j})(u_{\alpha,k}+s_{\alpha,k}) >= u_{\alpha,i}u_{\alpha,j}u_{\alpha,k} + u_{\alpha,i} < s_{\alpha,j}s_{\alpha,k} >_\alpha \\ &+ u_{\alpha,j} < s_{\alpha,i}s_{\alpha,k} >_\alpha + u_{\alpha,k} < s_{\alpha,i}s_{\alpha,j} >_\alpha + < s_{\alpha,i}s_{\alpha,j}s_{\alpha,k} >_\alpha\end{aligned} \tag{2.39}$$

Then I_{ij}^2 becomes,

$$\begin{aligned}I_{ij}^2 =& \frac{\partial}{\partial x_k}(n_\alpha < v_i v_j v_k >) = \frac{\partial}{\partial x_k}(n u_{\alpha,i}u_{\alpha,j}u_{\alpha,k}) + \frac{1}{m_\alpha}\frac{\partial}{\partial x_k}(u_{\alpha,i}\mathcal{P}_{\alpha,jk}) + \frac{1}{m_\alpha}\frac{\partial}{\partial x_k}(u_{\alpha,j}\mathcal{P}_{\alpha,ik}) \\ &+ \frac{1}{m_\alpha}\frac{\partial}{\partial x_k}(u_{\alpha,k}\mathcal{P}_{\alpha,ij}) + \frac{1}{m_\alpha}\frac{\partial}{\partial x_k}(\mathcal{Q}_{ijk}) = u_{\alpha,i}u_{\alpha,j}u_{\alpha,k}\frac{\partial n_\alpha}{\partial x_k} + n_\alpha u_{\alpha,j}u_{\alpha,k}\frac{\partial u_{\alpha,i}}{\partial x_k} + n_\alpha u_{\alpha,i}u_{\alpha,k}\frac{\partial u_{\alpha,j}}{\partial x_k} \\ &+ \frac{u_{\alpha,i}}{m_\alpha}\frac{\partial \mathcal{P}_{\alpha,jk}}{\partial x_k} + \frac{P_{\alpha,jk}}{m_\alpha}\frac{\partial u_{\alpha,i}}{\partial x_k} + \frac{u_{\alpha,j}}{m_\alpha}\frac{\partial \mathcal{P}_{\alpha,ik}}{\partial x_k} + \frac{P_{\alpha,ik}}{m_\alpha}\frac{\partial u_{\alpha,j}}{\partial x_k} + \frac{u_{\alpha,k}}{m_\alpha}\frac{\partial \mathcal{P}_{\alpha,ij}}{\partial x_k} + \frac{P_{\alpha,ij}}{m_\alpha}\frac{\partial u_{\alpha,k}}{\partial x_k} \\ &+ \frac{1}{m_\alpha}\frac{\partial \mathcal{Q}_{\alpha,ijk}}{\partial x_k}\end{aligned} \tag{2.40}$$

Thus,

$$
\begin{aligned}
I^1_{ij}+I^2_{ij} = \frac{1}{m_\alpha}\frac{\partial \mathcal{P}_{\alpha,ij}}{\partial t} + u_{\alpha,i}u_{\alpha,j}\underbrace{\left(\frac{\partial n_\alpha}{\partial t}+\frac{\partial (u_{\alpha,k}n_\alpha)}{\partial x_k}\right)}_{=0:\ \mathbf{CE}} + n_\alpha u_{\alpha,i}\underbrace{\left(\frac{\partial u_{\alpha,j}}{\partial t}+u_{\alpha,k}\frac{\partial u_{\alpha,j}}{\partial x_k}+\frac{1}{m_\alpha n_\alpha}\frac{\partial P_{\alpha,jk}}{\partial x_k}\right)}_{=\frac{e_\alpha}{m_\alpha}(E_j+\varepsilon_{ijk}u_{\alpha,k}B_i)+\frac{\Upsilon^{\alpha,\mathcal{M}}_j}{m_\alpha}\ \mathbf{ME}} \\
+ n_\alpha u_{\alpha,j}\underbrace{\left(\frac{\partial u_{\alpha,i}}{\partial t}+u_{\alpha,k}\frac{\partial u_{\alpha,i}}{\partial x_k}+\frac{1}{m_\alpha n_\alpha}\frac{\partial P_{\alpha,ik}}{\partial x_k}\right)}_{=\frac{e_\alpha}{m_\alpha}(E_i+\varepsilon_{ijk}u_{\alpha,j}B_k)+\frac{\Upsilon^{\alpha,\mathcal{M}}_i}{m_\alpha}:\ \mathbf{ME}} + \frac{u_{\alpha,k}}{m_\alpha}\frac{\partial P_{\alpha,ij}}{\partial x_k}+\frac{\mathcal{P}_{\alpha,ij}}{m_\alpha}\frac{\partial u_{\alpha,k}}{\partial x_k} \\
+ \frac{\mathcal{P}_{\alpha,ik}}{m_\alpha}\frac{\partial u_{\alpha,j}}{\partial x_k}+\frac{\mathcal{P}_{\alpha,jk}}{m_\alpha}\frac{\partial u_{\alpha,i}}{\partial x_k}+\frac{1}{m_\alpha}\frac{\partial \mathcal{Q}_{\alpha,ijk}}{\partial x_k},
\end{aligned}
\tag{2.41}
$$

where in the previous calculation, we define the heat flux triad as

$$
\mathcal{Q}_{ijk} = mn_\alpha < s_{i,\alpha}s_{j,\alpha}s_{k,\alpha} >_\alpha, \tag{2.42}
$$

For the electric and magnetic parts, we write

$$
\begin{aligned}
I^E_{ij} = -\frac{e_\alpha n_\alpha}{m_\alpha}E_l\Big\langle\frac{\partial}{\partial v_l}(v_iv_j)\Big\rangle_\alpha = -\frac{e_\alpha n_\alpha}{m_\alpha}E_l < \delta_{il}v_j+\delta_{jl}v_i >_\alpha = -\frac{e_\alpha n_\alpha}{m_\alpha}E_i < v_j >_\alpha \\
-\frac{e_\alpha n_\alpha}{m_\alpha}E_j < v_i >_\alpha = -\frac{e_\alpha n_\alpha}{m_\alpha}(E_iu_{\alpha,j}+E_ju_{\alpha,i})
\end{aligned}
\tag{2.43}
$$

and,

$$
\begin{aligned}
I^B_{ij} = -\frac{e_\alpha n_\alpha}{m_\alpha}\varepsilon_{mnk}B_k\Big\langle\frac{\partial}{\partial v_m}(v_nv_iv_j)\Big\rangle = -\frac{e_\alpha n_\alpha}{m_\alpha}\varepsilon_{mnk}B_k\Big\langle\underbrace{\delta_{nm}v_iv_j}_{=0\,:\,\varepsilon_{mmk}=0}+\delta_{im}v_nv_j+\delta_{jm}v_nv_i\Big\rangle \\
= -\frac{e_\alpha n_\alpha}{m_\alpha}\varepsilon_{ink}B_k < v_nv_j >_\alpha -\frac{e_\alpha n_\alpha}{m_\alpha}\varepsilon_{jnk}B_k < v_nv_i >_\alpha = -\frac{e_\alpha n_\alpha}{m_\alpha}\varepsilon_{ink}B_k\Big(u_{\alpha,n}u_{\alpha,j}+\frac{\mathcal{P}_{\alpha,nj}}{m_\alpha n_\alpha}\Big) \\
-\frac{e_\alpha n_\alpha}{m_\alpha}\varepsilon_{jnk}B_k\Big(u_{\alpha,n}u_{\alpha,i}+\frac{\mathcal{P}_{\alpha,ni}}{m_\alpha n_\alpha}\Big)
\end{aligned}
\tag{2.44}
$$

where $\Upsilon^{\alpha,\mathcal{P}} = m_\alpha I^C_\alpha(\chi(\mathbf{v}))$ represents the change in the distribution function of $\alpha-$particles due to pressure transfer from other particles (viscous interactions, or pressure transfer)

$$
\Upsilon^{\alpha,\mathcal{P}} = \sum_\beta \int m_\alpha \mathbf{vv} C_B(f_\alpha, f_\beta)d\mathbf{v} \tag{2.45}
$$

Now, substituting Eqs.(2.41-2.45) into Eq.(2.19), the full pressure tensor equation (**FPE**) takes the following form:

$$
\begin{aligned}
\frac{\partial \mathcal{P}_{\alpha,ij}}{\partial t}+u_{\alpha,k}\frac{\partial \mathcal{P}_{\alpha,ij}}{\partial x_k}+\mathcal{P}_{\alpha,ij}\frac{\partial u_{\alpha,k}}{\partial x_k}+\mathcal{P}_{\alpha,ik}\frac{\partial u_{\alpha,j}}{\partial x_k}+\mathcal{P}_{\alpha,jk}\frac{\partial u_{\alpha,i}}{\partial x_k}+\frac{\partial \mathcal{Q}_{\alpha,ijk}}{\partial x_k} \\
= \frac{e_\alpha}{m_\alpha}\Big(\varepsilon_{ink}B_k\mathcal{P}_{\alpha,nj}+\varepsilon_{jnk}B_k\mathcal{P}_{\alpha,ni}\Big)+\Upsilon^{\alpha,\mathcal{P}}_{ij}-n_\alpha u_{\alpha,i}\Upsilon^{\alpha,\mathcal{M}}_j-n_\alpha u_{\alpha,j}\Upsilon^{\alpha,\mathcal{M}}_i.
\end{aligned}
\tag{2.46}
$$

Now we need a new equation to express the evolution of heat transfer triad $\mathcal{Q}_{\alpha,ijk}$ which in turn gives a new tensor with a higher rank. Alternatively, we close the system applying a closure

relation for $\mathcal{Q}_{ijk}$ -one simple closure relation is the divergence-free heat transfer triad (No heat flux) $\nabla \cdot \mathcal{Q} = 0$, or even a vanishing heat flux triad $\mathcal{Q} = 0$. This simple closure, combined with appropriate relationships for transport quantities due to collisions with other particles and combined with Eqs.(2.26, 2.36, 2.46) coupled with Maxwell equations, constitute a closed system which can be solved for $\mathbf{E}$, $\mathbf{B}$, n_α, $\mathbf{u}_\alpha$, and $\mathcal{P}_\alpha$.

2.2.5 Energy Equation

There are many regimes in which describing the relevant physics does not require extending the model to include the full pressure tensor. Therefore, we can derive some relations that close the system of equations. The derivation of these relations, known as constitutive equations, depends strongly on the physics and properties of the studied medium. Before going further with this idea, we obtain in this section an equation that describes the time evolution of the scalar pressure p. Here, we take $\chi(\mathbf{v}) = \frac{v^2}{2}$. Before calculating the different terms in Eq.(2.19), we calculate the following two terms,

$$< v^2 >_\alpha = < (u_{\alpha,i} + s_{\alpha,i}) \cdot (u_{\alpha,i} + s_{\alpha,i}) >_\alpha = u_{\alpha,i}^2 + \frac{3}{m_\alpha n_\alpha} p_\alpha, \tag{2.47}$$

$$\begin{aligned} < v^2 v_j >_\alpha &= < (u_{\alpha,i} + s_{\alpha,i}) \cdot (u_{\alpha,i} + s_{\alpha,i}) \otimes (u_{\alpha,j} + s_{\alpha,j}) >_\alpha = u_{\alpha,i}^2 u_{\alpha,j} + 2u_{\alpha,i} < s_{\alpha,i} s_{\alpha,j} >_\alpha \\ &+ u_{\alpha,j} < s_{\alpha,i}^2 >_\alpha + < s_{\alpha,i}^2 s_{\alpha,j} >_\alpha = u_{\alpha,i}^2 u_{\alpha,j} + \frac{2u_{\alpha,i}}{m_\alpha n_\alpha} \mathcal{P}_{\alpha,ij} + \frac{3u_{\alpha,j}}{m_\alpha n_\alpha} p_\alpha + \frac{2}{m_\alpha n_\alpha} q_{\alpha,j}, \end{aligned} \tag{2.48}$$

$$I^1 = \frac{\partial}{\partial t}\Big(\frac{n}{2} < v^2 >_\alpha \Big) = \frac{\partial}{\partial t}(\frac{n_\alpha}{2} u_{\alpha,i}^2) + \frac{3}{2m_\alpha}\frac{\partial p_\alpha}{\partial t} = \frac{u_{\alpha,i}^2}{2}\frac{\partial n_\alpha}{\partial t} + n_\alpha u_{\alpha,i}\frac{\partial u_{\alpha,i}}{\partial t} + \frac{3}{2m_\alpha}\frac{\partial p_\alpha}{\partial t}, \tag{2.49}$$

$$\begin{aligned} I^2 &= \frac{\partial}{\partial x_j}\Big(\frac{n_\alpha}{2} < v^2 v_j >_\alpha \Big) = \frac{\partial}{\partial x_j}(\frac{n_\alpha}{2} u_{\alpha,i}^2 u_{\alpha,j}) + \frac{\partial}{\partial x_j}(\frac{u_{\alpha,i}}{m_\alpha}\mathcal{P}_{\alpha,ij}) + \frac{\partial}{\partial x_j}(\frac{3u_{\alpha,j}}{2m_\alpha} p_\alpha) + \frac{1}{m_\alpha}\frac{\partial q_{\alpha,j}}{\partial x_j} \\ &= \frac{u_{\alpha,i}^2}{2} u_{\alpha,j}\frac{\partial n_\alpha}{\partial x_j} + n_\alpha \frac{u_{\alpha,i}^2}{2}\frac{\partial u_{\alpha,j}}{\partial x_j} + n_\alpha u_{\alpha,i} u_{\alpha,j}\frac{\partial u_{\alpha,i}}{\partial x_j} + \frac{\mathcal{P}_{\alpha,ij}}{m_\alpha}\frac{\partial u_{\alpha,i}}{\partial x_j} + \frac{u_{\alpha,i}}{m_\alpha}\frac{\partial \mathcal{P}_{\alpha,ij}}{\partial x_j} \\ &+ \frac{3}{2m_\alpha} p_\alpha \frac{\partial u_{\alpha,j}}{\partial x_j} + \frac{3}{2m_\alpha} u_{\alpha,j}\frac{\partial p_\alpha}{\partial x_j} + \frac{1}{m_\alpha}\frac{\partial q_{\alpha,j}}{\partial x_j} \end{aligned} \tag{2.50}$$

Then,

$$\begin{aligned} I^1 + I^2 = \frac{u_{\alpha,i}^2}{2} \underbrace{\Big(\frac{\partial n_\alpha}{\partial t} + u_{\alpha,j}\frac{\partial n_\alpha}{\partial x_j} + n_\alpha \frac{\partial u_{\alpha,j}}{\partial x_j}\Big)}_{=0\,:\mathbf{CE}} + \underbrace{n_\alpha u_{\alpha,i}\Big(\frac{\partial u_{\alpha,i}}{\partial t} + u_{\alpha,j}\frac{\partial u_{\alpha,i}}{\partial x_j} + \frac{1}{m_\alpha n_\alpha}\frac{\partial \mathcal{P}_{\alpha,ij}}{\partial x_j}\Big)}_{= \frac{e_\alpha n_\alpha u_{\alpha,i}}{m_\alpha} E_i + \frac{e_\alpha n_\alpha u_{\alpha,i}}{m_\alpha}\varepsilon_{ijk} u_{\alpha,j} B_k + \frac{n_\alpha u_{\alpha,i}}{m_\alpha}\Upsilon_i^{\alpha,\mathcal{M}}} \\ + \frac{3}{2m_\alpha}\Big(\frac{\partial}{\partial t} + u_{\alpha,j}\frac{\partial}{\partial x_j}\Big) p_\alpha + \frac{3}{2m_\alpha} p_\alpha \frac{\partial u_{\alpha,j}}{\partial x_j} + \frac{\mathcal{P}_{\alpha,ij}}{m_\alpha}\frac{\partial u_{\alpha,i}}{\partial x_j} + \frac{1}{m_\alpha}\frac{\partial q_{\alpha,j}}{\partial x_j} \end{aligned} \tag{2.51}$$

$$I^E = -\frac{e_\alpha n_\alpha}{m_\alpha} E_l \Big\langle \frac{\partial}{\partial v_l}(\frac{v^2}{2}) \Big\rangle_\alpha = -\frac{e_\alpha n_\alpha}{m_\alpha} E_l < v_l \delta_{il} >_\alpha = -\frac{e_\alpha n_\alpha}{m_\alpha} E_i u_{\alpha,i}, \tag{2.52}$$

$$
\begin{aligned}
I^B &= -\frac{e_\alpha n_\alpha}{m_\alpha}\varepsilon_{ijk}B_k\Big\langle\frac{\partial}{\partial v_i}(\frac{v^2}{2}v_j)\Big\rangle = -\frac{e_\alpha n_\alpha}{m_\alpha}\varepsilon_{ijk}B_k < v_i v_j >_\alpha \\
&= -\frac{e_\alpha n_\alpha}{m_\alpha}\underbrace{u_{\alpha,j}\varepsilon_{ijk}u_{\alpha,j}B_k}_{=0:\ \mathbf{u}\perp\mathbf{u}\times\mathbf{B}} - \underbrace{\frac{e_\alpha n_\alpha}{m_\alpha}\varepsilon_{ijk}B_k\frac{\mathcal{P}_{\alpha,ij}}{m_\alpha n_\alpha}}_{=0:\ \textbf{symmetry of }\mathcal{P}} = 0,
\end{aligned}
\tag{2.53}
$$

Explicitly, the second term in previous equation takes the following form:

$$
\begin{aligned}
\varepsilon_{ijk}B_k\mathcal{P}_{ij} &= \varepsilon_{123}B_3\mathcal{P}_{12} + \varepsilon_{312}B_2\mathcal{P}_{31} + \varepsilon_{231}B_1\mathcal{P}_{23} \\
&+ \varepsilon_{213}B_3\mathcal{P}_{21} + \varepsilon_{132}B_2\mathcal{P}_{13} + \varepsilon_{321}B_1\mathcal{P}_{32} = 0, \\
\varepsilon_{ijk} &= -\varepsilon_{jik}\ \textit{and}\ \mathcal{P}_{ij} = \mathcal{P}_{ji}
\end{aligned}
\tag{2.54}
$$

The rate of energy transfer due to collisions is $\Upsilon^{\alpha,p} = m_\alpha I^C_\alpha(\frac{v^2}{2})$, then

$$
\Upsilon^{\alpha,p} = m_\alpha\sum_\beta\int\frac{v^2}{2}C_B(f_\alpha, f_\beta)d\mathbf{v},
\tag{2.55}
$$

Now, substituting Eqs.(2.51-2.55) into Eq.(2.19), one obtains the energy equation

$$
\frac{3}{2}\Big(\frac{\partial}{\partial t} + u_{\alpha,j}\frac{\partial}{\partial x_j}\Big)p_\alpha + \frac{3p_\alpha}{2}\nabla\cdot\mathbf{u}_\alpha + \mathcal{P}_\alpha{:}\nabla\mathbf{u}_\alpha + \nabla\cdot\mathbf{q}_\alpha = \Upsilon^{\alpha,p} - n_\alpha\mathbf{u}_\alpha\cdot\boldsymbol{\Upsilon}^{\alpha,\mathcal{M}}
\tag{2.56}
$$

where $\mathcal{P}_\alpha{:}\nabla\mathbf{u}_\alpha = \mathcal{P}_{\alpha,ij}\frac{\partial u_{\alpha,i}}{\partial x_i}$. This equation, in addition to appropriate relationships for collisional terms and heat flux, a constitutive equation for pressure tensor, Eqs.(2.26-2.36), and Maxwell equations constitute a closed system which can be solved to find n_α, $\mathbf{u}_\alpha$, p_α, $\mathbf{E}$, and $\mathbf{B}$.

2.3 The Closure Problem of Extended Fluid Models

We have shown in the previous discussion that any attempt to take a higher moment to close the system leads to a new macroscopic quantity leaving it open again. Accordingly, the closure is a trade-off between describing the correct physics and avoiding increasing the system's complexity. In this section, we present some standard closures and explain their building blocks.

2.3.1 Full Pressure Tensor Description

If the plasma is collisionless, then all the collisional terms (I^C) vanishes. This leads to introducing a first closed `MHD` system which reads

$$
\frac{dn_\alpha}{dt} + n\nabla\cdot\mathbf{u}_\alpha = 0,
\tag{2.57}
$$

$$
\begin{aligned}
\frac{\partial\mathbf{u}_\alpha}{\partial t} + \mathbf{u}_\alpha\cdot\nabla\mathbf{u}_\alpha &= -\frac{1}{m_\alpha n_\alpha}\nabla\cdot\mathcal{P}_\alpha + \frac{e_\alpha}{m_\alpha}\Big(\mathbf{E} + \mathbf{u}_\alpha\times\mathbf{B}\Big) \\
&= -\frac{1}{m_\alpha n_\alpha}\nabla p_\alpha - \frac{1}{m_\alpha n_\alpha}\nabla\cdot\Pi_\alpha + \frac{e_\alpha}{m_\alpha}\Big(\mathbf{E} + \mathbf{u}_\alpha\times\mathbf{B}\Big),
\end{aligned}
\tag{2.58}
$$

$$\begin{aligned}\frac{\partial \mathcal{P}_{\alpha,ij}}{\partial t} + u_{\alpha,k}\frac{\partial P_{\alpha,ij}}{\partial x_k} + \mathcal{P}_{\alpha,ij}\frac{\partial u_{\alpha,k}}{\partial x_k} + \mathcal{P}_{\alpha,ik}\frac{\partial u_{\alpha,j}}{\partial x_k} + \mathcal{P}_{\alpha,jk}\frac{\partial u_{\alpha,i}}{\partial x_k} + \frac{\partial \mathcal{Q}_{\alpha,ijk}}{\partial x_k} \\ = \frac{e_\alpha}{m_\alpha}\Big(\varepsilon_{ink}B_k\mathcal{P}_{\alpha,nj} + \varepsilon_{jnk}B_k\mathcal{P}_{\alpha,ni}\Big),\end{aligned} \tag{2.59}$$

with

$$\frac{\partial \mathcal{Q}_{\alpha,ijk}}{\partial x_k} = 0, \tag{2.60}$$

The previous equations describe a non-relativistic regime. Assuming a vanishing heat transfer triad led us to this system. However, while the physics behind this assumption is very delicate, it helps us to study several interesting regimes in which the full pressure tensor contributes, such as non-relativistic Weibel instability [182] or magnetic reconnection [183, 184].

It is possible to cast the full pressure tensor equation into the following form:

$$\frac{\partial \mathcal{P}_{\alpha,ij}}{\partial t} + \mathcal{L}(\mathcal{P}_{\alpha,ij}) = \mathcal{M}(\mathcal{P}_{\alpha,ij}), \tag{2.61}$$

where,

$$\mathcal{L}(\mathcal{P}_{\alpha,ij}) = u_{\alpha,k}\frac{\partial P_{\alpha,ij}}{\partial x_k} + \mathcal{P}_{\alpha,ij}\frac{\partial u_{\alpha,k}}{\partial x_k} + \mathcal{P}_{\alpha,ik}\frac{\partial u_{\alpha,j}}{\partial x_k} + \mathcal{P}_{\alpha,jk}\frac{\partial u_{\alpha,i}}{\partial x_k}, \tag{2.62a}$$

$$\mathcal{M}(\mathcal{P}_{\alpha,ij}) = \frac{e_\alpha}{m_\alpha}\Big(\varepsilon_{ink}B_k\mathcal{P}_{\alpha,nj} + \varepsilon_{jnk}B_k\mathcal{P}_{\alpha,ni}\Big) = \sigma_\alpha\omega_{c,\alpha}\Big(\varepsilon_{ink}b_k\mathcal{P}_{\alpha,nj} + \varepsilon_{jnk}b_k\mathcal{P}_{\alpha,ni}\Big) \tag{2.62b}$$

where $\omega_{c,\alpha} = \frac{|e_\alpha|B}{m_\alpha}$, $\sigma_\alpha = sign(e_\alpha)$, and $b_k = \frac{B_k}{B}$. Dividing the contributions to the pressure tensor into two parts is productive because it identifies sources of different nature with separated differential operators, and thus allows the ordering of these operators in terms of some perturbation parameters. The first operator $\mathcal{L}$ is related to the velocity gradient, which in the absence of the magnetic field relates the pressure tensor to the stress tensor that encompasses all the deformation effects in the fluid element. The second operator, $\mathcal{M}$, describes the magnetic gyromotion effects on the pressure tensor. Therefore, as soon as we define the appropriate lengths and time scales for these operators, we can give estimations to their magnitudes. Then, different approximations can be obtained. The length and time scales are

$$\partial_t \sim \omega, \quad \mathcal{L} \sim v_0 k, \quad \mathcal{M} \sim \omega_{c,\alpha}, \tag{2.63}$$

where ω is the characteristic frequency of the problem, v_0 is the characteristic velocity, k is the wave number. One of the main assumption behind derivation of the MHD model is that the cyclotron frequency is much larger that any of macroscopic perturbation frequencies. We can represent this assumption by defining an order parameter ϵ_P given by

$$\frac{\mathcal{L}}{\mathcal{M}} \sim \frac{v_0 k}{\omega_{c,\alpha}} \ll 1, \implies \epsilon_P = \frac{\mathcal{L}}{\mathcal{M}}, \tag{2.64}$$

Later, we depend on this parameter to first linearize the full pressure equation and then finding the zeroth and first-order corrections to the pressure tensor. For example, if we neglect the velocity gradient operator, we obtain the high-frequency regimes where $\omega \sim \omega_c \to \frac{\partial \mathcal{P}_{\alpha,ij}}{\partial t} = \mathcal{M}(\mathcal{P}_{\alpha,ij})$. Also, when we are in a low-frequency regime $\frac{\mathcal{L}}{\mathcal{M}} \sim \frac{\partial_t}{\mathcal{M}} \ll 1$, the magnetic part dominates over the remaining terms in the equation by a factor of ϵ_P, which will be the starting point in the derivation of different closed systems which are based on incorporating the pressure tensor and its corrections as we are going to discuss later.

2.3.2 Cold Plasma Model

In this case, one simply neglects the pressure and thus assumes the cold isotropic limit ($T_\alpha = 0$), then Eqs.[2.57,2.58,2.59,2.60] gives the cold plasma model with the following equations

$$\frac{dn_\alpha}{dt} + n\nabla \cdot \mathbf{u}_\alpha = 0, \tag{2.65}$$

$$\frac{\partial \mathbf{u}_\alpha}{\partial t} + \mathbf{u}_\alpha \cdot \nabla \mathbf{u}_\alpha = \frac{e_\alpha}{m_\alpha}\Big(\mathbf{E} + \mathbf{u}_\alpha \times \mathbf{B}\Big), \tag{2.66}$$

In this model, the effects of the thermal motions of the particles and the viscous forces are neglected. However, It is possible to keep the effects of momentum transfer between α particles and other particles due to their mutual collisions in Eq.(2.66) by approximating $\frac{\Upsilon^{\alpha,\mathcal{M}}}{m_\alpha} = -\sum_\beta \nu_{\alpha,\beta}(\mathbf{u}_\alpha - \mathbf{u}_\beta)$. Therefore, the second equation becomes

$$\frac{\partial \mathbf{u}_\alpha}{\partial t} + \mathbf{u}_\alpha \cdot \nabla \mathbf{u}_\alpha = \frac{e_\alpha}{m_\alpha}\Big(\mathbf{E} + \mathbf{u}_\alpha \times \mathbf{B}\Big) - \sum_\beta \nu_{\alpha,\beta}\Big(\mathbf{u}_\alpha - \mathbf{u}_\beta\Big), \tag{2.67}$$

This model is advantageous when analysing the propagation of electromagnetic waves with phase velocities much larger than the thermal velocity of the particles (high frequencies). For example, in a two-species plasma (ions and electrons), we can derive, by summing Eq.(2.67) for electrons and ions after multiplying each of them with $e_\alpha n_\alpha$, a version of generalized Ohm's law that involves the resistivity ($\eta = \frac{m_e \nu_{e,i}}{ne^2}$).

2.3.3 Adiabatic Approximation

According to this approximation, we can close the system by neglecting the effects of the viscosity, thermal conductivity, and the energy transfer due to collisions. Then, substituting that in energy equation (2.56), one obtains

$$\frac{3}{2}\Big(\frac{\partial}{\partial t} + u_{\alpha,j}\frac{\partial}{\partial x_j}\Big)p_\alpha + \frac{3p_\alpha}{2}\nabla \cdot \mathbf{u}_\alpha = \frac{3}{2}\frac{Dp_\alpha}{Dt} - \underbrace{\frac{5p_\alpha}{3n_\alpha}\frac{Dn_\alpha}{Dt}}_{\text{Using } \mathbf{CE}} = 0 \implies \boxed{p_\alpha n^{-\frac{5}{3}} = const}, \tag{2.68}$$

This relationship is known as the adiabatic energy equation. The remaining two equations are

$$\frac{\partial \mathbf{u}_\alpha}{\partial t} + \mathbf{u}_\alpha \cdot \nabla \mathbf{u}_\alpha = \frac{e_\alpha}{m_\alpha}\Big(\mathbf{E} + \mathbf{u}_\alpha \times \mathbf{B}\Big) - \frac{1}{m_\alpha n_\alpha}\nabla p_\alpha, \tag{2.69}$$

$$\frac{dn_\alpha}{dt} + n\nabla \cdot \mathbf{u}_\alpha = 0, \tag{2.70}$$

Maxwell equations, coupled with adiabatic approximation given by Eqs[2.68, 2.69, 2.70], form a closed system.

2.3.4 Double Adiabatic Approximation

According to the discussion in section 2.3.1, both $\mathcal{L}$ and ∂_t are smaller than $\mathcal{M}$ by a factor ϵ_P. Therefore, the behavior of the pressure tensor is determined, to the zeroth order, by the magnetic tensor $\mathcal{M}$. This allows us to expand the pressure tensor as follow,

$$\mathcal{P}_\alpha = \mathcal{P}^0_\alpha + \mathcal{P}^1_\alpha, \tag{2.71}$$

where $\mathcal{P}^0_\alpha \sim O[\epsilon^0_P]$, and $\mathcal{P}^1_\alpha = O[\epsilon^1_P]$. Thus, Eq.(2.61) reads

$$\frac{\partial}{\partial t}\Big(\mathcal{P}^0_\alpha + \mathcal{P}^1_\alpha\Big) = \mathcal{L}\Big(\mathcal{P}^0_\alpha + \mathcal{P}^1_\alpha\Big) + \mathcal{M}\Big(\mathcal{P}^0_\alpha + \mathcal{P}^1_\alpha\Big), \tag{2.72}$$

where, we also have $\partial_t \sim O[\epsilon^1_P]$, $\mathcal{L} \sim O[\epsilon^1_P]$ and $\mathcal{M} \sim 1$. Hence, the zeroth and the first-order approximations to the low-frequency regimes are given by the following equations

$$\mathcal{M}(\mathcal{P}^0_\alpha) = 0, \tag{2.73}$$

and,

$$\mathcal{M}(\mathcal{P}^1_\alpha) = \frac{\partial \mathcal{P}^0_\alpha}{\partial t} + \mathcal{L}(\mathcal{P}^0_\alpha), \tag{2.74}$$

Now, we solve the zeroth approximation equation (2.73). Using Eq.(2.62b), this equation reads

$$\varepsilon_{ink} b_k \mathcal{P}^0_{\alpha,nj} + \varepsilon_{jnk} b_k \mathcal{P}^0_{\alpha,ni} = 0, \tag{2.75}$$

Without any loss of generality, we assume the direction of the magnetic field along z ($k = z$), then we have the following possible cases

1. $i = x, j = y$, or $i = y, j = x$, then Eq.(2.75) becomes

$$\underbrace{\varepsilon_{xnz} b_z \mathcal{P}^0_{\alpha,ny}}_{\varepsilon_{xnz} \neq 0\,:\, n=y} + \underbrace{\varepsilon_{ynz} b_z \mathcal{P}^0_{\alpha,nx}}_{\varepsilon_{ynz} \neq 0\,:\, n=x} = 0, \implies \boxed{\mathcal{P}^0_{\alpha,xx} = \mathcal{P}^0_{\alpha,yy} = \mathcal{P}^0_{\alpha,\perp}} \tag{2.76}$$

2. $i = j = x$, or $i = j = y$, then one obtains

$$\underbrace{\varepsilon_{xnz} b_z \mathcal{P}^0_{\alpha,nx} + \varepsilon_{xnz} b_z \mathcal{P}^0_{\alpha,nx}}_{\varepsilon_{xnz} \neq 0\,:\, n=y} = 0, \implies \mathcal{P}^0_{\alpha,yx} = \mathcal{P}^0_{\alpha,xy} = 0, \tag{2.77}$$

   The symmetry of the pressure tensor, and the isotropicity in the perpendicular plan to magnetic field have been used in the previous equation.

3. $i = j = xz$, then Eq.(2.75) is always satisfied despite the value of taken by $\mathcal{P}^0_{\alpha,zz}$. Then, in general we have

$$\boxed{\mathcal{P}^0_{\alpha,xx} = \mathcal{P}^0_{\alpha,yy} = \mathcal{P}^0_{\alpha,\perp} \neq 0, \textit{and } \mathcal{P}^0_{\alpha,zz} = \mathcal{P}^0_{\alpha,||} \neq 0} \tag{2.78}$$

4. When $i = x$, and $j = z$

$$\underbrace{\varepsilon_{xnz} b_z \mathcal{P}^0_{\alpha,nz} = 0}_{\varepsilon_{xnz} \neq 0\,:\, n=y}, \implies \mathcal{P}^0_{\alpha,yz} = \mathcal{P}^0_{\alpha,zy} = 0, \tag{2.79}$$

   Or when $i = y$, and $j = z$

$$\underbrace{\varepsilon_{ynz} b_z \mathcal{P}^0_{\alpha,nz} = 0}_{\varepsilon_{ynz} \neq 0\,:\, n=x}, \implies \mathcal{P}^0_{\alpha,xz} = \mathcal{P}^0_{\alpha,zx} = 0, \tag{2.80}$$

Substituting these components into the full pressure tensor gives us the double adiabatic pressure tensor which reads

$$\mathcal{P}^0_\alpha = \begin{bmatrix} \mathcal{P}^0_{\alpha,\perp} & 0 & 0 \\ 0 & \mathcal{P}^0_{\alpha,\perp} & 0 \\ 0 & 0 & \mathcal{P}^0_{\alpha,||} \end{bmatrix} \tag{2.81}$$

This formula is written in a coordinate system with a magnetic field directed along z. For an arbitrary orientation of the magnetic field (local coordinate system), it becomes

$$\mathcal{P}^0_{\alpha,ij} = \mathcal{P}^0_{\alpha,\perp}\delta_{ij} + \Big(\mathcal{P}^0_{\alpha,||} - \mathcal{P}^0_{\alpha,\perp}\Big) b_i b_j, \tag{2.82}$$

which simply gives Eq.(2.81) when $b_x = b_y = 0$, that is $\mathbf{b} = \mathbf{e}_z$. This relationship reduces the number of unknowns in the pressure tensor to two. This allows expanding the previous discussed models to study more general problems. Now, after substituting Eq.(2.82) in Eq.(2.56), and neglecting the momentum and kinetic energy transfers due to collisions, and also the heat flux, one finds

$$\frac{3}{2}\frac{d}{dt}\{\frac{1}{3}(2p_{\alpha,\perp}+p_{\alpha,||})\}+\frac{3}{2}\{\frac{1}{3}(2p_{\alpha,\perp}+p_{\alpha,||})\}\frac{\partial u_{\alpha,i}}{\partial x_i}+\Big(p_{\alpha,\perp}\delta_{ij}+(p_{\alpha,||}-p_{\alpha,\perp})b_i b_j\Big)\frac{\partial u_{\alpha,i}}{\partial x_j} = 0, \tag{2.83}$$

In the previous equation, we substituted $p_\alpha = \frac{1}{3}Tr(\mathcal{P}_\alpha) = \frac{1}{3}(2p_{\alpha,\perp} + p_{\alpha,||})$, where Tr refers to the trace of the matrix. Remembering that the particles move freely along the magnetic field lines, then their contributions to the total thermal energy satisfy an equation of the same form, which allows us to decompose the previous equation into two given by

$$\frac{dp_{\alpha,\perp}}{dt} + 2p_{\alpha,\perp}\frac{\partial u_{\alpha,i}}{\partial x_i} - p_{\alpha,\perp}b_i b_j\frac{\partial u_{\alpha,i}}{\partial x_j} = 0, \tag{2.84a}$$

$$\frac{dp_{\alpha,||}}{dt} + p_{\alpha,||}\frac{\partial u_{\alpha,i}}{\partial x_i} + 2p_{\alpha,||}b_i b_j\frac{\partial u_{\alpha,i}}{\partial x_j} = 0, \tag{2.84b}$$

Eqs[2.84b, 2.84a] lead to the well know Chew-Goldberger-Low equations (CGL)[185]. These equations do not impose any restriction on the magnetic field. In one-fluid model, the Maxwell-Faraday equation can be coupled with Ohm law to further simplify Eq.(2.84). Generalized Ohm's law (see section 2.4.3) reads

$$\mathbf{E} + \mathbf{u}\times\mathbf{B} = \mathbf{\Psi}, \tag{2.85}$$

where $\mathbf{\Psi}$ is a function of many non-ideal parameters. Now, substituting Ohm law into the Maxwell-Faraday equation, one easily finds,

$$\begin{aligned} \frac{\partial B_i}{\partial t} &= \epsilon_{ijk}\partial_j(\mathbf{u}\times\mathbf{B})_k - \epsilon_{ijk}\partial_j\Psi_k = \epsilon_{ijk}\epsilon_{kmn}\partial_j(u_m B_n) - \epsilon_{ijk}\partial_j\Psi_k \\ &= \underbrace{u_i\partial_j B_j}_{=0:\nabla\cdot\mathbf{B}=0} + B_j\partial_j u_i - B_i\partial_j u_j - u_j\partial_j B_i - \epsilon_{ilk}\partial_l\Psi_k \end{aligned} \tag{2.86}$$

In the above calculation, we used the identity $\epsilon_{ijk}\epsilon_{mnk} = \delta_{im}\delta_{jn} - \delta_{in}\delta_{jm}$. Knowing that $\frac{d}{dt} = \frac{\partial}{\partial t} + u_i\partial_i$, and using density equation, one finds,

$$\frac{\partial u_i}{\partial x_j} = \frac{1}{B_j}\Big\{\frac{dB_i}{dt} - \frac{B_i}{n}\frac{dn}{dt} + \epsilon_{ijk}\frac{\partial\Psi_k}{\partial x_j}\Big\}, \tag{2.87}$$

Assuming the limit of ideal Ohm law ($\mathbf{\Psi} = 0$), and substituting Eq.(2.87) into Eqs.[2.84b,2.84a], we easily obtain CGL closure relationships, given by

$$\frac{d}{dt}\Big(\frac{p_\perp}{nB}\Big) = 0, \quad \frac{d}{dt}\Big(\frac{p_{||}B^2}{n^3}\Big) = 0, \tag{2.88}$$

2.3.5 Finite Larmor Radius Correction

The first collisionless correction introduced to the pressure was the anisotropy effect resulting from the existence of a magnetic field. In that case, the perpendicular and parallel components of the pressure decouple from each other, hence CGL equations, given by Eq.(2.88), have been obtained. A second correction, due the finite Larmor radius (hereafter, FLR), can be introduced using several approaches [186, 187, 188, 189]. One of the simplest is to linearize the full pressure tensor equation, that is to directly solve Eq.(2.74). In the following, we consider the magnetic field is aligned along the z axis, which simplifies the analysis. In this case, the left-hand side of Eq.(2.74) reads,

$$\mathcal{M}(\mathcal{P}^1_\alpha) = \omega_{c,\alpha}\begin{bmatrix} 2\mathcal{P}^1_{\alpha,xy} & \mathcal{P}^1_{\alpha,yy} - \mathcal{P}^1_{\alpha,xx} & \mathcal{P}^1_{\alpha,yz} \\ \mathcal{P}^1_{\alpha,yy} - \mathcal{P}^1_{\alpha,xx} & -2\mathcal{P}^1_{\alpha,xy} & -\mathcal{P}^1_{\alpha,xz} \\ \mathcal{P}^1_{\alpha,yz} & -\mathcal{P}^1_{\alpha,xz} & 0 \end{bmatrix} \tag{2.89}$$

While expanding the right hand side using Eqs[2.46, 2.82], we find

$$\Big(\frac{d\mathcal{P}^0_\alpha}{dt}\Big) = \begin{bmatrix} \frac{d\mathcal{P}^0_{\alpha,\perp}}{dt} & 0 & 0 \\ 0 & \frac{d\mathcal{P}^0_{\alpha,\perp}}{dt} & 0 \\ 0 & 0 & \frac{d\mathcal{P}^0_{\alpha,||}}{dt} \end{bmatrix}, \quad \Big(\mathcal{P}^0_{\alpha,ij}\frac{\partial u_{\alpha,k}}{\partial x_k}\Big) = \begin{bmatrix} \mathcal{P}^0_{\alpha,\perp}\frac{\partial u_{\alpha,k}}{\partial x_k} & 0 & 0 \\ 0 & \mathcal{P}^0_{\alpha,\perp}\frac{\partial u_{\alpha,k}}{\partial x_k} & 0 \\ 0 & 0 & \mathcal{P}^0_{\alpha,||}\frac{\partial u_{\alpha,k}}{\partial x_k} \end{bmatrix} \tag{2.90}$$

and,

$$\Big(\mathcal{P}^0_{\alpha,ik}\frac{\partial u_{\alpha,j}}{\partial x_k} + \mathcal{P}^0_{\alpha,jk}\frac{\partial u_{\alpha,i}}{\partial x_k}\Big) = \begin{bmatrix} 2\mathcal{P}^0_{\alpha,\perp}\frac{\partial u_{\alpha,x}}{\partial x} & \mathcal{P}^0_{\alpha,\perp}(\frac{\partial u_{\alpha,x}}{\partial y} + \frac{\partial u_{\alpha,y}}{\partial x}) & \mathcal{P}^0_{\alpha,\perp}\frac{\partial u_{\alpha,z}}{\partial x} + \mathcal{P}^0_{\alpha,||}\frac{\partial u_{\alpha,x}}{\partial z} \\ \mathcal{P}^0_{\alpha,\perp}(\frac{\partial u_{\alpha,x}}{\partial y} + \frac{\partial u_{\alpha,y}}{\partial x}) & 2\mathcal{P}^0_{\alpha,\perp}\frac{\partial u_{\alpha,y}}{\partial y} & \mathcal{P}^0_{\alpha,\perp}\frac{\partial u_{\alpha,z}}{\partial y} + \mathcal{P}^0_{\alpha,||}\frac{\partial u_{\alpha,y}}{\partial z} \\ \mathcal{P}^0_{\alpha,\perp}\frac{\partial u_{\alpha,z}}{\partial x} + \mathcal{P}^0_{\alpha,||}\frac{\partial u_{\alpha,x}}{\partial z} & \mathcal{P}^0_{\alpha,\perp}\frac{\partial u_{\alpha,z}}{\partial y} + \mathcal{P}^0_{\alpha,||}\frac{\partial u_{\alpha,y}}{\partial z} & 2\mathcal{P}^0_{\alpha,||}\frac{\partial u_{\alpha,z}}{\partial z} \end{bmatrix} \tag{2.91}$$

Two important remarks are obvious here. First, as the trace of a matrix is invariant under the basis transformation, then Eq.(2.89) implies $\mathcal{T}r(\mathcal{P}^1_\alpha) = 0 \implies \mathcal{P}^1_{\alpha,xx} = -\mathcal{P}^1_{\alpha,yy}$. The second observation is that $\mathcal{P}^1_{\alpha,zz} = 0$. Substituting the previous relations into Eq.(2.74), we easily find the FLR correction to the pressure tensor. It reads,

$$\mathcal{P}^1_{\alpha,xy} = \sigma_\alpha\frac{\mathcal{P}^0_{\alpha,\perp}}{2\omega_{c,\alpha}}\Big(\frac{\partial u_{\alpha,x}}{\partial x} - \frac{\partial u_{\alpha,y}}{\partial y}\Big), \tag{2.92a}$$

$$\mathcal{P}^1_{\alpha,yy} = -\mathcal{P}^1_{\alpha,xx} = \sigma_\alpha\frac{\mathcal{P}^0_{\alpha,\perp}}{2\omega_{c,\alpha}}\Big(\frac{\partial u_{\alpha,x}}{\partial y} + \frac{\partial u_{\alpha,y}}{\partial x}\Big), \tag{2.92b}$$

$$\mathcal{P}^1_{\alpha,xz} = -\frac{\sigma_\alpha}{\omega_{c,\alpha}}\Big(\mathcal{P}^0_{\alpha,\perp}\frac{\partial u_{\alpha,z}}{\partial y} + \mathcal{P}^0_{\alpha,||}\frac{\partial u_{\alpha,y}}{\partial z}\Big), \tag{2.92c}$$

$$\mathcal{P}^1_{\alpha,yz} = \frac{\sigma_\alpha}{\omega_{c,\alpha}}\Big(\mathcal{P}^0_{\alpha,\perp}\frac{\partial u_{\alpha,z}}{\partial x} + \mathcal{P}^0_{\alpha,||}\frac{\partial u_{\alpha,x}}{\partial z}\Big), \tag{2.92d}$$

where we have used Eq.(2.84a) to substitute the value of $\frac{d\mathcal{P}^0_{\alpha,\perp}}{dt}$. $\sigma_\alpha = sign(e_\alpha)$. It is interesting to notice that the terms $-\mathcal{P}^0_{\alpha,\perp}\frac{\partial u_z}{\partial z}$ and $\mathcal{P}^0_{\alpha,\perp} b_i b_j \frac{\partial u_i}{\partial x_j}$ cancel each other in this case ($\mathbf{b} = \mathbf{e}_z$). This does not require the use of Eq.(2.87) and then of generalized Ohm's law. Moreover, the block zz of Eq.(2.74) leads again to Eq.(2.84b). Therefore, there is no FLR correction along the magnetic field, which is intuitively understood. Accordingly, the pressure tensor now consists of two components: *gyrotropic* pressure ($\mathcal{P}^0_\alpha$) and *agyrotropic* correction (FLR) given by $\mathcal{P}^1_\alpha$ (the role of generalized Ohm's law in FLR and double adiabatic approximation has been discussed in details by Del Sarto and Pegoraro [190]). That is

$$\mathcal{P}_\alpha = \mathcal{P}^0_\alpha + \mathcal{P}^1_\alpha, \tag{2.93}$$

A more elegant independent coordinate system formula can be obtained for the FLR correction [191]. This can be done by first writing Eq.(2.74) as

$$\mathcal{M}(\mathcal{P}_\alpha) = \mathcal{S}_{b,\alpha}\mathcal{P}_\alpha - \mathcal{P}_\alpha\mathcal{S}_{b,\alpha} = [\mathcal{S}_{b,\alpha}, \mathcal{P}_\alpha] = \mathcal{R}_\alpha, \tag{2.94}$$

where,

$$\mathcal{R}_\alpha = \frac{\partial \mathcal{P}^0_\alpha}{\partial t} + \mathcal{L}(\mathcal{P}^0_\alpha), \quad \mathcal{S}_{b,\alpha} = \frac{e_\alpha}{m_\alpha}\epsilon_{ijk}B_k, \tag{2.95}$$

where [] is the commutator defined as $[A, B] = AB - BA$, where A and B are matrices. The previous equation represents a continuous Lyapunov equation [192], which is a subset of a more general one known as Sylvester equation [193]. In general, this equation does not have analytic solution for an arbitrary matrices $\mathcal{S}_{b,\alpha}$ and $\mathcal{R}_\alpha$, or it could have an infinite number of solutions. However, $\mathcal{S}_{b,\alpha}$ is a skew-matrix, and $\mathcal{P}_\alpha$ and $\mathcal{R}_\alpha$ are symmetric matrices. Thus it will be possible to construct, taking into account the nature of $\mathcal{P}_\alpha$ and $\mathcal{R}_\alpha$, an inverse of the commutator matrix. This gives the following equation for the FLR correction to pressure tensor

$$\begin{aligned}\mathcal{P}^1_\alpha = &\frac{\mathcal{P}^0_{\alpha,\perp}}{4\omega^2_{c,\alpha}}\Big\{(I + 3\mathbf{bb})(\mathcal{D} + \mathcal{D}^T)\mathcal{S}_{b,\alpha} + \mathcal{S}^T_{b,\alpha}(\mathcal{D} + \mathcal{D}^T)(I + 3\mathbf{bb})\Big\} \\ &+ \frac{2}{\omega^2_{c,\alpha}}(\mathcal{P}^0_{\alpha,||} - \mathcal{P}^0_{\alpha,\perp})\Big\{\mathbf{bb}\mathcal{D}^T\mathcal{S}_{b,\alpha} + \mathcal{S}^T_{b,\alpha}\mathcal{D}\mathbf{bb}\Big\}.\end{aligned} \tag{2.96}$$

In the above equation, $\mathbf{b}$ has an arbitrary orientation in the corresponding coordinate system. $\mathcal{D}_{ij} = \partial_j u_i$. When $\mathbf{b} = \mathbf{e}_z$, Eq.(2.96) reduces to Eq.(2.92).

2.3.6 Constitutive Closure Equation: Hydrodynamic Limit

In this section, we are going to discuss how to close the system of equations (2.26, 2.36, and 2.56) by finding a constitutive equation between the full pressure tensor and the fluid velocity -more precisely its gradient. One should be extremely careful about this derivation. First of all, it does not account for the magnetic field (purely hydrodynamic fluid). Second, it helps us to obtain the term which incorporates the ion viscosity into reduced, collisional MHD model. Furthermore, it clearly distinguishes between diffusion effects of the fluid velocity due to non-zero viscosity (divergence of the strain tensor), and the compressibility of the fluid (varying density).

In general, we can decompose the fluid element motion into three dominant components[194, 195, 196]. The first is a translational motion along the streamlines of the fluid, which characterizes the macroscopic behaviour of the fluid. The second is a pure rotation characterized by the vorticity vector $\mathbf{\Omega} = \nabla \times \mathbf{u}$, which depends on the frame of reference. For example, we can choose

a rotating reference in which the vorticity vanishes. The third component is the deformation of the fluid elements due to viscosity of the fluid (generally speaking, due to kinetic effects). One can easily show, as we are going to do next, that matrices can represent the last two components of the motion[197],[198], [195]. These matrices are the anti-symmetric rotation matrix $\mathcal{R}$ (skew-matrix), which varies with the frame of reference, and the symmetric strain matrix $\mathcal{D}$, which represents the deformation of fluid elements due to kinetic effects and is invariant under Galilean transformation. In effect, this invariance property is one of the critical assumptions that allow us to obtain a general relationship between the (hydro)-full pressure tensor and the velocity gradient [199]. The decomposition of the gradient velocity tensor $\mathcal{G}^{\mathbf{v}}$ gives,

$$\mathcal{G}^{\mathbf{v}}{}_{ij} = \frac{\partial u_{\alpha,i}}{\partial x_j} = \underbrace{\frac{1}{2}\left(\frac{\partial u_{\alpha,i}}{\partial x_j} + \frac{\partial u_{\alpha,j}}{\partial x_i}\right)}_{\mathcal{D}_{\alpha,ij}\,:\,\textbf{Symmetric Tensor}} + \frac{1}{2}\underbrace{\left(\frac{\partial u_{\alpha,i}}{\partial x_j} - \frac{\partial u_{\alpha,j}}{\partial x_i}\right)}_{\mathcal{R}_{\alpha,ij}\,:\,\textbf{Anti-symmetric Tensor}} = \mathcal{D}_\alpha + \frac{1}{2}\mathcal{R}_\alpha \tag{2.97}$$

where $\mathcal{R}_{ij} = -\varepsilon_{ijk}\Omega_k$.

However, the fluid can be divided, concerning viscosity, into two categories: *Newtonian fluid* and *Non-Newtonian fluid*. The former is the fluid in which the pressure tensor is linearly dependent on the rate of deformation, and the proportionality factor, in this case, is the viscosity tensor which is independent of the strain tensor (velocity gradient). Whereas the later is the fluid in which the viscosity tensor depends on applied pressures or forces. Therefore the relationship between the full pressure tensor and the strain tensor is no longer a linear one. In this section, we focus only on Newtonian fluid. When the fluid moves, the pressure tensor takes the form given by Eq.(2.32),

$$\mathcal{P}_{\alpha,ij} = p_\alpha \delta_{ij} + \Pi_{\alpha,ij} \tag{2.98}$$

The most general form of constitutive equation for Newtonian fluid is

$$\Pi_{\alpha,ij} = -\tau_{\alpha,ij} = -\mathcal{K}_{ijqr} D_{qr}, \tag{2.99}$$

where $\mathcal{K}_{ijqr}$ is fourth-order tensor known as viscosity cofficients, and $\tau_{\alpha,ij}$ is the viscous stress tensor. We should be careful about interpreting the minus sign, which results from the different definitions of the two quantities: stress and pressure. The pressure exerted on a fluid element is the force per unit area applied on its surface and points in the opposite direction of the surface unit vector $\hat{\mathbf{n}}$, that is $\mathbf{f_n} = -\mathcal{P}_\alpha \cdot \hat{\mathbf{n}}$. In contrast, the stress is the force per unit area exerted by the fluid on the side toward which the $\hat{\mathbf{n}}$ points -equals $\mathbf{f_n}$ but in the opposite direction. $\mathcal{K}_{ijqr}$ must be isotropic. This property ensures that the linear relationship between the viscous tensor $\Pi_{\alpha,ij}$ and strain tensor remains independent of the coordinate system in isotropic fluid. One can prove that any isotropic fourth-order tensor can be written in terms of Kronecker second-order tensor[200]. This relationship is given by,

$$\mathcal{K}_{ijqr} = \lambda\delta_{ij}\delta_{qr} + \mu\delta_{iq}\delta_{jr} + \gamma\delta_{ir}\delta_{jq}, \tag{2.100}$$

But, we also know that the viscous tensor is symmetric ($\Pi_{ij} = \Pi_{ji}$), then $\mathcal{K}_{ijqr} = \mathcal{K}_{jiqr} \implies \gamma = \mu$. Therefore the previous equation becomes

$$\mathcal{K}_{ijqr} = \lambda\delta_{ij}\delta_{qr} + 2\mu\delta_{iq}\delta_{jr}, \tag{2.101}$$

Substituting this previous equation into Eq.(2.99), one obtains

$$\Pi_{\alpha,ij} = -2\mu\mathcal{D}_{ij} - \lambda D_{qq}\delta_{ij}, \tag{2.102}$$

where $\mathcal{D} = \sum_q \frac{\partial u_{\alpha,q}}{\partial x_q} = \nabla \cdot \mathbf{u}_\alpha$ which represents the volumetric strain (the *compressibility* of the fluid). We can define the *mean pressure* as the average of the diagonal elements of the full pressure tensor ($\tilde{p}_\alpha = \frac{1}{3}\mathbf{Tr}(\mathcal{P}_\alpha)$), knowing that these three diagonal elements are not necessarily equals. For example, this is the case of magnetized plasma in which there is equipartition of the energy in the two different directions perpendicular to the magnetic field, but this is not the case for parallel direction -we are going to study this case (double adiabatic closure) in details later. Substituting Eq.(2.102) into Eq.(2.98), and summing on the diagonal elements, we obtain:

$$\begin{aligned} \mathcal{P}_{\alpha,ii} = 3p_\alpha - (2\mu_\alpha + 3\lambda_\alpha)\mathcal{D}_{\alpha,qq} \quad &\Longrightarrow \; p_\alpha = \frac{1}{3}\mathcal{P}_{\alpha,ii} + (\frac{2}{3}\mu_\alpha + \lambda_\alpha)\mathcal{D}_{\alpha,qq} \\ p_\alpha - \tilde{p}_\alpha = (\frac{2}{3}\mu_\alpha + \lambda_\alpha)\mathcal{D}_{\alpha,qq} &= (\frac{2}{3}\mu_\alpha + \lambda_\alpha)\nabla \cdot \mathbf{u}_\alpha = \kappa_\alpha \nabla \cdot \mathbf{u}_\alpha, \end{aligned} \tag{2.103}$$

κ_α is known as the bulk viscosity coefficient. We can understand the term on the right-hand side of the previous equation to be the difference between the thermodynamic pressure and mean (mechanical) pressure. In general, one can consider it due to the time lag with which the thermodynamics conditions are reached. On the one hand, neglecting this term (Stokes assumption [201]) allows obtaining simplified models which in turn give accurate descriptions of the fluid dynamics, and their results are in excellent agreement with experiments. On the other hand, justifying this assumption, by considering that the bulk viscosity is negligible, had shown to be not satisfying. That is because, except for mono-atomic gases, $\kappa_\alpha > \mu_\alpha$ for many fluids [202], and their ratio spans a wide range of values from small to huge ones. Therefore, κ_α may play a key role in some cases, such as shock/hydrogen bubble interaction [203]. Furthermore, contrary to the usual claim that κ_α is one of the fundamental results of kinetic theory, Truesdell showed [204] that this zero value was implicitly assumed in the kinetic theory of gases. In summary, to justify this assumption on a physical ground, we can postulate that the `RHS` of Eq.(2.103) is negligible as long as $|\kappa_\alpha \nabla \cdot \mathbf{u}_\alpha| << p_\alpha$[205, 206] which may appear "logical" because the term $\nabla \cdot \mathbf{u}_\alpha$ contributes to the volumetric compression of the fluid element.

Now, by applying the Stokes assumption, and substituting Eq.(2.102) into Eq.(2.98), taking into account that $\kappa_\alpha = \frac{2}{3}\mu_\alpha + \lambda$, one finds,

$$\mathcal{P}_{\alpha,ij} = p_\alpha \delta_{ij} - 2\mu_\alpha[\mathcal{D}_{\alpha,ij} - \frac{1}{3}\mathcal{D}_{\alpha,qq}\delta_{ij}] \;\Longrightarrow\; \mathcal{P}_{\alpha,ij} = p_\alpha \delta_{ij} - \mu_\alpha W_{\alpha,ij}, \tag{2.104}$$

where,

$$W_{\alpha,ij} = \Big[\frac{\partial u_{\alpha,i}}{\partial x_j} + \frac{\partial u_{\alpha,j}}{\partial x_i} - \frac{2}{3}(\nabla \cdot \mathbf{u}_\alpha)\delta_{ij}\Big], \tag{2.105}$$

This relationship allows closing the system of equations for Newtonian fluid as it provides us with a dependence of the higher-dimensional quantity ($\mathcal{P}_\alpha$) on lower one u through a transport coefficient, which is, in this case, the viscosity. Now, substituting Eq.2.104 into momentum equation, and assuming an incompressible fluid, one easily obtains,

$$\nabla \cdot \mathcal{P} = \nabla p - \nu \Delta u, \tag{2.106}$$

where ν is the viscosity, and u is the averaged velocity of the plasma. Therefore, this model accounts for some kinetic effects through the viscous term, which measures the deformation of the fluid element. We can apply this closure with either multi-fluid models where we consider each species consists a fluid, and thus the viscosity in the previous relationship will be either the ion viscosity or the electron one. It is also possible to use this closure with one fluid model in which ions carry the bulk motion of the plasma, and hence the viscosity here will be the ion viscosity.

2.4 One Fluid Model

In the previous sections, we derived the multi-fluid models (or two-fluid model if the plasma consists of ions and electrons) by introducing macroscopic measures which ignore the detailed information involved in the velocity space. Hence, it allows obtaining evolution equations for these quantities at some price: the closure problem. However, there is another drawback: the lack of ability of this model to explain some kinetic phenomena and adequately describe many others, but we assume for now that they are not of main concern here.

However, even if the two-fluid model accounts precisely for the physics in the studied case adopting physically-suitable closure relationships, this model still encompasses a wide spectrum of time and spatial scales. Scanning a wide range of scales might not be essential for understanding various interesting phenomena (ideal MHD activities, instabilities of the bulk plasma, design considerations of fusion machines, etc..). Therefore, further reduced models might be preferable. The first step when deriving these models is to clearly write down the characteristic scales of the problem and then normalize all the quantities to them. This provides information about their magnitudes. Thus, as for the specific model we attempt to obtain, all reduced models use some asymptotic ordering introduced to eliminate undesirable information. In this context, two essential approximations are introduced to eliminate high frequencies and short-wavelengths. Therefore, they lead to non-relativistic one-fluid model. First, the displacement current in the Maxwell-Ampere equation is neglected if the phase velocities are much smaller than the light speed, which can be accomplished by formally requiring the limit $c \to \infty$. It hence ensures the quasi-neutrality assumption of the hot plasma. The second approximation is to neglect the electrons' inertia due to their low mass (formally by seeking the limit $m_e \to 0$). This assumption is justified by the fast response of the electrons ($\omega \ll \omega_{pe}$), which means a large number of electron plasma oscillations occurs before one period of the wave is completed. Hence these activities last over time scales quite far from the characteristic one of the wave (However, this hypothesis is not always valid in the context of magnetic reconnection which can be initiated by the electron inertia -thus the name collisionless magnetic reconnection). A third approximation, strongly connected to the second one, corresponds to neglecting terms proportional to electron-ion mass ration ($\epsilon_m = \frac{m_e}{m_i}$). We summarize the parameters' range for non-relativistic one-fluid model, as obtained in Refs.[207, 208], in the following form

$$\text{Length: } a \gg \rho_i \gg \rho_e \sim \lambda_{De}, \tag{2.107a}$$

$$\text{Frequency: } \nu_{ei} \ll \frac{v_{Ti}}{a} \ll \omega_{ci} \ll \omega_{pi} \sim \omega_{pe}, \tag{2.107b}$$

$$\text{Velocity: } v_{Ti} \sim v_A \ll v_{Te} \ll c, \tag{2.107c}$$

with the perturbation parameter,

$$\epsilon_m = \frac{m_e}{m_i}, \tag{2.108}$$

In the previous equation, a is the characteristic length of the problem, ρ_i the ion-Larmor radius, ρ_e is the electron-Larmor radius, λ_{De} is the Debye length, ν_{ei} is the ion-electron collision frequency, v_{Ti} is ion thermal velocity, v_{Te} is the electron thermal velocity, v_A is the Alfvén velocity, and c is the speed of light, while ω_{ci} is the ion–cyclotron frequency, ω_{pi} is the ion-plasma frequency, and ω_{pe} is the electron-plasma frequency. The details of this ordering will be clearly understood when writing down the derivation.

Nevertheless, it is worth stressing the fact that other models can be obtained by completely following another ordering. For example, this is the case of electron-MHD model in which the dynamic of the system evolves on fast time scales such that ions form a neutralizing background.

In this case, the electron dynamic decouples from ions' one and occurs on spatial length "smaller" than ion-skin depth (d_i) -we are going to see this later.

2.4.1 One-Fluid Density Equation

We define the one-fluid density as the sum of the two species densities making up the plasma: ions and electrons. It reads,

$$\rho = m_i n_i + m_e n_e = n(m_i + m_e) \approx m_i n, \tag{2.109}$$

where we used the quasi-neutrality principle ($n_i = n_e = n$), and neglected the electron mass $m_e \ll m_i$. The density equation can be obtained by summing the averaging Vlasov equation over momentum space, and the summing it over the species consisting the plasma. We denote this as $\sum_\alpha \int\int\int m_\alpha V(f_\alpha) d\mathbf{v}$. That is,

$$\begin{aligned}\sum_\alpha \int\int\int m_\alpha V(\alpha) d\mathbf{v} = \sum_\alpha \int\int\int m_\alpha \Big[&\frac{\partial f_\alpha(\mathbf{r},\mathbf{v},t)}{\partial t} + \mathbf{v}\cdot\nabla_\mathbf{r} f_\alpha(\mathbf{r},\mathbf{v},t) \\ &+ \frac{e_\alpha}{m_\alpha}\Big[\mathbf{E} + \mathbf{v}\times\mathbf{B}\Big]\cdot\nabla_\mathbf{v} f_\alpha(\mathbf{r},\mathbf{v},t)\Big] d\mathbf{v} = 0,\end{aligned} \tag{2.110}$$

which gives

$$\frac{\partial n}{\partial t} + \nabla\cdot(n\mathbf{u}) = 0, \tag{2.111}$$

where $\mathbf{u}$ is the total averaged velocity given by,

$$\rho\mathbf{u} = m_i n_i \mathbf{u}_i + m_e n_e \mathbf{u}_e, \implies \mathbf{u} = \mathbf{u}_i + \epsilon_m \mathbf{u}_e \approx \mathbf{u}_i, \tag{2.112}$$

where we used Eq.(2.109). The main consequence of the previous line is that the momentum of the plasma is carried by the ions. This equation can be written in dimensionless form by introducing the characteristic length L_0, the characteristic velocity u_0, and the characteristic time τ_0. Then the dimensionless quantities become:

$$n = n_0\tilde{n}, \quad \mathbf{u} = u_0\tilde{\mathbf{u}}, \quad t = \tau_0\tilde{t}, \tag{2.113}$$

Substituting this equation into Eq.(2.111), and removing the sign $\sim$, the dimensionless density equation becomes,

$$\frac{\partial n}{\partial t} + \frac{\tau_0 u_0}{L_0}\nabla\cdot(n\mathbf{u}) = 0, \tag{2.114}$$

To preserve the shape of the density equation, we take $\tau_0 = \frac{L_0}{u_0}$, which gives again Eq.(2.111) but with dimensionless quantity now. u_o in this model is Alfvén velocity $u_i = B/\sqrt{\mu_0 m_i n}$ which characterizes the electromagnetic wave propagation in one-fluid plasma (MHD activities), and thus $\tau_0 = \tau_A = L_0/v_A$.

2.4.2 One-Fluid Momentum Equation

We can obtain the motion equation of one-fluid model by summing the equations of motion of the two species or calculating

$$\sum_{\alpha=i,e} \int\int\int m_\alpha \mathbf{v} V(f_\alpha) d\mathbf{v}, \tag{2.115}$$

where $V(f_\alpha)$ is given by Eq.(2.18). However, before going on with the derivation, we should be aware of three reference frames exist here. When approximating the plasma as one-fluid, three averaged velocities naturally appear, namely:$\mathbf{u}_e$, $\mathbf{u}_i$, and $\mathbf{u}$. The pressure tensor of $\alpha-$type species is estimated in a reference frame moving with speed equals to $\mathbf{u}_\alpha$ [Eq.(2.31)]. In contrast, the bulk plasma has an averaged velocity equals to $\mathbf{u}$. These different frames introduce three characteristic velocities: two random velocities, and a diffusive one. The first random velocity ($\mathbf{s}_\alpha = \mathbf{v} - \mathbf{u}_\alpha$) is used to calculate $\mathcal{P}_\alpha$ in the correct reference frame. The second one is the total random velocity ($\mathbf{s_t} = \mathbf{v} - \mathbf{u}$) allowing estimating the local deviation of the absolute velocity ($\mathbf{v}$) from the bulk velocity ($\mathbf{u}$), which is required when averaging over momentum space. The third one ($\mathbf{w}_\alpha = \mathbf{u}_\alpha - \mathbf{u}$) is a measure of the relative motions between the three reference frames. The relation between these velocities is given by

$$\mathbf{w}_\alpha = \mathbf{s}_t - \mathbf{s}_\alpha, \tag{2.116}$$

Now, with the help of Eqs.[2.20, 2.21, 2.22, 2.23], one finds

$$I^1 = \frac{\partial}{\partial t}\Big(\sum_{\alpha=i,e}\int m_\alpha \mathbf{v} f_\alpha dv\Big) = \frac{\partial}{\partial t}\Big(\sum_{\alpha=i,e}\int m_\alpha(\mathbf{s}_\alpha+\mathbf{u}_\alpha) f_\alpha d\mathbf{v}\Big) = \frac{\partial}{\partial t}[(\sum_{\alpha=i,e}\int (m_\alpha n_\alpha \mathbf{u}_\alpha)] = \frac{\partial}{\partial t}(\rho\mathbf{u}), \tag{2.117}$$

$$\begin{aligned} I^2 &= \nabla\cdot\Big[\sum_{\alpha=i,2}\int m_\alpha \mathbf{v}\mathbf{v} f_\alpha d\mathbf{v}\Big] = \nabla\cdot\Big[\sum_{\alpha=i,e}\int m_\alpha(\mathbf{s}_\alpha+\mathbf{w}_\alpha+\mathbf{u})(\mathbf{s}_\alpha+\mathbf{w}_\alpha+\mathbf{u}) f_\alpha d\mathbf{v}\Big] \\ &= \nabla\cdot\Big[\sum_{\alpha=i,2}\int m_\alpha(\mathbf{s}_\alpha\mathbf{s}_\alpha+\mathbf{w}_\alpha\mathbf{w}_\alpha+\mathbf{u}\mathbf{u}) f_\alpha d\mathbf{v} = \nabla\cdot\sum_{\alpha=i,2}\Big(\mathcal{P}_\alpha + m_\alpha n_\alpha \mathbf{w}_\alpha\mathbf{w}_\alpha\Big) + \nabla\cdot(\rho\mathbf{u}\mathbf{u}) \\ &= \nabla\cdot\mathcal{P} + \nabla\cdot(\rho\mathbf{u}\mathbf{u}), \end{aligned} \tag{2.118}$$

where we used Eq.(2.31), and Eq.(2.116). $\mathcal{P}$ is the total pressure tensor of the plasma, and it is given by

$$\mathcal{P} = \sum_{\alpha=i,e}[\mathcal{P}_\alpha + m_\alpha n_\alpha \mathbf{w}_\alpha\mathbf{w}_\alpha] = \sum_{\alpha=i,e}[\mathcal{P}_\alpha + m_\alpha n_\alpha \mathbf{u}_\alpha\mathbf{u}_\alpha] - \rho\mathbf{u}\mathbf{u}, \tag{2.119}$$

In obtaining Eq.(2.118), we also used the fact that the total momentum of the plasma is conserved, and the only allowed momentum transfer is between the two species. Therefore, ($\sum_{\alpha=i,e} m_\alpha n_\alpha \mathbf{w}_\alpha = m_e n\mathbf{w}_e + m_i n\mathbf{w}_i = m_e n\mathbf{u}_e + m_i n\mathbf{u}_i - \rho\mathbf{u} = 0$). Then, for example, $m_e n_e \mathbf{w}_e$ will represent the momentum transfer from electron fluid to ions. Now, Eq.(2.22) gives,

$$I^E_j = \sum_{\alpha=i,e} -e_\alpha E_j \int \delta_{ij} f_\alpha d\mathbf{v} = -E_i \sum_{\alpha=i,e}(e_\alpha n_\alpha) = 0, \quad j = 1,2,3.\ \text{(quasi-neutrality)}, \tag{2.120}$$

Finally, the magnetic part reads

$$I^B_j = -\epsilon_{ijk} B_k \sum_{\alpha=i,e} e_\alpha n_\alpha u_{\alpha,j} = -\epsilon_{ijk} B_k J_j = -\mathbf{J}\times\mathbf{B}|_j, \tag{2.121}$$

In the previous equation we used Eq.(2.34). The one-fluid current density is given by

$$\mathbf{J} = \sum_{\alpha=i,e} e_\alpha n_\alpha \mathbf{u}_\alpha = en(\mathbf{u}_i - \mathbf{u}_e), \tag{2.122}$$

Substituting Eqs.[2.117, 2.118, 2.120, 2.121] in Eq.(2.115), we find the equation of motion

$$\frac{\partial}{\partial t}(\rho \mathbf{u}) + \nabla \cdot (\rho \mathbf{u}\mathbf{u}) = -\nabla \cdot \mathcal{P} + \mathbf{J} \times \mathbf{B}, \tag{2.123}$$

It is possible, under some conditions (to be discussed later), to approximate the pressure tensor using the constitutive relationship given by Eq.(2.105). Hence,

$$\frac{\partial}{\partial t}(\rho \mathbf{u}) + \nabla \cdot (\rho \mathbf{u}\mathbf{u}) = -\nabla p + \mathbf{J} \times \mathbf{B} + \nu \Delta \mathbf{u}, \tag{2.124}$$

p is the total mechanical pressure defined as the average of the diagonal elements of the pressure tensor. It reads,

$$p = \frac{1}{3}\sum \mathcal{P}_{ii} = \sum_{\alpha=i,e} [p_\alpha + \frac{1}{3} m_\alpha n_\alpha w_\alpha^2], \tag{2.125}$$

Two interesting consequences follows from Eq.(2.122). One one hand, due to the quasi-neutrality, the leading order velocity ($\mathbf{v}_{\mathbf{E}\times\mathbf{B}}$) does not contribute to the current density because it is the same for all species. One the other hand, we can write the current density in terms of $\mathbf{u}$ which equals to $\mathbf{u}_i$ in this model. Therefore, one obtains

$$\mathbf{u} \times \mathbf{B} = (\mathbf{u}_e + \frac{\mathbf{J}}{en}) \times \mathbf{B} = \mathbf{u}_e \times \mathbf{B} + \frac{\mathbf{J}}{en} \times \mathbf{B}, \tag{2.126}$$

Eq.(2.126) implies that the magnetic field is carried by electrons. Finally we discuss the dimensionless form of Eqs.(2.123, 2.124). The dimensionless quantities are given by,

$$\rho = \rho_0 \tilde{\rho},\ t = \tau_0 \tilde{t},\ \mathbf{u} = u_0 \tilde{\mathbf{u}},\ p = p_0 \tilde{p},\ \mathbf{B} = B_0 \tilde{\mathbf{B}},\ \mathbf{J} = J_0 \tilde{J} = \frac{B_0}{\mu_0 L_0} \tilde{\mathbf{J}},\ x = L_0 \tilde{x} \tag{2.127}$$

where Maxwell-Ampere equation has been employed to relate the normalization of current density and magnetic filed. After substituting into Eq.(2.124) and removing $\sim$ sign, the dimensionless equation of motion reads

$$\frac{\partial}{\partial t}(\rho \mathbf{u}) + \nabla \cdot (\rho \mathbf{u}\mathbf{u}) = -\nabla p + \mathbf{J} \times \mathbf{B} + R^{-1} \Delta \mathbf{u}, \tag{2.128}$$

where $R = \frac{\rho L_0 u_0}{\nu}$ is the fluid Reynolds number. This equation can be further simplified by using the continuity equation and Eq.(B.28), which gives

$$\rho \frac{\partial \mathbf{u}}{\partial t} + \rho \mathbf{u} \cdot \nabla \mathbf{u} = -\nabla p + \mathbf{J} \times \mathbf{B} + R^{-1} \Delta \mathbf{u}, \tag{2.129}$$

We stress the fact that in conserving the shape of the dimensional equation, we assumed the following orderings are made for the dimensionless Navier-Stokes equation:

$$u_0 \sim \frac{L_0}{\tau_0}, \quad p_0 \sim \rho_0 u_0^2 \sim \frac{B_0^2}{\mu_0}, \quad u_0 \sim u_A = \frac{B_0}{\sqrt{\mu_0 \rho_0}}, \tag{2.130}$$

This ordering is consistent with one of the main assumptions behind the derivation of Reduced-MHD: the strong guide field. B_0, appearing in the ordering above, is the magnetic field in a perpendicular plane to the guide field. Also, this ordering is suitable for low-β plasma where $\frac{p_0 \mu_0}{B_{guide}^2} \ll 1$ [180, 33].

2.4.3 Generalized Ohm's Law

The equation of motion, derived in the previous section, describes the time evolution of the plasma momentum. At the same time, generalised Ohm's law covers the current density evolution, which does not appear in the equation in its most simplified form (ideal Ohm law). Ideal Ohm's law imposes a solid restriction on the dynamic of particles and magnetic field. It states that the magnetic field and plasma are co-moving together. Therefore, the topology of the field lines is conserved with time, meaning that the magnetic energy will remain stored in the field topology, and thus prevents the plasma from evolving toward lower energy state, thereby converting some of the stored magnetic energy into kinetic energy. Generalized Ohm's law can be obtained by calculating

$$\sum_{\alpha=i,e} \int\int\int e_\alpha \mathbf{v} V(f_\alpha) d\mathbf{v}, \tag{2.131}$$

where $V(f_\alpha)$ is given by Eq.(2.18). Again using Eqs.[2.20, 2.21, 2.22, 2.23], one finds

$$I^1 = \frac{\partial}{\partial t}\Big(\sum_{\alpha=i,e} e_\alpha \int \mathbf{v} f_\alpha d\mathbf{v}\Big) = \frac{\partial}{\partial t}\Big(\sum_{\alpha=i,e} e_\alpha n_\alpha u_\alpha\Big) = \frac{\partial \mathbf{J}}{\partial t}, \tag{2.132}$$

$$\begin{aligned} I^2 &= \nabla \cdot \sum_{\alpha=i,e} e_\alpha \int \mathbf{v}\mathbf{v} f_\alpha d\mathbf{v} = \nabla \cdot \sum_{\alpha=i,e} e_\alpha \int (\mathbf{s}_\alpha \mathbf{s}_\alpha + \mathbf{w}_\alpha \mathbf{w}_\alpha + \mathbf{s}_\alpha \mathbf{w}_\alpha + \mathbf{w}_\alpha \mathbf{s}_\alpha + \mathbf{u}\mathbf{u}) f_\alpha d\mathbf{v} \\ &= \nabla \cdot \sum_{\alpha=i,e} \frac{e_\alpha}{m_\alpha} \mathcal{P}_\alpha + \nabla \cdot \sum_{\alpha=i,e} e_\alpha n_\alpha \mathbf{w}_\alpha \mathbf{w}_\alpha + \sum_{\alpha=i,e} e_\alpha n_\alpha \mathbf{u}_\alpha \mathbf{w}_\alpha + \sum_{\alpha=i,e} e_\alpha n_\alpha \mathbf{w}_\alpha \mathbf{u}_\alpha + \sum_{\alpha=i,e} e_\alpha n_\alpha \mathbf{u}\mathbf{u}, \end{aligned} \tag{2.133}$$

The last term in the previous equation vanishes because of the quasi-neutrality assumption. On the other hand, as a consequence of equalities $\mathbf{u} = \mathbf{u}_i$ and $\mathbf{u}_e = \mathbf{u}_i - \frac{\mathbf{J}}{en}$, it can be easily shown using the definition of diffusive velocity and Eq.(2.122) that

$$\mathbf{w}_i = 0, \quad \mathbf{w}_e = -\frac{\mathbf{J}}{en}, \tag{2.134}$$

Therefore, expanding Eq.(2.133), and substituting Eq.(2.134) in it, we find

$$I^2 = \frac{e}{m_i} \nabla \cdot \mathcal{P}_i - \frac{e}{m_e} \nabla \cdot \mathcal{P}_e - \nabla \cdot \{\frac{\mathbf{J}\mathbf{J}}{en}\} + \nabla \cdot \{\mathbf{J}\mathbf{u} + \mathbf{u}\mathbf{J}\}, \tag{2.135}$$

Now, the electric and magnetic field's contributions are given by summing over Eqs.[2.22, 2.23]

$$I_i^E = -E_j \sum_{\alpha=i,e} \frac{e_\alpha^2}{m_\alpha} \int \delta_{ij} f_\alpha d\mathbf{v} = -e^2 n \underbrace{(\frac{1}{m_i} + \frac{1}{m_e})}_{m_i \gg m_e} E_i = -\frac{e^2 n}{m_e} E_i, \tag{2.136}$$

while,

$$\begin{aligned} I_i^B &= -\epsilon_{ljk} B_k \sum_{\alpha=i,e} \frac{e_\alpha^2 n_\alpha}{m_\alpha} < \frac{\partial (v_i v_j)}{\partial v_l} >_\alpha = -e^2 n \epsilon_{ijk} B_k \{\frac{u_{i,j}}{m_i} + \frac{u_{e,j}}{m_e}\} \\ &= -e^2 n \epsilon_{ijk} B_k \{\underbrace{\frac{u_j}{m_i} + \frac{u_j}{m_e}}_{m_i \gg m_e} - \frac{J_j}{m_e e n}\} = -\frac{e^2 n}{m_e} \mathbf{u} \times \mathbf{B}|_i + \frac{e}{m_e} \mathbf{J} \times \mathbf{B}|_i, \end{aligned} \tag{2.137}$$

In the previous equation we used $\mathbf{u} = \mathbf{u}_i$, $\mathbf{u}_e = \mathbf{u} - \frac{J}{en}$, and Eq.(2.34). Substituting Eqs.[2.132, 2.135, 2.136, 2.137] into Eq.(2.131), and after multiplying two the sides with $\frac{m_e}{e^2 n}$, one obtains

$$\mathbf{E}+\mathbf{u}\times\mathbf{B} = \frac{m_e}{e^2 n}\frac{\partial \mathbf{J}}{\partial t} + \epsilon_m \frac{1}{en}\nabla\cdot\mathcal{P}_i - \frac{1}{en}\nabla\cdot\mathcal{P}_e + \frac{m_e}{e^2 n}\nabla\cdot\{\mathbf{uJ}+\mathbf{Ju}\} - \frac{m_e}{e^2 n}\nabla\cdot\{\frac{\mathbf{JJ}}{en}\} + \frac{1}{en}\mathbf{J}\times\mathbf{B} + \eta\mathbf{J}, \tag{2.138}$$

The last term in Eq.(2.138) did not result from averaging procedure of Vlasov equation (it is clearly a transport coefficient). Rather, it was included depending on heuristic argument starting with the momentum equations of ions and electrons Eqs.[2.36]. In these equations we approximate $\Upsilon^{\alpha,\mathcal{M}}$ as follow

$$\Upsilon^{i,\mathcal{M}} = -m_i n \nu_{ie}(\mathbf{u}_i - \mathbf{u}_e), \quad \Upsilon^{i,\mathcal{M}} = -m_e n \nu_{ei}(\mathbf{u}_e - \mathbf{u}_i), \tag{2.139}$$

then,

$$\sum_{\alpha=i,e}\frac{e_\alpha}{m_\alpha}\Upsilon^{\alpha,\mathcal{M}} = \frac{e}{m_i}\Upsilon^{i,\mathcal{M}} - \frac{e}{m_e}\Upsilon^{e,\mathcal{M}} = -en\nu_{ei}(\mathbf{u}_i - \mathbf{u}_e)\underbrace{\{1+\epsilon_m\}}_{\epsilon_m \ll 1} = -\nu_{ei}\mathbf{J}, \tag{2.140}$$

In the previous equation, we used the fact that $m_i\nu_{ie} = m_e\nu_{ie}$. Then multiplying this term with $\frac{m_e}{e^2 n}$, one obtains the term $\eta\mathbf{J}$, where

$$\eta = \frac{m_e \nu_{ei}}{e^2 n}, \tag{2.141}$$

The previous estimation of η is simplified and does not account for anisotropy introduced by the magnetic field, or the effects of the electric field, many-body interactions, etc... In this case, the transport coefficients are calculated by first ordering the kinetic equation in the power of a perturbation parameter ϵ_v, that is $f_\alpha = f^0_\alpha(1 + \epsilon_v\phi(\mathbf{v}) + \epsilon_v^2\psi(\mathbf{v}) + ..)$ [178, 209]. Then we integrate all the terms, including collision term, over velocity space, and match the terms of the same power of ϵ_v[15] which finally give the accurate closure equations which relate quantities from higher dimensions with those of lower ones through transport coefficients, which is clearly more accurate than those discussed in section 2.3 [210, 211, 212].

Before discussing the normalization of the generalized Ohm's law, Eq.(2.138) can be written in terms of electron skin depth d_e, given by

$$d_e = \frac{c}{\omega_{pe}} = \sqrt{\epsilon_m} d_i, \quad d_e^2 = \frac{m_e}{\mu_0 e^2 n_0}, \tag{2.142}$$

Then,

$$\mathbf{E}+\mathbf{u}\times\mathbf{B} = \mu_0 d_e^2\frac{\partial \mathbf{J}}{\partial t} + \epsilon_m \frac{1}{en}\nabla\cdot\mathcal{P}_i - \frac{1}{en}\nabla\cdot\mathcal{P}_e + \mu_0 d_e^2\nabla\cdot\{\mathbf{uJ}+\mathbf{Ju}\} - \mu_0 d_e^2\nabla\cdot\{\frac{\mathbf{JJ}}{en}\} + \frac{1}{en}\mathbf{J}\times\mathbf{B} + \eta\mathbf{J}, \tag{2.143}$$

Before the normalization of the generalized Ohm's law, we write some useful relationships which used frequently when normalizing MHD equations. They are

$$\omega_{c,i} = \epsilon_m\omega_{c,e}, \quad u_0 = \frac{B_0}{\sqrt{\mu_0 m_i n_0}} = \omega_{c,i}d_i = \epsilon_m^{\frac{1}{2}}\omega_{c,e}d_e, \quad \rho_s = \epsilon_m^{\frac{1}{2}}\frac{v_{th,e}}{\omega_{c,i}}, \quad v_{th,\alpha} = \sqrt{\frac{kT_\alpha}{m_\alpha}}, \tag{2.144}$$

We can utilise these relationships, in addition to auxiliary scalings resulting from Maxwell equations, to find the non-dimensional form of generalised Ohm law. Still, the reference pressure

[15] In fact, ϵ_v is a formal expansion parameter which shows the importance of the collisions. It helps us to group together the terms of the same order (see Chapman and Cowling [178] for details).

p_0 can be chosen based on different physical arguments. For example, if the pressure in the perpendicular plane is of the same order of the magnetic energy in that plane, then it will seem natural to choose as a reference pressure the magnetic energy ($p_0 \sim \rho u_0^2 \sim B_0^2/\mu_0$). Another choice is the thermodynamic pressure ($p_0 \sim n_0 k T_{\alpha,0}$) . In the former, the ion skin depth (d_i) enters the scene, while in the latter the ion-sound Larmor radius (ρ_s) appears as a spatial scale into the equation. With this in mind, the first choice gives

$$\mathbf{E}+\mathbf{u}\times\mathbf{B} = d_e^2\frac{\partial \mathbf{J}}{\partial t}+\epsilon_m d_i\frac{\nabla\cdot\mathcal{P}_i}{n}-d_i\frac{\nabla\cdot\mathcal{P}_e}{n}+d_e^2\nabla\cdot\{\mathbf{uJ}+\mathbf{Ju}\}-d_e^2 d_i\nabla\cdot\{\frac{\mathbf{JJ}}{n}\}+d_i\frac{\mathbf{J}\times\mathbf{B}}{n}+S^{-1}\mathbf{J}, \tag{2.145}$$

where, S is known as Lundquist number (magnetic Reynolds number),given by

$$S = \frac{\mu_0 L_o u_0}{\eta}, \tag{2.146}$$

The second choice leads to the following equation where only the pressure terms change

$$\mathbf{E}+\mathbf{u}\times\mathbf{B} = d_e^2\frac{\partial \mathbf{J}}{\partial t}+\epsilon_m \frac{\rho_i^2}{d_i}\frac{\nabla\cdot\mathcal{P}_i}{n}-\frac{\rho_s^2}{d_i}\frac{\nabla\cdot\mathcal{P}_e}{n}+d_e^2\nabla\cdot\{\mathbf{uJ}+\mathbf{Ju}\}-d_e^2 d_i\nabla\cdot\{\frac{\mathbf{JJ}}{n}\}+d_i\frac{\mathbf{J}\times\mathbf{B}}{n}+S^{-1}\mathbf{J}, \tag{2.147}$$

In the previous equation, the ion pressure tensor has been normalized to the ion thermodynamic pressure ($p_{0,i} = k n_0 T_i$), while the electrons to electron thermodynamic pressure ($p_{0,e} = k n_0 T_e$). ρ_i is the ion Larmor radius given by,

$$\rho_i = \frac{v_{th,i}}{\omega_{c,i}} = \sqrt{\frac{T_i}{T_e}}\rho_s, \quad \rho_e = \frac{v_{th,e}}{\omega_{c,e}}, \tag{2.148}$$

where ρ_e is the electron Larmor radius. Now, noticing that the ion pressure tensor is of order ϵ_m, it can then be neglected compared to other terms. Then, the generalized Ohm law becomes

$$\mathbf{E}+\mathbf{u}\times\mathbf{B} = d_e^2\frac{\partial \mathbf{J}}{\partial t}-\frac{\rho_s^2}{d_i}\frac{\nabla\cdot\mathcal{P}_e}{n}+d_e^2\nabla\cdot\{\mathbf{uJ}+\mathbf{Ju}\}-d_e^2 d_i\nabla\cdot\{\frac{\mathbf{JJ}}{n}\}+d_i\frac{\mathbf{J}\times\mathbf{B}}{n}+S^{-1}\mathbf{J}, \tag{2.149}$$

This equation and momentum equation is the starting point in the derivation of reduced models, such as Reduced-MHD. However, any further simplification will not be trivial to justify. As discussed in section 1.2.1, the topology of the field is preserved as long as we are in ideal MHD regime. This ideality is violated when taking into account the `RHS` terms of the previous equation.

However, some of these terms might break the topology and therefore allowing reconnecting events, while others cannot. The first term on the `RHS` represents the evolution of the current density on spatial lengths of the order of electron skin depth -that is when the inertia of electrons becomes important. This term breaks the field topology and removes the singularity at null points, and thus resulting in a reconnection process (see chapter 7). The second term represents the divergence of the electron pressure tensor, which can be understood as a force exerted on a unit volume of the plasma due to the random motions of its electrons. This term can break the topology of field lines, and thus leading to reconnection (the same can be said on the divergence of ion pressure tensor). The third and fourth terms represent the convective motion of electrons, which becomes essential as soon as the electron inertia can no longer be neglected. This term preserves the topology of the magnetic field. The fifth term is the Hall term, which also preserves the topology of field lines (see section 5.5.1 for the proof), but it has an interesting consequence on magnetic reconnection. It makes the reconnection process `3D` due to the generation of a

magnetic field perpendicular to the reconnection plane (see section 5.5 for a detailed discussion). It is worth to mention the fact that ignoring this term in Ohm law is difficult to justify in realistic situations. For example, in order to neglect it in the purely resistive case, we must have $\omega_{c,e} \ll \nu_{ei}$, which is rarely achieved in space plasma [213, 37]. In contrast, the reconnection can be considered a 2D process in many other models. The last term is the resistive term which describes the variation of the electric field due to the collisions between ions and electrons, and thus describes the diffusion of field lines (this is obvious when using Ampere-Maxwell equation). In general, the resistivity is a tensorial quantity, which might be inhomogeneous, unsteady, or strongly anisotropic depending on the existence of magnetic field [168, 214, 215].

2.4.4 Motion of Magnetic Field Lines

The fully ionized quasi-neutral plasma is composed of ions and electrons which move together collectively. To the first order, ions and electrons velocities are equal to electromagnetic drift velocity. However, in most cases, higher-order corrections are needed for both. These corrections are not necessarily the same neither in value nor in their nature (physical source). Nevertheless, it remains possible to relate them through the equation of current density which is given in terms of total velocities of both electron and ions: Eq.(2.122).

As we are only interested in the motion of field lines -specifically their velocity, it is sufficient to keep only the resistive and Hall terms in generalized Ohm law. Then,

$$\mathbf{E} + \mathbf{u} \times \mathbf{B} = \frac{1}{en}\mathbf{J} \times \mathbf{B} + \eta \mathbf{J} \tag{2.150}$$

From Eq.(2.122), we write

$$\mathbf{u} \approx \mathbf{u}_i = \frac{\mathbf{J}}{en} + \mathbf{u}_e, \tag{2.151}$$

substituting Eq.(2.151) into Eq.(2.150), one finds

$$\mathbf{E} + \mathbf{u}_e \times \mathbf{B} = \eta \mathbf{J}, \tag{2.152}$$

where Hall term is cancelled by $\mathbf{J}$ term in electron velocity. The previous equation assures us that the electron velocity is the convective velocity of field lines. Accordingly, the magnetic topology breaking will occur on spatial scales strongly related to that of characteristic lengths of electrons.

3

Numerical Methods for Solving Vlasov System

Contents

In this chapter, we are going to explain the numerical methods used to solve Vlasov-Maxwell system given by the following equations,

$$\frac{\partial f_\alpha(\mathbf{r},\mathbf{v},t)}{\partial t} + \mathbf{v}\cdot\nabla_{\mathbf{r}} f_\alpha(\mathbf{r},\mathbf{v},t) + \frac{e_\alpha}{m_\alpha}\Big[\mathbf{E}+\mathbf{v}\times\mathbf{B}\Big]\cdot\nabla_{\mathbf{v}} f_\alpha(\mathbf{r},\mathbf{v},t) = 0, \tag{3.1a}$$

$$\nabla\cdot\mathbf{E} = \frac{\rho}{\epsilon_0}, \tag{3.1b}$$

$$\nabla\cdot\mathbf{B} = 0, \tag{3.1c}$$

$$\frac{\partial\mathbf{B}}{\partial t} = -\nabla\times\mathbf{E}, \tag{3.1d}$$

$$\frac{\partial\mathbf{E}}{\partial t} = c^2\nabla\times\mathbf{B} - \frac{1}{\epsilon_0}\mathbf{J}, \tag{3.1e}$$

where $\mathbf{v} = \mathbf{p}/m_\alpha\gamma$, and γ is the Lorentz factor. The main focus of this chapter is on the code `VLEM` designed to solve the previous system of equations using the semi-Lagrangian method on an Eulerian grid,, coupled with Yee algorithm , used to solve the electromagnetic part. Therefore, we start by presenting Yee algorithm employed to solve Maxwell equations; then we briefly explain some history, and the PIC method. The kinetic simulations that we are going to dicuss in next Chapters have been indeed run by using both the VLEM solver [2], and the PIC code SMILEI [1]. After that, we detail the semi-Lagrangian procedure starting with the operator splitting idea representing the main element of this method. Then, we collect all the elements of the code in one figure. Finally, we close this chapter by discussing the eigenvalue solver used to study the scaling laws of reconnection instabilities in different regimes.

3.1 Yee Algorithm

`VLEM` code uses the Yee algorithm [216] for the advancement of the electromagnetic fields. This algorithm is based on a finite difference time domain (`FDTD`) method to solve Maxwell's equations based on second-order central finite difference schemes [217, 218]. The main features of this method are the following:

- A staggered spatial mesh is used for interleaved placement of the electric and magnetic fields.
- The fields are also updated at interleaved points in time, staggered in such a way that they "leapfrog" over each other (leapfrog method).
- The time discretization is explicit. This excludes the problem associated matrix inversions, and reduce the number of arithmetic operations, which leads to a much faster simulation.
- The finite-difference stencil is second-order accurate for both time and space coordinates.

We recall for convenience here the set of Maxwell's equations that we need to discretize

$$\nabla \cdot \mathbf{E} = \frac{\rho}{\epsilon_0}, \tag{3.2a}$$

$$\nabla \cdot \mathbf{B} = 0, \tag{3.2b}$$

$$\frac{\partial \mathbf{B}}{\partial t} = -\nabla \times \mathbf{E}, \tag{3.2c}$$

$$\frac{\partial \mathbf{E}}{\partial t} = c^2 \nabla \times \mathbf{B} - \frac{1}{\epsilon_0}\mathbf{J}, \tag{3.2d}$$

In the following, we present a derivation for a $2D$ case: (x, y). Then, the generalization to `3D`-space will be straightforward, and we summarize the general results in a table. It is indeed possible to explain the idea behind the method by first making the simplifying assumption that the electromagnetic fields just depend on two coordinates. The derivation of $2D$ case will allow us to investigate the different aspects of this algorithm.

As stated before, Yee algorithm is a centred finite difference, second-order accurate both in time and space. In our case $\mathbf{E} = \mathbf{E}(x, y)$ and $\mathbf{B} = \mathbf{B}(x, y)$. We start by discretizing Eq.(3.2c)

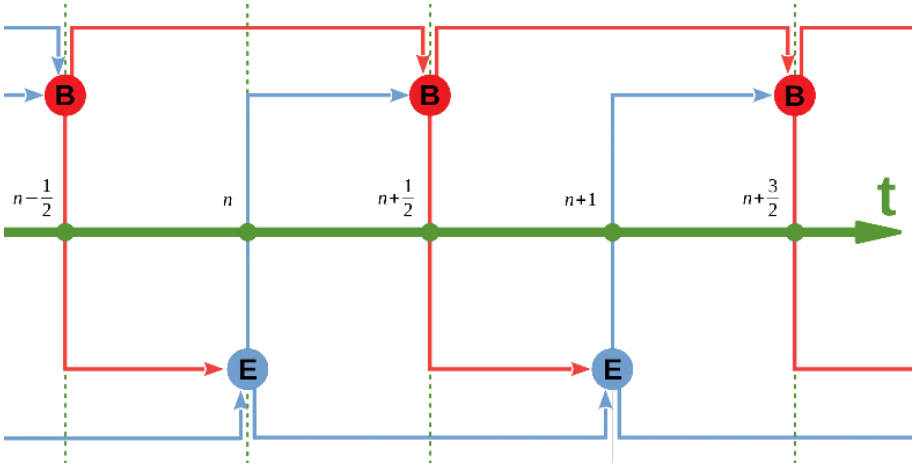

Figure 3.1: Temporal part of of Yee algorithm. As shown, estimating magnetic field $\mathbf{B}$ at time step $n+\frac{1}{2}$ requires providing the values of fields $\mathbf{E}$, and $\mathbf{B}$ at steps n and $n-\frac{1}{2}$, respectively.

using using a stencil centered at $t=t_n$, then

$$\begin{aligned} \frac{\partial \mathbf{B}}{\partial t}\Big|^n &= -\nabla\times\mathbf{E}\Big|^n, \implies \\ \mathbf{B}^{n+\frac{1}{2}} &= \mathbf{B}^{n-\frac{1}{2}} - \Delta t\nabla\times\mathbf{E}|^n + O[(\Delta t)^2], \end{aligned} \tag{3.3}$$

Applying the same argument to Eq.(3.2d) at $t=t_{n+\frac{1}{2}}$ with a second order accurate stencil, one easily finds,

$$\mathbf{E}^{n+1} = \mathbf{E}^n + c^2\Delta t\nabla\times\mathbf{B}\Big|^{n+\frac{1}{2}} - \frac{\Delta t}{\epsilon_0}\mathbf{J}^{n+\frac{1}{2}}, \tag{3.4}$$

The two previous staggered equations allow us to update the fields at interleaved time steps. Fig.3.1 shows the time discretization strategy of Yee algorithm, where the magnetic field is calculated at half integer time steps, while the electric field at the integer ones. As shown in the figure, at every time step n, information from two previous steps are required. Now, we turn our attentions to discretizations along spatial dimensions

Fig.3.2 shows a cell of Yee grid in a `3D`-space. As shown in the figure, on the one hand, electric fields components are placed in the middle of the edges of the cells and oriented parallel the corresponding edges. On the other hand, magnetic fields are placed at face centres and are directed perpendicularly to the respective faces. With this method, the space will be filled with these cells which, naturally, take into account the laws of Maxwell-Ampére, and Maxwell-Faraday, Eqs[(3.2d),(3.2c)], respectively. For example, it is easy to notice that four electric field vectors surround a magnetic field vector, and curl around it, thus fulfilling Maxwell-Faraday equation. According to this, Yee algorithm looks very natural. Now, we try to obtain a full descritization for the $x-$component of Maxwell-Farady law, then the remaining components are estimated in the same manner. Eq.(3.3) gives,

$$\begin{aligned} B_x^{n+\frac{1}{2}} &= B_x^{n-\frac{1}{2}} - \Delta t\nabla\times\mathbf{E}\Big|_x^n = B_x^{n-\frac{1}{2}} - \Delta t\Big\{\frac{\partial E_z^n}{\partial y} - \frac{\partial E_y^n}{\partial z}\Big\} \implies \\ B_{x\ i,j+\frac{1}{2},k+\frac{1}{2}}^{n+\frac{1}{2}} &= B_{x\ i,j+\frac{1}{2},k+\frac{1}{2}}^{n-\frac{1}{2}} - \frac{\Delta t}{\Delta y}\Big(E_{z\ i,j+1,k+\frac{1}{2}}^n - E_{z\ i,j,k+\frac{1}{2}}^n\Big) \\ &+ \frac{\Delta t}{\Delta z}\Big(E_{y\ i,j+\frac{1}{2},k+1}^n - E_{y\ i,j+\frac{1}{2},k}^n\Big), \end{aligned} \tag{3.5}$$

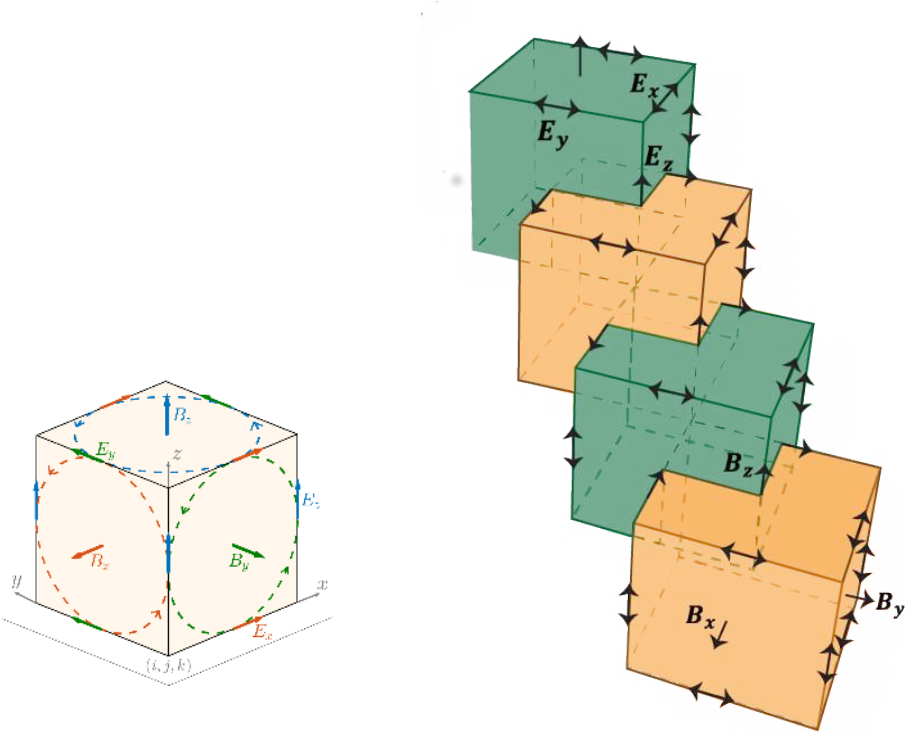

Figure 3.2: To left: 3D Yee cell. The node (i, j, k) is shown with $\mathbf{E}$ and $\mathbf{B}$ located at edges', and faces' centres, respectively. To the right: many Yee cells.

Now, $x-$ component of Eq.(3.4) leads to

$$E_x^{n+1} = E_x^n + c^2\Delta t \nabla \times \mathbf{B}\Big|_x^{n+\frac{1}{2}} - \frac{\Delta t}{\epsilon_0} J_x^{n+\frac{1}{2}} = E_x^n + c^2\Delta t\Big(\frac{\partial B_z^{n+\frac{1}{2}}}{\partial y} - \frac{\partial B_y^{n+\frac{1}{2}}}{\partial z}\Big) - \frac{\Delta t}{\epsilon_0} J_x^{n+\frac{1}{2}} \tag{3.6}$$

After discretizing the equation along spatial coordinates, one finds

$$\begin{aligned} E^{n+1}_{x\ i+\frac{1}{2},j,k} = E^n_{x\ i+\frac{1}{2},j,k} &+ \frac{c^2\Delta t}{\Delta y}\Big(B^{n+\frac{1}{2}}_{z\ i+\frac{1}{2},j+\frac{1}{2},k} - B^{n+\frac{1}{2}}_{z\ i+\frac{1}{2},j-\frac{1}{2},k}\Big) \\ &- \frac{c^2\Delta t}{\Delta z}\Big(B^{n+\frac{1}{2}}_{y\ i+\frac{1}{2},j,k+\frac{1}{2}} - B^{n+\frac{1}{2}}_{y\ i+\frac{1}{2},j,k-\frac{1}{2}}\Big) - \frac{\Delta t}{\epsilon_0} J^{n+\frac{1}{2}}_{x\ i+\frac{1}{2},j,k}, \end{aligned} \tag{3.7}$$

Following the same argument of the two previous results, the descritized components of Maxwell-Farady and Maxwell-Ampére equations are given by,

$$\begin{aligned} B^{n+\frac{1}{2}}_{y\ i+\frac{1}{2},j,k+\frac{1}{2}} = B^{n-\frac{1}{2}}_{y\ i+\frac{1}{2},j,k+\frac{1}{2}} &- \frac{\Delta t}{\Delta z}\Big(E^n_{x\ i+\frac{1}{2},j,k+1} - E^n_{x\ i+\frac{1}{2},j,k}\Big) \\ &+ \frac{\Delta t}{\Delta x}\Big(E^n_{z\ i+1,j,k+\frac{1}{2}} - E^n_{z\ i,j,k+\frac{1}{2}}\Big), \end{aligned} \tag{3.8}$$

$$\begin{aligned} B^{n+\frac{1}{2}}_{z\ i+\frac{1}{2},j+\frac{1}{2},k} = B^{n-\frac{1}{2}}_{z\ i+\frac{1}{2},j+\frac{1}{2},k} &- \frac{\Delta t}{\Delta x}\Big(E^n_{y\ i+1,j+\frac{1}{2},k} - E^n_{y\ i,j+\frac{1}{2},k}\Big) \\ &+ \frac{\Delta t}{\Delta y}\Big(E^n_{x\ i+\frac{1}{2},j+1,k} - E^n_{x\ i+\frac{1}{2},j,k+\frac{1}{2}}\Big), \end{aligned} \tag{3.9}$$

$$E^{n+1}_{y\ i,j+\frac{1}{2},k} = E^{n}_{y\ i,j+\frac{1}{2},k} + \frac{c^2\Delta t}{\Delta z}\left(B^{n+\frac{1}{2}}_{x\ i,j+\frac{1}{2},k+\frac{1}{2}} - B^{n+\frac{1}{2}}_{x\ i,j+\frac{1}{2},k-\frac{1}{2}}\right) - \frac{c^2\Delta t}{\Delta x}\left(B^{n+\frac{1}{2}}_{z\ i+\frac{1}{2},j+\frac{1}{2},k} - B^{n+\frac{1}{2}}_{z\ i-\frac{1}{2},j+\frac{1}{2},k}\right) - \frac{\Delta t}{\epsilon_0} J^{n+\frac{1}{2}}_{y\ i,j+\frac{1}{2},k}, \tag{3.10}$$

$$E^{n+1}_{z\ i,j,k+\frac{1}{2}} = E^{n}_{z\ i,j,k+\frac{1}{2}} + \frac{c^2\Delta t}{\Delta x}\left(B^{n+\frac{1}{2}}_{y\ i+\frac{1}{2},j,k+\frac{1}{2}} - B^{n+\frac{1}{2}}_{y\ i-\frac{1}{2},j,k+\frac{1}{2}}\right) - \frac{c^2\Delta t}{\Delta y}\left(B^{n+\frac{1}{2}}_{x\ i,j+\frac{1}{2},k+\frac{1}{2}} - B^{n+\frac{1}{2}}_{x\ i,j-\frac{1}{2},k+\frac{1}{2}}\right) - \frac{\Delta t}{\epsilon_0} J^{n+\frac{1}{2}}_{z\ i,j,k+\frac{1}{2}}, \tag{3.11}$$

Quantity	x	y	z	t	*in cell*
E_x	$i+\frac{1}{2}$	j	k	n	$E^n_{x\ i+\frac{1}{2},j,k}$
E_y	i	$j+\frac{1}{2}$	k	n	$E^n_{y\ i,j+\frac{1}{2},k}$
E_z	i	j	$k+\frac{1}{2}$	n	$E^n_{z\ i,j,k+\frac{1}{2}}$
ρ	i	j	k	n	$\rho^n_{i,j,k}$
J_x	$i+\frac{1}{2}$	j	k	$n+\frac{1}{2}$	$J^{n+\frac{1}{2}}_{x\ i+\frac{1}{2},j,k}$
J_y	i	$j+\frac{1}{2}$	k	$n+\frac{1}{2}$	$J^{n+\frac{1}{2}}_{y\ i,j+\frac{1}{2},k}$
J_z	i	j	$k+\frac{1}{2}$	$n+\frac{1}{2}$	$J^{n+\frac{1}{2}}_{z\ i,j,k+\frac{1}{2}}$
B_x	i	$j+\frac{1}{2}$	$k+\frac{1}{2}$	$n+\frac{1}{2}$	$B^{n+\frac{1}{2}}_{x\ i,j+\frac{1}{2},k+\frac{1}{2}}$
B_y	$i+\frac{1}{2}$	j	$k+\frac{1}{2}$	$n+\frac{1}{2}$	$B^{n+\frac{1}{2}}_{y\ i+\frac{1}{2},j,k+\frac{1}{2}}$
B_z	$i+\frac{1}{2}$	$j+\frac{1}{2}$	k	$n+\frac{1}{2}$	$B^{n+\frac{1}{2}}_{z\ i+\frac{1}{2},j+\frac{1}{2},k}$

Table 3.1: Characterization of Yee grid in $3D-$space.

Table 3.1 lists the main features of Yee algorithm in 3-dimensional space, including the interleaved positions, both in time and space, where we evaluate fields and currents. Lagrangian methods, such as PIC simulation, and semi-Lagrangian ones provide us with ways to calculate current and mass densities relying on our knowledge of the distribution function which can be estimated either as the sum over macro-particles in the former or as a scalar field in a six-dimensional phase space in the latter. Maxwell-Gauss and Maxwell-Thomson must be solved at $t = 0$; then they are satisfied at any time, as we are going to see in the following sections.

Therefore, it is evident that starting from specific initial conditions on the electric and magnetic fields; one can calculate them at later time steps by only using Maxwell-Faraday, and Maxwell-Ampére equations associated with appropriate methods to compute densities. However, Maxwell equations are four. Accordingly, any solution must fulfill simultaneously all the equations, not only two of them. This raises two questions

- Does the computed magnetic field **B** satisfy Eq.3.2b?
- Does the computed electric field **E** satisfy Eq.3.2a?

3.1.1 Temporal Advancement of the Magnetic Field

If the initial magnetic field satisfies $\nabla \cdot \mathbf{B} = 0$, and its time evolution is always governed by Eq.3.2c, then $\nabla \cdot \mathbf{B} = 0$ is true at all time. To prove this, it is sufficient to take the divergence of Faraday-Maxwell equation,

$$\frac{\partial(\nabla \cdot \mathbf{B})}{\partial t} = \nabla \cdot \frac{\partial \mathbf{B}}{\partial t} = -\nabla \cdot \nabla \times \mathbf{E} = 0, \ \textit{because} \ \nabla \cdot \nabla \times \mathbf{A} = 0, \ \textit{for any} \ \mathbf{A}, \tag{3.12}$$

Therefore, updating $\mathbf{B}$ with Eqs.[(3.5),(3.8),(3.9)] preserves the discretized version of Thomson-Maxwell equation, given by

$$\frac{B^{n+\frac{1}{2}}_{x\ i+1,j+\frac{1}{2},k+\frac{1}{2}} - B^{n+\frac{1}{2}}_{x\ i,j+\frac{1}{2},k+\frac{1}{2}}}{\Delta x} + \frac{B^{n+\frac{1}{2}}_{y\ i+\frac{1}{2},j+1,k+\frac{1}{2}} - B^{n+\frac{1}{2}}_{y\ i+\frac{1}{2},j,k+\frac{1}{2}}}{\Delta y} + \frac{B^{n+\frac{1}{2}}_{z\ i+\frac{1}{2},j+\frac{1}{2},k+1} - B^{n+\frac{1}{2}}_{z\ i+\frac{1}{2},j+\frac{1}{2},k}}{\Delta z} = 0, \tag{3.13}$$

3.1.2 Temporal Advancement of the Electric Field

The discretized Gauss-Maxwell equation takes the following form

$$\frac{E^{n}_{x\ i+\frac{1}{2},j,k} - E^{n}_{x\ i-\frac{1}{2},j,k}}{\Delta x} + \frac{E^{n}_{y\ i,j+\frac{1}{2},k} - E^{n}_{y\ i,j-\frac{1}{2},k}}{\Delta y} + \frac{E^{n}_{z\ i,j,k+\frac{1}{2}} - E^{n}_{z\ i,j,k-\frac{1}{2}}}{\Delta z} = \frac{\rho^{n}_{ijk}}{\epsilon_0}, \tag{3.14}$$

The current density ($\mathbf{J}$) obtained from the distribution function does not necessarily lead, after substituting in the Maxwell-Ampére equation, to an electric field that automatically satisfies the previous equation. This problem does not owe its origin to the numerical computation of the distribution function. It is instead related to the discrete approximation of the differential operators, such as $\nabla\times$ and $\nabla\cdot$; hence correction schemes are required. To understand this problem, we take the divergence of Eq.(3.2d):

$$\nabla \cdot \frac{\partial \mathbf{E}}{\partial t} = -c^2 \nabla \cdot \nabla \times \mathbf{B} - \frac{1}{\epsilon_0} \nabla \cdot \mathbf{J}, \tag{3.15}$$

Knowing that $\nabla \cdot \nabla \times \mathbf{A} = 0$, and substituting Eq.(3.2a) into the previous equations, one finds

$$\frac{\partial}{\partial t}\Big(\rho - \epsilon_0 \nabla \cdot \mathbf{E}\Big) = \nabla \cdot \mathbf{J} + \frac{\partial \rho}{\partial t} \overset{?}{=} 0, \tag{3.16}$$

Hence, updating the electric field using Eqs.[(3.7),(3.10),(3.11)] preserves Eq.(3.14), meaning that the continuity equation (Eq.(3.16)) is satisfied at all time. In practical terms, it means that substituting a current density $\mathbf{J}$, which fulfills Eq.(3.16), into Eq.(3.2d) gives an electric field that always satisfies Maxwell-Gauss equation. Before going further and explaining the suggested solutions to this problem, the discretized continuity equation can easily be obtained from the previous equation. It reads

$$\frac{\rho^{n+1}_{ijk} - \rho^{n}_{ijk}}{\Delta t} = -\frac{J^{n+\frac{1}{2}}_{x\ i+\frac{1}{2},j,k} - J^{n+\frac{1}{2}}_{x\ i-\frac{1}{2},j,k}}{\Delta x} - \frac{J^{n+\frac{1}{2}}_{y\ i,j+\frac{1}{2},k} - J^{n+\frac{1}{2}}_{y\ i,j-\frac{1}{2},k}}{\Delta y} - \frac{J^{n+\frac{1}{2}}_{z\ i,j,k+\frac{1}{2}} - J^{n+\frac{1}{2}}_{z\ i,j,k-\frac{1}{2}}}{\Delta z}, \tag{3.17}$$

3.1.3 Boris Correction Method

In Boris method [219, 220], at each iteration, the values of $\mathbf{E}$ obtained from the Ampére-Maxwell equation are corrected through invoking a static potential $\delta\Phi$ satisfying the following equation

$$\Delta(\delta\Phi) = \nabla \cdot \mathbf{E} - \frac{\rho}{\epsilon_0}, \tag{3.18}$$

Thus the corrected values of the field are

$$\mathbf{E}_c = \mathbf{E} - \nabla(\delta\Phi), \tag{3.19}$$

$\mathbf{E}_c$ satisfies Maxwell-Gauss equation. However, this method requires solving a Poisson equation on the grid point at each time step, which can be done using methods such as spectral methods [221, 222], iteration solvers [223], or multi-grid methods [224, 225].

3.2 Eulerian, Lagrangian and Semi-Lagrangian Methods: Introduction

An observer can watch the physics which takes place in a continuum medium (for example, a fluid) from two different points of view -to be precise, they might be three. Either, she keeps her eyes on fixed points of the domain and follows the time evolution of the physical quantities there (scalar and vector fields), or she watches the world around her while travelling with the fluid particles. In the former case, we call the person an Eulerian observer, while in the latter is known as a Lagrangian observer. Also, it will be possible to mix between these approaches as we are going to see when speaking about the semi-Lagrangian method.

These approaches can be applied to numerically solve the Vlasov-Maxwell System (hereafter, `VM`). Each of these methods has its advantages/disadvantages. In the Eulerian scheme, the distribution function is considered as a scalar field to be estimated at grid points of the discretized phase space. This grid has six dimensions (3 for each of spatial and momentum coordinates, that is `3D3V` phase space). Therefore, the equations will be solved on grid points. While this makes Eulerian numerical algorithms easy to implement and parallelize on super-computers, the method has the disadvantage of being computationally expensive. For example, for a $6D$ phase space with 100 points in each direction, the total number of points will be 10^{12}.

Another drawback of this scheme was one of the main motivations of the semi-lagrangian technique: it is the restriction on time step imposed by `CFL` condition (Courant–Friedrichs–Lewy [226]) which, in the Eulerian approach, pose an upper bound on it to ensure the stability of the numerical scheme. This means that one can not increase the spatial resolution by reducing the spatial step, without decreasing the time step. In summary, the Eulerian method is a trade-off between accuracy and stability.

In the Lagrangian scheme, the distribution function f is defined as the sum over macro-particles having some statistical weight. These particles move according to Newton's law. Therefore, by knowing the forces acting on these particles at some initial time, we can solve their motion equations using a specific numerical algorithm, such as second-order leapfrog method to find their new positions and momenta. Higher-order methods, such as the Runge–Kutta [227, 228], are numerically very expensive which limits their use to simple cases, such as the `1D-1V` geometry [229, 230]. The next stage is to calculate the mass and current densities at grid points depending on the weight used in the definition of f. Then, one solves Maxwell equations and interpolates

the solution using the positions of the particles. Finally, we repeat this procedure in the next time step. One of the most famous methods in this class is PIC (Particle-in-Cell) simulations[231, 232]. It is evident here that there is no need to discretize the velocity space. Two essential consequences follow. First, the absence of discretization is attractive from the computational point of view because the numerical domain becomes smaller by several order of magnitude. Second, dealing with velocity as a dependent variable allows studying regimes with significant variation in velocities, which is not the case of Eulerian schemes where the velocity coordinates are independent variables. Thus they are restricted by the dimensions of the phase space grid. Another positive aspect of this scheme is that it allows a longer time step, and avoid the complexities resulting from CFL condition. However, there still disadvantages. Due to the statistical definition of f, a source of statistical noise related to the number of particles (N_p) exists, which means that these methods will face difficulties in studying cases with finite N_p. However, even when N_p is large enough, Lagrangian approaches will suffer when investigating phenomena which include particles in the tail of distribution function. In these cases, the Eulerian schemes proved to be better[233, 234, 235].

Therefore, having a method combining advantages from the Eulerian and Lagrangian descriptions is promising, and here comes the semi-Lagrangian (SL) scheme. The SL method avoids damping effects and phase errors associated with the Eulerian method and takes benefits from their high spatial resolution through discretization of the whole phase space. Hence, SL schemes have a very low numerical noise [236, 237]. At the same time, they relax the restrictions imposed by CFL conditions and allow a much longer time step (Lagrangian approach), while they avoid the statistical noise of PIC codes, that results from the finite value if N_p.

Following the previous discussion, it will not be strange to expect that one of the main fields in which SL methods emerged is weather forecasting. This domain depends mainly on numerical weather prediction models (hereafter, NWP). In these models, the time step plays a vital role, especially if the model is designed so to work in real-time to update weather forecasts or to predict and respond to some environmental emergency. Therefore, the choice of time integration scheme is of crucial importance when designing an efficient NWP (see Refs.[238, 239] for historical reviews). As mentioned in Ref.[238], a considerable amount of work has been done about SL techniques. These works included the first application of the scheme in meteorology (1952) in a paper by Fjørtoft[240], followed with another one by Welander in 1955 [241]. In his paper, Welander proved that, following a set of fluid particles (fluid parcel) in a Lagrangian sense by the means of the ordinary equations of motion, might make the numerical integration of physical quantities, due to the statistical nature of the method, extremely challenging. The reason is that the fluid parcel is twisted and strongly deformed by the nonlinear dynamics and forms a long, thin filament in the phase-space (filamentation). In another paper published in 1959 [242], Wien-Nielsen used Lagrangian approaches to solve advection equation, but he focused on the particles that arrive at grid points and then traced them back to their departure locations which do not necessarily coincide with the grid points. It is this idea which draws the difference between Lagrangian and semi-Lagrangian method. In the former, the set of particles (fluid particles, electrons or ions in the plasma, etc..) changes at every time step, while in the latter, we are interested in the particles that arrive at grid vertices. In his paper, Nielsen calls this method quasi-Lagrangian. The term "semi-Lagrangian" appeared in the title of a paper by Sawyer published in 1963 [243], where the author solved the basic barotropic equation by following a system composed of atmospheric parcels. Sawyer showed that calculating vorticity field on fixed grid results in a method with similar accuracy to those obtained by Eulerian approaches, and he showed its main strength, in allowing the integrations over much longer time steps on a coarse

grid (see [244] for more details).

The main advantage of the SL methods is their numerical stablity, and allowing time integrations with longer time steps compared to equivalent Eulerian methods. In Ref.[245], the Canadian meteorologist André Robert formally demonstrated this general property of SL methods. Then Bates and McDonald confirmed this result and extended it in Ref.[238] to study many different cases in 2D space. At the same time, Stainforth, Coté and others massively contributed to the development of this field of numerical methods (NWPs)[239, 246, 247, 248].

In the context of the plasma physics, the semi-Lagrangian method was first introduced by *Cheng et Knorr* [249] who proposed a second-order time splitting method [250] to solve the Vlasov equation. Then with the growing power of the super-computers, the method was extended to higher phase space dimensions [251, 252]. These works were followed by many other contributions to the development of the method in plasma physics [233, 253, 254, 255] (see [256, 257] and references therein).

Let us now briefly discuss the PIC method.

3.3 Particle-in-Cell Method

As an example of application of the Lagrangian approach, the PIC method is briefly explained in this section. Because of its Lagrangian nature, the PIC method is exposed to all the numerical issues and difficulties associated to the statistical definition of the distribution function as a sum over macro-particles, which reads

$$f(t,\mathbf{x},\mathbf{p}) = \sum_{\alpha=1}^{N} S(\mathbf{x}-\mathbf{x}_\alpha)\delta(\mathbf{p}-\mathbf{p}_\alpha) \tag{3.20}$$

Here S represents the form factor, which plays a crucial role in distributing the contribution of each macro-particle to the current and mass densities at different points of the fixed spatial grid. This grid is made of *cells*, defined as the region centred around the grid points. For example, in the $2D$ case, the cell (i,j) is a rectangle of dimensions $(\Delta x, \Delta y)$ with the point (i,j) at its centre. The form factor can take various forms. For example, the zeroth-order approximation, known as nearest grid point strategy NGP [258], is the simplest one. Here, the particle charge is wholly assigned to the nearest grid point. However, in this approach, the force between two particles is discontinuous and becomes zero if they are in the same cell, while approximately follows the physical law of electrostatic interaction when the particles are separated by a few cells. Therefore, several problems, such as self-heating and substantial levels of numerical noise [259, 241], are associated with this method and thus limit its application. Consequently, in order to overcome these issues, other techniques have been suggested. For instances, it is possible to employ linear, quadratic, or cubic interpolations.

A proper interpretation of the concept of macro-particles helps in understanding the error source in PIC codes. This concept can be viewed from two different points of view. On the one hand, one can interpret the particle geometrically as a "rectangle" (rectangular cloud) that may cover many cells. Accordingly, the charge can be distributed linearly between the nearest centres. Hence the term Cloud-in-Cell which has been adopted to the first time by *Birdsall* and *Fuss* in Ref.[259]. On the other hand, the particle might be defined as a point with its charge linearly interpolated to the nearest cell centres, hence the term Particle-in-Cell [260, 261, 262]. Besides, higher-order interpolation schemes, such as splines, can be used for the form factor, which in turn reduce the numerical noise and heating problems. For example, *SMILEI* [1], which is a

collaborative, open-source, object-oriented ($C++$) PIC code, can use an interpolation scheme up to fourth-order.

Fig.3.3 shows the typical main loop of a `PIC` solver. Grey colour represents the past and future time steps, while the warm colours show an ongoing iteration inside the loop. The electromagnetic `PIC` cycle can be summarized with the following steps

1. **Gathering Fields**: This is represented by stage 2 in the figure, where $\mathbf{E}$ and $\mathbf{B}$ fields are registered at time t_n. The electric field is estimated at t_n, while $\mathbf{B}$ at t_n is averaged from its values at $t_{n-\frac{1}{2}}$ and $t_{n+\frac{1}{2}}$.

2. **Particle Pusher**: This is shown in the figure by stages 3 and 4 for the momentum $\mathbf{p}_\alpha$ and the positions $\mathbf{x}_\alpha$, respectively. Many different time advancement schemes can be employed here, the one which is represented in Fig.3.3 is the leapfrog method. The discretization of characteristic equations reads,

$$\left.\frac{d\mathbf{p}_\alpha}{dt}\right|^n = \frac{\mathbf{p}_\alpha^{n+\frac{1}{2}} - \mathbf{p}_\alpha^{n-\frac{1}{2}}}{\Delta t} = q\left[\mathbf{E}(\mathbf{x}_\alpha^{\mathbf{n}}) + \frac{\mathbf{p}_\alpha^{\mathbf{n}}}{\mathbf{m}_\alpha \gamma_\alpha^{\mathbf{n}}} \times \mathbf{B}(\mathbf{x}_\alpha^{\mathbf{n}})\right], \tag{3.21a}$$

$$\left.\frac{d\mathbf{x}_\alpha}{dt}\right|^{n+\frac{1}{2}} = \frac{\mathbf{x}_\alpha^{n+1} - \mathbf{x}_\alpha^{n}}{\Delta t} = \frac{\mathbf{p}_\alpha^{n+\frac{1}{2}}}{m_\alpha \gamma_\alpha^{n+\frac{1}{2}}}, \tag{3.21b}$$

   Adopting an appropriate time integration scheme is crucial issue in `PIC` approach because the chosen scheme must be a compromise between the accuracy and the duration of the simulation. For example, `SMILEI` code [1] implements Boris pusher[219], and Vay pusher [263], which provide an alternative formulation of leapfrog solver that avoids the additional errors introduced when calculating the relativistic particles in specific configurations. As expected, this further increases the computational cost.

3. **Current Deposition**: At this stage, shown by 5 in Fig.3.3, current and mass densities are estimated using definitions of the distribution function. ρ is determined at t_n while $\mathbf{J}$ at $t_{n+\frac{1}{2}}$. However, the current densities obtained here do not necessarily satisfy the continuity equation. Therefore, their values must be corrected before substituting them into the Ampére-Maxwell equation to update the electric field at the subsequent time step. We will address this issue in the following section. Many correction schemes are available to this purpose -see Refs.[264, 265, 219] for more details.

4. **EM Solver**: This is shown in the Fig.3.3 by stages 1, and 6 which employ Yee algorithm for finding $\mathbf{B}$ and $\mathbf{E}$ at $t_{n+\frac{1}{2}}$ and t_{n+1}, respectively. These fields are calculated at the grid points. In Fig.3.3, it is obvious that estimating $\mathbf{E}^{n+1}$ requires knowing $\mathbf{E}^n$, $\mathbf{B}^{n+\frac{1}{2}}$ and $\mathbf{J}^{n+\frac{1}{2}}$ (Ampére-Maxwell equation). Thus, the simulation estimates first $\mathbf{B}^{n+\frac{1}{2}}$ from our knowledge of $\mathbf{E}^n$ and $\mathbf{B}^{n-\frac{1}{2}}$ (Faraday-Maxwell equation) -see next section for the details. After calculating the fields at cell centres, they are interpolated to the particles' locations (1*, and 6* in the figure, where α stands for the species, h refers to fields estimated at centres of edges of Yee cell for electric field, and centres of faces of the cube for the magnetic field). Finally, another stage starts again with the registering of the electromagnetic fields at the next time step.

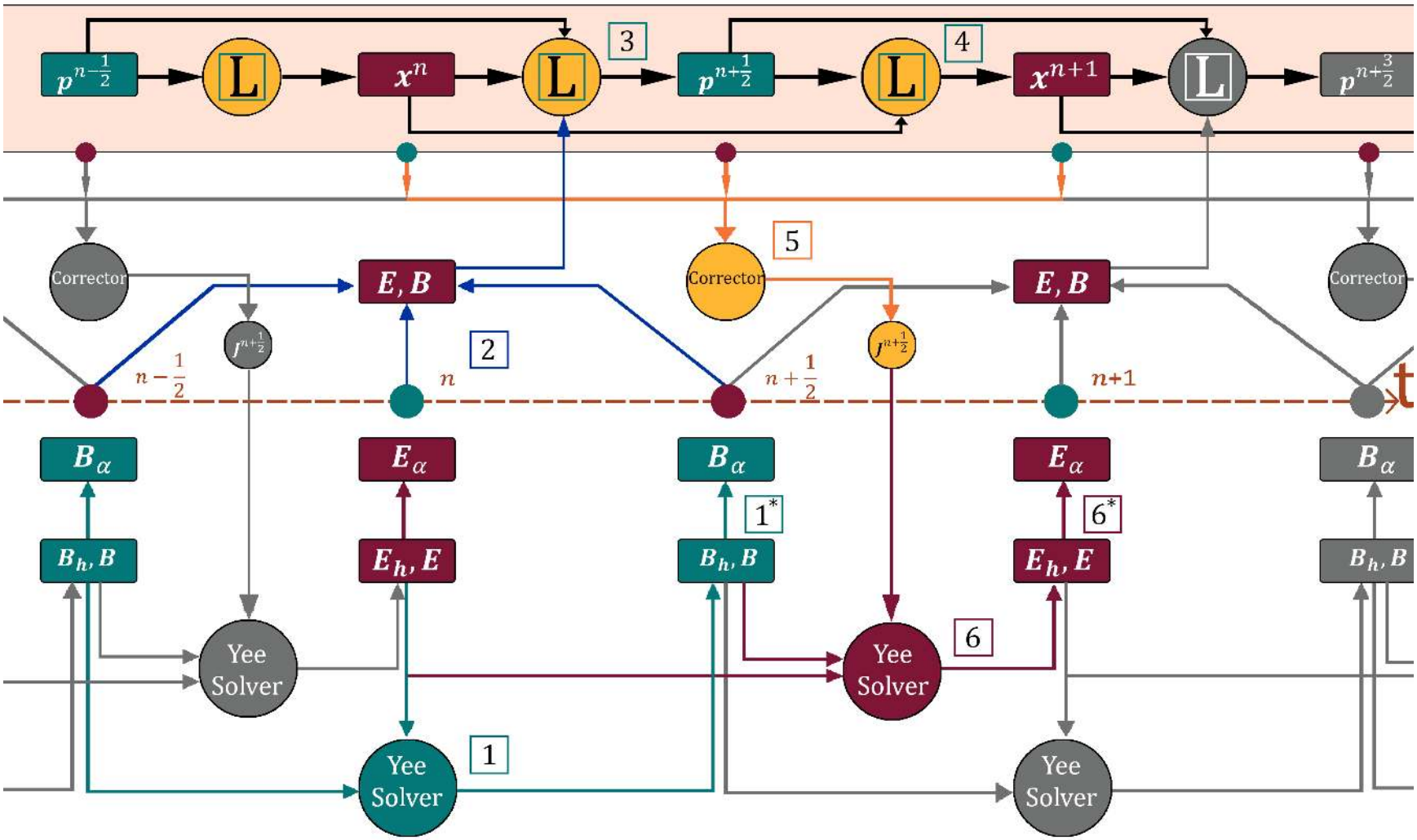

Figure 3.3: Representation of PIC simulations. The numbers inside square boxes indicates the solution steps.

Eq.(3.21) gives the evolution of the trajectories of the macro-particles. Therefore, even if the initial regime consisted of a uniform distribution of particles, the final state can be highly irregular. An example is that of a state composed of very narrow bands of particles, where their concentration can be enormous in some areas, and pretty small in others [241]. The semi-Lagrangian approach overcomes this limitation because the distribution function is always interpolated from quantities evaluated in the positions where particles are located at phase-space grid points, meaning that we are constantly interested in a specific set of particles that exist only at grid points (this is the main feature of the Eulerian-type description).

3.4 Operator Splitting: the Main Element of the Semi-Lagrangian Method

Before going further and joining Yee algorithm with semi-Lagrangian method to solve the `VM` system, it worth saying some words about the primary technique that allowed exploiting the strength of the semi-Lagrangian approach: the operator splitting, also known as *Strang splitting*, after the scientist who suggested it in Ref.[250] so to establish a finite difference scheme of second-order in order to solve the advection equation [266]. Around the same period, Marchuk independently found identical results [267, 268]. The operator splitting is a powerful tool for solving the differential equations numerically. It separates the original equation into many parts over each time step, it integrates them at each time step, and then combines these solutions so to get the global solution of the original problem. To understand the operator splitting, we take the following equation,

$$\frac{\partial f}{\partial t} = A_x f + A_y f + A_z f. \tag{3.22}$$

Here $f = f(t, x, y, z)$ can represent a distribution function, while the operators (or finite difference matrices) A_x, A_y, and A_z can represent the advection along different directions. In general, these matrices are non-commutative ($[A, B] = AB - BA \neq 0$). The solution to the previous equation is

$$f(h) = e^{h(A_x + A_y + A_z)} f(0). \tag{3.23}$$

In most practical cases, finding $e^{h(A_x+A_y+A_z)}$ is impossible, hence some approximations might improve the situation. In our study, we are interested in applying Strang splitting to the numerical solution of Eq.(3.22), hence we do not estimate Eq.(3.23) for large $\Delta t = h$ because the error will be very large. Therefore, the approximations we are going to perform are in principle more accurate as smaller is Δt. Next, we replace h in the exponential with Δt.

The first thing that comes to mind is approximating the exponential operator with

$$e^{\Delta t(A_x+A_y+A_z)} \approx e^{\Delta t A_x} e^{\Delta t A_y} e^{\Delta t A_z}, \tag{3.24}$$

The operators on the `RHS` result from the exact solutions to the following equations

$$\frac{\partial f}{\partial t} = A_x f, \quad \frac{\partial f}{\partial t} = A_y f, \quad \frac{\partial f}{\partial t} = A_z f, \tag{3.25}$$

Adopting the approximation given by Eq.(3.24) is equivalent to finding a solution to each equation of the system (3.25) over a complete-time step, and then joining them together to approximate that of Eq.(3.22). The question now is: *what is the accuracy of Eq.(3.24)*? We can answer this question by expanding the two sides of each equation in powers of Δt, and then see

to which power p of Δt, the coefficients remain identical. Hence, we say the approximation is locally accurate to the $(p+1)^{th}$ order, while it is globally p^{th}-order accurate. In our example, Taylor expansion of Eq.(3.24) gives

$$e^{\Delta t(A_x+A_y+A_z)} = \mathbf{I} + \Delta t(A_x + A_y + A_z) + \frac{(\Delta t)^2}{2}(A_x^2 + A_y^2 + A_z^2 + A_xA_y + A_yA_x + A_xA_z + A_zA_x + A_yA_z + A_zA_y) + O[(\Delta t)^3] \tag{3.26}$$

$$e^{\Delta tA_x}e^{\Delta tA_y}e^{\Delta tA_z} = \mathbf{I} + \Delta t(A_x + A_y + A_z) + \frac{(\Delta t)^2}{2}(A_x^2 + A_y^2 + A_z^2 + 2A_xA_y + 2A_xA_z + 2A_yA_z) + O[(\Delta t)^3], \tag{3.27}$$

The two previous relations are identical up to the first order. The coefficients of second power are not equal because the operators are not commutative (for instance, $2A_xA_y \neq A_xA_y + A_yA_x$). So the scheme is locally second-order accurate, but since the total number of the time steps is inversely proportional to Δt, the approximation is globally first-order accurate (henceforth, the accuracy order always refers to the global one). If $A_z = 0$, the approximation is simply obtained by substituting it in the previous equations. In Ref.[250], Strang proposed a second-order accurate splitting (with $A_z = 0$), given by

$$e^{\Delta t(A_x+A_y)} = e^{\frac{\Delta t}{2}A_x}e^{\Delta tA_y}e^{\frac{\Delta t}{2}A_x} + O[(\Delta t)^3], \tag{3.28}$$

This means we first solve the 1^{st} equation of system (3.25) over $\frac{\Delta t}{2}$. Then, the 2^d one over Δt. Finally, we continue solving the 1^{st} one over the remaining half time step $\frac{\Delta t}{2}$. If the operators involve the advection velocities ($A_i = u_i\frac{\partial}{\partial x_i}$), we say that f is advected along the x direction over $\frac{\Delta t}{2}$, followed by a complete advection along y, then by another advection along x over $\frac{\Delta t}{2}$. It is straightforward to obtain the accuracy order of Eq.(3.28) by applying the same expansion method. As the name tells, it is second-order accurate. Also, a generalization of this 2^d-order splitting to the case with three operators given by Eq.(3.22) yields

$$e^{\Delta t(A_x+A_y+A_z)} = e^{\frac{\Delta t}{2}A_x}e^{\frac{\Delta t}{2}A_y}e^{\Delta tA_z}e^{\frac{\Delta t}{2}A_y}e^{\frac{\Delta t}{2}A_x} + O[(\Delta t)^3], \tag{3.29}$$

Higher accuracy with splitting methods are possible, but they require further substeps or going back in time, and a much more complicated algebra. For example, in `2D3V` version of the `VLEM`, we use Eq.(3.28) to advect the distribution function in `2D` space grid. If one intends to adopt a higher splitting approximation, the main consequence is a massive increase in the computational costs and complexity of the code. Nevertheless, we briefly explain the method for obtaining a higher-order splitting that can be helpful if the dimensions of the phase space are relatively low, and also help us to understand the general idea behind it [269, 270].

The problem can be stated as follows: given two operators A_x and A_y, find the set of real numbers $(a_1, a_2, ..., a_k)$ and $(b_1, b_2, ..., b_k)$ such that the following equation holds,

$$e^{\Delta t(A_x+A_y)} = \prod_{i=1}^{k} e^{a_i\Delta tA_x}e^{b_i\Delta tA_y} + O[(\Delta t)^{p+1}], \tag{3.30}$$

which is equivalent to

$$M(\Delta t) := \prod_{i=1}^{k} e^{a_i\Delta tA_x}e^{b_i\Delta tA_y} = e^{\{\Delta t(A_x+A_y)+O[(\Delta t)^{p+1}]\}} \tag{3.31}$$

To do so, we expand the LHS of the equality in the power of Δt and match the coefficients of equal powers up to the order p. In this way, Neri [269] and Forest and Ruth [271] proposed a 4^{th}-order integrator for a Hamiltonian system. As a simple example, if $p = 1$, then Eq.(3.30) yields

$$a_1 + a_2 + ... + a_k = 1, \quad b_1 + b_2 + ... + b_k = 1,$$

The simplest solution is $k = 1$, $a_1 = b_1 = 1$, with $a_i = b_i = 0$ for $i > 1$ which is the 1^{st}-order splitting obtained above -Eq.(3.24) with $A_z = 0$. However, the procedure and involved algebra are very long and they are quite difficult to follow when trying to find a much higher-order splitting (≥ 4). A beautiful, yet extremely powerful solution came in a paper of Yoshida published in 1990 [272] . In his paper, Yoshida made use of Baker-Campbell-Hausdorff (BCF) formula [273] to find splitting of any order. This method is the subject of the next section.

3.4.1 Construction of High-Order Splitting

BCF Formula states that for any non-commutative operators C and D, the product $e^C e^D$ can be expressed in terms of the exponential of one operator B, which is given as an infinite series of commutators of these operators [274]. The formula is

$$\begin{aligned} &e^C e^D = e^B, \quad where \\ &B = C + D + \frac{1}{2}[C,D] + \frac{1}{12}\Big([C,C,D] + [D,D,C]\Big) + \frac{1}{24}[C,D,D,C] \\ &- \frac{1}{720}\Big([C,C,C,C,D] + [D,D,D,D,C]\Big) + \frac{1}{360}\Big([C,D,D,D,C] + [D,C,C,C,D]\Big) \\ &+ \frac{1}{120}\Big([C,C,D,D,C] + [D,D,C,C,D]\Big) + ... \end{aligned} \tag{3.32}$$

Where the higher-order commutators (Poisson brackets) are given by

$$[A,B] = AB - BA, \quad [A,B,C] = [A,[B,C]], \quad [A,B,C,D] = [A,[B,[C,D]]], \tag{3.33}$$

Eq.(3.28) is a product of three operators. Therefore, it will be useful to extend BCF to include this case. It is easy to show by repeatedly applying this formula to $e^C e^D e^C$, that one finds $e^B = e^C e^D e^C$, where

$$\begin{aligned} B = 2C + D + \frac{1}{6}[D,D,C] - \frac{1}{6}[C,C,D] + \frac{7}{360}[C,C,C,C,D] - \frac{1}{360}[D,D,D,D,C] \\ + \frac{1}{90}[C,D,D,D,C] + \frac{1}{45}[D,C,C,C,D] - \frac{1}{60}[C,C,D,D,C] + \frac{1}{30}[D,D,C,C,D] + ... \end{aligned} \tag{3.34}$$

Now, taking $C = \frac{\Delta t}{2}A_x$, and $D = \Delta t A_y$ which represent the splitting operators in Eq.(3.28), the previous identity gives

$$\begin{aligned} B = \Delta t(A_x + A_y) + \frac{(\Delta t)^3}{12}[A_y,A_y,A_x] - \frac{(\Delta t)^3}{24}[A_x,A_x,A_y] + \frac{7(\Delta t)^5}{5760}[A_x,A_x,A_x,A_x,A_y] \\ - \frac{(\Delta t)^5}{720}[A_y,A_y,A_y,A_y,A_x] + \frac{(\Delta t)^5}{360}[A_x,A_y,A_y,A_y,A_x] + \frac{(\Delta t)^5}{360}[A_y,A_x,A_x,A_x,A_y] \\ - \frac{(\Delta t)^5}{480}[A_x,A_x,A_y,A_y,A_x] + \frac{(\Delta t)^5}{120}[A_y,A_y,A_x,A_x,A_y] + ... \end{aligned} \tag{3.35}$$

Thus Eq.(3.28) can be written as follows

$$M_2(\Delta t) = e^{\frac{\Delta t}{2}A_x} e^{\Delta t A_y} e^{\frac{\Delta t}{2}A_x} = e^{B} = e^{[\Delta t \alpha_1 + (\Delta t)^3 \alpha_3 + (\Delta t)^5 \alpha_5 + ...]}, \tag{3.36}$$

where α_1, α_3, and α_5 are the coefficient of the powers (Δt), $(\Delta t)^3$, and (Δt^5), respectively. For example, $\alpha_1 = (A_x + A_y)$, and $\alpha_3 = \frac{1}{12}[A_y, A_y, A_x] - \frac{1}{24}[A_x, A_x, A_y]$.

Now we turn our attention to use the previous discussion in constructing splitting schemes of a higher order. However, before doing so, we introduce a special class of operators: operators with exact time reversibility.

A symmetric operator $M(\Delta t)$ displays exact time reversibility if

$$M_2(\Delta t) M_2(-\Delta t) = M_2(-\Delta t) M_2(\Delta t) = \mathcal{I}, \tag{3.37}$$

Due to the exact time reversibility and symmetry of the operator $M(\Delta t)$, all the terms of even powers of Δt are equal to zero. The main consequence of this property is that it allows us to construct higher-order splitting schemes (4^{th}, 6^{th}, 8^{th}...) by taking the symmetric product of splitting schemes of a lower order. For example, we can establish a 4^{th}-order splitting by a symmetric product of a 2^d-order one, as it follows:

$$M_4(\Delta t) = M_2(d_2 \Delta t) M_2(d_1 \Delta t) M_2(d_2 \Delta t), \tag{3.38}$$

Now substituting Eq.(3.36) for $M_2(d_2\Delta t)$ and $M_2(d_1\Delta t)$ in the previous equation, we find

$$M_4(\Delta t) = e^{[\Delta t (d_1 + 2d_2)\alpha_1 + (\Delta t)^3 (d_1^3 + 2d_2^3)\alpha_3 + (\Delta t)^5 (d_1^5 + 2d_2^5)\alpha_5 + ...]}, \tag{3.39}$$

Keeping in mind that $\alpha_1 = A_x + A_y$, we demand $d_1 + 2d_2 = 1$ and $d_1^3 + 2d_2^3 = 0$ to ensure that M_4 is 4^{th}-order accurate. The solution is $d_1 = -\frac{2^{1/3}}{2 - 2^{1/3}}$, $d_2 = \frac{1}{2 - 2^{1/3}}$. Thus M_4 reads,

$$M_4(\Delta t) = e^{\frac{d_2 \Delta t}{2}A_x} e^{d_2 \Delta t A_y} e^{\frac{d_2 \Delta t}{2}A_x} e^{\frac{d_1 \Delta t}{2}A_x} e^{d_1 \Delta t A_y} e^{\frac{d_1 \Delta t}{2}A_x} e^{\frac{d_2 \Delta t}{2}A_x} e^{d_2 \Delta t A_y} e^{\frac{d_2 \Delta t}{2}A_x} \tag{3.40}$$

The preceding analysis gives an idea about the operator splitting and how complex the method becomes when increasing its accuracy. For example, in 2^d-order splitting (M_2), three equations must be solved consecutively, and the solution of each will be a starting point for the subsequent one. When adopting $M4$, the number of intermediate steps increases to $9 = 3^2$, while it becomes $27 = 3^3$ for M_6. The complexity increases when a third operator A_z is involved in the problem. Nevertheless, a method that combines the principles of the time splitting, the semi-Lagrangian approach, and the conservation of the distribution function along the characteristics allows a robust numerical modeling of the `VM` system and allows us to explore a broad spectrum of kinetic plasma phenomena.

3.5 Semi-Lagrangian Approach for the Vlasov Equation

In this section, we explain one of the cornerstones of the `VLEM` code: the conservation of the distribution function along the characteristics. We start by writing the advective form of Vlasov equation which gives deep insight on the Eulerian approach. Then, we formulate the problem in the Lagrangian form and introduce the notion of the invariance of the distribution function. Lastly, we explain the main idea behind the semi-Lagrangian method. Vlasov equation reads

$$\frac{\partial f}{\partial t} + \frac{\mathbf{p}}{m\gamma} \cdot \frac{\partial f}{\partial \mathbf{r}} + q\Big(\mathbf{E} + \frac{\mathbf{p}}{m\gamma} \times \mathbf{B}\Big) \cdot \frac{\partial f}{\partial \mathbf{p}} = 0. \tag{3.41}$$

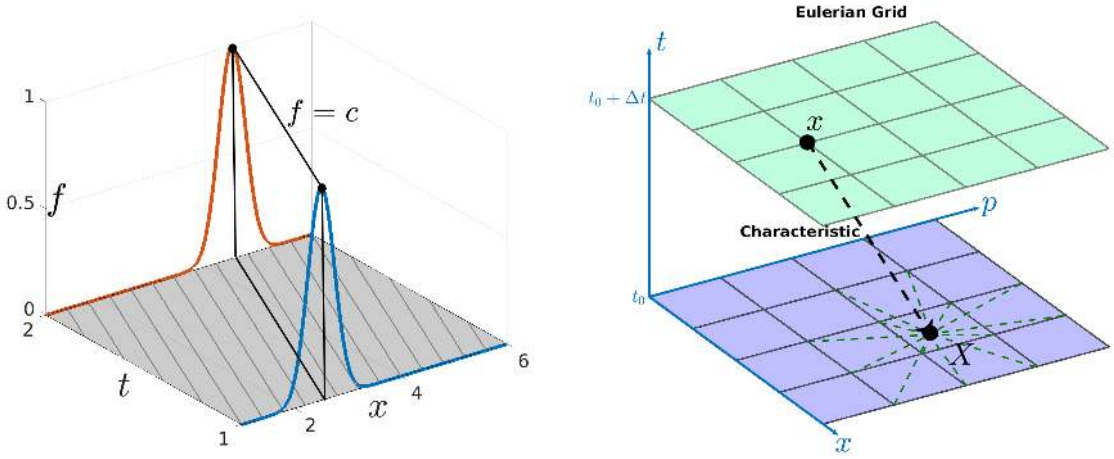

Figure 3.4: A Gaussian wave (left) propagates in the x-positive direction with constant velocity $v = 2$, at two different times $t_1 = 1$, and $t_2 = 2$. As shown, the function f is exactly the same at the extremities of any characteristics, that is $f\{x(t)\} = f\{x(t) - v\Delta t\}$. For example, $f\{x(2)\} = f\{x(2) - 2 * (t_2 - t_1)\} = f(2.5) = 1$, where $x(2) = 4.5$. The curve will flatten with time if the diffusion is involved. Therefore, in this case, f is no longer conserved along the characteristics. On the right, we plot the principle behind the backward semi-Lagrangian method. At every time step $t_0 + \Delta t$, we trace back in time, for all the points of the Eulerian phase space grid, the distribution function along its characteristics to estimate its current values.

In the previous line, we wrote the Vlasov equation in its purely advective form. In principle, it therefore corresponds to the same family of Eq.(3.22). The first term gives the evolution of f with time at a fixed point in the phase-space, $(x_{i_1}, y_{i_2}, z_{i_3}, p_{x;j_1}, p_{y;j_2}, p_{z;j_3})$. The second and the third terms of this equation represent the advection of the distribution function in the spatial and momentum parts of the phase space, respectively. The vector field responsible for this advection in the real space is the velocity ($\mathbf{v} = \frac{\mathbf{p}}{m\gamma}$), while the Lorentz force ($\mathbf{F}_L = q(\mathbf{E} + \frac{\mathbf{p}}{m\gamma} \times \mathbf{B})$) is responsible of the advection in the momentum space. The absence of the collision term on the `RHS` of the equation implies the absence of diffusion, which promotes further the choice of a 2^d-order semi-Lagrangian method for its numerical integration. It also means that particles' trajectories can not intersect. Accordingly, it strongly motivates employing the idea of the conservation of f along the characteristic curves of this partial differential equation.

As mentioned in section 3.2, in the Eulerian approach, we trace the evolution of physical quantities at fixed points in the phase space. Thus, if we directly discretize Eq.(3.41), considering the momentum and positions as independent variables, the result is a Eulerian grid. The distribution function, in this case, is a scalar `6D` field.

Now we turn our attention to the characteristics and to the Lagrangian formulation of Vlasov equation. Combining the two advective fields ($\mathbf{v}_r$,$\mathbf{F}_L$) into one field $\mathbf{V}$ given by

$$\mathbf{V} = \Big(\mathbf{v}_r, \mathbf{F}_L\Big), \quad \nabla_{tot} = \Big(\frac{\partial}{\partial \mathbf{r}}, \frac{\partial}{\partial \mathbf{p}}\Big)^T \tag{3.42}$$

then, Eq.(3.41) reads,

$$\frac{\partial f}{\partial t} + \mathbf{V}.\nabla_{tot} f = 0. \tag{3.43}$$

The left frame of Fig.3.4 shows the solution for a one-dimensional advection problem at two

different times $t = 1, 2$, respectively. In this example, the wave propagates along x-direction with velocity $v = 2$, in absence of diffusion. Therefore, the shape of the perturbation remains the same as time passes, and the function is constant along the characteristics of the equation, which are given by $\frac{dx}{dt} = v = 2 \implies x(t) = 2 * t + c_0$. We can express this fact by stating $f\{x(t)\} = const$. Basically, Eq.(3.43) has the same form, which implies the conservation of the distribution function along its characteristics. Thus, Eq.(3.43) gives

$$\frac{df}{dt} = 0, \implies f\{\mathbf{x}(t; \mathbf{X}, s)\} = const \tag{3.44}$$

This equation asserts that the distribution function at point $\mathbf{x}$ in phase space and at time t is equal to its value at point $\mathbf{X}$ at previous time s, knowing that these two locations represent the extremities of the characteristic passing through them at the prescribed times, as shown in the right frame of Fig.3.4. In this figure, f is obtained at time $t_0 + \Delta t$ and the position $\mathbf{x}$ in the phase space by advecting its value from point $\mathbf{X}$ at earlier time t_0. The characteristic equations are given by

$$\frac{d\mathbf{r}}{dt} = \frac{\mathbf{p}}{m\gamma}, \tag{3.45a}$$

$$\frac{d\mathbf{p}}{dt} = q\Big(\mathbf{E} + \frac{\mathbf{p}}{m\gamma} \times \mathbf{B}\Big), \tag{3.45b}$$

If we now relax the condition that $\mathbf{x}$ is a fixed point in the phase space, Eq.(3.44) represents the Lagrangian formulation of the problem. In this formulation, we are not interested in evaluating the fields at distinct positions (Eulerian grid) at every time step. Instead, we follow the evolution of a set of characteristics that can end anywhere in the continuum phase-space domain, that is, we let the system evolve freely without forcing it to always settle on locations corresponding to point of the Eulerian grid in the phase-space. Even if the simulation started with a highly uniform distribution, the system can lead to the formation of narrow particle filaments in the phase-space, which in turn feeds the statistical and numerical noise in the solution [241].

So, how to join advantages from the two approaches? For instance, can we maintain the high resolution achievable in Eulerian methods, while avoiding `CFL` stability criterion and damping issues? Also, is it possible to find a way allowing us to incorporate the positive sides of Lagrangian methods, such as the absence of `CFL` conditions, as it is the case in Eqs.(3.45a,3.45b)? Can we minimize the numerical noise as much as possible? The answer is yes by using the following semi-Lagrangian receipt:

> *Follow the evolution of the distribution function along the characteristics (Lagrangian thinking), but at definite positions at the end of every time step (Eulerian thinking).*

The right frame of Fig.3.4 shows the backward semi-Lagrangian algorithm. Here, at each time step, the distribution function at $\mathbf{x}\{t_0 + \Delta t; \mathbf{X}, t_0\}$ is estimated by following back in time the characteristic passing through this point toward its starting point at previous time step $\mathbf{X}(t_0)$ (black-dotted arrow). The value of the distribution function is constant along this path. However, $\mathbf{X}(t_0)$ is not necessarily a distinct point on the predefined grid. If so, interpolation techniques are employed to approximate f at $\mathbf{X}(t_0)$ from its neighbourhood. With interpolation in mind, we have now all the elements of `VLEM` code.

3.6 Domain Decomposition in VLEM

In the preceding sections, we described in some details the central tools used to design VLEM code. VLEM is a semi-Lagrangian code that allows one to solve both relativistic and non-relativistic VM systems. It does so by combining the advantages of the different tools, previously explained, namely the semi-Lagrangian approach, the Yee algorithm, the conservation of distribution function along the characteristics, together with interpolation schemes, which we are going to address in a later section. Before going further, we briefly say some words about the parallelization of VLEM.

i	j	l	$[i_s, i_e]$	$[j_s, j_e]$
0	0	0	$[0, 15]$	$[0, 15]$
0	1	1	$[16, 31]$	$[0, 15]$
...	...	...	...	...
1	0	16	$[0, 15]$	$[16, 31]$
...	...	...	...	...
2	3	35	$[48, 63]$	$[32, 47]$
...	...	...	...	...
5	10	90	$[160, 175]$	$[80, 195]$
8	3	131	$[48, 63]$	$[128, 143]$
...	...	...	...	...
11	8	184	$[128, 143]$	$[176, 191]$
...	...	...	...	...
15	15	255	$[240, 255]$	$[240, 255]$

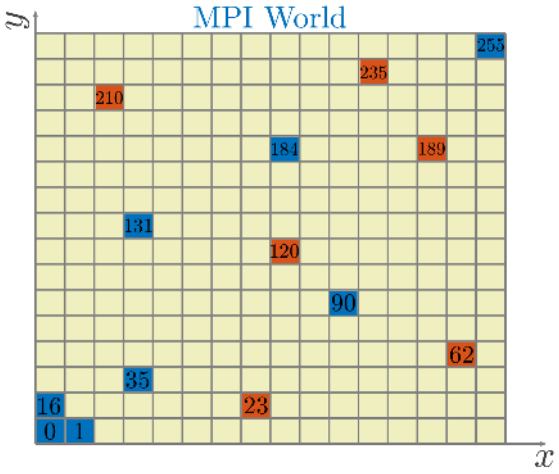

Table 3.2: Domain decomposition among $N_{proc,t} = 256$ computing nodes, 16 along each direction $N_{proc,x} = N_{proc,y} = 16$. Here $i_s = j * N_{proc,x}$, $i_e = i_s + N_{proc,x} - 1$, $j_s = i * N_{proc,y}$, and $j_e = j_s + N_{proc,y} - 1$. In the left frame, we record the coordinates of some processors and their attached patches. In the right frame, we show an illustration of the MPI world (domain decomposition). The blue squares display the patches listed in the table, while the orange ones exemplify other patches.

VLEM code takes advantage of two parallelization levels: MPI and OMP [see Ref.[2, 275] for details]. On the one hand, the spatial domain is decomposed into subdomains. Each subdomain (*patch*) is assigned to a computing node (MPI). This domain decomposition starts by specifying the number of patches along each spatial direction. In the version VLEM-2D3V of the code, $N_{proc,x}$, and $N_{proc,y}$ denotes these numbers along x and y directions, respectively. On the other hand, the momentum part of the grid is treated globally that is, the whole domain $(p_{x;j_1}, p_{y;j_2}, p_{z;j_3})$ is accessible to all computing nodes (here, the parallelization level is OMP). Therefore, each computing node has its patch of f with the following size in VLEM2D3V

$$patch\Big|_l = [x_{i_s}, x_{i_e}] \times [y_{j_s}, y_{j_e}] \times [p_{x;min}, p_{x;max}] \times [p_{y;min}, p_{y;max}] \times [p_{z;min}, p_{z;max}] \tag{3.46}$$

Here $l = N_{proc,x} * i + j$ labels the computing node inside the MPI parallel world. $[x_{i_s}, x_{i_e}] \times [y_{j_s}, y_{j_e}]$ are the area defined by patch l; (i, j) represents its indices in the decomposed domain: $i = \texttt{int}(\frac{l}{N_{proc,x}})$, and $j = \texttt{mod}(\frac{l}{N_{proc,x}})$. What is left is the complete momentum space assigned

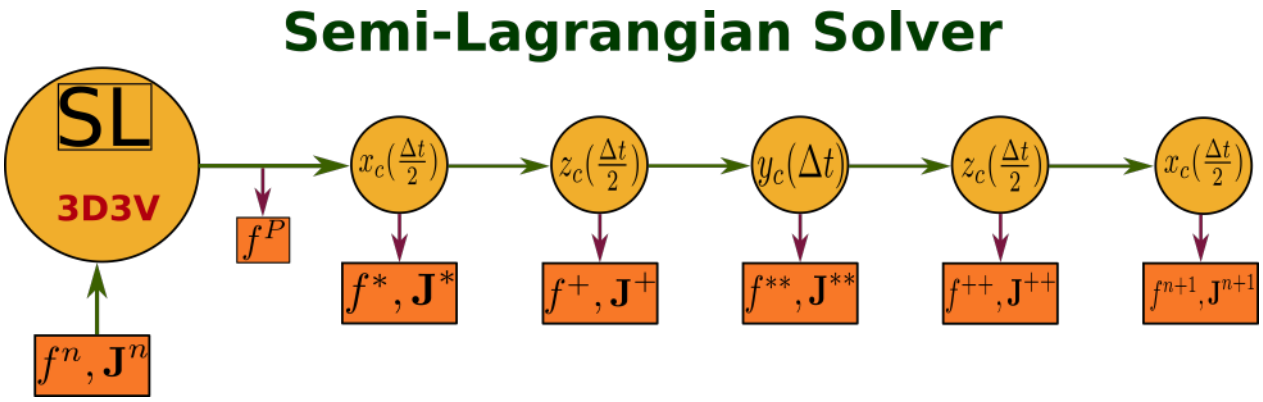

Figure 3.5: Strang Splitting for 3D3V phase space. At each advection step, the updated values of the distribution function and of the current density are stored to be used later with Esirkepov correction method.

to each processor -see Fig.3.2 for a detailed illustration of the domain decomposition. This method of domain decomposition was successfully used in gyrokinetic simulations for the study of gyrokinetic transport in Tokamaks [276] that has led to the development of the code GYSELA5D, which performs a two-dimensional advection in the space (r, θ) (GYSELA5D stands for GYro SEmi LAgrangian code [277],[2]).

3.7 Vlasov Solver in VLEM

VLEM solves the Vlasov equation using time splitting method introduced in section 3.4 [250, 249, 278]. This method enables us to divide Vlasov equation into several parts, then to solve each of them in a sub-space with lower dimensions compared to the original phase space. This procedure starts with the initial distribution function resulting from the previous time step $f^n(\mathbf{r}, \mathbf{p})$, where $(\mathbf{r}, \mathbf{p})$ are points of the predefined Eulerian grid. Then the split advection equations are solved subsequently so to obtain $f^{n+1}(\mathbf{r}, \mathbf{p})$. In the following we present the strategy of solving Eq.(3.41) in a 3D3V phase space.

1. First, we split the force and velocity operators. The situation is identical to Eq.(3.22) with $A_x = \mathbf{v}_r . \frac{\partial}{\partial \mathbf{r}}$, $A_y = \mathbf{F}_L \cdot \frac{\partial}{\partial \mathbf{p}}$ and $A_z = 0$. Therefore, the time splitting gives the following two differential equations,

$$\frac{\partial f}{\partial t} + \frac{\mathbf{p}}{m\gamma} \cdot \frac{\partial f}{\partial \mathbf{r}} = 0, \tag{3.47a}$$

$$\frac{\partial f}{\partial t} + q\Big(\mathbf{E} + \frac{\mathbf{p}}{m\gamma} \times \mathbf{B}\Big) \cdot \frac{\partial f}{\partial \mathbf{p}} = 0, \tag{3.47b}$$

2. The 3D advection equation Eq.(3.47b) is solved in the momentum space by applying

Eq.(3.28). Thus, we again split the problem into two equations, namely

$$\frac{\partial f}{\partial t} + q\mathbf{E}\cdot\frac{\partial f}{\partial \mathbf{p}} = 0, \tag{3.48a}$$

$$\frac{\partial f}{\partial t} + q\Big(\frac{\mathbf{p}}{m\gamma}\times\mathbf{B}\Big)\cdot\frac{\partial f}{\partial \mathbf{p}} = 0, \tag{3.48b}$$

Here, the Eq.(3.48b) is advected over Δt, while the Eq.(3.48a) over $\frac{\Delta t}{2}$ for two times. The magnetic advection equation (Eq.3.48b) has an interesting feature: the conservation of the particle's Lorentz factor during its gyro-motion around the field lines. We are going to detail this property in the next section. Furthermore, we can no longer split Eqs.(3.48b) because the three components of $\mathbf{p}$ will appear in the resulting system. Therefore, at each time step, this equation is solved concurrently (one `patch` per `cpu`).

The result of this step is

$$f^P(\mathbf{r},\mathbf{p}) = f^n\{(\mathbf{r},\mathbf{P}(t_n;\mathbf{p},t_{n+1})\} \tag{3.49}$$

$\mathbf{P}$ and $\mathbf{p}$ represent the extremities of the characteristics corresponding to Eq.(3.47b), that is, $\mathbf{p}$ at t_{n+1} is the point on a characteristic which starts from the point $\mathbf{P}$ at the previous time step t_n.

3. We split Eq.(3.47a) into three $1D$-advection equations. These equations read

$$\frac{\partial f}{\partial t} + \frac{p_x}{m\gamma}\frac{\partial f}{\partial x} = 0, \quad \frac{\partial f}{\partial t} + \frac{p_y}{m\gamma}\frac{\partial f}{\partial y} = 0, \quad \frac{\partial f}{\partial t} + \frac{p_z}{m\gamma}\frac{\partial f}{\partial z} = 0, \tag{3.50}$$

Then, we apply Eq.(3.29).

4. We perform half advection along the $x-$direction, which means solving the first equation of (3.50) for $\frac{\Delta t}{2}$, and then updating the values of the distribution function (f^P) resulted from the `3D` advection in momentum space. The new distribution function is given by

$$f^*(x,y,z,\mathbf{p}) = f^P(x - \frac{p_x}{m\gamma}\frac{\Delta t}{2}, y, z, \mathbf{p}), \tag{3.51}$$

5. We perform half advection along the $z-$direction, which means solving the third equation of (3.50) for $\frac{\Delta t}{2}$. The new distribution function is given by

$$f^+(x,y,z,\mathbf{p}) = f^*(x,y,z - \frac{p_z}{m\gamma}\frac{\Delta t}{2}, \mathbf{p}), \tag{3.52}$$

6. We solve the second equation of Eqs.(3.50) over a complete time step (Δt), which leads to

$$f^{**}(x,y,z,\mathbf{p}) = f^+(x, y - \frac{p_y \Delta t}{m\gamma}, z, \mathbf{p}), \tag{3.53}$$

7. Repeat the step 5, then the distribution function becomes

$$f^{++}(x,y,z,\mathbf{p}) = f^{**}(x,y,z - \frac{p_z}{m\gamma}\frac{\Delta t}{2}, \mathbf{p}), \tag{3.54}$$

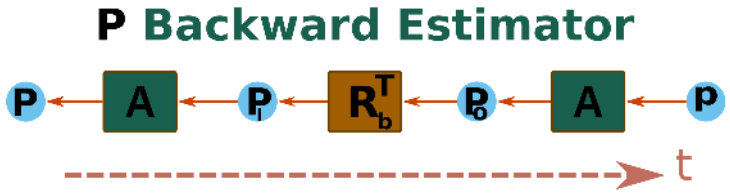

Figure 3.6: P-Backward estimator. $\mathbf{P}, \mathbf{p}$ are the momenta at t_n and t_{n+1}, respectively. $\mathbf{A}$ represents a solver for Eq.(3.48a) over $\frac{\Delta t}{2}$, while $\mathbf{R}_b$ is a solver for Eq.(3.48b). $\mathbf{R}$ stands for the rotation, and the subscript $\mathbf{b}$ for the unit vector of magnetic field.

8. Finally, we complete the advection along x for the remaining half time step $\frac{\Delta t}{2}$. This allows us to calculate f^{n+1}; this yields the sought solution of the Vlasov equation

$$f^{n+1}(x, y, z, \mathbf{p}) = f^{++}(x - \frac{p_x}{m\gamma}\frac{\Delta t}{2}, y, z, \mathbf{p}), \tag{3.55}$$

These steps are schematized in Fig.3.5 . In the version `VLEM2D3V` of the code, we follow the previous procedure, but we remove the steps 5 and 7. It is evident here that $(\mathbf{r}, \mathbf{P})$, $(x - \frac{p_x}{m\gamma}\frac{\Delta t}{2}, y, z, \mathbf{p})$, $(x, y, z - \frac{p_z}{m\gamma}\frac{\Delta t}{2}, \mathbf{p})$, or $(x, y - \frac{p_y \Delta t}{m\gamma}, z, \mathbf{p})$ may not correspond to points belonging to the phase space grid. Therefore, some interpolation methods are employed to obtain the fields at these positions.

3.8 3D Advection in Momentum Space And Rotation Tensor

The magnetic part of splitting reads

$$\frac{\partial f}{\partial t} + q\Big(\frac{\mathbf{p}}{m\gamma} \times \mathbf{B}\Big) \cdot \frac{\partial f}{\partial \mathbf{p}} = 0, \tag{3.56}$$

In the preceding equation, the temporal advancement is due to Lorentz force. The main consequence is the conservation of the kinetic energy of the particles during their gyro-motions around the field lines because the magnetic force does not perform any work on the particle -it is perpendicular to particle trajectory. Therefore, the effect of this force is solely to rotate the particle and to continuously distribute its kinetic energy between the two eigen-directions in the plane locally perpendicular to the field (mathematically, $\mathbf{p} \cdot \frac{d\mathbf{p}}{dt} = q\mathbf{p} \cdot (\frac{\mathbf{p}}{m\gamma} \times \mathbf{B}) = 0 \implies p^2 = const$). We also notice that the magnetic field is assumed to be constant during the integration of this equation. The main question to answer in this section is: *what is the relation between* $\mathbf{P}$ *at* t_n *and* $\mathbf{p}$ *at* t_{n+1}*? Or, how to find* $\mathbf{P}$ *for the given Eulerian grid points* $\mathbf{p}$*?* .

We start answering this question by first presenting an algorithm for calculating $\mathbf{P}$, then we turn our attention to explain in details the rotation effect of magnetic field.

3.8.1 Backward Estimation of the Momentum

As soon as the values of $\mathbf{P}$ at t_n are estimated, it is straightforward to obtain f^P by applying Eq.(3.49). Fig.3.6 shows the algorithm for finding $\mathbf{P}(t_n)$. As already stated in section 3.7, we first perform a half advection of $\mathbf{E}$ (olive colored boxes in Fig.3.6), followed by a complete advection of $\mathbf{B}$ (light-brown box in Fig.3.6), then another half advection of $\mathbf{E}$.

Since $\mathbf{p}$ is a point in the Eulerian phase space grid, it is always known. Therefore, we start here; then we trace the characteristic backwards in time to obtain $\boldsymbol{P}$. The characteristic equation of Eq.(3.48a) reads

$$\frac{d\mathbf{p}}{dt} = q\mathbf{E} \implies \frac{\mathbf{p} - \mathbf{P}_O}{\frac{\Delta t}{2}} = q\mathbf{E} \implies \mathbf{P}_O = \mathbf{p} - \frac{q(\Delta t)}{2}\mathbf{E}. \tag{3.57}$$

This step is shown in the right part of Fig.3.6. At the introduction of this section, we proved the conservation of the kinetic energy and the rotation effect of the magnetic force. Hence, $\mathbf{P}_O$ is just a rotation of $\mathbf{P}_I$ under a transformation represented by the tensor $\mathbf{R_b}$. However, this rotation must conserve the value of P^2, which implies that $\mathbf{R_b}$ is an orthogonal tensor (A matrix $\mathbf{R_b}$ is orthogonal if ${\mathbf{R_b}}^T = {\mathbf{R_b}}^{-1}$, where T stands for the transpose).

Therefore, $\mathbf{P}_I$, which represents the momentum before the rotation, reads

$$\mathbf{P}_I = {\mathbf{R_b}}^T \cdot \mathbf{P}_O = {\mathbf{R_b}}^T \cdot \Big(\mathbf{p} - \frac{q(\Delta t)}{2}\mathbf{E}\Big), \tag{3.58}$$

Fig.3.6 shows this procedure as a light-brown box. To complete solving Vlasov equation into momentum space, we continue tracing back the characteristic of Eq.(3.48a) over the remaining $\frac{\Delta t}{2}$ so to calculate $\mathbf{P}$ at t_n (olive box on the left part of Fig.3.6). This leads us to an expression identical to Eq.(3.57): by replacing $\mathbf{P}_O$ with $\mathbf{P}$, and $\mathbf{p}$ with $\mathbf{P}_I$, then substituting Eq.(3.58) for $\mathbf{P}_I$, one easily obtains:

$$\mathbf{P} = {\mathbf{R_b}}^T \cdot \Big(\mathbf{p} - \frac{q(\Delta t)}{2}\mathbf{E}\Big) - \frac{q(\Delta t)}{2}\mathbf{E}, \tag{3.59}$$

with this in hand, we turn our attention now to finding the rotation tensor $\mathbf{R}_b$.

3.8.2 Rotation Tensor

We start the discussion in this section by a simple observation: the cross product $\mathbf{b} \times \mathbf{P}$ can also be expressed as a matrix acting on $\mathbf{P}$ as follows

$$\mathbf{b} \times \mathbf{P} = \mathbf{S_b} \cdot \mathbf{P}, \ \textit{where} \quad \mathbf{S}_b = \begin{pmatrix} 0 & -b_z & by \\ b_z & 0 & -b_x \\ -b_y & b_x & 0 \end{pmatrix} \tag{3.60}$$

where $\mathbf{S_b}$ is a *skew-symmetric* tensor (a tensor that satisfies $\mathbf{S}_\mathbf{b}^T = -\mathbf{S_b}$). $\mathbf{b}$ is called the vector invariant (or axial vector) of the skew-symmetric tensor, while the unit vector $\mathbf{k}$ (see Fig.3.7) is known as the *skew vector*. Now, from the characteristic equation of Eq.(3.56), we write

$$\frac{d\mathbf{P}}{dt} \approx \frac{\Delta \mathbf{P}}{\Delta t} \approx -\frac{qB}{m\gamma}\mathbf{b} \times \mathbf{P}_I, \implies \Delta \mathbf{P} = \Theta \mathbf{b} \times \mathbf{P}_I = \Theta \mathbf{S_b} \cdot \mathbf{P}_I, \tag{3.61}$$

where $\mathbf{b} = \frac{\mathbf{B}}{||\mathbf{B}||}$, $\Theta = -\phi_r$, $\phi_r = \frac{qB(\Delta t)}{m\gamma}$ is the rotation angle as shown in Fig.3.7. In this figure, we plot the momenta before the rotation ($\mathbf{P}_I$), and after it, ($\mathbf{P}_O$). The green shaded sphere represents a constant kinetic energy surface ($||\mathbf{P}|| = const$), while the mauve shaded one defines a normalized magnetic energy surface. At this stage (`3D` advection in momentum space), on one hand, $\mathbf{b}$ remains constant in magnitude ($\mathbf{b}$ shown in Fig.3.7 corresponds to a distinct point in the spatial part of the Eulerian grid (x, y, z)). On the other hand, for fixed $\mathbf{b}$, $\mathbf{P}_I$ takes any possible direction in the sub-sphere depending on its location in the momentum sub-domain of the grid.

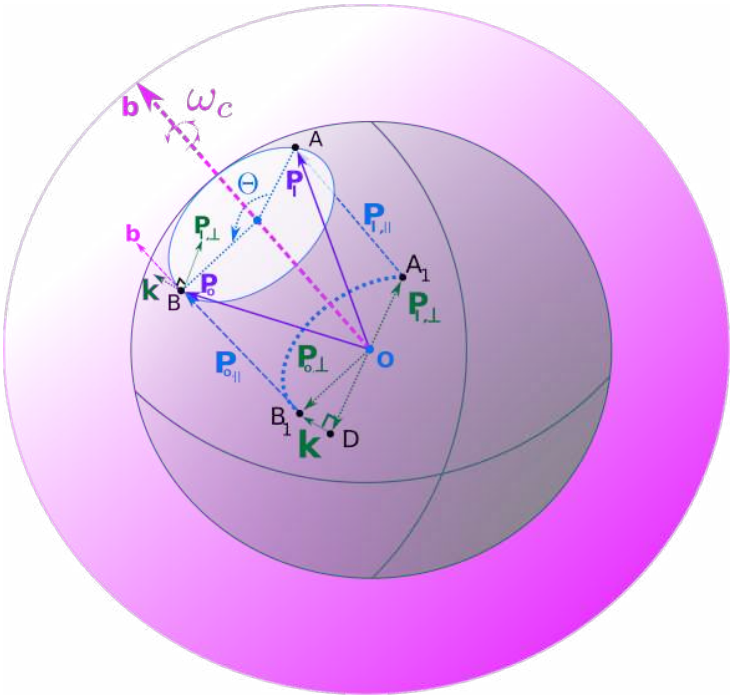

Figure 3.7: The physics involved when advecting the Vlasov equation in momentum space with only the magnetic part of the Lorentz force. $\mathbf{b}$ is the unit vector tangent to magnetic field lines. $\mathbf{P}_I$, and $\mathbf{P}_O$ are the momenta before and after the rotation, respectivly. $\perp$ refers to the perpendicular direction to $\mathbf{b}$, while $||$ refers to the parallel one.

However, $\mathbf{P}_O$ is completely determined by $\mathbf{P}_I$ and $\mathbf{b}$. In principle, if the number of grid points in momentum space is infinite, all the points on the kinetic energy surface will be scanned.

Now, we try to find how $\mathbf{P}_I$ is transformed into $\mathbf{P}_O$ in terms of $\mathbf{b}$ and ϕ_r. From Fig.3.7, one writes

$$\mathbf{P}_O = \overrightarrow{OB} = \overrightarrow{OB_1} + \overrightarrow{B_1B} = \overrightarrow{OB_1} + \mathbf{P}_{(O;||)} = \overrightarrow{OB_1} + \mathbf{P}_{(I;||)}, \tag{3.62}$$

It is easy to show by direct projection that a vector $\mathbf{P}$ can be decomposed into a parallel component $\mathbf{P}_{||}$ along $\mathbf{b}$, and a perpendicular one $\mathbf{P}_\perp$. The projection operators are $\mathbf{b}\otimes\mathbf{b}$, and $[\mathbf{I}-\mathbf{b}\otimes\mathbf{b}]$, respectively. Then,

$$\mathbf{P} = (\mathbf{b}\otimes\mathbf{b})\cdot\mathbf{P} + [\mathbf{I}-\mathbf{b}\otimes\mathbf{b}]\cdot\mathbf{P}, \tag{3.63}$$

Substituting this relationship into Eq.(3.62) for $\mathbf{P}_{(I;||)}$, one finds

$$\overrightarrow{OB} = \overrightarrow{OB_1} + (\mathbf{b}\otimes\mathbf{b})\cdot\mathbf{P}_I \tag{3.64}$$

Also, we have

$$\overrightarrow{OB_1} = \overrightarrow{OD} + \overrightarrow{DB_1}, \tag{3.65}$$

Now using the definition of Θ, and Eq.(3.63), we obtain

$$\overrightarrow{OD} = -||OD||\hat{\mathbf{P}}_{I,\perp} = -\cos(\pi-\Theta)\mathbf{P}_{I,\perp} = \cos(\phi_r)\Big[I-\mathbf{b}\otimes\mathbf{b}\Big]\cdot\mathbf{P}_I \tag{3.66}$$

where the "$\hat{}$" refers to the unit vector. From the figure, we write for $\overrightarrow{DB_1}$

$$\overrightarrow{DB_1} = ||\mathbf{P}_{I,\perp}|| \sin(\pi - \Theta)\mathbf{k} = ||\mathbf{P}_{I,\perp}|| \sin(\Theta)\mathbf{k} = -\sin(\phi_r)||\mathbf{P}_{I,\perp}||\mathbf{k} \tag{3.67}$$

Knowing that $\mathbf{k} = \frac{\mathbf{b}\times\mathbf{P}_{I,\perp}}{||\mathbf{b}\times\mathbf{P}_{I,\perp}||} = \frac{\mathbf{b}\times\mathbf{P}_{I,\perp}}{||\mathbf{P}_{I,\perp}||}$, and using Eq.(3.60), the previous equation becomes

$$\overrightarrow{DB_1} = -\sin(\phi_r)\mathbf{S}_b \cdot \mathbf{P}_I, \tag{3.68}$$

Now substituting Eqs.[3.68,3.66] into Eq.(3.64), one finds the following formula for the rotation

$$\begin{aligned} \mathbf{P}_O &= \mathbf{R}_\mathbf{b} \cdot \mathbf{P}_I, \\ \mathbf{R}_\mathbf{b} &= \Big\{ \cos(\phi_r)\mathbf{I} + (1-\cos(\phi_r))\mathbf{b}\otimes\mathbf{b} - \sin(\phi_r)\mathbf{S}_\mathbf{b} \Big\} \cdot \mathbf{P}_I, \end{aligned} \tag{3.69}$$

where $\mathbf{S}_b$ is the skew-symmetric tensor given by Eq.(3.60), and $\mathbf{R}_\mathbf{b}$ is the rotation tensor shown in Fig.3.6. As mentioned before, this tensor is orthogonal (It is easy to prove this by direct substitution which shows $\mathbf{R}_\mathbf{b}^T = \mathbf{R}_\mathbf{b}^{-1}$), otherwise it won't conserve the kinetic energy. Therefore,

$$\mathbf{P}_I = \mathbf{R}_b^T \cdot \mathbf{P}_O,$$
$$\mathbf{R}_b = \begin{pmatrix} b_x^2 + (1-b_x^2)cos(\phi_r) & b_x b_y(1-\cos(\phi_r)) + b_z\sin(\phi_r) & b_x b_z(1-\cos(\phi_r)) - b_y\sin(\phi_r) \\ b_y b_x(1-\cos(\phi_r)) - b_z\sin(\phi_r) & b_y^2 + (1-b_y^2)cos(\phi_r) & b_y b_z(1-\cos(\phi_r)) + b_x\sin(\phi_r) \\ b_z b_x(1-\cos(\phi_r)) + b_y\sin(\phi_r) & b_z b_y(1-\cos(\phi_r)) - b_x\sin(\phi_r) & b_z^2 + (1-b_z^2)cos(\phi_r) \end{pmatrix} \tag{3.70}$$

The form of Eq.(3.69) is quite general. It is a representation of the rotation in a local coordinate system which always follows the dynamics of the field lines. This remarkable feature enables us to apply this equation in any coordinate system by merely knowing the corresponding field components. With this equation in hand, we now have all the required ingredients to determine $\mathbf{P}$ given by Eq.(3.59).

3.9 Esirkepov Correction Method

We explored in section 3.7 the algorithm utilised to solve the Vlasov equation by means of the Strang splitting at t_n. After each advection, the distribution function is re-estimated, and the new value will be the initial condition for the subsequent advection. At the end, we calculate f^{n+1}. To ensure that Maxwell-Gauss equation is satisfied, most `PIC` codes use correction methods to adjust the current density $\mathbf{J}^{n+\frac{1}{2}}$ before injecting it into Yee solver in order to find the electric field $\mathbf{E}^{n+1}$. In section 3.1.2, we proved that a necessary and sufficient condition for $\mathbf{J}$ to satisfy Eq.(3.2a) is to initially fulfil it, and automatically respects the continuity equation given by Eq.(3.17) at each time step.

`VLEM` employs Esirkepov-type method, initially proposed for `PIC` simulations, to correct the current density. In his paper [264], Esirkepov suggested a density decomposition correction scheme to overcome this issue. This technique is a generalization to those proposed in Refs[279, 280, 281] in which we interpret the form factor as a charge density of the macro-particle. Then, Esirkepov imposed the following assumptions

- Due to its linearity, we can write Eq.(3.17) for just one particle; then the total current density is simply the sum of the contributions coming from each macro-particle.

- The total charge density of the macro-particles must remain constant

$$\sum_{(x_i,y_j,z_k)} S\Big[(x_i - x_\alpha)(y_j - y_\alpha)(z_k - z_\alpha)\Big] = const, \tag{3.71}$$

  where (x_i, y_j, z_k) is the Euler spatial grid, and α refers to the particles of α-species.

- The trajectory of the macro-particle is a straight line over the interval t. Otherwise, it will not be possible to decompose the form factor in a simple and self-consistent manner.

- The macro-particle moves less than one cell per time step.

- The geometry is Cartesian.

Following this line of thought, Esirkepov defined the corrected current density in terms of newly proposed functions -the so-called density decomposition functions (W_1, W_2, W_3). After that, he wrote each of (W_1, W_2, W_3) as a linear combination of the possible differences of the form factor. Then, he proved that, under the prior assumptions, only one linear combination exists such that the continuity equation, written now as $W_1 + W_2 + W_3 = S(x + \Delta x, y + \Delta y, z + \Delta z) - S(x, y, z)$, remains true at each time step[264].

We can apply an equivalent strategy to correct the current density in `VLEM`. We start by considering the characteristics as trajectories of the particles. In this sense, the interpolation to the grid points can be interpreted as a particle's form factor($S_{spline} \rightarrow f$). Furthermore, the `3D`-advection in momentum space does not influence the current density at distinct spatial points because Eq.(3.56) preserves it at all positions in this space. Therefore, the differences of the distribution function in momentum part are neglected. Now, we write

$$W = W_x + W_y + W_z = f^{n+1}(x, y, z) - f^n(x, y, z), \tag{3.72}$$

We know that $f^{n+1}(x, y, z) = f^n(x - \delta x, y - \delta y, z - \delta z)$, thus the above equation becomes

$$W_x + W_y + W_z = f^n(x - \delta x, y - \delta y, z - \delta z) - f^n(x, y, z), \tag{3.73}$$

Where $\delta x = \frac{p_x}{m\gamma}\Delta t,\ \delta y = \frac{p_y}{m\gamma}\Delta t,\ \delta z = \frac{p_z}{m\gamma}\Delta t$. Now we substitute the algorithm given in section 3.7 into the previous equation ($\delta x/2 \rightarrow \delta z/2 \rightarrow \delta y \rightarrow \delta z/2 \rightarrow \delta x/2$), then one finds

$$\begin{aligned}
W = W_x + W_y + W_z = {} & \underbrace{f^n(x_i - \delta x, y_j - \delta y, z_k - \delta z)}_{f^{n+1}} - \underbrace{f(x_i - \frac{\delta x}{2}, y_j - \delta y, z_k - \delta z)}_{f^{++}} \\
& \underbrace{f(x_i - \frac{\delta x}{2}, y_j - \delta y, z_k - \delta z)}_{f^{++}} - \underbrace{f(x_i - \frac{\delta x}{2}, y_j - \delta y, z_k - \frac{\delta z}{2})}_{f^{**}} \\
& + \underbrace{f(x_i - \frac{\delta x}{2}, y_j - \delta y, z_k - \frac{\delta z}{2})}_{f^{**}} - \underbrace{f(x_i - \frac{\delta x}{2}, y_j, z_k - \frac{\delta z}{2})}_{f^{+}} \\
& + \underbrace{f(x_i - \frac{\delta x}{2}, y_j, z_k - \frac{\delta z}{2})}_{f^{+}} - \underbrace{f(x_i - \frac{\delta x}{2}, y_j, z_k)}_{f^{*}} \\
& + \underbrace{f(x_i - \frac{\delta x}{2}, y_j, z_k)}_{f^{*}} - \underbrace{f(x_i, y_j, z_k)}_{f^{n}}
\end{aligned} \tag{3.74}$$

Therefore, we obtain

$$W_x = f^{n+1} - f^{++} + f^{*} - f^{n}, \tag{3.75a}$$
$$W_y = f^{**} - f^{+}, \tag{3.75b}$$
$$W_z = f^{++} - f^{**} + f^{+} - f*, \tag{3.75c}$$

By taking the limit $W_z = 0$, and $+ \rightarrow *$, $f^{++} \rightarrow f^{**}$, we recover the relation for the code `VLEM2D3V` [275]. A nice remark about the distribution function decomposition is that the acceptable shiftings of f appear in a very natural manner in the context of the semi-Lagrangian approach as they can be computed from the advection equations, whereas in `PIC` solvers, the allowed combinations of S are estimated to serve only one primary objective , that is the current density correction.

Now, multiplying Eqs.(3.75a, 3.75b, 3.75c) by $-ev_x$, $-ev_y$, $-ev_z$, respectively, and by then integrating the results over the momentum space, one easily obtains

$$-e < v_x W_x >= J_{x\ i,j,k}^{n+1} - J_{x\ i,j,k}^{++} + J_{xi,j,k}^{*} - J_{x\ i,j,k}^{n}, \tag{3.76a}$$
$$-e < v_y W_y >= J_{y\ i,j,k}^{**} - J_{y\ i,j,k}^{+}, \tag{3.76b}$$
$$-e < v_z W_z >= J_{z\ i,j,k}^{++} - J_{z\ i,j,k}^{**} + J_{z\ i,j,k}^{+} - J_{z\ i,j,k}^{*}, \tag{3.76c}$$

In the previous relations, $-e < v_y W_y >$ represents the current density J_y transported at point (x_i, y_j, z_k) over Δt, then $-e < v_y W_y >= -\nabla \cdot \mathbf{J}|_y$. By substituting the divergence component from Eq.(3.17), we find

$$J_{y\ i,j+\frac{1}{2},k}^{n+\frac{1}{2}} = \frac{1}{4}\Big(J_{y\ i,j,k}^{n} + J_{y\ i,j-1,k}^{n} + J_{y\ i,j,k}^{n+1} + J_{y\ i,j-1,k}^{n+1}\Big) - \Big(J_{y\ i,j,k}^{**} - J_{y\ i,j,k}^{+}\Big), \tag{3.77}$$

where we approximated

$$J_{y\ i,j-\frac{1}{2},k}^{n+\frac{1}{2}} = \frac{1}{4}\Big(J_{y\ i,j,k}^{n} + J_{y\ i,j-1,k}^{n} + J_{y\ i,j,k}^{n+1} + J_{y\ i,j-1,k}^{n+1}\Big) \tag{3.78}$$

By taking $+ \rightarrow *$, $f^{+} \rightarrow f^{*}$, and removing the subscript k, we recover $J_{y\ i,j+\frac{1}{2}}^{n+\frac{1}{2}}$ for `VLEM2D3V`. Now, by repeating this argument for J_x, and J_z, one easily finds

$$J_{x\ i+\frac{1}{2},j,k}^{n+\frac{1}{2}} = \frac{1}{4}\Big(J_{x\ i,j,k}^{n} + J_{x\ i-1,j,k}^{n} + J_{x\ i,j,k}^{n+1} + J_{x\ i-1,j,k}^{n+1}\Big) - \frac{1}{2}\Big(J_{x\ i,j,k}^{n+1} - J_{x\ i,j,k}^{++} + J_{x\ i,j,k}^{*} - J_{x\ i,j,k}^{n}\Big), \tag{3.79}$$

where we approximated

$$J_{x\ i-\frac{1}{2},j,k}^{n+\frac{1}{2}} = \frac{1}{4}\Big(J_{x\ i,j,k}^{n} + J_{x\ i-1,j,k}^{n} + J_{x\ i,j,k}^{n+1} + J_{x\ i-1,j,k}^{n+1}\Big), \tag{3.80}$$

and,

$$J_{z\ i,j,k+\frac{1}{2}}^{n+\frac{1}{2}} = \frac{1}{4}\Big(J_{z\ i,j,k}^{n} + J_{z\ i,j,k-1}^{n} + J_{z\ i,j,k}^{n+1} + J_{z\ i,j,k-1}^{n+1}\Big) - \frac{1}{2}\Big(J_{z\ i,j,k}^{++} - J_{z\ i,j,k}^{**} + J_{z\ i,j,k}^{+} - J_{z\ i,j,k}^{*}\Big), \tag{3.81}$$

where we approximated

$$J_{z\ i,j,k-\frac{1}{2}}^{n+\frac{1}{2}} = \frac{1}{4}\Big(J_{z\ i,j,k}^{n} + J_{z\ i,j,k-1}^{n} + J_{z\ i,j,k}^{n+1} + J_{z\ i,j,k-1}^{n+1}\Big), \tag{3.82}$$

By now eliminating the correction on J_z because it does not enter into the continuity equation in the 2D3V case ($\frac{\partial}{\partial z} = 0$), taking $++ \rightarrow **$, $f^{++} \rightarrow f^{**}$, and by removing the subscript k, we recover $J_{y\ i+\frac{1}{2},j}^{n+\frac{1}{2}}$ for VLEM2D3V. All required variables for correcting the current density have been already stored before reaching this stage as shown Fig.3.5.

3.10 Vlasov-Maxwell Solver in VLEM2D3V

In the preceding discussions of this chapter, we examined in details all the required elements to design the VLEM solver. In this section, we close the discussion by summarizing the complete algorithm for solving the Vlasov-Maxwell system in 2D3V phase space with VLEM2D3V. These steps, shown in Fig.3.8 in colors for an ongoing iteration, are

1. A Yee solver (1) computes the magnetic filed ($\mathbf{B}^{n+\frac{1}{2}}$) knowing $\mathbf{B}^{n-\frac{1}{2}}$, and $\mathbf{E}^{n}$ from the previous iteration. [see section 3.1].

2. Magnetic field at t_n is interpolated using $\mathbf{B}^{n} = \frac{\mathbf{B}^{n+\frac{1}{2}}+\mathbf{B}^{n-\frac{1}{2}}}{2}$ (2). Also, VLEM2D3V interpolates the magnetic and electric fields to the spatial grid points before starting the Vlasov Solver.

3. Vlasov Solver (3, see also Fig.3.5) starts working by performing the following steps

   - 3D-advection in momentum space [see section 3.8.1].
   - 1D-advection along $x-$direction over $\frac{\Delta t}{2}$, then storing J^{*} and f^{*} [see section 3.7].
   - 1D-advection along $y-$direction over a complete time step, then storing J^{**} and f^{**} [see section 3.7].
   - Another 1D-advection along $x-$direction over the remaining $\frac{\Delta t}{2}$, then storing J^{n+1} and f^{n+1} [see section 3.7].

4. Correct the current density $\mathbf{J}^{n+\frac{1}{2}}$ using Esirkepov corrector (4) [see section 3.9]

5. A Yee solver (5) starts working to calculate the electric field at t_{n+1} with the inputs: the corrected current density $\mathbf{J}^{n+\frac{1}{2}}$, magnetic fields $\mathbf{B}^{n+\frac{1}{2}}$, and electric field $\mathbf{E}^{n}$.

6. Repeat the procedure starting from step 1.

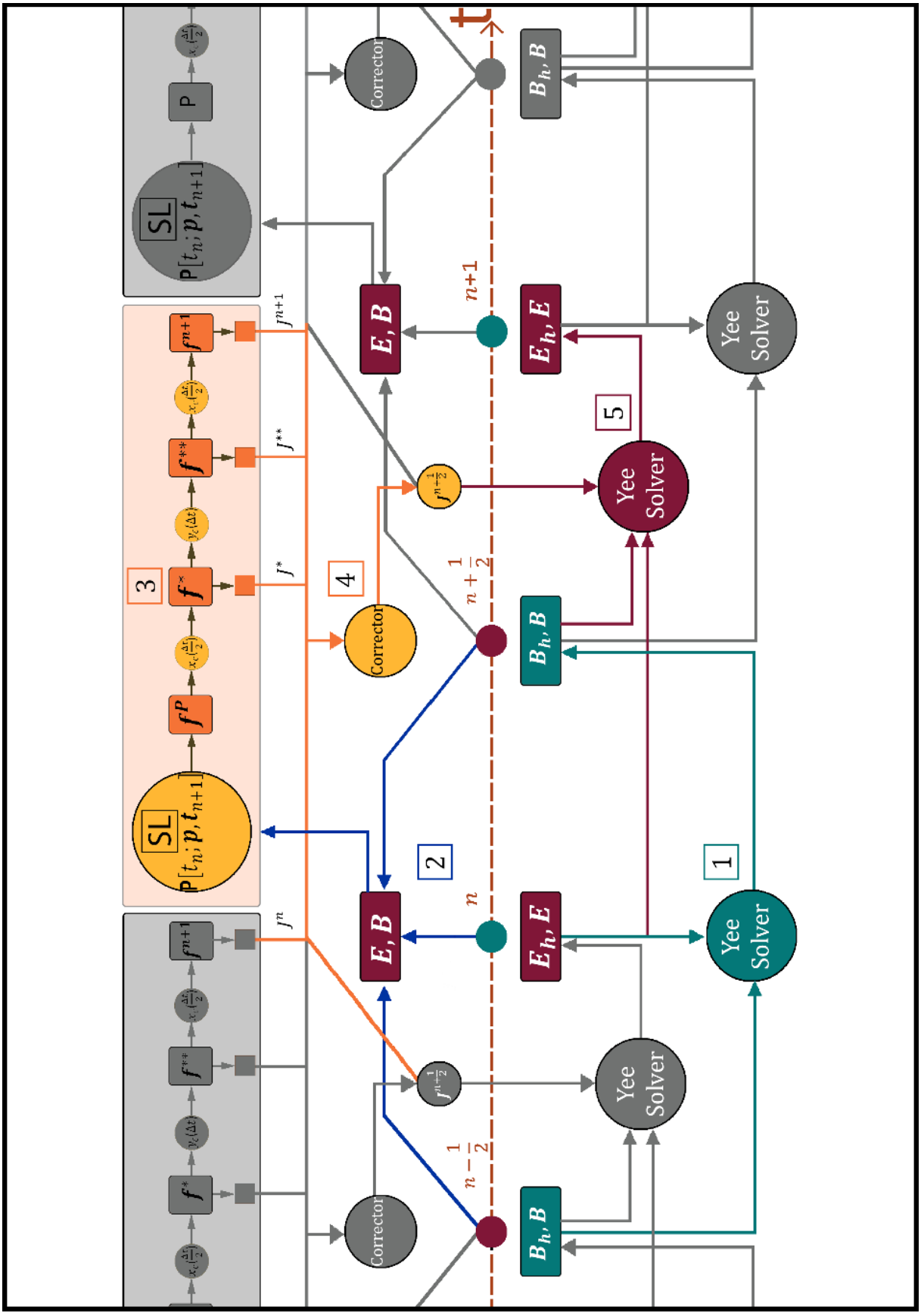

Figure 3.8: Representation of `VLEM2D3V` code. The numbers inside square boxes indicates the solution steps in time order.The colored objects represent the actual computations performed by the simulation in a current iteration inside the main loop. Grey objects are either future (right), or past (left).

4

Numerical Methods for Solving Multi-Scales Eigenvalue Problems

Contents

4.1 Introduction

When studying the linear phase of reconnection instabilities, and of secondary ones occurring in the non-linear phase of the process, we always encounter a generalized eigenvalue problem, such as that given by

$$\gamma B_x = \frac{\eta}{\mu_0}(\frac{d^2}{dx^2} - k^2)B_x \tag{4.1}$$

An exact analytical solution to these kinds of problems generally do not exist due to the multi-scale nature of the partial differential equation involved, which depend on a non-homogeneous equilibrium configuration. The generalized eigenvalue problem takes the following form [282, 283, 284],

$$\gamma \mathcal{A}\mathbf{u} = \mathcal{B}\mathbf{u}, \tag{4.2}$$

where γ and $\mathbf{u}$ are the eigenvalue and the eigenvectors to be found. $\mathcal{A}$ and $\mathcal{B}$ represent in our case the numerical operators resulting, for example, from the discretization of the problem using finite difference stencils. For instance, in the case of Eq.(1.26), $\mathcal{B}$ can be the finite difference stencil approximating the second derivative with respect to x, that is $\frac{\partial^2}{\partial x^2}$, and $\mathbf{u}$ is the magnetic field. This eigenvalue problem in turn depends on matrix decomposition and on numerical algorithms, such as the QR method to find the eigenvalues and eigenvectors. From a computational point of view we have tackled it by developing an algorithm in MATLAB.

To solve this generalized eigenvalue problem correctly for cases such as magnetic reconnection, we should employ a high resolution (very small step) to resolve the inner reconnecting layer. As discussed in the introduction, the inner layer in which the reconnection takes place is very narrow, and of the order of non-ideal parameters. For example, the width of this layer (δ) scales as $\eta^{-1/3}$

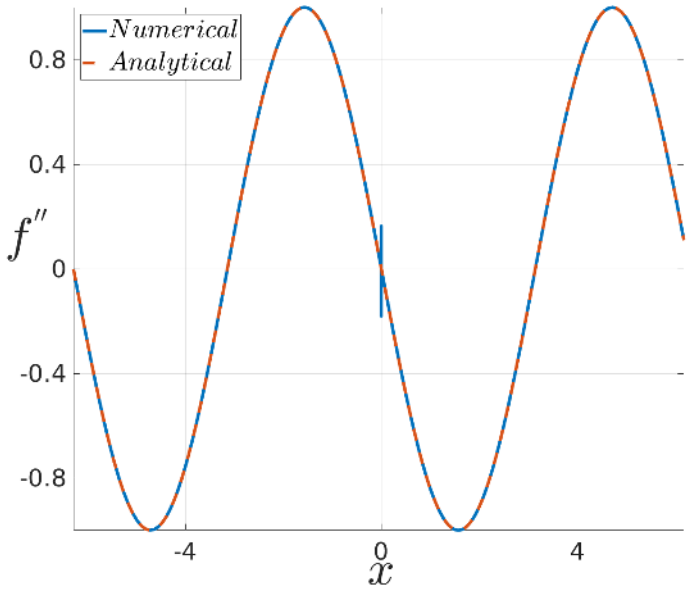

Figure 4.1: The second derivative of the $\sin(x)$ using a double precision non-uniform stencil of the fourth order (blue), and the exact one (orange). The bad estimation of the derivative is clearly shown in the vicinity of $x = 0$.

and $\eta^{-2/5}$ for different purely resistive regimes (see chapters 1 and 7). Therefore, as resistivity (η) approaches its realistic values (for example, 10^{-12}), the width of the reconnection region is of the order 10^{-5} in units of the reference length. This, in turns, means that the step Δx, used in the finite difference stencil, must be much smaller than that, so to ensure having enough points inside the inner layer. Hence, we adopt a non-uniform grid with a varying step that becomes smaller as we approach the neutral line (see section 4.1.2). But due to the double precision storage of numbers in computers, the stencils, used to estimate derivatives, become ill-conditioned when the step reaches very small values. The effect of this ill-conditioning is shown in Fig.4.1, where we present the second derivative of $\sin(x)$ estimated numerically on a non-uniform grid. It is obvious that the stencil fails to give a good approximation for the second derivative near the center of the inner layer ($x = 0$) where the grid spacing becomes very small. To overcome this problem, we use a multi-precision algorithm (section 4.1.2). In the following section, we detail the method that can be followed so to build an arbitrary accurate stencil for the derivative of any order, and then we conclude this short Chapter by explaining the idea behind the non-uniform grid.

4.1.1 A t^{th}-order Accurate Finite Difference Stencil for the n^{th} Derivative on a Non-uniform Grid

In the eigenesolver, derivatives are numerically computed using the standard compact difference method [285]. The general, explicit form for a non-uniform approximation of the n^{th} derivative on a non-uniform grid by using a centered stencil with N_t points and accuracy up to order

$t = N_t - n$ reads

$$\left.\frac{\partial^n f}{\partial x^n}\right|_i = \sum_{m=-\frac{N_t-1}{2}}^{\frac{N_t-1}{2}} a_{i+m} f_{i+m} + e^{(t^{th})} \tag{4.3}$$

Note that, even though the stencils we are considering are centered (and therefore N_t is an odd number), they are in general not symmetric because of the non-uniformity of the grid (see section 4.1.2).

Coefficients a_{i+m} are evaluated by following the standard compact difference approach, using Taylor expansion. For the points to the left and to the right of the center of the stencil, x_i, we respectively find

$$f_{i-j} = \sum_{m=0}^{N_t-1} \frac{h_{i-j}^l}{m!} \left.\frac{\partial^m f}{\partial x^m}\right|_i - \frac{h_{i-j}^{N_t}}{N_t!} \left.\frac{\partial^{N_t}}{\partial x^{N_t}} f\right|_i, \tag{4.4}$$

$$f_{i+j} = \sum_{m=0}^{N_p-1} (-1)^m \frac{h_{i+j}^m}{m!} \left.\frac{\partial^m f}{\partial x^m}\right|_i + \frac{h_{i+j}^{N_p}}{N_p!} \left.\frac{\partial^{N_p}}{\partial x^{N_p}} f\right|_i. \tag{4.5}$$

Using Eqs.(4.4-4.5) combined with (4.3) we obtain a system of N_t equations for the coefficients $a_{i\pm m}$, with $1 \le m \le (N_t - 1)/2$. We write it as

$$\underbrace{\begin{pmatrix} h_{i+\frac{N_t-1}{2}} & \cdots & h_{i+1} & -h_{i-1} & \cdots & -h_{i-\frac{N_t-1}{2}} \\ h^2_{i+\frac{N_t-1}{2}} & \cdots & h^2_{i+1} & h^2_{i-1} & \cdots & h^2_{i-\frac{N_t-1}{2}} \\ \vdots & \cdots & \vdots & \vdots & \cdots & \vdots \\ \vdots & \cdots & \vdots & \vdots & \cdots & \vdots \\ h^J_{i+\frac{N_t-1}{2}} & \cdots & h^J_{i+1} & h^J_{i-1} & \cdots & h^J_{i-\frac{N_t-1}{2}} \\ \vdots & \cdots & \vdots & \vdots & \cdots & \vdots \\ \vdots & \cdots & \vdots & \vdots & \cdots & \vdots \\ h^{N_t-1}_{i+\frac{N_t-1}{2}} & \cdots & h^{N_t-1}_{i+1} & h^{N_t-1}_{i-1} & \cdots & h^{N_t-1}_{i-\frac{N_t-1}{2}} \end{pmatrix}}_{[\boldsymbol{A_t}]} \times \underbrace{\begin{pmatrix} a_{i+\frac{N_t-1}{2}} \\ a_{i+\frac{N_t-1}{2}-1} \\ \vdots \\ \vdots \\ a_{i+\frac{N_t-1}{2}-J-1} \\ \vdots \\ \vdots \\ a_{i-\frac{N_t-1}{2}} \end{pmatrix}}_{\boldsymbol{a}} = \underbrace{\begin{pmatrix} 0 \\ 0 \\ 0 \\ 0 \\ J! \\ 0 \\ 0 \\ 0 \end{pmatrix}}_{\boldsymbol{b}}, \tag{4.6}$$

where "$\times$" stands here for matrix product. Naming $[\tilde{\boldsymbol{A}}_j]$ the matrix that results from replacing the column j in $[\boldsymbol{A}_t]$ with vector $\boldsymbol{b}$, the coefficients $a_{i\pm j}$ can be found for example, by using Cramer's method:

$$a_{i\pm j} = \frac{\det[\tilde{\boldsymbol{A}}_j]}{\det[\boldsymbol{A}_t]} \qquad a_0 = -\sum_{j=-\frac{N_t-1}{2}, j\neq 0}^{\frac{N_t-1}{2}} a_{i+j}, \tag{4.7}$$

Above, the index j runs over $j = 1, 2, .., (N_t - 1)/2$. The determinant of $[\boldsymbol{A_t}]$ can be computed using the fact that $\boldsymbol{A_t}$ is a matrix of Vandermonde-type. After some algebra we can write a general formula for calculating the determinant of a stencil matrix of size $t \times t$,

$$\det[\boldsymbol{A_t}] = \Big(\prod_{l=-N_s, l\neq 0}^{N_t} h_{i+l} \Big) \Big(\prod_{k=1}^{N_t-1} \prod_{l=k+1}^{N_t} [h_{i\pm k} - h_{i\pm l}] \Big) \times \Big(\prod_{k=1}^{N_t} \prod_{l=1}^{N_t} [h_{i+k} + h_{i-l}] \Big), \tag{4.8}$$

with "$\times$" is now expressing standard algebraic product. From Eqs.(4.4-4.5) we can then re-write the local truncation error of the scheme of $t^{th} = (N_t - n)^{th}$ order:

$$e^t = \Big[\sum_{j=1}^{N_t} h_{i+j}^{N_t} a_{i+j} - \sum_{j=1}^{N_t} h_{i-j}^{N_t} a_{i-j} \Big] \times \frac{1}{N_t!} \frac{\partial^{N_t} f}{\partial x^{N_t}}\Big|_i. \tag{4.9}$$

It should be noted that in Eq.(4.9) the number of multiplications of ill-conditioned terms like $h_{i\pm k} - h_{i\pm l}$ increases with the sought accuracy t of the scheme: this provides a source of roundig-error, which eventually forces to reduce the machine-epsilon (i.e., to increase the precision of number representation). Notice that this is an unavoidable drawback of finite-difference schemes, which must be "payed" in order to overcome ill-conditioning problems, when higher order stencils are used.

Previous formulae can be used to compute the coefficients of compact schemes for an arbitrary derivative with arbitrary accuracy. As an explicit example we can consider a fourth order accurate stencil ($t = 4$) for the first derivative ($n = 1$), such as it has been used for the numerical calculations discussed here.
Using these values, whence $N_t = t + n = 5$, Eq.(4.3), (4.4) and (4.5) respectively read:

$$\frac{\partial f}{\partial x}|_i = \sum_{m=-2}^{2} a_{i+m} f_{i+m} + e^{(4)}, \tag{4.10}$$

$$f_{i-j} = \sum_{l=0}^{4} \frac{h_{i-j}^l}{l!} \frac{\partial^l f}{\partial x^l}\Big|_i - \frac{h_{i-j}^5}{5!} \frac{\partial^5 f}{\partial x^5}\Big|_i, \tag{4.11}$$

$$f_{i+j} = \sum_{l=0}^{4} (-1)^l \frac{h_{i+j}^l}{l!} \frac{\partial^l f}{\partial x^l}\Big|_i + \frac{h_{i+j}^5}{5!} \frac{\partial^5 f}{\partial x^5}\Big|_i. \tag{4.12}$$

This leads to a linear system of $N_t = 5$ equations: to the following linear system

$$\underbrace{\begin{pmatrix} h_{i+2} & h_{i+1} & -h_{i-1} & -h_{i-2} \\ h_{i+2}^2 & h_{i+1}^2 & h_{i-1}^2 & h_{i-2}^2 \\ h_{i+2}^3 & h_{i+1}^3 & -h_{i-1}^3 & -h_{i-2}^3 \\ h_{i+2}^4 & h_{i+1}^4 & h_{i-1}^4 & h_{i-2}^4 \end{pmatrix}}_{[\boldsymbol{A_4}]} \cdot \underbrace{\begin{pmatrix} a_{i+2} \\ a_{i+1} \\ a_{i-1} \\ a_{i-2} \end{pmatrix}}_{\boldsymbol{a}} = \underbrace{\begin{pmatrix} 1 \\ 0 \\ 0 \\ 0 \end{pmatrix}}_{\boldsymbol{b}} \tag{4.13}$$

we must add the equation for $a_i = -(a_{i-2} + a_{i-2} + a_{i+1} + a_{i+2})$, as it is given by the second of Eqs.(4.7). Applying Eq.(4.8), one finds

$$\begin{aligned} \det[\boldsymbol{A}_4] = & h_{i+2} h_{i+1} h_{i-1} h_{i-2} (h_{i+2} + h_{i-2})(h_{i+1} + h_{i-2}) \times \\ & (h_{i-1} - h_{i-2})(h_{i+2} + h_{i-1})(h_{i+1} + h_{i-1})(h_{i+1} - h_{i+2}) \end{aligned} \tag{4.14}$$

Finally, using (4.8) and (4.14) in the first of (4.7) we explicitly obtain the sought coefficients:

$$a_{i+2} = \frac{h_{i+1}h_{i-1}h_{i-2}}{h_{i+2}(h_{i+2}+h_{i-2})(h_{i+2}+h_{i-1})(h_{i+1}-h_{i+2})} \tag{4.15}$$

$$a_{i+1} = \frac{-h_{i+2}h_{i-1}h_{i-2}}{h_{i+1}(h_{i+1}+h_{i-2})(h_{i+1}+h_{i-1})(h_{i+1}-h_{i+2})} \tag{4.16}$$

$$a_{i-1} = \frac{h_{i+2}h_{i+1}h_{i-2}}{h_{i-1}(h_{i+2}+h_{i-1})(h_{i+1}+h_{i-1})(h_{i-1}-h_{i-2})} \tag{4.17}$$

$$a_{i-2} = \frac{-h_{i+2}h_{i+1}h_{i-1}}{h_{i-2}(h_{i+2}+h_{i-2})(h_{i+1}+h_{i-2})(h_{i-1}-h_{i-2})} \tag{4.18}$$

For example, if the grid is uniform, then $h_{i+2} = h_{i-2} = 2\Delta x$, and $h_{i+1} = h_{i-1} = \Delta x$. Substituting these values in the previous equations give

$$a_{i+2} = -\frac{1}{12\Delta x},\ a_{i+1} = \frac{8}{12\Delta x},\ a_{i-2} = \frac{1}{12\Delta x},\ a_{i-1} = -\frac{8}{12\Delta x}, a_0 = 0, \tag{4.19}$$

Then substituting the values of these coefficients in Eq.(4.3), one finds the known 4^{th} order centered difference approximation for the first derivative,

$$\frac{\partial f}{\partial x} \approx \frac{-f_{i+2} + 8f_{i+1} - 8f_{i-1} + f_{i+2}}{12\Delta x}, \tag{4.20}$$

4.1.2 Non-uniform Grid and Machine Precision

The non-uniform grid with a fine spacing around $x = 0$ is generated by applying the function

$$x_i = \frac{x_i^* \left[\left(\frac{2|x_i^*|}{L_x} \right)^\beta + b \right]}{1+b}. \tag{4.21}$$

to a uniform grid of spacing h^* centered around $x_0^* = 0$ and defined by $x_i^* = ih^*$, where $i = -N_x/2, ..., N_x/2$, with N_x number of sub-intervals in the interval $[-L_x/2, L_x/2]$. The choice of the real parameters $\beta > 0$ and $b > 0$ allows us to control the degree of non-uniformity, which increases as β increases and/or b decreases. The generic spacing h_i is indeed given in terms of the uniform mesh size L_x/N_x by the relation

$$h_i = \frac{L_x}{N_x} \frac{\left[(2|i+1|N_x)^\beta + b \right] + i\,(2N_x)^\beta \left(|i+1|^\beta - |i|^\beta \right)}{1+b}. \tag{4.22}$$

Notice that small values of h_i can lead to truncation errors comparable to, or smaller than the machine epsilon for a given precision. Therefore, in order to avoid ill-conditioning problems related to the subtraction of too close numbers, both the parameters β and b for a fixed machine precision ϵ_p and the machine precision itself must be made vary at the varying of the non-ideal parameters allowing reconnection, once the number of grid points $N_x + 1$ is fixed: on the one hand, the smallest h_j must be small enough to allow a sufficient resolution of the reconnecting layer width δ; on the other hand, h_j/a must be larger than the machine epsilon.

Lower constraints on h_j/a are indeed posed by rounding errors of the order of the machine precision: by taking into account the implicit rounding error of truncated numbers given by ϵ_{pr} (e.g., in decimal single precision $pr \to s$, $\epsilon_s = 5 \times 10^{-7}$), Eq.(4.3) should be rewritten as:

$$\frac{\partial^2 f}{\partial x^2}|_i = \sum_{m=-4}^{m=4} a_{i+m}(f_{i+m} + \epsilon_{pr}) + e^{t^{th}}. \tag{4.23}$$

It follows that the condition

$$\left| \left.\frac{\partial^2 f}{\partial x^2}\right|_{x_i} - \sum_{m=-4}^{m=4} a_{i+m} f_m \right| \leq \underbrace{e_i^{(t^{th})} + \sum_{m=-4}^{m=4} a_{i+m}\epsilon_{pr}}_{\Lambda_i(h_{i-4},\ldots,h_{i+4})}, \tag{4.24}$$

must be respected, where $\Lambda_i(h_{i-4}, ..., h_{i+4})$ is a polynomial of the mesh spacing $h_{i-4}, ..., h_{i+4}$ (cf. Eq.(4.9) and (4.15-4.18) above).

In order to find a quantitative threshold on h_j we could underestimate $\Lambda_i(h_{i-4}, ..., h_{i+4})$ by means of the function $\Lambda_i^*(\min_m\{h_{i+m}\})$ obtained by calculating $\Lambda_i(h_{i-4}, ..., h_{i+4})$ after substituting, at the varying of m, each of the h_{i+m} with $\min_m\{h_{i+m}\} = h^*$. The numerical value of the latter can be thus computed by finding the minimum of $\Lambda_i^*(h^*)$ imposing:

$$\frac{\partial \Lambda_i^*(h^*)}{\partial h^*} = 0. \tag{4.25}$$

This gives us a restrictive lower threshold on the smallest value of h_j on the grid, which is compatible with a given machine epsilon ϵ_p. If this is not the case, the machine precision must be increased (i.e., ϵ_p must be decreased).

However, in the present version of the code, we don't start by finding the minimum value allowed for the step, by solving the previous equation. In fact, we follow somehow "empirical" way by refining the non-uniform grid until the numerical solution converges.

5

Reduced MHD Models

Contents

5.1 Introduction

Reduced magnetohydrodynamics models are a compromise between simplicity and realism. They ground on the general properties of MHD [33, 286]. Roughly speaking, from a mathematical point of view, they fall into three categories: two-, three-, and four-fields models, where for each field, we have an evolution equation. Their derivations start with the ordering of various terms in the two-fluid model with respect to some small parameter. These parameters can be the ratio of parallel and perpendicular components of the magnetic field, the ratio of large and small radius of a tokamak, e.g., the ratio between the kinetic and magnetic energy (or pressure). The first family of reduced models is the two-field RMHD. In this model, the dynamic is described by two scalar fields: magnetic stream function and the velocity stream function. The former gives the poloidal component of the field, while the gradient components of the later represent the poloidal velocities. The derivation of this model primary depends on the strong guide field assumption. According to this assumption, the guide field is a strong, almost uni-directional field. Thus, the perpendicular components of the field will be smaller than the parallel one by a factor $\epsilon_B = |\frac{\mathbf{B}_\perp|}{B_{||}}$. Another critical assumption is the low-β limit of the plasma, which in most cases, by granting a leading order incompressibility of the plasma fluid, allows the elimination

of the pressure and density gradients from the system, leaving us with two nonlinear equations describing the evolution of the stream functions.

The plasma fluid velocity in this model is mainly due to the mean $\boldsymbol{E} \times \boldsymbol{B}$-drift velocity ($\mathbf{u}_{\mathbf{E}\times\mathbf{B}}$), while drifts resulting from other effects, such as polarization drift and diamagnetic drift, are neglected (or at most retained as first-order corrections, e.g. when ion-sound FLR effects are retained). Furthermore, we ignore the parallel perturbed magnetic field compared to the perpendicular components. These models started separately with the seminal works by Strauss [76, 77], Rosenbluth [78], and Kadomtsev [79]. These works considered resistivity as a dissipative parameter in Ohm law, and neglected `FLR` effects, Hall effects, temperature and density gradients, which can become important in many realistic cases [287]. Two-fields `RMHD` models for toroidal geometry, with density profile scaling as R^{-2}, have been proposed in Refs [288, 289]. Other collisionless models, which include other non-ideal parameters in Ohm law, such as the electron inertia and the effect of electron compressibility, have also been derived by Schep and Pegoraro [83]. Also, resistive models with a general steady, inhomogeneous density profile have been proposed to study instabilities, such as the current halo in tokamaks [290, 291]. Schep and Pegoraro [83] also derived a generalized two-fluid model, which accounts for the effect of a finite ion temperature.

Three-field models [292], which represent a reduction of the more general two-fluid models, is obtained under the assumptions of a : low$-\beta$ plasma dominated by a strong guide field along the ignorable direction, say z; an incompressible flow; a constant electron temperature; and a cold ion limit. The three scalar fields are the magnetic stream function, the velocity stream function, and the electron density. The dynamic in this model is intrinsically `2D`.

A more general set of reduced equations (four-field model [293]) governing the 2D dynamics of magnetic reconnection for small and large guide field and that includes the effects of Hall term can be obtained, by using an ordering that assumes the compressional Alfvén waves to propagate much faster than other waves in the system. Therefore, these waves decouple from others and can be thus eliminated. The four fields here are the magnetic stream function, the velocity stream function, the z-component of ion velocity, and the perturbation b_z along the guide field. This model is a generalization of those obtained for studying the dynamics with an infinite guide field [294, 295, 84, 296, 149, 297]. It is also worth mentioning other reduced models, such as that obtained in Ref.[298], which use a multiple time scale expansion to separate the three time scales associated with the problem. These time scales are the characteristics times of the equilibrium, of the perturbations propagating parallel to the magnetic field, and of the perturbations with wave vectors perpendicular to the field.

In two-field `RMHD` models, Hall term, in generalized Ohm law, is neglected. It was Sonnerup (1979) [86] who first observed the importance of the decoupling between the motion of electrons and ions. The two-field models, in which ions and electrons are constrained to move together, fail to describe this decoupling that becomes important for phenomena occurring on length scales of the order of the ion skin depth or smaller, where Hall effect plays crucial role [299, 300, 301, 302]. In the context of magnetic reconnection, although both ions and electrons move in the direction of the plasma flow toward the X point, ions are slower due to their inertia. This difference is at the origin of the Hall current whose direction is opposite to the convective inflow of the plasma. However, the idea is somehow more subtle and depends on the regime's nature [213].

On the one hand, if the current sheet is collisionless, its width will be smaller than the mean free path of particles, and approximately of the same order of ion skin depth. On the other hand, if ion gyro-radius is larger than its skin depth, the plasma will be collisionless within the current

sheet where ions follow their inertia. Therefore, inside the current sheet, there is only a convective electron current which generates an opposite Hall current. This current, in turn, generates an out-of-plane (Hall) magnetic field which has a quadrupole $3D$ structure (see Fig.5.2) modifying the parallel component of the field when a strong guide field exists. However, the compressibility of the plasma can contribute to this variation of the field in the out-of-plane direction [300, 302]. The linear analysis of tearing mode for a resistive regime with Hall effects was first carried by Terasawa (1983) [303] and has been recently extended to investigate how the "ideal" tearing mode critical aspect ratio is modified due to Hall effects in the absence of the guiding field [304], and to study oblique tearing mode [305], and the occurrence of fast recursive reconnection [306]. A review paper about the applications of the Hall-magnetohydrodynamic regime in space and laboratory plasma can be found in Ref.[307]. At the same time, several models have been devised for the transition from Alfvénic to whistler mediated reconnection, occurring when perturbations at scales d_i are nonlinearly generated. These models, which trace back to the "whistler mediated reconnection" by Mandt, Denton and Drake [94] provide estimates of the growth rate that do not rely on the boundary layer solution of the linear equations, but are rather obtained with heuristic type arguments: they are nevertheless supported by several nonlinear simulations [94].

5.2 Two-Fields Reduced MHD Ordering

Before we discuss a derivation of the two-field `RMHD` model [180], we start by describing the main idea behind it. The derivation of this model depends on ordering the different terms in MHD equations in powers of some small parameters. This ordering is very sensitive to the physics we wish to study. As mentioned in the introduction, the derivation starts with two assumptions: a strong, almost uni-directional guide field and low-β plasma. However, after finding the model, further corrections can be introduced, which include, for example, finite electron temperature effects. Saying that the field is strong would mean that the pressure and kinetic energy are small compared to the magnetic energy. At the same time, the uni-directional assumption implies that the component of the magnetic field along this direction (say $B_z = B_0 + b$, where B_0 is the strong, constant guide field, and b is the perturbation along its direction which is disregarded on this model) is much larger than these components in the perpendicular plane ($\mathbf{B}_\perp = B_x\mathbf{e}_x + B_y\mathbf{e}_y$). If we have in mind the tokamak geometry, then we know that $\frac{B_\perp}{B_\varphi} \sim \frac{r}{R_0}$, where r is the small radius and R_0 is the major radius. So, one writes the following ordering

$$\frac{B_\perp}{B_z} \sim \frac{B_\perp}{B_0} \sim \frac{r}{R} \sim \epsilon_B \tag{5.1}$$

Moreover, a strong guide field along z implies a slowly changing dynamic both in time and space along that direction, while it is the opposite for the perpendicular dynamic. Thus we have,

$$\frac{\partial}{\partial t} \sim O[\epsilon_B], \quad \frac{\partial}{\partial z} \sim O[\epsilon_B], \quad \frac{\partial}{\partial x} \sim \frac{\partial}{\partial y} \sim O[1]. \tag{5.2}$$

A low-β assumption with a constant density profile will, then, implies

$$\rho u_\perp^2 \sim p \sim \frac{B_\perp^2}{2\mu_0} \implies p \sim u_\perp^2 \sim B_\perp^2 \sim \epsilon_B^2 B_0^2, \quad \rho \sim 1, \tag{5.3}$$

Using the previous ordering with Maxwell-Ampere equation, and $\mathbf{B} = \nabla \times \mathbf{A}$, we find that

$$J_x \sim J_y \sim O[\epsilon_B^2], \quad J_z \sim O[\epsilon_B] \quad A_x \sim A_y \sim O[\epsilon_B^2], \quad A_z \sim O[\epsilon_B] \tag{5.4}$$

The Ordering of $\mathbf{J}$ has been obtained using Faraday equation. It is important to notice that for the consistency of the model, any perturbation of the $z-$ component of the field, must be of second order. Therefore, the magnetic field can be written as

$$\mathbf{B} = \mathbf{B}_\perp + (B_0 + b)\mathbf{e}_z, \tag{5.5}$$

where $b \sim O[\epsilon_B^2]$. Now, the $z-$ component of the equation of motion (2.128), neglecting Reynolds term, gives

$$\rho\frac{\partial u_z}{\partial t} + \rho\mathbf{u}\cdot\nabla u_z = \underbrace{-\frac{\partial p}{\partial z} + (J_x B_y - J_y B_x)}_{\sim O[\epsilon_B^3]}, \implies u_z \sim O[\epsilon_B^2] \tag{5.6}$$

The previous equation is of order $O[\epsilon_B^3]$, thus it is reasonable to assume $u_z \approx 0$. This means that we are moving in a reference frame in which the $z-$component of the force vanishes, $F_z = 0$. As we are interested in using this model to study reconnection, we start by adopting a purely resistive regime in order to only focus on the ordering and the derivation of the model. Later, we are going to extend the model. In this case, the generalized Ohm law becomes

$$\mathbf{E} + \mathbf{u}\times\mathbf{B} = \eta\mathbf{J}, \tag{5.7}$$

The $z-$component of the left hand side is of order ϵ_B^2, thus $\eta \sim O[\epsilon_B]$. Table 5.1 summarize the ordering of different terms.

$B_{\|\|}$	$B_\perp$	$J_\perp$	$J_{\|\|}$	$A_\perp$	$A_{\|\|}$	$u_\perp$	$u_{\|\|}$	p	b	∂_t	$\partial_{\|\|}$	$\partial_\perp$
1	$O[\epsilon_B]$	$O[\epsilon_B^2]$	$O[\epsilon_B]$	$O[\epsilon_B^2]$	$O[\epsilon_B]$	$O[\epsilon_B]$	$O[\epsilon_B^2]$	$O[\epsilon_B^2]$	$O[\epsilon_B^2]$	$O[\epsilon_B]$	$O[\epsilon_B]$	1

Table 5.1: Two-fields `RMHD` orderings. $\perp$ refers to the directions perpendicular to that of the guid field, while $||$ denotes the parallel direction.

We know that the magnetic field must be divergence-free. Then, taking the divergence of Eq.(5.5), we see that $\frac{\partial b}{\partial z} \sim O[\epsilon_B^3]$, meaning that $\nabla_\perp \cdot \mathbf{B}_\perp = 0$. Therefore, the perpendicular part of the magnetic field can be written as the curl of a stream function $\psi(x, y)$ (this stream function here is nothing than the z component of the vector potential, $A_z = -\psi$). Hence,

$$\mathbf{B} = \nabla\times(\psi\mathbf{e}_z) + (B_0 + b)\mathbf{e}_z = \nabla\psi\times\mathbf{e}_z + (B_0 + b)\mathbf{e}_z, \tag{5.8}$$

Taking the perpendicular component of Ohm law, one finds

$$\mathbf{E}_\perp + (\mathbf{u}\times\mathbf{B})_\perp = \eta\mathbf{J}_\perp, \tag{5.9}$$

$\perp$ refers to x or y components. However, the right-hand side of the previous equation scales as ϵ_B^3, thus it can be ignored. This means, for example, $u_y \sim E_x/B_z$ and $u_x \sim E_y/B_z$, where we neglected the third-order terms. The main consequence here is that the perpendicular velocity, to the first order, is completely defined by the $\boldsymbol{E}\times\boldsymbol{B}$-drift motion: $\mathbf{v}_{\mathbf{E}\times\mathbf{B}}$. In this model, we only keep terms up to second order. The continuity equation provides another essential information about the velocity, which allows us to write it in term of another stream function. This reduces

the complexity of the model because, instead of working with vector fields, we now use just a few scalar fields. From Eq.(2.26), we have

$$\nabla \cdot \mathbf{u} = 0, \implies \nabla_\perp \cdot \mathbf{u}_\perp + \underbrace{\frac{\partial u_z}{\partial z}}_{\sim O[\epsilon_B^3]} = 0, \implies \nabla_\perp \cdot \mathbf{u}_\perp = 0, \tag{5.10}$$

Therefore, the velocity can be written as

$$\mathbf{u}_\perp = -\nabla \times (\phi \mathbf{e}_z) = \mathbf{e}_z \times \nabla\phi, \tag{5.11}$$

From Eq.(5.9), it easy to prove that $\phi = \chi/B_z$, where χ is the electrostatic scalar potential, and $B_z \sim B_0$. ϕ is known as the velocity stream function. As it follows from their definition, ψ and ϕ scales as ϵ_B. The use of a minus sign in the previous definition is optional, and this choice allows us to assign the same sign for both ϕ and the scalar potential.

Now substituting Eqs(5.7,5.8) into Maxwell-Faraday equation, and neglecting the third order terms, the $z-$component becomes

$$\frac{\partial \psi}{\partial t} = (\mathbf{u} \times \mathbf{B})_z - \eta J_z, \tag{5.12}$$

Assuming a non-relativistic case, Maxwell-Ampere equation gives

$$\mathbf{J} = -\frac{1}{\mu_0}\Delta\psi \mathbf{e}_z + \frac{1}{\mu_0}\nabla b \times \mathbf{e}_z, \tag{5.13}$$

In the previous equation, the first term is of the first order, while the second term is of second order and lays perpendicular plane. In the derivation, we used Eqs(B.20,B.21).

Using the definitions of ϕ and ψ, and Eq.(B.22), we find

$$\mathbf{u} \times \mathbf{B} = \Big[(\nabla\psi \times \nabla\phi) \cdot \mathbf{e}_z\Big]\mathbf{e}_z + (B_0 + b)\nabla\phi = [\psi, \phi]\mathbf{e}_z + (B_0 + b)\nabla\phi, \tag{5.14}$$

where,

$$[\psi, \phi] = (\nabla\psi \times \nabla\phi) \cdot \mathbf{e}_z = \frac{\partial\psi}{\partial x}\frac{\partial\phi}{\partial y} - \frac{\partial\phi}{\partial x}\frac{\partial\psi}{\partial y}, \tag{5.15}$$

is the Poisson bracket (see appendix C for details). Now noticing that the second term of Eq.(5.14) is in the perpendicular plane, we find, after substituting Eqs(5.13,5.14) into Eq.(5.12)

$$\frac{\partial\psi}{\partial t} + [\phi, \psi] = \frac{\eta}{\mu_0}\nabla^2\psi, \tag{5.16}$$

This equation expresses the z-component of the resistive Ohm law in terms of stream functions. It is a linear second-order partial differential equation which describes the evolution of the magnetic stream function. It involves two unknowns: ψ and ϕ. Hence, another equation for ϕ is required to close the system. This equation can be obtained by taking the z-component of `curl` of Eq.(2.124), which allows us to eliminate the pressure term, and thus to find the vorticity equation. The `curl` of Eq.(2.124) gives,

$$\rho\frac{\partial \nabla \times \mathbf{u}}{\partial t} + \rho\nabla \times (\mathbf{u} \cdot \nabla\mathbf{u}) = \nabla \times (\mathbf{J} \times \mathbf{B}) + \nu\nabla \times \Delta\mathbf{u}, \tag{5.17}$$

where the vorticity vector $\mathbf{\Omega}$ is given by

$$\mathbf{\Omega} = \nabla \times \mathbf{u} = -\nabla \times \nabla \times (\phi\mathbf{e}_z) = \nabla^2\phi\mathbf{e}_z = U\mathbf{e}_z. \tag{5.18}$$

where we used Eq.(B.21), and $U = \nabla^2\phi$. Now we calculate the second term. First we start by estimating the convective operator $\mathbf{u}\cdot\nabla$ by using Eq.(5.11) and Poisson bracket notation,

$$\mathbf{u}\cdot\nabla = (\mathbf{e}_z\times\nabla\phi)\cdot\nabla = (-\frac{\partial\phi}{\partial y}\mathbf{e}_x + \frac{\partial\phi}{\partial x}\mathbf{e}_y)\cdot(\mathbf{e_x}\frac{\partial}{\partial x} + \mathbf{e}_y\frac{\partial}{\partial y}) = \frac{\partial\phi}{\partial x}\frac{\partial}{\partial y} - \frac{\partial\phi}{\partial y}\frac{\partial}{\partial x} = [\phi,.], \quad (5.19)$$

Applying this operator on $\mathbf{u}$, one finds

$$\mathbf{u}\cdot\nabla\mathbf{u} = [\phi,.](-\frac{\partial\phi}{\partial y}\mathbf{e}_x + \frac{\partial\phi}{\partial x}\mathbf{e}_y) = -[\phi,\frac{\partial\phi}{\partial y}]\mathbf{e}_x + [\phi,\frac{\partial\phi}{\partial x}]\mathbf{e}_y, \quad (5.20)$$

Now using the previous relation and Eq.(C.34), the second term of Eq.(5.17) has only a $z-$component and can be calculated as follows

$$\nabla\times(\mathbf{u}\cdot\nabla\mathbf{u}) = \Big(\frac{\partial}{\partial x}[\phi,\frac{\partial\phi}{\partial x}] + \frac{\partial}{\partial y}[\phi,\frac{\partial\phi}{\partial y}]\Big)\mathbf{e}_z = \Big([\phi,\frac{\partial^2\phi}{\partial x^2}] + [\phi,\frac{\partial^2\phi}{\partial y^2}]\Big)\mathbf{e}_z = [\phi,\Delta\phi]\mathbf{e}_z = [\phi,U]\mathbf{e}_z, \quad (5.21)$$

Following again the same procedure, using Eqs(B.22, B.23), the definitions of the current density, the magnetic field, and the Poisson bracket, we obtain

$$\begin{aligned}\mathbf{J}\times\mathbf{B} &= (-\frac{1}{\mu_0}\Delta\psi\mathbf{e}_z + \frac{1}{\mu_0}\nabla b\times\mathbf{e}_z)\times(\nabla\psi\times\mathbf{e}_z + (B_0+b)\mathbf{e}_z)\\ &= -\frac{1}{\mu_0}\nabla^2\psi\nabla\psi - \frac{1}{\mu_0}[\psi,b]\mathbf{e}_z - \frac{B_0}{\mu_0}\nabla b - \frac{b}{\mu_0}\nabla b,\end{aligned} \quad (5.22)$$

Notice that all the terms are of second order, except the fourth term which is of third order. Then, using Eqs(B.24, B.23), one easily finds

$$\nabla\times(\mathbf{J}\times\mathbf{B}) = \frac{1}{\mu_0}[\psi,\nabla^2\psi]\mathbf{e}_z - \frac{1}{\mu_0}\nabla[\psi,b]\times\mathbf{e}_z, \quad (5.23)$$

and the last term in Eq.(5.17) becomes

$$\nabla\times\Delta\mathbf{u} = \nabla^2U\mathbf{e}_z, \quad (5.24)$$

Now, substituting Eqs(5.18, 5.21, 5.23, 5.24) into Eqs.(5.17), the $z-$component gives the evolution equation of the vorticity. That is,

$$\frac{\partial U}{\partial t} + [\phi,U] = \frac{1}{\mu_0}[\psi,\nabla^2\psi] + \nu\nabla^2U, \quad (5.25)$$

The dimensionless version of this equation is

$$\frac{\partial U}{\partial t} + [\phi,U] = [\psi,\nabla^2\psi] + R^{-1}\nabla^2U, \quad (5.26)$$

where the Reynolds number is given by

$$R = \frac{\rho_0 u_0 L_0}{\nu} \quad (5.27)$$

Eqs(5.16, 5.25) form the `RMHD` equations of viscous-resistive, low-β regime in slab geometry. We can further extend this model by including additional terms from generalized Ohm law. Before

extending the model, it is worth writing the vector expression of Faraday equation without neglecting any term. Substituting Eqs(5.8, 5.7,5.13) into Faraday equation we find,

$$\frac{\partial \nabla\psi}{\partial t} \times \mathbf{e}_z + \frac{\partial b}{\partial t}\mathbf{e}_z = \nabla[\psi, \phi] \times \mathbf{e}_z + \frac{\eta}{\mu_0}\nabla(\nabla^2\psi) \times \mathbf{e}_z + \frac{\eta}{\mu_0}\nabla^2 b\ \mathbf{e}_z + [b, \phi]\ \mathbf{e}_z \tag{5.28}$$

We see that Eq.(5.16) follows from the first term on the left-hand side, and from the first and second terms on the right-hand side, while another decoupled equation for b , is obtained from remaining terms, and reads

$$\frac{\partial b}{\partial t} + [\phi, b] = \frac{\eta}{\mu_0}\nabla^2 b, \tag{5.29}$$

but is obviously negligible being of third order in ε_B.

5.2.1 Collisionless Regime

As previously mentioned, we can further extend the model by including other terms in Ohm law. We start by discussing the effect of electron inertia; then we briefly discuss the Hall term. Using Eq.(5.13), the first term on right hand side of Eq.(2.143) becomes

$$\mu_0 d_e^2 \frac{\partial \mathbf{J}}{\partial t} = -d_e^2 \frac{\partial \nabla^2\psi}{\partial t}\mathbf{e}_z + d_e^2 \frac{\partial}{\partial t}(\frac{\partial b}{\partial y})\mathbf{e}_x - d_e^2 \frac{\partial}{\partial t}(\frac{\partial b}{\partial x})\mathbf{e}_y, \tag{5.30}$$

Noticing that the last two terms in the previous equation are third-order terms, they can be neglected. That is,

$$\frac{\partial}{\partial t} \sim O[\epsilon_B], b \sim O[\epsilon_B^2], \frac{\partial}{\partial y} \sim 1 \implies \frac{\partial}{\partial t}(\frac{\partial b}{\partial y}) \sim O[\epsilon_B^3], \tag{5.31}$$

The same argument is applied to the last term. Hence,

$$\mu_0 d_e^2 \frac{\partial \mathbf{J}}{\partial t} = -d_e^2 \frac{\partial \nabla^2\psi}{\partial t}\mathbf{e}_z, \tag{5.32}$$

The $\mu_0 d_e^2 \nabla \cdot \{\mathbf{J}\mathbf{u} + \mathbf{u}\mathbf{J}\}$ term, which is of the same order of $\frac{\partial \mathbf{J}}{\partial t}$, becomes

$$\mu_0 d_e^2 \nabla \cdot \{\mathbf{J}\mathbf{u} + \mathbf{u}\mathbf{J}\} = \mu_0 d_e^2 (\nabla \cdot \mathbf{J})\mathbf{u} + \mu_0 d_e^2 (\mathbf{J} \cdot \nabla)\mathbf{J} + \mu_0 d_e^2 (\nabla \cdot \mathbf{u})\mathbf{J} + \mu_0 d_e^2 (\mathbf{u} \cdot \nabla)\mathbf{J}, \tag{5.33}$$

Using Eq.(5.13), it is easy to prove that

$$\nabla \cdot \mathbf{J} = 0. \tag{5.34}$$

The current density advection term becomes

$$\mathbf{J} \cdot \nabla = \frac{1}{\mu_0}\frac{\partial b}{\partial y}\frac{\partial}{\partial x} - \frac{1}{\mu_0}\frac{\partial b}{\partial x}\frac{\partial}{\partial y} - \frac{1}{\mu_0}\nabla^2\psi\frac{\partial}{\partial z} = -\frac{1}{\mu_0}[b, .] - \frac{1}{\mu_0}\nabla^2\psi\frac{\partial}{\partial z}. \tag{5.35}$$

Thus,

$$(\mathbf{J} \cdot \nabla)\mathbf{u} = \frac{1}{\mu_0}[b, \frac{\partial \phi}{\partial y}]\mathbf{e}_x - \frac{1}{\mu_0}[b, \frac{\partial \phi}{\partial x}]\mathbf{e}_y \sim O[\epsilon_B^3] \sim 0. \tag{5.36}$$

In the above relation, all the $z-$derivative vanishes because stream functions are independent of z. The third term on the right hand side of Eq.(5.33) is zero because of Eq.(5.10). Using Eq.(5.19) and Eq.(5.13), one finds

$$(\mathbf{u}\cdot\nabla)\mathbf{J} = -\frac{1}{\mu_0}[\phi,\nabla^2\psi]\mathbf{e}_z + \frac{1}{\mu_0}[\phi,\frac{\partial b}{\partial y}]\mathbf{e}_x - \frac{1}{\mu_0}[\phi,\frac{\partial b}{\partial x}]\mathbf{e}_y, \tag{5.37}$$

Noticing again that the second and third terms scale as ϵ_B^3, the second order relationship becomes

$$(\mathbf{u}\cdot\nabla)\mathbf{J} = -\frac{1}{\mu_0}[\phi,\nabla^2\psi]\mathbf{e}_z, \tag{5.38}$$

Now substituting Eqs(5.34, 5.36, 5.10, 5.38) into Eq.(5.33), we obtain

$$\mu_0 d_e^2 \nabla\cdot\{\mathbf{J}\mathbf{u}+\mathbf{u}\mathbf{J}\} = -d_e^2[\phi,\nabla^2\psi]\mathbf{e}_z \tag{5.39}$$

Substituting Eqs(5.32 5.39) into Ohm law (Eq.(5.12)), we find

$$\frac{\partial\mathcal{F}}{\partial t} + [\phi,\mathcal{F}] = \frac{\eta}{\mu_0}\nabla^2\psi, \tag{5.40}$$

where

$$\mathcal{F} = \psi - d_e^2\nabla^2\psi, \tag{5.41}$$

The dimensionless version of this equation reads

$$\frac{\partial\mathcal{F}}{\partial t} + [\phi,\mathcal{F}] = S^{-1}\nabla^2\psi, \tag{5.42}$$

where $S = \frac{\mu_0 L_o u_0}{\eta}$ is the Lundquist number, and the remaining reference values are given by

$$\psi_0 = B_0 L_0, \quad \phi_0 = u_0 L_0, \quad t_0 = \frac{L_0}{u_0}, \quad u_0\frac{B_0}{\sqrt{\mu_0 n m_i}}. \tag{5.43}$$

The time here is normalized with respect to Alfvén time, the magnetic field to a reference field (for example, in the reconnection case the value of the shear field evaluated in some point −typically far from the neutral line), and the spatial lengths to a reference length L_0, which , in reconnection, can represent the equilibrium shear length. When $\eta = 0$, the previous equation is called the collisionless Ohm law. Notice that we have omitted the hat "ˆ" form the dimensionless quantities to simplify the notation. For example, $\mathcal{F} = \psi_0\hat{\mathcal{F}} = B_0 L_0\hat{\mathcal{F}}$. [1]

5.2.2 Electron Compressibility Effect

As we are going to see later, the inclusion of the electron compressibility effects increase the growth rate of the collisionless regime by $(\frac{\rho_s}{d_e})^{2/3}$. The starting point of the derivation is to obtain the pressure tensor contribution to the Ohm law and to the fluid velocity equation under the assumption of a strong guide field. As obtained in the previous sections, the reduced equation (Eq.(5.40)) has been derived by taking the z component of Ohm law. Thus the earlier results hold, but two modifications are introduced. First, we calculate the contribution of electron pressure tensor, then its contribution to the term $\mathbf{u}\times\mathbf{B}$.

From Eq.(2.92), the electron pressure tensor, under the existence of strong guid field ($\frac{\partial}{\partial z} = 0$), becomes

[1] We repeatedly do that in this thesis.

$$\mathcal{P}_e = \mathcal{P}_e^0 + \mathcal{P}_e^1 = \begin{bmatrix} \frac{\mathcal{P}_{e,\perp}^0}{2\omega_{c,e}}(\frac{\partial u_{e,x}}{\partial y} + \frac{\partial u_{e,y}}{\partial x}) & -\frac{\mathcal{P}_{e,\perp}^0}{2\omega_{c,e}}(\frac{\partial u_{e,x}}{\partial x} - \frac{\partial u_{e,y}}{\partial y}) & \frac{\mathcal{P}_{e,\perp}^0}{\omega_{c,e}}\frac{\partial u_{e,z}}{\partial y} \\ -\frac{\mathcal{P}_{e,\perp}^0}{2\omega_{c,e}}(\frac{\partial u_{e,x}}{\partial x} - \frac{\partial u_{e,y}}{\partial y}) & -\frac{\mathcal{P}_{e,\perp}^0}{2\omega_{c,e}}(\frac{\partial u_{e,x}}{\partial y} + \frac{\partial u_{e,y}}{\partial x}) & -\frac{\mathcal{P}_{e,\perp}^0}{\omega_{c,e}}\frac{\partial u_{e,z}}{\partial x} \\ \frac{\mathcal{P}_{e,\perp}^0}{\omega_{c,e}}\frac{\partial u_{e,z}}{\partial y} & -\frac{\mathcal{P}_{e,\perp}^0}{\omega_{c,e}}\frac{\partial u_{e,z}}{\partial x} & \mathcal{P}_{e,||}^0 \end{bmatrix} \tag{5.44}$$

where,

$$\mathcal{P}_{e,\perp}^0 \approx \mathcal{P}_{e,||}^0 = kT_e^0 n_e, \tag{5.45}$$

where T_e^0 is a constant, uniform reference electron temperature. Now we calculate the $z-$contribution of electron pressure tensor term in Eq.(2.143), thus using Eqs(5.44, 5.45), we find

$$\begin{aligned} I_{\mathcal{P}_e,z} &= -\frac{1}{en_e}(\nabla\cdot\mathcal{P}_e)\cdot\mathbf{e}_z = -\frac{1}{en_e}(\frac{\partial\mathcal{P}_{e,xz}}{\partial x} + \frac{\mathcal{P}_{e,yz}}{\partial y}) = -\frac{kT_e^0}{en_e\omega_{c,e}}\Big[\frac{\partial}{\partial x}(n_e\frac{\partial u_{e,z}}{\partial y}) - \frac{\partial}{\partial y}(n_e\frac{\partial u_{e,z}}{\partial x})\Big] \\ &= -\frac{kT_e^0}{e\omega_{c,e}}[ln(n_e), u_{e,z}], \end{aligned} \tag{5.46}$$

where,

$$\nabla\cdot\mathcal{P}_e = (\frac{\partial\mathcal{P}_{e,xx}}{\partial x} + \frac{\partial\mathcal{P}_{e,yx}}{\partial y})\mathbf{e}_x + (\frac{\partial\mathcal{P}_{e,xy}}{\partial x} + \frac{\partial\mathcal{P}_{e,yy}}{\partial y})\mathbf{e}_y + (\frac{\partial\mathcal{P}_{e,xz}}{\partial x} + \frac{\partial\mathcal{P}_{e,yz}}{\partial y})\mathbf{e}_z \tag{5.47}$$

We are interested in the $z-$component of the current density. Along the guide field, the electron velocity is larger than that of the ion with a factor equal to ϵ_m^{-1}, where the dominant force there is electrostatic. Thus, $j_z = -en_e u_{e,z}$, then using Eq.(5.13), we write

$$u_{e,z} = \frac{1}{\mu_0 en_e}\nabla^2\psi, \tag{5.48}$$

Hence, Eq.(5.46) becomes

$$I_{\mathcal{P}_e,z} = -\frac{kT_e^0}{\mu_0 e^2 n_0\omega_{c,e}}\frac{\psi_0}{L_0^2}[ln(n_e), \frac{\nabla^2\psi}{n_e}] = -\epsilon_m d_i\rho_s^2[ln(n_e), \frac{\nabla^2\psi}{n_e}], \tag{5.49}$$

with the previous writing, the quantity between Poisson brackets is dimensionless. Also, Eqs.(2.144, 2.148) have been used to obtain the previous equation. This equation will be neglected now because it is of order ϵ_m. Nevertheless, even if terms of this order are kept, this term is cancelled by another one that results from the convective term $\mathbf{u}_{e,\perp}.\nabla$ in Ohm law (see Ref[308]). The exact cancellation of the bracket terms proportional to $\epsilon_m\rho_s^2 d_i$ is known as gyrofluid cancellation [186].

Now we turn our attention to the $\mathbf{u}\times\mathbf{B}$ term. We know that one-fluid velocity is equal to ion velocity, meaning that the plasma fluid moves with ion velocity. Then,

$$\mathbf{u}\times\mathbf{B} = (\frac{\mathbf{J}}{en} + \mathbf{u_e})\times\mathbf{B}. \tag{5.50}$$

The $z-$component of the previous equation is

$$(\mathbf{u}\times\mathbf{B})\cdot\mathbf{e}_z = \mathbf{e}_z\cdot(\mathbf{u}_e\times\mathbf{B}) = \mathbf{u}_{e,\perp}\cdot(\mathbf{B}\times\mathbf{e}_z) = \mathbf{u}_{e,\perp}\cdot\nabla\psi, \tag{5.51}$$

In the previous equation, the $z-$ component of the contribution resulting from the current density is zero. Also, we have used Eq.(5.8). The electron velocity can be estimated from the equation of motion: Eq.(2.36). The leading order terms, neglecting the inertia of electrons, gives

$$\mathbf{u}_e \times \mathbf{B} = -\frac{1}{en_e}\nabla \cdot \mathcal{P}_e - \mathbf{E}, \tag{5.52}$$

Taking the cross product with $\mathbf{e}_z$, and using the definitions of stream functions, it is easy to obtain

$$\mathbf{u}_{e,\perp} = \mathbf{e}_z \times \nabla\phi + (\nabla\psi \times \mathbf{e}_z)u_{e,z} - \frac{\rho_s^2}{d_i}\mathbf{e}_z \times \frac{\nabla \cdot \mathcal{P}_e}{n_e}. \tag{5.53}$$

All quantities in the previous equation are dimensionless. Now, substituting this equation into Eq.(5.52), and noticing the zero contribution of the second term, we find

$$(\mathbf{u} \times \mathbf{B}) \cdot \mathbf{e}_z = -(\mathbf{e}_z \times \nabla\phi) \cdot \nabla\psi + \frac{\rho_s^2}{d_i}(\mathbf{e}_z \times \frac{\nabla \cdot \mathcal{P}_e}{n_e}) = [\psi, \phi] + \frac{\rho_s^2}{d_i}(\mathbf{e}_z \times \frac{\nabla \cdot \mathcal{P}_e}{n_e}) \cdot \nabla\psi \tag{5.54}$$

Using Eq.(5.44), Poisson bracket, and the definitions of the stream function we easily find,

$$\frac{\rho_s^2}{d_i}\mathbf{e}_z \times \frac{\nabla \cdot \mathcal{P}_e}{n_e} = \frac{\rho_s^2}{d_i}\mathbf{e}_z \times \nabla ln(n_e) + R \tag{5.55}$$

The remaining terms R are of order $\epsilon_B\epsilon_m$, and thus neglected. Substituting this equation into Eq.(5.54), one finds

$$(\mathbf{u} \times \mathbf{B}) \cdot \mathbf{e}_z = [\psi, \phi] - \frac{\rho_s^2}{d_i}[ln(n_e), \psi], \tag{5.56}$$

The generalized Ohm law is the same as derived in section 2.4.3, with only one additional term that takes into account a two-fluid effect which results from the compressibility of the electrons as we are going to see in this section. However, to close our system, we need to write the gradient of electron density, if possible, as a function of the stream functions. Here, the quasi-neutrality assumption plays the main rule. Contrary to the electrons' case, ion inertia cannot be neglected as it represents, approximately, the inertia of the plasma. On the other hand, the $z-$component of ion velocity and the ion pressure tensor part can be neglected because they scale as ϵ_m. Then, the equation of motion of the ions gives

$$\mathbf{u}_{i,\perp} = \mathbf{e}_z \times \nabla\phi - d_i\frac{\partial\nabla\phi}{\partial t} - d_i[\phi, \nabla\phi], \tag{5.57}$$

This equation is dimensionless, and it is easy to obtain it by taking the curl of Eq.(2.36), while keeping only the inertia, electrostatic, and the magnetic terms. Also, we used Eq.(5.11), and Poisson bracket notation.

Now continuity equation of ions, combined with Eqs(5.57, 5.19) give

$$\frac{d}{dt}ln(n_i) = d_i\frac{d}{dt}\nabla^2\phi \implies ln(n_e) = ln(n_i) = d_i\nabla^2\phi, \tag{5.58}$$

Where we have used the quasi-neutrality assumption $n_e = n_i$. Substituting this equation into Eq.(5.56), one finds

$$(\mathbf{u} \times \mathbf{B}) \cdot \mathbf{e}_z = [\psi, \phi] - \rho_s^2[\nabla^2\phi, \psi] = [\psi, \phi] - \rho_s^2[U, \psi]. \tag{5.59}$$

Finally substituting this into Eq.(5.12), with the collisionless corrections added in the previous section and given by Eq.(5.42), becomes

$$\frac{\partial \mathcal{F}}{\partial t} + [\phi, \mathcal{F}] = \rho_s^2 [U, \psi] + S^{-1} \nabla^2 \psi. \tag{5.60}$$

In other words we only add one term to the right hand side of Eq.(5.42). This term is $\rho_s^2[U, \psi]$. The vorticity equation remains the same as given by Eq.(5.26).

5.3 Two-Field RMHD Equations

The dimensionless two-field RMHD equations read

$$\frac{\partial \mathcal{F}}{\partial t} + [\phi, \mathcal{F}] = \rho_s^2 [U, \psi] + S^{-1} \nabla^2 \psi, \tag{5.61}$$

$$\frac{\partial U}{\partial t} + [\phi, U] = [\psi, \nabla^2 \psi] + R^{-1} \nabla^2 U, \tag{5.62}$$

with

$$\mathcal{F} = \psi - d_e^2 \nabla^2 \psi, \quad U = \nabla^2 \phi, \tag{5.63}$$

and,

$$\mathbf{u} = \mathbf{e}_z \times \nabla \phi, \quad \mathbf{B} = \nabla \psi \times \mathbf{e}_z + B_{0,z} \mathbf{e}_z, \tag{5.64}$$

where $R = (\rho L_0 u_0)/\nu$ and $S = (\mu_0 L_0 u_0)/\eta$, are the Reynolds and Lundquist number, respectively. η is the magnetic resistivity, and ν is the plasma viscosity. L_0 and u_0 are the characteristic lengths and Alfvén velocity, respectively. This system represents a 2D-initial value problem where the dependent variables are ψ, and ϕ. Later, we are going to linearize these equations with an equilibrium that enables us to study the linear phase of magnetic reconnection in different regimes. This system can be solved by numerical methods, such as spectral methods for periodic boundary conditions [222], or with other methods like finite difference, or multigrid methods that allows us to study the reconnection layer with high spatial resolution [309, 310, 224, 311].

5.4 Linear Analysis of RMHD Equations

In this section, we are going to linearize RMHD equations. However, the linearized equations of this section are slightly modified. They are a generalization of the Padé approximation [312] and include only one additional term which describes the diffusion of the vorticity and takes into account the effects of a finite temperature of ions [83, 313, 314]. The equations read,

$$\frac{\partial \mathcal{F}}{\partial t} + [\phi, \mathcal{F}] = \rho_s^2 [U, \psi] + S^{-1} \nabla^2 \psi, \tag{5.65}$$

$$\frac{\partial U}{\partial t} + [\phi, U] = [\psi, \nabla^2 \psi] + R^{-1} \nabla^2 U, \tag{5.66}$$

with

$$\mathcal{F} = \psi - d_e^2 \nabla^2 \psi, \quad U - \rho_i^2 \nabla^2 U = \nabla^2 \phi, \tag{5.67}$$

and,

$$\mathbf{u} = \mathbf{e}_z \times \nabla \phi, \quad \mathbf{B} = \nabla \psi \times \mathbf{e}_z + B_{0,z} \mathbf{e}_z. \tag{5.68}$$

Since in this chapter the focus is on the formal derivation and discussion of the model, we consider now all non-ideal terms together before to linearize them.

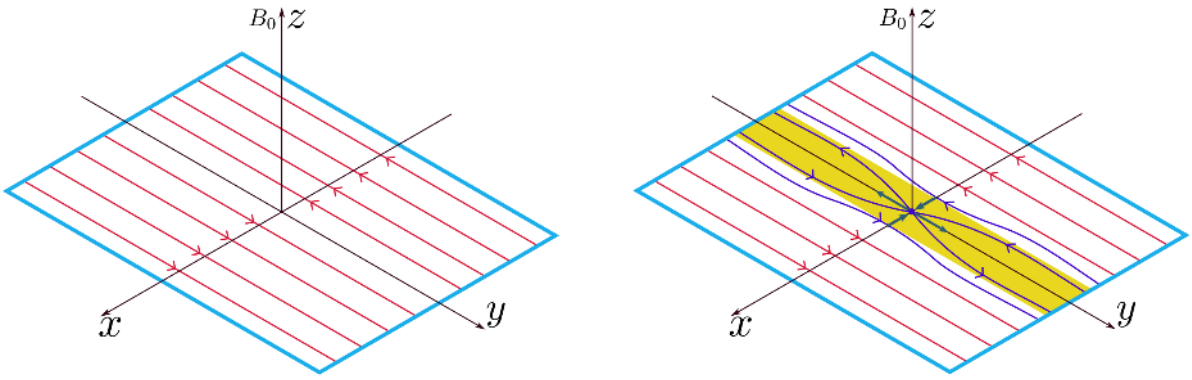

Figure 5.1: To the left: an equilibrium configuration of Magnetic reconnection in Cartesian geometry. B_0 is the strong guide field along $z-$direction, while $B_y(x)$ is a sheared in-plane magnetic field which changes its topology and thus converts the magnetic energy stored into field lines into kinetic energy. To the right: the formation of a magnetic island and the reconnecting of field lines at $X-$point.The yellow region represents the reconnection layer whom width depends on the non-ideal parameters.

5.4.1 Equilibrium

Fig.5.1 shows an in-plane equilibrium in a slab geometry which is unstable for the reconnection of magnetic field lines when the terms allowing the change of magnetic line topology are included in Ohm law. The reconnection occurs in a small narrow region (current sheet) centred around the y axis. The equilibrium magnetic stream function is a function of x and given by

$$\mathbf{B}_{eq} = B_{eq,y}(x)\mathbf{e}_y + B_{eq,z}\mathbf{e}_z = -\frac{\partial \psi_{eq}(x)}{\partial x}\mathbf{e}_y + B_{eq,z}\mathbf{e}_z, \tag{5.69}$$

It is clear that $\mathbf{B}_{eq}$ is divergence-free. However, a current density in the z direction ($\mathbf{J}_{eq} = -\frac{1}{\mu_0}\frac{\partial B_{eq,y}(x)}{\partial x}\boldsymbol{e}_z$) is associated to this equilibrium field. Thus there is a force along the x direction ($\mathbf{J}_{eq} \times \mathbf{B}_{eq} = \frac{1}{2\mu_0}\frac{\partial B^2_{eq,y}(x)}{\partial x}$). Therefore the equilibrium condition implies the existence of another force which results from the $x-$component of the pressure gradient ($\frac{\partial p(x)}{\partial x}$).

Far from the current sheet, the plasma follows ideal `MHD` equations, and the frozen-in condition is respected. Thus, in that region, the plasma and the magnetic field lines are co-moving together, and therefore the plasma cannot slip across field lines. However, around the singular surface, $x = 0$, the inclusion of a diffusive effect into the ideal `MHD` equations is required to remove the singularity into the problem. It is this diffusive mechanism which allows a finite magnetic field along $x-$direction to make the particles jump between different field lines, and thus the reconnection instability to occur.

An extended model that includes the full pressure tensor can also be derived by keeping the pressure tensor in the equation of motion and by adding the evolution equation of the pressure tensor. However, one must pay attention to the consistency of this model with the kinetic description, where a meaningful comparison between fluid and kinetic models will be only possible for small values of $k^2\rho_i^2$, and of $k^2 d_i^2$ (k is the wavenumber), as discussed in Ref. [315].

5.4.2 Linearization of RMHD Equations

Now we linearize the equations by adding perturbations to the equilibrium quantities ($f = f_{eq} + f_1$). These perturbations are periodic along y (Fig.(5.1)), which allows us to use Fourier analysis, and thus to study the linear phase of the instability. After linearization, Eqs.(5.65, 5.66) become

$$\frac{\partial \mathcal{F}_1}{\partial t} + [\phi_{eq}, \mathcal{F}_1] + [\phi_1, \mathcal{F}_{eq}] = \rho_s^2[U_{eq}, \psi_1] + \rho_s^2[U_1, \psi_{eq}] + S^{-1}\nabla^2\psi_1, \tag{5.70}$$

$$\frac{\partial U_1}{\partial t} + [\phi_{eq}, U_1] + [\phi_1, U_{eq}] = [\psi_{eq}, \nabla^2\psi_1] + [\psi_1, \psi_{eq}^{''}] + R^{-1}\nabla^2 U_1, \tag{5.71}$$

with,

$$\mathcal{F}_{eq} = \psi_{eq} - d_e^2\psi_{eq}^{''}, \quad U_{eq} - \rho_i^2 U_{eq}^{''} = \phi_{eq}^{''}, \tag{5.72}$$

$$\mathcal{F}_1 = \psi_1 - d_e^2\nabla^2\psi_1, \quad U_1 - \rho_i^2\nabla^2 U_1 = \nabla^2\phi_1, \tag{5.73}$$

The "prime" denotes the derivation with respect to x. Now, the perturbed stream functions are

$$\psi_1 = \tilde{\psi}(x)e^{\gamma t}e^{iky}, \quad \phi_1 = i\tilde{\phi}(x)e^{\gamma t}e^{iky}, \tag{5.74}$$

For example with this perturbation, a straightforward derivation gives

$$\begin{aligned} &\frac{\partial \mathcal{F}_1}{\partial t} = \gamma\Big[1 - d_e^2(\partial_x^2 - k^2)\Big]\tilde{\psi}(x)e^{\gamma t}e^{iky}, \quad \nabla^2\psi_1 = (\partial_x^2 - k^2)\tilde{\psi}(x)e^{\gamma t}e^{iky}, \\ &[\psi_1, \psi_{eq}^{''}] = -\psi_{eq}^{'''}\frac{\partial \psi_1}{\partial y} = -ik\psi_{eq}^{'''}\psi_1. \end{aligned} \tag{5.75}$$

Therefore, after substituting these perturbations, as detailed in appendix D, into Eq.(5.70, 5.72, 5.73), one obtains the following eigenvalue problem,

$$\gamma \begin{bmatrix} \mathcal{D} & 0 \\ 0 & i\Lambda \end{bmatrix} \begin{bmatrix} \tilde{\psi}(x) \\ \tilde{\phi}(x) \end{bmatrix} = \begin{bmatrix} \mathcal{L}_1 & \mathcal{L}_2 \\ \mathcal{L}_3 & \mathcal{L}_4 \end{bmatrix} \begin{bmatrix} \tilde{\psi}(x) \\ \tilde{\phi}(x) \end{bmatrix} \tag{5.76}$$

where,

$$\begin{aligned} &\mathcal{D} = \mathcal{I} - d_e^2\mathcal{A}, \quad \mathcal{A} = \frac{\partial^2}{\partial x^2} - k^2, \quad \mathcal{E} = \frac{\partial^4}{\partial x^4} - 2k^2\frac{\partial^2}{\partial x^2} + k^4, \quad \Lambda = \rho_i^2\mathcal{E} + \mathcal{A}, \quad \mathcal{V} = \rho_i^2\mathcal{A}\mathcal{E} + \mathcal{E}, \\ &\mathcal{L}_1 = -ik\phi_{eq}^{'}\mathcal{D} + ik\rho_s^2 U_{eq}^{'} + S^{-1}\mathcal{A}, \quad \mathcal{L}_2 = k\rho_s^2\psi_{eq}^{'}\Lambda - k\mathcal{F}_{eq}^{'}, \quad \mathcal{L}_3 = ik\psi_{eq}^{'}\mathcal{A} - ik\psi_{eq}^{'''}, \\ &\mathcal{L}_4 = iR^{-1}\mathcal{V} + k\phi_{eq}^{'}\Lambda - kU_{eq}^{'}, \end{aligned} \tag{5.77}$$

Here $\mathcal{I}$ is the identity operator. This eigenvalue problem can be used to study a wide range of instabilities, from the Kelvin-Helmholtz instability to primary and secondary reconnection instabilities. For example, when taking the limit $\rho_i = 0$, and $\phi_{eq} = 0$, it is possible, as we are going to see later, to study different reconnection regimes for the primary instability. Among the possibilities we find the:

- **Cold collisionless regime**: Here $\rho_i = S^{-1} = R^{-1} = \rho_s = 0$, and $d_e \neq 0$ with no flow $\phi_{eq} = 0$.

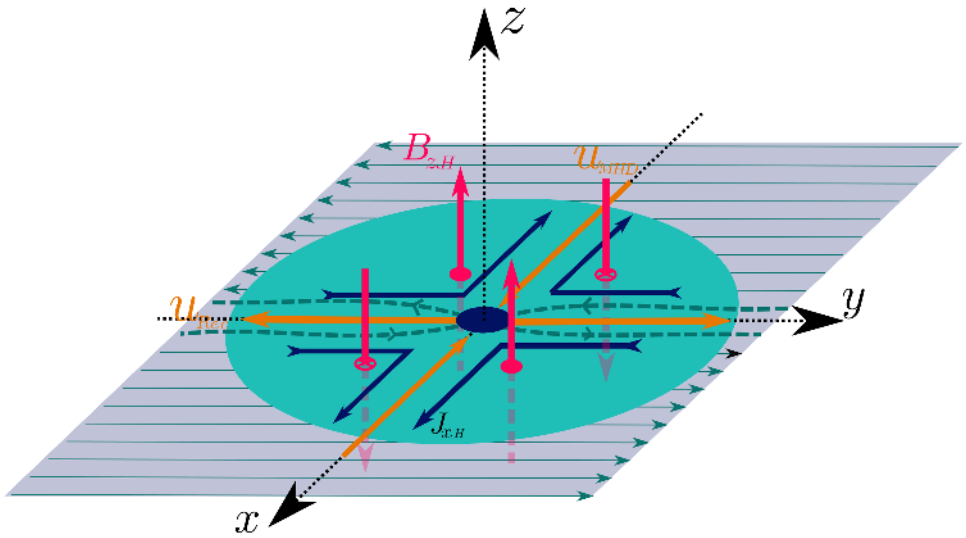

Figure 5.2: Effects of Hall term on reconnection: the outer circle represents the width of the collisionless current sheet where the motion of the ions starts to decouple from that of electrons. Black arrows denote the Hall current which is opposite to the electrons convective motion (orange arrows) toward X point shown as a small black circle. Hall term generates a Hall magnetic field (red arrows) in a direction perpendicular to the reconnection plane.

- **Warm Collisionless regime**: Here $\rho_i = S^{-1} = R^{-1} = 0$, and $d_e \neq 0 \neq \rho_s$ with no flow $\phi_{eq} = 0$.
- **Purely resistive regime**: Here $\rho_i = \rho_s = d_e = R^{-1} = 0$, and $S^{-1} \neq 0$ with no flow $\phi_{eq} = 0$.
- **Viscous-resistive regime**: Here $\rho_i = \rho_s = d_e = 0$, and $S^{-1} \neq 0 \neq R^{-1}$ with no flow $\phi_{eq} = 0$.
- **Semi-Collisional regime**: Here $\rho_i = d_e = R^{-1} = 0$, and $S^{-1} \neq 0 \neq \rho_s$ with no flow $\phi_{eq} = 0$.
- **Hybrid regime**: Here $\rho_i = \rho_s = R^{-1} = 0$, and $S^{-1} \neq 0 \neq d_e$ with no flow $\phi_{eq} = 0$.

5.5 Hall Effect in Magnetic Reconnection: New Results

In the previous sections, we went into the details of the two-field `RMHD` equations. We extended this model to include the effect of electron compressibility through the ion-sound Larmor radius term. However, when Hall term is taken into account, the geometry of reconnection at `X`-point is modified due to an emerging magnetic field (Hall field) perpendicular to the reconnection plane (3D structure).

Fig.5.2 shows Hall effects on the reconnection process. In this figure, we present a collisionless regime. Hence the width of the diffusion region is smaller than the mean free paths of particles. Also, if the width of the current sheet is smaller than the ion cyclotron radius, but of the order of the ion skin depth, ions behave as unmagnetized particles, and its motion decouples of that of electrons. This separation between ion and electron motions starts at the boundary of the current

sheet (outer green circle in the figure), leaving behind a flow of electrons, which remains in co-motion with magnetic field lines until they reach the `X-` point, where the topology of field lines breaks and lines reconnect (the inner black circle in the figure). This electrons inflow generates an opposite Hall current (black arrows in the figure) that induces an out-of-plane magnetic field (Hall field shown as red arrows in the figure).

In the following, we are going to linearize `MHD` equation while keeping Hall term into generalized Ohm Law. The equations of the Hall system read,

$$\mathbf{E}+\mathbf{u}\times\mathbf{B}=\mu_0 d_e^2\frac{\partial\mathbf{J}}{\partial t}+\mu_0 d_e^2\nabla\cdot\{\mathbf{uJ}+\mathbf{Ju}\}+\frac{1}{en}\mathbf{J}\times\mathbf{B}+\eta\mathbf{J}, \tag{5.78}$$

$$\frac{\partial\mathbf{B}}{\partial t}=-\nabla\times\mathbf{E},\quad \mathbf{J}=\frac{1}{\mu_0}\nabla\times\mathbf{B}, \tag{5.79}$$

$$mn\frac{\partial\mathbf{u}}{\partial t}+mn\mathbf{u}\cdot\nabla\mathbf{u}=-\nabla p+\mathbf{J}\times\mathbf{B}, \tag{5.80}$$

The equilibrium magnetic field is composed of two parts: the sheared field (B_0) in the `(x-y)` plane (see Fig.5.2), and the guide field (B_g) along the $z-$direction. It reads,

$$\mathbf{B}=\nabla\times(\psi\mathbf{e}_z)+B_g\mathbf{e}_z=B_0 f(x)\mathbf{e}_y+B_g\mathbf{e}_z. \tag{5.81}$$

The equilibrium current densities, and $\mathbf{J}\times\mathbf{B}$ force are

$$\mathbf{J}_{eq}=\frac{1}{\mu_0}\nabla\times\mathbf{B}_{eq}=\frac{B_0}{\mu_0}f^{'}(x)\mathbf{e}_z,\quad \mathbf{F}_{\mathbf{J}_{eq}\times\mathbf{B}_{eq}}=\mathbf{J}_{eq}\times\mathbf{B}_{eq}=-\frac{B_0^2}{\mu_0}f(x)f^{'}(x)\mathbf{e}_x, \tag{5.82}$$

Therefore to sustain this equilibrium, the magnetic force is balanced by a force resulting from a gradient of the pressure along the $x-$direction, that is,

$$p(x)+\frac{B_0^2}{2\mu_0}=const. \tag{5.83}$$

Now, after linearizing Eqs.(5.78, 5.80, 5.79) [see appendix E for detailed derivation], one finds

$$\frac{\partial}{\partial t}(1-d_e^2\nabla^2)B_{1x}=[f(x)-d_e^2 f^{''}(x)]\frac{\partial u_x}{\partial y}-d_i f(x)\frac{\partial^2 B_{1z}}{\partial y^2}+S^{-1}\nabla^2 B_{1x}, \tag{5.84}$$

$$\frac{\partial}{\partial t}(1-d_e^2\nabla^2)B_{1z}=f(x)\frac{\partial u_z}{\partial y}+d_i[f(x)\nabla^2-f^{''}(x)]B_{1x}+S^{-1}\nabla^2 B_{1z}, \tag{5.85}$$

$$\frac{\partial}{\partial t}\nabla^2 u_x=[f(x)\nabla^2-f^{''}(x)]\frac{\partial B_{1x}}{\partial y}+R^{-1}\nabla^2\nabla^2 u_x, \tag{5.86}$$

$$\frac{\partial}{\partial t}\frac{\partial u_z}{\partial y}=f(x)\frac{\partial^2 B_{1z}}{\partial y^2}+R^{-1}\nabla^2\frac{\partial u_z}{\partial y}. \tag{5.87}$$

This closed system is composed of four dimensionless equations where the dependent functions are B_{1x}, B_{1z}, u_x, and u_z. The derivation of these equations is based on two main assumptions: a constant uniform guide magnetic field, and an incompressible plasma with a periodic perturbation propagating along the $y-$direction. The magnetic fields are normalized to the shear field (B_0). At the same time, the remaining reference quantities are the Alfvén velocity u_A, the Alfvén time τ_A, and the characteristic width L_0 of the equilibrium current sheet (see appendix E).

Notice that the guide field does not appear in the previous equations. However, in the case of an oblique propagating mode, the guide field will play an entirely different role and contribute to the growth rate of the reconnecting mode even if its magnitude is constant. In other words, the problem can be further generalized to include an oblique mode that propagates in the $y-z$ plane with both an x dependent guide field (B_g) and a shear field (B_0).

If we assume the case in which the perturbation is periodic along the $y-$direction, then we can apply Fourier decomposition along this direction. Thus, any perturbed quantity A_1 can be written as $A_1 = \tilde{A}(x)e^{\gamma t}e^{iky}$, where γ is the growth rate (frequency) of any possible instability driven by the equilibrium 5.81. Substituting this decomposition into Eqs.(5.84, 5.85, 5.86, 5.87), and changing the sign in the dependent quantities, we obtain

$$\gamma \begin{bmatrix} \mathcal{D} & 0 & 0 & 0 \\ 0 & \mathcal{D} & 0 & 0 \\ 0 & 0 & \mathcal{A} & 0 \\ 0 & 0 & 0 & \mathcal{I} \end{bmatrix} \begin{bmatrix} B_{1x} \\ B_{1z} \\ u_x \\ u_z \end{bmatrix} = \begin{bmatrix} S^{-1}\mathcal{A} & d_i\mathcal{L}_1 & \mathcal{L}_2 & 0 \\ d_i\mathcal{L}_3 & S^{-1}\mathcal{A} & 0 & \mathcal{L}_4 \\ \mathcal{L}_5 & 0 & R^{-1}\mathcal{L}_6 & 0 \\ 0 & \mathcal{L}_7 & 0 & R^{-1}\mathcal{A} \end{bmatrix} \begin{bmatrix} B_{1x} \\ B_{1z} \\ u_x \\ u_z \end{bmatrix} \tag{5.88}$$

where,

$$\mathcal{A} = \frac{\partial^2}{\partial x^2} - k^2, \quad \mathcal{D} = \mathcal{I} - d_e^2\mathcal{A}, \mathcal{L}_1 = k^2 f(x)\mathcal{I}, \quad \mathcal{L}_2 = -k[f(x) - d_e^2 f''(x)], \quad \mathcal{L}_3 = [f(x)\mathcal{A} - f''(x)], \tag{5.89a}$$

$$\mathcal{L}_4 = -kf(x)\mathcal{I}, \quad \mathcal{L}_5 = k[f(x)\mathcal{A} - f''(x)], \quad \mathcal{L}_6 = \frac{\partial^4}{\partial x^4} - 2k^2\frac{\partial^2}{\partial x^2} + k^4, \quad \mathcal{L}_7 = kf(x)\mathcal{I}, \tag{5.89b}$$

Eq.(5.88) represents a generalized eigenvalue problem which can be solved numerically to find the eigen functions ($B_{1x},\ B_{1z},\ u_x,\ u_z$) and eigenvalue γ (the growth rate). Notice that when $d_i = 0$, $z-$ and $x-$ variables decouple from each others, and the $x-$component equations reduces to the RMHD equation.

5.5.1 Why Hall Effect Preserves the Field Topology

We mentioned when discussing Ohm law in section 2.4.3 that the Hall term preserves the magnetic topology, and we are now in an excellent position to answer why. Since we are only interested in knowing if Hall term can lead to a reconnection event or no, we simplify the eigenvalue problem, given by Eq.(5.88) as much as we can. Therefore, we follow the same line of thoughts of chapter 1. We take $R^{-1} = S^{-1} = d_e = 0$, then Eqs.[5.84, 5.85, 5.86, 5.87] become

$$\gamma B_{1x} = ikf(x)u_x + d_i k^2 f(x)B_{1z}, \tag{5.90}$$

$$\gamma B_{1z} = ikf(x)u_z + d_i\Big[f(x)(\frac{\partial^2}{\partial x^2} - k^2) - f''(x)\Big]B_{1x}, \tag{5.91}$$

$$\gamma(\frac{\partial^2}{\partial x^2} - k^2)u_x = ik\Big[f(x)(\frac{\partial^2}{\partial x^2} - k^2) - f''(x)\Big]B_{1x}, \tag{5.92}$$

$$ik\gamma u_z = ik^2 f(x)B_{1z}, \tag{5.93}$$

As discussed in the introduction, the reconnection occurs on singular surfaces where $kf(x) = 0$. Therefore, when $f(x) = 0$ at the neutral line, the first and the last equations gives $u_x \to \infty$

and $u_z \to \infty$, respectively. Since these are non-physical results, then the only solution is $\gamma = 0$, and hence no reconnection occurs. This is in agreement with the equivalence in the form of the ideal Ohm's law and Hall-MHD Ohm's law (cf. Section 1.1 and Pegoraro et al. [107]). Otherwise, when $\gamma \neq 0$, one needs to include non-ideal parameters that allow removing the singularity of the problem, which gives a finite fluid velocity.

5.6 Reduced MHD in Toroidal Geometry with Steady Inhomogenous Density: New Results

In this thesis, we are interested in studying magnetic reconnection, which is a local phenomenon that takes place in regions where current sheets form. When looking for the scaling laws of the growth rate and for the width of reconnecting layer, this allows us to locally approximate the r coordinate (see Fig.5.3) as the shear variable x, and to approximate θ as the variable y along which the initial perturbation propagates (for details, see chapter 7 and Ref. [153]).

As discussed in the introduction of this chapter, two-fields resistive RMHD models for toroidal geometry, with density profile scaling as R^{-2}, have been proposed in Refs[288, 289]. Also, resistive models with a general steady, inhomogeneous density profile have been proposed to study instabilities, such as halo current in tokamak [290, 291]. In this section, we are going to extend these models to include the effects of electron inertia, and to obtain the formulae of the differential operators in (r, θ, φ) coordinate system (hereafter, CS). The difference with respect to the models mentioned in previous references is that in the latter only resistive effects are included and the equations are written with respect to the (R, φ, Z) CS. The two CSs are shown in Fig.5.3. These CSs and the transformation between them are discussed in details in appendix C.

We are now going to follow the same line of thought that we developed when we derived the RMHD equations in Cartesian geometry. It is easier to first derive the equations in the (R, Z, φ) CS, and only later we will re-write them in the (r, θ, φ) CS.

In the remaining of this section, we use the axisymmetry assumption. According to this hypothesis, the dynamic is symmetric under rotation over the toroidal angle φ. This assumption implies that the solution space's dimensions reduce from three to two dimensions, meaning $\frac{\partial}{\partial \varphi} = 0$. By first looking at the continuity equation, and taking into account that the density is steady but inhomogeneous, one finds,

$$\nabla \cdot (\rho \mathbf{u}) = 0 \implies \mathbf{u} = \frac{1}{\rho} \nabla \times (\Phi \nabla \varphi) = \frac{1}{\rho R} \nabla \Phi \times \mathbf{e}_\varphi = \begin{cases} -\frac{1}{\rho R} \frac{\partial \Phi}{\partial Z} \\ 0 \\ \frac{1}{\rho R} \frac{\partial \Phi}{\partial R} \end{cases}, \tag{5.94}$$

while in (r, θ, φ) CS, one obtains

$$\mathbf{u} = \frac{1}{\rho} \nabla (\Phi \nabla \varphi) = \frac{1}{\rho R} \nabla \times \Phi \times \mathbf{e}_\varphi = \begin{cases} \frac{1}{\rho R r} \frac{\partial \Phi}{\partial \theta} \\ -\frac{1}{\rho R} \frac{\partial \Phi}{\partial r} \\ 0 \end{cases}, \tag{5.95}$$

After having obtained the velocity, we turn our attention to the magnetic field. We assume again axis-symmetry along the φ direction, $\partial / \partial \varphi = 0$, which is justified by the strong guide field hypothesis, here valid for the toroidal magnetic component. Therefore, the magnetic field can be written in term of a stream function $\psi = \psi(R, Z))$, and reads

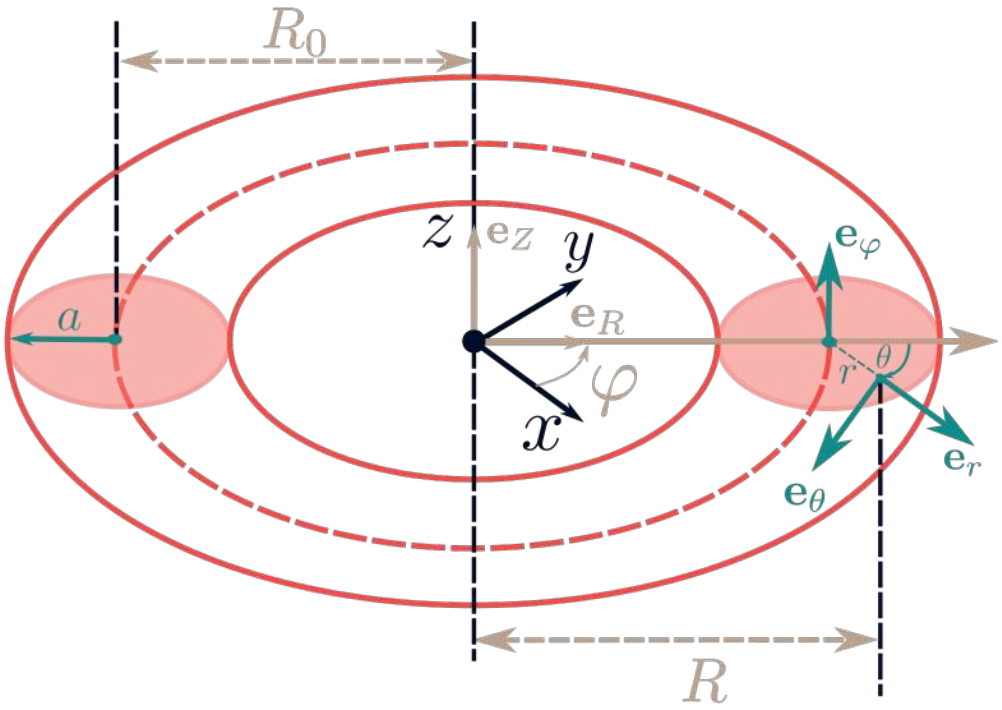

Figure 5.3: An isometric illustration of the toroidal geometry. We show the three different coordinate systems: the Cartesian, (R, φ, Z), and (r, θ, φ) coordinate systems.

$$\mathbf{B} = \frac{B_{\varphi,0}}{R}\mathbf{e}_\varphi + \nabla \times (\psi \nabla \varphi) = \frac{B_{\varphi,0}}{R}\mathbf{e}_\varphi + \frac{1}{R}\nabla\psi \times \mathbf{e}_\varphi = \begin{cases} -\frac{1}{R}\frac{\partial \psi}{\partial Z} \\ \frac{B_{\varphi,0}}{R} \\ \frac{1}{R}\frac{\partial \psi}{\partial R} \end{cases} \tag{5.96}$$

In the (r, θ, φ) CS, one obtains

$$\mathbf{B} = \frac{B_{\varphi,0}}{R}\mathbf{e}_\varphi + \frac{1}{R}\nabla\psi \times \mathbf{e}_\varphi = \begin{cases} \frac{1}{Rr}\frac{\partial \psi}{\partial \theta} \\ -\frac{1}{R}\frac{\partial \psi}{\partial r} \\ \frac{B_{\varphi,0}}{R} \end{cases} , \tag{5.97}$$

Here $B_{\varphi,0}$ is a strong constant guide field. It is easy to notice that this magnetic field is, by construction, divergence free (using Eq.(C.7b)). Now, in order to obtain the first RMHD equation in the (R, φ, Z) coordinate system, we substitute the generalized Ohm law, given by Eq.(2.143), into Faraday-Maxwell equation. This gives

$$\frac{\partial \mathbf{B}}{\partial t} = \nabla \times (\mathbf{u} \times \mathbf{B}) - \mu_0 d_e^2 \frac{\partial}{\partial t}\nabla \times \mathbf{J} - \mu_0 d_e^2 \nabla \times \nabla \cdot \{\mathbf{uJ}\} - \mu_0 d_e^2 \nabla \times \nabla \cdot \{\mathbf{Ju}\} - \eta \nabla \times \mathbf{J}, \tag{5.98}$$

To simplify the derivation, we have neglected for the moment the pressure tensor, Hall, and **JJ** terms. We are going later to use the same argument discussed in section 5.2.2, to include the effects of the electron pressure tensor. Our derivation consists in estimating all the terms in the previous equation and then taking the one that describes the dynamics along $\mathbf{e}_\varphi$. This procedure

gives an equation which governs the evolution of the magnetic stream function ψ in (R, φ, Z) CS. Then, to obtain this equation in the (r, θ, φ) CS, we either follow the same algorithm, or we use the transformation relation derived in appendix C.

We start by estimating the current density. Neglecting the displacement current in Ampere-Maxwell equation, one finds,

$$\mathbf{J} = \frac{1}{\mu_0}\nabla \times \mathbf{B} = -\frac{1}{\mu_0 R}\Delta^* \psi \mathbf{e}_\varphi \tag{5.99}$$

In the previous equation, Δ^* is known as Grad-Shafranov operator, which reads in (R, φ, Z),

$$\Delta^* = R\Big\{\frac{\partial}{\partial R}(\frac{1}{R}\frac{\partial}{\partial R}) + \frac{\partial}{\partial Z}(\frac{1}{R}\frac{\partial}{\partial Z})\Big\}, \tag{5.100}$$

To derive the previous equation for the current density, we used Eq.(C.7c). To obtain the same equation in (r, θ, φ), we either follow the same procedure, or we use the transformations between coordinate systems given by Eq.(C.30). Therefore, one finds

$$\mathbf{J} = \frac{1}{\mu_0}\nabla \times \mathbf{B} = -\frac{1}{\mu_0 R}\Delta^+ \psi \mathbf{e}_\varphi \tag{5.101}$$

Here Δ^+ is the Grad-Shafranov operator in (r, θ, φ) coordinate system. It reads,

$$\Delta^+ = \Delta_\perp - \frac{2}{R}(\nabla R)\cdot\nabla, \tag{5.102}$$

$\Delta_\perp$ and ∇ are the Laplacian and the gradient in (r, θ, φ) system given by Eq.(C.15d), and Eq.(C.15a), respectively (see appendix C for details). Now, we estimate the first $\mathbf{u} \times \mathbf{B}$, which gives

$$\mathbf{u}\times\mathbf{B} = -\frac{B_{\varphi,o}}{\rho R^2}\mathbf{e}_\varphi \times (\nabla\Phi\times\mathbf{e}_\varphi) + \frac{1}{\rho R^2}(\nabla\Phi\times\mathbf{e}_\varphi)\times(\nabla\psi\times\mathbf{e}_\varphi) = -\frac{B_{\varphi,o}}{\rho R^2}\nabla_\perp\Phi + \frac{1}{\rho R^2}[\psi,\Phi]\mathbf{e}_\varphi, \tag{5.103}$$

where $\nabla_\perp$ is given by Eq.(C.7a), and $[\ ,\ ]$ is the Poisson bracket in (R, φ, Z) CS given by

$$[\psi,\Phi] = \frac{\partial\psi}{\partial R}\frac{\partial\Phi}{\partial Z} - \frac{\partial\psi}{\partial Z}\frac{\partial\Phi}{\partial R}, \tag{5.104}$$

In the (r, θ, φ) CS

$$\mathbf{u}\times\mathbf{B} = -\frac{B_{\varphi,o}}{\rho R^2}\nabla_\perp\Phi - \frac{1}{\rho R^2}[\psi,\Phi]\mathbf{e}_\varphi, \tag{5.105}$$

where $\nabla_\perp$ is given by Eq.(C.15a), and

$$[\psi,\Phi] = \frac{1}{r}\Big\{\frac{\partial\psi}{\partial r}\frac{\partial\Phi}{\partial\theta} - \frac{\partial\psi}{\partial\theta}\frac{\partial\Phi}{\partial r}\Big\}, \tag{5.106}$$

This formula can be obtained by either using Eq.(5.97) and Eq.(5.95), or directly from the transformations between the Css - Eq.(C.33).

Now, we estimate

$$\nabla\cdot\Big\{\mathbf{J}\mathbf{u} + \mathbf{u}\mathbf{J}\Big\} = (\nabla\cdot\mathbf{J})\mathbf{u} + (\mathbf{J}\cdot\nabla)\mathbf{u} + (\nabla\cdot\mathbf{u})\mathbf{J} + (\mathbf{u}\cdot\nabla)\mathbf{J}, \tag{5.107}$$

where we used Eq.(B.28). We have for both coordinate systems

$$\nabla \cdot \mathbf{J} = \frac{1}{\mu_0} \nabla \cdot (\nabla \times \mathbf{B}) = 0, \tag{5.108}$$

Also, in (R, φ, Z) we write

$$\mathbf{J} \cdot \nabla = -\frac{\Delta^* \psi}{\mu_0 R} \mathbf{e}_\varphi \cdot \nabla = -\frac{\Delta^* \psi}{\mu_0 R^2} \frac{\partial}{\partial \varphi} \tag{5.109}$$

While in (r, θ, φ), it reads,

$$\mathbf{J} \cdot \nabla = -\frac{\Delta^+ \psi}{\mu_0 R} \mathbf{e}_\varphi \cdot \nabla = -\frac{\Delta^+ \psi}{\mu_0 R^2} \frac{\partial}{\partial \varphi} \tag{5.110}$$

Then, in the (R, φ, Z) `CS`, we obtain

$$\mathbf{J} \cdot \nabla \mathbf{u} = -\frac{\Delta^* \psi}{\mu_0 \rho R^3} \nabla \Phi \times \frac{\partial}{\partial \varphi} \mathbf{e}_\varphi = \frac{\Delta^* \psi}{\mu_0 \rho R^3} \nabla \Phi \times \mathbf{e}_R = \frac{\Delta^* \psi}{\mu_0 \rho R^3} \frac{\partial \Phi}{\partial Z} \mathbf{e}_\varphi, \tag{5.111}$$

In the (r, θ, φ) `CS`, it takes the following form

$$\mathbf{J} \cdot \nabla \mathbf{u} = -\frac{\Delta^+ \psi}{\mu_0 \rho R^3} \nabla \Phi \times \frac{\partial}{\partial \varphi} \mathbf{e}_\varphi = \frac{\Delta^+ \psi}{\mu_0 \rho R^3} \nabla \Phi \times \mathbf{e}_R = -\frac{\Delta^+ \psi}{\mu_0 \rho R^3} (\sin\theta \frac{\partial \Phi}{\partial r} + \frac{\cos\theta}{r} \frac{\partial \Phi}{\partial \theta}) \mathbf{e}_\varphi, \tag{5.112}$$

This equation can be obtained by either performing straightforward calculations in (r, θ, φ), or by simply applying the transformations, given by Eq.(C.22) and Eq.(C.30), on Eq.(5.111). Now, we proceed to find the velocity convective term with respect to the (R, φ, Z) `CS`. Using the definitions of the velocity given by Eq.(5.94) and Eq.(5.95), and the corresponding gradients, we easily find in the (R, φ, Z) `CS`

$$\mathbf{u} \cdot \nabla = \frac{1}{\rho R} (\nabla \Phi \times \mathbf{e}_\varphi) \cdot \nabla = \frac{1}{\rho R} [\Phi, \cdot] \tag{5.113}$$

Instead, in the (r, θ, φ) `CS`

$$\mathbf{u} \cdot \nabla = \frac{1}{\rho R} (\nabla \Phi \times \mathbf{e}_\varphi) \cdot \nabla = -\frac{1}{\rho R} [\Phi, \cdot] \tag{5.114}$$

Now, applying the previous relation to the current density, one obtains in the (R, φ, Z) `CS`

$$(\mathbf{u} \cdot \nabla)\mathbf{J} = -\frac{1}{\mu_0 \rho R} [\Phi, \frac{\Delta^* \psi}{R}] \mathbf{e}_\varphi = -\frac{1}{\mu_0 \rho R^2} [\Phi, \Delta^* \psi] \mathbf{e}_\varphi - \frac{\Delta^* \psi}{\mu_0 \rho R^3} \frac{\partial \Phi}{\partial Z} \mathbf{e}_\varphi \tag{5.115}$$

while in the (r, θ, φ) `CS`, one finds

$$(\mathbf{u} \cdot \nabla)\mathbf{J} = \frac{1}{\mu_0 \rho R^2} [\Phi, \Delta^+ \psi] \mathbf{e}_\varphi + \frac{\Delta^+ \psi}{\mu_0 \rho R^3} (\sin\theta \frac{\partial \Phi}{\partial r} + \frac{\cos\theta}{r} \frac{\partial \Phi}{\partial \theta}) \mathbf{e}_\varphi, \tag{5.116}$$

Finally, using the continuity equation, one finds in the (R, φ, Z) `Cs`

$$\nabla \cdot \mathbf{u} = -\frac{1}{\rho} (\mathbf{u} \cdot \nabla) \rho = -\frac{1}{\rho^2 R} [\Phi, \rho] \tag{5.117}$$

and in the (r,θ,φ) CS

$$\nabla\cdot\mathbf{u}=-\frac{1}{\rho}(\mathbf{u}\cdot\nabla)\rho=\frac{1}{\rho^2 R}[\Phi,\rho] \tag{5.118}$$

In the (R,φ,Z) CS, we write

$$(\nabla\cdot\mathbf{u})\mathbf{J}=\frac{\Delta^*\psi}{\mu_0\rho^2R^2}[\Phi,\rho]\mathbf{e}_\varphi, \tag{5.119}$$

and for (r,θ,φ) CS,

$$(\nabla\cdot\mathbf{u})\mathbf{J}=-\frac{\Delta^+\psi}{\mu_0\rho^2R^2}[\Phi,\rho]\mathbf{e}_\varphi, \tag{5.120}$$

Now, substituting the previous relations into Eq.(5.107), one finds for (R,φ,Z),

$$\nabla\cdot\Big\{\mathbf{J}\mathbf{u}+\mathbf{u}\mathbf{J}\Big\}=-\frac{1}{\mu_0\rho R^2}[\Phi,\Delta^*\psi]\mathbf{e}_\varphi+\frac{\Delta^*\psi}{\mu_0\rho^2R^2}[\Phi,\rho]\mathbf{e}_\varphi, \tag{5.121}$$

and for (r,θ,φ),

$$\nabla\cdot\Big\{\mathbf{J}\mathbf{u}+\mathbf{u}\mathbf{J}\Big\}=\frac{1}{\mu_0\rho R^2}[\Phi,\Delta^+\psi]\mathbf{e}_\varphi-\frac{\Delta^+\psi}{\mu_0\rho^2R^2}[\Phi,\rho]\mathbf{e}_\varphi, \tag{5.122}$$

Substituting the previous equations in Faraday-Maxwell equation, given by Eq.(5.98), one finally obtains the first equation of the RMHD regime in toroidal geometry. In (R,φ,Z), it reads

$$\frac{\partial\mathcal{F}}{\partial t}+\frac{1}{\rho R}[\Phi,\mathcal{F}]=-\frac{d_e^2}{\rho^2R}\Delta^*\psi[\Phi,\rho]+\frac{\eta}{\mu_0}\Delta^*\psi, \tag{5.123}$$

where,

$$\mathcal{F}=\psi-d_e^2\Delta^*\psi, \tag{5.124}$$

and in (r,θ,φ) coordinates, it becomes

$$\frac{\partial\mathcal{F}}{\partial t}-\frac{1}{\rho R}[\Phi,\mathcal{F}]=\frac{d_e^2}{\rho^2R}\Delta^+\psi[\Phi,\rho]+\frac{\eta}{\mu_0}\Delta^+\psi, \tag{5.125}$$

where,

$$\mathcal{F}=\psi-d_e^2\Delta^+\psi, \tag{5.126}$$

Our next step is to find the equation of motion in terms of the velocity stream function (or, more explicitly, in terms of the vorticity). We start by re-writing the curl of the equation of motion, which reads,

$$\frac{\partial}{\partial t}\nabla\times\mathbf{u}+\nabla\times\Big\{\mathbf{u}\cdot\nabla\mathbf{u}\Big\}=\nabla\times\Big\{\frac{\mathbf{J}\times\mathbf{B}}{\rho}\Big\}+\nu\nabla\times\frac{\Delta\mathbf{u}}{\rho}, \tag{5.127}$$

By taking the curl of the equation of motion, it was possible to eliminate the scalar pressure gradient. Now, we estimate these terms one by one as we have done when we derived Eq.(5.123). The curl of the velocity is the vorticity. Now, using Eq.(5.94) and Eq.(C.7c), one easily finds in (R,φ,Z) CS

$$\mathbf{U}=\nabla\times\mathbf{u}=-\frac{1}{\rho R}\Delta_\rho\Phi\mathbf{e}_\varphi, \tag{5.128}$$

where Δ_ρ is the generalized Grad-Shafranov operator (diffusion operator), which is given by

$$\Delta_\rho = \rho R \frac{\partial}{\partial R}\Big[\frac{\partial}{\partial R}\Big(\frac{1}{\rho R}\frac{\partial}{\partial R}\Big) + \frac{\partial}{\partial Z}\Big(\frac{1}{\rho R}\frac{\partial}{\partial Z}\Big)\Big] = \Delta^* - \frac{1}{\rho}\nabla\rho\cdot\nabla, \tag{5.129}$$

Notice that the Grad-Shafranov operator is a special case of this operator when $\rho = 1$ (for more details, see appendix C).

In (r, θ, φ), and following the same procedure, or using the transformation between the two coordinate systems, we obtain

$$\mathbf{U} = \nabla \times \mathbf{u} = -\frac{1}{\rho R}\Delta_\rho^+ \Phi \mathbf{e}_\varphi, \tag{5.130}$$

where

$$\Delta_\rho^+ = \Delta_\perp - \frac{2}{R}(\nabla R)\cdot\nabla - \frac{1}{\rho}(\nabla\rho)\cdot\nabla, \tag{5.131}$$

Here $\Delta_\perp$ and ∇ are given by Eq.(C.15d) and Eq.(C.15a), respectively. Now, we turn our attention to the second term on the LHS of the equation of motion. To simplify the upcoming calculations, we are going to define the components of the velocity as

$$a = -\frac{1}{\rho R}\frac{\partial\Phi}{\partial Z}, \quad b = \frac{1}{\rho R}\frac{\partial\Phi}{\partial R} \tag{5.132}$$

Hence,

$$\mathbf{u}\cdot\nabla\mathbf{u} = (a\frac{\partial a}{\partial R} + b\frac{\partial a}{\partial Z})\mathbf{e}_R + (a\frac{\partial b}{\partial R} + b\frac{\partial b}{\partial Z})\mathbf{e}_Z \tag{5.133}$$

Then, using Eq.(C.7c) and after some algebra, the curl of the previous relationship gives,

$$\nabla\times\Big\{\mathbf{u}\cdot\nabla\mathbf{u}\Big\} = \Big\{(\frac{\partial a}{\partial R} + \frac{\partial b}{\partial Z})(\frac{\partial a}{\partial Z} - \frac{\partial b}{\partial R}) + (a\frac{\partial}{\partial R} + b\frac{\partial}{\partial Z})(\frac{\partial a}{\partial Z} - \frac{\partial b}{\partial R})\Big\}\mathbf{e}_\varphi, \tag{5.134}$$

We then calculate each term in the previous equation. Using Eq.(5.132), we obtain

$$\frac{\partial a}{\partial R} + \frac{\partial b}{\partial Z} = -\frac{1}{\rho R^2}[\Phi, R] - \frac{1}{\rho^2 R}[\Phi, \rho], \tag{5.135}$$

and using the definition of the diffusion operator in (R, φ, Z) given by Eq.(5.129), one obtains

$$\frac{\partial a}{\partial Z} - \frac{\partial b}{\partial R} = -\frac{1}{\rho R}\Delta_\rho\Phi, \tag{5.136}$$

$$a\frac{\partial}{\partial R} + b\frac{\partial}{\partial Z} = \frac{1}{\rho R}[\Phi, .], \tag{5.137}$$

Then, substituting the last three equation in Eq.(5.134), we find

$$\nabla\times\Big\{\mathbf{u}\cdot\nabla\mathbf{u}\Big\} = \Big\{\frac{2\Delta_\rho\Phi}{\rho^2 R^3}[\Phi, R] + \frac{2\Delta_\rho\Phi}{\rho^3 R^2}[\Phi, \rho] - \frac{1}{\rho^2 R^2}[\Phi, \Delta_\rho\Phi]\Big\}\mathbf{e}_\varphi, \tag{5.138}$$

Either following the same procedure (this will be very long and tedious), or by using the transformation relations (see appendix C), this term takes the following form in (r, θ, φ) CS,

$$\nabla\times\Big\{\mathbf{u}\cdot\nabla\mathbf{u}\Big\} = \Big\{-\frac{2\Delta_\rho^+\Phi}{\rho^2 R^3}[\Phi, R] - \frac{2\Delta_\rho^+\Phi}{\rho^3 R^2}[\Phi, \rho] + \frac{1}{\rho^2 R^2}[\Phi, \Delta_\rho^+\Phi]\Big\}\mathbf{e}_\varphi, \tag{5.139}$$

Now, using the definitions of the magnetic field and of the current density, it is straightforward to show that the first term in the RHS of the equation of motion can be written as

$$\nabla\Big\{\frac{\mathbf{J}\times\mathbf{B}}{\rho}\Big\} = \Big\{\frac{1}{\mu_0\rho R^2}[\Delta^*\psi,\psi] - \frac{\Delta^*\psi}{\mu_0\rho^2R^2}[\rho,\psi] - \frac{2\Delta^*\psi}{\mu_0\rho R^3}[R,\psi]\Big\}\mathbf{e}_\varphi, \tag{5.140}$$

while in (r,θ,φ), after a direct calculation, the previous equation becomes

$$\nabla\Big\{\frac{\mathbf{J}\times\mathbf{B}}{\rho}\Big\} = \Big\{-\frac{1}{\mu_0\rho R^2}[\Delta^+\psi,\psi] + \frac{\Delta^+\psi}{\mu_0\rho^2R^2}[\rho,\psi] + \frac{2\Delta^+\psi}{\mu_0\rho R^3}[R,\psi]\Big\}\mathbf{e}_\varphi, \tag{5.141}$$

Finally, for the last term, we either write it in its exact form as

$$\nabla\times\frac{\Delta\mathbf{u}}{\rho}\cdot\mathbf{e}_\phi = \frac{1}{\rho}(\Delta\mathbf{U})\cdot\mathbf{e}_\varphi. \tag{5.142}$$

or, following the suggestion in Ref. [290],

$$\nabla\times\frac{\Delta\mathbf{u}}{\rho}\cdot\mathbf{e}_\phi = -\frac{1}{\rho^2R}\Delta_\rho\Delta_\rho\Phi, \tag{5.143}$$

Now, defining the vorticity $\Omega=\Delta_\rho\Phi$, and substituting all the previous equation in Eq.(5.127), we find

$$\frac{\partial\Omega}{\partial t} + \frac{1}{\rho R}[\Phi,\Omega] - \frac{2\Omega}{\rho R^2}[\Phi,R] - \frac{2\Omega}{\rho^2R}[\Phi,\rho] = \frac{1}{\mu_0R}[\psi,\Delta^*\psi] - \frac{\Delta^*\psi}{\mu_0\rho R}[\psi,\rho] - \frac{2\Delta^*\psi}{\mu_0R^2}[\psi,R] + \frac{1}{\nu\rho}\Delta_\rho\Omega, \tag{5.144}$$

which becomes in (r,θ,φ) Cs

$$\frac{\partial\Omega}{\partial t} - \frac{1}{\rho R}[\Phi,\Omega] + \frac{2\Omega}{\rho R^2}[\Phi,R] + \frac{2\Omega}{\rho^2R}[\Phi,\rho] = -\frac{1}{\mu_0R}[\psi,\Delta^*\psi] + \frac{\Delta^+\psi}{\mu_0\rho R}[\psi,\rho] + \frac{2\Delta^+\psi}{\mu_0R^2}[\psi,R] + \frac{1}{\nu\rho}\Delta_\rho^+\Omega, \tag{5.145}$$

Here $\Omega=\Delta_\rho^+\Phi$. For the seek of completeness, we should mention the fact that in the above derivation, we neglected the term $\nabla\times\frac{\nabla p}{\rho} = -(1/\rho^2)\nabla\rho\times\nabla p$. The justification of this step lay in the strong guide field assumption (low-β plasma) used when ordering the effects of different quantities when we derive RMHD regime. It should be noted, however, that this term also vanishes when a polytropic closure is assumed, which implies $P=P(\varrho)$. To summarize the results of this section, we list the closed system of RMHD equations in (R,φ,Z):

$$\frac{\partial\mathcal{F}}{\partial t} + \frac{1}{\rho R}[\Phi,\mathcal{F}] = -\frac{d_e^2}{\rho^2R}\Delta^*\psi[\Phi,\rho] + \rho_s^2[\Omega,\psi] + \frac{\eta}{\mu_0}\Delta^*\psi, \tag{5.146}$$

$$\begin{aligned}\frac{\partial\Omega}{\partial t} + \frac{1}{\rho R}[\Phi,\Omega] - \frac{2\Omega}{\rho R^2}[\Phi,R] - \frac{2\Omega}{\rho^2R}[\Phi,\rho] &= \frac{1}{\mu_0R}[\psi,\Delta^*\psi] - \frac{\Delta^*\psi}{\mu_0\rho R}[\psi,\rho] \\ &\quad - \frac{2\Delta^*\psi}{\mu_0R^2}[\psi,R] + \frac{1}{\nu\rho}\Delta_\rho\Omega,\end{aligned} \tag{5.147}$$

where,

$$\mathcal{F} = \psi - d_e^2\Delta^*\psi,\ \ \Omega=\Delta_\rho\Phi. \tag{5.148}$$

In the previous system, we added the effect of electron compressibility as discussed in section 5.2.2. The equations in the (r,θ,φ) CS, instead read

$$\frac{\partial\mathcal{F}}{\partial t} - \frac{1}{\rho R}[\Phi,\mathcal{F}] = \frac{d_e^2}{\rho^2R}\Delta^+\psi[\Phi,\rho] - \rho_s^2[\Omega,\psi] + \frac{\eta}{\mu_0}\Delta^+\psi, \tag{5.149}$$

$$\frac{\partial \Omega}{\partial t} - \frac{1}{\rho R}[\Phi, \Omega] + \frac{2\Omega}{\rho R^2}[\Phi, R] + \frac{2\Omega}{\rho^2 R}[\Phi, \rho] = -\frac{1}{\mu_0 R}[\psi, \Delta^+ \psi] + \frac{\Delta^+ \psi}{\mu_0 \rho R}[\psi, \rho] + \frac{2\Delta^+ \psi}{\mu_0 R^2}[\psi, R] + \frac{1}{\nu \rho}\Delta_\rho^+ \Omega, \tag{5.150}$$

where,

$$\mathcal{F} = \psi - d_e^2 \Delta^+ \psi, \ \Omega = \Delta_\rho^+ \Phi. \tag{5.151}$$

As mentioned in the introduction of this section, the coordinates r and θ can be locally approximated to the shear variable x and y, receptively. However, a very subtle difference exists when comparing reconnecting modes in astrophysics and in tokamaks. In the former, very long and elongated current sheets might form. Neglecting the possible occurrence of spatially localised modes and assuming that a Fourier-type analysis valid under periodic boundary conditions still holds, this allows the excitation of a broad spectrum of wavenumbers, which will be later dominated by the fastest growing mode. On the other hand, reconnecting modes occur on specific resonant surfaces in tokamaks (e.g. for a specific poloidal and toroidal wavenumbers, that is a few discrete values of wavelengths) which rules out the notion of a continuum spectrum of wavenumbers. In order to find the scaling laws, we perturb the previous equations with Fourier modes of the form $f(r)e^{im\theta - in\varphi}$. The resulting system of equations can be solved numerically for arbitrary steady density and equilibrium profiles in the intended geometry. Due to the small values of the non-ideal parameters and aiming to study realistic situations, we need to build a multi-precision solver that can resolve the reconnecting layer with very high precision. The work done in this section is the first step in our work aiming to build an eigensolver to study the linear phase of tearing instabilities, and also to simulate the non-linear stage of the reconnection in geometries similar to those met in real tokamak devices.

6

Electron MHD and Extended Electron MHD Regimes

Contents

6.1 Introduction

In this chapter, we consider magnetic reconnection in the Electron Magnetohydrodynamic (EMHD) limit, which we have briefly introduced in Chapter 2. The reason is two-fold: first, being EMHD a reduced model, relatively simpler under some respect than Hall-MHD, its study allows to shed light into complex fundamental features of magnetic reconnection that can furnish the basis for the understanding of analogous ingredients in richer, two-fluid models; second, the modelling of fluid EMHD reconnection provides a first, useful element of comparison with "electron-only" magnetic reconnection in full kinetic models, which is easier to be studied in a numerical Vlasov description thanks to the complete neglect of the dynamics of the ion species. In chapter 8, in

particular, we will discuss kinetic simulations about the coupling of magnetic reconnection with some beam-plasma instabilities, namely of Weibel-type, that can be indeed described also with fluid modelling, in the framework of an `EMHD` description.

Electron magnetohydrodynamics (`EMHD`) [91] is a theory that describes the plasma behaviour at small spatial lengths ($L \ll d_i$) and short time scales ($\omega_{c,i} \ll \omega \ll \omega_{c,e}$). In this theory, ions are considered immobile and forming a neutralizing background. Therefore, the dynamic is entirely determined by electrons, which preserve the quasi-neutrality and carry all the current. The characteristic time scale of this regime is the whistler time (τ_w), which means that, in `EMHD`, whistler waves replace Alfvén waves in driving the dynamics [108].

`EMHD` theory has been successfully applied to investigate a wide range of plasma phenomena, such as studying non-linear skin effects [91, 316], magnetic and electron vorticities [317, 318, 319, 320], plasma turbulence [143, 321], laser-plasma interactions [87], Weibel instability [322, 2, 275], and all magnetic reconnection [89, 90, 93, 323, 324, 325, 326].

Here, we distinguish two regimes. The first one assumes the electron fluid incompressible [93]. In this case, the divergence of the velocity vanishes, which is a direct result of the negligible density perturbation and gradients. Therefore, neglecting density perturbation, and displacement current in Ampere equation allows expressing the velocity in terms of the magnetic field. Note that neglecting the displacement current goes together with the incompressibility assumption, which, in turns, implies the restriction to non-relativistic phase velocities. Then, by substituting Ampere and Faraday equations into the momentum equation of electrons, one ends up, after taking the curl of the later, with `EMHD` equations. This incompressible model is `3D`, and the only unknown in the differential equations is the magnetic field components, which allows determining all the remaining unknowns. A `2D` model can be derived when, for some reasons, a translation invariance can be assumed.

However, including the effects of the compressibility resulting from the density perturbation and inhomogeneities is possible, and lead to a slight modification of the incompressible model as long as the full pressure tensor effects and displacement current are ignored. These modifications involve introducing a new parameter known as the renormalized skin depth ($\lambda_e = d_e^2(1 + \frac{\omega_{c,e}}{\omega_{p,e}})$) into the z component of the equations. This parameter also accounts for the effects of the charge separation [323, 313, 108].

Ignoring the displacement current in the derivation of the incompressible (or slightly compressible) `EMHD` equations has been justified by the requiring a phase velocity of the phenomenon under consideration to be much smaller than the velocity of light, which is not always true. It is also assumed that the pressure is isotropic: a polytropic relation between the pressure and the electron density suffices to this purpose. From both a numerical and an analytical point of view, the model which follows the mentioned assumptions is much easier to address, compared to a model with a full pressure tensor and a displacement current(to be discussed later in this chapter).

In this latter case, taking a non-relativistic limit of the fluid equations (we neglect the Lorentz gamma factor), the `EMHD` equations are given by,

$$\frac{\partial \mathbf{u}_e}{\partial t} + \mathbf{u}_e \cdot \nabla \mathbf{u}_e = -\frac{e}{m_e}\Big(\mathbf{E} + \mathbf{u}_e \times \mathbf{B}\Big) - \frac{\nabla \cdot \mathcal{P}_e}{m_e n_e}, \tag{6.1}$$

$$\frac{\partial \mathbf{B}}{\partial t} = -\nabla \times \mathbf{E}, \tag{6.2}$$

$$\nabla \times \mathbf{B} = \mu_0 \mathbf{J} + \frac{1}{c^2}\frac{\partial \mathbf{E}}{\partial t}, \tag{6.3}$$

with the full pressure tensor dynamics described by

$$\frac{\partial \mathcal{P}_e}{\partial t} + (\nabla \cdot \mathbf{u}_e)\mathcal{P}_e + (\mathbf{u}_e \cdot \nabla)\mathcal{P}_e + \mathcal{P}_e \cdot \nabla \mathbf{u}_e + [\mathcal{P}_e \cdot \nabla \mathbf{u}_e]^T + \frac{e}{m_e}\Big(\mathcal{P}_e \times \mathbf{B} + [\mathcal{P}_e \times \mathbf{B}]^T\Big) = 0, \quad (6.4)$$

The above system can be heuristically closed, for simplicity, by assuming a zero heat triad. In the following, we first proceed by deriving the incompressible EMHD model under the assumptions of constant density, negligible displacement current, and a scalar pressure. Then, we modify the model to include the effects of compressiblity, and discuss in detail the linear analysis of these models. Finally, we discuss in details the extended EMHD, which includes the full pressure tensor. In the remaining of this chapter, we omit the subscript "e" to simplify the notation.

6.2 EMHD Regime

In this section, we are going to obtain the equations governing the incompressible and weakly compressible EMHD regimes. Furthermore, we perform the linear analysis of these equations with a sheared equilibrium magnetic field. This configuration allows studying the linear phase of magnetic reconnection in EMHD regimes.

6.2.1 Incompressible EMHD Regime

In this regime, we consider a scalar pressure, constant density, and negligible displacement current. This allows us, after taking the curl of Eq.(6.1) to eliminate the pressure term. Then, substituting Faraday and Ampere equations into the result, we easily obtain the incompressible EMHD equation given by

$$\frac{\partial \Omega}{\partial t} = \nabla \times (\mathbf{u} \times \Omega), \text{ or, } \frac{\partial}{\partial t}\Big(\mathbf{B} - d_e^2 \nabla^2 \mathbf{B}\Big) = -\frac{1}{\mu_0}\nabla \times \Big(\nabla \times \mathbf{B} \times \Big[\mathbf{B} - d_e^2 \nabla^2 \mathbf{B}\Big]\Big), \quad (6.5)$$

Where Ω is the generalized vorticity,

$$\Omega = -\frac{m}{e}\nabla \times \mathbf{u} + \mathbf{B} = \mathbf{B} - d_e^2 \nabla^2 \mathbf{B}, \quad (6.6)$$

In the derivation of the previous equation we made use of the canonical momentum of electrons ($\mu_e = m\mathbf{u} - e\mathbf{A}$, therefore $\Omega = -\frac{1}{e}\nabla \times \mu_e$). This equation is nothing than Ohm law, so we can include resistive term if necessary. Therefore, it reads

$$\frac{\partial}{\partial t}\Big(\mathbf{B} - d_e^2 \nabla^2 \mathbf{B}\Big) = -\frac{1}{\mu_0}\nabla \times \Big(\nabla \times \mathbf{B} \times \Big[\mathbf{B} - d_e^2 \nabla^2 \mathbf{B}\Big]\Big) + D\nabla^2 \mathbf{B}, \quad (6.7)$$

with,

$$D = \frac{\eta}{\mu_0} = c^2 \epsilon_0 \eta, \quad (6.8)$$

where η is the resistivity. This is a closed system of equations for the three components of the magnetic field $\mathbf{B}$, which can be solved with different numerical methods [327, 286, 328, 329]. It is interesting to notice that the previous system is 3D and the magnetic field can depend on all the coordinates ($\mathbf{B} = \mathbf{B}(x, y, z)$).

This model is applied to phenomena with $\omega \ll \omega_{p,e}$, a characteristic length L_0 which is larger than Debye length, while still smaller than the ion-skin depth, and $\frac{d_e^2}{L_0^2}(\frac{\omega_{c,e}}{\omega_{p,e}})^2 \ll 1$. The last condition can be understood by looking at dimensionless Ampere equation, where the spatial

lengths are normalized to L_0, time to whistler time, and magnetic field to a background field. It reads,

$$\mathbf{u} = -\nabla \times \mathbf{B} + (\frac{d_e}{L_0})^2(\frac{\omega_{c,e}}{\omega_{p,e}})^2\frac{\partial \mathbf{E}}{\partial t}, \tag{6.9}$$

The previous equation implies that the incompressible EMHD is suitable for regimes in which the plasma is weakly magnetized, or the equilibrium characteristic length is large compared to the electron-skin depth. However, this condition appears again in the dimensionless Gauss equation which reads,

$$\tilde{n} = -(\frac{d_e}{L_0})^2(\frac{\omega_{c,e}}{\omega_{p,e}})^2\nabla \cdot \mathbf{E}, \tag{6.10}$$

Where the total density is $n = n_{eq} + \tilde{n}$, and $\tilde{n}$ is the density perturbation. However, in the presence of a strong guide field ($\omega_{c,e} \geq \omega_{p,e}$), the electron cyclotron frequency overtakes the role of the plasma frequency into the system. Hence, as explicitly written in Eq.(6.9) and Eq.(6.10), nor the density perturbation, neither the displacement current (relativistic effects) are negligible anymore ([108]).

6.2.2 Linear Waves in Incompressible EMHD

To study the propagation of linear waves in this regime, we first linearize Eq.(6.7) with a uniform equilibrium magnetic field ($\mathbf{B}_0 = (0, 0, B_0)$). Then we take the Fourier transformation of the resulting system by allowing the perturbed quantities (Q) to be of the following form

$$Q(y, z) = \tilde{Q}e^{i(k_y y + k_z z - \omega t)}, \tag{6.11}$$

Where k_y and k_z are the components of the wavevector $\mathbf{k}$ of the wave that propagates in (y, z) plane to find the dispersion relation we first calculate (see appendix F for detailed derivation)

$$\mathcal{D}_w \cdot \mathbf{B} = 0, \tag{6.12}$$

$\mathbf{B}$ here is the perturbed Fourier component of the field where we omit "$\sim$" to simplify writing, and

$$\mathcal{D}_w = \begin{bmatrix} -i\omega(1 + k^2d_e^2) + Dk^2 & \alpha k_z^2 B_0 & -\alpha k_y k_z B_0 \\ -\alpha k_z^2 B_0 & -i\omega(1 + k^2d_e^2) + Dk^2 & 0 \\ \alpha k_y k_z B_0 & 0 & -i\omega(1 + k^2d_e^2) + Dk^2 \end{bmatrix}, \tag{6.13}$$

where $\alpha = \frac{1}{\mu_0 en}$. Eq.(6.12) has a non-trivial solution if the determinant of $\mathcal{D}_w$ is equal to zero ($|\mathcal{D}_w| = 0$), which in turn gives the dispersion relation. It is important to notice that the three components of the perturbed field are coupled. Equating the determinant to zero gives one of the following two possible solutions

$$\begin{aligned} \omega &= -i\frac{Dk^2}{1 + k^2d_e^2}, \\ \omega &= \pm\frac{\alpha k k_z B_0}{1 + k^2d_e^2} - i\frac{Dk^2}{1 + k^2d_e^2} = \pm\frac{k k_z d_e^2 \omega_{c,e}}{1 + k^2d_e^2} - i\frac{Dk^2}{1 + k^2d_e^2}, \end{aligned} \tag{6.14}$$

Here we used Eq.(2.142). First equation in 6.14 describes a damped wave due to the plasma resistivity. If $D = 0$, then the second equation represents the frequency of an oscillatory wave that will also be damped if the resistivity is included. The wave of these nature are known as whistler waves. They are transverse right circularly polarized waves, which propagate parallel to the magnetic field in a cold plasma [167, 330, 331, 176]. Therefore, it is a natural choice to use whistler time ($\tau_w = \frac{1}{\omega_w} = \frac{L^2}{d_e^2\omega_{c,e}}$) as reference time when obtaining the dimensionless EMHD equations.

6.2.3 Derivation of Compressible EMHD Regime

In the previous section, we derived the incompressible electron MHD model, which is more suitable for a weakly magnetized plasma or a plasma with an electron skin-depth much smaller than the characteristic length of the equilibrium. As can be seen from Eq.(6.10), the density perturbation starts to play an important rule if a strong guide field exists. Therefore, the previous model must be modified to account for density perturbation (electron compressibility effects). Now, considering the electron inertia, and the pressure gradient terms as second-order quantities in Eq.(6.1), the electric force is therefore balanced by Lorentz force ($\mathbf{E} = -\mathbf{u} \times \mathbf{B}$). Then substituting this into Eq.(6.10), one finds

$$\tilde{n} = (\frac{d_e}{L_0})^2(\frac{\omega_{c,e}}{\omega_{p,e}})^2 \nabla \cdot (\mathbf{u} \times \mathbf{B}), \tag{6.15}$$

Now taking only the zeroth-order component of the velocity from Eq.(6.9), and substituting it into the previous equation, we obtain

$$\tilde{n} = (\frac{d_e}{L_0})^2(\frac{\omega_{c,e}}{\omega_{p,e}})^2 \mathbf{e}_{eq} \cdot \nabla^2 \mathbf{B}_1, \tag{6.16}$$

Where $\mathbf{e}_{eq} = \frac{\mathbf{B}_0}{B_0}$, B_0 is a reference value (for $\mathbf{B}_1$, see appendix F). It is again clear that the density perturbation is strongly connected to the perturbation of the magnetic field. Under the assumption of a strong guide field, say directed along z, the previous equation indicates the fact that the density perturbation is proportional to the z-component of the magnetic perturbation, and it is therefore due to the parallel dynamics and can be neglected as long as the coefficient $(\frac{d_e}{L_0})^2(\frac{\omega_{c,e}}{\omega_{p,e}})^2$ is very small. At the same time, it remains relevant even when it is of the order of unity $(\frac{d_e}{L_0})^2(\frac{\omega_{c,e}}{\omega_{p,e}})^2 \sim O[1]$. Now, we proceed to derive the compressible model starting from Eq.(6.5). Therefore using the identity given by Eq.(B.26), Eq.(6.5) becomes

$$\Big(\frac{\partial}{\partial t} + \mathbf{u} \cdot \nabla\Big)\mathbf{\Omega} = -\mathbf{\Omega}(\nabla \cdot \mathbf{u}) + \mathbf{\Omega} \cdot \nabla \mathbf{u}, \tag{6.17}$$

Where we used the fact that $\nabla \cdot \mathbf{\Omega} = 0$ (see Eq.(6.6)). Now substituting the divergence of the velocity, calculated from the Eq.(2.26), into the previous equation, one easily obtains

$$(\frac{\partial}{\partial t} + \mathbf{u} \cdot \nabla)\mathbf{\Omega}^* = \mathbf{\Omega}^* \cdot \nabla \mathbf{u}, \tag{6.18}$$

Where $\mathbf{\Omega}^* = \frac{\mathbf{\Omega}}{n}$ is known as potential generalized vorticity [313]. Knowing that $n = n_{eq} + \tilde{n}$ and $\tilde{n} << n_0$, where n_0 is the reference density, Taylor expansion allows us to approximate $\mathbf{\Omega}^*$ as

$$\mathbf{\Omega}^* \approx \frac{\mathbf{\Omega}}{n_0} - \frac{\mathbf{\Omega}_0}{n_0}\frac{\tilde{n}}{n_0} = \frac{\mathbf{B}}{n_0} - \frac{d_e^2}{n_0}\nabla^2 \mathbf{B} - \frac{\mathbf{B}_0}{n_0}\frac{\tilde{n}}{n_0}, \tag{6.19}$$

The previous definition of the potential generalized vorticity is dimensional. The set of equations composed of Eqs[6.18, 6.19, 6.16] constitute a closed system, where the main difference compared to the incompressible model is the inclusion of density perturbation. The dispersion relation of the linear waves that characterize the dynamics in this model is a slightly modified one of that of the incompressible case given by Eq.(6.14), which can be obtained following the same approach in appendix F. In this case, the whistler frequency reads [313],

$$\omega = \pm \frac{k k_z d_e^2 \omega_{c,e}}{\sqrt{(1 + \lambda_e k^2 d_e^2)(1 + k^2 d_e^2)}}, \quad \lambda_e = 1 + \frac{\omega_{c,e}^2}{\omega_{p,e}^2}, \tag{6.20}$$

Therefore, in weakly magnetized plasma, $\lambda_e = 1$. Hence, we recover Eq.(6.14).

6.2.4 2D-EMHD Regime

The models discussed in the previous section are 3D. In some cases, such as a plasma immersed in a strong background guide field, the dynamics is essentially 2D, meaning it varies much slower along the field direction (ignorable coordinate) compared to the perpendicular plane. In such situations, a simpler 2D model can be derived, and usefully applied to study various interesting phenomena. The crucial difference compared to the RMHD is that the current is entirely carried by electrons in the EMHD regimes, which implies the importance of retaining a magnetic field perturbation along the guide field direction. At the same time, the usefullness of this model is also a consequence of being able to neglect the displacement current. Following the same line of thoughts in section 5.2, the incompressible EMHD has the ordering shown in table 6.1.

b	ψ	$J_\perp$	$J_{\|\|}$	$A_\perp$	$A_{\|\|}$	$u_\perp$	$u_{\|\|}$	p	ρ	∂_t	$\partial_\perp$
$O[\epsilon_B]$	$O[\epsilon_B]$	$O[\epsilon_B]$	$O[\epsilon_B]$	$O[\epsilon_B]$	$O[\epsilon_B]$	$O[\epsilon_B]$	$O[\epsilon_B]$	$O[\epsilon_B^2]$	1	$O[\epsilon_B]$	1

Table 6.1: Two-fields EMHD orderings. $\perp$ refers to the directions perpendicular to that of the guid field, while $||$ denotes the parallel direction.

The main idea behind this model is to write the equations in terms of stream functions. In this case, these functions are ψ, and b, which scales as $O[\epsilon_B]$. Therefore, the magnetic field and velocity read

$$\mathbf{B} = \nabla\psi \times \mathbf{e}_z + (B_0 + b)\mathbf{e}_z, \quad \mathbf{u} = \frac{1}{\mu_0 e n}\nabla \times \mathbf{B}, \tag{6.21}$$

Here we neglect the displacement current in Faraday law. After substituting the previous relationship into Eq.(6.7), we find the two following dimensionless coupled partial differential equations (see appendix G for detailed derivation):

$$\frac{\partial F}{\partial t} + [b, F] = S^{-1}\nabla^2\psi, \tag{6.22}$$

$$\frac{\partial W}{\partial t} + [b, W] = [\psi, \nabla^2\psi] + S^{-1}\nabla^2 b, \tag{6.23}$$

Where,

$$F = \psi - d_e^2\nabla^2\psi, \quad W = b - d_e^2\nabla^2 b, \tag{6.24}$$

And S is the EMHD Lundquist number. The magnetic field, lengths, and time are normalized to a background magnetic field B_0, characteristic length L_0, and whistler time $\tau_w = \frac{L^2}{d_e^2\omega_{c,e}} = \tau_A\frac{L}{d_i}$ (see appendix G).

6.2.5 Linear Analysis of EMHD Regime

Following the same line of thoughts in section 5.4.2, the linear versions of Eqs[6.22, 6.23] read

$$\frac{\partial F_1}{\partial t} + [b_{eq}, F_1] + [b_1, F_{eq}] = S^{-1}\nabla^2\psi_1, \tag{6.25}$$

$$\frac{\partial W_1}{\partial t} + [b_{eq}, W_1] + [b_1, W_{eq}] = [\psi_1, \nabla^2\psi_{eq}] + [\psi_{eq}, \nabla^2\psi_1] + S^{-1}\nabla^2 b, \tag{6.26}$$

Where,

$$F_1 = \psi_1 - d_e^2\nabla^2\psi_1, \quad W_1 = b_1 - d_e^2\nabla^2 b_1, F_{eq} = \psi_{eq} - d_e^2\nabla^2\psi_{eq}, \quad W_{eq} = b_{eq} - d_e^2\nabla^2 b_{eq}, \quad (6.27)$$

We assume the equilibrium quantities are in general functions only of x, that is $b_{eq} = b_{eq}(x)$ and $\psi_{eq} = \psi_{eq}(x)$ which allows us to study different phenomena, such as magnetic reconnection in EMHD regime. Now, assuming $\psi_1 = \tilde{\psi}(x)e^{iky}e^{\gamma t}$, and $b = i\tilde{b}(x)e^{iky}e^{\gamma t}$, the previous two equations lead to the following eigenvalue problem for the incompressible EMHD regime,

$$\gamma \begin{bmatrix} \mathcal{D} & 0 \\ 0 & \mathcal{D} \end{bmatrix} \begin{bmatrix} \psi(x) \\ \phi(x) \end{bmatrix} = \begin{bmatrix} \mathcal{L}_1 & \mathcal{L}_2 \\ \mathcal{L}_3 & \mathcal{L}_4 \end{bmatrix} \begin{bmatrix} \psi(x) \\ b(x) \end{bmatrix} \quad (6.28)$$

Where,

$$\mathcal{D} = \mathcal{I} - d_e^2\mathcal{A}, \quad \mathcal{A} = \frac{\partial^2}{\partial x^2} - k^2, \quad \mathcal{L}_1 = S^{-1}\mathcal{A} - ikb_{eq}^{'}\mathcal{D}, \quad \mathcal{L}_2 = -kF_{eq}^{'}, \quad \mathcal{L}_3 = k\Big[\psi_{eq}^{'}\mathcal{A} - \psi_{eq}^{'''}\Big],$$
$$\mathcal{L}_4 = ik\Big[W_{eq}^{'} - b_{eq}^{'}\mathcal{D}\Big] + S^{-1}\mathcal{A}, \quad (6.29)$$

However, a slightly simple modification can be added to the equation to include the compressibility effects studied before. This can be done by replacing d_e into the parallel component equation of magnetic field (b), by the effective skin depth $\lambda_e = 1 + \frac{\omega_{c,e}^2}{\omega_{p.e}}$. Therefore, the matrices in ψ equation remain the same, while only $\mathcal{D}$ and $\mathcal{L}_4$ are modified in b-equation, and read

$$\mathcal{D}_1 = \mathcal{I} - \lambda^2\mathcal{A}, \quad \mathcal{L}_4 = ik\Big[W_{eq}^{'} - b_{eq}^{'}\mathcal{D}_1\Big] + S^{-1}\mathcal{A}, \quad (6.30)$$

6.3 Extended EMHD Regime with Full Pressure Tensor: New Results

We re-write the EMHD equations as follow

$$\frac{\partial \mathbf{u}}{\partial t} + \mathbf{u}\cdot\nabla\mathbf{u} = -\frac{e}{m_e}\Big(\mathbf{E} + \mathbf{u}\times\mathbf{B}\Big) - \frac{\nabla\cdot\mathcal{P}}{mn}, \quad (6.31)$$

$$\frac{\partial \mathbf{B}}{\partial t} = -\nabla\times\mathbf{E}, \quad (6.32)$$

$$\nabla\times\mathbf{B} = \mu_0\mathbf{J} + \frac{1}{c^2}\frac{\partial \mathbf{E}}{\partial t}, \quad (6.33)$$

with the full pressure tensor given by,

$$\frac{\partial \mathcal{P}}{\partial t} + (\nabla\cdot\mathbf{u})\mathcal{P} + (\mathbf{u}\cdot\nabla)\mathcal{P} + \mathcal{P}\cdot\nabla\mathbf{u} + [\mathcal{P}\cdot\nabla\mathbf{u}]^T + \frac{e}{m}\Big(\mathcal{P}\times\mathbf{B} + [\mathcal{P}\times\mathbf{B}]^T\Big) = 0, \quad (6.34)$$

In this section we are going to linearize the previous system of equations for a general case in which the density is no longer uniform. First, we are going to identify a consistent equilibrium pressure tensor, then we linearize the full pressure tensor. Finally we use the results to obtain the eigenvalue problem after substituting the pressure tensor components into linearized versions of Eqs[6.31, 6.32, 6.33]. When linearizinng these equations, the equilibrium quantities are assumed to be functions of x, while the perturbations are periodic along y-direction, and of the form

$f_1 = \tilde{f}(x)e^{\gamma t}e^{iky}$. The problem is also independent of z, which means $\frac{\partial}{\partial z} = 0$. It should be noted that this system of equations still requires relativistic corrections to be negligible for fluid velocities and kinetic pressure, in order to neglect the Lorentz relativistic factor. We recall indeed that relativistic effects, as seen in previous section, should be in principle taken into account when relaxing the incompressible fluid hypothesis. On the other hand, the set of Eqs.[6.31-6.34] has been shown to give results in excellent agreement with kinetic ones, for example for the description of Weibel-type instabilities [182].

6.3.1 Equilibrium Pressure Tensor

In this section, we discuss a consistent choice of the equilibrium pressure tensor, which is necessary when studying the effect of full pressure tensor on reconnection. The equilibrium magnetic field reads,

$$\mathbf{B}_0 = B_s f(x)\mathbf{e}_y + B_g \mathbf{e}_z, \tag{6.35}$$

Where B_s is the amplitude of the shear field, and B_g is the guide field. Under the assumption of strong guide field, we have $B_s \ll B_g$, and $-1 \leq f(x) \leq 1$. At equilibrium the displacement current vanishes, thus the equilibrium velocity can be estimated from Maxwell-Ampere law. Then,

$$\mathbf{u}_0 = -\frac{\mathbf{J}}{en_0} = -\frac{1}{\mu_0 en_0}\nabla \times \mathbf{B}_0 = -\frac{B_s}{\mu_0 en_0} f^{'}(x)\mathbf{e}_z, \quad \frac{d\mathbf{u}_0}{dx} = \frac{du_{z0}}{dx}\mathbf{e}_z = -\bar{\omega}_{c,e} d_e^2 f^{''}\mathbf{e}_z, \tag{6.36}$$

Above, we used Eq.(2.142), and $\bar{\omega}_{c,e}$ is the shear frequency. The superscript "$'$" denotes the derivative with respect to x. We define the following cyclotron frequencies for the guide and shear fields, respectively

$$\omega_{c,e} = \frac{eB_g}{m}, \quad \bar{\omega}_{c,e} = \frac{eB_s}{m} \tag{6.37}$$

The equilibrium equation of motion for electrons becomes

$$-\frac{e}{m}\mathbf{u}_0 \times \mathbf{B}_0 - \frac{\nabla \cdot \mathcal{P}^0}{mn_0} = 0, \tag{6.38}$$

From Eqs[6.35, 6.36], the different components of $\mathbf{u}_0 \times \mathbf{B}_0$ force read

$$\mathbf{u}_0 \times \mathbf{B}_0 = \begin{cases} \frac{B_s^2}{\mu_0 en_0} f(x)f^{'}(x), \\ 0, \\ 0, \end{cases} \tag{6.39}$$

We have $\mathbf{E}_0 = 0$, and then this force must be balanced by the force which results from the divergence of the pressure tensor. After substituting the previous equation into Eq.(6.38), one finds

$$[\nabla \cdot \mathcal{P}^0]_x - \frac{B_s^2}{\mu_0} f(x)f^{'}(x) = 0, \tag{6.40}$$

Using Eq.(B.29), we have $[\nabla \cdot \mathcal{P}^0]_x = \frac{d\mathcal{P}^0_{xx}}{dx}$, where the equilibrium depends only on x. Substituting this into the previous equation one easily finds,

$$\mathcal{P}^0_{xx} = \frac{B_s^2}{2\mu_0}[f(x)]^2, \tag{6.41}$$

However, to be consistent, the previous result must satisfy the pressure tensor equation at equilibrium. Then, other non-vanishing terms of the pressure tensor exist. To identify them, we write the full pressure tensor equation at equilibrium using Eq.(6.34). The equilibrium equation reads,

$$(\nabla\cdot\mathbf{u}_0)\mathcal{P}^0 + (\mathbf{u}_0\cdot\nabla)\mathcal{P}^0 + \mathcal{P}^0\cdot\nabla\mathbf{u}_0 + [\mathcal{P}^0\cdot\nabla\mathbf{u}_0]^T + \frac{e}{m_e}\Big(\mathcal{P}^0\times\mathbf{B}_0 + [\mathcal{P}^0\times\mathbf{B}_0]^T\Big) = 0, \tag{6.42}$$

After estimating the different terms into the previous equation (see appendix H for detailed calculations), we find the following set of equations for the elements of the euqilibrium pressure tensor

$$\omega_{c,e}\mathcal{P}^0_{xy} - \bar{\omega}_{c,e}f(x)\mathcal{P}^0_{xz} = 0, \tag{6.43}$$

$$\omega_{c,e}\mathcal{P}^0_{yy} - \omega_{c,e}\mathcal{P}^0_{xx} - \bar{\omega}_{c,e}f(x)\mathcal{P}^0_{yz} = 0, \tag{6.44}$$

$$\omega_{c,e}\mathcal{P}^0_{yz} + \bar{\omega}_{c,e}f(x)\mathcal{P}^0_{xx} - \bar{\omega}_{c,e}f(x)\mathcal{P}^0_{zz} + \frac{\partial u_{z0}}{\partial x}\mathcal{P}^0_{xx} = 0, \tag{6.45}$$

$$-2\omega_{c,e}\mathcal{P}^0_{xy} = 0, \tag{6.46}$$

$$\omega_{c,e}\mathcal{P}^0_{xz} - \bar{\omega}_{c,e}f(x)\mathcal{P}^0_{xy} - \frac{\partial u_{z0}}{\partial x}\mathcal{P}^0_{xy} = 0, \tag{6.47}$$

$$\bar{\omega}_{c,e}f(x)\mathcal{P}^0_{xz} + \frac{\partial u_{z0}}{\partial x}\mathcal{P}^0_{xz} = 0, \tag{6.48}$$

It is obvious from these equations that $\mathcal{P}^0_{xy} = \mathcal{P}^0_{xz} = 0$. Hence, only Eqs.[6.44, 6.45] define the equilibrium pressure tensor. Following these argument, we end with two possible equilibrium given by

1. $\mathcal{P}^0_{yz} = 0$, then Eqs[6.44, 6.45, 6.41, 6.36, 2.142] give

$$\mathcal{P}^0_{xx} = \mathcal{P}^0_{yy} = \frac{B_s^2}{2\mu_0}[f(x)]^2, \quad \mathcal{P}^0_{zz} = \frac{B_s^2}{2\mu_0}[f(x) - d_e^2 f''(x)]f(x), \tag{6.49}$$

2. $\mathcal{P}^0_{yz} \neq 0$. In this case there will be anisotropic in the plane $(x-y)$, that is

$$\mathcal{P}^0_{yy} - \mathcal{P}^0_{xx} = \frac{\bar{\omega}_{c,e}}{\omega_{c,e}}f(x)\mathcal{P}^0_{yz}, \tag{6.50}$$

Accordingly, the main effect of $\mathcal{P}^0_{yz}$ is to generate an anisotropy in the plane perpendicular to the guide field. This anisotropy effect increases with reducing the intensity of the guide field. Nevertheless, this argument is correct far from the singular surface (on which f vanishes). In the very vicinity of this surface, the function f reaches very small values. Hence, even if $\omega_{c,e} \approx \bar{\omega}_{c,e}$, it remains possible to identify a region around the singular surface where $\mathcal{P}^0_{xx} \approx \mathcal{P}^0_{yy}$. The existence of a strong guide field ($\omega_{c,e} \gg \bar{\omega}_{c,e}$) strengthens this argument. Strictly speaking, from a mathematical point of view, when requiring $\mathcal{P}^0_{zz} = 0$, we are then forced to consider $\mathcal{P}^0_{yz} \neq 0$ in order to satisfy the set of equations [6.43 - 6.48].

6.3.2 Linear Analysis of the Pressure Tensor Equation with Strong Guide Field

First, we assume an equilibrium magnetic field with two components. The first is a shear field in (x-y) plane: $B_y(x) = B_s f(x)$, while the second is a constant strong guide field along z direction (B_g), as given by Eq.(6.35). Furthermore, at equilibrium and in the vicinity $X-$point (it is the point at which the shear field vanishes), where the reconnection occurs, we assume that the pressure is dominated by the gyrotropic part, which also implies that the non-diagonal elements are neglected compared to the diagonal ones. Additionally, the existence of a guide field produces an anisotropy in the diagonal elements of the equilibrium pressure tensor. Therefore, we adopt the equilibrium given by Eq.(6.49), that is

$$\mathcal{P}^0_{xx} = \mathcal{P}^0_{yy} = \mathcal{P}^0_{\perp}(x),\ \mathcal{P}^0_{zz} = \mathcal{P}^0_{||}(x),\ \mathcal{P}^0_{xz} = \mathcal{P}^0_{zx} = \mathcal{P}^0_{xy} = \mathcal{P}^0_{yx} = \mathcal{P}^0_{zy} = \mathcal{P}^0_{yz} = 0, \tag{6.51}$$

Where "0" refers to equilibrium, " $\perp$ " to perpendicular direction to the guide field, and ||" to parallel direction. The equilibrium pressure tensor components are functions of the shear variable x, which can be understood since a gradient of the pressure is needed to establish stationary equilibrium. Because of the equilibrium we chose, and the absence of a shear velocity, one can assume a vanishing equilibrium velocity. Under these assumptions, the linear version of Eq.(6.34) reads

$$\begin{aligned}&\frac{\partial \mathcal{P}^1}{\partial t} + (\nabla\cdot\mathbf{u}_1)\mathcal{P}^0 + (\mathbf{u}_1\cdot\nabla)\mathcal{P}^0 + \mathcal{P}^0\cdot\nabla\mathbf{u}_1 + [\mathcal{P}^0\cdot\nabla\mathbf{u}_1]^T + +\mathcal{P}^1\cdot\nabla\mathbf{u}_0 + [\mathcal{P}^1\cdot\nabla\mathbf{u}_0]^T \\ &+ \frac{e}{m}\Big(\mathcal{P}^0\times\mathbf{B}_1 + \mathcal{P}^1\times\mathbf{B}_0 + [\mathcal{P}^0\times\mathbf{B}_1]^T + [\mathcal{P}^1\times\mathbf{B}_0]^T\Big) = 0,\end{aligned} \tag{6.52}$$

The previous system is composed of six differential equations for the independent components of the pressure tensor. After solving it, as detailed in appendix H, these components read,

$$\mathcal{P}^1_{xy} = \frac{\mathcal{P}^0_{\perp}}{2\omega_{c,e}}\Big(\frac{\partial u_{y1}}{\partial y} - \frac{\partial u_{x1}}{\partial x}\Big), \tag{6.53}$$

$$\mathcal{P}^1_{xz} = \frac{e}{m\omega_{c,e}}(\mathcal{P}^0_{||} - \mathcal{P}^0_{\perp})B_{x1} + \frac{\mathcal{P}^0_{\perp}}{\omega_{c,e}}\frac{\partial u_{z1}}{\partial y}, \tag{6.54}$$

$$\begin{aligned}\mathcal{P}^1_{xx} = &-\frac{2\mathcal{P}^0_{\perp}}{\gamma}\Big(\frac{\partial u_{x1}}{\partial x} + \frac{\partial u_{y1}}{\partial y}\Big) - \frac{1}{\gamma}\frac{d\mathcal{P}^0_{\perp}}{dx}u_{x1} \\ &+ \frac{2\bar{\omega}_{c,e}}{\gamma}f(x)\Big[\frac{e}{m\omega_{c,e}}(\mathcal{P}^0_{||} - \mathcal{P}^0_{\perp})B_{x1} + \frac{\mathcal{P}^0_{\perp}}{\omega_{c,e}}\frac{\partial u_{z1}}{\partial y}\Big],\end{aligned} \tag{6.55}$$

$$\begin{aligned}\mathcal{P}^1_{yy} = &-\frac{\mathcal{P}^0_{\perp}}{\omega_{c,e}}\Big(\frac{\partial u_{x1}}{\partial y} + \frac{\partial u_{y1}}{\partial x}\Big) - \frac{2\mathcal{P}^0_{\perp}}{\gamma}\Big(\frac{\partial u_{x1}}{\partial x} + \frac{\partial u_{y1}}{\partial y}\Big) - \frac{1}{\gamma}\frac{d\mathcal{P}^0_{\perp}}{dx}u_{x1} \\ &+ \frac{2\bar{\omega}_{c,e}}{\gamma}f(x)\Big[\frac{e}{m\omega_{c,e}}(\mathcal{P}^0_{||} - \mathcal{P}^0_{\perp})B_{x1} + \frac{\mathcal{P}^0_{\perp}}{\omega_{c,e}}\frac{\partial u_{z1}}{\partial y}\Big],\end{aligned} \tag{6.56}$$

$$\begin{aligned}\mathcal{P}^1_{zz} = &-\frac{1}{\gamma}\frac{d\mathcal{P}^0_{||}}{dx}u_{x1} - \frac{\mathcal{P}^0_{||}}{\gamma}\Big(\frac{\partial u_{x1}}{\partial x} + \frac{\partial u_{y1}}{\partial y}\Big) \\ &- \frac{2\bar{\omega}_{c,e}}{\gamma}\Big[f(x) - d_e^2 f''(x)\Big]\Big[\frac{e}{m\omega_{c,e}}(\mathcal{P}^0_{||} - \mathcal{P}^0_{\perp})B_{x1} + \frac{\mathcal{P}^0_{\perp}}{\omega_{c,e}}\frac{\partial u_{z1}}{\partial y}\Big],\end{aligned} \tag{6.57}$$

$$\begin{aligned}\mathcal{P}^1_{yz} = &-\frac{1}{\omega_{c,e}}\mathcal{P}^0_{\perp}\frac{\partial u_{z1}}{\partial x} - \frac{e}{m\omega_{c,e}}(\mathcal{P}^0_{\perp} - \mathcal{P}^0_{||})B_{y1} \\ &+ \frac{\bar{\omega}_{c,e}}{\omega_{c,e}}f(x)\Big\{\frac{1}{\gamma}\mathbf{u}\cdot\nabla(\mathcal{P}^0_{\perp} - \mathcal{P}^0_{||}) + \frac{1}{\gamma}(2\mathcal{P}^0_{\perp} - \mathcal{P}^0_{||})(\frac{\partial u_{x1}}{\partial x} + \frac{\partial u_{y1}}{\partial y})\Big\} \\ &- \frac{\bar{\omega}_{c,e}}{\omega_{c,e}}d_e^2 f''(x)\Big\{\frac{2\mathcal{P}^0_{\perp}}{\gamma}(\frac{\partial u_{x1}}{\partial x} + \frac{\partial u_{y1}}{\partial y}) + \frac{1}{\gamma}\frac{d\mathcal{P}^0_{\perp}}{dx}u_{x1}\Big\},\end{aligned} \tag{6.58}$$

6.3.3 Linearization of the Continuity Equation

The linearization of continuity equation with an equilibrium profile depending only on x gives

$$\frac{\partial n_1}{\partial t} + \mathbf{u}_1\cdot\nabla n_0 + n_0\nabla\cdot\mathbf{u}_1 = 0 \implies n_1 = -\frac{1}{\gamma}\frac{dn_0}{dx}u_{x1} - \frac{n_0}{\gamma}\frac{\partial u_{x1}}{\partial x} - \frac{n_0}{\gamma}\frac{\partial u_{y1}}{\partial y}, \tag{6.59}$$

We used the fact that $\nabla\cdot\mathbf{u}_0 = 0$, and $n_0 = n_0(x)$. n_0 is the equilibrium electron density. Taking into account that the problem is independent of the z variable and taking the Fourier transformation of it ($n_1 = \tilde{n}_1 e^{\gamma t}e^{iky}$), one finds

$$\tilde{n}_1 = -\frac{1}{\gamma}\frac{dn_0}{dx}\tilde{u}_{x1} - \frac{n_0}{\gamma}\frac{\partial\tilde{u}_{x1}}{\partial x} - \frac{ikn_0}{\gamma}\tilde{u}_{y1}, \tag{6.60}$$

This equation is fundamental and gives us the density perturbation. It will be combined with linearized motion, Faraday, and Ampere equations so to formulate an eigenvalue problem. It is important to mention the fact that any equilibrium density profile must satisfies the following equation

$$\mathbf{u}_0\cdot\nabla n_0 + n_0\nabla\cdot\mathbf{u}_0 = 0, \tag{6.61}$$

According to the chosen equilibrium velocity, given by Eq.(6.36), we have $\nabla\cdot\mathbf{u}_0 = 0$, therefore any equilibrium density profile, satisfying $\mathbf{u}_0\cdot\nabla n_0 = 0$ (that is, $n_0 = n_0(x,y)$), can be studied. Obviously, the simplest one is the equilibrium homogeneous density $n_0 = const$.

6.3.4 Linear Analysis of Faraday-Maxwell Equation with Strong Guide Field and Full Pressure Tensor

The linearization of Faraday-Maxwell equation, given by Eq.(6.32), leads to the following system of differential equations (see appendix I for a detailed derivation):

$$\frac{\partial B_{x1}}{\partial t} = \Big[B_s f + \frac{mB_s}{\mu_0 e^2}(-\frac{f''}{n_0} + \frac{f' n_0'}{n_0^2})\Big]\frac{\partial u_{x1}}{\partial y} + \frac{m}{e}\frac{\partial}{\partial t}(\frac{\partial u_{z1}}{\partial y}) + \frac{1}{en_0}\Big(\frac{\partial^2\mathcal{P}^1_{xz}}{\partial x\partial y} + \frac{\partial^2\mathcal{P}^1_{yz}}{\partial y^2}\Big), \tag{6.62}$$

$$\begin{aligned}\frac{\partial B_{y1}}{\partial t} = &\Big[-B_s f' + \frac{mB_s}{\mu_0 e^2}\times\Big(\frac{f'''}{n_0} - \frac{2f'' n_0'}{n_0} + \frac{2f' {n_0'}^2}{n_0^3} - \frac{f' n_0''}{n_0^2}\Big)\Big]u_{x1} - \Big[B_s f - \frac{mB_s}{\mu_0 e^2}\Big(\frac{f''}{n_0} \\ &- \frac{f' n_0'}{n_0^2}\Big)\Big]\frac{\partial u_{x1}}{\partial x} - \frac{m}{e}\frac{\partial}{\partial t}(\frac{\partial u_{z1}}{\partial x}) - \frac{1}{en_0}\frac{\partial^2\mathcal{P}^1_{xz}}{\partial x^2} - \frac{1}{en_0}\frac{\partial^2\mathcal{P}^1_{yz}}{\partial x\partial y} + \frac{n_0'}{en_0^2}\frac{\partial\mathcal{P}^1_{xz}}{\partial x} + \frac{n_0'}{en_0^2}\frac{\partial\mathcal{P}^1_{yz}}{\partial y},\end{aligned} \tag{6.63}$$

$$\begin{aligned}\frac{\partial B_{z1}}{\partial t} = &-\frac{B_s^2}{\mu_0 e}\frac{ff'}{n_0^2}\frac{\partial n_1}{\partial y} - \Big[\frac{B_s}{\mu_0 en_0}f''(x) - \frac{B_s}{\mu_0 e}\frac{n_0' f'(x)}{n_0^2}\Big]B_{x1} - B_g(\frac{\partial u_{x1}}{\partial x} + \frac{\partial u_{y1}}{\partial y}) + B_s f(x)\frac{\partial u_{z1}}{\partial y} \\ &+ \frac{m}{e}\frac{\partial}{\partial t}(\frac{\partial u_{y1}}{\partial x} - \frac{\partial u_{x1}}{\partial y}) + \frac{1}{en_0}\frac{\partial^2}{\partial x\partial y}(\mathcal{P}^1_{yy} - \mathcal{P}^1_{xx}) + \frac{1}{en_0}\frac{\partial^2\mathcal{P}^1_{xy}}{\partial x^2} - \frac{1}{en_0}\frac{\partial^2\mathcal{P}^1_{xy}}{\partial y^2} - \frac{n_0'}{en_0^2}\frac{\partial\mathcal{P}^1_{xy}}{\partial x} - \frac{n_0'}{en_0^2}\frac{\partial\mathcal{P}^1_{yy}}{\partial y},\end{aligned} \tag{6.64}$$

The previous equations are general where we kept the effects of electron inertia and full pressure tensor. They are also dimensional, and can be applied to regimes with arbitrary equilibrium density profiles, which make them very useful to study realistic cases after, numerically, solving them.

6.3.5 Linear Analysis of Ampere-Maxwell Equation with Full Pressure Tensor

Now, we turn our attention to Ampere-Maxwell equation. After linearizing, it takes the following form

$$n_0\mathbf{u}_1 + n_1\mathbf{u}_0 = -\frac{1}{\mu_0 e}\nabla\times\mathbf{B}_1 + \frac{1}{\mu_0 e c^2}\frac{\partial\mathbf{E}_1}{\partial t} = -\frac{1}{\mu_0 e}\nabla\times\mathbf{B}_1 - \frac{1}{\mu_0 e c^2}\frac{\partial}{\partial t}\Big[(\mathbf{u}_0\times\mathbf{B}_1) + (\mathbf{u}_1\times\mathbf{B}_0) + (\mathbf{u}_0\times\mathbf{B}_0)\frac{n_1}{n_0} + \frac{m}{e}\frac{\partial\mathbf{u}_1}{\partial t} + \frac{m}{e}\mathbf{u}_1\cdot\nabla\mathbf{u}_0 + \frac{\nabla\cdot\mathcal{P}^1}{e n_0}\Big], \tag{6.65}$$

Where,

$$\nabla\times\mathbf{B}_1 = \begin{cases} \frac{\partial B_{z1}}{\partial y}, \\ -\frac{\partial B_{z1}}{\partial x}, \\ \frac{\partial B_{y1}}{\partial x} - \frac{\partial B_{x1}}{\partial y}, \end{cases} \tag{6.66}$$

Now substituting Eq.(6.66), and all the needed relationships from appendix I, into the previous equation, one finds the following system of equations

$$\frac{1}{\omega_{p,e}^2}\frac{\partial^2 u_{x1}}{\partial t^2} + \frac{\omega_{c,e}}{\omega_{p,e}^2}\frac{\partial u_{y1}}{\partial t} - \frac{\bar{\omega}_{c,e}}{\omega_{p,e}^2} f\frac{\partial u_{z1}}{\partial t} + \frac{\bar{\omega}_{c,e}\alpha}{\omega_{p,e}^2} f'\frac{\partial B_{y1}}{\partial t} + \frac{1}{\mu_0 e^2 n_0^2 c^2}\frac{\partial}{\partial t}\Big(\frac{\partial \mathcal{P}^1_{xx}}{\partial x} + \frac{\partial \mathcal{P}^1_{xy}}{\partial y}\Big) = -u_{x1} - \alpha\frac{\partial B_{z1}}{\partial y}, \tag{6.67}$$

$$\frac{1}{\omega_{p,e}^2}\frac{\partial^2 u_{y1}}{\partial t^2} - \frac{\omega_{c,e}}{\omega_{p,e}^2}\frac{\partial u_{x1}}{\partial t} - \frac{\bar{\omega}_{c,e}\alpha}{\omega_{p,e}^2} f'\frac{\partial B_{x1}}{\partial t} + \frac{1}{\mu_0 e^2 n_0^2 c^2}\frac{\partial}{\partial t}\frac{\partial \mathcal{P}^1_{xy}}{\partial x} + \frac{1}{\mu_0 e^2 n_0^2 c^2}\frac{\partial}{\partial t}\frac{\partial \mathcal{P}^1_{yy}}{\partial y} + = -u_{y1} + \alpha\frac{\partial B_{z1}}{\partial x} \tag{6.68}$$

$$\frac{1}{\omega_{p,e}^2}\frac{\partial^2 u_{z1}}{\partial t^2} + \frac{\bar{\omega}_{c,e}}{\omega_{p,e}^2}(f - d_e^2 f'')\frac{\partial u_{x1}}{\partial t} + \frac{1}{\mu_0 e^2 n_0^2 c^2}\frac{\partial}{\partial t}\frac{\partial \mathcal{P}^1_{xz}}{\partial x} + \frac{1}{\mu_0 e^2 n_0^2 c^2}\frac{\partial}{\partial t}\frac{\partial \mathcal{P}^1_{yz}}{\partial y} = -\frac{u_{z0}}{n_0}n_1 - u_{z1} + \alpha\frac{\partial B_{x1}}{\partial y} - \alpha\frac{\partial B_{y1}}{\partial x} \tag{6.69}$$

Which give, after substituting the values the pressure tensor's elements and its derivatives (see appendix H),

$$\frac{\gamma^2}{\omega_{p,e}^2}u_{x1} - \gamma\frac{c^2\bar{\omega}_{c,e}^2}{2\omega_{p,e}^4}\frac{f^2}{2\omega_{c,e}}\frac{\partial^2 u_{x1}}{\partial y\partial x} + \gamma\frac{\omega_{c,e}}{\omega_{p,e}^2}u_{y1} + \gamma\frac{c^2\bar{\omega}_{c,e}^2}{2\omega_{p,e}^4}\frac{f^2}{2\omega_{c,e}}\frac{\partial^2 u_{y1}}{\partial y^2} - \gamma\frac{\bar{\omega}_{c,e}}{\omega_{p,e}^2}f u_{z1} + \gamma\frac{\bar{\omega}_{c,e}\alpha}{\omega_{p,e}^2}f' B_{y1}$$
$$= -u_{x1} + \frac{c^2\bar{\omega}_{c,e}^2}{2\omega_{p,e}^4}(2f^2\frac{\partial^2}{\partial x^2} + 4f'f\frac{\partial}{\partial x} + f^{2'}\frac{\partial}{\partial x} + 2f_3 + 2f'^2)u_{x1} + \frac{c^2\bar{\omega}_{c,e}^2}{2\omega_{p,e}^4}(2f^2\frac{\partial^2}{\partial x\partial y} + 4f'f\frac{\partial}{\partial y})u_{y1}$$
$$- \frac{c^2\bar{\omega}_{c,e}^2}{2\omega_{p,e}^4}\frac{2\bar{\omega}_{c,e}}{\omega_{c,e}}(f^3\frac{\partial^2}{\partial x\partial y} + 3f'f^2\frac{\partial}{\partial y})u_{z1} + \frac{c^2\bar{\omega}_{c,e}^2}{2\omega_{p,e}^4}\frac{2e\bar{\omega}_{c,e}d_e^2}{m\omega_{c,e}}(f_1\frac{\partial}{\partial x} + f_1')B_{x1} - \alpha\frac{\partial B_{z1}}{\partial y}, \tag{6.70}$$

$$\frac{\gamma^2}{\omega_{p,e}^2}u_{y1}-\gamma\frac{\omega_{c,e}}{\omega_{p,e}^2}u_{x1}-\gamma\frac{c^2\bar{\omega}_{c,e}^2}{2\omega_{p,e}^4}\frac{1}{\omega_{c,e}}\Big[\frac{f^2}{2}\frac{\partial^2}{\partial x^2}+ff^{'}\frac{\partial}{\partial x}-f^2\frac{\partial^2}{\partial y^2}\Big]u_{x1}+\gamma\frac{c^2\bar{\omega}_{c,e}^2}{2\omega_{p,e}^4}\frac{1}{\omega_{c,e}}\Big[\frac{f^2}{2}\frac{\partial^2}{\partial x\partial y}$$
$$+ff^{'}\frac{\partial}{\partial y}-f^2\frac{\partial^2}{\partial y\partial x}\Big]u_{y1}-\gamma\frac{\bar{\omega}_{c,e}\alpha}{\omega_{p,e}^2}f^{'}B_{x1}=\frac{c^2\bar{\omega}_{c,e}^2}{2\omega_{p,e}^4}\Big[f^{2'}\frac{\partial}{\partial y}+2f^2\frac{\partial^2}{\partial y\partial x}\Big]u_{x1}-u_{y1}+\frac{c^2\bar{\omega}_{c,e}^2}{2\omega_{p,e}^4}2f^2\times$$
$$\frac{\partial^2u_{y1}}{\partial y^2}-\frac{c^2\bar{\omega}_{c,e}^2}{2\omega_{p,e}^4}\frac{2\bar{\omega_{c,e}}}{\omega_{c,e}}f^3\frac{\partial^2u_{z1}}{\partial y^2}+\frac{c^2\bar{\omega}_{c,e}^2}{2\omega_{p,e}^4}\frac{2e\bar{\omega}_{c,e}d_e^2}{m\omega_{c,e}}f_1\frac{\partial B_{x1}}{\partial y}+\alpha\frac{\partial B_{z1}}{\partial x}, \tag{6.71}$$

$$\frac{\gamma^2}{\omega_{p,e}^2}u_{z1}+\gamma\frac{\bar{\omega}_{c,e}}{\omega_{p,e}^2}(f-d_e^2f^{''})u_{x1}+\gamma\frac{c^2\bar{\omega}_{c,e}^2}{2\omega_{p,e}^4}(\frac{f^2}{\omega_{c,e}}\frac{\partial^2}{\partial x\partial y}+\frac{2ff^{'}}{\omega_{c,e}}\frac{\partial}{\partial y})u_{z1}-\gamma\frac{c^2\bar{\omega}_{c,e}^2}{2\omega_{p,e}^4}\frac{1}{\omega_{c,e}}f^2\frac{\partial^2u_{z1}}{\partial y\partial x}$$
$$-\gamma\frac{c^2\bar{\omega}_{c,e}^2}{2\omega_{p,e}^4}\frac{ed_e^2}{m\omega_{c,e}}(f_3\frac{\partial}{\partial x}+f_3^{'})B_{x1}-\gamma\frac{c^2\bar{\omega}_{c,e}^2}{2\omega_{p,e}^4}\frac{ed_e^2}{m\omega_{c,e}}f_3\frac{\partial B_{y1}}{\partial y}=-\frac{c^2\bar{\omega}_{c,e}^2}{2\omega_{p,e}^4}\frac{\bar{\omega}_{c,e}d_e^2}{\omega_{c,e}}f_5\frac{\partial u_{x1}}{\partial y}-\frac{c^2\bar{\omega}_{c,e}^2}{2\omega_{p,e}^4}\times$$
$$\frac{\bar{\omega}_{c,e}}{\omega_{c,e}}f_6\frac{\partial^2u_{x1}}{\partial y\partial x}-\frac{c^2\bar{\omega}_{c,e}^2}{2\omega_{p,e}^4}\frac{\bar{\omega}_{c,e}}{\omega_{c,e}}f_6\frac{\partial^2u_{y1}}{\partial y^2}-u_{z1}+\alpha\frac{\partial B_{x1}}{\partial y}-\alpha\frac{\partial B_{y1}}{\partial x}-\frac{u_{z0}}{n_0}n_1, \tag{6.72}$$

In writing the above equations, we used the following useful relationships,

$$\frac{B_g}{\mu_0en_0c^2}=\frac{\omega_{c,e}}{\omega_{p,e}^2},\quad \frac{B_s}{\mu_0^2e^2n_0^2c^2}=\frac{\bar{\omega}_{c,e}\alpha}{\omega_{p,e}^2},\quad \frac{B_s^2}{2\mu_0^2e^2n_0^2c^2}=\frac{1}{2}\frac{c^2\bar{\omega}_{c,e}^2}{\omega_{p,e}^4}, \tag{6.73}$$

6.3.6 Homogeneous Equilibrium Density

Now, we group the linear equations derived in the previous sections to formulate a generalized eigenvalue problem. These equations are: linearized equations of density, Faraday, and Ampere. The the eigenvalue to be found is the growth rate γ, and the eigenvector is $\mathbf{V}_\gamma = [B_x, B_y, B_z, u_x, u_y, u_z, n]^T$ (see appendix J for details). This eigenvalue problem takes the following form

$$\gamma^2\begin{bmatrix}\mathcal{I}&0&0&0&0&kd_e^2\mathcal{I}&0\\0&\mathcal{I}&0&0&0&\mathcal{S}_{22z}&0\\0&0&0&0&0&0&0\\0&0&0&d_e^4\mathcal{I}&0&0&0\\0&0&0&0&d_e^4\mathcal{I}&0&0\\0&0&0&0&0&d_e^4\mathcal{I}&0\\0&0&0&0&0&0&0\end{bmatrix}\begin{bmatrix}B_x\\B_y\\B_z\\u_x\\u_y\\u_z\\n\end{bmatrix}+\gamma\begin{bmatrix}\mathcal{M}_{11x}&\mathcal{M}_{11y}&0&\mathcal{S}_{11x}&0&\mathcal{S}_{11z}&0\\\mathcal{M}_{21x}&\mathcal{M}_{21y}&0&\mathcal{S}_{21x}&0&\mathcal{S}_{21z}&0\\0&0&\mathcal{I}&-kd_e^2\mathcal{I}&\mathcal{S}_{31y}&0&0\\0&\mathcal{M}_{41y}&0&\mathcal{S}_{41x}&\mathcal{S}_{41y}&\mathcal{S}_{41z}&0\\\mathcal{M}_{51x}&0&0&\mathcal{S}_{51x}&\mathcal{S}_{51y}&0&0\\\mathcal{M}_{61x}&\mathcal{M}_{61y}&0&\mathcal{S}_{61x}&0&\mathcal{S}_{61z}&0\\0&0&0&0&0&0&\mathcal{I}\end{bmatrix}$$
$$\times\begin{bmatrix}B_x\\B_y\\B_z\\u_x\\u_y\\u_z\\n\end{bmatrix}+\begin{bmatrix}0&0&0&\mathcal{S}_{10x}&\mathcal{S}_{10y}&0&0\\0&0&0&\mathcal{S}_{20x}&\mathcal{S}_{20y}&0&0\\\mathcal{M}_{30x}&0&0&\mathcal{S}_{30x}&\mathcal{S}_{30y}&\mathcal{S}_{30z}&\mathcal{N}_{30n}\\\mathcal{M}_{40x}&0&\mathcal{M}_{40z}&\mathcal{S}_{40x}&\mathcal{S}_{40y}&\mathcal{S}_{40z}&0\\\mathcal{M}_{50x}&0&\mathcal{M}_{50z}&\mathcal{S}_{50x}&\mathcal{S}_{50y}&\mathcal{S}_{50z}&0\\\mathcal{M}_{60x}&\mathcal{M}_{60y}&0&\mathcal{S}_{60x}&\mathcal{S}_{60y}&\mathcal{S}_{60z}&\mathcal{N}_{60n}\\0&0&0&\mathcal{S}_{70x}&\mathcal{S}_{70y}&0&0\end{bmatrix}\begin{bmatrix}B_x\\B_y\\B_z\\u_x\\u_y\\u_z\\n\end{bmatrix}=0, \tag{6.74}$$

Where,

$$S_{11x} = k\frac{\bar{\omega}_{c,e}}{\omega_{c,e}}\Big[f - d_e^2 f''\Big], \quad S_{11z} = -\frac{i}{2}(\frac{\bar{\omega}_{c,e}}{\omega_{c,e}})^2 k^2 d_e^2\Big[\frac{\partial}{\partial x} - f^2\frac{\partial}{\partial x} - 2ff'\Big], \quad M_{11x} = -\frac{1}{2}(\frac{\bar{\omega}_{c,e}}{\omega_{c,e}})^2 k\times$$
$$d_e^2\Big[f_3\frac{\partial}{\partial x} + f_3'\Big], M_{11y} = -\frac{i}{2}(\frac{\bar{\omega}_{c,e}}{\omega_{c,e}})^2 k^2 d_e^2 f_3, \quad S_{10x} = \frac{i}{2}(\frac{\bar{\omega}_{c,e}}{\omega_{c,e}})^3 k^2\Big[f_6\frac{\partial}{\partial x} + d_e^2 f_5\Big], \quad S_{10y} = \frac{i}{2}(\frac{\bar{\omega}_{c,e}}{\omega_{c,e}})^3$$
$$\times k^2\Big[f_6\frac{\partial}{\partial x} + d_e^2 f_5\Big], S_{22z} = d_e^2\frac{\partial}{\partial x}, \quad S_{21x} = (\frac{\bar{\omega}_{c,e}}{\omega_{c,e}})\Big[f\frac{\partial}{\partial x} - d_e^2 f''\frac{\partial}{\partial x} + f' - d_e^2 f'''\Big], S_{21z} = -\frac{1}{2}\times$$
$$(\frac{\bar{\omega}_{c,e}}{\omega_{c,e}})^2 k\Big[2ff'\frac{\partial}{\partial x} + 2f_3 + 2f'^2\Big], M_{21x} = -\frac{1}{2}(\frac{\bar{\omega}_{c,e}}{\omega_{c,e}})^2 d_e^2\Big[f_3\frac{\partial^2}{\partial x^2} + 2f_3'\frac{\partial}{\partial x} + f_3''\Big], \quad M_{21y} = \frac{1}{2}(\frac{\bar{\omega}_{c,e}}{\omega_{c,e}})^2$$
$$\times k d_e^2\Big[f_3\frac{\partial}{\partial x} + f_3'\Big], \tag{6.75}$$

$$S_{20x} = -\frac{1}{2}(\frac{\bar{\omega}_{c,e}}{\omega_{c,e}})^3 k\Big[f_6\frac{\partial^2}{\partial x^2} + (f_6' + d_e^2 f_5)\frac{\partial}{\partial x} + d_e^2 f_5'\Big], S_{20y} = -i\frac{1}{2}(\frac{\bar{\omega}_{c,e}}{\omega_{c,e}})^3 k^2\Big[f_6\frac{\partial}{\partial x} + f_6'\Big],$$
$$S_{31y} = -d_e^2\frac{\partial}{\partial x}, S_{30x} = \Big\{\frac{\partial}{\partial x} + \frac{1}{2}(\frac{\bar{\omega}_{c,e}}{\omega_{c,e}})^2 d_e^2\Big[\frac{f^2}{2}\frac{\partial^3}{\partial x^3} + 2ff'\frac{\partial^2}{\partial x^2} + (f_3 + f'^2)\frac{\partial}{\partial x} - ik^2 f^2\frac{\partial}{\partial x} - 2ik^2$$
$$\times ff' + \frac{i}{2}k^2 f^2\frac{\partial}{\partial x}\Big]\Big\}, S_{30y} = -k\Big[1 + \frac{1}{4}(\frac{\bar{\omega}_{c,e}}{\omega_{c,e}})^2 d_e^2\Big(f^2\frac{\partial^2}{\partial x} - 2f_3 - 2f'^2 - k^2\frac{f^2}{2}\Big)\Big], N_{30n} = -(\frac{\bar{\omega}_{c,e}}{\omega_{c,e}})^2$$
$$\times kff'\frac{\partial}{\partial y}, S_{30z} = (\frac{\bar{\omega}_{c,e}}{\omega_{c,e}})kf, M_{30x} = (\frac{\bar{\omega}_{c,e}}{\omega_{c,e}})f'', \quad S_{41x} = \frac{d_e^4}{4}(\frac{\bar{\omega}_{c,e}}{\omega_{c,e}})^2 kf^2\frac{\partial}{\partial x}, S_{41y} = d_e^2\Big[1 - \frac{i}{2}(\frac{\bar{\omega}_{c,e}}{\omega_{c,e}})^2$$
$$\times k^2 d_e^2 f^2\Big], \quad S_{41z} = -d_e^2(\frac{\bar{\omega}_{c,e}}{\omega_{c,e}})f, M_{41y} = d_e^2(\frac{\bar{\omega}_{c,e}}{\omega_{c,e}})f', \quad S_{40x} = \Big[(\frac{\omega_{p,e}}{\omega_{c,e}})^2 - \frac{d_e^2}{2}(\frac{\bar{\omega}_{c,e}}{\omega_{c,e}})^2\times$$
$$\Big(2f^2\frac{\partial^2}{\partial x^2} + 4f'f\frac{\partial}{\partial x} + f^{2'}\frac{\partial}{\partial x} + 2f_3 + 2f'^2\Big)\Big], \tag{6.76}$$

$$S_{40y} = \frac{kd_e^2}{2}(\frac{\bar{\omega}_{c,e}}{\omega_{c,e}})^2\Big[2f^2\frac{\partial}{\partial x} + 4f'f\Big], S_{40z} = -kd_e^2(\frac{\bar{\omega}_{c,e}}{\omega_{c,e}})^3\Big[f^3\frac{\partial}{\partial x} + 3f'f^2\Big], M_{40x} = -d_e^2(\frac{\bar{\omega}_{c,e}}{\omega_{c,e}})^3\Big[f_1\frac{\partial}{\partial x}$$
$$+ f_1'\Big], \quad M_{40z} = -k(\frac{\omega_{p,e}}{\omega_{c,e}})^2, \quad S_{51x} = -d_e^2\Big[1 + \frac{d_e^2}{2}(\frac{\bar{\omega}_{c,e}}{\omega_{c,e}})^2\Big(\frac{f^2}{2}\frac{\partial^2}{\partial x^2} + ff'\frac{\partial}{\partial x} + if^2k^2\Big)\Big],$$
$$M_{51x} = -d_e^2(\frac{\bar{\omega}_{c,e}}{\omega_{c,e}})f', \tag{6.77}$$

And,

$$S_{51y} = -\frac{d_e^4}{2}(\frac{\bar{\omega}_{c,e}}{\omega_{c,e}})^2 k\Big[\frac{f^2}{2}\frac{\partial}{\partial x} + ff' - f^2\frac{\partial}{\partial x}\Big], \quad S_{50x} = \frac{d_e^2}{2}(\frac{\bar{\omega}_{c,e}}{\omega_{c,e}})^2 k\Big[f^{2'} + 2f^2\frac{\partial}{\partial x}\Big], \quad S_{50z} = -id_e^2\times$$
$$(\frac{\bar{\omega}_{c,e}}{\omega_{c,e}})^3 k^2 f^3, S_{50y} = \Big[(\frac{\omega_{p,e}}{\omega_{c,e}})^2 + id_e^2(\frac{\bar{\omega}_{c,e}}{\omega_{c,e}})^2 k^2 f^2\Big], \quad M_{50x} = d_e^2(\frac{\bar{\omega}_{c,e}}{\omega_{c,e}})^3 k f_1, \quad M_{50z} = -(\frac{\omega_{p,e}}{\omega_{c,e}})^2\frac{\partial}{\partial x},$$
$$S_{61x} = d_e^2(\frac{\bar{\omega}_{c,e}}{\omega_{c,e}})\Big[f - d_e^2 f''\Big], \quad S_{61z} = d_e^4(\frac{\bar{\omega}_{c,e}}{\omega_{c,e}})^2 ff'\frac{\partial}{\partial y}, \quad M_{61x} = -\frac{d_e^4}{2}(\frac{\bar{\omega}_{c,e}}{\omega_{c,e}})^2\Big[f_3\frac{\partial}{\partial x} + f_3'\Big],$$
$$M_{61y} = \frac{d_e^4}{2}(\frac{\bar{\omega}_{c,e}}{\omega_{c,e}})^2 k f_3, \quad S_{60x} = -\frac{d_e^2}{2}(\frac{\bar{\omega}_{c,e}}{\omega_{c,e}})^3 k[f_6\frac{\partial}{\partial x} + d_e^2 f_5\Big], \quad S_{60y} = -\frac{id_e^2}{2}(\frac{\bar{\omega}_{c,e}}{\omega_{c,e}})^3 k^2 f_6,$$
$$S_{60z} = (\frac{\bar{\omega}_{c,e}}{\omega_{c,e}})^3, \quad M_{60x} = (\frac{\omega_{p,e}}{\omega_{c,e}})^2 k, \quad M_{60y} = (\frac{\omega_{p,e}}{\omega_{c,e}})^2\frac{\partial}{\partial x}, \quad N_{60n} = -\frac{\bar{\omega}_{c,e}\omega_{p,e}^2}{\omega_{c,e}^3}f', \quad S_{70x} = \frac{\partial}{\partial x},$$
$$S_{70y} = ik, \tag{6.78}$$

In the above formulation, the perturbation is assumed to be periodic in the $y-$direction. These equations represent a first step for the development of a numerical eigensolver to be used for the extension of tearing mode theory in the EMHD regime (so far performed only in the incompressible EMHD regime) and for the interpretation of and comparison with numerical results for kinetic studies of electron-only reconnection. However, building a numerical eigen solver to address this eigenvalue problem in its full generality will be very challenging, especially if one takes into account that the problem is a second-order eigenvalue problem. It is also interesting to notice that the highest degree of the growth rate (γ^2) is multiplied by d_e^4, which can take small values -for example, $d_e = 10^{-4} \implies d_e^4 = 10^{-16}$. This small values in turn, will lead to the formation of thin current layers. Therefore, in order to correctly resolve these narrow regions, we must take very small spatial steps, which in turns lead to issues related to ill-conditioning of finite-difference stencils (see section 4.1 for details).

6.3.7 Linear Analysis of the Full Pressure Tensor Equation without Strong Guide Field

Following exactly the same line of thoughts considered when calculating the components of perturbed pressure tensor when a strong guide field exists (see appendix H for detailed derivation), we obtain

$$\begin{aligned}\mathcal{P}_{xx}^1 = &\frac{1}{\gamma}\frac{f}{l_0}\Lambda_6 - \frac{2}{\bar{\omega}_{c,e}}\frac{f}{l_3}\Lambda_3 + \frac{1}{\gamma}\frac{l_4}{l_3}\Lambda_1 = -\frac{1}{\gamma}\frac{f}{l_0}\mathcal{P}_{zz}^0\frac{\partial u_{x1}}{\partial x} - \frac{1}{\gamma}\frac{f}{l_0}\frac{d\mathcal{P}_{zz}^0}{dx}u_{x1} - 3\frac{1}{\gamma}\frac{l_4}{l_3}\mathcal{P}_{xx}^0\frac{\partial u_{x1}}{\partial x}\\ &- \frac{1}{\gamma}\frac{l_4}{l_3}\frac{d\mathcal{P}_{xx}^0}{dx}u_{x1} - \frac{1}{\gamma}\frac{l_4}{l_3}\mathcal{P}_{xx}^0\frac{\partial u_{y1}}{\partial y} - \frac{1}{\gamma}\frac{f}{l_0}\mathcal{P}_{zz}^0\frac{\partial u_{y1}}{\partial y} + \frac{2}{\bar{\omega}_{c,e}}\frac{f}{l_3}\mathcal{P}_{xx}^0\frac{\partial u_{z1}}{\partial x} - \frac{2e}{m\bar{\omega}_{c,e}}\times\\ &\frac{f}{l_3}(\mathcal{P}_{zz}^0 - \mathcal{P}_{xx}^0)B_{y1},\end{aligned} \tag{6.79}$$

$$\mathcal{P}_{yy}^1 = -\frac{\mathcal{P}_{yy}^0}{\gamma}\frac{\partial u_{x1}}{\partial x} - \frac{1}{\gamma}\frac{d\mathcal{P}_{yy}^0}{dx}u_{x1} + \frac{3\mathcal{P}_{yy}^0}{\gamma}\frac{\partial u_{y1}}{\partial y}, \tag{6.80}$$

$$\mathcal{P}^1_{zz} = \frac{2}{\bar{\omega}_{c,e}}\frac{l_0}{l_3}\Lambda_3 - \frac{2}{\gamma}\frac{l_0^2}{l_3}\Lambda_1 = 3\frac{2}{\gamma}\frac{l_0^2}{l_3}\mathcal{P}^0_{xx}\frac{\partial u_{x1}}{\partial x} + \frac{2}{\gamma}\frac{l_0^2}{l_3}\frac{d\mathcal{P}^0_{xx}}{dx}u_{x1} + \frac{2}{\gamma}\frac{l_0^2}{l_3}\mathcal{P}^0_{xx}\frac{\partial u_{y1}}{\partial y} - \frac{2}{\bar{\omega}_{c,e}}\frac{l_0}{l_3}\mathcal{P}^0_{xx}\frac{\partial u_{z1}}{\partial x} + \frac{2e}{m\bar{\omega}_{c,e}}\frac{l_0}{l_3}(\mathcal{P}^0_{zz} - \mathcal{P}^0_{xx})B_{y1}, \tag{6.81}$$

$$\mathcal{P}^1_{xy} = \frac{1}{\bar{\omega}_{c,e}}\frac{f}{l_1}\Lambda_4 + \frac{\gamma}{\bar{\omega}^2_{c,e}}\frac{1}{l_1}\Lambda_2 = -\frac{\gamma}{\bar{\omega}^2_{c,e}}\frac{1}{l_1}\mathcal{P}^0_{yy}\frac{\partial u_{x1}}{\partial y} - \frac{\gamma}{\bar{\omega}^2_{c,e}}\frac{1}{l_1}\mathcal{P}^0_{xx}\frac{\partial u_{y1}}{\partial x} - \frac{1}{\bar{\omega}_{c,e}}\frac{f}{l_1}\mathcal{P}^0_{yy}\frac{\partial u_{z1}}{\partial y} + \frac{e}{m\bar{\omega}_{c,e}}\frac{f}{l_1}(\mathcal{P}^0_{yy} - \mathcal{P}^0_{zz})B_{x1} + \frac{e\gamma}{m\bar{\omega}^2_{c,e}}\frac{1}{l_1}(\mathcal{P}^0_{xx} - \mathcal{P}^0_{yy})B_{z1}, \tag{6.82}$$

$$\mathcal{P}^1_{xz} = \frac{1}{2\bar{\omega}_{c,e}}\frac{1}{l_0}\Lambda_6 - \frac{\gamma}{\bar{\omega}^2_{c,e}}\frac{1}{l_3}\Lambda_3 + \frac{1}{\bar{\omega}_{c,e}}\frac{l_0}{l_3}\Lambda_1 = -\frac{1}{2\bar{\omega}_{c,e}}\frac{1}{l_0}\mathcal{P}^0_{zz}\frac{\partial u_{x1}}{\partial x} - \frac{1}{2\bar{\omega}_{c,e}}\frac{1}{l_0}\frac{d\mathcal{P}^0_{zz}}{dx}u_{x1} - 3\frac{1}{\bar{\omega}_{c,e}}\frac{l_0}{l_3}\mathcal{P}^0_{xx}\frac{\partial u_{x1}}{\partial x} - \frac{1}{\bar{\omega}_{c,e}}\frac{l_0}{l_3}\frac{d\mathcal{P}^0_{xx}}{dx}u_{x1} - \frac{1}{\bar{\omega}_{c,e}}\frac{l_0}{l_3}\mathcal{P}^0_{xx}\frac{\partial u_{y1}}{\partial y} - \frac{1}{2\bar{\omega}_{c,e}}\frac{1}{l_0}\mathcal{P}^0_{zz}\frac{\partial u_{y1}}{\partial y} + \frac{\gamma}{\bar{\omega}^2_{c,e}}\frac{1}{l_3}\mathcal{P}^0_{xx}\frac{\partial u_{z1}}{\partial x} - \frac{e\gamma}{m\bar{\omega}^2_{c,e}}\frac{1}{l_3}(\mathcal{P}^0_{zz} - \mathcal{P}^0_{xx})B_{y1}, \tag{6.83}$$

$$\mathcal{P}^1_{yz} = \frac{\gamma}{\bar{\omega}^2_{c,e}l_1}\Lambda_4 - \frac{l_0}{\bar{\omega}_{c,e}l_1}\Lambda_2 = \frac{1}{\bar{\omega}_{c,e}}\frac{l_0}{l_1}\mathcal{P}^0_{yy}\frac{\partial u_{x1}}{\partial y} + \frac{1}{\bar{\omega}_{c,e}}\frac{l_0}{l_1}\mathcal{P}^0_{xx}\frac{\partial u_{y1}}{\partial x} - \frac{\gamma}{\bar{\omega}^2_{c,e}}\frac{1}{l_1}\mathcal{P}^0_{yy}\frac{\partial u_{z1}}{\partial y} + \frac{e\gamma}{m\bar{\omega}^2_{c,e}}\frac{1}{l_1}(\mathcal{P}^0_{yy} - \mathcal{P}^0_{zz})B_{x1} - \frac{e}{m\bar{\omega}_{c,e}}\frac{l_0}{l_1}(\mathcal{P}^0_{xx} - \mathcal{P}^0_{yy})B_{z1}, \tag{6.84}$$

Where,

$$l_0 = f - d_e^2 f'', \quad l_1 = \frac{\gamma^2}{\bar{\omega}^2_{c,e}} + l_0 f, \quad l_2 = \frac{\gamma^2}{\bar{\omega}^2_{c,e}} + 2l_0 f, \quad l_3 = l_2 + 2l_0 f, \quad l_4 = l_2 + 4l_0 f, \tag{6.85}$$

When looking at Eq.(6.85), it is clear that a new difficulty appears when trying to formulate the eigenvalue problem. This is due to the fact that l_1, l_2, l_3, l_4 depend on the growth rate, and also on x. If we do not neglect $\frac{\gamma^2}{\bar{\omega}^2_{c,e}}$ in Eq.(6.85), two consequences follow,

- Calculating the derivatives of the perturbed pressure tensor components become tedious and very challenging, even when ignoring this ratio.
- The eigenvalue problem will be of fifth order, which is larger than the case when a strong guide field exists ($2^d - order$).

Having in mind the aim of solving the previous system numerically, in order to overcome this issue, we suggest to first integrate the linear versions of Ampere and Faraday equations, and then to apply the numerical methods on the resulting system. Using this procedure, the integration with respect to x becomes an operator (integration stencil in the numerical method), which might make the problem a little bit less complicated. However, even with this procedure, many other problems remain. These issues include the degree of the eigenvalue problem, and the ill-conditioned finite-difference matrices resulting from the discretization of the problem.

7

Results of the Study of Tearing Modes in Thin Current Sheets

Contents

In this chapter, we discuss the stability of thin current sheets in different regimes, where we study, for each regime, the scaling laws of both the growth rate and the width of the reconnecting layer, and then we obtain the scalings of the fastest growing modes. The text of sections 7.1, 7.2, 7.3, 7.5, 7.6, 7.7, and 7.9 is the text, slightly adapted from a published article (Betar et al. (2020) [153]), while the text of sections 7.4 and 7.10 concerns a paper to be submitted and section 7.11 concerns a contribution to the JET-WPJET1 and JET1-2020-C39 EURfusion campaigns (see chapter 9).

7.1 Thin Current Sheets: Introduction

In this chapter, we discuss the stability of thin current sheets using the results of numerical simulations of the eigenvalue problem 5.76 in the cold ion limit. Thin current sheets can occur in laboratory plasmas, such as in the $m = 1$ mode in tokamaks [332], and in a variety of space

plasmas. They are also observed in numerical simulations of MHD turbulence [144]. They are characterized by large aspect ratios L/a ,with L being the length of the sheet and a its width, a background magnetic field B_0, and a sheet magnetic field B_{cs}, not necessarily of the same order as B_0. Thin current sheets generally possess a broad range of unstable modes, ranging from a minimum wavenumber k_{min} of order $1/L$ to a maximum wavenumber k_{max} of order $1/a$. The spectrum has usually a maximum at a wavenumber k_M such that $1/L \ll k_M \ll 1/a$. The maximum growth rate γ_M is important to assess the eventual fate of the current sheet in the context of an evolving plasma. The notion of the maximum growth rate, and the fastest mode have been discussed in section 1.4.

Although the growth rates and the properties of the eigenfunctions of tearing-type modes in different wavelength limits and different regimes had been already investigated in the past, mostly by means of boundary layer techniques, an exhaustive numerical survey of the validity of these estimates had not been performed before.

We have addressed this issue by using the multi-precision linear solver (Eigen Solver) that uses finite difference schemes with tunable precision on a non-uniform grid with double periodic boundary conditions, which has been discussed in detail in chapter 4. It must also be noted that integration of the linear problem in regimes where the non-ideal parameters are sufficiently small, so as to justify the application of the asymptotic matching techniques of the boundary layer theory, is challenging also from a computational point of view because one must resolve strong spatial gradients in intervals of the domain with thickness that scales as some positive power of the small non-ideal parameters (see chapter 4 for more details about the eigen solver).

We explicitly re-write the eigenvalue problem, given by Eqs.[5.70-5.73] for the cold-ion regime ($\rho_i = 0$) with vanishing equilibrium shear velocity ($\phi_0 = 0$),

$$\gamma\Big[1 - d_e^2\Big(\frac{\partial^2}{\partial x^2} - k^2\Big)\Big]\psi = k\rho_s^2\psi_0'\Big(\frac{\partial^2}{\partial x^2} - k^2\Big)\phi - kF_0'\phi + S^{-1}\Big(\frac{\partial^2}{\partial x^2} - k^2\Big)\psi, \tag{7.1}$$

$$\gamma\Big(\frac{\partial^2}{\partial x^2} - k^2\Big)\phi = k\Big[\psi_0'\Big(\frac{\partial^2}{\partial x^2} - k^2\Big) - \psi_0'''\Big]\psi + \Big[R^{-1}\Big(\frac{\partial^4}{\partial x^4} - 2k^2\frac{\partial^2}{\partial x^2} + k^4\Big)\Big]\phi, \tag{7.2}$$

An exact analytical solution to this general eigenvalue problem does not generally exist in a closed form, but approximated analytical solutions, using a boundary layer approach [154, 333] , can be obtained in the purely resistive constant-ψ regime [57] and internal kink [151, 150] regimes or in purely collisionless reconnection regimes [63, 82, 81]. Heuristic estimations, to be discussed later, can be sometimes used to evaluate the scalings of the growth rates and of the reconnecting layer width by relying on an appropriate balancing of the terms of Eqs.[7.1,7.2], without working out all the calculations of the asymptotic matching of the boundary layer approach. This kind of simplified analysis has been first applied to kinetic tearing equations [67]. Even in this case, however, the support of numerical calculations may be required, as for regimes in which finite Larmor radius effects are included. We are also going to show that the use of this analysis is more complex when more than one ideal parameters are taken into account.

A numerical approach to this eigenvalue problem is therefore useful to determine the scalings and eigenmode profiles in the different reconnection regimes. For this, one needs to resolve accurately the thin layer (hereafter named the "*inner layer*") around the reconnecting current sheet, where non-ideal `MHD` effects become important. We indicate with δ the thickness of such layer (see Fig.1.5).

To this purpose, we have developed an eigensolver for a slab periodic box of dimensions $[-L_x/2, L_x/2] \times [-L_y/2, L_y/2]$ that uses compact finite difference schemes of tunable precision

for the derivatives on a non-uniform grid along the x-direction (see section 4.1). The non-uniformity of the grid ensures the spatial resolution of the inner layer, where the grid spacing can be chosen to be much smaller than in the outer layer, where the non-ideal parameters can be neglected. While this guarantees a faster convergence of the solution of the eigenvalue problem, it also leads to ill-conditioned finite difference matrices when the non-uniformity is high and the non-ideal parameters take asymptotically small values. This is especially true for the eigenfunctions which converge much more slowly than the eigenvalues. It should be noted that this ill-conditioning is an unavoidable feature of the numerical solution, when finite-difference schemes are used to compute the derivatives inside the inner layer. We have solved this latter problem by developing a multi-precision algorithm that relies on the Advanpix Multiprecision Computing Toolbox for *MATLAB* [334] for arbitray machine precision calculations, and that solves the eigenvalue problem related to the finite difference scheme described above with a generalized Schur decomposition (or QZ decomposition) [335, 282].

Although different magnetic equilibrium profiles can be considered that are compatible with this choice, we focus here on "Grasso's equilibrium", first proposed in Ref.[336]:

$$\psi_0 = \frac{1}{2\cosh^2(x)}, \tag{7.3}$$

In Eqs[7.1, 7.2, 7.3], the quantities are normalized according to Eq.(5.43) where B_0 in this case is equal to the sheet magnetic field B_{cs}, the velocity here is Alfvén velocity given by $v_A = B_0/\sqrt{4\pi m_i n_0}$, and $L_0 = a$ is the width of the current sheet (see Fig.1.5).

Equilibrium (7.3), which has $k_{max}a = \sqrt{5}$, was introduced because at fixed k it provides comparably higher values of Δ' than, for example, the $\psi_0 = \cos(x/a)$ profile in an interval with $L_x = 2\pi$. In this sense it is particularly useful for the numerical modelling of large-Δ' modes, both for the linear (i.e. scaling analysis) and nonlinear dynamics. It must be noted that this equilibrium is periodic in x only in the formal limit $L_x/a \to \infty$. Therefore, the periodic conditions in x, required by the present version of the code (they can be in principle relaxed in the numerical scheme) are granted by taking a sufficiently large interval L_x. For example, for a choice $L_x = 4\pi a$, which is typical for numerical simulations of tearing modes in numerical boxes with aspect ratios of order of unity, $\psi_0(\pm 2\pi) \simeq 7 \times 10^{-6}$. The numerical error introduced in this way is shown to be negligible by the results presented later in this chapter. We note however that a slightly modified version of equilibrium (7.3) has been also considered in Ref.[337], where constant values have been added to the first terms of the Fourier expansion in x of ψ_0, in order to ameliorate the convergence of its numerical Fourier series in boxes with finite values of L_x/a.

This chapter will start by a discussion of the instability parameter Δ', which can be found solving the equations into the outer layer, governed by ideal MHD. Then, we give an example of the strength of the heuristic estimations in the purely resistive regime, and goes on to understand the difficulty of applying this approach in some other regimes. Next, we follow that with sections that discuss the different regimes, including the viscous-resistive regime, warm-resistive regime, warm-inertial regime, and inertial-resistive regime. Finally, we conclude the chapter with some new results in both `EMHD`, and warm-ion limit ($\rho_i \neq 0$).

7.2 Estimating the Instability parameter Δ'

As explained in section 1.3.1, this parameter can be calculated by solving the system of equations in the outer layer. Therefore, it only depends on the choice of the equilibrium, and the wavenumber. The definition of Δ' in term of the stream function reads,

$$\Delta' \equiv \lim_{\epsilon \to 0} \frac{\psi'_{out}(\epsilon) - \psi'_{out}(-\epsilon)}{\psi_{out}(0)}, \tag{7.4}$$

In the outer layer, the regime is governed by the ideal MHD (all the non-ideal parameter terms become negligible in Ohm law), therefore Eqs[5.61, 5.62], once linearized give

$$[\psi_{out}, \psi_0''] + [\psi_0, \nabla^2 \psi_{out}] = 0, \tag{7.5}$$

It is therefore obvious from the previous equation that $\Delta' = \Delta'(k, \psi_0)$. This differential equation can be solved for the chosen equilibrium. Then, Δ' is estimated using Eq.(7.4). Table 7.1 shows the formulae of Δ' for different equilibria and the corresponding references.

$\psi_0(x/a)$	$B_y^0(x/a) = -d\psi_0/dx$	Ref.	$\Delta'(ka)$	Ref.	$\lim_{ka\to 0} \Delta' \sim (ka)^{-p}$	p
$B_{cs} a \ln\lvert\cosh(x/a)\rvert$	$B_{cs}\tanh(x/a)$	[[156]]	$2\left(\frac{1}{ka} - ka\right)$	[[57]]	$\frac{2}{ka}$	1
$\begin{cases} 0 \quad \text{for} \quad x \le -a \\ B_{cs}(x/a) \quad \text{for} \quad -a < x \le a \\ 0 \quad \text{for} \quad x > a \end{cases}$	$\begin{cases} 0 \quad \text{for} \quad x \le -a \\ B_{cs} \quad \text{for} \quad -a < x \le a \\ 0 \quad \text{for} \quad x > a \end{cases}$	[[57]]	$2(ka)\left(\frac{(1-ka) - ka\tanh(ka)}{ka - (1-ka)\tanh(ka)}\right)$	[[57]]	$\frac{2}{ka}$	1
$B_{cs} a \cos(x/a)$	$B_{cs}\sin(x/a)$	[[58]]	$2\sqrt{1-(ka)^2}\tan\left(\frac{\pi}{2}\sqrt{1-(ka)^2}\right)$	[[152]]	$\frac{8}{\pi(ka)^2}$	2
$\frac{B_{cs} a}{2\cosh^2(x/a)}$	$B_{cs}\frac{\tanh(x/a)}{\cosh^2(x/a)}$	[[336]]	$2\left(\frac{-(ka)^4 + 2(ka)^2 + 15}{(ka)^2\sqrt{4+(ka)^2}}\right)$	[[336]]	$\frac{15}{(ka)^2}$	2

Table 7.1: : Equilibrium profiles and related expression of $\Delta'(ka)$ (both with a bibliographical reference about where the former had been first used for tearing mode analysis and about where a formula for the second has been provided), and corresponding scaling of $\Delta'(ka)$ with respect to ka for $ka \ll 1$. In this table, dimensional units have been reintroduced. Notice that k is dimensional in the table.

In the presence of a continuum spectrum of wavenumbers, the large wavelength limit $k \to 0$ and the small wavelength limit $k \to k_{max}$ of the dispersion relation respectively correspond to the large-Δ' ($\Delta'\delta \gg 1$) or internal-kink regime [151, 150] or to the small-Δ' or constant-ψ regime ($\Delta'\delta \ll 1$) [57], where δ is the width of the reconnecting layer. These regions are shown in Fig. 7.1.

The main goal of this chapter is to find the scaling laws for the growth rate and width of the reconnecting modes in large-, small-Δ' limits (hereafter, LD, and SD, respectively), and of the fastest growing mode. However, even if a general procedure has been suggested to estimate the scaling of the fastest mode in collisionless, purely resistive, and viscous-resistive regimes in Refs.[24, 164] by equating $\gamma_{SD}(k_M) = \gamma_{LD}(k_M)$ and assuming $\Delta'(k) \sim k^{-p}$, for $k \ll 1$, the dependence of the fastest mode on the magnetic equilibrium profile invokes the importance of using the numerical approach.

As discussed in section 1.4, the scaling of the fastest growing mode was already addressed in a series of papers by Cross and Van Hoven [58, 59, 60, 61] that were mainly focused on applications to astrophysical plasmas. In these papers the typical aspect ratio of the current sheet is taken to be very large, so the approximation $L/a \to \infty$ can be adopted. A paradigmatic example, already considered by Dungey in his first formalization of the notion of reconnection [26, 338], is provided by the terrestrial magnetotail. Its instability to reconnecting modes in a continuous

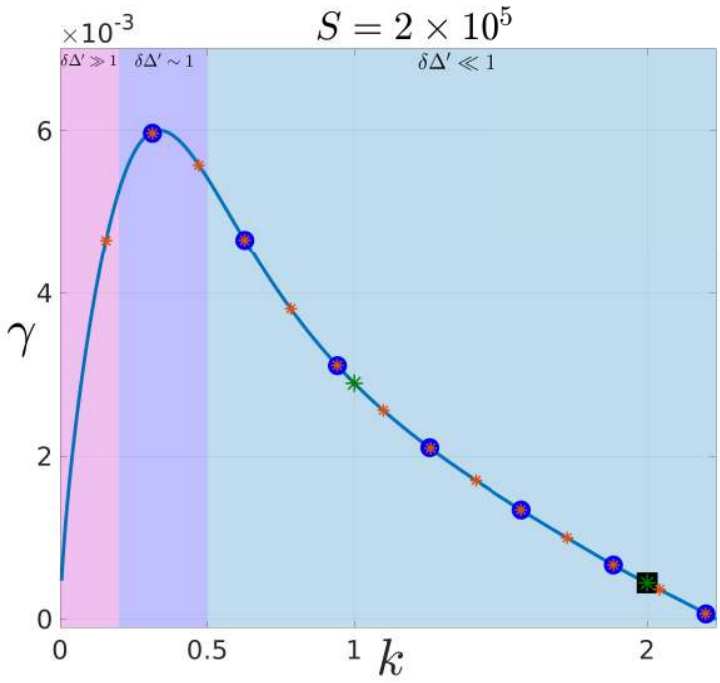

Figure 7.1: The continuous line shows the dependence of γ on k in the continuous interval $[0, k_{max}a]$, for tearing modes due resistivity ($S^{-1} = 5\times10^{-6}$). Dots, stars and squares correspond instead to the discrete modes that can be destabilized when $L/a = \pi$ (black square), 2π (green star), 20 (blue dots), 40 (red stars) respectively, the largest oscillation number corresponding to $\lfloor k_{mg}L/(2\pi) \rceil$, where "$\lfloor ... \rceil$" means "integer part of". Here $k_{max}a = \sqrt{5}$ is fixed by the equilibrium profile (7.3), whereas, for comparison, $k_{max}a = 1$ in the case of Harris' pinch equilibrium [156].

spectrum of wavelengths has been addressed in a kinetic framework in Ref. [66], and then, by considering resistive slab tearing modes, in Refs.[339, 59]. Other astrophysical applications of tearing theory to large aspect ratio current sheets have been then considered for coronal mass ejections (see Refs. [340, 142, 157, 341]), whose occurrence close to neutral magnetic points noted by Giovanelli [20] had indeed motivated Hoyle [25] and Dungey [26, 338] to explore and formalize the mechanism that would have been later dubbed "*magnetic reconnection*[19]" (see the general introduction of this dissertation for a brief review of the history of the subject). In particular, as noted by Velli and Hood[157], an aspect ratio of the order of $L/a \sim 20$ is typically sufficient to allow the instability of mode with a wavenumber close enough to that of the fastest growing mode as computed by considering a continuous spectrum. This is clearly shown in Fig. 7.1. In the numerical results that follow, however, the fastest mode has been identified by selecting, for each fixed couple of non-ideal parameters at play, the wave number which displayed the maximum growth rate after a scan over about 40 modes in the $(0, \sqrt{5})$ interval of the (normalized) k variable.

7.3 Example on the Heuristic Estimation of the Scaling Law for Purely Resistive Regime

Heuristic estimation combines the boundary layer approach with some ansatz about the ordering of terms in the linearized equations. This way, we avoid solving the equations using the asymptotic matching expansion methods. Nevertheless, in some regimes, such as warm-inertial, warm-resistive, and EMHD regimes, it is not possible to use such a technique (we are going to discuss this in the next section). Hence, the numerical analysis becomes necessary when attempting to verify the known analytical scaling laws or to explore new regimes. For illustrative purposes, let us now proceed by considering for simplicity the case of the purely resistive tearing. In this case, Eqs [7.1, 7.2] become

$$\gamma\psi = -k\psi_0'\phi + S^{-1}\psi'' - k^2\psi, \tag{7.6}$$

$$\gamma\phi'' - \gamma k^2\phi = k\psi_0'\psi'' - k^3\psi - \psi_0'''\psi, \tag{7.7}$$

When we consider the solution of Eqs.(7.6-7.7) at a distance from the neutral line of the order of the reconnecting layer width δ, we can neglect k^2 with respect to the second order derivative in x of the perturbed quantities. We can also approximate $\psi_0'|_{x\simeq\delta} \sim \delta\psi_0''|_{x\simeq\delta}$ and neglect the ψ_0''' term. By ordering $\psi_1''/\psi_1 \sim 1/\delta^2$ for the large limit, we then obtain the two time scales

$$\gamma \sim \frac{S^{-1}}{\delta^2}, \quad \frac{\psi}{\phi} \sim \frac{k\delta}{\gamma}, \quad \text{and} \quad \gamma \sim k\delta, \tag{7.8}$$

The first time scale is the resistive diffusion time along x over the scale δ, while the last one is essentially the shear-Alfvén wave dispersion relation at the scale $x \sim \delta$. It is related to the *natural* time scale τ_0 and it does not depend explicitly on the current sheet width a nor on the characteristic system length L (when restoring the dimensions, it becomes $\gamma\tau_0 \sim \hat{k}\hat{\delta}$, where $\hat{k} = k/a$, $\hat{\delta} = \delta a$). The above estimate is valid in the large Δ' limit, that is, as long as $\Delta'\delta \gg 1$. The second term results from balancing the $\gamma\psi$ term with $k\psi_0'\phi$.
In the small-Δ' limit, one must assume $\psi_1'/\psi_1 \sim \Delta'$ and $\psi_1''/\psi_1 \sim \Delta'/\delta$. One then has, following the same procedure, the two conditions

$$\gamma \sim k\delta(\Delta'\delta)^{1/2} \qquad \text{and} \qquad \gamma \sim \frac{S^{-1}\Delta'}{\delta}, \tag{7.9}$$

We have thus heuristically obtained the following scalings in the large- (label "LD") and in the small-Δ' (label "SD") limits, respectively:

$$\gamma_{LD} \sim k\delta_{LD}, \qquad \delta_{LD} \sim (kS)^{-1/3} \tag{7.10}$$

$$\gamma_{SD} \sim k\delta_{SD}(\Delta'\delta_{SD})^{1/2}, \qquad \delta_{SD} \sim (kS)^{-2/5}\,\Delta'^{1/5} \tag{7.11}$$

Scalings (7.10-7.11) then define the two ranges of the spectrum of unstable modes which meet at a wavenumber such that $\delta_{LD} \sim \delta_{SD} \sim \Delta'^{-1}$. This situation is illustrated in Fig. 7.1, where the dependence of γ is represented with respect both to a continuum spectrum and to a discrete spectrum in k, the latter for different values of L/a. One observes that the wavenumber at which the two ranges meet corresponds to the most unstable mode if L/a is sufficiently large. Eventhough this simple procedure allows us to recover the well-known scalings in the purely resistive regime [57, 59, 151], it sometimes does not work when attempting to find the scaling laws in other regimes, such as the large-Δ' limit of the warm-inertial regime [85] or in the collisionless `EMHD` regime [93].

7.4 Heuristic Estimation: A Missing Characteristic Length

To present the difficulty encountered when trying to apply the heuristic approach to other regimes, we consider here the warm-collisionless regime. In this section, we will attempt to employ the method we have used in the previous section to obtain the scaling laws of the warm-collisionless case. We are going to see that taking $\psi''/\psi \sim 1/\delta^2$ in the large wavelength limit won't allow us to recover the scaling laws since we did not account for the additional complexity imposed by the inclusion of more than one non-ideal parameter into the problem.

In the warm-collisionless regime, Eqs [7.1, 7.2] become

$$\gamma\psi - \gamma d_e^2\psi'' = k\rho_s^2\psi_0'\phi'' - k^3\rho_s^2\psi_0'\phi - k\psi_0'\phi, \tag{7.12}$$

$$\gamma\phi'' - \gamma k^2\phi = k\psi_0'\psi'' - k^3\psi - \psi_0'''\psi, \tag{7.13}$$

We again consider the solution of the previous system, composed of Eq.(7.12) and Eq.(7.13), in the inner reconnecting layer. In this region, we can neglect the terms proportional to k^2, and approximate the derivative of the equilibrium magnetic stream function as $\psi_0'|_{x\simeq\delta} \sim \delta\psi_0''|_{x\simeq\delta}$, and we neglect the ψ_0'''. Then, the previous equations read

$$\gamma\psi - \gamma d_e^2\psi'' = k\rho_s^2\delta\phi'' - k\delta\phi, \tag{7.14}$$

$$\gamma\phi'' = k\delta\psi'', \tag{7.15}$$

When we derive the scaling laws using the heuristic estimation, as we have done in the purely resistive regime in the previous section, we assume the following relations

$$\frac{\psi''}{\psi} \sim \frac{1}{\delta^2} \quad \text{for} \quad \Delta'\delta \gg 1, \qquad \frac{\psi''}{\psi} \sim \frac{\Delta'}{\delta} \quad \text{for} \quad \Delta'\delta \ll 1. \tag{7.16}$$

Neglecting the signs, Eq.(7.15) gives

$$\phi'' = \frac{k\delta}{\gamma}\psi'', \tag{7.17}$$

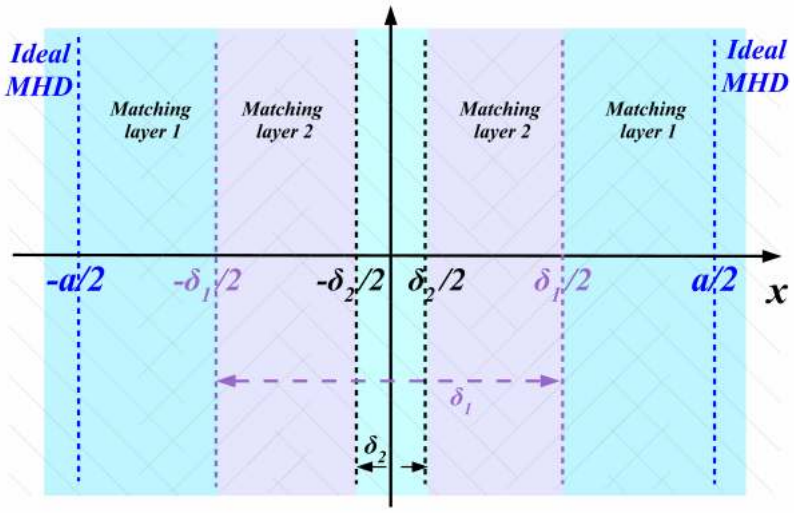

Figure 7.2: Sketch of the boundary layer decomposition when two boundary layers are required (e.g., case of the warm collisionless RMHD). The reconnecting layer width, δ, is not defined a priori since it can differ from δ_1 and δ_2.

While balancing the current density term on the LHS of Eq.(7.14) with the first term on the RHS of the same equation gives

$$\phi'' = \frac{\gamma d_e^2}{k\rho_s^2 \delta}\psi''. \tag{7.18}$$

Substituting Eq.(7.18) in Eq.(7.17), one finds

$$\gamma \sim k\delta \frac{\rho_s}{d_e} \tag{7.19}$$

The previous equation alone is not sufficient to obtain the scaling laws of γ and δ. Therefore, we need an additional equation to close the system. The first thing that comes to mind is to rely on the same method used in the previous section. Hence, we depend on the definitions given by Eq.(7.16), and balancing different terms in Eq.(7.14) and Eq.(7.15) to find the required relation to close the system. However, while this procedure perfectly works for the small wavelength limit (or tearing modes: $\Delta'\delta \ll 1$), no combinations between different terms in the equations allow us to recover the scaling laws of the large wavelength limit ($\Delta'\delta \gg 1$; this is also true for the large wavelength limit in the collisionless EMHD regime). In these cases, the problem is due to the presence of at least two boundary layers and therefore of two matching regions (see Fig.7.2), whose characteristic widths (δ_1 and δ_2), depend on the spatial scales of the problem in a non-trivial way. Moreover the notion of "reconnection layer width", which we can keep on naming δ, in this case can not be a priori related to the width of one of the boundary layers.

One important observation can be made regarding Eq.(7.16): the characteristic length l related to the first derivative of the magnetic function via $\psi' \sim \psi/l$ is always determined by the larger value between δ and $(\Delta')^{-1}$. Therefore, instead of the definition given by Eq.(7.16), we suggest a more general definition that incorporates the new characteristic length l,

$$\psi' \sim \frac{\psi}{l}, \qquad \psi'' \sim \frac{\psi'}{\delta} \sim \frac{\psi}{\delta l}, \tag{7.20}$$

Here l is not limited to be either $(\Delta')^{-1}$ or δ. It can be another characteristic length hidden in the problem. Our numerical analysis shows that in both collisionless RMHD and EMHD and a

quite extended interval spanning at least the inner region and part of the matching region, it is generally valid that $\psi \sim d_e^2 \psi''$. This relation can be intuitively understood in the context of the conversion of magnetic energy into kinetic energy due to the reconnection: $\gamma\psi$ term represents the breaking and reconnecting of the field lines (releasing the magnetic energy). In contrast, $\gamma d_e^2 \psi''$ presents the growth of the current density due to the reconnection event inside the inner layer (i.e., kinetic energy growth). Hence, $\psi \sim d_e^2 \psi''$ with Eq.(7.20) give

$$\delta \sim \frac{d_e^2}{l}. \tag{7.21}$$

The previous discussion of the characteristic length l suggests that it can take the value of another parameter involved in the problem (not just δ or $(\Delta)^{'-1}$). However, since our problem includes two eigenfunctions, ψ and ϕ, whose characteristic length related to their second derivatives is the width of the reconnecting layer (δ), and since $\Delta^{'}$ is the instability parameter determined by the magnetic configuration in the ideal-MHD outer layer, we anticipate a further characteristic length whose inverse we name $\Delta_v^{'}$, because of its definition which we give in analogy with the usual $\Delta^{'}$. We so define the logarithmic jump of the derivative of the fluid velocity component parallel to the neutral line:

$$\Delta_v^{'} \equiv \lim_{\epsilon \to 0} \frac{v'_{y,out}(\epsilon) - v'_{y,out}(-\epsilon)}{v_{y,out}(0)}. \tag{7.22}$$

This definition of $\Delta_v^{'}$ is applied to both RMHD and EMHD regimes. In RMHD regime, it becomes

$$\Delta_v^{'} = \Delta_\phi^{'} \equiv \lim_{\epsilon \to 0} \frac{\phi''_{out}(\epsilon) - \phi''_{out}(-\epsilon)}{\phi'_{out}(0)} \tag{7.23}$$

where the outflow velocity along the neutral line is $v_y = \phi^{'}$ (see chapter 5 for a detailed study of RMHD regime). Therefore, this discussion suggests the following definition of the characteristic length l

$$l = max\{(\Delta')^{-1},\ (\Delta_\phi)^{-1},\ \delta\}, \tag{7.24}$$

We mentioned above that taking l to be either δ or $(\Delta^{'})^{-1}$ does not lead to the correct scaling laws obtained by boundary layer approach in the large wavelength limit.

Since the heuristic derivation did not lead to the correct scalings when we choose only between two characteristic lengths (δ and $(\Delta)^{'-1}$), we expect that the largest characteristic length in the problem can be $l = (\Delta_\phi^{'})^{-1}$. Therefore, substituting this value for l in Eq.(7.21), and then substituting the resulting relation in Eq.(7.19), one finds

$$\gamma \sim k \Delta_\phi^{'} \rho_s d_e \tag{7.25}$$

It is interesting to notice that this scaling law for the large wavelength limit of the warm-collisionless regime is identical to the scaling law of the small wavelength limit of the same regime, except that we replace $\Delta^{'}$ with $\Delta_\phi^{'}$ (see table 7.2, or section 7.7). However, as shown in table 7.2, the scaling law, obtained by boundary layer approach, is given by $\gamma \sim k \rho_s^{2/3} d_e^{1/3}$. Therefore, the question that arises: *does the dependence of $\Delta_\phi^{'}$ on d_e and ρ_s, if exists, leads to this scaling?* That is, we must prove that the scalings of δ and $\Delta_\phi^{'}$, obtained by the numerical solver, must lead to the same results of γ, obtained by both Eq.(7.19) and Eq.(7.25). This growth rate, in turn, should also coincide with its scaling given in table 7.2.

Before going on to answer this question, we first discuss the method by which the numerical solver calculates $\Delta^{'}$, and $\Delta_\phi^{'}$, then we provide an operational definition of the reconnecting layer width δ. Finally, we go back to answer the question.

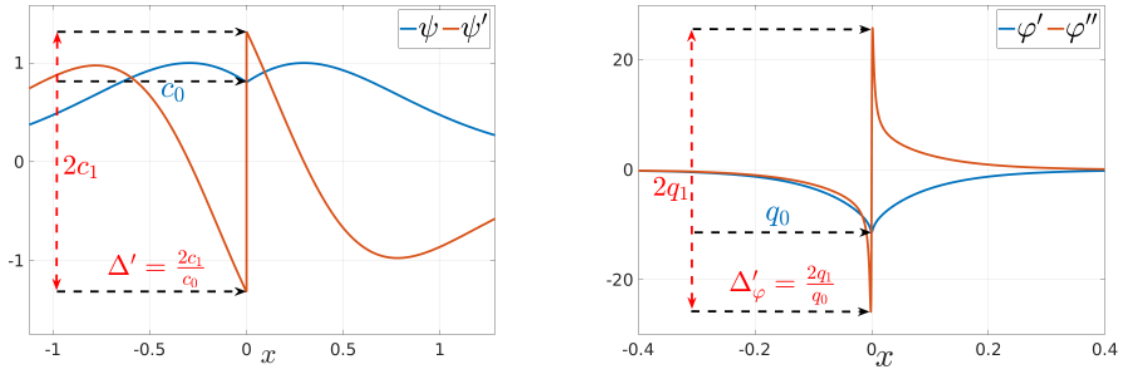

Figure 7.3: Left frame: Example of numerical evaluation of the coefficients c_0 and c_1 of Eq.(7.26), once the profile of $\psi(x)$ and of its derivative $\psi^{'}(x)$ have been computed. In practice, an accurate evaluation of the ψ_{out} part of the eigenfunction $\psi(x)$ is sufficient, even though this procedure results to be appropriate only when a single boundary layer exists. Right frame: analogous example of evaluation of q_0 and q_1 of Eq.(7.26) from $\phi^{'}$ and $\phi^{''}$, once the eigenfunction ϕ has been computed.

7.4.1 Numerical Estimation of $\Delta^{'}$ and $\Delta^{'}_{v}$

It must be noted that the numerical evaluation of both $\Delta^{'}$ and $\Delta^{'}_{v}$ according to their definitions is made possible by the geometrical interpretation that can be given of the instability parameter in terms of a local expansion of the outer solution as $x \to 0$. Since we can write $\psi_{out} \sim c_0 + c_1|x|$ and $v_{y,out}(x)|_{x\to 0} = \phi^{'}_{out}(x)|_{x\to 0} \sim q_0 + q_1|x|$, once the eigenfunctions have been computed we can calculate (cf. Fig.7.3)

$$\Delta^{'} \equiv 2\frac{c_1}{c_0}, \qquad \Delta^{'}_{v} \equiv 2\frac{q_1}{q_0}. \tag{7.26}$$

The definitions, given by Eq.(7.26), are formally correct and in agreement with definitions Eq.(7.4) and Eq.(7.22) also in the large wavelength regime, when analytical expressions of $\Delta^{'}$ that depend only on the outer eigenmode solutions loose of validity. Fig.7.3 shows an example of the numerical estimation of $\Delta^{'}$ and $\Delta^{'}_{\phi}$.

7.4.2 Operational Definition of the Reconnecting Layer Width δ

The reconnecting layer can be identified as the region around the neutral line in which the current density related to the perturbation is concentrated. In our notation this current density is $J_z = -\nabla^2\psi$. Inside of this region a velocity field is also concentrated, corresponding to an outflow parallel to the neutral line outwardly directed from the X-point, which is a hyperbolic point of the flow (that is $v_y = \phi^{'}$ in RMHD and $v_y = -b^{'}$ in EMHD).

In previous works which dealt with nonlinear simulation results, the characteristic width of such a current sheet or of the reconnecting layer itself has been identified in terms of the global profile of the eigenmode superposed to the equilibrium function: e.g., by looking at the distance between the local minima of $J_z(x) + J_{z,0}(x, y0)$ (Ali et al. (2014) [342]), or of the local minima of what we would here name $B_x(x, y_0) \sim \psi(x)cos(k(y - y_0))$ (Tenerani et al. (2015) [343]), with y_0 corresponding to the ordinate of the X-point. In the nonlinear simulations of Papini et al. (2019b) [344], the full width at half maximum of the total current $J_{t,z}$ minus the background one (i.e., the width at half height of an estimation of J_z) has been taken as the reference value for δ.

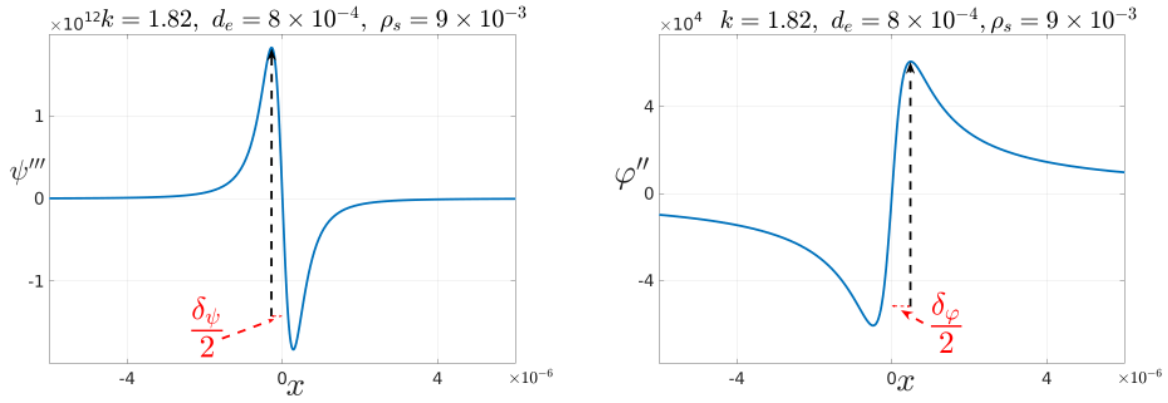

Figure 7.4: Examples of evaluation of half-width of the current layer as the distance of the inflection point of $\psi^{''}$ (left) and $\phi^{'}$ (right) from the neutral line.

Here, instead, by making reference to the eigenfunctions only, the ansatz we heuristically assume (and which we will a posteriori show to be coherent with other assumptions) is to identify δ as follows

δ is the twice the distance from the neutral line of the inflection point of J_z or of v_y.

This clearly corresponds to the distance from the neutral line of the local maxima (or minima) of the gradient of the current density ($J_z^{'}$) and of the vorticity $\phi^{''}$. Since these two distances can in principle differ, we respectively name them δ_ψ and δ_ϕ:

$$\delta_\psi : J_z^{''}\Big|_{x=\delta_\psi} = \psi^{IV}\Big|_{x=\delta_\psi} = 0, \qquad \delta_\phi : v_y^{''}\Big|_{x=\delta_\psi} = \psi^{'''}\Big|_{x=\delta_\phi} = 0. \tag{7.27}$$

As shown in Fig.7.4, these values can be easily calculated once the profiles of the corresponding eigenfunctions have been computed. In the whole parameter range we have scanned with the numerical eigensolver, we have verified that δ_ψ and δ_ψ display the same asymptotic scaling. We can so write $\delta_\psi \sim \delta_\phi$, even if a proportionality factor not much different from unity can be present (for example we measured $\delta_\phi = 2\delta_\psi$ in for the case presented in Fig.7.4).

7.4.3 Scaling Law of the Large Wavelength Limit in Warm-Collisionless Regime: Collecting all the Ingredients

We are now in a position allowing us to answer the question whether Eq.(7.19) and Eq.(7.25) leads to the same scaling law of γ, and therefore confirming the definition of the characteristic length l, given by Eq.(7.24). To do so, we perform several numerical simulations using a multi-precision resolution in order to resolve the inner layer. Fig.7.5 shows the results of two sets of numerical simulations (each set lasted for ~ 36 hours). On the left frame, we plot the dependence of the characteristic lengths $(\Delta^{'}_{num})^{-1}$ (blue color; it is the equivalent to $\Delta^{'}$ only in the small wavelength limit and numerically estimated with Eq.(7.4)), $(\Delta^{'}_{\phi})^{-1}$ (orange color), and δ (black color), as function of the skin depth. As shown in this frame the largest characteristic length is $(\Delta^{'}_{\phi})^{-1}$ which scales as $d_e^{2/3}$. On the right frame, we show these characteristic lengths as function of ρ_s. We again observe that $(\Delta^{'}_{\phi})^{-1}$ is the largest one and scales as $\rho_s^{1/3}$. Therefore according to Eq.(7.24), one finds

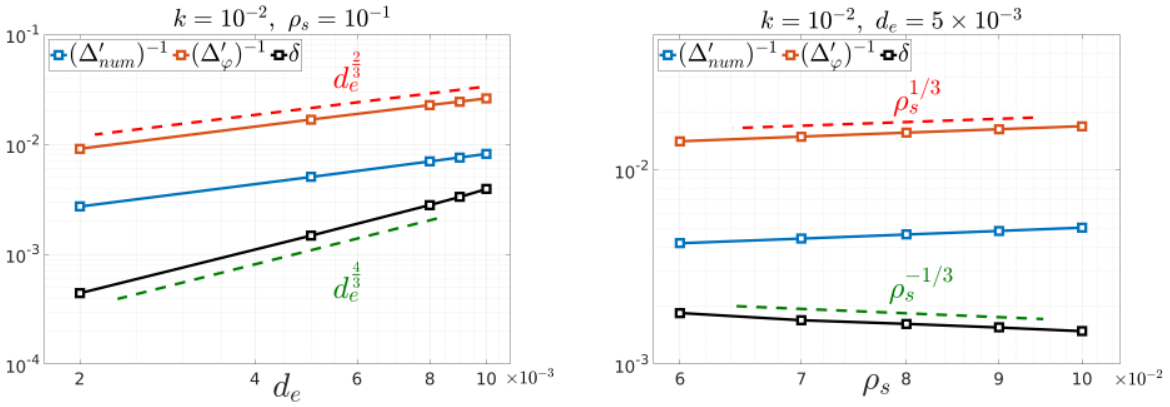

Figure 7.5: Scalings of $(\Delta'_{num})^{-1}$ (blue color), $(\Delta'_{\phi})^{-1}$ (orange color), and δ (black color) as function of the electron skin depth d_e on the left frame, and of the ion-sound Larmor radius ρ_s on the right frame.

$$l = (\Delta'_{\phi})^{-1} \sim d_e^{\frac{2}{3}} \rho_s^{\frac{1}{3}}, \tag{7.28}$$

It is also shown in Fig.7.5 that the scaling of the width of the inner layer δ is

$$\delta \sim d_e^{4/3} \rho_s^{-\frac{1}{3}}, \tag{7.29}$$

By either substituting Eq.(7.29) into Eq.(7.19), or Eq.(7.28) into Eq.(7.25), we obtain

$$\gamma \sim k \rho_s^{\frac{2}{3}} d_e^{\frac{1}{3}}, \tag{7.30}$$

which is identical to its scaling obtained by boundary layer approach (see table 7.2). Therefore, we conclude that it is the dependence on the definition given by Eq.(7.16), the absence of a third characteristic length and of the numerical simulations that made the heuristic estimation fail in recovering the known scalings. However, we can write identical formulae for the scaling laws of γ and δ in both large wavelength, and small wavelength limits, by only replacing Δ' in the latter with Δ'_{ϕ} defined by Eq.(7.23) in order to obtain the scaling of the large wavelength limit.

Hence, for $\Delta' \delta \ll 1$, we write

$$\gamma \sim k \Delta' \rho_s d_e, \qquad \delta \sim \Delta' d_e^2 \tag{7.31}$$

while for $\Delta' \delta \gg 1$, we have

$$\gamma \sim k \Delta'_{\phi} \rho_s d_e, \qquad \delta \sim \Delta'_{\phi} d_e^2 \tag{7.32}$$

where Δ'_{ϕ} is given by Eq.(7.28).

7.5 Viscous-Resistive Regime (S^{-1}, R^{-1})

We here identify as "viscous-resistive" the regime in which we can set $d_e = \rho_s = 0$ in Eqs.(7.1-7.2). Although linear tearing modes in this regime have been already extensively studied in literature (see Refs. [345, 346, 347, 348, 343]), they are considered here for two reasons. The first one is that previous studies in this regime chose different equilibria than (7.3). The second one is that comparison with previous results which do not depend on the choice of the equilibrium profile

(notably the results in the constant-ψ, or small-Δ' limit) provides a benchmark test for the newly developed eigensolver.

We have recovered the well known scaling laws both in the *purely resistive* [57, 59, 151] regime,

$$\gamma_{LD} \sim k^{2/3} S^{-1/3}, \qquad \delta_{LD} \sim k^{-1/3} S^{-1/3}, \tag{7.33}$$

$$\gamma_{SD} \sim k^{2/5} \Delta'^{4/5} S^{-3/5}, \qquad \delta_{SD} \sim k^{-2/5} \Delta'^{1/5} S^{-2/5}, \tag{7.34}$$

and in the *viscous-resistive* regime [345],

$$\gamma_{LD} \sim k^{2/3} R^{1/3} S^{-2/3}, \qquad \delta_{LD} \sim k^{-1/3} R^{-1/6} S^{-1/6}, \tag{7.35}$$

$$\gamma_{SD} \sim k^{1/3} \Delta' R^{1/6} S^{-5/6}, \qquad \delta_{SD} \sim k^{-1/3} R^{-1/6} S^{-1/6} \tag{7.36}$$

Note that the reconnecting layer width in the viscous-resistive regime has the same scaling in both the large- and small-Δ' limit (Eqs.(7.35-7.36). Scalings (7.33-7.34) correspond to (7.10) and (7.11), respectively.

These benchmark results are shown in the right frames of Fig. 7.6. For the growth rates, these scalings had been already numerically verified in the past, for example in Refs. [346, 347, 348], although with a different magnetic equilibrium (which does not affect these results). It is however in the more recent work by Tenerani et al.[343] that a more extensive numerical study has been performed, also for the scaling of the reconnecting layer width and in all wave-length limits of the slab dispersion relation, with a different eigensolver than the one used here.

The scalings (7.33-7.36) can be estimated by means of the heuristic-type argument outlined in section 7.3. A relation is obtained by balancing the dominant terms of Eq.(7.2), which, by assuming $\phi^{(N)} \sim \phi/\delta^N$ (with $^{(N)}$ expressing the N^{th}-order derivative with respect to x), we write as $\gamma\phi/\delta^2 \sim k\delta\psi'' + R^{-1}\phi/\delta^4$. Using the latter and the estimates obtained from (7.1) so to eliminate ϕ and ψ'' in terms of ψ we get the qualitative expression:

$$\gamma \sim R^{-1}\delta^{-2} - k^2\delta^4 S. \tag{7.37}$$

Combination of (7.37) with the relations obtained from Ohm's law (second relation of 7.8 and 7.9) yelds two polynomial relations for γ (or δ), whose solution gives the sought scalings. Eqs.(7.35-7.36) are obtained by assuming the R^{-1}-related terms to be dominant, which, by developing the algebra, is seen to correspond to $R^{-1} \gg S^{-1}$ for $\Delta'\delta_{LD} \gg 1$ and to $\gamma \sim (S^{-1}\Delta'/\delta_{SD} \ll R^{-1}\delta_{SD}^{-2})$ for $\Delta'\delta_{SD} \ll 1$ (see [349, 350] for detailed estimations for different regimes using heuristic approach).

A further scaling which is of physical interest in a large aspect ratio current sheet, is that of the mode with the highest growth rate [57]. The scalings of this mode occurring at $\Delta'\delta \sim 1$ do depend on the choice of the equilibrium profile [24], as it had been already numerically found by Cross and Van Hoven [58]. Previous studies of this mode in the viscous-resistive regime have focussed [343] on a Harris-pinch equilibrium [156]. In Ref. [24], however, general formulae for the maximum growth rate for a general equilibrium profile have been proposed for the collisionless, purely resistive and viscous-resistive regimes (see Eqs.23-25 therein): these scalings can be estimated by equating $\gamma_{SD}(k_M) = \gamma_{LD}(k_M) = \gamma_M$, while assuming $\Delta'(k) \sim k^{-p}$ for $k \ll 1$. These formulae agree with the results obtained for a Harris-pinch profile[57, ?, 343] (case $p = 1$), and they have been verified also for equilibrium (7.3), indirectly in the warm collisionless case in Ref. [24] (by comparison with previous results by Comisso et al [158]), and directly with another numerical solver in the purely resistive, inviscid regime, in Ref. [164]. For convenience we rewrite here these general scalings for the fastest growing mode $\Delta'\delta \sim 1$ by

including also the corresponding estimates for k_M and δ_M (they can be then easily rewritten in terms of Prandtl number $P \equiv \nu/\eta = S/R$):

$$\text{Viscous-Resistive regime } (P \gg 1) \text{ for } \lim_{k\to 0} \Delta' \sim k^{-p} \qquad \begin{cases} \gamma_M \sim R^{\frac{p}{1+3p}} S^{-\frac{1+2p}{1+3p}} \\ k_M \sim \left(R^{-1/2} S^{-1/2}\right)^{\frac{1}{1+3p}} \\ \delta_M \sim \left(R^{-1/2} S^{-1/2}\right)^{\frac{p}{1+3p}} \end{cases} \tag{7.38}$$

$$\text{Resistive regime } (P \ll 1) \text{ for } \lim_{k\to 0} \Delta' \sim k^{-p} \qquad \begin{cases} \gamma_M \sim S^{-\frac{1+p}{1+3p}} \\ k_M \sim S^{-\frac{1}{1+3p}} \\ \delta_M \sim S^{-\frac{p}{1+3p}} \end{cases} \tag{7.39}$$

In the left and center frames of Fig. 7.6, we have plotted the scalings of γ_M and k_M, with respect to Reynolds's and Lundquist's numbers, that we have numerically obtained by solving the eigenvalue problem for equilibrium (7.3). The complete set of numerical results is summarized by:

$$\text{Viscous-Resistive regime } (P \gg 1) \quad \begin{cases} \gamma_M \sim R^{2/7} S^{-5/7} \\ k_M \sim R^{-1/14} S^{-1/14} \\ \delta_M \sim R^{-1/7} S^{-1/7} \end{cases} \quad , \quad \text{Resistive regime } (P \ll 1) \quad \begin{cases} \gamma_M \sim S^{-3/7} \\ k_M \sim S^{-1/7} \\ \delta_M \sim S^{-2/7} \end{cases} \tag{7.40}$$

Eq.(7.40) corresponds to the analytical estimations (7.38-7.39) after the substitution $p = 2$, valid for equilibrium (7.3). The transition to a purely resistive regime in which the effects of viscosity become negligible is qualitatively in agreement with that obtained in Ref. [343] for a Harris equilibrium, and the scalings for γ_M and k_M of (7.40) coincide with those already verified in Ref. [164].

Two distinct regions are visible in Fig. 7.6. The first one is for $R \leq S$ (see, e.g., the yellow line in the top frames of Fig. 7.6 for $R \leq S = 10^6$). This region represents the visco-resistive case, and its scalings confirm those at left of Eq.7.40. The second region is for $R \geq S$ (see, e.g., the yellow line of Fig. 7.6 for $R > S = 10^6$) and corresponds to a purely resistive limit in which viscosity negligibly contributes. Its scalings are given by those at the right of Eq.7.40. A transition region between these two limit regimes is also visible. This region is characterized by a reversal of the slope in the scaling of k_M with R^{-1} –see the top-center frame of Fig. 7.6, where a relative minimum of $k_M(R^{-1})$ is clearly visible. No power law scaling has been measured here.

The growth rates of the fastest mode in both viscous-resistive and purely resistive regimes for equilibrium (7.3) can be compared by re-writing their ratio in terms of the Prandtl number: $\gamma_{M_S} \sim P^{2/7} \gamma_{M_{S,R}}$, where $\gamma_{M_{S,R}}$ stands for the scaling at the left of Eq.(7.40) and γ_{M_S} for that at the right of (7.40). This relationship indicates the intuitive role of the viscosity in slowing down the tearing growth rate as P overtakes unity (cf. the values of γ_M plotted in the right frames of Fig. 7.6).

7.6 Warm-Resistive Regime (S^{-1}, ρ_s)

We now consider the regime in which only temperature effects and a finite collision rate dominate. That is, we can assume $R^{-1} = d_e = 0$ in Eqs.(7.1,7.2).

The linear problem in this warm-resistive regime has been first studied analytically by means of a boundary layer theory in Ref.[81]. Although in that treatment diamagnetic drift effects

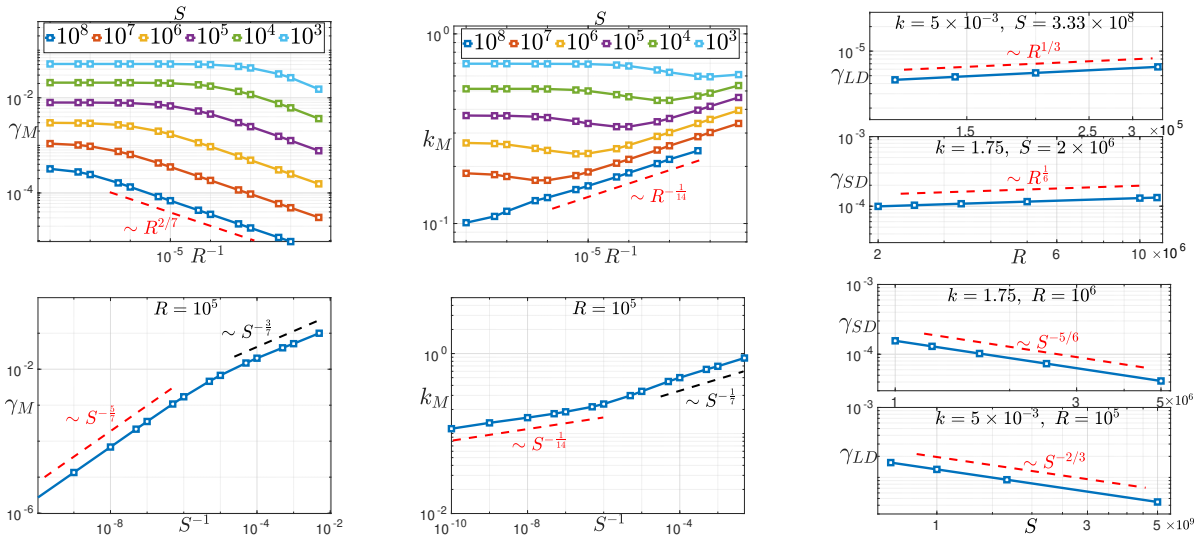

Figure 7.6: Scaling laws in the visco-resistive regime of Sec. 7.5 (dots are numerically obtained values). Left frames: growth rate of the fastest growing mode γ_M as function of R (top) and of S (bottom). Center frames: wavenumber of the fastest growing mode k_M as function of R (top) and S (bottom). Right frames: growth rates in the large-Δ' and small-Δ' limits (labels γ_{LD} and γ_{SD}, respectively) as a function of R and S.

were also included, here we neglect them, as equilibrium density fluctuations are not retained in the model of Eqs.(7.1,7.2). In the same paper, the effect of finite ion Larmor radius corrections were also retained by means of a (gyro)-kinetic modelling of the ion response [80]. Although ion FLR effects can be included in the model by means of Padé-type approximants [312, 83] or by means of more refined approximations[351, 352] which in the collisionless limit preserve the Hamiltonian character of the system for arbitrary values of ρ_i, we have chosen not to include them in the present analysis. In this sense we depart from the "semi-collisional" limit, identified in the kinetic study by Drake and Lee[67] through the condition $\gamma d_e^2 \ll S^{-1} \ll (kd_e)\Delta'^{-1/2}\rho_i^{3/2}$.

The scalings given in Refs.[81, 82] for the warm-resistive case and in Ref. [85] for the warm-collisionless case can be recovered from those discussed in this chapter with the substitution $\rho_s^2 \to \rho_i^2 + \rho_s^2$. However, the loss of symmetry between ρ_s^2 and ρ_i^2 in the warm-collisionless growth rate, which was noted in Ref. [314] requires further investigation. The warm-collisionless scalings ($d_e \neq 0$, $\rho_s \neq 0$) were also obtained by Zocco and Scheckochihin[353], starting from a reduced semi-kinetic model somewhat different from the one considered in Ref. [80, 81, 85] (see also Ref. [351]), and by integrating the boundary layer equations in coordinate space.

The heuristic estimation of the tearing scalings in presence of ρ_s are much more difficult than in "cold" (i.e. $\rho_s = 0$) regimes. However, as it happens for the "cold" collisionless limit with $\rho_s = 0$ and $d_e \neq 0$, in which the collisionless scalings can be deduced from those of the purely resistive regime after substituting [354] $d_e^2 \to S^{-1}/\gamma$, it is easy to verify that the scalings of the warm-resistive regime below can be equally recovered from those of the warm collisionless case first discussed in Ref. [85]. This is also the criterion used in Ref.[353] to re-obtain the results of Refs.[81, 82] and to deduce the corresponding scalings for the inner layer width from boundary analysis calculations in a semi-kinetic warm-collisionless regime.

The corresponding scaling laws, confirmed by the numerical solutions, are:

$$\gamma_{LD} \sim k^{6/7}\rho_s^{4/7}S^{-1/7}, \quad \delta_{LD} \sim k^{-4/7}\rho_s^{-5/7}S^{-4/7} \tag{7.41}$$

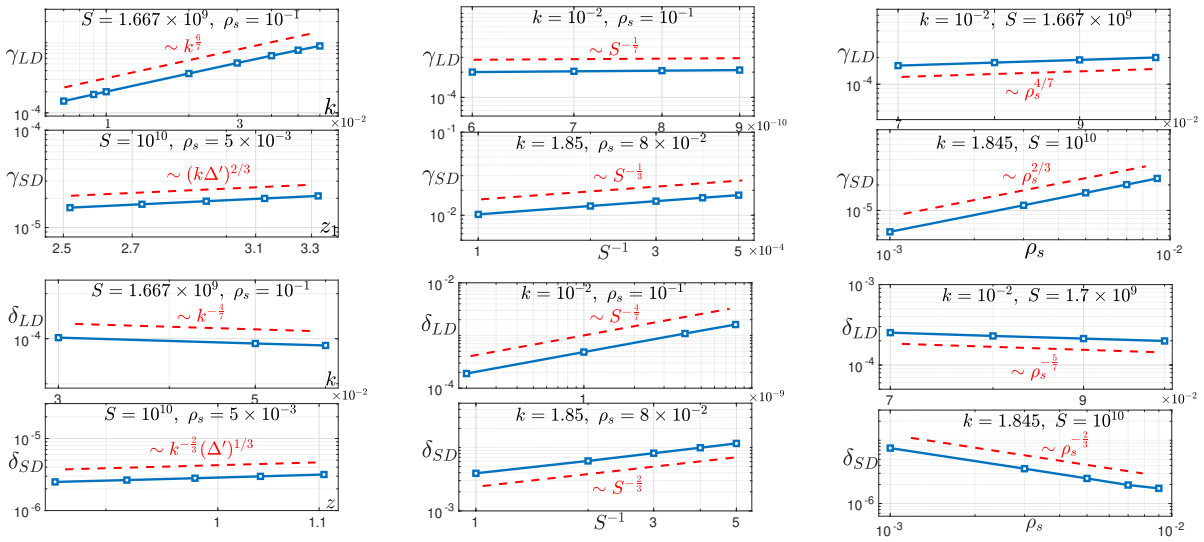

Figure 7.7: Scaling laws in the warm-resistive regime of Sec.7.6 (blue dots are numerically obtained values): growth rates γ are displayed in the two upper panels, and reconnecting layer widths δ are displayed in the two lower panels. In left figures (SD case) the abscissa variables are $z = k^{-2/3}\Delta'^{1/3}$ and $z_1 = (k\Delta')^{2/3}$.

$$\gamma_{SD} \sim (k\Delta')^{2/3}\rho_s^{2/3}S^{-1/3}, \quad \delta_{SD} \sim k^{-2/3}\Delta'^{1/3}\rho_s^{-2/3}S^{-2/3}. \tag{7.42}$$

In Fig. 7.7 we plot the growth rates γ_{SD} and γ_{LD} versus different parameters (k, S, and ρ_s), and the corresponding scaling laws of δ_{SD} and δ_{LD}. The conditions of validity of these scalings are obtained from the normalization scales of the boundary layer analysis, which give [81, 353] $\rho_s \gg (kS)^{1/3}$ in the large-Δ' limit and $\Delta' \ll \rho_s^{-1/7}(kS)^{2/7}$ in the small-Δ' limit. Outside of this range, the effect of ρ_s is negligible and scalings (7.33-7.34) of the purely resistive regime are recovered.

Using the same argument described in the previous section to estimate the growth rate of the fastest growing mode, we obtain from (7.41-7.42) the following scalings:

$$\text{Warm-Resistive Regime} \qquad \begin{cases} \gamma_M \sim \rho_s^{5/8}S^{-1/4} \\ k_M \sim \rho_s^{1/16}S^{-1/8} \\ \delta_M \sim \rho_s^{-3/4}S^{-1/2} \end{cases} \tag{7.43}$$

These are confirmed by numerical results. Fig. 7.8 shows the scalings of γ_M (left frame) and of k_M (right frame) versus the different parameters. Here, again, two limit regions can be recognized where scalings (7.40) and (7.43) respectively hold. In the top-left frame of Fig. 7.8 we see that, when $S \gtrsim 10^6$, the scaling of $\gamma_M \propto \rho_s^{5/8}$ agrees with Eq. (7.43) for all chosen values of ρ_s. For values of $S \lesssim 10^6$, we recognize a threshold value for ion sound Larmor radius $\tilde{\rho}_s$ above which we recover the semi-collisional regime of Eq. (7.43). When $\rho_s < \tilde{\rho}_s$, the scaling of γ_M becomes independent on ρ_s. In the bottom left frame of Fig. 7.8, when $S > \tilde{S}$ we recover the scaling $\gamma_M \sim S^{-1/4}$ of Eq. (7.43) (see, e.g., the blue line in bottom-left frame of Fig. 7.8, where we can identify $\tilde{S} = 10^7$ for $\rho_s = 10^{-2}$). The second limit regime (purely resistive) governed by Eq. (7.40) corresponds to $\gamma_M \sim S^{-3/7}$ and is observed when $S < \tilde{S}$ (see again, e.g., the blue line in bottom-left frame of Fig. 7.8 for $\rho_s = 10^{-2}$). In the right frame of Fig. 7.8 we recognize the same features as above. Here, a threshold value of the Lundquist number $\tilde{S}$ for each value of ρ_s

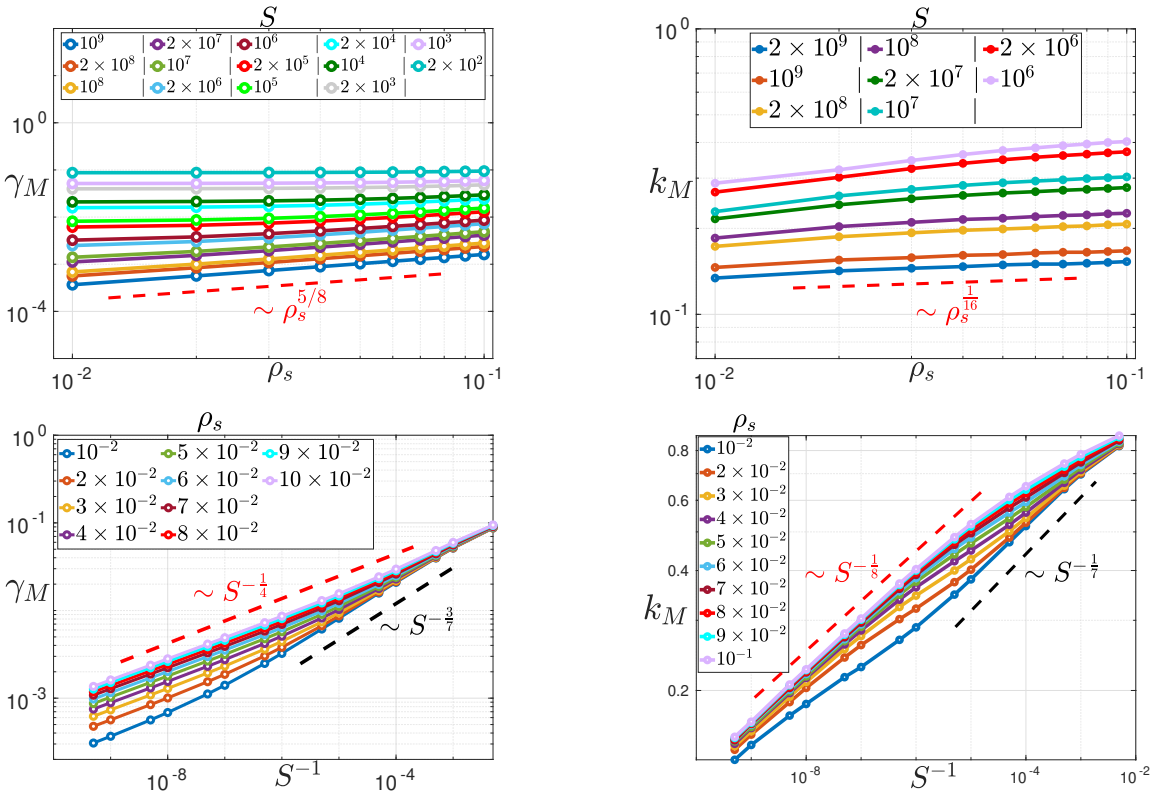

Figure 7.8: Scaling laws of the the fastest growing mode ($\Delta'\delta \sim 1$) in the warm-resistive regime (Sec.7.6).

is visible. For larger values of S, the wavenumber of the fastest growing mode follows the scaling $k_M \sim S^{-1/8}$ of the warm-resistive regime given by Eq. (7.43), while below this threshold value the wavenumber of the fastest growing mode is once more governed by the scaling $k_M \sim S^{-1/7}$.

Finally, the scalings of Eqs. (7.43) can be generalized to an arbitrary equilibrium profile. Proceeding as before we obtain:

$$\begin{array}{c}\text{Warm-Resistive}\\ \text{Regime for } \lim\limits_{k\to 0}\Delta' \sim k^{-p}\end{array} \qquad \begin{cases} \gamma_M \sim \rho_s^{\frac{2+4p}{2+7p}} S^{-\frac{2+p}{2+7p}}, \\ k_M \sim \rho_s^{\frac{1}{2+7p}} S^{-\frac{2}{2+7p}}, \\ \delta_M \sim \rho_s^{-\frac{2+5p}{2+7p}} S^{-\frac{4p}{2+7p}}, \end{cases} \tag{7.44}$$

7.7 Warm-inertial Regime (ρ_s, d_e)

This regime differs from previous one in that a finite electron inertia replaces a finite resistivity as the mechanism that allows reconnection by violating the ideal Lagrangian invariance of ψ. We then assume $R^{-1} = S^{-1} = 0$ in Eqs.(7.1,7.2).

Scalings of the growth rate in this regime have been first obtained by Porcelli [85] and had been provided for the layer width δ by Zocco and Schekochihin [353]. For the fastest growing mode they had been first numerically obtained by Comisso et al. [158] for the same equilibrium (7.3) we consider here, and they had been generalized to different equilibria in Ref.[24].

As previously mentioned, scalings in this regime mirror those of the warm-resistive case previous the substitution $S^{-1} \to \gamma d_e^2$. While in the regime where both d_e and ρ_s contribute, which is delimited by the condition $\rho_s \gtrsim d_e$, we rewrite below all of the relevant scalings, we present in Fig. 7.9 the numerical results for the small- and large-Δ' regimes, only, since the fastest growing mode with $p = 2$ has been already studied [158]:

$$\gamma_{LD} \sim k\rho_s^{2/3} d_e^{1/3}, \qquad \delta_{LD} \sim \rho_s^{-1/3} d_e^{4/3}, \tag{7.45}$$

$$\gamma_{SD} \sim k\Delta' \rho_s d_e, \qquad \delta_{SD} \sim \Delta' d_e^2, \tag{7.46}$$

$$\begin{array}{c}\text{Warm-Inertial}\\ \text{Regime for } \lim\limits_{k\to 0}\Delta' \sim k^{-p}\end{array} \qquad \begin{cases} \gamma_M \sim \rho_s^{\frac{1+2p}{3p}} d_e^{\frac{2+p}{3p}}, \\ k_M \sim \rho_s^{\frac{1}{3p}} d_e^{\frac{2}{3p}}, \\ \delta_M \sim \rho_s^{-1/3} d_e^{4/3}. \end{cases} \tag{7.47}$$

Note, in the large-Δ' limit, the localization of the reconnecting layer in a scale δ_{LD} smaller than d_e because of $\rho_s > d_e$, and, in the small-Δ' limit, the independence of δ_{SD} from ρ_s.

It is well known, however, that for $d_e \gg \rho_s$ the purely inertial (i.e., cold collisionless) regime is entered. Its scalings in the large- and small-Δ' limits have been provided in Refs. [85, 354], and in Refs. [63, 67, 354], respectively.

$$\gamma_{LD} \sim k d_e, \qquad \delta_{LD} \sim d_e, \tag{7.48}$$

$$\gamma_{SD} \sim k(\Delta')^2 d_e^3, \qquad \delta_{SD} \sim \Delta' d_e^2, \tag{7.49}$$

Again, we do not present here the numerical results of this case, as they have been already addressed elsewhere [354, 24] but we note that we found the condition $d_e \gg \rho_s$ delimiting the validity of (7.48-7.49) to be numerically satisfied already for $d_e/\rho_s \gtrsim 0.1$.

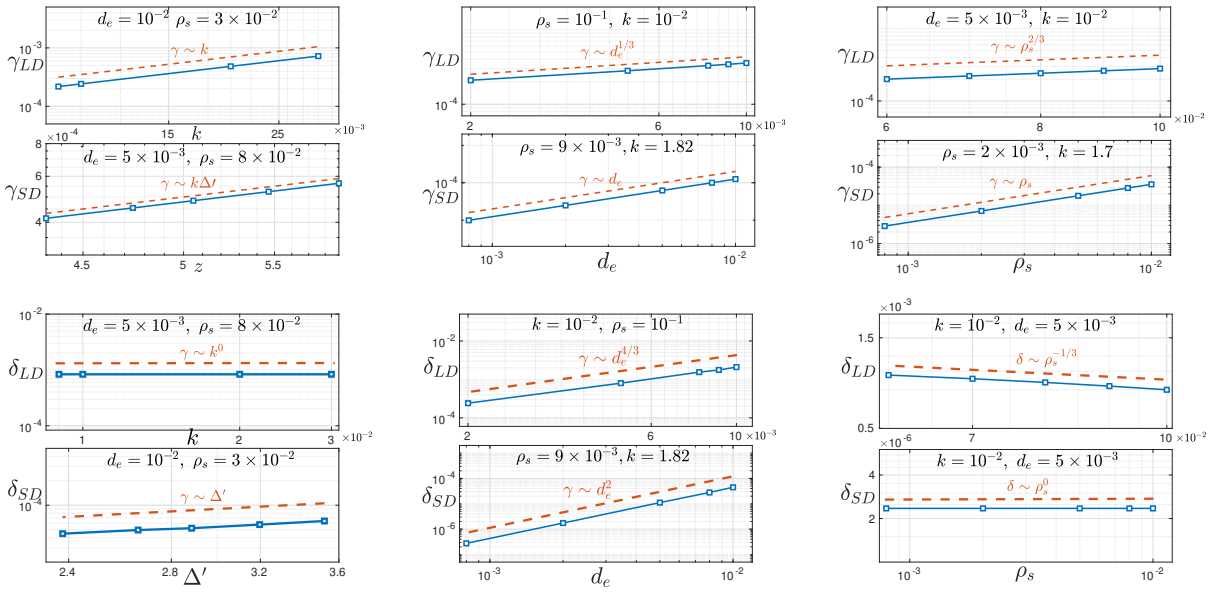

Figure 7.9: Scaling laws in the warm-inertial regime of Sec.7.7 (blue dots are numerically obtained values): growth rates γ are displayed in the two upper panels, and reconnecting layer widths δ are displayed in the two lower panels. Labels "LD" and "SD" correspond to the large-Δ' and small-Δ' limits, respectively.

In this cold, collisionless case, the fastest growing mode in a large aspect ratio current sheet has been first considered in Ref.[60], where the scaling $\gamma_M \sim d_e^{3/2}$ has been numerically obtained for the equilibrium $\psi_0 = \cos(x)$. This agrees with the more general estimates given in Ref. [24]:

$$\begin{array}{c}\text{Cold-Inertial}\\ \text{Regime } (d_e^2 \gg \rho_s^2)\\ \text{for } \lim_{k\to 0}\Delta' \sim k^{-p}\end{array} \qquad \begin{cases}\gamma_M \sim d_e^{\frac{1+p}{p}},\\ k_M \sim d_e^{\frac{1}{p}},\\ \delta_M \sim d_e,\end{cases} \tag{7.50}$$

which have been verified also for a Harris pinch equilibrium [24] and, here, for equilibrium (7.3) (see section. 7.8, next).

Finally, Figures 7.10 evidence the formal equivalence of d_e and S^{-1} by showing the practically identical shape of the eigenfunctions obtained when inertia and resistivity, respectively, are the only non-ideal mechanisms at play and when the values are chosen so that $\gamma d_e^2 = S^{-1}$. We recall instead that ρ_s, like R^{-1}, is per se not sufficient to regularize the singularity that in ideal MHD would develop at the neutral line, since it does not violate the topological invariance of magnetic field lines in ideal MHD, as they are dragged by the flow: although, as $d_e = S^{-1} = 0$, ρ_s appears in front of a source term in the equation for the Lagrangian invariance of ψ, it can be re-absorbed in a redefinition of the fluid stream function with respect to which the total (i.e. material) time derivative of ψ results to be zero ($\varphi \to \varphi - \rho_s^2 U$). More in general, both ρ_s-corrections to the $\mathbf{E}\times\mathbf{B}$ velocity, as they are derived in the $\delta B_z \sim (|\mathbf{B}_{perp}|/B_0)^2$ limit, and the $\mathbf{J}\times\mathbf{B}$ term in Ohm's law of Hall-MHD model do not allow, alone, reconnection (see, e.g., Ref. [355]). After redefinition of the fluid velocity, both terms can be indeed reabsorbed into a null Lie-derivative of $\mathbf{B}(\mathbf{x}, t)$ that expresses the impedement of magnetic reconnection [108].

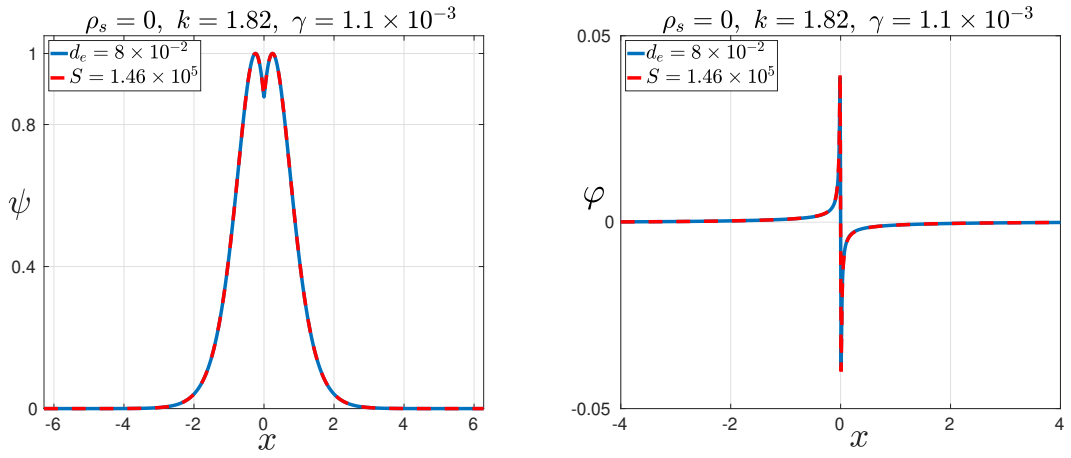

Figure 7.10: Eigenmode profiles of ψ (left panel) and ϕ (right panel) obtained for a case in which d_e (blue curve) and S^{-1} (red curve) are, respectively, the only non zero non-ideal parameter. The values of the parameters have been chosen so that $\gamma d_e^2 \simeq S^{-1}$; the blue and red curves are practically superimposable.

7.8 Inertial-resistive Regime (d_e, S^{-1})

In this regime, where $R^{-1} = \rho_s = 0$ in Eqs.(7.1,7.2). Three regions in parameter spaces can be identified, depending on the relative magnitude of γd_e^2 and S^{-1}. These three regions can be classified as two asymptotic regimes, in which resistivity or electron inertia respectively dominate, and an intermediate region at the intersection of these two regimes.

The existence of these three regions, and in particular of a parameter range in which both d_e and S^{-1} contribute to the growth rate when $\gamma d_e^2 \sim S^{-1}$, had been already noted in the pioneering numerical study of Ref.[60] although specific scalings have been there provided for the $\gamma d_e^2 \gg S^{-1}$ limit, only.

The scalings in the two asymptotic regimes are easily obtained. The first regime, valid for $\gamma d_e^2 \ll S^{-1}$ can be so identified as purely resistive. This has been already discussed and summarized with Eq.(7.39). In this case the inertia-related terms $(\gamma d_e^2 \psi)$ can be neglected with respect to the resistivity contribution.

The second one, valid in the opposite limit $\gamma d_e^2 \gg S^{-1}$, is the cold-inertial regime of Sec. 7.7. The intermediate parameter range is defined by the constraint $\gamma d_e^2 \sim S^{-1}$. We note that the scalings for tearing modes in presence of both electron inertia and resistivity can be deduced by considering for example the scalings (7.48) and (7.49) of the cold inertial case and by rescaling $d_e^2 \to \hat{d}_e{}^2 \equiv d_e^2 + S^{-1}/\gamma$ [354] . For the growth rates this leads to the implicit relations

$$\gamma_{LD} \sim k \left(d_e^2 + \frac{S^{-1}}{\gamma_{LD}} \right)^{1/2}, \quad \gamma_{SD} \sim k(\Delta')^2 \left(d_e^2 + \frac{S^{-1}}{\gamma_{SD}} \right)^{3/2}, \tag{7.51}$$

which are useful to interpret the results in the transition region.

Using for γ the scalings (7.48-7.49) of the collisionless tearing modes or the scalings (7.33-7.34) of the purely resistive case, it is possible to reformulate the condition of transition between the the two asymptotic regimes in terms of the wavenumber as:

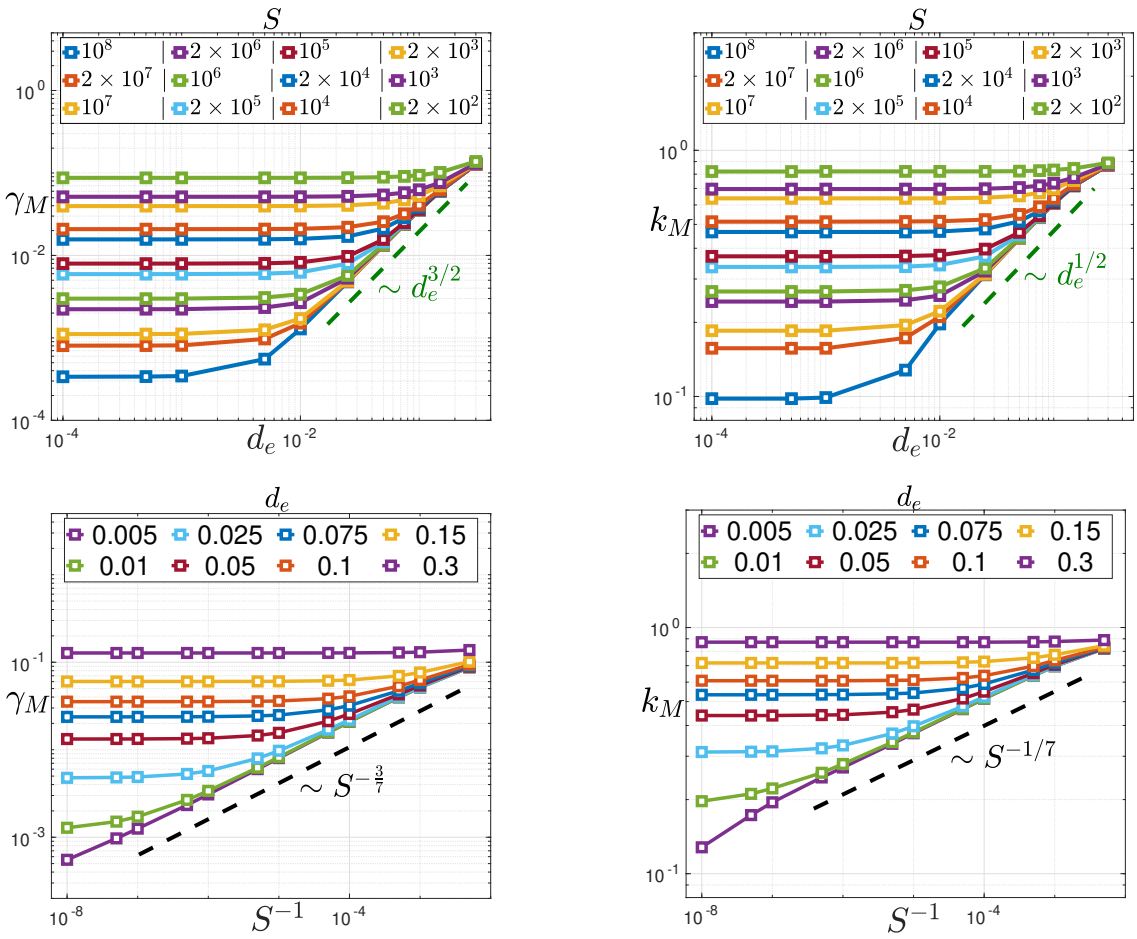

Figure 7.11: Scaling laws of the fastest growing mode occurring for $\Delta'\delta \sim 1$ in the inertial-resistive regime. The dashed green lines of the upper frames indicate the scaling of the purely collisionless regime (7.50), while the black ones in the lower frames indicate the scalings of the purely resistive regime, (7.40).

$$\text{Inertial-resistive range } \gamma d_e^2 \sim S^{-1} \quad \begin{cases} k \sim d_e^{-3} S^{-1} & (\Delta'\delta \gg 1), \\ k(\Delta')^2 \sim d_e^{-5} S^{-1} & (\Delta'\delta \ll 1) \end{cases} \tag{7.52}$$

In a numerical scan of the parameter space, it is easier to identify the three regions (i.e., the two asymptotic regimes and the transition region) by focussing first on the scalings of the fastest growing mode, for which the wavenumber is fixed by the non-ideal parameters.

Fig.(7.11) displays the results of a set of numerical integrations performed by varying of both d_e and S^{-1} and by selecting the corresponding fastest growing mode in a formally continuous spectrum of unstable modes. The dependence of γ_M and k_M on d_e and on S^{-1} is displayed in the top and bottom frames, respectively. For each line, the transition from one asymptotic regime to the other, occurring when $\gamma d_e^2 \sim S^{-1}$, is quite evident. In each frame, the dashed line evidentiates the scaling dependence on the dominant parameter of the mostly inertial (7.50) or mostly resistive regime (7.40). The results of this chapter are listed in table 7.2.

	viscous-resistive: $(R^{-1},\ S^{-1})$		warm-resistive: $(\rho_s,\ S^{-1})$		warm-inertial: $(\rho_s,\ d_e)$	
γ_{LD}	$k^{\frac{2}{3}}R^{\frac{1}{3}}S^{-\frac{2}{3}}$		$k^{\frac{6}{7}}\rho_s^{\frac{4}{7}}S^{-\frac{1}{7}}$		$k\rho_s^{\frac{2}{3}}d_e^{\frac{1}{3}}$	
δ_{LD}	$k^{-\frac{1}{3}}R^{-\frac{1}{6}}S^{-\frac{1}{6}}$		$k^{-\frac{4}{7}}\rho_s^{-\frac{5}{7}}S^{-\frac{4}{7}}$		$\rho_s^{-\frac{1}{3}}d_e^{\frac{4}{3}}$	
γ_{SD}	$k^{\frac{1}{3}}\Delta' R^{\frac{1}{6}}S^{-\frac{5}{6}}$		$(k\Delta')^{\frac{2}{3}}\rho_s^{\frac{2}{3}}S^{-\frac{1}{3}}$		$k\Delta'\rho_s d_e$	
δ_{SD}	$k^{-\frac{1}{3}}R^{-\frac{1}{6}}S^{-\frac{1}{6}}$		$k^{-\frac{2}{3}}\Delta'^{\frac{1}{3}}\rho_s^{-\frac{2}{3}}S^{-\frac{2}{3}}$		$\Delta' d_e^2$	
	$\Delta' \sim (ka)^{-1}$	$\Delta' \sim (ka)^{-2}$	$\Delta' \sim (ka)^{-1}$	$\Delta' \sim (ka)^{-2}$	$\Delta' \sim (ka)^{-1}$	$\Delta' \sim (ka)^{-2}$
γ_M	$R^{\frac{1}{4}}S^{-\frac{3}{4}}$	$R^{\frac{2}{7}}S^{-\frac{5}{7}}$	$\rho_s^{\frac{2}{3}}S^{-\frac{1}{3}}$	$\rho_s^{\frac{5}{8}}S^{-\frac{1}{4}}$	$\rho_s d_e$	$\rho_s^{\frac{5}{6}}d_e^{\frac{2}{3}}$
k_M	$\left(R^{-\frac{1}{2}}S^{-\frac{1}{2}}\right)^{\frac{1}{4}}$	$\left(R^{-\frac{1}{2}}S^{-\frac{1}{2}}\right)^{\frac{1}{7}}$	$\rho_s^{\frac{1}{9}}S^{-\frac{2}{9}}$	$\rho_s^{\frac{1}{16}}S^{-\frac{1}{8}}$	$\rho_s^{\frac{1}{3}}d_e^{\frac{2}{3}}$	$\rho_s^{\frac{1}{6}}d_e^{\frac{1}{3}}$
δ_M	$\left(R^{-\frac{1}{2}}S^{-\frac{1}{2}}\right)^{\frac{1}{4}}$	$\left(R^{-\frac{1}{2}}S^{-\frac{1}{2}}\right)^{\frac{2}{7}}$	$\rho_s^{-\frac{7}{9}}S^{-\frac{4}{9}}$	$\rho_s^{-\frac{3}{4}}S^{-\frac{1}{2}}$	$\rho_s^{-\frac{1}{3}}d_e^{\frac{4}{3}}$	$\rho_s^{-\frac{1}{3}}d_e^{\frac{4}{3}}$
$\left(\frac{a}{L}\right)_{\text{crit}}$	$R^{*\frac{1}{6}}S^{*-\frac{1}{2}}$	$R^{*\frac{1}{10}}S^{*-\frac{1}{2}}$	$\rho_s^{*\frac{1}{3}}S^{*-\frac{1}{6}}$	$\rho_s^{*\frac{1}{3}}S^{*-\frac{2}{15}}$	$\rho_s^{*\frac{1}{3}}d_e^{*\frac{1}{3}}$	$\rho_s^{*\frac{1}{3}}d_e^{*\frac{4}{15}}$

Table 7.2: : Asymptotic scalings of resistive reduced-MHD tearing modes in presence of viscosity and electron temperature, and of collisionless modes in presence of electron temperature. Bottom line refers to the scaling of the critical aspect ratio $(a/L)_{crit}$ discussed in Sec. 7.9.

7.9 Critical Scaling in Different Regimes

In what follows in this section, let us consider current sheets triggered by some dynamics that take place inside the plasma, such as turbulence. Pucci and Velli [161] proved that a critical inverse aspect ratio exists and separates the slowly evolving unstable current sheets from those violently unstable. They dubbed the instability occurring at this threshold "ideal" tearing because the growth rate, normalized to the macroscopic Alfvén time ($\tau_A^* = \frac{L}{v_A}$, where L is the length of the current sheet, and the dimensionless quantities normalized to L are labeled with the apex *), becomes of the order of unity and does not depend explicitly on Lundquist number. This concept might, on the one hand, help in explaining the mechanisms behind the observed fast reconnection phenomena [356]. On the other hand, it helps understanding the restricitions on naturally occurning current sheets, and hence solving the problem of diverging growth rate. The linear analysis, first performed by Pucci and Velli for the purely resistive regime, was later extended to the viscous-resistive regime by Tenerani et al. [357], and further generalized to include inertial and EMHD regimes by Del Sarto et al. [24]. In this context, non-linear studies have been performed to investigate the onset of "ideal" tearing in thin current sheet and its dependence on the magnetic equilibrium [164, 358, 359]. This idea can be understood by re-normalizing Eq.(7.40) with respect to L, this gives for Harris sheet ($p = 1$),

$$\text{Resistive Regime} \qquad \begin{cases} \gamma^*\tau_A^* \sim S_L^{-1/2}(\frac{a}{L})^{-3/2}, \\ k_M^* L \sim S_L^{-1/4}(\frac{a}{L})^{-5/4}, \\ \delta_M^* \sim S_L^{-1/4}(\frac{a}{L})^{-5/4}, \end{cases} \tag{7.53}$$

From the previous equation, as the inverse aspect ratio grows, more and more modes become unstable, initially in the small Δ' range as shown in Fig.(7.1). Of these, the fastest growing mode is associated with the smallest possible wavenumber $k \sim 1/L$, which gives from the second equation of 7.53: $L/a \sim S_L^{1/5}$, therefore the maximum growth rate allowed for this regime is such that

$$\gamma^*\tau_A^* \sim S_L^{-1/5}, \tag{7.54}$$

The characteristic time at which the current sheet shrinks is assumed to be of the order of

τ_A^*. It is obvious that the previous growth rate is still smaller that the characteristic rate of shrinking $\sim 1/\tau_A^*$. Therefore, the shrinking process can continue producing modes in the lower wavenumber portion of the spectrum. This process goes on until the growth rate becomes of the order of characteristic rate $\gamma_M^*\tau_A^* \sim 1$ reached when

$$\left(\frac{L}{a}\right)_{\rm crit} \sim S_L^{1/3} \tag{7.55}$$

This is the smallest possible aspect ratio compatible with the stability condition. Below this value, the current sheet would be destroyed by a mode growing at a faster rate than the one at which the sheet is produced. The corresponding critical wave-number scales as

$$(k^*L)_{\rm crit} \sim S_L^{1/6} \tag{7.56}$$

which gives a measure of the size of the smaller structures produced when the sheet is destroyed, a quantity that can, in principle, be compared with observations.

As mentioned in the introduction of this section, the critical scalings (7.55-7.56) can be generalized to any reconnection regime, similarly to what was shown in Ref.[24]. Let us do this in the regimes discussed in previous sections. From a practical point of view it is sufficient to consider the scalings of the fastest growing modes which we have provided as written by normalizing lengths to a and magnetic fields to B_0, and to rewrite them as normalized to L. The characteristic time of the process governing the current sheet evolution is therefore τ_A^* and the limit $\gamma_M^* \sim O(1)$ must be posed for consistency with the linear analysis. This provides an asymptotic scaling of the critical aspect ratio $(L/a)_{\rm crit}$ with the non-ideal parameters involved.

In the viscous-resistive regime of section 7.5 we thus re-write Eqs.(7.38) as:

$$\begin{cases} \gamma_M^* \sim \left(\frac{L}{a}\right)^{\frac{2+4p}{1+3p}} R^{*\frac{p}{1+3p}} S^{*-\frac{1+2p}{1+3p}}, \\ k_M^* \sim \left(\frac{L}{a}\right)^{\frac{2+3p}{1+3p}} \left(R^{*-1/2} S^{*-1/2}\right)^{\frac{1}{1+3p}}, \\ \delta_M^* \sim \left(\frac{L}{a}\right)^{-\frac{1+4p}{1+3p}} \left(R^{*-1/2} S^{*-1/2}\right)^{\frac{p}{1+3p}}, \end{cases} \tag{7.57}$$

The critical scalings (7.55) and (7.56) so read

$$\left(\frac{L}{a}\right)_{\rm crit} \sim R^{*-\frac{p}{2+4p}} S^{*\frac{1}{2}} = P^{*-\frac{p}{2+4p}} S^{*\frac{1+p}{2+4p}}, \tag{7.58}$$

$$(k_M L)_{\rm crit} \sim R^{*-\frac{1+p}{2+4p}} S^{*1/2}. \tag{7.59}$$

This result can be specialized: for $p = 1$ it corresponds to both the Harris-pinch equilibrium $\psi_0 = a \ln|\cosh(x/a)|$ and to the piece-wise equilibrium defined by $\psi_0(x) = x/a$ in the interval $-a < x \leq a$ and by $\psi_0 = 0$ for $x \leq -a$ and $x > a$ (Ref.[57]). For $p = 2$ it corresponds to the case of Eq.(7.3) and to the case of the equilibrium $\psi_0(x) = a\cos(x/a)$ (Ref.[152]):

$$\left(\frac{L}{a}\right)_{\rm crit}^{[p=1]} \sim R^{*-\frac{1}{6}} S^{*\frac{1}{2}}, \qquad \left(\frac{L}{a}\right)_{\rm crit}^{[p=2]} \sim R^{*-\frac{1}{10}} S^{*\frac{1}{2}}, \tag{7.60}$$

The scalings of γ_M^* in Eq.(7.57) and the critical condition of Eqs.(7.58-7.60) specialized to the $p = 1$ case had been first obtained numerically by Tenerani *et al.* in Ref. [343].

A current sheet with an aspect ratio (asymptotically) larger than that indicated above is met for example in the case of a Sweet-Parker type steady-reconnection assumption on the current sheet aspect ratio. In the purely resistive case it corresponds to $L/a \sim S_L^{1/2}$. Its application to the evaluation of the fastest growing mode in the purely resistive regime gives [162, 163] $\gamma_M^* \sim S_L^{1/4}$: in literature this has been often referenced to as the "*plasmoid instability*" regime[163, 360]. In the viscous-resistive case the corresponding assumption has been discussed in Ref. [361] (see also Ref.[362]).

Analogous results are obtained in the warm-resistive regime of Sec. 7.6. Eqs.(7.47), re-scaled to L, become:

$$\begin{cases} \gamma_M^* \sim \left(\dfrac{L}{a}\right)^{\frac{6+12p}{2+7p}} \rho_s^{*\frac{2+4p}{2+7p}} S^{*-\frac{2+p}{2+7p}}, \\ k_M^* \sim \left(\dfrac{L}{a}\right)^{\frac{5+7p}{2+7p}} \rho_s^{*\frac{1}{2+7p}} S^{*-\frac{2}{2+7p}}, \\ \delta_M^* \sim \left(\dfrac{L}{a}\right)^{-\frac{4+8p}{2+7p}} \rho_s^{*-\frac{2+5p}{2+7p}} S^{*-\frac{4p}{2+7p}}, \end{cases} \tag{7.61}$$

Here the critical aspect ratio and fastest growing mode read

$$\left(\frac{L}{a}\right)_{\text{crit}} \sim \rho_s^{*-\frac{1}{3}} S^{*\frac{2+p}{3(2+4p)}} \tag{7.62}$$

$$(k_M L)_{\text{crit}} \sim \rho_s^{*-\frac{1}{3}} S^{*\frac{p-1}{3(2+4p)}}. \tag{7.63}$$

As it happens in the warm-collisionless case [24], the equilibrium choice does not affect the scaling dependence of the critical aspect ratio on ρ_s. For $p = 1$ and $p = 2$ Eq.(7.62) specializes to:

$$\left(\frac{L}{a}\right)_{\text{crit}}^{[p=1]} \sim \rho_s^{*-\frac{1}{3}} S^{*\frac{1}{6}}, \qquad \left(\frac{L}{a}\right)_{\text{crit}}^{[p=2]} \sim \rho_s^{*-\frac{1}{3}} S^{*\frac{2}{15}}. \tag{7.64}$$

Also note that for $p = 1$ critical wave vector does not depend on resistivity.

We finally report for completeness the critical scalings already evaluated in Ref. [24] for the warm-inertial regime,

$$\begin{cases} \gamma_M^* \sim \left(\dfrac{L}{a}\right)^{\frac{1+2p}{p}} \rho_s^{*\frac{1+2p}{3p}} d_e^{*\frac{2+p}{3p}}, \\ k_M^* \sim \left(\dfrac{L}{a}\right)^{\frac{1+p}{p}} \rho_s^{*\frac{1}{3p}} d_e^{*\frac{2}{3p}}, \\ \delta_M^* \sim \rho_s^{*-\frac{1}{3}} d_e^{*\frac{4}{3}}, \end{cases} \tag{7.65}$$

The critical aspect ratio and fastest growing mode are

$$\left(\frac{L}{a}\right)_{\text{crit}} \sim \rho_s^{*-\frac{1}{3}} d_e^{*\frac{-2-p}{3(1+2p)}} \tag{7.66}$$

$$(k_M L)_{\text{crit}} \sim \rho_s^{*-\frac{1}{3}} d_e^{*\frac{1-p}{3(1+2p)}}. \tag{7.67}$$

and for $p = 1$ and $p = 2$ the critical ratii read:

$$\left(\frac{L}{a}\right)_{\text{crit}}^{[p=1]} \sim \rho_s^{*-\frac{1}{3}} d_e^{*-\frac{1}{3}}, \qquad \left(\frac{L}{a}\right)_{\text{crit}}^{[p=2]} \sim \rho_s^{*-\frac{1}{3}} d_e^{*-\frac{4}{15}}. \tag{7.68}$$

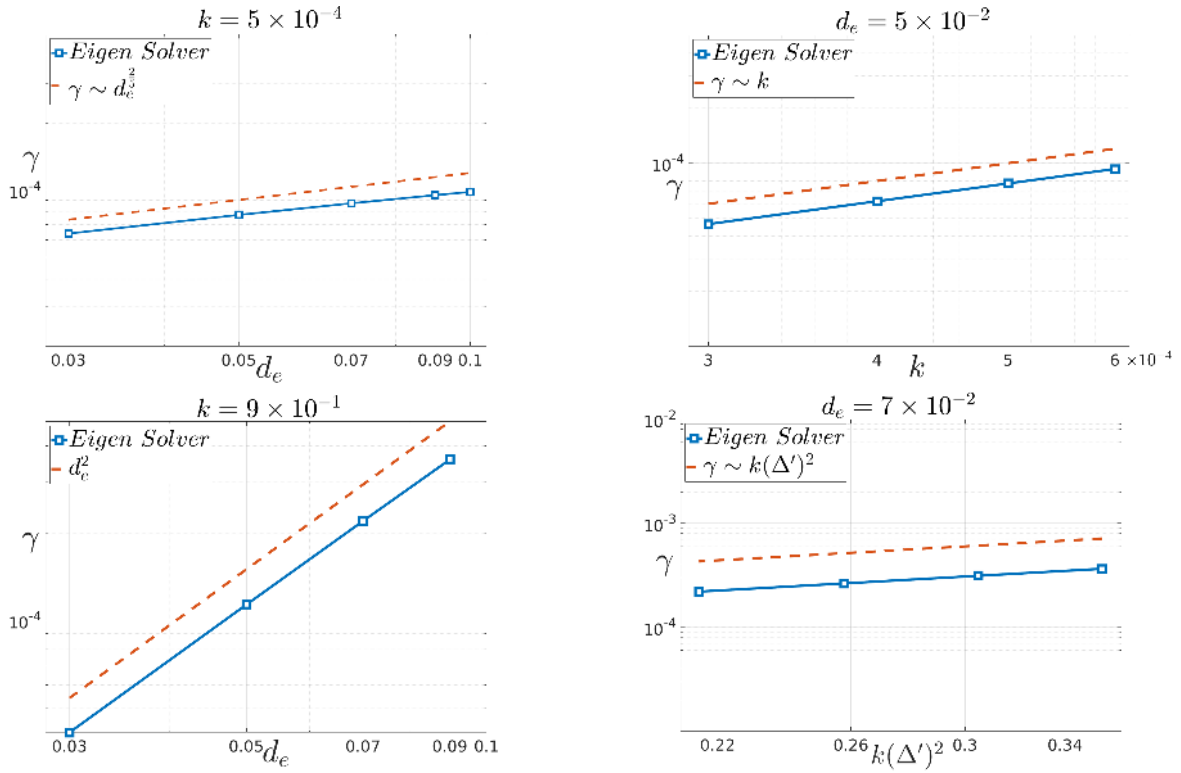

Figure 7.12: Scaling laws of the EMHD regime. The scalings of γ in the large wavelength and small wavelength limits are shown in the top and the bottom frames, respectively.

These results perfectly mirror those of the warm-resistive case above, according to the correspondence $S^{-1} \leftrightarrow \gamma d_e^2$, which corresponds to $S^{-1} \leftrightarrow d_e^2$ since the critical ratii above are the same of the "ideal" tearing, $\gamma_M^* = \gamma_{IT} \sim O(1)$.

The critical scalings we have written in the three regimes are summarized in the last line of Table 7.2.

It should be noted that it is left open the question of whether values of p different from 1 and 2 are admitted for different magnetic equilibrium profiles with a single resonant point. The change of regime indicated by Eqs.(7.63) and (7.67) when $p < 1$ suggests to exclude the possibility of fractional values smaller than unity. Finally, it is also interesting to notice that the size of the smallest structures, measured by k_M^*, is independent of the non-ideal parameter that leads to the reconnection (d_e, or S) for Harris equilibrium ($p = 1$), while this does not hold for equilibria given by Eq.7.3, or $\psi_0 = cos(x/a)$.

7.10 Scaling in Collisionless EMHD

The reference works for the linear analysis of tearing-type modes in EMHD are those of (Bulanov et al. (1992) [89]; Erba and Pegoraro (1993) [92]; Attico et al.(2000) [93]), where the scalings of the growth rates in both the resistive and the collisionless regimes have been first provided. These theoretical scalings have been partially revised and also numerically verified in the collisionless case by Attico et al. (2000) [93]. The analysis we have performed in the purely collisionless limit essentially confirms such results but for a small discrepancy with respect to the growth rate scalings in the large wavelength limit.

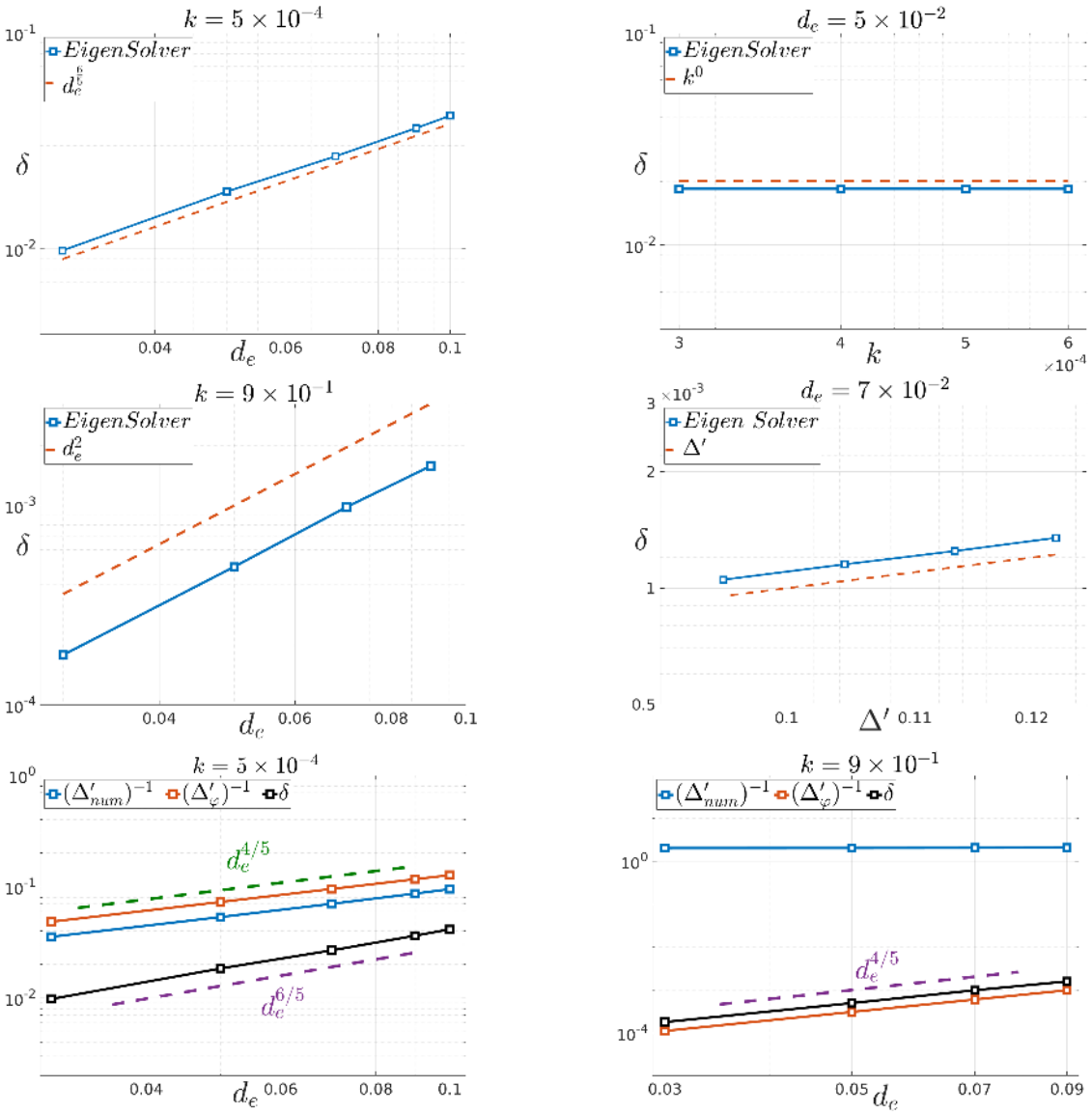

Figure 7.13: Scaling laws of the EMHD regime. The scalings of δ in the large wavelength and small wavelength limits are shown in the top and the middle frames, respectively. In the bottom frames, we plot the scalings of $(\Delta'_{num})^{-1}$ (blue color), $(\Delta'_{\phi})^{-1}$ (orange color), and δ (black color) for the large wavelength limit on the left-bottom frame, and for the small wavelength limit on the right-bottom frame.

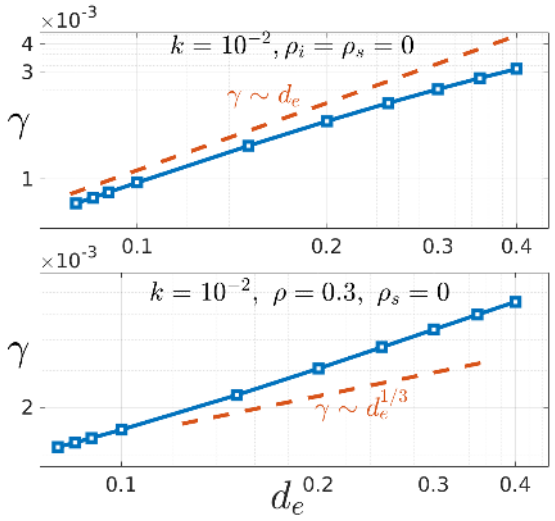

Figure 7.14: The growth rate as function of d_e in the large wavelength limit. The values of d_e are taken to be the same of those in Ref.[314]. The deviation from the correct scaling is evident for $d_e > 0.1$, for both cold ($\rho_i = \rho_s = 0$), and warm-ion ($\rho_i \neq 0$) regimes.

Besides of that, in the present analysis we provide the scalings of the reconnecting layer width in both the small and large wavelength limit, which agree with the generalized heuristic analysis of section 7.4. Fig.7.12 and Fig.7.13 show the scalings, obtained by the numerical solver, for both γ and δ, respectively. These scalings read

$$\begin{aligned} &\gamma \sim k d_e^{\frac{2}{5}}, \quad \delta \sim d_e^{\frac{6}{5}}, \quad \text{for } \Delta^{'}\delta \gg 1, \\ &\gamma \sim k(\Delta^{'})^2 d_e^2, \quad \delta \sim \Delta^{'} d_e^2, \quad \text{for } \Delta^{'}\delta \ll 1, \end{aligned} \tag{7.69}$$

Using the relation $\delta l \sim d_e^2$, we find that

$$l \sim d_e^{\frac{4}{5}} \quad (\text{for } \Delta^{'}\delta \gg 1), \qquad l \sim (\Delta^{'})^{-1} \quad (\text{for } \Delta^{'}\delta \ll 1). \tag{7.70}$$

These scalings agree with the definition of l given by Eq.(7.24), and also with the discussion in section 7.4. For example, we can recognize in the bottom frames of Fig.7.13 that $l = (\Delta^{'}_{\phi})^{-1}$ for the large wavelength limit (left frame), while it is $l = (\Delta^{'})^{-1}$ for the small wavelength limit (right frame). It is also evident in the right-bottom frame that $\Delta^{'}$ does not depend on the non-ideal parameter, but only on the wavenumber and the width of the equilibrium, which agrees with the definition of the instability parameter for the tearing modes (see section 1.3.1).

7.11 Scaling Laws in the Warm-ion Regime

In this section, we briefly present two results of our study of the warm-ion regime for the case in which only ρ_s, ρ_i, and d_e are non-zero in the eigenvalue problem given by Eq.(5.76). The complete results concerning the wide scan of different regimes are in preparation to be published (see chapter 9). In this study, the scaling by Porcelli [85] have been confirmed for $\rho_s,\ \rho_i > d_e$, where ρ_i and ρ_s enter symmetrically in the growth rate via power of a geometric mean ($\sqrt{\rho_s^2 + \rho_i^2}$).

For example, in order to obtain the scalings of the small wavelength limit, we substitute $\sqrt{\rho_s^2 + \rho_i^2}$ for ρ_s in Eq.(7.31).

However, in Ref.[314], Del Sarto, Marchetto, et al observed an "asymmetry" between ion and electron FLR (ρ_i and ρ_s) both in linear and nonlinear dynamics. In the present work, we found that this is likely due to the non-asymptotically small value of the electron skin depth; that is the values of d_e might be outside the interval in which the method of matched asymptotic expansions (boundary layer approach) does apply. This is clearly shown in Fig.7.14, where the deviation from the correct scaling laws is evident for the values of d_e studied in Ref.[314].

We also found two new regimes that had not been evidenced before with analytical estimations. These regimes are shown in Fig.7.15 at the right-top and the bottom frames. In the left-top frame, we plot the scalings of γ as function of both d_e and $r = \sqrt{\rho_i^2 + \rho_s^2}$ in the Porcelli limit (that is, when $r > d_e$, $\gamma < r$, and $\Delta' d_e \gg 1$, see Comisso et al.[158]). These scalings can be easily obtained by replacing ρ_s with r in the warm-inertial regime discussed in section 7.7.

In the right-top frame, we obtain the scaling $\gamma \sim r^{2/5} d_e$ when $d_e \rho_i \gg \rho_s^2$, and $r \sim d_e$. However, we can neglect this regime as it spans a very narrow region for ρ_s. The more interesting regime is that occurring for $r \sim d_e$ and $d_e \rho_i \sim \rho_s^2$, as shown in the bottom frame of Fig.7.15. This regime will be discussed in detail a future work (see 9).

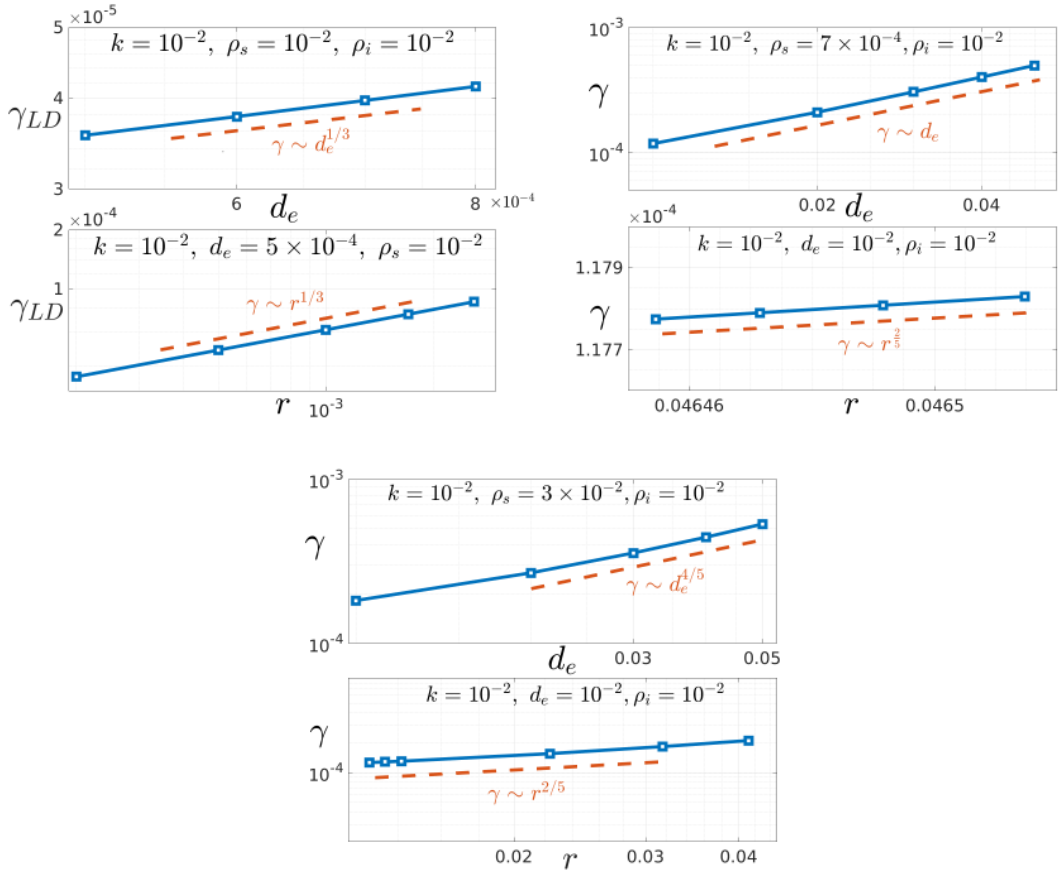

Figure 7.15: The growth rate as function of d_e in the large wavelength limit. The values of d_e are taken to be the same of those in Ref.[314]. The deviation from the correct scaling is evident for the $d_e > 0.1$, for both cold ($\rho_i = \rho_s = 0$), and warm-ion ($\rho_i \neq 0$) regimes.

8

Competition of Magnetic Reconnection and Weibel-type Instabilities

Contents

In this chapter, we investigate, by means of nonlinear kinetic simulations, the competition of magnetic reconnection with Weibel type instabilities. To this purpose, we present simulations performed using VLEM2D3V code, detailed in chapter 3. Additionally, we also show PIC simulations performed with SMILEI code [1]. VLEM code has been extensively used to study two-stream instability, Weibel-type instabilities [2], and more recently, the oblique modes [3]. In this chapter, we are interested in the kinetic study of the linear and nonlinear evolution of some plasma configurations, which consist of two counter-propagating beams. These configurations are unstable to Weibel-type instabilities, and possibly to reconnecting modes. We start this chapter by introducing Weibel-type instabilities, and then presenting the results. We have addressed in particular two kind of problems, for which we have performed two sets of "numerical experiments" related to Weibel modes for two counter-propagating electron beams (the so called "current filamentation instability", or CFI):

In the first set of simulations, we considered the CFI-instability of two counter-propagating electron beams having a finite radial width [4, 5], which are expected to be subject of magnetic reconnection processes related to the merging of parallel oriented current beams.

In the second set of simulations, we have addressed, although with a preliminary study, the competition between CFI and magnetic reconnection that, in Ref.[363] had been already

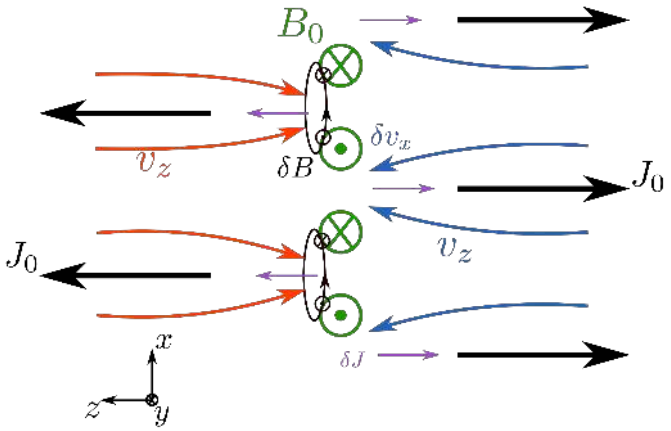

Figure 8.1: The mechanism of the CFI instability, a kind of Weibel instability. Here, an initial configuration of two counter-propagating beams along the z direction (orange and blue colours) is perturbed with a perpendicular magnetic field in the y-direction (green colour). This field is modulated in the x-direction. Due to the existence of this field, and to the well-known fact that currents propagating in the same direction attract each other, the beams on the left and right sides tend to move toward points with minimum magnetic fields. Therefore, a current density **J** (black arrows), modulated in the x direction, is generated (current filamentations). This current density creates a magnetic field (black circles) in the (x,y) plane. This latter field amplifies the initial one and generates a new current density (purple arrows) that enhances that produced by the original field; this further enhances the filamentation phenomenon and finally magnetic reconnection.

evidenced to occur one subsequent of the other, with tearing-type magnetic reconnection being dominated by the pressure anisotropy related to the primary CFI-dynamics.

8.1 Weibel-type Instabilities

This type of instability concerns a somehow opposite mechanism of that involved in magnetic reconnection. The latter is a process that leads to the conversion of the magnetic energy, stored in field topology, into kinetic and thermal energies of charged particles inside the plasma. The former involves the inverse mechanism: conversion of thermal and kinetic energies of the particles into electromagnetic energy, which leads to the amplification of an existing magnetic field if the plasma is magnetized.

Weibel proved in 1958 [7] that the existence of anisotropy in temperatures between parallel and perpendicular directions can excite this type of instabilities, which tend to reduce the degree of the anisotropy, and therefore isotropize the plasma temperatures. These anisotropic temperatures were observed in magnetospheric plasma [364], and also in numerical simulations of turbulent plasma [365]. The distribution function, in this case, is represented by a Bi-Maxwellian distribution which accounts for the different temperatures in different directions (different thermal motions in different directions). It reads,

$$f = n_0 \sqrt{\frac{m}{2\pi k_B T_\perp}} \left(\frac{m}{2\pi k_B T_{||}}\right) e^{-\frac{v_x^2+v_y^2}{2k_B T_\perp} - \frac{v_z^2}{2k_B T_{||}}} \tag{8.1}$$

All quantities refer here to electrons, since at the scales relevant to this instability, ions constitute a neutralizing background. Aiming to understand the mechanism behind this instability using a simpler image, Fried (1959) [8] showed that this instability also occurs in the limit in which the bi-Maxwellian distribution function is substituted by two counter-propagating electron beams along z direction with homogeneous velocities v_1 and v_2 and cold temperature parallel to the beams: the perpendicular temperature will be in this case represented by the difference between the two Dirac peaks. Therefore, f becomes

$$f = \Big(n_1\delta(v_z - v_1) + n_2\delta(v_z - v_2)\Big)\delta(v_x)\delta(v_y) \tag{8.2}$$

where n_1 and n_2 here are the densities of the beams (and not the perturbed quantities), and their sum is n_0, which represents the total density of the plasma.

This simple representation allows us to understand the mechanism behind the amplification of an initial magnetic field, and also to understand the reasons behind the formation of current filamentation inside magnetized plasmas. As shown in Fig.8.1, we have two counter-propagating electron beams along the z-direction with an initial magnetic perturbation B_0 (green colour).

We know that two currents, propagating in the same direction, attract each other, while the opposite is true for two counter-propagating currents. We also know that the electrons are right-handed with respect to the field, meaning that they gyrate counterclockwise when the field is pointing outside of the plane of the "paper" (Lorentz force).

Taking these facts into account, the electron beams (orange and blue coloured arrows), while reaching the perturbed region, will deflect toward points with minimum values of magnetic fields, as shown in the figure. This kind of motion, initiated by $\mathbf{B}_0$, will, in turn, generate a current density $\mathbf{J}_0$ pointing in the direction opposite to these of electron beams, as shown with black coloured arrows in Fig.8.1. Then, this current density generates a magnetic field $\delta\mathbf{B}$ (black circles in the figure) which points in the same direction of the original field, leading to the amplification of the initial field and to the generation of a new current density $\delta\mathbf{J}$ (purple coloured arrows) which further enhances the current density $\mathbf{J}_0$. This process, first devised by Fried, to give a picture of Weibel instability, is now called current filamentation instability (`CFI`).

The invariance of the problem in the z direction implies the conservation of canonical momentum in this direction. This means, for example, that

$$P_{c,z} = mv_z - eA_z(x) = mv_{z,0} = const, \tag{8.3}$$

where $P_{c,z}$ is the canonical momentum, A_z is the vector potential, and $v_{z,0}$ is the initial velocity. See the thesis by Sarrat [275] for a detailed study (kinetic and fluid descriptions) of `CFI`.

8.2 `CFI` with `VLEM2D3V`: A Benchmark Test

Contrary to the `CFI` instability, magnetic reconnection is a `2D` process occurring inside the current layer plane, say (`x-y`) plane. This means that when studying magnetic reconnection (or even "magnetic annihilitaion" [366]), we allow the streaming of the beams along the direction perpendicular to the reconnection plane. This is the first time we employ `VLEM` to investigate such cases. Therefore, before using the code to study magnetic reconnection, we start by testing its symmetry with respect to the physics, which can be done by studying `CFI` instability using two different configurations. In the first one, the beams propagate along the y direction, with a magnetic perturbation along z direction; while in the second test, the beams stream along the z

direction, with a magnetic perturbation in y direction (in both cases, the initial magnetic field is modulated in x direction). The initial magnetic fields for these numerical tests are given by

$$\delta B_{z,0} = B_0 \cos(k_x x), \quad \delta B_{y,0} = B_0 \cos(k_x x), \tag{8.4}$$

where $B_{z,0}$ and $B_{y,0}$ are the initial magnetic fields for the first and second simulations, respectively. As explained in section 8.1, these configurations are `CFI` unstable, and therefore the initial magnetic field will be amplified due to the magnetic field generated by the instability[16]. The initial distribution function for beams propagating in the y direction is given by

$$\begin{aligned} f = \frac{n_1}{(2\pi m k_B T_1)^{3/2}} exp\Big[- \frac{p_x^2 + (p_y - p_1)^2 + p_z^2}{2 m k_B T_1} \Big] \\ + \frac{n_2}{(2\pi m k_B T_2)^{3/2}} exp\Big[- \frac{p_x^2 + (p_y - p_2)^2 + p_z^2}{2 m k_B T_2} \Big], \end{aligned} \tag{8.5}$$

In both simulations the density profile is homogeneous and symmetric ($n_1 = n_2 = 0.5$). The normalized momenta of the beams are taken to be $p_1 = 0.95$, and $p_2 = -0.95$ in both simulations. The velocity in the code is normalized to the speed of light (c). Therefore, the Lorentz factor is $\gamma = \sqrt{1 + p^2} = \frac{1}{\sqrt{1 - v^2}}$, meaning that the previous value of the momentum is equivalent to $|v_1| = |v_2| = 0.689c$. The beams are also assumed to be cold $T_1 = T_2 = 2\ keV$, while the rest mass energy of electron is 511 keV. Time is normalized to plasma electron frequency ($\omega_{p,e}$). Hence, the lengths are normalized to the electron skin depth (d_e). $k_x = \frac{2\pi m}{L_x}$, and $k_y = \frac{2\pi n}{L_y}$, where m, n, L_x, and L_y are the number of modes, and the lengths of the simulation box in both directions x and y, respectively. The time step is $\Delta t = 0.003$ which respects the `CFL` condition imposed by Yee solver ($(c\Delta t)^2 \leq \frac{1}{(\Delta x)^{-2} + (\Delta y)^{-2}}$). All other simulations' parameters are identical, and are shown in table 8.1.

Simulation	N_x	N_y	N_{p_x}	N_{p_y}	N_{p_z}	n_1	n_2	p_1	p_2	Δt	B_0	m	n
1	128	16	32	32	32	0.5	0.5	0.95	−0.95	0.003	10^{-4}	1	0
2	128	16	32	32	32	0.5	0.5	0.95	−0.95	0.003	10^{-4}	1	0

Table 8.1: The parameters of two CFI simulations performed to ensure that the code is physically symmetric. N_x, and N_y are the number of grid points in x and y directions, respectively. N_{p_x}, N_{p_y}, and N_{p_z} are the corresponding number of points in momentum space. B_0 is the amplitude of the initial field. n_1 and n_2 are the densities of the beams.

This benchmark test is also important due to the fact that the semi-Lagrangian method here includes advecting the Vlasov equation along with both directions: x and y. Therefore, when the beams are along y direction, there will be an advection parallel to the beams, while it won't be the case when the beams are in the z-direction (the code is independent of this coordinate).

[16] It is important to mention that here, and in all the remaining sections of this chapter, we do not perturb the quantities in the propagation direction of the beams for two reasons. One the one hand, we always want to avoid configurations which are unstable to two-stream instability and oblique mode [367, 3], occurring when the perturbations have components parallel to the beams. On the other hand, the existence of this parallel component of the perturbations will invoke the necessity of extending the `VLEM2D3V` code to be `3D3V` one in order to study the coupling of these instabilities with initial conditions that might lead to magnetic reconnection. This is the next step in developing `VLEM` code.

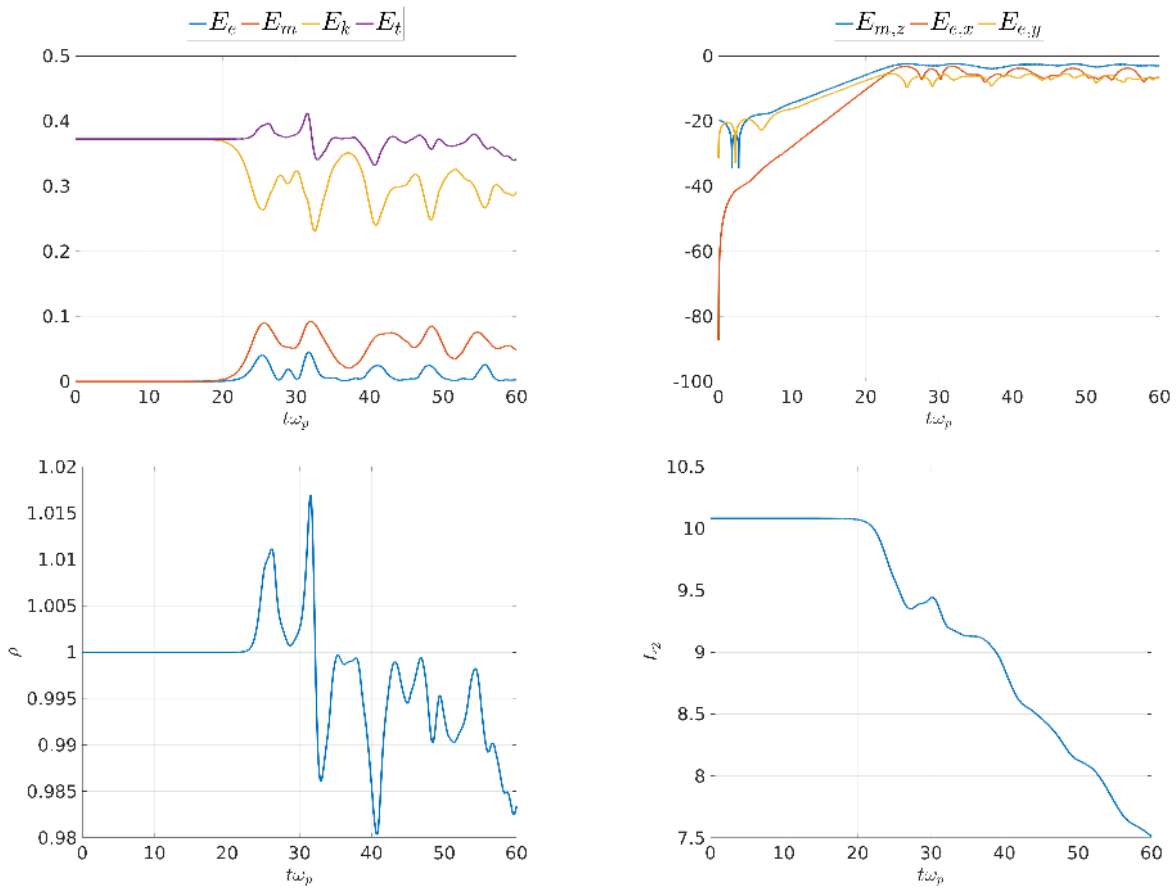

Figure 8.2: Time evolution of the first simulation (beams along the y direction). The top-left frame shows the energies evolution with time. E_e (blue), E_m (orange), E_k (yellow), and E_t (purple) are electric, magnetic, kinetic, and total energies, respectively. In the top-right frame of the figure, we show the evolution of magnetic energy associated with B_z component: $E_{m,z}$ (blue), the electric energies $E_{e,x}$ (orange) and $E_{e,y}$ (yellow), associated with E_x and E_y components of the electric field. Bottom-left frames shows the evolution of mean plasma density ρ, while the bottom-right frame represents the L_2-norm. The loss of conservation of these two quantities is not only a result of the low resolution of the grid in the momentum space, but also due to the loss of information which arises when the filamentation reaches the size of the cells in the phase space.

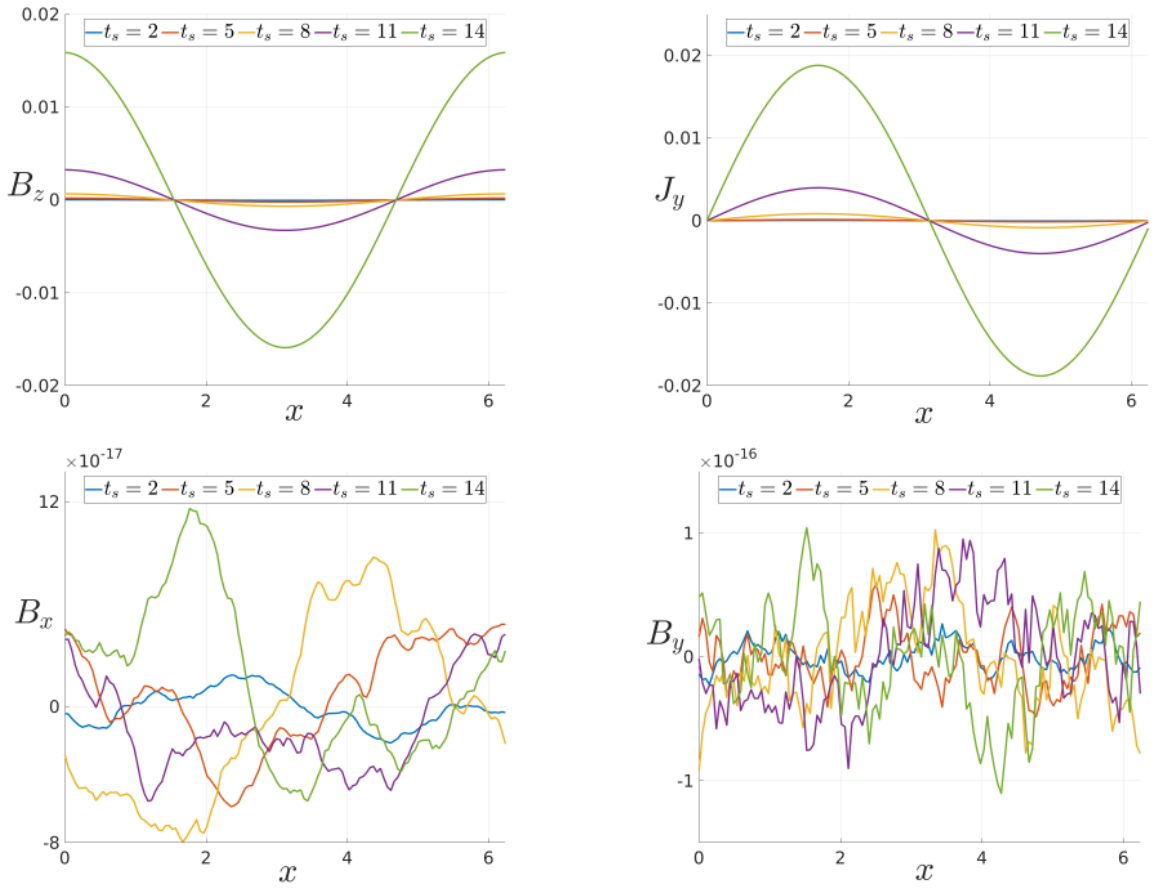

Figure 8.3: The magnetic field components, and the current density along the beams' direction at different times for the first simulation for the beams propagating along the $y-$direction, and a background magnetic field along the $z-$direction. Notice that at all these times, the total energy, L_2- norm and the mean plasma density are precisely conserved (at the order of the machine epsilon).

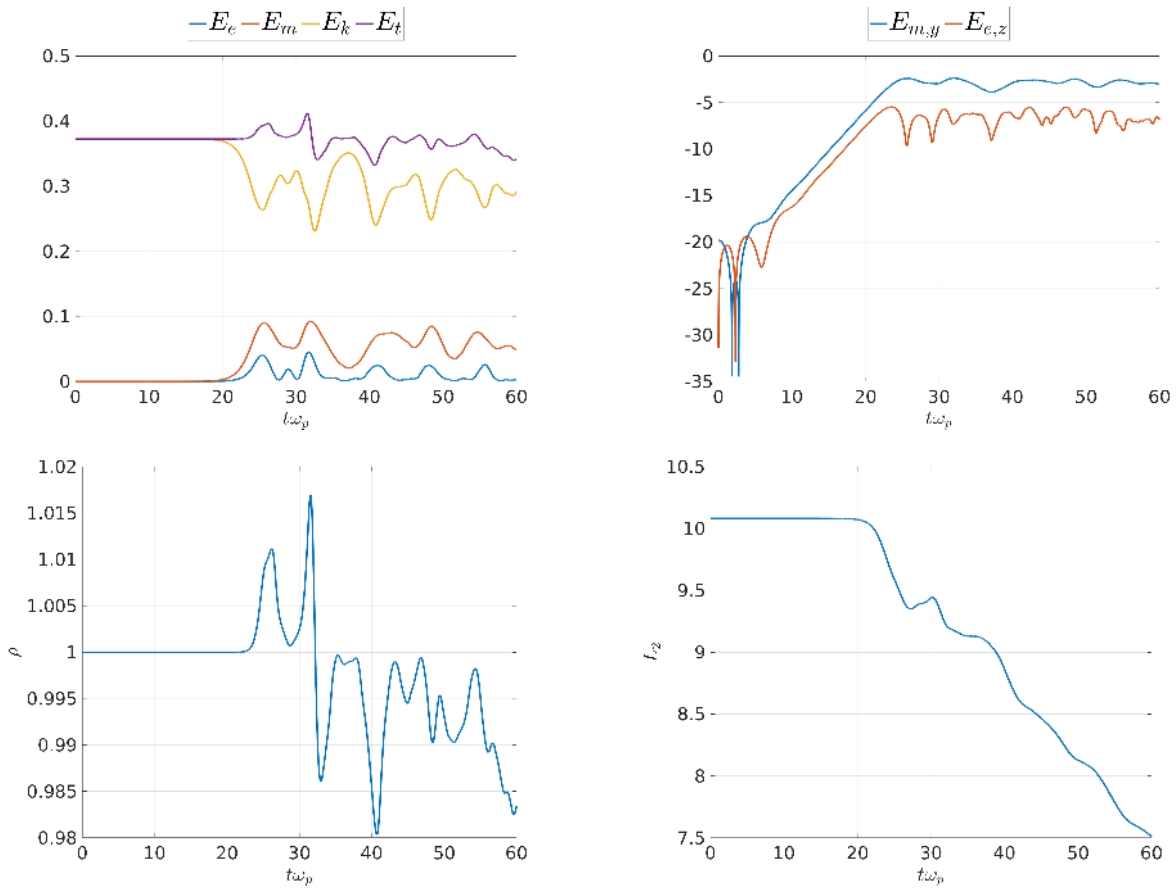

Figure 8.4: Time evolution of the second simulation (beams along z direction). The top-left frame shows the energies evolution with time. E_e (blue), E_m (orange), E_k (yellow), and E_t (purple) are electric, magnetic, kinetic, and total energies, respectively. In the top-right frame of the figure, we show the evolution of magnetic energy associated with B_y component: $E_{m,y}$ (blue), and the electric energy $E_{e,z}$ (orange) associated with E_z component of the electric field. No contribution of $E_{e,x}$ due to the independence of the problem of z coordinate. Bottom-left frames shows the evolution of mean plasma density ρ, while the bottom-right frame represents the L_2-norm. The loss of conservation of these two quantities is not only a result of the low resolution of the grid in the momentum space, but also due to the loss of information which arises when the filamentation reaches the size of the cells in the phase space.

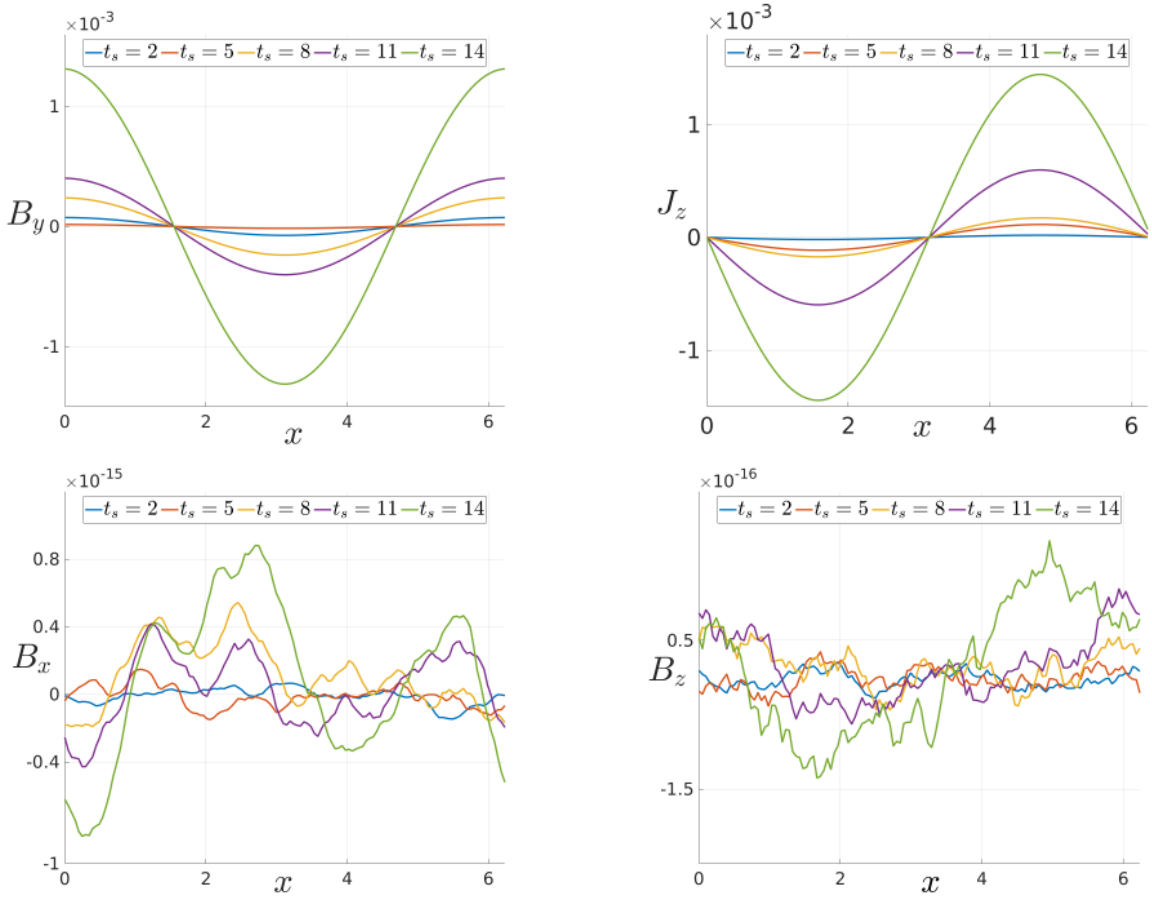

Figure 8.5: The magnetic field components and the current density along the beams' direction at different times for the second simulation for the beams propagating along the $z-$direction, and a background magnetic field along the $y-$direction. Notice that at all these times, the total energy, L_2- norm and the mean plasma density are precisely conserved (at the order of the machine epsilon).

Here comparisons have been carried out over short times for which two-stream instability can be considered as negligible.

The electric, magnetic, kinetic, and total energies are calculated from the following equations,

$$\begin{aligned} E_e &= \int \frac{\epsilon_0}{2} E^2 d\mathbf{r}, \\ E_m &= \int \frac{1}{2\mu_0} B^2 d\mathbf{r}, \\ E_k &= \int_{\mathbf{r}} \int_{\mathbf{p}} \mathbf{p}(\gamma - 1) mc^2 f d\mathbf{p} d\mathbf{r}, \\ E_t &= E_e + E_m + E_k, \end{aligned} \tag{8.6}$$

where $E^2 = E_x^2 + E_y^2 + E_z^2$, $B^2 = B_x^2 + B_y^2 + B_z^2$, and $d\mathbf{r} = dxdy$. The electric energy $E_{e,i}$, and magnetic energy $E_{m,i}$ associated with i^{th} component of the electric and magnetic fields, respectively, are given by

$$\begin{aligned} E_{e,i} &= \int_{\mathbf{r}} \frac{\epsilon_0}{2} E_i^2 d\mathbf{r}, \\ E_{m,i} &= \int_{\mathbf{r}} \frac{1}{2\mu_0} B_i^2 d\mathbf{r}, \end{aligned} \tag{8.7}$$

Here $i = x,\ y,\ z$. The mean density and the L_2 norm are calculated from the following two integrals,

$$\rho = \int_{\mathbf{r}} \int_{\mathbf{p}} d\mathbf{r} d\mathbf{p} f, \quad L_2 = \int_{\mathbf{r}} \int_{\mathbf{p}} d\mathbf{r} d\mathbf{p} f^2, \tag{8.8}$$

The total energy provides a measure of the accuracy of a simulation. An important loss of the conservation of the total energy implies , in principle, that the results of the simulation are no longer accurate. It should be however mentioned that recent results [367], involving the nonlinear dynamics of oblique modes, have suggested that a local (and essentially reversible) variation of the Casimir invariants related to the distribution function (notably, the entropy and L_2 norm) can occur in association to small scale fluctuations of f.

Figs[8.2, 8.4] show the time evolution of energies, mean density, and L_2-norm of the two simulations. As shown in the figures, the typical behavior of `CFI` instability is evident: an increase of the magnetic energy associated with a decrease of the kinetic energy (top-left frames of the two figures). This behavior is further confirmed by looking at the magnetic energy associated with the direction of the initial magnetic field ($E_{m,z}$ in the first simulation, and $E_{m,y}$ in the second). In both cases, these energies increase with the same rates, indicating the amplification of the initial magnetic field, as shown in the top-right frames of the two figures. The loss of the conservation of total energy, mean density, and L_2 norm, as shown in the bottom frames, is due to usual coarse-graining and is related to the low resolution of the grid in the momentum space ($N_{p_x} = N_{p_y} = N_{p_z} = 32$, see table 8.1).

Figs.[8.3, 8.5] show the magnetic field components at different times for both cases. It is obvious that B_z and J_y in the first simulation, and B_y and J_z in the second one, grow with time due to the mechanism explained in section 8.1. This growth goes on until the saturation of the instability. As also shown in the figures, the other components of the magnetic field are not identically zero, but we observe that they grow starting from machine epsilon. However, their values remain negligible compared to the amplified field, and can therefore be ignored.

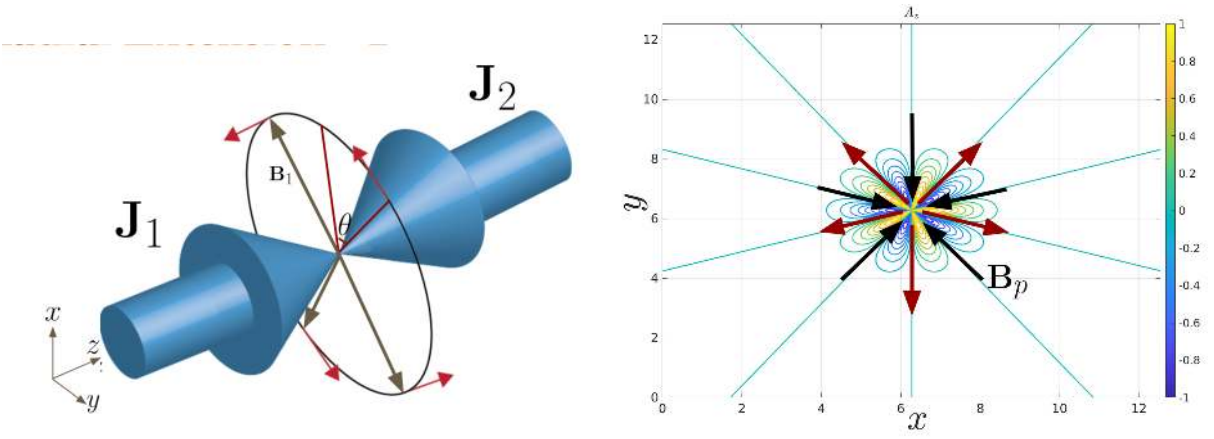

Figure 8.6: The left frame shows two counter-propagating electron beams along z direction. The initial magnetic field is periodic in θ direction, and modulated in r. The small red arrows show the wave vector of the magnetic field. On the right, we show a contour plot for the initial vector potential and magnetic field given by Eq.(8.10) and Eq.(8.11) for $m = 5$, where $\mathbf{B}_p = \sqrt{B_x^2 + B_y^2}$.

Now, we start to address the problem of two cylindrical, symmetric, counter-propagating beams in background vector potential having the same symmetry of the beams.

8.3 Simulations of Cylindrical Symmetric, Counter-Propagating Beams

In this section, we considered the `CFI`-instability of two counter-propagating electron beams having a finite radial width, which are expected to be subject to magnetic reconnection processes related to the merging of parallel oriented current beams. We are going to present the results of a set of simulations, performed with the `VLEM` code [2], and the `PIC` code (SMILEI [1]). First, we start by briefly presenting the problem. We have two counter-propagating gaussian electrons' beams along the z direction. The following equation gives the profiles of their velocities

$$\mathbf{v}_i = v_i e^{-\frac{r^2}{\sigma}} \mathbf{e}_z, \quad i = 1, 2 \tag{8.9}$$

Here $r^2 = (x - L_x/2)^2 + (y - L_y/2)^2$, where L_x and L_y are the lengths of the simulation box in x, and y directions, respectively. $\sigma = 1$ for all the simulations.

As an initial magnetic perturbation, we choose a cylindrical symmetric vector potential in z direction. The initial vector potential reads,

$$\mathbf{A} = A_z \mathbf{e}_z = cos(m\theta) e^{-\frac{r^2}{\sigma}}, \tag{8.10}$$

where $r^2 = (x - L_x/2)^2 + (y - L_y/2)^2$, $\theta = \arccos((x - L_x/2)/r)$, and m is the number of modes. This kind of configuration has been studied in Refs.[4, 5]. Our problem is invariant with respect to the z direction, which means, in terms of Hamiltonian mechanics, that the canonical momentum $P_{c,z}$ is conserved. Therefore, the problem is intrinsically `2D` with periodic boundary conditions. Given Eq.(8.10), the resulting initial components of the magnetic fields read

$$
\begin{aligned}
B_x &= -B_0\Big[\frac{2(y-L_y/2)}{\sigma}\cos(m\theta) + \frac{m(x-L_x/2)}{r^2}\sin(m\theta)\Big]e^{-\frac{r^2}{\sigma}},\\
B_y &= B_0\Big[\frac{2(x-L_x/2)}{\sigma}\cos(m\theta) - \frac{m(y-L_y/2)}{r^2}\sin(m\theta)\Big]e^{-\frac{r^2}{\sigma}},
\end{aligned}
\tag{8.11}
$$

where B_0 is the amplitude of the initial perturbation. Obviously this field is divergence-free (see Fig.8.6).

8.3.1 VLEM Simulations

In this section, we present the preliminary results of the simulations performed using VLEM2D3V code. In this case, the two initial beams have cylindrical, symmetric shape, given by Eq.(8.9), where $v_i = 0.688$ for both beams. We also perturb the two beams with an initial vector potential along the $z-$direction given by Eq.(8.10). The components of the initial magnetic fields are therefore given by Eq.(8.11), where the initial amplitude is $B_0 = 10^{-4}$. The dimension of the simulation box is $(L_x, L_y) = (4\pi, 4\pi)$, where $N_x = N_y = 256$. The grid resolution in the momentum space is $N_{p_x} = N_{p_y} = N_{p_z} = 64$ with an extension $-2 < p_i < 2,\ i = x, y, z$ in each direction in momentum space. The time step is $\Delta t = 5\times10^{-3}$, which respects the CFL conditions introduced by Yee solver.

For this configuration, the number of threads per process in VLEM2D3V code is $N_{threads} = 8$, and the total number of the MPI processes is $N_{mpi} = 256$. This corresponds to a total number of cores equal to $N_{mpi} \times N_{threads} = 2048$. The beams temperatures are $T_1 = T_2 = 2keV$.

In the top-left frame of Fig.8.7, we plot the evolution of different forms of energy. As expected, after an initial phase, we measure a decrease in the kinetic energy, associated with a growth in the electromagnetic energy at $t \sim 4$. This growth in the electromagnetic energy is due to the onset of the CFI instability, that leads to the amplification of the in-plane initial magnetic fluctuations given by Eq.(8.11). The signature of this instability, which has been detailed in the introduction of this chapter, is evident in the plots of the in-plane magnetic energies (two bottom frames of Fig.8.7) associated with the magnetic fields B_x, and B_y, where the exponential growth of these components is evidenced.

Fig.8.8 shows the profiles of the vector potential A_z (left frames), and of the current density J_z (right frames) at different times: $t = 7.5,\ 12.5,\ 15,\ 30$. At the first stage of the simulation, we observe the formation of many electrons beams, as shown in the top-left frame in Fig.8.8. However, as the dynamic evolves, beams with different directions repel each other. In contrast, those streaming in the same directions merge due to a sort of coalescence instability [368, 369, 370, 371], originating from the tendency of two current beams to attract one another when propagating in the same direction [372], which is an example of magnetic reconnection. This phenomenon, typically referred to as "magnetic annihilation", is clearly seen in the remaining frames of the vector potential and the current density. The final configuration consists of two counter-propagating, well-separated beams as shown in the bottom frames in Fig.8.8.

However, one interesting point deserves further investigation in VLEM simulation: the increase in the total energy ($\sim 23\%$) starting at $t \sim 5$, and which later decreases. In order to investigate the reasons behind this process, we performed a second simulation with a lower resolution in the momentum phase ($N_{p_x} = N_{p_y} = N_{p_z} = 32$), while all other parameters has been kept identical to those in the first simulation presented in the previous discussion.

Fig.8.9 shows the energy evolution in the two simulations. In the left-top frame, we plot the evolution of different forms of energy for the simulation with higher resolution (64 points in

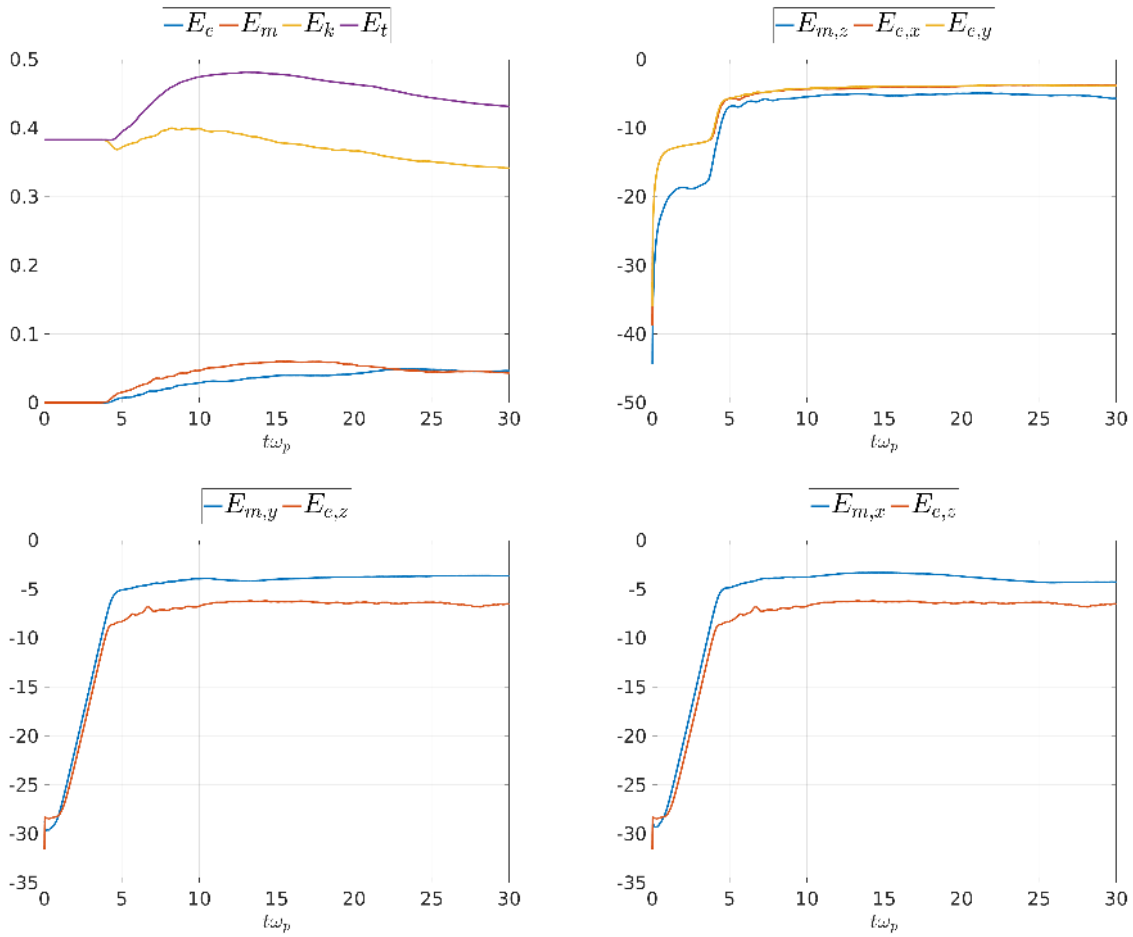

Figure 8.7: Energy conservation (top-left frame), and the evolution of the energies associated with different directions for `VLEM2D3V` simulation of the mode $m = 5$. The counterstreaming beams are gaussian (Eq.8.9), and symmetric ($n_1 = n_2$). See section 8.3.1 for the details.

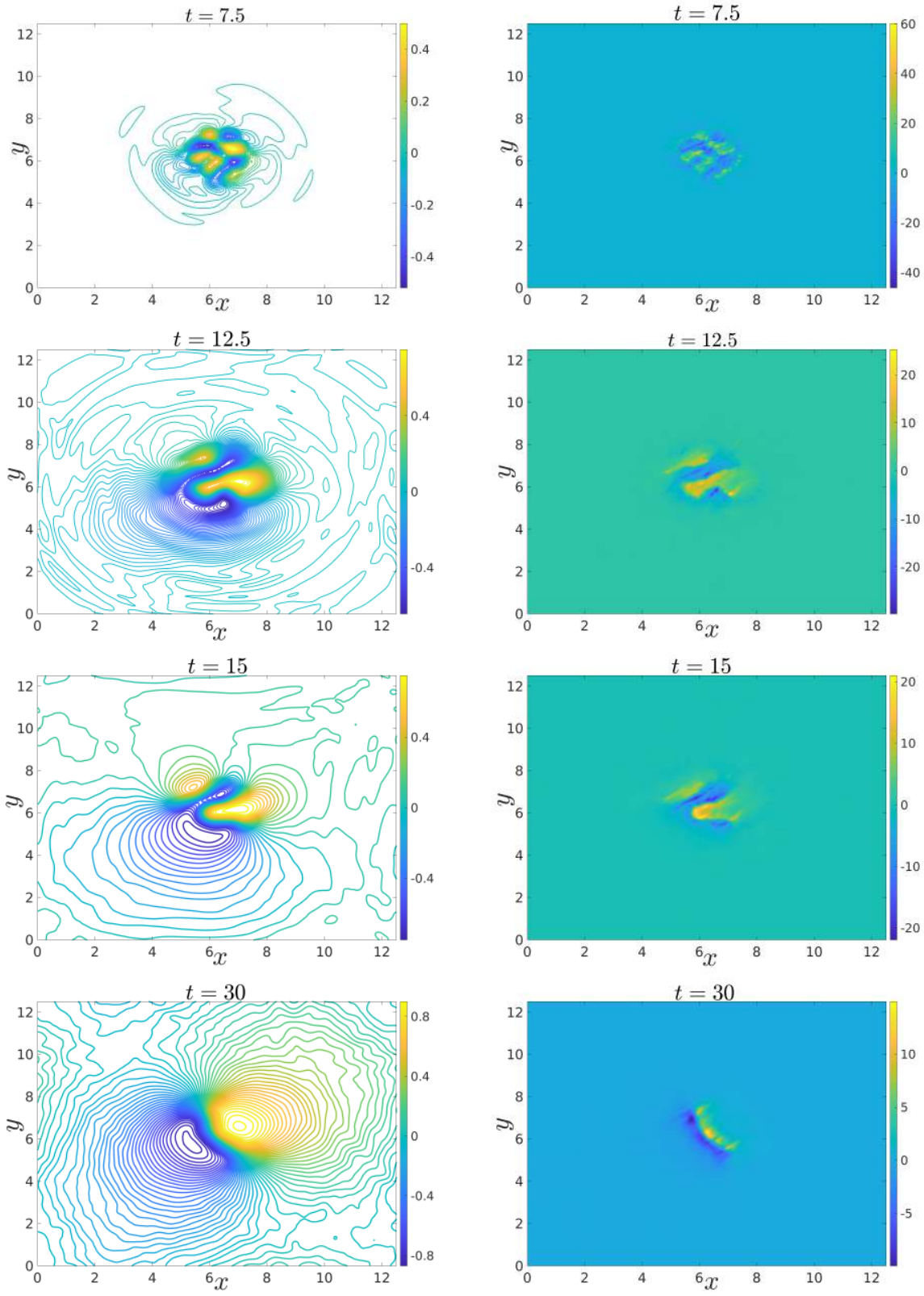

Figure 8.8: A_z (left frames), and J_z (right frames) for the `VLEM2D3V` simulation of the mode $m = 5$. The counterstreaming beams are gaussian (Eq.(8.9)), and symmetric ($n_1 = n_2$). Their velocity amplitude is $v_i = 0.688$. The reconnection events, and the formation of `X`-points, seen in the vector potential contours are due to the coalescence instability, that is the merging of the beams oriented in the same direction.

each direction of the momentum space; hereafter S_{64}); while in the left-bottom frame, we show the results of the simulation with lower resolution (32 in each direction of the momentum space; hereafter S_{32}). As shown in the figure, the growth of the total energy in S_{32} ($\sim 100\%$) is much larger than its counterpart in S_{64} ($\sim 23\%$). It is also interesting to notice that this growth in the total energy is smoother in S_{64}, and it is not associated with any sudden variation in the total density. However, the case is completely different for S_{32} where an initial decrease (of the order of 2.5%), followed by a large and sharp increase ($\sim 18\%$) in the total density have been evidenced in the right-bottom frame of Fig.8.9. Nevertheless, a further investigation of this behaviour is in fact needed to eliminate any physical process that might be responsible of it; and to also know whether this effect is purely due to the numerical methods introduced by the discretization and interpolation methods, or there are some other processes which enhance the violation of the total energy conservation. Due to time constraint, we will address this problem in future work.

Due to the complexity of the problem discussed above and to the very long time duration of any `VLEM` simulation with higher resolution, we found that it will also be useful to rely on `PIC` simulations in order to address the problem of two inhomogeneous, counterstreaming, symmetric beams. In what follows we do not intend at all to make any comparison between PIC and semi-Lagrangian codes for studying this kind of problems since this will require a precise selection of the parameters in both cases: PIC and semi-Lagrangian simulations. This comparison study deserves future investigations. Here, we limit our self in the next section to the study of the underlying physics of the problem.

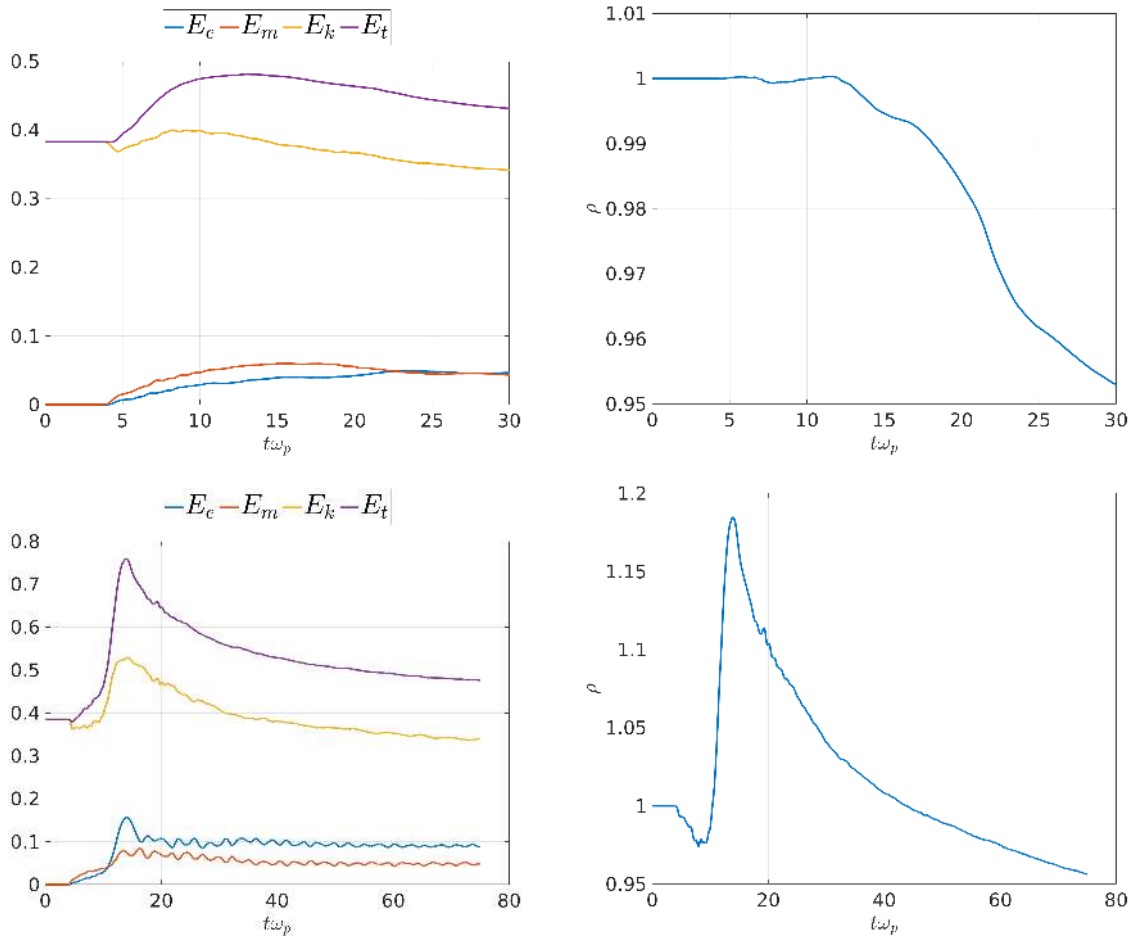

Figure 8.9: Temporal evolution of different forms of energy for two `VLEM` simulations (left frames), and of the total plasma density (right frames). The parameters are identical in the two simulations, except for the resolution in the momentum space. The resolution in the momentum space for the simulation shown in the top frames, is $N_{p_x} = N_{p_y} = N_{p_z} = 64$; while it is $N_{p_x} = N_{p_y} = N_{p_z} = 32$ for the simulation results in the bottom frames.

8.3.2 PIC Simulations

In this section, we are going to present the results of a set of simulations, performed with the PIC code (SMILEI [1]). The velocities of the beams and the vector potential are given by Eq.(8.9) and Eq.(8.10), respectively. The dimensions of the simulation box are $(L_x, L_y) = (4\pi, 4\pi)$. Table 8.2 shows the parameters of the different simulations.

The velocity in SMILEI code is normalized to the speed of light c, the charge to the electron charge e, the mass to electron mass m_e, the kinetic energy to the rest energy m_0c^2. However, SMILEI leaves open to the user the possibility to choose the reference length, depending on the problem under investigation. In our case, the reference length and time are the electron skin depth and the inverse of the electron plasma frequency, respectively. This choice of the reference frequency and length can be explicitly made in the code. For example, if one chooses the total density of the beams to be equal to the reference density n_r, defined in the code by $n_r = m_e\epsilon_0 w_r^2/e^2$, then the reference frequency ω_r will be the electron plasma frequency $\omega_{p,e}$; and the reference length, defined in the code by $L = c/\omega_r$, becomes the electron skin depth. Therefore, in the following, all times and lengths are given in units of the electron skin depth and the electron plasma frequency.

m	N_x	N_y	L_x	L_y	NPPC	IP	Δt	n_1	n_2	v_1	v_2	B_0
2	512	512	4π	4π	1024	*regular*	0.005	0.5	0.5	0.5	-0.5	5×10^{-5}
2	512	512	4π	4π	1024	*random*	0.005	0.5	0.5	0.5	-0.5	5×10^{-5}
5	512	512	4π	4π	1024	*random*	0.005	0.5	0.5	0.5	-0.5	5×10^{-5}
5	512	512	4π	4π	1024	*regular*	0.005	0.5	0.5	0.5	-0.5	5×10^{-5}
5	512	512	4π	4π	1024	*regular*	0.005	0.7	0.3	0.3	-0.7	5×10^{-5}
5	512	512	4π	4π	1024	*regular*	0.005	0.5	0.5	0.9	-0.9	5×10^{-5}

Table 8.2: The parameters of the simulations performed with PIC code (SMILEI). The simulated system involves two counter-propagating gaussian beams, with cylindrical symmetric initial vector potential. m is the the mode number. N_x and N_y are the number of cells in x and y directions, respectively. NPPC is the number of particles per cell (the total number of particles in the simulation box is $N_t = N_xN_yNPPC$). IP the initialization method of the particles' positions. n_1, n_2, v_1, v_2 are the densities and velocities of the first and second beams, respectively. Δt is the time step, and B_0 is the amplitude of the initial fields. The boundary conditions are periodic in both x and y for these simulations.

Fig.8.10 shows the evolution of the kinetic and electromagnetic energies for two simulations of the mode $m = 2$ (see table 8.2 for the details of each simulation). The only difference between these two simulations is the initialization of the particles' positions. In the first, denoted by superscript "1" in the figure, the particles' initial positions have a regular distribution inside the cells. In contrast, in the second, denoted by superscript "2" in the figure, the particles have been randomly loaded in the box at the beginning of the simulation.

As shown in the left frame of the figure, the total energy is very well conserved during the simulations. The kinetic and the electromagnetic energies of both simulations are approximately the same. Three distinct phases characterize these curves. The first one, until $t = 25$, involves a tiny increase in the electromagnetic energy due to the smooth merging of small bunches of the electrons having the same directions. This process is clearly shown in Fig.8.11. In the top-

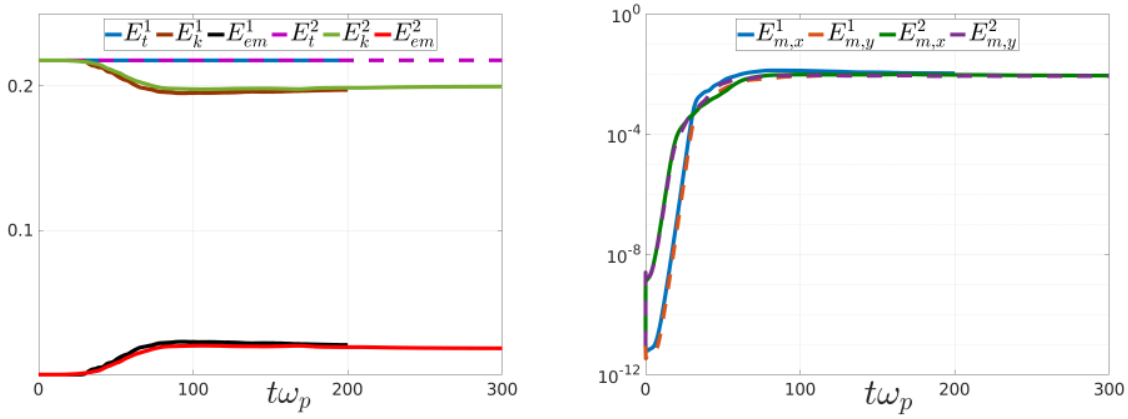

Figure 8.10: Results of two simulations for the mode $m = 2$ with different initializations of the particles' positions in PIC code. The superscripts 1 and 2 refer to the first and second simulations with regular and random initializations, respectively (see table 8.2). On the left, we show the energy conservation curves for the two simulations. As expected, they are in a very well agreement. On the right frame, we plot the electromagnetic energies associated with magnetic field components in (x-y) plane which are perpendicular to the beams direction. The growth of these fields is due to CFI instability.

right frame of this figure, we observe many small separated electrons' beams, which gradually disappear due to merging process, as shown in the middle-right and bottom-right frames of the same figure.

However, in the case with random initialization of the particles' positions, the number of merging processes is much larger than that in the "regular" case (compare the current densities of the two cases by looking at Fig.8.11 and Fig.8.13). This merging can be ascribed to the coalescence instability [368, 369, 370, 371]. Therefore, the magnetic "vortices" (or "islands", although unrelated in principle to tearing type modes) forming at the beginning of the simulation, especially for the case with the random initialization, merge to form larger islands. This merging mechanism does not involve tearing-type modes, of which no signature can be recognized.

The second phase includes a much faster increase in the electromagnetic energy, which is also associated with a decrease in the kinetic energy, meaning the conversion of the latter into the former. This growth of electromagnetic energy is due to CFI instability. The configuration of the problem is CFI unstable. The prominent signature of CFI, discussed in the introduction of this chapter, is evident in the right frame of the Fig.8.10, where we plot the electromagnetic energies associated with the magnetic field components in the perpendicular plane to the beams (in our case: (x-y) plane). The exponential growth of these components is due to CFI, where the current densities start to concentrate in the regions with the minimum values of the perpendicular field and generate a new magnetic field having the same direction of the original one, leading to its amplification (this mechanism is explained in the introduction of this chapter, and summarized in Fig.8.1). The concentration of the current density in the region with minimum magnetic field is evident when looking at Fig.8.13. In this figure, we show the evolution of the $z-$ component of the current density, and the square root of the perpendicular magnetic pressure $B_p = \sqrt{B_x^2 + B_y^2}$ at three different times ($t = 36,\ 56,\ 182$). It is apparent from this figure that the centers of maximum values of current density exist at the locations where the magnetic pressure reaches its minimum values. The same result holds for the simulations of $m = 5$ shown in Fig.8.14 and

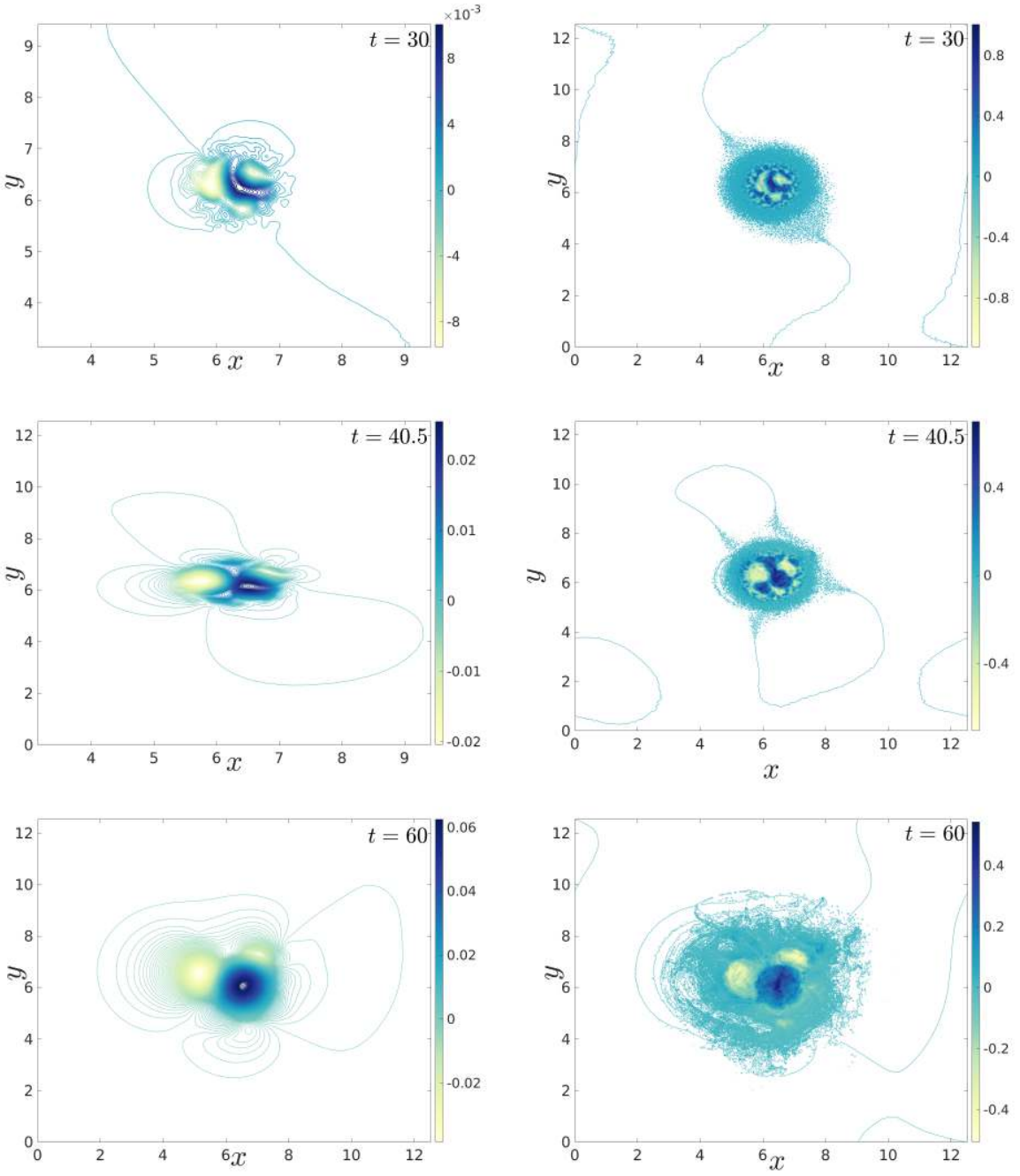

Figure 8.11: z components of the vector potential (left frames) and the current density (right frames) for a simulation of two symmetric, Gaussian, counter-propagating beams along z direction. The densities are $n_1 = n_2 = 0.5$, and the amplitude of the velocities are $v_1 = v_2 = 0.5$. The initial magnetic perturbation is cylindrical symmetric in (`x-y`) plane, with $m = 2$ and $B_0 = 5 \times 10^{-5}$. The number of particles per cell is 1024, and their positions have been randomly initialized in Smilei.

Fig.8.15 for the random and regular initialization of the particles' positions, respectively.

As a manifestation of the merging process between beams, due to the attraction/repulsion forces, we show in Fig.8.12 the trajectory of a bunch of electrons at different times. These electrons were first repelled by the two beams with opposite direction (shown in yellow color). Due to the underlying dynamics and the periodicity of the boundary conditions, this beam merges at a later time with the one which is shown in the figure as a blue colored large spot centered at the point $(8, 4)$.

The third phase is the saturation phase, where no further large variations are observed in the electromagnetic and kinetic energies. This phase starts at $t \sim 80$ in both simulations of the mode $m = 2$.

When comparing the different simulations shown in table 8.2, we can summarize our discussion of the cases considered here in three main points. The first one is the effects resulting from the initialization method of the particles' positions. We notice that in the case of symmetric gaussian beams for $m = 2$ ($n_1 = n_2,\ v_1 = v_2$), the final configuration is composed of three beams if the positions' initialization is random, as shown in Fig.8.11. Then, these beams, as shown in Fig.8.12, move far from each due to the mutual forces and the boundary conditions. In contrast, if the initialization of the particles' positions is regular, the simulation of $m = 2$ ends with two beams, as shown in Fig.8.13, where we plot $B_p = \sqrt{B_x^2 + B_y^2}$ (left frames), and the current density (right frames) at times $t = 36,\ 56.\ 182$.

The previous discussion implies that the initialization method of the particles' positions influences the final configuration of the system. This effect is also evident for the simulations of $m = 5$ as shown in Fig.8.14 and Fig.8.15 for random and regular initializations, respectively (see table 8.2 for the details of these simulations). In Fig.8.14, we show the vector potential (left frames), the current density (middle frames), and B_p (right frames) at three different times ($t = 42,\ 78,\ 180$). It is obvious in this case that the final configuration consists of two counterstreaming beams localized at the locations of the minimum magnetic pressure (see the right frames of the figure). In contrast for the case with regular initialization, Fig.8.15 shows the vector potential (left frames), current density (middle frames), and B_p at three different times ($t = 42,\ 78,\ 180$). Here, we observe that at $t = 42$, four distinct beams forms, and the subsequent dynamics of these beams evolve in accordance with their mutual forces, and the boundary conditions.

The second point concerns the consequences of the boundary conditions, which are periodic in our simulations. Fig.8.17 shows the mechanisms by which the periodicity of the boundary conditions affects the problem. In this figure, we plot the z component of the current density at $t = 180$ for the simulation of the mode $m = 2$, and with random initialization of the particles' positions. As shown in the figure, the periodicity of the boundary conditions, combined with the random initialization lead to a configuration, where any further merging between beams needs very long time to take a place. This configuration is completely determined by the mutual forces between the beams, which are shown in the figure as arrows pointing in the direction of the forces and whose lengths reflect the amplitude of the force, and boundary conditions. This result of obtaining different final configurations, depending on the initialization method of the particles' positions and on the boundary conditions, needs further investigation in order to identify the reasons responsible of it, which can depend on the initialization method, the number of particles per cell, and/or on the initial perturbation.

The third point concerns the case of non-symmetric gaussian beams, shown in the left frame of Fig.8.16. In this frame, we plot the current density of two non-symmetric counter-propagating beams ($n_1 = 07,\ v_1 = 0.3,\ n_2 = 0.3$, and $v_2 = -0.7$), where we observe the formation of four

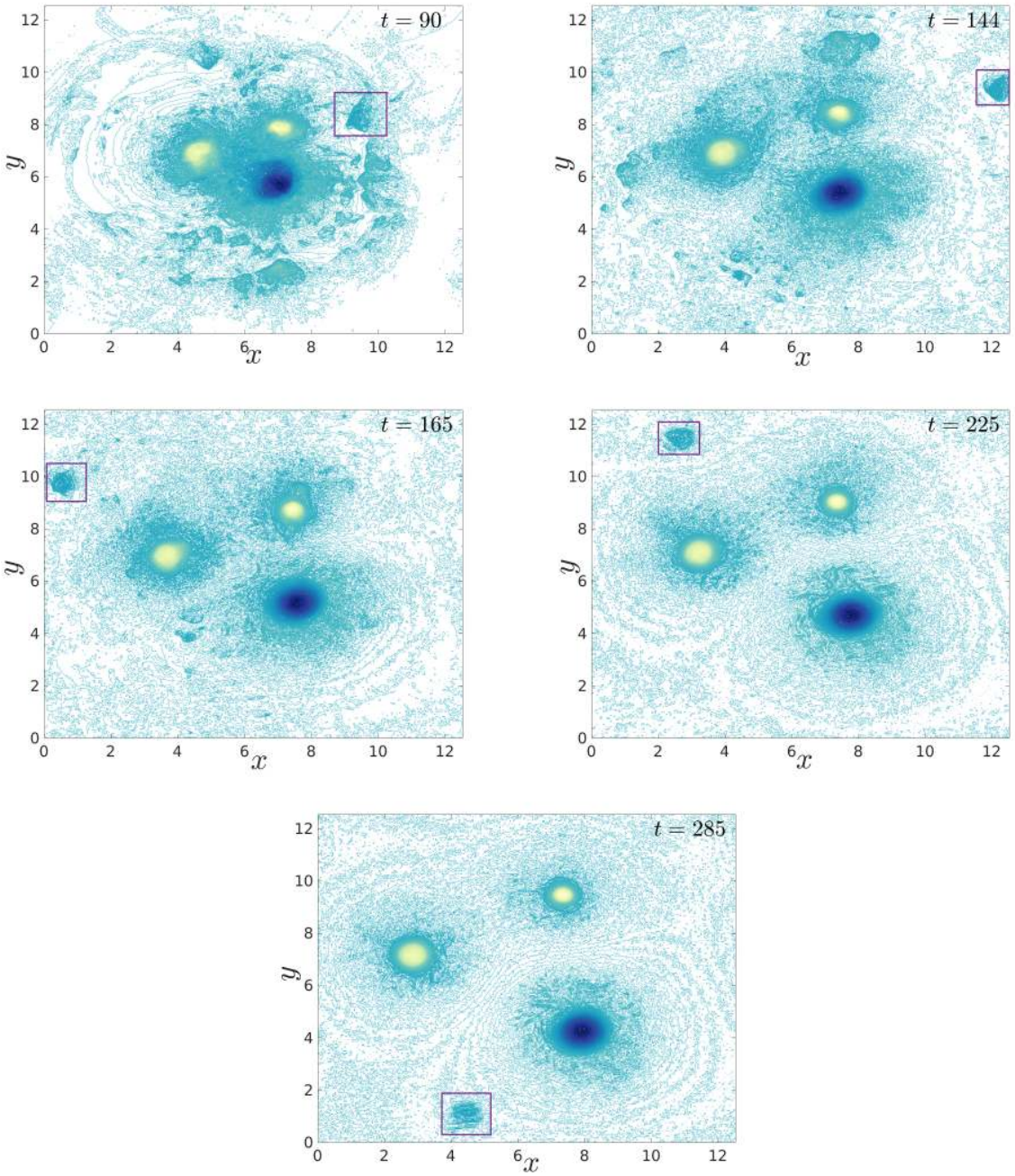

Figure 8.12: z component of the current density at different times for the simulation of two symmetric, gaussian, counter-propagating beams along z direction (the same parameters of Fig.8.11). The trajectory of a bunch of electrons, encircled by purple square, and flowing in the positive direction of z axis is shown. This electron beam feels a repulsive force due to the interaction with the two "stronger" beams (shown in light yellow) and therefore drifts, due to the attraction force, toward the third one (shown in blue at $x = 8,\ y = 5$), until it merges with it at a later time.

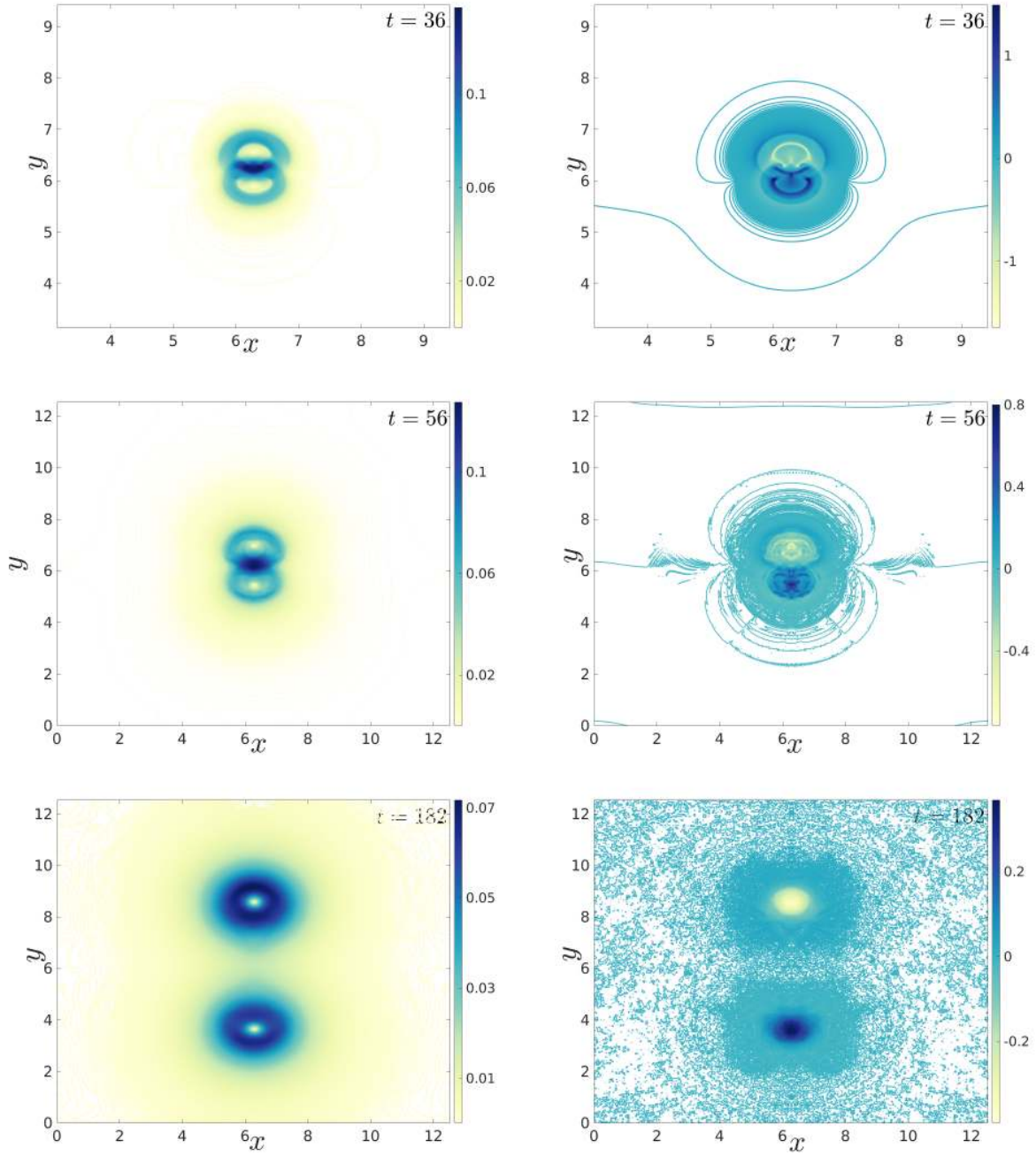

Figure 8.13: Results of the simulation for $m = 2$ with regular initialization of the particles' positions at three different times, $t = 36,\ 56,\ 182$. On the left frames, we plot $B_p = \sqrt{B_x^2 + B_y^2}$, while the evolution of the current density is shown on the right frames. See table 8.2 for other parameters of the simulation.

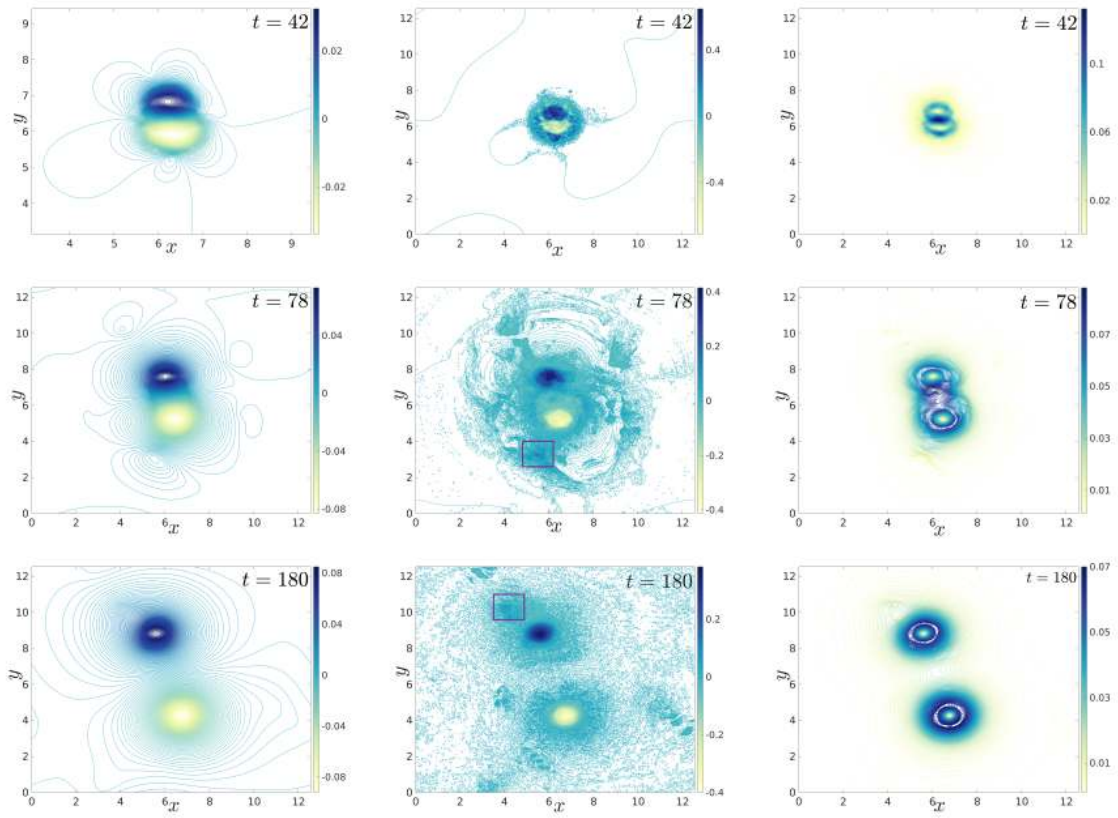

Figure 8.14: Results of the simulation for $m = 5$, with random initialization of the particles' positions at three different times, $t = 42,\ 78,\ 180$. Vector potential, current density, and the $B_p = \sqrt{B_x^2 + B_y^2}$ are shown on the left, the middle, and the right frames, respectively. In the frames of the current density we also show the trajectory of a bunch of electrons towards its final destination, where it merges with the upper beam due to the attraction force resulting between two currents propagating in the same direction. See table 8.2 for other parameters of the simulation.

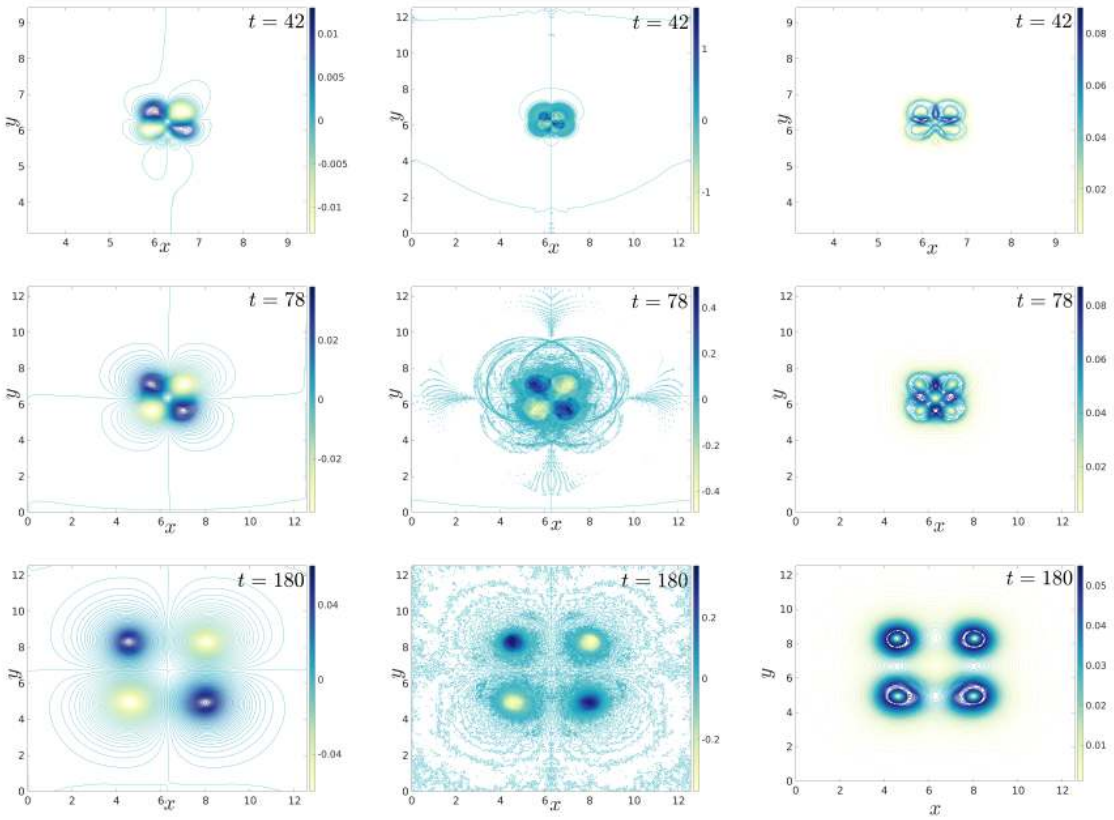

Figure 8.15: Results of the simulation for $m = 5$, with "regular" initialization of the particles' positions (i.e., symmetrically distributed in space) at three different times, $t = 42,\ 78,\ 180$ (same times in Fig.8.14). Vector potential, current density, and $B_p = \sqrt{B_x^2 + B_y^2}$ are shown in the left, the middle, and the right, respectively. See table 8.2 for other parameters of the simulation.

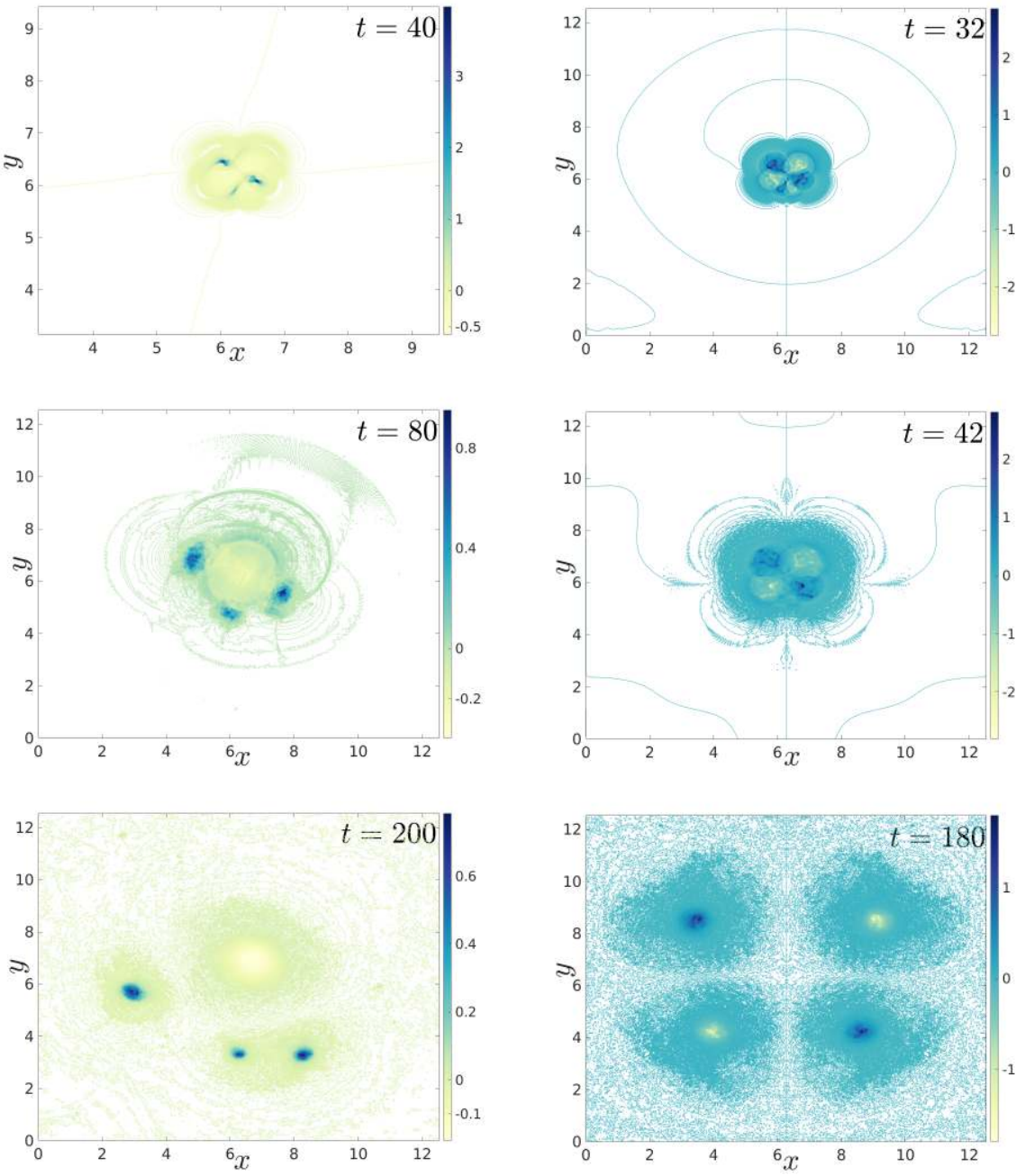

Figure 8.16: z components of the current densities resulting from two different simulations at different times ($t = 40,\ 80,\ 200$ for the left frames, and $t = 32,\ 42,\ 180$ for the right ones). To the left, we plot the current density of the simulation for $m = 5$ and non-symmetric gaussian beams ($n_1 = 0.7,\ v_1 = 0.3$, and $n_2 = 0.3,\ v_2 = -0.7$). In the right frames, we show the current density of the simulation with symmetric, gaussian beams, but with much larger relativistic velocity ($v = 0.9c$). The initialization of particles' positions are regular in both simulations. See table 8.2 for other parameters of these two simulations.

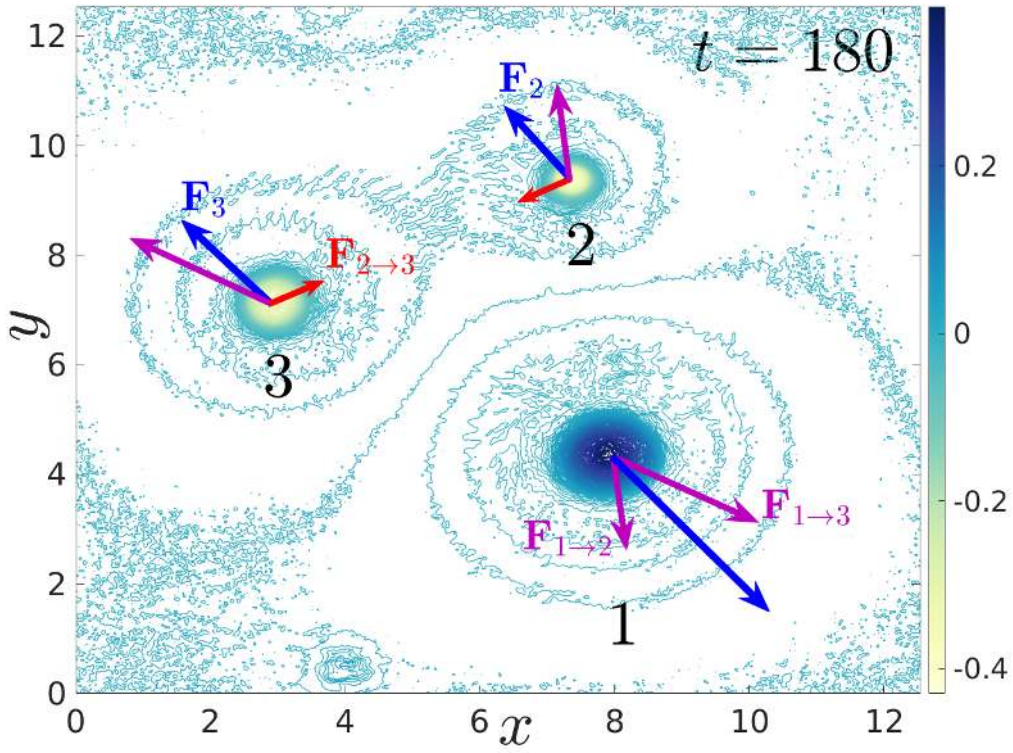

Figure 8.17: Forces between different beams for the simulation of symmetric gaussian beams of the mode $m = 2$, and random initialization of the particles' positions. As shown in the figure, the attraction force between beams 2 and 3 ($\mathbf{F}_{2\to3}$) is not sufficient to overcome the repulsive forces $\mathbf{F}_{1\to2}$ and $\mathbf{F}_{1\to3}$ between these beams, and first one, respectively. This fact, combined with the periodicity of the boundary conditions led to this configuration. A final configuration with only two counter-propagating beams can take a very long time to occur for this case. See table 8.2 for other parameters of these two simulations.

beams, three of them in the same directions, although the initial distribution of the particles is regular (those three beams correspond to the second particles with the initial velocity $v_2 = -0.7$). However, this point, which is similar to that mentioned above, also requires further investigation to understand the reason leading to these different nonlinear phases. Aiming to understand this effect, we started different sets of large simulations in some of which we increased the number of particles per cell, while in other we keep the same parameters, but we perform longer simulations to investigate the long term dynamics of these separated beams (where it is expected for those of the same direction to merge although this can take a very long time). Hopefully, by the time I defend this PhD work, we will have the answer to this problem.

8.4 Simulations of Homogeneous-Symmetric Beams: Tearing Mode vs CFI

In this section we are going to focus on studying the case of two counter-propagating, homogeneous ($n_i = const$, $v_i = const$), symmetric ($n_1 = n_2$, $v_1 = v_2$) beams in a background equilibrium, which is unstable to tearing modes. We start by presenting the simulations performed using `PIC` code (`SMILEI`), and then the preliminary results of the semi-Lagrangian code: `VLEM2D3V`. This kind of configuration has been already studied in the past by Califnao te al. [363], and this will be the first step for studying new configurations in which the beams might be non-symmetric, and highly relativistic.

The beams in both type of simulations propagate in the $z-$direction inside a `2D` box with dimensions $(L_x, L_y) = (2\pi, 2\pi)$. The initial background magnetic field is composed of two parts. The first one is an $x-$dependent field along y, allowing the `CFI` instability, which will be amplified due to the involved mechanism in this instability. The second part, is a divergence-free magnetic noise (B_n), that allows the development of magnetic reconnection. The background field reads,

$$\mathbf{B} = B_n \sum_{i,j} \sin(k_x x + k_y y + \varphi_{i,j})\mathbf{e}_x + \Big[B_0 \sin(x) - B_n \sum_{i,j} \sin(k_x x + k_y y + \varphi_{i,j}\Big]\mathbf{e}_y, \qquad (8.12)$$

where $\varphi \in [0, 2\pi]$ is a random phase. For `PIC` simulations, the number of `MPI` process (N_{mpi}) used in each simulation is 1024 with one thread per one `MPI` process. The particles' positions have been initialized with regular distribution inside each cell. In contrast, the number of threads per process in `VLEM2D3V` code is $N_{threads} = 8$, and a total number of processors $N_{mpi} = 256$. This corresponds to a total number of cores equals to $N_{mpi} \times N_{threads} = 2048$.

8.4.1 Results of PIC Simulations

In this section, we present the results of three `PIC` simulations to investigate the importance of both the beams' velocity and the amplitude of the background magnetic noise. The different parameters of these simulations are shown in table 8.3.

Simulation	N_x	N_y	`NPPC`	Δt	n_1	n_2	v_1	v_2	B_0	B_n
S_1	512	512	1024	0.005	0.5	0.5	0.4	-0.4	10^{-3}	5×10^{-6}
S_2	512	512	1024	0.005	0.5	0.5	0.4	-0.4	10^{-3}	10^{-7}
S_3	512	512	1024	0.005	0.5	0.5	0.9	-0.9	10^{-3}	5×10^{-6}

Table 8.3: The parameters of the simulations performed using PIC code (`Smilei`). This initialization implies a total number of macro-particles equal to 2.68×10^8 inside the simulation box.

In Fig.8.18, we plot the evolution of the different forms of energy, and the pressure tensor components as a function of time in the left and right frames, respectively (S_1 on the top, S_2 in the middle, and S_3 in the bottom). While in Fig.8.19 and Fig.8.20, we show the contour plots of A_z, J_z, $B_p = \sqrt{B_x^2 + B_y^2}$, and B_y at different times for the simulations S_1 and S_2, respectively.

As expected for the three simulations, we observe in Fig.8.18 that, after a first slow phase, a large decrease in the kinetic energy, associated with exponential growth in the electromagnetic

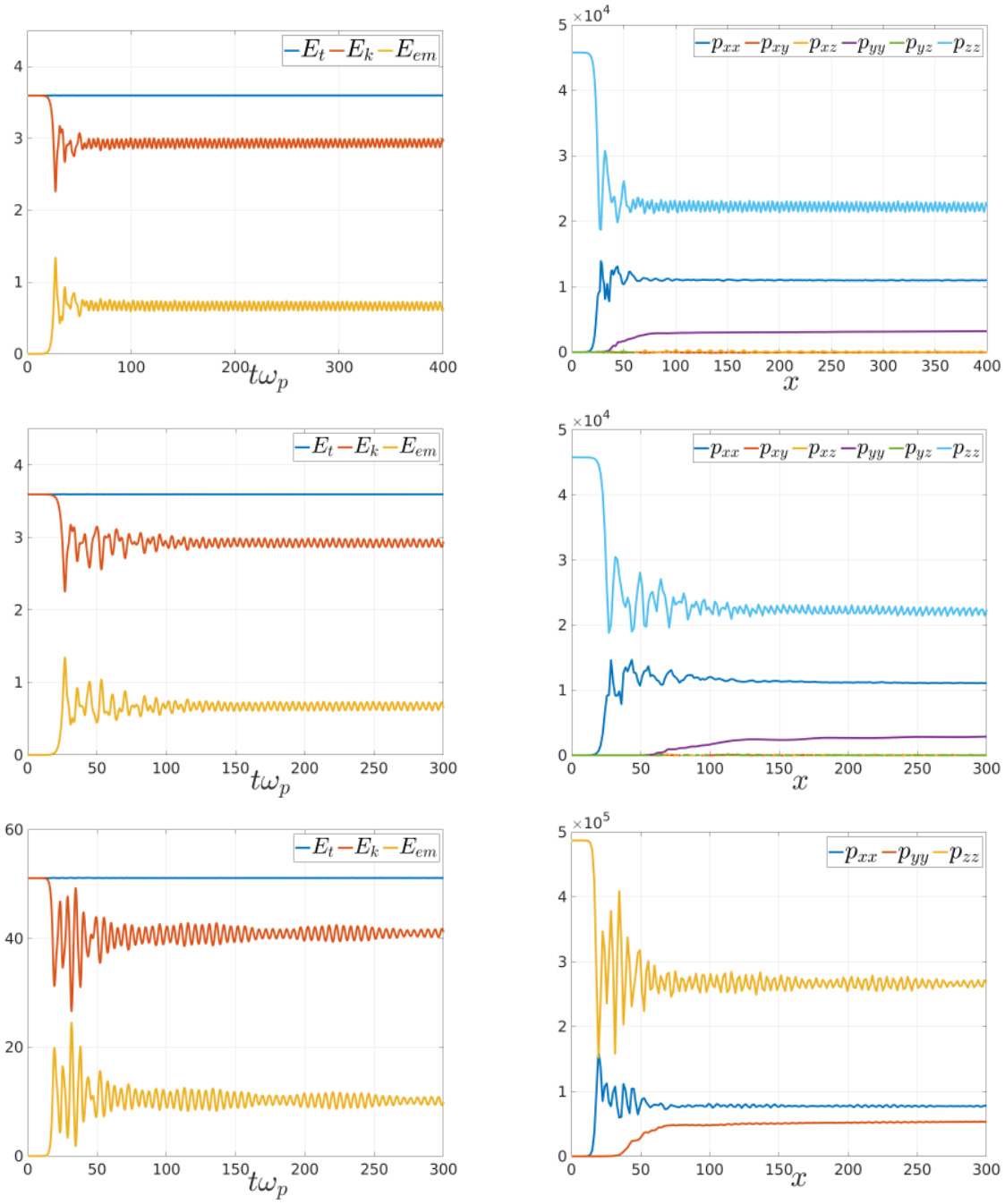

Figure 8.18: Energy conservation (left frames), and the evolution of different pressure tensor components as function of time (right frames). Simulations, S_1, S_2, and S_3, are shown in the top, the middle, and the bottom frames of the figure, respectively. The only difference between simulations S_1 and S_3 is the value of the velocity, which equals to $v = 0.4c$ in the S_1, and $v = 0.9c$ in S_3. On the another hand, the difference between S_1 and S_2 is the amplitude of the background noise magnetic field. In S_1, it equals to $B_n = 5 \times 10^{-6}$, while in S_2, $B_n = 10^{-7}$, which is 50 times smaller than its value in S_1. All other parameters of the simulation are shown in table 8.3

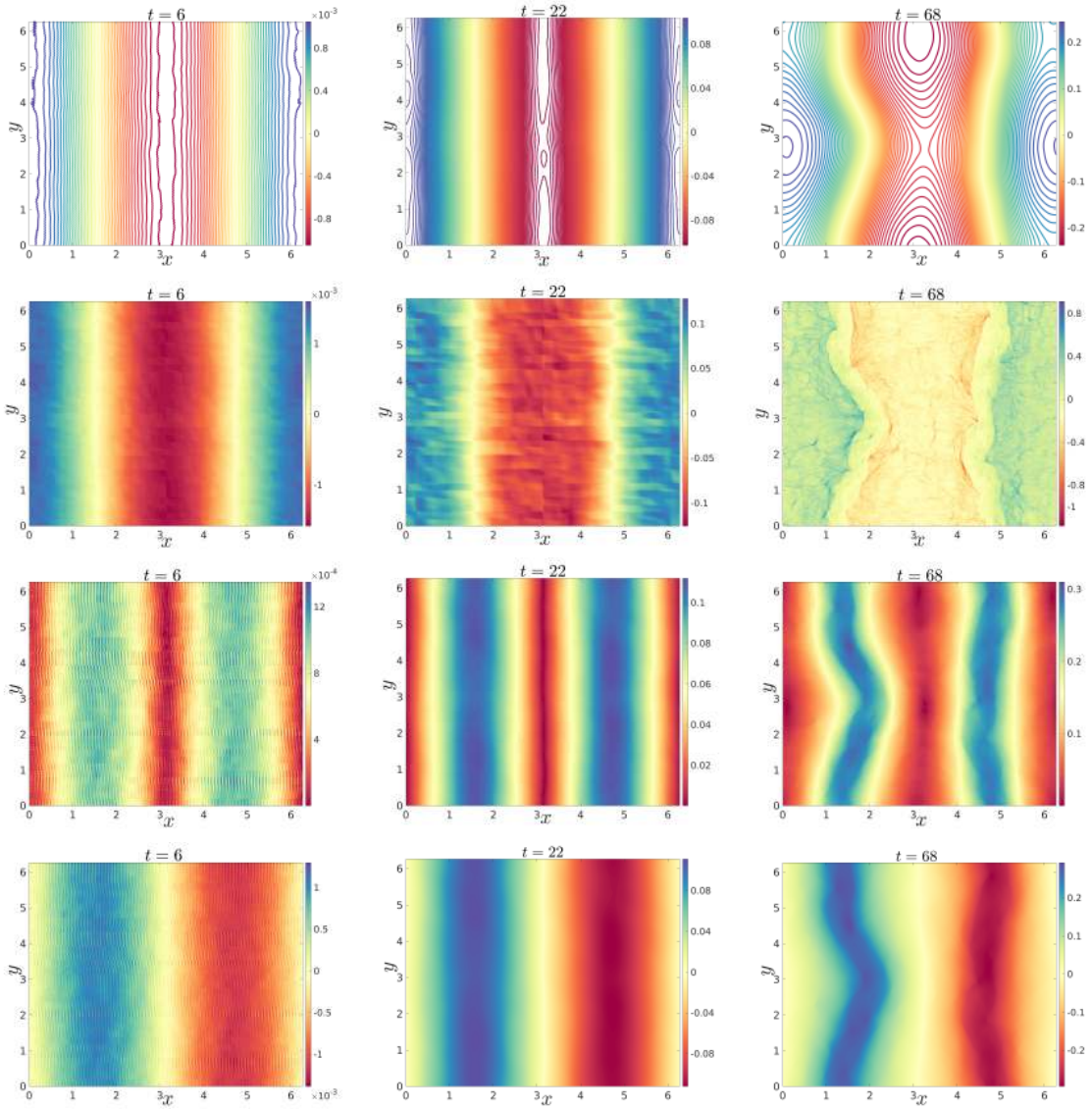

Figure 8.19: A_z (top frames), J_z (second frames), $B_p = \sqrt{B_x^2 + B_y^2}$ (third frames), and B_y (bottom frames) profiles at different times of the simulation S_1, where the background magnetic perturbation is $B_n = 5 \times 10^{-6}$. All other parameters of the simulation are shown in table 8.3

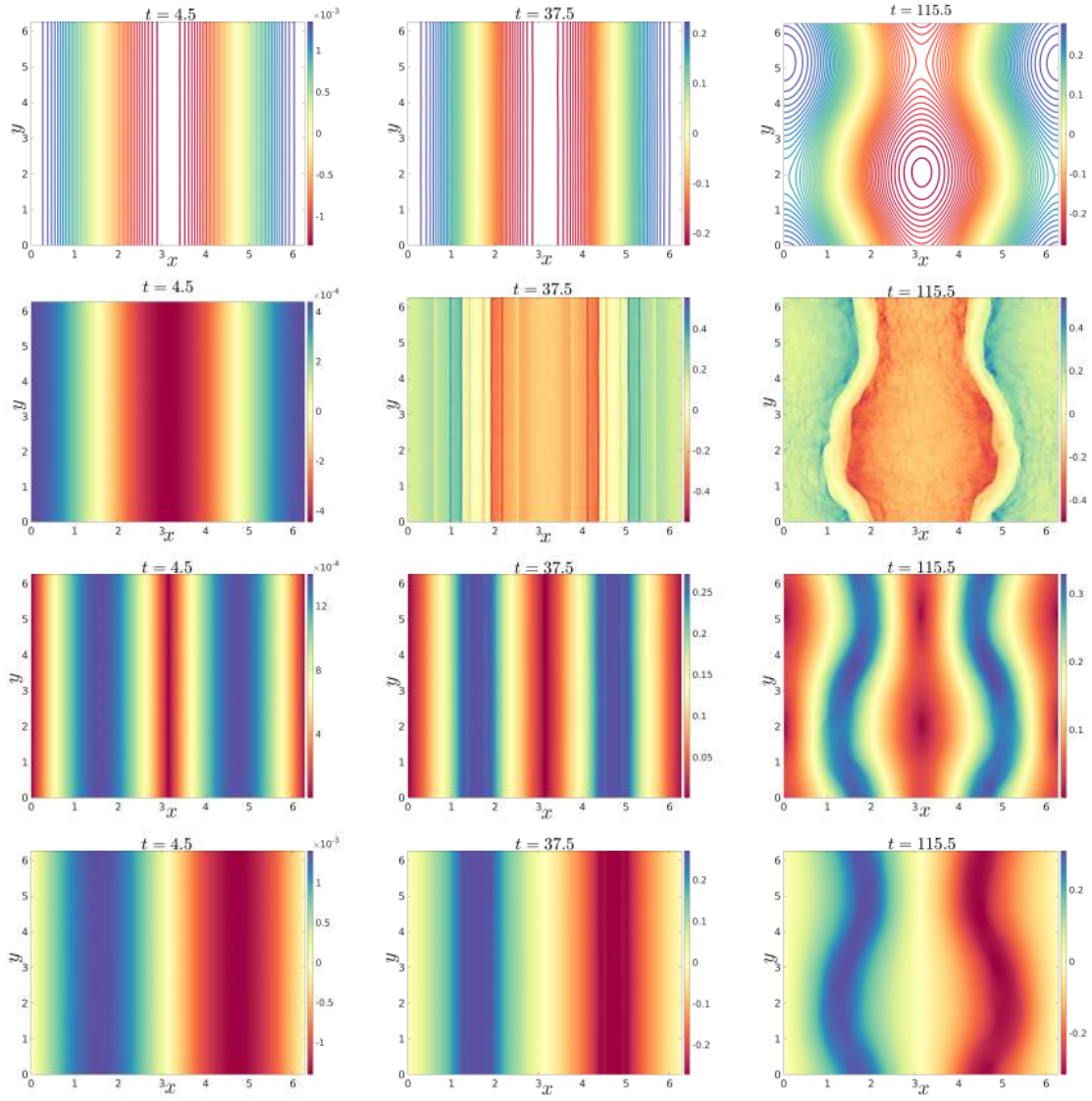

Figure 8.20: A_z (top frames), J_z (second frames), $B_p = \sqrt{B_x^2 + B_y^2}$ (third frames), and B_y (bottom frames) profiles at different times of the simulation S_2, where the background magnetic perturbation is $B_n = 10^{-7}$, which is 50 times smaller than that in simulation S_1. All other parameters of the simulation are shown in table 8.3

energy (the typical behaviour of CFI instability). This phase includes the conversion of the kinetic energy of the particles into magnetic energy and is shown as amplification in the initial magnetic field along y direction (see, for example, the B_y plotted in the bottom frames of Fig.8.19, where this amplification effect of the field is clear). However, it is not possible, with this type of initialization, to definitely tell if any reconnection event has been occurred by just looking at energy conservation curves, due to the fact that the instabilities may compete even in their respective liner stages. Other signatures must be then sought. Still, one can look at the vector potential, at the in-plane velocity field (which are expected to form hyperbolic patterns around reconnecting X-points), and at the evolution of the pressure tensors components to search for any sign of magnetic reconnection related to tearing-type instabilities.

In terms of the pressure tensor, which measures the spatially averaged kinetic energy, the three simulations we have performed start with an initial configuration having $T_{zz} \gg T_{xx} \sim T_{yy}$, where the pressure is calculated using $\mathcal{P}_{ij} = m_e n \int v_i p_j f d\mathbf{p}$, where $i, j = x, y, z$, and $T_{ii} = \mathcal{P}_{ii}/nk_B$ in dimensional units. As explained in the introduction, CFI instability works on restoring the isotropicity of the temperatures by converting a part of the particles' kinetic energy to magnetic energy. Therefore, this temperature anisotropy will be reduced due to the onset of CFI instability. This effect is evident when looking at the pressure tensor components' curves on the right frames of Fig.8.18. In the results of the three simulations, we observe a growth in the x component of the pressure tensor ($\mathcal{P}_{xx}$) associated with a decrease of $\mathcal{P}_{zz}$, leading to reduce the anisotropy in the non-linear phase of the CFI instability.

However, the reconnection and CFI processes occur simultaneously in the simulations S_1, and S_3. In both simulations, we observe a growth in the pressure tensor component $\mathcal{P}_{yy}$ starting at time $t \sim 30$, as shown in the right frames of Fig.8.18. This simultaneous developments of both instabilities can be clearly evidenced in the contour plots of the fields, as shown in Fig.8.19 for the simulation S_1. In the top frames of this figure, we plot the vector potential at three different times ($t = 6,\ 22,\ 68$). The formation of a magnetic island can be observed in the early stages of the simulation, where the CFI instability does not yet reach its saturation level. This observation is evident when looking at the evolution of the magnetic field component B_y shown in the bottom frames of Fig.8.19 (Compare B_y at times $t = 22$, and $t = 68$ where the saturation is reached with a well defined magnetic island).

To further investigate the simultaneous development of the two instabilities, we performed another simulation (S_2) in which the value of the background magnetic noise is 50 times smaller than its value in S_1 ($B_{n,S_2} = B_{n,S_1}/50 = 10^{-7}$). The temporal evolution of energy and pressure tensor components of S_2 are shown in the middle frame of Fig.8.18. As expected the sharp variations in both $\mathcal{P}_{zz}$ and $\mathcal{P}_{xx}$ start the same time compared to the simulation S_1 since they are due to the onset of CFI instability which seeds the B_y component of the magnetic field whose initial value remains the same in the two simulations. However, the situation is completely different for the component $\mathcal{P}_{yy}$. In the simulation S_2, $\mathcal{P}_{yy}$ growth starts at larger time compared to that in S_1, and it reaches its saturation level much slower in the simulation S_2. It is also evident that the saturation value is smaller in S_2 since the magnetic field which seeds the reconnection is smaller ($B_{n,S_2} \ll B_{n,S_1}$).

The previous discussion suggests that the formation of the magnetic island in S_2 will start after the saturation of B_y due to CFI instability, or, at least, at later time compared to the simulation S_1. In Fig.8.20, we present the results of the simulation S_2, where we show the contour plots of the fields A_z, J_z, B_p, and B_y at three different times ($t = 4.5,\ 37.5,\ 115.5$). The effects of the CFI instability are evident in the figure. On the one hand, we observe the growth of the magnetic field component B_y due to this instability, as shown in the three bottom frames of the figure. On the another hand, the concentration of the current density in the regions of

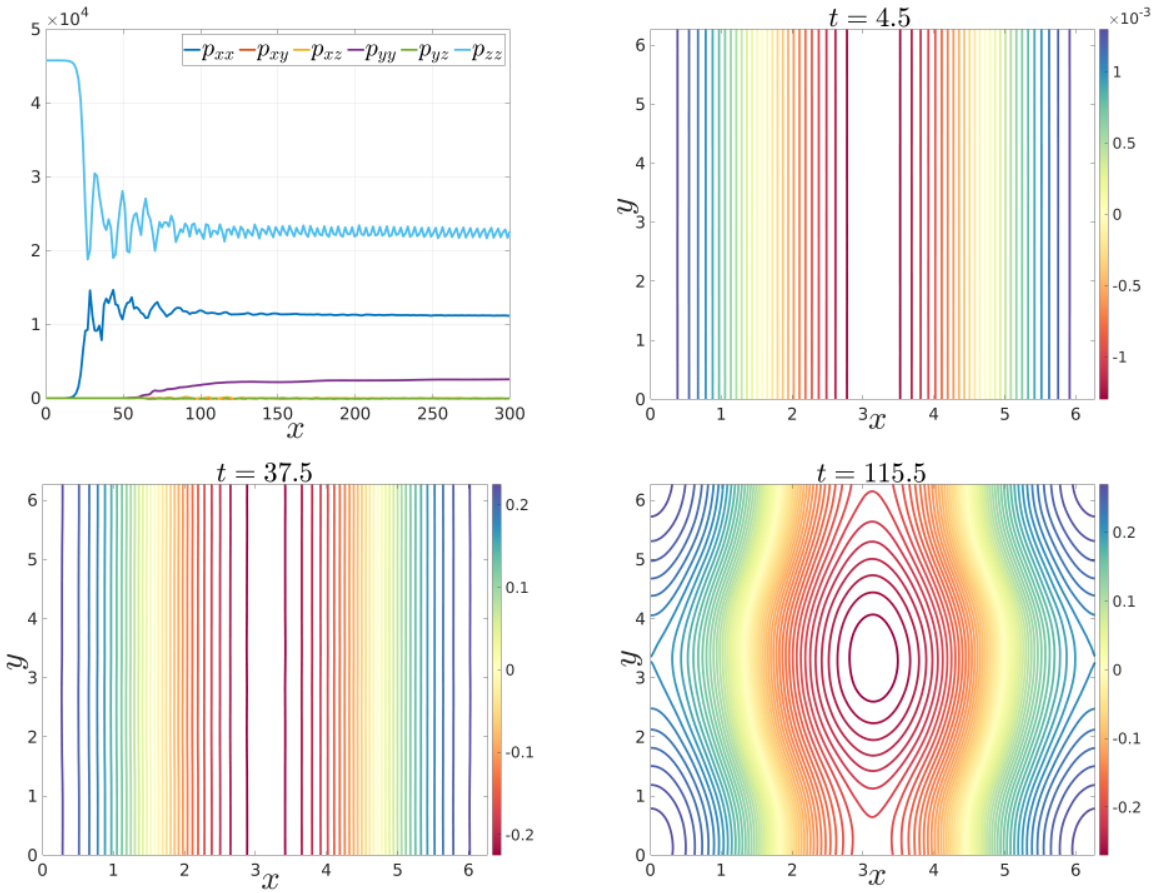

Figure 8.21: The evolution of the pressure tensor components (top-left frame), and the vector potential at three different times ($t = 4.5,\ 37.5,\ 115.5$). The only difference between this simulation and S_2 is the number of the macro-particles per cell, which equals to 1.1×10^9 in S_4, three times larger than its value in S_2.

the smallest magnetic pressure ($B_p^2 = B_x^2 + B_y^2$) is also evidenced in the profiles of the current density and B_p (the second, and the third frames from the top in Fig.8.20, respectively).

By looking at the middle frames ($t = 37.5$), it is obvious that B_y reaches its saturation value (compare B_y for $t = 37.5$ and $t = 115.5$) without the formation of any magnetic island (see the profile of vector potential at the top-middle frame). This means that any additional reduction in the background magnetic noise B_n will further delay the formation of the magnetic island.

Finally, to confirm our previous results, and also showing the effects of changing the number of macro-particles per cell, we perform another simulation (S_4) with identical parameters to those of S_2, except that the number of particles per cell is now 4096, that is four time larger than that in S_2. This leads to a total number of macro-particles equals to $\sim 1.1 \times 10^9$ inside the simulation box. Other parameters of the simulation are shown in table 8.4.

Fig.8.21 shows the results of the simulation S_4. In the top-left frame, we plot the evolution of the pressure tensor components, where they show identical behaviours and values compared to their counterparts in the simulation S_2 (the middle frame in Fig.8.18). Therefore, increasing the number of particles per cell has negligible effects on the evolution of the pressure tensor components. This is also correct for the vector potential and the remaining fields. However,

Simulation	N_x	N_y	NPPC	Δt	n_1	n_2	v_1	v_2	B_0	B_n
S_4	512	512	4096	0.005	0.5	0.5	0.4	-0.4	10^{-3}	10^{-7}

Table 8.4: The parameters of the simulation S_4. This initialization implies a total number of macro-particles equals to $1073741824 \sim 1.1 \times 10^9$ inside the simulation box.

we can observe that the location of the X-point change. In Fig.8.21, we also present the A_z profiles at three different times for the simulation S_4 ($t = 4.5,\ 37.5,\ 115.5$). It can be noticed, by looking at Fig.8.21 and Fig.8.20, that the values and the profiles of the vector potential are approximately the same in both simulations S_2 and S_4. Hence, we conclude that 1024 particles per cell are sufficient to study the cases we discussed in this section.

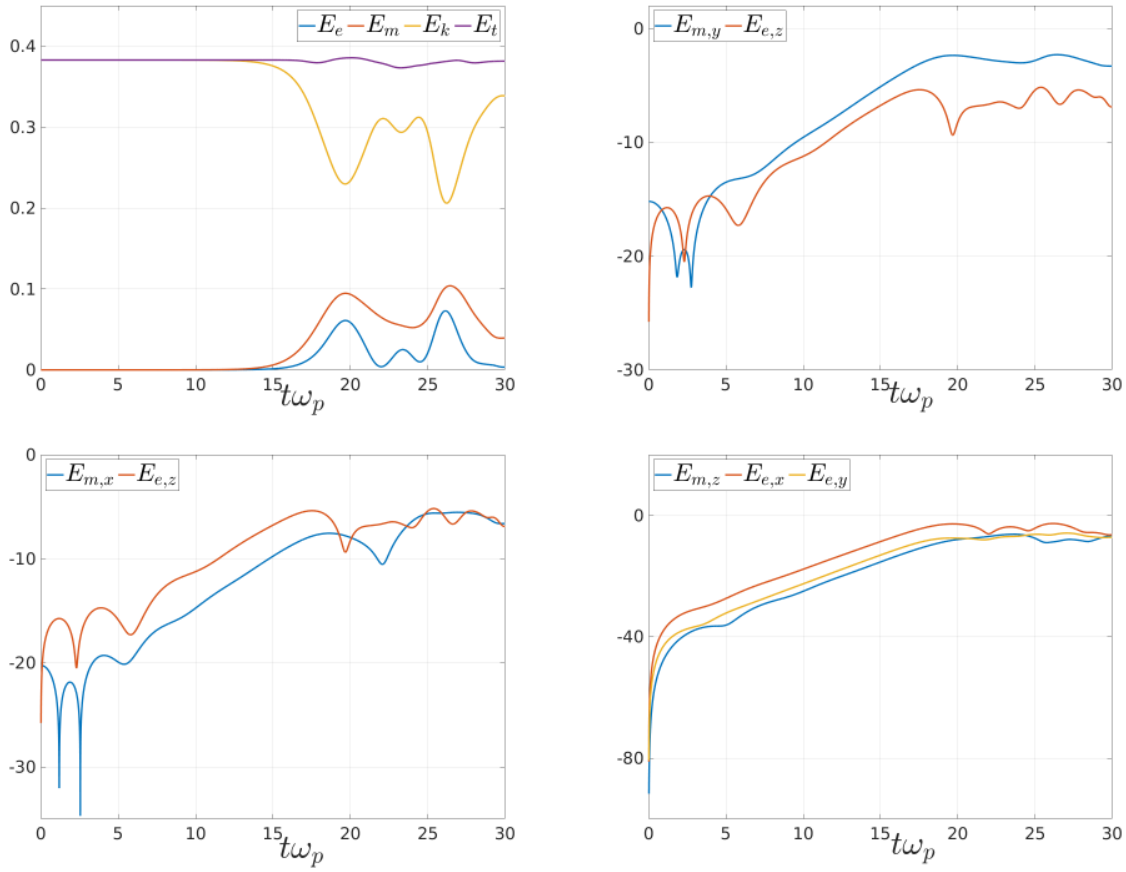

Figure 8.22: Energy conservation (top-left frame), and the evolution of the energies associated with different directions for `VLEM2D3V` simulation. see section 8.4.2 for details.

8.4.2 `VLEM2D3V` Semi-Lagrangian Simulation

In this section, we present the preliminary results of `VLEM2D3V` simulations for an initial magnetic field given by Eq.(8.12), where $B_0 = 10^{-3}$, and $B_n = 5{\times}10^{-6}$. The beams in `VLEM2D3V` simulation we present here propagate along $z-$direction. They are symmetric, homogeneous ($n_1 = n_2 = 0.5$, and $v_1 = 0.689,\ v_2 = -0.689$), and are assumed to be cold ($T_1 = T_2 = 2KeV$). The remaining parameters of the simulation are shown in table 8.5.

N_x	N_y	N_{p_x}	N_{p_y}	N_{p_z}	n_1	n_2	p_1	p_2	dt	B_0	B_n
256	256	64	64	64	0.5	0.5	0.95	-0.95	0.008	10^{-3}	5×10^{-6}

Table 8.5: The parameters of `VLEM2D3V` simulation for two counter-propagating symmetric, homogeneous beams.

In Fig.8.22, we plot the evolution of different forms of energy as function of time. In the top-left frame, we show the total, kinetic, magnetic, and electric energies in violet, yellow, orange, and blue colours, respectively. As expected, a growth of the magnetic energy, associated with decreasing kinetic energy, is evident due to the onset of the `CFI` instability. The amplification of

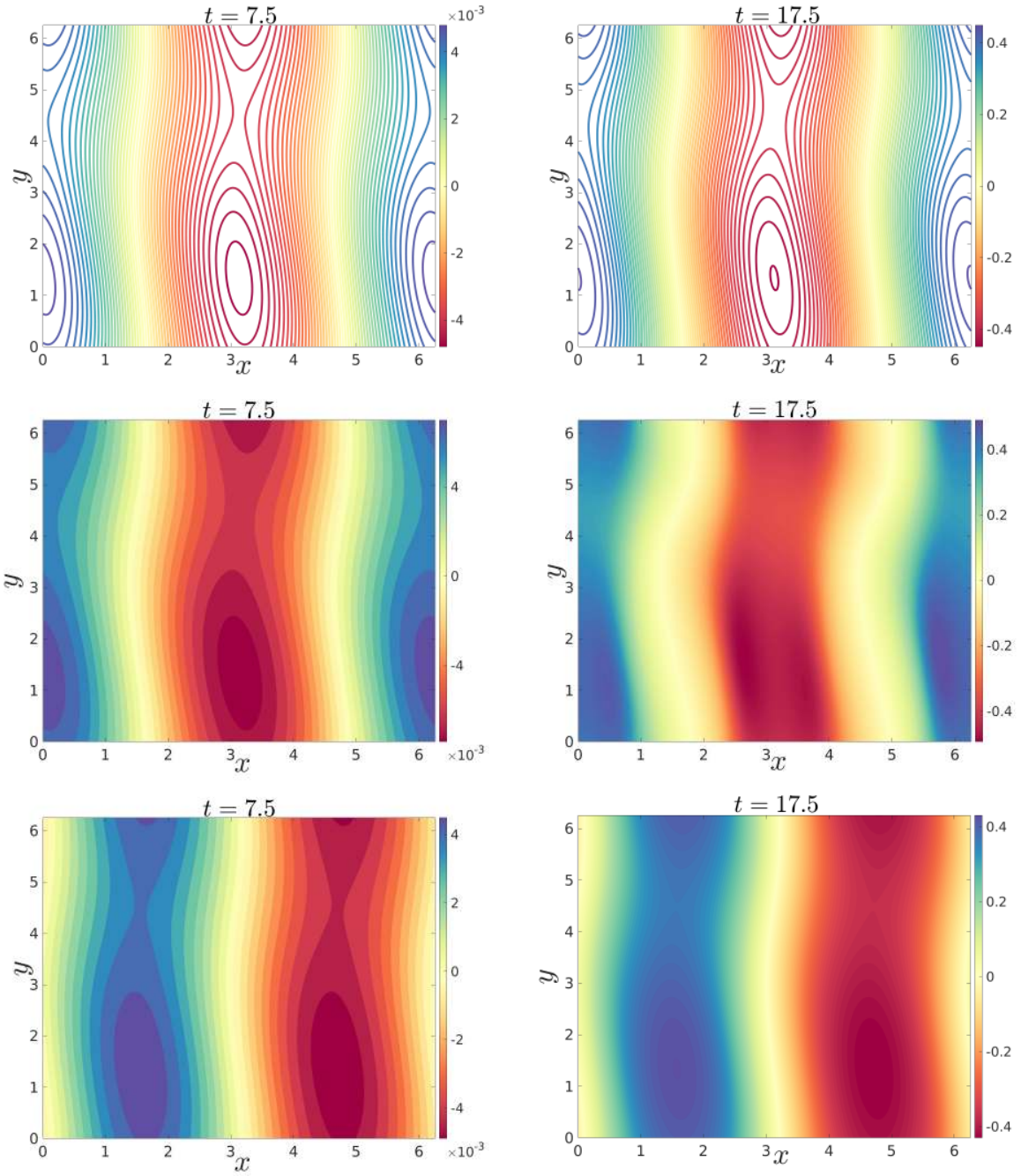

Figure 8.23: The profiles of A_z, J_z, and B_y at the top, middle, and bottom frames, respectively. These results, shown at different times, were obtained by the semi-Lagrangian code (`VLEM2D3V`). It is evident that the reconnection develops simultaneously with `CFI` instability. This is obvious when looking at the contour plot of B_y (bottom frames) where the increase in its value is due to `CFI`. see section 8.4.2 for details.

the background magnetic fluctuations along y direction ($B_0 sin(x)\mathbf{e}_y$) can be seen in the right-top frames, where we plot the evolution of the magnetic energy associated with this direction.

Fig.8.23 shows A_z, J_z, and B_y at two different times: $t = 7.5$, and $t = 17.5$. As shown in the figure, a full developed magnetic island, with $k_y = 1$ Fourier component and a width of the order of the electron skin depth (here $d_e = 1$ since all spatial variables are normalized to d_e), has formed while the seed magnetic field of `CFI` does not yet reach the saturation values. This field at $t = 7.5$ is of the same order of the initial magnetic fluctuations $B_0 = 10^{-3}$, as clearly evidenced in the bottom-left frame of the figure.

However, we anticipate that the case is similar to `PIC` simulations, meaning that the development of the magnetic island can be delayed by taking a smaller magnetic noise. Since the formation of the magnetic island occurs in the early stage of the kinetic simulation, before the onset of the `CFI`, one expects to observe an increase of the kinetic energy at some time $t < 7.5$. This growth is not seen in the top-left frame of Fig.8.23 due to its small values compared to the initial kinetic energy of the plasma. This is understood since the seed magnetic field of reconnection (B_n) is very small due to the background magnetic field (B_0) which have been amplified due to the development of `CFI`. In fact, when zooming on the kinetic and magnetic energy curves at $t \sim 2.5$, one can see a growth in the kinetic energy with a decrease in magnetic energy. However, the amplitude of this energy conversion is of the order of 10^{-6}, which is much smaller than the initial kinetic energy (~ 0.38).

8.5 A Remark on `PIC` vs Semi-Lagrangian Codes

As mentioned in the introduction of this chapter, we emphasize the fact that, in the present work, we do not make any comparison between the two methods since this kind of study must be performed by, carefully, fixing the parameters and the settings of the comparison tests (both methods have their advantages and disadvantages). However, for the sake of the completeness, we present in this section, the concept of the "graininess factor" for `PIC` method. Then, we provide a simple tool, discussed in Refs.[373, 374], that helps us when comparing the computation efforts required by the two methods.

We know that the collective behaviour characterizes the full ionized plasma. The parameter which allows us to identify the relative importance of the collective behaviour and the individual phenomena is the plasma graininess parameter g (see the book by Bertrand, Del Sarto and Ghizzo for a discussion of this parameter [177]), defined as follows,

$$g = \frac{1}{n\lambda_D^3}, \tag{8.13}$$

where n is the particle density, and $\lambda_D = (\frac{\epsilon_0 k_B T}{ne^2})^{1/2}$ is the Debye length. Therefore, the smaller this parameter is, the stronger the collective behaviour becomes. In Vlasov model, the plasma is collisionless, meaning that the individual collisions between particles are neglected, which is described by the limit: $g \to 0$. However, even though `PIC` codes allow us to study the collective behaviour of the plasma when the spatial grid step is of the order of Debye length ($\Delta x \sim \lambda_D$), it introduces individual effects due to the finite number of the macro-particles (N_p). These individual effects are mostly considered as normal noise, which can be quantified in terms of graininess factor of `PIC` simulations ($g_{\texttt{PIC}}$), as detailed in Refs.[373, 374, 375].

The factor $g_{\texttt{PIC}}$ reads

$$g_{\texttt{PIC}} = \frac{1}{n_0(\Delta x)^{d_x}}, \tag{8.14}$$

where n_0 is the density of the macro-particles in the PIC simulation (it is given by $n_0 = N_p/L^{d_x}$). $d_x = 1, 2, 3$ is the dimensions of the space, L is the spatial length of the simulation box. In the previous equation, we assumed that the spatial steps are equal in all directions and the same for the extensions of the simulation box. Substituting n_0 in Eq.(8.14), one finds,

$$g_{\texttt{PIC}} = \frac{1}{N_p}(\frac{L}{\Delta x})^{d_x}, \tag{8.15}$$

In all the simulations performed in the previous discussions, $d_x = 2$, and $N_x = N_y = \frac{L}{\Delta x} = 512 = 2^9$ is the number of cells in each directions. Then, Eq.(8.15) becomes

$$g_{\texttt{PIC}} = \frac{2^{18}}{N_p}, \tag{8.16}$$

For example, the graininess factor of the simulation S_2 for two homogeneous, symmetric, counter-propagating beams with a total number of particles $N_p = \texttt{NPPC} \times N_x \times N_y = 2^{10} \times 2^{18} = 2^{28}$ ($\texttt{NPPC} = 2^{10}$ is the number of particles per cell), becomes

$$g_{\texttt{PIC},S_2} = 9.7 \times 10^{-4}, \tag{8.17}$$

while for the simulation S_4, which is equivalent to S_2, except that $\texttt{NPPC} = 2^{12}$, $g_{\texttt{PIC},S_4}$ is

$$g_{\texttt{PIC},S_4} = 2.4 \times 10^{-4}, \tag{8.18}$$

For comparison, $g = 3 \times 10^{-8}$ in tokamaks, and $g = 3 \times 10^{-9}$ in Solar corona, and the interstellar plasma [177].

We now turn our attention to the computational efforts of the PIC and semi-Lagrangian methods. It is expected that the ratio between the numerical effort for the two methods will be proportional to the ratio between the total number of the points in the Eulerian grid in the semi-Lagrangian method $N_{\texttt{SL}}$, and the total number of macro-particles N_p in PIC method. $N_{\texttt{SL}}$ is given by

$$N_{\texttt{SL}} = N_v^{d_v}(\frac{L}{\Delta x})^{d_x}, \tag{8.19}$$

where N_v is the number of points along each direction in the velocity space, and $d_v = 1, 2, 3$ is the number of dimensions. Now, substituting Eq.(8.15) in the previous equation, one finds

$$\frac{N_{\texttt{SL}}}{N_p} = g_{\texttt{PIC}} N_v^{d_v}, \tag{8.20}$$

Substituting Eq.(8.15) in Eq.(8.19) was possible thanks to the fact that in both methods, the Maxwell equations are solved on the same spatial grid using the same method (when grids, and/or the methods are different this substitution is no longer allowed). For example, this ratio for the simulation S_2, and a semi-Lagrangian simulation with $N_v = 64$, becomes

$$\frac{N_{\texttt{SL}}}{N_p} \approx 254.3 \tag{8.21}$$

One should be careful that the previous discussion concerns the computational efforts, but not the accuracy.

8.6 Conclusions

Thanks to PIC (SMILEI) and semi-Lagrangian (VLEM) codes, we discussed in this chapter two beam-plasma configurations. In the first one, we performed several numerical experiments for two counter-propagating inhomogeneous, gaussian beams in a background, cylindrically-symmetric, vector potential. We have shown that these configurations are CFI unstable, but are tearing stable. In the second case, we discussed a system with two counterstreaming, homogeneous beams. As an initial condition, we chose a magnetic field composed of two parts. The first one is an x dependent magnetic field along y direction, which has been amplified due to CFI instability. In contrast, the second one is a divergence-free magnetic noise which seeds the development of magnetic reconnection. The development of reconnection depends on the strength of the magnetic noise. However, in Ref. [363], it was suggested that the growth rate of the secondary reconnection was driven by pressure tensor components. The linear theory of reconnection due to pressure tensor has been poorly explored. Therefore, the next step is to design an eigensolver to solve the eigenvalue problem, derived in chapter 6. This will allow us to interpret the results of the kinetic simulations, and to also test some hypotheses on the simultaneous occurrence and competition of CFI and tearing-type modes.

9

Conclusions and Future Work

Contents

Magnetic reconnection is a complex physical process by which the magnetic energy converts into kinetic energy, thermal energy, and acceleration of the charged particles. It occurs in both natural and laboratory plasmas. Therefore, understanding this phenomenon is an essential step towards the understanding of several phenomena, for which many open questions still exist, in our near-Earth environments, in the solar system, in the distant universe, and also here on Earth. Since, reconnecting-type instabilities can co-exist with other instabilities, the problem becomes very complex; not only from analytical point of view, but also from numerical point of view. For these reasons, it is likely to keep on being an active field of researches for many years to come.

9.1 Conclusions

We started this dissertation by introducing a simple description of magnetic reconnection, followed by a detailed discussion of the mathematical principles by which we can build numerical solvers in order to tackle the reconnection problem (chapters 1 and 2). The next two following chapters have been devoted to these subjects. In chapter 3, in particular, we explored and developed the numerical methods used to solve the `VM` system (semi-Lagrangian and particle-in-cell methods). In chapter 4, we addressed the generalized eigenvalue problems met when performing Fourier analysis to study the linear phase of reconnection instabilities: based on this, we have developed a finite difference multi-precision solver that can be applied to different reconnection regimes. After that, we discussed the fluid models and we have derived a collisionless `RMHD` model that account for the possible presence of inhomogeneous arbitrary density in toroidal geometry (Chapter 5); this analytical model provides the basis of an eigenvalue solver that can be implemented by adapting the solver discussed in Chapter 4. In Chapter 4, we also settled the analytical basis of the extension of such a numerical solver to the inclusion of Hall-term in Ohm's law. In chapter 6, we discussed an `EMHD` model which account for the density fluctuations and the relativistic effects. By linearizing this model, we have settled the basis of the complex, generalized eigenvalue problem, which had not been addressed before, in literature, in the non-relativistic, warm `EMHD` compressible regime, both with and without a strong guide field. We then presented, in Chapter 7, the results obtained using the numerical solver developed and discussed in chapters 4 and 5, which allowed us to verify some analytical estimations of the scaling law

that had been provided by previous theoretical studies but had never been systematically verified before. More importantly, our investigation has allowed us to complement such previous models by providing new insights in the physics of reconnecting instabilities of "tearing-type", notably about the identification of the microscopic scales of the unstable eigenmodes and about their scaling with the relevant parameters. We also identified a new reconnection regime for tearing modes in presence of finite ion Larmor radius effects. In the last chapter (chapter 8), we focused on the kinetic study of the linear and nonlinear evolution of some plasma configurations, which are unstable to Weibel-type instabilities, and possibly to reconnecting modes. In this chapter, we have performed benchmark tests to validate `VLEM2D3V` code for the study of reconnecting modes, and then we used the code to study Weibel-type instabilities and tearing modes. We have also used the `PIC` code (`SMILEI`) to investigate the same problems. Two problems have been addressed. The first one is the case of two counter-propagating, inhomogeneous, Gaussian beams with an initial cylindrically symmetric vector potential. This configuration is `CFI` unstable, but in principle tearing stable, although it can be subject to magnetic reconnection in the form of "merging" of current filaments (or magnetic annihilation). The second problem involves two counter-propagating, homogeneous, symmetric beams. In this case in order to single out specific features of the competition between Weibel-type and reconnecting modes, we have distinguished two kinds of magnetic fluctuations, combined together. The first one consists of a coherent magnetic field, which, depending on one coordinate only, excites the `CFI` alone and it is then amplified by its growth, The second one consists of a non-harmonic random noise which depends on two-coordinates and therefore seeds the development of both electrostatic (two-stream) and oblique modes, and of magnetic reconnection. We have then evidenced how the occurrence of tearing modes, whose onset as secondary instabiities to `CFI` had been already investigated in previous works, can indeed compete with `CFI` since the linear stage, depending on the amplitude of the `2D` part of the magnetic perturbation.

9.2 Future Work

What's left to be done is always much more than what one has done. There is still much to do to complete several ideas discussed in this thesis. This includes:

* Developing an eigensolver to numerically solve the generalized eigenvalue problem obtained in section 6.3.6 . In the light of the results of this eigensolver, we probably can interpret the results of the kinetic simulations using a fluid model, which will allow us to improve our understanding of the roles the electron pressure tensor plays in the dynamic of `EMHD` reconnection.

* It will also be interesting to develop a numerical solver for the extended `EMHD` system (Eqs.[6.31 - 6.34]). On the one hand, it will provide us with a tool to study the nonlinear phase of some configurations, that are unstable to both Weibel-type instabilities and tearing modes. On the other hand, this fluid simulation will also enable us to compare the fluid and the kinetic models (`PIC` and semi-Lagrangian).

* Understanding the linear phase of tearing-type instabilities in different regimes will be the next step in our work. This effort will include the compressible Hall-MHD regime (section 5.5), the warm-ion limit of reduced MHD (section 5.4), the secondary modes to resistive instability, and the effects of the existence of a shear velocity on the development of these instabilities. Some of these subjects have been started being addressed and the work is in progress.

* Developing a nonlinear code to integrate the collisionless reduced MHD model in the toroidal geometry, devised in section 5.6, is one of our main long term objectives. This part also includes designing an eigensolver, which will be useful for tokamak applications, notably for the stability analysis of the experimental profiles measured in machines like JET. All the work, which concerns the fusion applications, has been developed in connection with the FR-FCM project "Evolution of current sheets in low-collision plasmas" and WPEDU EURATOM program. In particular, the development of an eignesolver for the study of reconnection in toroidal geometry has been (and will be) carried out in the framework of the participation to the EUROfusion Horizon 2020 campaigns JET-WPJET1 and JET1-2020-C39.

* Performing further semi-Lagrangian simulations using a higher resolution in the phase space to complement and complete the preliminary results presented in section 8.4.2. This should also involve a further study of the effects of the magnetic noise that seeds the reconnection process.

* Assessing the combined role of Weibel-type instabilities, tearing modes, oblique mode, and two-stream instability, which, in principle, are all intervening when 2D-fluctuations are superposed to the CFI unstable configuration: of particular interest is the investigation of the competition of magnetic reconnection and oblique-type modes, in the light of the recent results discussed in Ref. [3]. The configurations leading to the simoultaneous co-existence of all these instabilities require a 3D3V version of the semi-Lagrangian code or the use of the 3D PIC code (e.g. SMILEI). Nevertheless, also investigations performed with reduced 2D geometries and a proper choice of the beam orientation can provide, thanks to the exploitation of the relevant translation invariances of the system (and thus of the conservation of the associated components of the canonical momentum) interesting insight in the role played by these different actors.

* Finally, we mention that, during this PhD research, we had also studied the problem of 2D turbulent decay in a magnetized electron Vlasov plasma in which ions form a neutralizing background: this study was meant as a first comparison test of a nonlinear phenomenon that only involved the electron dynamics, and that could be described by both a fluid EMHD model and a kinetic model. The idea was to identify, in this way, the parameter range of the kinetic description which corresponded to the "hydrodynamic limit", in which thermal effects can be neglected and thus kinetic results are expected to converge to fluid ones. Since the theory of cold EMHD incompresisble turbulence is well established, this subject represented and interesting test of comparison which could be afforded with a PIC code (SMILEI, in this case). However, this study has revealed to be less trivial and more "surprising" than expected, since the initialization of the problem in a kinetic framework has evidenced a nonlinear evolution which did not display the features of developed turbulence but rather, seemingly, the development of coherent structures. Preliminary results have been presented as a poster contribution at the international "Vlasovia conference" held in Strasbourg in July 2019. This work was developed in collaboration with researchers of Arcetry Observatory (Florence, Italy), within the framework the Egidee-Galilèe PHC project 39632WH "Generation and evolution of non-thermal particle distributions in the solar wind" . Further investigations, which went beyond the purpose of this PhD project are needed to better characterise the regime identified with these preliminary studies.

A

Brief Summary of the PhD Activities

The PhD research period that led to this dissertation involved some other activities ad scientific contributions beside of those reported in this manuscript. Here below, a comprehensive brief account of them:

Oral Communications (OC):

OC3. "Microscopic scales of linear tearing instabilities", Arcetri Workshop on plasma astrophysics, Arcetri Observatory, Florence - italy (2019).

OC2. "On the asymptotic scaling of the reconnection layer width in linear tearing analysis", Arcetri Workshop on plasma astrophysics, Arcetri Observatory, Florence - italy (2018).

OC1. "Magnetic reconnection", 06 June 2019, Ecole doctoral

Poster Communications (PC):

PC2. "Turbulence in an Electron Vlasov Plasma: Comparison with incompressible EMHD regime", Vlasovia 2019 (International workshop on the theory and applications of Vlasov equation), 22-25 July 2019.

PC1. "Magnetic Reconnection", Doctoriales de Lorraine -DocLor, Saint-Dié La Bolle Cap - France (2019).

Articles on international peer-reviewed journals (A):

A3. "Ion FLR Effects on Linear Tearing Modes", in progress, C Marchetto, H Betar, D. Del Sarto, and M. Ottaviani. (In the framework of the participation to the EUROfusion Horizon 2020 campaigns JET-WPJET1 and JET1-2020-C39)

A2. H Betar, D. Del Sarto, M. Ottaviani, and A. Ghizzo, "Microscopic scales of linear tearing instabilities", in progress, to be submitted to J. Plasma Phys.

A1. H Betar, D. Del Sarto, M. Ottaviani, and A. Ghizzo, "Multiparametric study of tearing modes in thin current sheets", Physics of Plasmas 27, 102106 (2020) [153].

In the framework of the participation to the EUROfusion Horizon 2020 campaigns JET-WPJET1 and JET1-2020-C39, we have participated in the following works (JET):

JET15. "Ion cyclotron resonance heating scenario for DEMO", D Van Ester, E. Lerche,R. Ragona,...,H Betar,..., I. Zychor (+ 1250 co-authors), Nucl. Fusion,59, 106051 (2019)

JET14. "Control of the hydrogen: deuterium isotope mixture using pellets in JET", M.Valovic, Y. Baranov, A. Boboc,...,H Betar,..., I. Zychor (+ 1250 co-authors), Nucl. Fusion, 59, 106047 (2019)

JET13. "Synthetic diagnostics for the JET scintillator probe lost alpha measurements", J. Varje, V.Kiptily, P. Siren,...,H Betar,..., I. Zychor (+ 1250 co-authors), J. Instrumentation, 14, C09018 (2019)

JET12. "Deep neural networks for plasma tomography with applications to JET and COMPASS", D. D. Carcvalho, D.R. Ferreira, P.J. Carvalho,...,H Betar,..., I. Zychor (+ 1250 co-authors), J. Instrumentation, 14, C09011(2019)

JET11. "A new mechanism for increasing density peaking in tokamaks: improvement of the inward particle pinch with edge ExB shearing", J. Garcia, H.Doerk, T. Goerler,...,H Betar,..., I. Zychor (+ 1250 co-authors), PlasmaPhys. Controll. Fusion, 61, 104002(2019)

JET10. "Role of fast ion pressure in the isotope effect in JET L-mode plasmas", N. Bonanomi, I. Casiraghi, P. Mantica,...,H Betar,..., I. Zychor (+ 1250co-authors), Nucl. Fusion, 59, 096030 (2019)

JET9. "Modification of the Alfven wave spectrum by pellet injection", H.J. Oliver,S.E. Sharapov, B.N. Breizman,...,H Betar,..., I. Zychor (+ 1250 co-authors),Nucl. Fusion, 59, 106031 (2019)9

JET8. "Multiphyiscs approach to plasma neutron source modelling at the JET tokamak", Z. Stancar, M. Gorelenkova, S. Conroy,...,H Betar,..., I. Zychor(+ 1250 co-authors), Nucl. Fusion, 59, 096020 (2019)

JET7. "Interpretative and predictive modelling of Joint European Torus collisionality scans", F. Eriksson, F. Fransson, M. Oberparleiter,...,H Betar,..., I.Zychor (+ 1250 co-authors), Plasma Phys. Controll. Fusion 61,115004(2019)

JET6. "First principles and integrated modelling achievements towards trust full power predictions for JET and ITER", J. Garcia, R.J. Dumont, J. Joly,...,HBetar,..., I. Zychor (+ 1250 co-authors), Nucl. Fusion, 59, 086047 (2019)

JET5. "Adaptive learning for disruption prediction in non-stationary conditions", A. Murari, M. Lungaroni, M. Gelfusa,...,H Betar,..., I. Zychor (+ 1250co-authors), Nucl. Fusion, 59, 086037 (2019)

JET4. "Self-consistent pedestal prediction for JET-ILW in preparation of the DT campaign", S. Saarelma, L. Frassinetti, P. Bilkova,...,H Betar,..., I. Zychor(+ 1250 co-authors), Phys. Pasmas, 26, 072501 (2019)

JET3. "COREDIV numerical simulation of high neutron rate JET-ILW DD pulsesin view of extension to JET-ILW DT experiments", G. Teleska, I. Ivanova-Stanik. R. Zagorski,...,H Betar,..., I. Zychor (+ 1250 co-authors), Nucl.Fusion, 59, 056026 (2019)

JET2. "Recurrence plot for dynamic analysis of type-I ELMs at JET with a carbon wall", B. Cannasa, A. Fanni, A. Murari,...,H Betar,..., I. Zychor (+ 1250co-authors), IEEE Trans. Plasma Sci., 47, 1871 (2019)

JET1. "Overview of the JET preparation for deuterium-tritium operation with the ITER-like wall", E. H. Joffrin, S. Abduallev, M. Abhangi,...,H Betar,...,I. Zychor (+ 1250 co-authors), Nucl. Fusion 59, 112021 (2019)

Finally, I mention in the following some scientific, and transversal courses I have followed

Graduate Courses Followed during the Doctoral Program (C):

C6. Stochastic Processes in Astrophysics and Cosmology at Paris observatory (30 hours)

C5. Symétrie de l'atome au solide atIJL(20 hours).

C4. Parallel Computing with MKL-intel (20 hours). This course was organized by EXPLOR in the collaboration with Intel (October/2019). **C3.** Machine learning data science and deep learning with python course (udemy platform).

C2. Deep Learning (https://www.deeplearningbook.org).

C1. Neural networks and deep learning (http://neuralnetworksanddeeplearning.com/).

B

Some Useful Formulae on Vectors, Tensor Algebra and Coordinate Changes

In this appendix, we present a brief review of the nonlinear coordinate changes and some vector identities and notions that have been extensively used in this thesis.

Introduction:

A basis for a vector space V is a set of linearly independent vectors which span V. This means that any $\mathbf{u} \in V$ can be uniquely defined as a linear combination of these vectors. Let us call these vectors $(\mathbf{e}_1, \mathbf{e}_2, \mathbf{e}_3)$ in the three dimensional basis, then any vector $\mathbf{u}$ is given by

$$\mathbf{u} = u_1\mathbf{e}_1 + u_2\mathbf{e}_2 + u_3\mathbf{e}_1, \tag{B.1}$$

We call $\mathbf{u}\cdot\mathbf{e}_1$, $\mathbf{u}\cdot\mathbf{e}_2$, and $\mathbf{u}\cdot\mathbf{e}_3$ the components of the vector in V space. They are given by the following matrix equation

$$\underbrace{\begin{bmatrix} \mathbf{e}_1\cdot\mathbf{e}_1 & \mathbf{e}_2\cdot\mathbf{e}_1 & \mathbf{e}_3\cdot\mathbf{e}_1 \\ \mathbf{e}_1\cdot\mathbf{e}_2 & \mathbf{e}_2\cdot\mathbf{e}_2 & \mathbf{e}_3\cdot\mathbf{e}_2 \\ \mathbf{e}_1\cdot\mathbf{e}_3 & \mathbf{e}_2\cdot\mathbf{e}_3 & \mathbf{e}_3\cdot\mathbf{e}_3 \end{bmatrix}}_{\mathcal{G}} \begin{bmatrix} u_1 \\ u_2 \\ u_3 \end{bmatrix} = \begin{bmatrix} \mathbf{u}\cdot\mathbf{e}_1 \\ \mathbf{u}\cdot\mathbf{e}_2 \\ \mathbf{u}\cdot\mathbf{e}_3 \end{bmatrix} \tag{B.2}$$

$\mathcal{G}$ contains all available information about the vector space (or the coordinate system). It tells us whether this space is orthogonal, curvilinear, orthonormal, etc. If it is diagonal, then the space is orthogonal, and becomes orthonormal when this matrix is equal to the identity matrix. We define the inner product on V space as the following matrix multiplication,

$$\mathbf{u}\cdot\mathbf{w} = \mathbf{u}^T\mathcal{G}\mathbf{w}, \tag{B.3}$$

Which reads $\mathbf{u}^T\mathbf{w}$ for orthonormal coordinate system where $\mathcal{G} = \mathbf{I}$.

Change of Basis:

Let us now assume that the vector decomposition expressed by Eq.(B.1) is already known, and we would like to change its representation to another coordinate system V' ($\mathbf{e'}_1$, $\mathbf{e'}_2$, $\mathbf{e'}_3$), then we write

$$\mathbf{u} = u_1\mathbf{e}_1 + u_2\mathbf{e}_2 + u_3\mathbf{e}_1 = u'_1\mathbf{e}'_1 + u'_2\mathbf{e}'_2 + u'_3\mathbf{e}'_1, \tag{B.4}$$

In order to find the i^{th} component in V', we simply take the inner product of the previous equation wit $\mathbf{e}'_i$. Then for all the components we take the inner product with $[\mathbf{e}'_1, \mathbf{e}'_2, \mathbf{e}'_3]^T$. One finds

$$\underbrace{\begin{bmatrix} \mathbf{e}_1\cdot\mathbf{e}'_1 & \mathbf{e}_2\cdot\mathbf{e}'_1 & \mathbf{e}_3\cdot\mathbf{e}'_1 \\ \mathbf{e}_1\cdot\mathbf{e}'_2 & \mathbf{e}_2\cdot\mathbf{e}'_2 & \mathbf{e}_3\cdot\mathbf{e}'_2 \\ \mathbf{e}_1\cdot\mathbf{e}'_3 & \mathbf{e}_2\cdot\mathbf{e}'_3 & \mathbf{e}_3\cdot\mathbf{e}'_3 \end{bmatrix}}_{\mathcal{T}} \begin{bmatrix} u_1 \\ u_2 \\ u_3 \end{bmatrix} = \underbrace{\begin{bmatrix} \mathbf{e}'_1\cdot\mathbf{e}'_1 & \mathbf{e}'_2\cdot\mathbf{e}'_1 & \mathbf{e}'_3\cdot\mathbf{e}'_1 \\ \mathbf{e}'_1\cdot\mathbf{e}'_2 & \mathbf{e}'_2\cdot\mathbf{e}'_2 & \mathbf{e}'_3\cdot\mathbf{e}'_2 \\ \mathbf{e}'_1\cdot\mathbf{e}'_3 & \mathbf{e}'_2\cdot\mathbf{e}'_3 & \mathbf{e}'_3\cdot\mathbf{e}'_3 \end{bmatrix}}_{\mathcal{G}'} \begin{bmatrix} u'_1 \\ u'_2 \\ u'_3 \end{bmatrix} \tag{B.5}$$

where $\mathcal{T}$ is the transformation matrix operating on the V space. In a more compact notation, we can express the previous relationship as follows

$$\mathcal{T}\mathbf{u} = \mathcal{G}'\mathbf{u}' \implies \mathbf{u}' = \mathcal{G}'^{-1}\mathcal{T}\mathbf{u}, \quad or \quad u'_i = \mathcal{G}'^{-1}_{im}\mathcal{T}_{ml}u_l \tag{B.6}$$

Notice that if the bases are orthonormal, then $\mathcal{G}'^{-1} = \mathcal{G}' = \mathcal{I}$. For the inverse, transformation $V' \to V$, we follow exactly the same procedure, then we find

$$\mathbf{u} = \mathcal{G}^{-1}\mathcal{T}^T\mathbf{u}' \implies u_i = \mathcal{G}_{im}\mathcal{T}^T_{ml}u'_l, \tag{B.7}$$

One interesting and very important remark is that when the base vectors are orthonormal (the unit vectors are perpendicular, and $\mathcal{G} = \mathcal{G}' = \mathcal{I}$), the transformation matrix becomes orthogonal (A matrix $\mathcal{T}$ is orthogonal when $\mathcal{T}^{-1} = \mathcal{T}^T$), which allows us to easily perform the transformation between different coordinate systems.

Curvilinear Coordinate Systems:

Curvilinear coordinate system is a coordinate system (C) for the Euclidean space in which the coordinate lines are generally curved. To derive general formulae for many differential operators in a curvilinear coordinate, we take as reference frame the Cartesian coordinates (E). We further restrict our analysis to three-dimensional spaces. Then any vector $\mathbf{r}$ has three components (q_1, q_2, q_3) along the three directions $\mathbf{e}_{q_1}, \mathbf{e}_{q_2}, \mathbf{e}_{q_3}$ of C, that is

$$\mathbf{r} = \mathbf{r}(q_1, q_2, q_3), \tag{B.8}$$

The unit vectors of the coordinate system can be easily derived by noticing, for example, that the unit vector $\mathbf{e}_{q_1}$ results from the change of $\mathbf{r}$ along this direction while keeping q_2 and q_3 constant, then one writes

$$\mathbf{e}_{q_i} = \frac{\frac{\partial\mathbf{r}}{\partial q_i}}{h_i}, \text{ where } h_i = \left|\frac{\partial\mathbf{r}}{\partial q_i}\right| \quad i = 1, 2, 3. \tag{B.9}$$

h_i are known as the scale factors of the coordinate system (Lamé coefficients). Then using the chain rule, the element length vector $d\mathbf{r}$ is written as,

$$d\mathbf{r} = h_1 dq_1\mathbf{e}_{q_1} + h_2 dq_2\mathbf{e}_{q_2} + h_3 dq_3\mathbf{e}_{q_3}, \tag{B.10}$$

Therefore, according to Eq.(B.3), one writes

$$dl = |d\mathbf{r}| = d\mathbf{r}^T\mathcal{G}d\mathbf{r} = \sqrt{h_i dq_i}, \text{ with, } dl_i = h_i dq_i, \tag{B.11}$$

Also, the surface element S_{ij} with a normal vector directed along k, and the volume elements are given by,

$$dS_{ij} = h_i h_j dq_i dq_j, \quad dV = h_i h_j h_k dq_i dq_j dq_k, \tag{B.12}$$

Now using the chain rule, the Cartesian total derivative for each component reads

$$dx_j = \frac{\partial x_j}{\partial q_i} dq_i = \mathcal{T}_{ji} dq_i, \tag{B.13}$$

where $\mathcal{T}$ is the orthogonal transformation matrix between the Cartesian and Curvilinear coordinate systems. We can obtain the gradient operator in C starting from the expression for the differential of a function f, given by

$$df = \frac{\partial f}{\partial q_1} dq_1 + \frac{\partial f}{\partial q_2} dq_2 + \frac{\partial f}{\partial q_3} dq_3, \tag{B.14}$$

Now substituting Eq.(B.11) into the previous equation, we obtain

$$df = \frac{1}{h_1}\frac{\partial f}{\partial q_1} dl_1 + \frac{1}{h_2}\frac{\partial f}{\partial q_2} dl_2 + \frac{1}{h_3}\frac{\partial f}{\partial q_3} dl_3 = \nabla f \cdot d\mathbf{r}, \tag{B.15}$$

Therefore, the **gradient** reads,

$$\nabla = \frac{\mathbf{e}_{q_1}}{h_1}\frac{\partial}{\partial q_1} + \frac{\mathbf{e}_{q_2}}{h_2}\frac{\partial}{\partial q_2} + \frac{\mathbf{e}_{q_3}}{h_3}\frac{\partial}{\partial q_3}, \tag{B.16}$$

In the following we list without proof the general formulae for the remaining operators [see [376] for more details]. However, it is straightforward to obtain them starting from their integral definitions.

The Divergence:

$$\nabla\cdot = \frac{1}{h_1 h_2 h_3}\Big\{\frac{\partial}{\partial q_1}(h_2 h_3) + \frac{\partial}{\partial q_2}(h_1 h_3) + \frac{\partial}{\partial q_3}(h_1 h_2)\Big\}, \tag{B.17}$$

The Curl:

$$\nabla \times \mathbf{A} = \frac{1}{h_1 h_2 h_3}\begin{vmatrix} h_1\mathbf{e}_{q_1} & h_2\mathbf{e}_{q_2} & h_3\mathbf{e}_{q_3} \\ \frac{\partial}{\partial q_1} & \frac{\partial}{\partial q_2} & \frac{\partial}{\partial q_3} \\ h_1 A_1 & h_2 A_2 & h_3 A_3 \end{vmatrix}, \tag{B.18}$$

The Laplacian:

$$\Delta = \frac{1}{h_1 h_2 h_3}\Big\{\frac{\partial}{\partial q_1}\Big(\frac{h_2 h_3}{h_1}\frac{\partial}{\partial q_1}\Big) + \frac{\partial}{\partial q_2}\Big(\frac{h_1 h_3}{h_2}\frac{\partial}{\partial q_2}\Big) + \frac{\partial}{\partial q_3}\Big(\frac{h_1 h_2}{h_3}\frac{\partial}{\partial q_3}\Big)\Big\}, \tag{B.19}$$

Now, we have all the necessary mathematical tools to obtain all formulae for the differential operators in toroidal coordinate system, which the subject of the following appendix.

Useful Vector Identities

$$\nabla \cdot (f\mathbf{A}) = \nabla f \cdot \mathbf{A} + f\nabla \cdot \mathbf{A}, \tag{B.20}$$

$$\Delta\mathbf{A} = \nabla(\nabla \cdot \mathbf{A}) - \nabla \times \nabla\mathbf{A}, \tag{B.21}$$

$$\mathbf{A} \times (\mathbf{B} \times \mathbf{C}) = (\mathbf{A} \cdot \mathbf{C})\mathbf{B} - (\mathbf{A} \cdot \mathbf{B})\mathbf{C}, \tag{B.22}$$

$$\nabla \times (f\mathbf{A}) = \nabla f \times \mathbf{A} + f\nabla \times \mathbf{A}, \tag{B.23}$$

$$\nabla \times (\nabla f) = 0, \tag{B.24}$$

$$\nabla \cdot \nabla \times \mathbf{A} = 0, \tag{B.25}$$

$$\nabla \times (\mathbf{A} \times \mathbf{B}) = \mathbf{A}(\nabla \cdot \mathbf{B}) - \mathbf{B}(\nabla \cdot \mathbf{A}) + (\mathbf{B} \cdot \nabla)\mathbf{A} - (\mathbf{A} \cdot \nabla)\mathbf{B}, \tag{B.26}$$

$$\nabla \cdot (\mathbf{A} \times \mathbf{B}) = \mathbf{B} \cdot \nabla \times \mathbf{A} - \mathbf{A} \cdot \nabla \times \mathbf{B}, \tag{B.27}$$

$$\nabla \cdot \{\mathbf{AB}\} = (\nabla \cdot \mathbf{A})\mathbf{B} + (\mathbf{A} \cdot \nabla)\mathbf{B}, \tag{B.28}$$

$$[\nabla \cdot \mathcal{P}]_i = \frac{\partial \mathcal{P}_{ij}}{\partial j}, \quad j = x,\ y,\ z \tag{B.29}$$

C

Torodial Coordinate System

In this appendix, we seek to summarise all the transformation rules between the most two popular coordinate systems used in Tokamak physics, and the Cartesian one, which is essential for the derivation of the equations into the toroidal geometry (see Fig.(C.1)).

These coordinate systems are (R, φ, Z), and (r, θ, φ).

$(R,\ \varphi,\ Z)$ Coordinate System:

As shown in Fig.(C.1), the relations between these coordinates and the Cartesian coordinates are

$$x = R\cos\varphi, \quad y = R\sin\varphi, \quad z = Z, \tag{C.1}$$

while the unit vectors are given by

$$\mathbf{e}_R = \cos\varphi\mathbf{e}_x + \sin\varphi\mathbf{e}_y, \tag{C.2a}$$
$$\mathbf{e}_\varphi = -\sin\varphi\mathbf{e}_x + \cos\varphi\mathbf{e}_y, \tag{C.2b}$$
$$\mathbf{e}_Z = \mathbf{e}_z, \tag{C.2c}$$

The metric tensor $\mathcal{G}$, whose elements are given by

$$g_{ij} = \sum_{k=1}^{3} \frac{\partial x_k}{\partial q_i}\frac{\partial x_k}{\partial q_j} \tag{C.3}$$

where $x_k = x,\ y,\ z$ and $q_i = R,\ \varphi,\ Z$, defines the distance between two points in the space. For $(R,\ \varphi,\ Z)$ coordinate system, it reads

$$\mathcal{G} = \begin{bmatrix} 1 & 0 & 0 \\ 0 & R^2 & 0 \\ 0 & 0 & 1 \end{bmatrix}, \tag{C.4}$$

Using Eq.(B.9), the scale factors read

$$h_R = 1, \quad h_\varphi = R, \quad h_Z = 1, \tag{C.5}$$

The one-to-one mapping between the two coordinate systems gives

$$R = \sqrt{x^2 + y^2}, \quad \varphi = \arctan\frac{y}{x}, \quad Z = z, \tag{C.6}$$

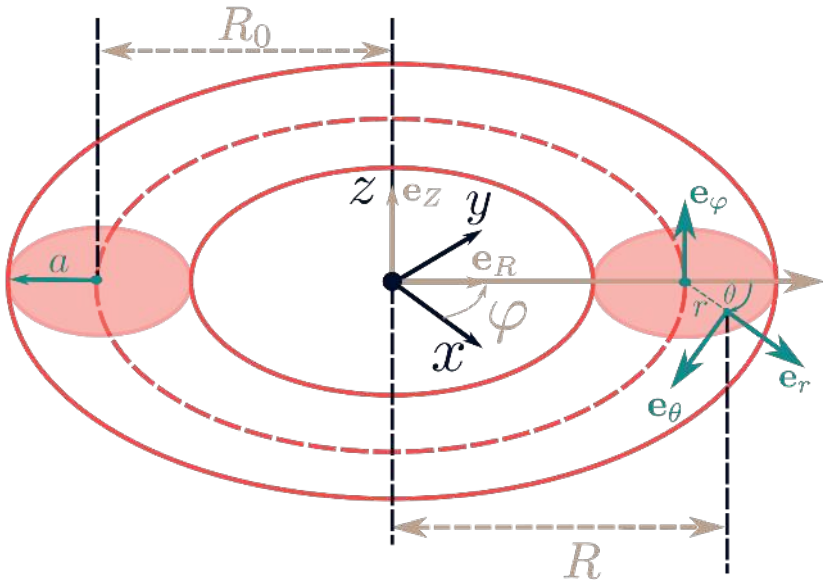

Figure C.1: An isometric illustration of the toroidal geometry. We show the three different coordinate systems: the Cartesian, (R, φ, Z), and (r, θ, φ) coordinate systems.

Differential operators, given by Eqs.[B.16, B.17, B.18, B.19], become

$$\nabla\psi = \mathbf{e}_R\frac{\partial\psi}{\partial R} + \frac{\mathbf{e}_\varphi}{R}\frac{\partial\psi}{\partial\varphi} + \mathbf{e}_Z\frac{\partial\psi}{\partial Z}, \tag{C.7a}$$

$$\nabla\cdot\mathbf{A} = \frac{1}{R}\Big\{\frac{\partial}{\partial R}(RA_R) + \frac{\partial A_\varphi}{\partial\varphi} + \frac{\partial}{\partial Z}(RA_Z)\Big\} \tag{C.7b}$$

$$\nabla\times\mathbf{A} = \frac{1}{R}\begin{vmatrix}\mathbf{e}_R & R\mathbf{e}_\varphi & \mathbf{e}_Z\\ \frac{\partial}{\partial R} & \frac{\partial}{\partial\varphi} & \frac{\partial}{\partial Z}\\ A_R & RA_\varphi & A_Z\end{vmatrix}, \tag{C.7c}$$

$$\Delta\psi = \frac{1}{R}\Big\{\frac{\partial}{\partial R}(R\frac{\partial\psi}{\partial R} + \frac{\partial}{\partial\varphi}(\frac{1}{R}\frac{\partial\psi}{\partial\varphi}) + \frac{\partial}{\partial Z}(R\frac{\partial\psi}{\partial Z})\Big\}, \tag{C.7d}$$

The Jacobian matrices $\mathcal{J}_{x,y,z}$, and $\mathcal{J}_{R,\varphi,Z}$ obtained from $dx_i = \frac{\partial x_i}{\partial q_j}dq_j$, and $dq_i = \frac{\partial q_i}{\partial x_j}dx_j$, respectively, are

$$\mathcal{J}_{x,y,z} = \begin{bmatrix}\cos\varphi & -R\sin\varphi & 0\\ \sin\varphi & R\cos\varphi & 0\\ 0 & 0 & 1\end{bmatrix}, \quad \mathcal{J}_{R,\varphi,Z} = \begin{bmatrix}\cos\varphi & \sin\varphi & 0\\ -\frac{\sin\varphi}{R} & \frac{\cos\varphi}{R} & 0\\ 0 & 0 & 1\end{bmatrix} \tag{C.8}$$

To obtain the previous equation, we used Eqs.(C.6, C.1). We conclude this section with some important relations, which we can obtain in a straightforward manner,

$$\nabla R = \mathbf{e}_R, \quad \nabla\varphi = \frac{1}{R}\mathbf{e}_\varphi, \quad \nabla Z = \mathbf{e}_Z, \tag{C.9a}$$

$$\nabla\cdot\mathbf{e}_R = \frac{1}{R}, \quad \nabla\times\mathbf{e}_R = 0, \quad \nabla\times\mathbf{e}_Z = 0 \tag{C.9b}$$

$$\nabla\cdot\mathbf{e}_\varphi = 0, \quad \nabla\times\mathbf{e}_\varphi = \frac{1}{R}\mathbf{e}_z, \tag{C.9c}$$

Notice that Eq.(C.9a) can be derived by multiplying the Jacobian $\mathcal{J}_{R,\varphi,Z}$ with $[\mathbf{e}_x, \mathbf{e}_y, \mathbf{e}_z]^T$.

(r, θ, φ) Coordinate System:
From Fig.(C.1), we have

$$x = (R_0 + r\cos\theta)\cos\varphi, \quad y = (R_0 + r\cos\theta)\sin\varphi, \quad z = -r\sin\theta, \tag{C.10}$$

where R_0 is the major radius of the tokamak (see Fig.C.1). In terms of Cartesian coordinates, the unit vectors read

$$\mathbf{e}_r = \cos\theta\cos\varphi\mathbf{e}_x + \cos\theta\sin\varphi\mathbf{e}_y - \sin\theta\mathbf{e}_z, \tag{C.11a}$$

$$\mathbf{e}_\theta = -\sin\theta\cos\varphi\mathbf{e}_x - \sin\theta\sin\varphi\mathbf{e}_y - \cos\theta\mathbf{e}_z, \tag{C.11b}$$

$$\mathbf{e}_\varphi = -\sin\varphi\mathbf{e}_x + \cos\varphi\mathbf{e}_y, \tag{C.11c}$$

The metric of this coordinate system reads

$$\mathcal{G} = \begin{bmatrix} 1 & 0 & 0 \\ 0 & r^2 & 0 \\ 0 & 0 & R^2 \end{bmatrix}, \tag{C.12}$$

The scale factors are obtained as shown in the previous section. They read,

$$h_r = 1, \quad h_\theta = r, \quad h_\varphi = R_0 + r\cos\theta = R, \tag{C.13}$$

r, θ, φ are given by

$$r = \sqrt{x^2+y^2+z^2-2R_0\sqrt{x^2+y^2}+R_0^2}, \quad \theta = \arctan\left(\frac{z}{R_0-\sqrt{x^2+y^2}}\right), \quad \varphi = \arctan\left(\frac{y}{x}\right), \tag{C.14}$$

Notice that when $R_0 = 0$, the previous relations become identical to those of the spherical coordinate system. Using Eqs.[B.16, B.17, B.18, B.19], the differential operators read

$$\nabla\psi = \mathbf{e}_r\frac{\partial\psi}{\partial r} + \frac{\mathbf{e}_\theta}{r}\frac{\partial\psi}{\partial\theta} + \frac{\mathbf{e}_\varphi}{R}\frac{\partial\psi}{\partial\varphi}, \tag{C.15a}$$

$$\nabla\cdot\mathbf{A} = \frac{1}{rR}\left\{\frac{\partial}{\partial r}(rRA_r) + \frac{\partial}{\partial\theta}(RA_\theta) + \frac{\partial}{\partial\varphi}(rA_\varphi)\right\} \tag{C.15b}$$

$$\nabla\times\mathbf{A} = \frac{1}{rR}\begin{vmatrix} \mathbf{e}_r & r\mathbf{e}_\theta & R\mathbf{e}_\varphi \\ \frac{\partial}{\partial r} & \frac{\partial}{\partial\theta} & \frac{\partial}{\partial\varphi} \\ A_r & rA_\theta & RA_\varphi \end{vmatrix}, \tag{C.15c}$$

$$\Delta\psi = \frac{1}{rR}\left\{\frac{\partial}{\partial r}\left(rR\frac{\partial\psi}{\partial r}\right) + \frac{\partial}{\partial\theta}\left(\frac{R}{r}\frac{\partial\psi}{\partial\theta}\right) + \frac{\partial}{\partial\varphi}\left(\frac{r}{R}\frac{\partial\psi}{\partial\varphi}\right)\right\}, \tag{C.15d}$$

while the Jacobians read

$$\mathcal{J}_{x,y,z} = \begin{bmatrix} \cos\theta\cos\varphi & -r\sin\theta\cos\varphi & -R\sin\varphi \\ \cos\theta\sin\varphi & -r\sin\theta\sin\varphi & R\cos\varphi \\ -\sin\theta & -r\cos\theta & 0 \end{bmatrix} \tag{C.16}$$

where $\mathcal{J}^{ij}_{x,y,z} = \frac{\partial x_i}{\partial q_j}$, with $i = x, y, z$ and $j = r, \theta, \varphi$, and,

$$\mathcal{J}_{r,\theta,\varphi} = \begin{bmatrix} \cos\theta\cos\varphi & \cos\theta\sin\varphi & -\sin\theta \\ -\frac{\sin\theta\cos\varphi}{r} & -\frac{\sin\theta\sin\varphi}{r} & -\frac{\cos\theta}{r} \\ -\frac{sin\varphi}{R} & \frac{\cos\varphi}{R} & 0 \end{bmatrix} \tag{C.17}$$

From Eq.(C.17) and operator formulae, we obtain

$$\nabla r = \mathbf{e}_r, \quad \nabla\theta = \frac{\mathbf{e}_\theta}{r}, \quad \nabla\varphi = \frac{\mathbf{e}_\varphi}{R} \tag{C.18a}$$

$$\nabla\cdot\mathbf{e}_r = \frac{1}{r}, \nabla\cdot\mathbf{e}_\theta = 0, \quad \nabla\cdot\mathbf{e}_\varphi = 0, \tag{C.18b}$$

$$\nabla\times\mathbf{e}_r = 0, \quad \nabla\times\mathbf{e}_\theta = \frac{\mathbf{e}_\varphi}{r}, \quad \nabla\times\mathbf{e}_\varphi = \frac{\mathbf{e}_z}{R}, \tag{C.18c}$$

$$\tag{C.18d}$$

Transformation between (R, φ, Z) and (r, θ, φ) Coordinates:

It is useful to establish the transformation relations between these two coordinate systems because they will be used repeatedly in this thesis. We have,

$$R = R_0 + r\cos\theta, \quad Z = -r\sin\theta, \quad \varphi = \varphi, \tag{C.19a}$$

$$r = \sqrt{(R-R_0)^2 + Z^2}, \quad \theta = \arctan(\frac{Z}{R_0 - R}), \quad \varphi = \varphi, \tag{C.19b}$$

while the unit vectors are given by,

$$\mathbf{e}_r = \cos\theta\mathbf{e}_R - \sin\theta\mathbf{e}_Z, \quad \mathbf{e}_\theta = -\sin\theta\mathbf{e}_R - \cos\theta\mathbf{e}_z, \tag{C.20a}$$

$$\mathbf{e}_R = \cos\theta\mathbf{e}_r - \sin\theta\mathbf{e}_\theta, \quad \mathbf{e}_Z = -\sin\theta\mathbf{e}_r - \cos\theta\mathbf{e}_\theta, \tag{C.20b}$$

Then, we obtain the reduced Jacobians

$$\mathcal{J}^{R,Z}_{r,\theta} = \begin{bmatrix} \cos\theta & -r\sin\theta \\ -\sin\theta & -r\cos\theta \end{bmatrix}, \quad \mathcal{J}^{r,\theta}_{R,Z} = \begin{bmatrix} \cos\theta & -\sin\theta \\ -\frac{\sin\theta}{r} & -\frac{\cos\theta}{r} \end{bmatrix} \tag{C.21}$$

where $\mathcal{J}^{R,Z}_{r,\theta,ij} = \frac{\partial q'_i}{\partial q_j}$, with $i = R, Z$, and $j = r, \theta$. The opposite is true for $\mathcal{J}^{r,\theta}_{R,Z}$. Now, we can establish the fundamental transformation relations for the partial derivatives by multiplying with the transpose of the Jacobian matrices. Therefore, $\partial_{R,Z} = {\mathcal{J}^{r,\theta}_{R,Z}}^T \cdot \partial_{r,\theta}$, and $\partial_{r,\theta} = {\mathcal{J}^{R,Z}_{r,\theta}}^T \cdot \partial_{R,Z}$. Explicitly, it reads

$$\begin{bmatrix} \frac{\partial}{\partial R} \\ \frac{\partial}{\partial Z} \end{bmatrix} = \begin{bmatrix} \cos\theta & -\frac{\sin\theta}{r} \\ -\sin\theta & -\frac{\cos\theta}{r} \end{bmatrix} \begin{bmatrix} \frac{\partial}{\partial r} \\ \frac{\partial}{\partial\theta} \end{bmatrix} = \begin{bmatrix} \cos\theta\frac{\partial}{\partial r} - \frac{\sin\theta}{r}\frac{\partial}{\partial\theta} \\ -\sin\theta\frac{\partial}{\partial r} - \frac{\cos\theta}{r}\frac{\partial}{\partial\theta} \end{bmatrix} \tag{C.22}$$

and,

$$\begin{bmatrix} \frac{\partial}{\partial r} \\ \frac{\partial}{\partial\theta} \end{bmatrix} = \begin{bmatrix} \cos\theta & -\sin\theta \\ -r\sin\theta & -r\cos\theta \end{bmatrix} \begin{bmatrix} \frac{\partial}{\partial R} \\ \frac{\partial}{\partial Z} \end{bmatrix} = \begin{bmatrix} \cos\theta\frac{\partial}{\partial R} - \sin\theta\frac{\partial}{\partial Z} \\ -r\sin\theta\frac{\partial}{\partial R} - r\cos\theta\frac{\partial}{\partial Z} \end{bmatrix} \tag{C.23}$$

Another two identities -the second derivatives $\frac{\partial^2}{\partial R^2}$ and $\frac{\partial^2}{\partial Z^2}$- will prove to be very useful for the derivation of the Laplacian and other operators. After some algebra, they read,

$$\frac{\partial^2}{\partial R^2} = \cos^2\theta\frac{\partial^2}{\partial r^2} + \frac{\sin^2\theta}{r^2}\frac{\partial^2}{\partial\theta^2} - \frac{\sin(2\theta)}{r}\frac{\partial^2}{\partial r\partial\theta} + \frac{\sin^2\theta}{r}\frac{\partial}{\partial r} + \frac{\sin(2\theta)}{r^2}\frac{\partial}{\partial\theta}, \tag{C.24a}$$

$$\frac{\partial^2}{\partial Z^2} = \sin^2\theta\frac{\partial^2}{\partial r^2} + \frac{\cos^2\theta}{r^2}\frac{\partial^2}{\partial\theta^2} + \frac{\sin(2\theta)}{r}\frac{\partial^2}{\partial r\partial\theta} + \frac{\cos^2\theta}{r}\frac{\partial}{\partial r} - \frac{\sin(2\theta)}{r^2}\frac{\partial}{\partial\theta}, \tag{C.24b}$$

Grad-Shafranov and Diffiusion Operators:

Grad-Shafranov operator is an elliptic operator arise naturally in (R,φ,Z) coordinate system when modelling the plasma equilibrium [377, 378]. When $\frac{\partial}{\partial\varphi} = 0$, Grad-Shafranov operator reads

$$\Delta^*\psi = \frac{\partial^2\psi}{\partial R^2} + \frac{\partial^2\psi}{\partial Z^2} - \frac{1}{R}\frac{\partial\psi}{\partial R} = \Delta_{R,Z}\psi - \frac{2}{R}\frac{\partial\psi}{\partial R}, \tag{C.25}$$

where $\Delta_{R,Z}$ is the Laplacian given by Eq.(C.7d). It is straightforward to obtain this operator in (r,θ,φ) coordinate after substituting Eqs.(C.24) in the previous one. Then, we find

$$\Delta^+\psi = \Delta^*|_{r,\theta}\psi = \frac{\partial^2\psi}{\partial r^2} + \frac{1}{r}\frac{\partial\psi}{\partial r} + \frac{1}{r^2}\frac{\partial^2\psi}{\partial\theta^2} - \frac{1}{R}\Big(\cos\theta\frac{\partial}{\partial r} - \frac{\sin\theta}{r}\frac{\partial}{\partial\theta}\Big)\psi, \tag{C.26}$$

After expanding the Laplacian Eq.(C.15d), and substituting Eqs.[C.20b, C.15a] into the previous equation, we obtain

$$\Delta^+ = \Delta_\perp - \frac{2}{R}(\nabla R)\cdot\nabla, \tag{C.27}$$

Here all the operators are written in (r,θ,φ) coordinate system. $\Delta_\perp$ is the poloidal Laplacian which can be obtained from Eq.(C.15d) in the limit $\frac{\partial}{\partial\varphi} = 0$. When we seek to extend the reduced MHD model, by for example including a varying density profile, we encounter another operator, known as the diffusion operator, which can be viewed as a generalization of the Grad-Shafranov operator. It is given in (R,φ,Z) by

$$\Delta_\rho\psi = \rho R\Big\{\frac{\partial}{\partial R}\Big(\frac{1}{\rho R}\frac{\partial\psi}{\partial R}\Big) + \frac{\partial}{\partial Z}\Big(\frac{1}{\rho R}\frac{\partial\psi}{\partial Z}\Big)\Big\} = \Delta^*\psi - \frac{1}{\rho}(\nabla\rho)\cdot\nabla\psi, \tag{C.28}$$

We obtain Eq.(C.28) following the same procedure in the derivation of Eq.(C.27). Notice that when $\rho = const$, diffusion operator reduces to Grad-Shafranov operator: Eq.(C.25). We can transform Δ_ρ to (r,θ,φ) with different methods. The straightforward one is by using Eq.(C.27), which gives

$$\Delta^+_\rho = \Delta_\perp - \frac{2}{R}(\nabla R)\cdot\nabla - \frac{1}{\rho}(\nabla\rho)\cdot\nabla, \tag{C.29}$$

Again, Δ^+_ρ reduced to Δ^+ when $\rho = const$. All the operators are written in (r,θ,φ). In two lines,

$$\boxed{\Delta^*_{R,Z} \longrightarrow \Delta^+_{r,\theta}, \quad \Delta_{\rho,RZ} \longrightarrow \Delta^+_{\rho,r\theta},} \tag{C.30}$$

Poisson Brackets:

In general, these brackets result from the advective terms into the equations of reduced and electron MHD. Poisson bracket for two functions f and g defined in a two-dimensional Cartesian coordinate system is given by,

$$[f,g] = \frac{\partial f}{\partial x}\frac{\partial g}{\partial y} - \frac{\partial g}{\partial x}\frac{\partial f}{\partial y}, \tag{C.31}$$

For example, the advection of the density n with velocity $\mathbf{u}$ could leads to a term of the form $[\phi, n]$, where ϕ might be the velocity stream function. By the direct substituting for t he Cartesian coordinates into the previous equation, and using the Jacobians of each coordinate system, we obtain

$$[f,g]_{R,Z} = \frac{\partial f}{\partial R}\frac{\partial g}{\partial Z} - \frac{\partial g}{\partial R}\frac{\partial f}{\partial Z}, \tag{C.32a}$$

$$[f,g]_{r,\theta} = \frac{1}{r}\Big\{\frac{\partial f}{\partial r}\frac{\partial g}{\partial \theta} - \frac{\partial g}{\partial r}\frac{\partial f}{\partial \theta}\Big\}, \tag{C.32b}$$

In this case, we have

$$\boxed{[\ ,\ ]_{R,Z} \longrightarrow -[\ ,\ ]_{r,\theta},} \tag{C.33}$$

The minus sign is due to the fact that $\mathbf{e}_R \times \mathbf{e}_Z = -\mathbf{e}_\varphi$, while $\mathbf{e}_r \times \mathbf{e}_\theta = \mathbf{e}_\varphi$. A useful identity of Poisson bracket is the following one

$$\frac{d}{d\mathbf{r}}[A,B] = [\frac{dA}{d\mathbf{r}}, B] + [A, \frac{dB}{d\mathbf{r}}], \tag{C.34}$$

D

Linear Analysis of RMHD Model

In this appendix, we explicitly present and discuss all terms appearing in the linear RMHD equation Eqs.[5.70, 5.71]. The basic perturbation quantities are

$$\psi_1 = \tilde{\psi}(x)e^{\gamma t}e^{iky}, \quad \phi_1 = \tilde{\phi}(x)e^{\gamma t}e^{iky}, \tag{D.1}$$

Linear Analysis of Equations:

Here we write the expressions for the terms appearing in the linearized RMHD equations in section 5.4.2, namely Eqs(5.70, 5.73). All equilibrium quantities are functions of x only.

$$\nabla^2\psi_1 = (\frac{\partial}{\partial x^2}-k^2)\tilde{\psi}(x)e^{iky}e^{\gamma t} = \mathcal{A}\tilde{\psi}(x)e^{iky}e^{\gamma t}, \quad \nabla^2\phi_1 = i(\frac{\partial}{\partial x^2}-k^2)\tilde{\phi}(x)e^{iky}e^{\gamma t} = i\mathcal{A}\tilde{\phi}(x)e^{iky}e^{\gamma t}, \tag{D.2}$$

$$\mathcal{F}_1 = \Big\{\mathcal{I} - d_e^2(\frac{\partial^2}{\partial x^2} - k^2)\Big\}\tilde{\psi}(x)e^{iky}e^{\gamma t} = (\mathcal{I} - d_e^2\mathcal{A})\tilde{\psi}(x)e^{iky}e^{\gamma t} = \mathcal{D}\tilde{\psi}(x)e^{iky}e^{\gamma t}, \tag{D.3}$$

$$\begin{aligned} U_1 &= i\Big(\rho_i^2\Big[\frac{\partial^4}{\partial x^4} - 2k^2\frac{\partial^2}{\partial x^2} + k^4\Big] + (\frac{\partial^2}{\partial x^2} - k^2)\Big)\tilde{\phi}(x)e^{iky}e^{\gamma t} = i(\rho_i^2\mathcal{E} + \mathcal{A})\tilde{\phi}(x)e^{iky}e^{\gamma t} \\ &= i\Lambda\tilde{\phi}(x)e^{iky}e^{\gamma t}, \end{aligned} \tag{D.4}$$

$$\begin{aligned} \nabla^2 U_1 &= i\Big(\rho_i^2(\frac{\partial^2}{\partial x^2} - k^2)\Big[\frac{\partial^4}{\partial x^4} - 2k^2\frac{\partial^2}{\partial x^2} + k^4\Big] + \Big[\frac{\partial^4}{\partial x^4} - 2k^2\frac{\partial^2}{\partial x^2} + k^4\Big]\Big)\tilde{\phi}(x)e^{iky}e^{\gamma t} \\ &= i(\rho_i^2\mathcal{A}\mathcal{E} + \mathcal{E})\tilde{\phi}(x)e^{iky}e^{\gamma t} = i\mathcal{V}\tilde{\phi}(x)e^{iky}e^{\gamma t}, \end{aligned} \tag{D.5}$$

$$\begin{aligned} \frac{\partial\mathcal{F}_1}{\partial t} &= \gamma\{1 - d_e^2\mathcal{A}\}\tilde{\psi}(x)e^{iky}e^{\gamma t} = \gamma\mathcal{D}\tilde{\psi}(x)e^{iky}e^{\gamma t}, \\ \frac{\partial U_1}{\partial t} &= i\gamma\{\rho_i^2\mathcal{E} + \mathcal{A}\}\tilde{\phi}(x)e^{iky}e^{\gamma t} = i\Lambda\tilde{\phi}(x)e^{iky}e^{\gamma t}, \end{aligned} \tag{D.6}$$

$$[\phi_{eq}, \mathcal{F}_1] = \frac{\partial\phi_{eq}}{\partial x}\frac{\partial\mathcal{F}_1}{\partial y} - \frac{\partial\mathcal{F}_1}{\partial x}\frac{\partial\phi_{eq}}{\partial y} = \frac{\partial\phi_{eq}}{\partial x}\frac{\partial\mathcal{F}_1}{\partial y} = \frac{\partial\phi_{eq}}{\partial x}\frac{\partial\mathcal{F}_1}{\partial y} = ik\phi'_{eq}\mathcal{D}\tilde{\psi}(x)e^{iky}e^{\gamma t}, \tag{D.7}$$

$$[\phi_1, \mathcal{F}_{eq}] = k\mathcal{F}'_{eq}\tilde{\phi}(x)e^{iky}e^{\gamma t}, \tag{D.8}$$

$$[U_{eq}, \psi_1] = ikU'_{eq}\tilde{\psi}(x)e^{iky}e^{\gamma t}, \tag{D.9}$$

$$[U_1, \psi_{eq}] = k\psi'_{eq}\{\rho_i^2\mathcal{E} + \mathcal{A}\}\tilde{\phi}(x)e^{iky}e^{\gamma t} = k\psi'_{eq}\Lambda\tilde{\phi}(x)e^{iky}e^{\gamma t}, \tag{D.10}$$

$$[\phi_{eq}, U_1] = -k\phi'_{eq}\{\rho_i^2\mathcal{E} + \mathcal{A}\}\tilde{\phi}(x)e^{iky}e^{\gamma t} = -k\phi'_{eq}\Lambda\tilde{\phi}(x)e^{iky}e^{\gamma t}, \tag{D.11}$$

$$[\phi_1, U_{eq}] = kU'_{eq}\tilde{\phi}(x)e^{iky}e^{\gamma t}, \tag{D.12}$$

$$[\psi_{eq}, \nabla^2\psi_1] = ik\psi'_{eq}\mathcal{A}\tilde{\psi}(x)e^{iky}e^{\gamma t}, \tag{D.13}$$

$$[\psi_1, \nabla^2\psi_{eq}] = -ik\psi'''_{eq}\tilde{\psi}(x)e^{iky}e^{\gamma t}, \tag{D.14}$$

Above, the matrices $\mathcal{A}$, $\mathcal{D}$, $\mathcal{E}$, Λ and $\mathcal{V}$ are given by Eq.(5.77). Substituting the previous relations into Eqs(5.70, 5.71), we obtain the eigenvalue problem 5.76.

E

Linear Analysis in the Hall Regime

In this appendix, we linearize the system of equations of Hall MHD which takes into account the Hall term.

Linearization in the Hall Regime:

After substituting Eq.(5.78) into Eq.(5.79), and perturbing each equilibrium quantity $\mathbf{A}_{eq}$, with $\mathbf{A}_1$ such that $|\mathbf{A}_1| << |\boldsymbol{A}_{eq}|$, the linearized Maxwelll-Faraday equation becomes

$$\begin{aligned}\frac{\partial \mathbf{B}_1}{\partial t} &= \nabla \times (\mathbf{u} \times \mathbf{B}_{eq}) - \mu_0 d_e^2 \nabla \times (\frac{\partial \mathbf{J}_1}{\partial t}) - \mu_0 d_e^2 \nabla \times (\nabla \cdot \{\mathbf{u}\mathbf{J}_{eq} + \mathbf{J}_{eq}\mathbf{u}\}) - \frac{1}{en} \nabla \times (\mathbf{J}_{eq} \times \mathbf{B}_1) \\ &\quad - \frac{1}{en} \nabla \times (\mathbf{J}_1 \times \mathbf{B}_{eq}) - \eta \nabla \times (\mathbf{J}_1),\end{aligned} \tag{E.1}$$

In the previous equation, the equilibrium velocity is taken to be zero, and thus $\mathbf{u} = \mathbf{u}_1$. The perturbation quantities $\mathbf{A}_1$ are $\mathbf{A}_1 = A_{1x}\mathbf{e}_x + A_{1y}\mathbf{e}_y + A_{1z}\mathbf{e}_z$. Also, we assumed the incompressible limit ($\nabla \cdot \mathbf{u} = 0$). Now using Eqs.(5.82, 5.81, 5.79), the terms in linearized Faraday equation are

$$\mathbf{u} \times \mathbf{B}_{eq} = \begin{cases} B_g u_y - B_0 f(x) u_z, \\ -B_g u_x, \\ B_0 f(x) u_x \end{cases} \tag{E.2}$$

$$\nabla \times (\mathbf{u} \times \mathbf{B}_{eq}) = \begin{cases} B_0 f(x) \frac{\partial u_x}{\partial y}, \\ -B_0 f^{'}(x) u_x - B_0 f(x) \frac{\partial u_x}{\partial x}, \\ \underbrace{-B_g \dfrac{\partial u_x}{\partial x} - B_g \dfrac{\partial u_y}{\partial y}}_{=0, \nabla \cdot \mathbf{u} = 0.} + B_0 f(x) \frac{\partial u_z}{\partial y} = B_0 f(x) \frac{\partial u_z}{\partial y}, \end{cases} \tag{E.3}$$

$$\mathbf{J}_{eq} \times \mathbf{B}_1 = \frac{B_0}{\mu_0} \begin{cases} -f^{'}(x) B_{1y}, \\ f^{'}(x) B_{1x}, \\ 0, \end{cases} \tag{E.4}$$

$$\nabla\times(\mathbf{J}_{eq}\times\mathbf{B}_1)=\frac{B_0}{\mu_0}\begin{cases}0,\\0,\\f^{''}(x)B_{1x}+f^{'}(x)\underbrace{\dfrac{\partial B_{1x}}{\partial x}+\dfrac{\partial B_{1y}}{\partial y}}_{=-\frac{\partial B_{1z}}{\partial z}}=f^{''}(x)B_{1x}-\underbrace{f^{'}(x)\dfrac{\partial B_{1z}}{\partial z}}_{=0\ if\ \frac{\partial}{\partial z}=0.}=f^{''}(x)B_{1x},\end{cases}\tag{E.5}$$

$$\mathbf{J}_1=\frac{1}{\mu_0}\nabla\times\mathbf{B}_1=\frac{1}{\mu_0}\begin{cases}\frac{\partial B_{1z}}{\partial y},\\-\frac{\partial B_{1z}}{\partial x},\\\frac{\partial B_{1y}}{\partial x}-\frac{\partial B_{1x}}{\partial y}\end{cases}\tag{E.6}$$

$$\nabla\times\mathbf{J}_1=\frac{1}{\mu_0}\begin{cases}\frac{\partial^2 B_{1y}}{\partial x\partial y}-\frac{\partial^2 B_{1x}}{\partial x^2}=-\nabla^2 B_{1x},\\-\frac{\partial^2 B_{1y}}{\partial x^2}+\frac{\partial^2 B_{1x}}{\partial x\partial y},\\-\frac{\partial^2 B_{1z}}{\partial x^2}-\frac{\partial^2 B_{1z}}{\partial y^2}=-\nabla^2 B_{1z},\end{cases}\tag{E.7}$$

$$\mathbf{J}_1\times\mathbf{B}_{eq}=\frac{1}{\mu_0}\begin{cases}-B_g\frac{\partial B_{1z}}{\partial x}-B_0 f(x)\frac{\partial B_{1y}}{\partial x}+B_0 f(x)\frac{\partial B_{1x}}{\partial y},\\-B_g\frac{\partial B_{1z}}{\partial y},\\B_0 f(x)\frac{\partial B_{1z}}{\partial y},\end{cases}\tag{E.8}$$

$$\nabla\times(\mathbf{J}_1\times\mathbf{B}_{eq})=\frac{1}{\mu_0}\begin{cases}B_0 f(x)\frac{\partial^2 B_{1z}}{\partial y^2},\\-B_0 f^{'}(x)\frac{\partial B_{1z}}{\partial y}-B_0 f(x)\frac{\partial^2 B_{1z}}{\partial x\partial y},\\B_0 f(x)(\frac{\partial^2 B_{1y}}{\partial x\partial y}-\frac{\partial^2 B_{1x}}{\partial y^2})=-B_0 f(x)\nabla^2 B_{1x},\end{cases}\tag{E.9}$$

$$\nabla\cdot\{\mathbf{u}\mathbf{J}_{eq}+\mathbf{J}_{eq}\mathbf{u}\}=(\nabla\cdot\mathbf{u})\mathbf{J}_{eq}+\mathbf{u}\cdot\nabla\mathbf{J}_{eq}+(\nabla\cdot\mathbf{J}_{eq})\mathbf{u}+\mathbf{J}_{eq}\cdot\nabla\mathbf{u}=\frac{B_0}{\mu_0}f^{''}(x)u_x\mathbf{e}_z,\tag{E.10}$$

Where $\nabla\cdot\mathbf{u}=\nabla\cdot\mathbf{J}_{eq}=\mathbf{J}_{eq}\cdot\nabla=0$.

$$\nabla\times\Big[\nabla\cdot\{\mathbf{u}\mathbf{J}_{eq}+\mathbf{J}_{eq}\mathbf{u}\}\Big]=\frac{B_0}{\mu_0}\begin{cases}f^{''}(x)\frac{\partial u_x}{\partial y},\\-f^{'''}(x)u_x-f^{''}(x)\frac{\partial u_x}{\partial x},\\0,\end{cases}\tag{E.11}$$

After substituting these relations into Eq.(E.1), $x-$ and $z-$ components give the following two equations,

$$\frac{\partial}{\partial t}(1-d_e^2\nabla^2)B_{1x}=B_0[f(x)-d_e^2 f^{''}(x)]\frac{\partial u_x}{\partial y}-\frac{B_0}{\mu_0 en}f(x)\frac{\partial^2 B_{1z}}{\partial y^2}+\frac{\eta}{\mu_0}\nabla^2 B_{1x},\tag{E.12}$$

$$\frac{\partial}{\partial t}(1-d_e^2\nabla^2)B_{1z}=B_0 f(x)\frac{\partial u_z}{\partial y}+\frac{B_0}{\mu_0 en}[f(x)\nabla^2-f^{''}(x)]B_{1x}+\frac{\eta}{\mu_0}\nabla^2 B_{1z},\tag{E.13}$$

The linearization of Eq.(5.80), gives

$$mn\frac{\partial \mathbf{u}}{\partial t} = -\nabla p_1 + \mathbf{J}_1 \times \mathbf{B}_{eq} + \mathbf{J}_{eq} \times \mathbf{B}_1 + \nu\nabla^2\mathbf{u}, \tag{E.14}$$

Now, taking the `curl` of this equation to eliminate the pressure, one finds

$$mn\frac{\partial \mathbf{\Omega}}{\partial t} = \nabla \times (\mathbf{J}_1 \times \mathbf{B}_{eq}) + \nabla \times (\mathbf{J}_{eq} \times \mathbf{B}_1) + \nu\nabla^2\mathbf{\Omega}, \tag{E.15}$$

Where

$$\mathbf{\Omega} = \nabla \times \mathbf{u} = \begin{cases} \frac{\partial u_z}{\partial y} \\ -\frac{\partial u_z}{\partial x} \\ \frac{\partial u_y}{\partial x} - \frac{\partial u_x}{\partial y} \end{cases}, \tag{E.16}$$

Using Eqs(E.9, E.5), one easily obtains

$$mn \begin{cases} \frac{\partial \Omega_x}{\partial t} \\ \frac{\partial \Omega_y}{\partial t} \\ \frac{\partial \Omega_z}{\partial t} \end{cases} = \begin{cases} \frac{B_0}{\mu_0} f(x) \frac{\partial^2 B_{1z}}{\partial y^2} + \nu\nabla^2\Omega_x, \\ -\frac{B_0}{\mu_0} f'(x) \frac{\partial B_{1z}}{\partial y} - \frac{B_0}{\mu_0} f(x) \frac{\partial^2 B_{1z}}{\partial x \partial y} + \nu\nabla^2\Omega_y, \\ -\frac{B_0}{\mu_0} f(x)\nabla^2 B_{1x} + \frac{B_0}{\mu_0} f''(x) B_{1x} + \nu\nabla^2\Omega_z, \end{cases} \tag{E.17}$$

Evaluating the derivative $\frac{\partial}{\partial y}$ of the $z-$component of the vorticity equation, one finds

$$\frac{\partial \Omega_z}{\partial} = -\nabla^2 u_x, \tag{E.18}$$

Then, the $z-$component equation becomes

$$mn\frac{\partial}{\partial t}\nabla^2 u_x = \frac{B_0}{\mu_0}[f(x)\nabla^2 - f''(x)]\frac{\partial B_{1x}}{\partial y} + \nu\nabla^2\nabla^2 u_x, \tag{E.19}$$

The x- and $z-$ components of vorticity equation in addition to the $x-$ and $z-$ components of Faraday equation form a closed-generalized eigenvalue problem. Now, if we normalize quantities with respect to $B_0,\ L_0, u_0 = u_A,\ \tau_0 = \tau_A = \frac{L_0}{u_0}$, the dimensionless system of equations becomes

$$\frac{\partial}{\partial t}(1 - d_e^2\nabla^2)B_{1x} = [f(x) - d_e^2 f''(x)]\frac{\partial u_x}{\partial y} - d_i f(x)\frac{\partial^2 B_{1z}}{\partial y^2} + S^{-1}\nabla^2 B_{1x}, \tag{E.20}$$

$$\frac{\partial}{\partial t}(1 - d_e^2\nabla^2)B_{1z} = f(x)\frac{\partial u_z}{\partial y} + d_i[f(x)\nabla^2 - f''(x)]B_{1x} + S^{-1}\nabla^2 B_{1z}, \tag{E.21}$$

$$\frac{\partial}{\partial t}\nabla^2 u_x = [f(x)\nabla^2 - f''(x)]\frac{\partial B_{1x}}{\partial y} + R^{-1}\nabla^2\nabla^2 u_x, \tag{E.22}$$

$$\frac{\partial}{\partial t}\frac{\partial u_z}{\partial y} = f(x)\frac{\partial^2 B_{1z}}{\partial y^2} + R^{-1}\nabla^2\frac{\partial u_z}{\partial y}, \tag{E.23}$$

Remark on Phase Difference between Velocity and Magnetic Field Perturbations:
However, if we assume that the perturbation quantities are of the form $\tilde{A}(x)e^{\gamma t}e^{iky}$, and substitute this into Eq.(E.12) with $d_i = d_e = S^{-1} = 0$, one easily finds,

$$\gamma B_{1x} = ikf(x)u_x, \tag{E.24}$$

The previous equation means that u_x and B_{1x} have opposite spatial parity and are de-phased by $\frac{\pi}{2}$. Therefore, $B_{1x} \sim \cos(ky) \sim e^{iky}$, while $u_x \sim \sin(ky) \sim ie^{iky}$ at O point. Hence, we take perturbations to be as follows

$$B_{1i} = B_{1i}(x)e^{\gamma t}e^{iky}, \quad u_i = iu_i(x)e^{\gamma t}e^{iky}, \tag{E.25}$$

Where $i = x, y, z$. This is also true for the magnetic and velocity stream functions: ψ and ϕ, receptively.

F

Linear Analysis of Incompressible EMHD

Homogeneous Periodic Perturbations:

Due to the uniformity of the background magnetic field, the equilibrium electron velocity given by Ampere law vanishes. The linear version of Eq.(6.7) becomes

$$\frac{\partial \mathbf{B}_1}{\partial t} - d_e^2 \frac{\partial}{\partial t}\nabla^2 \mathbf{B}_1 = \nabla \times (\mathbf{u} \times \mathbf{B}_0) + D\nabla^2 \mathbf{B}_1, \tag{F.1}$$

We proceed by estimating all the terms. The electron velocity is given by

$$\mathbf{u}_1 = -\frac{1}{\mu_0 e n_0}\nabla \times \mathbf{B}_1 = -\frac{1}{\mu_0 e n_0}\begin{cases} \frac{\partial B_{z1}}{\partial y} - \frac{\partial B_{y1}}{\partial z}, \\ \frac{\partial B_{x1}}{\partial z} - \frac{\partial B_{z1}}{\partial x}, \\ \frac{\partial B_{y1}}{\partial x} - \frac{\partial B_{x1}}{\partial y}, \end{cases} \tag{F.2}$$

while

$$\mathbf{u}_1 \times \mathbf{B}_0 = -\frac{B_0}{\mu_0 e n_0}\begin{cases} \frac{\partial B_{x1}}{\partial z} - \frac{\partial B_{z1}}{\partial x}, \\ \frac{\partial B_{y1}}{\partial z} - \frac{\partial B_{z1}}{\partial y}, \\ 0, \end{cases} \tag{F.3}$$

$$\nabla \times (\mathbf{u}_1 \times \mathbf{B}_0) = -\frac{B_0}{\mu_0 e n_0}\begin{cases} \frac{\partial^2 B_{z1}}{\partial z \partial y} - \frac{\partial^2 B_{y1}}{\partial z^2}, \\ \frac{\partial^2 B_{x1}}{\partial z^2} - \frac{\partial^2 B_{z1}}{\partial z \partial x}, \\ \frac{\partial^2 B_{y1}}{\partial x \partial z} - \frac{\partial^2 B_{x1}}{\partial y \partial z}, \end{cases} \tag{F.4}$$

Substituting into Eq.(F.1), we find the following three coupled differential equations

$$\begin{aligned} \frac{\partial B_{x1}}{\partial t} - d_e^2 \frac{\partial}{\partial t}\nabla^2 B_{x1} &= \frac{B_0}{\mu_0 e n_0}\frac{\partial^2 B_{y1}}{\partial z^2} - \frac{B_0}{\mu_0 e n_0}\frac{\partial^2 B_{z1}}{\partial z \partial y} + D\nabla^2 B_{x1}, \\ \frac{\partial B_{y1}}{\partial t} - d_e^2 \frac{\partial}{\partial t}\nabla^2 B_{y1} &= -\frac{B_0}{\mu_0 e n_0}\frac{\partial^2 B_{x1}}{\partial z^2} + \frac{B_0}{\mu_0 e n_0}\frac{\partial^2 B_{z1}}{\partial z \partial x} + D\nabla^2 B_{y1}, \\ \frac{\partial B_{z1}}{\partial t} - d_e^2 \frac{\partial}{\partial t}\nabla^2 B_{z1} &= \frac{B_0}{\mu_0 e n_0}\frac{\partial^2 B_{x1}}{\partial y \partial z} - \frac{B_0}{\mu_0 e n_0}\frac{\partial^2 B_{y1}}{\partial x \partial z} + D\nabla^2 B_{z1}, \end{aligned} \tag{F.5}$$

This system of linearized equations can be used for a wave with an arbitrary directions. However, going back to our chosen perturbation quantities, the previous set of equations becomes

after applying Fourier transformation using Eq.(6.11)

$$\begin{aligned}
-i\omega B_{x1} - ik^2 d_e^2 \omega B_{x1} &= -\alpha k_z^2 B_0 B_{y1} + \alpha k_y k_z B_0 B_{z1} - Dk^2 B_{x1},\\
-i\omega B_{y1} - ik^2 d_e^2 \omega B_{y1} &= \alpha k_z^2 B_0 B_{x1} - Dk^2 B_{y1},\\
-i\omega B_{z1} - ik^2 d_e^2 \omega B_{z1} &= -\alpha k_y k_z B_0 B_{x1} - Dk^2 B_{z1},
\end{aligned} \tag{F.6}$$

where $\alpha = \frac{1}{\mu_0 e n_o}$. In the previous equations, B_{x1}, B_{y1}, B_{z1} are the Fourier components $\tilde{Q}$, but we omit the tilde ($\sim$) to simplify writing. Eq.(F.6) can be cast in the following matrix form

$$\begin{bmatrix}
-i\omega(1+k^2d_e^2)+Dk^2 & \alpha k_z^2 B_0 & -\alpha k_y k_z B_0\\
-\alpha k_z^2 B_0 & -i\omega(1+k^2d_e^2)+Dk^2 & 0\\
\alpha k_y k_z B_0 & 0 & -i\omega(1+k^2d_e^2)+Dk^2
\end{bmatrix}
\begin{bmatrix} B_{x1}\\ B_{y1}\\ B_{z1}\end{bmatrix} = 0, \tag{F.7}$$

which represents the dispersion relation of the model.

Inhomogeneous Perturbation:

In this section, we write the different values of terms in Eqs[6.25, 6.26, 6.27] for inhomogeneous perturbation along x, and periodic one along y. The perturbed quantity Q_1 takes the following form

$$Q_1 = \tilde{Q}(x) e^{iky} e^{\gamma t}, \tag{F.8}$$

Hence, the different terms become

$$\frac{\partial F_1}{\partial t} = \gamma e^{iky} e^{\gamma t}\Big(1 - d_e^2(\frac{\partial^2}{\partial x^2} - k^2)\Big) = \gamma e^{iky} e^{\gamma t}\Big(1 - d_e^2 \mathcal{A}\Big)\tilde{\psi} = \gamma e^{iky} e^{\gamma t} \mathcal{D}\tilde{\psi}, \tag{F.9}$$

$$[b_{eq}, F_1] = ike^{iky} e^{\gamma t} b'_{eq} \mathcal{D}\tilde{\psi}, \tag{F.10}$$

$$[b_1, F_{eq}] = ke^{iky} e^{\gamma t} F'_{eq} \tilde{b}, \tag{F.11}$$

$$\nabla^2 \psi_1 = e^{iky} e^{\gamma t}(\frac{\partial^2}{\partial x^2} - k^2)\tilde{\psi} = e^{iky} e^{\gamma t} \mathcal{A}\tilde{\psi}, \tag{F.12}$$

$$\frac{\partial W}{\partial t} = i\gamma e^{iky} e^{\gamma t} \mathcal{D}\tilde{b}, \tag{F.13}$$

$$[b_{eq}, W_1] = i^2 k e^{iky} e^{\gamma t} b'_{eq} \mathcal{D}\tilde{b}, \tag{F.14}$$

$$[b_1, W_{eq}] = -i^2 k e^{iky} e^{\gamma t} W'_{eq} \tilde{b}, \tag{F.15}$$

$$[\psi_{eq}, \nabla^2 \psi_1] = ike^{iky} e^{\gamma t} \psi'_{eq} \mathcal{A}\tilde{\psi}(x), \tag{F.16}$$

$$[\psi_1, \nabla^2 \psi_{eq}] = -ike^{iky} e^{\gamma t} \psi'''_{eq} \tilde{\psi}(x), \tag{F.17}$$

$$\nabla^2 b_1 = ie^{iky} e^{\gamma t} \mathcal{A}\tilde{b}, \tag{F.18}$$

Now, substituting these expression into equations 6.25, and 6.26, one easily obtains the eigenvalue problem given by Eq.(6.28).

G

Derivation of 2D-EMHD Model

Some Remarks on the Derivation of the 2D-EMHD Model:

To derive this model, we calculate each term in Eq.(6.7) which is given by,

$$\frac{\partial}{\partial t}\Big(\mathbf{B} - d_e^2\nabla^2\mathbf{B}\Big) = \frac{1}{\mu_0 en}\nabla\times\Big(\mathbf{B}\times(\nabla\times\mathbf{B})\Big) - \frac{d_e^2}{\mu_0 en}\nabla\times\Big(\nabla^2\mathbf{B}\times(\nabla\times\mathbf{B})\Big) + D\nabla^2\mathbf{B}, \quad \text{(G.1)}$$

Using the definition of the magnetic field 6.21, we have

$$\nabla\times\mathbf{B} = -\nabla^2\psi\mathbf{e}_z + \nabla b\times\mathbf{e}_z, \quad \text{(G.2)}$$

$$\mathbf{B}\times(\nabla\times\mathbf{B}) = \nabla^2\psi\nabla\psi - [b,\psi]\mathbf{e}_z + (B_g + b)\nabla b, \quad \text{(G.3)}$$

$$\nabla\times\Big(\mathbf{B}\times(\nabla\times\mathbf{B})\Big) = [\nabla^2\psi,\psi]\mathbf{e}_z - \nabla[b,\psi]\times\mathbf{e}_z, \quad \text{(G.4)}$$

$$\nabla^2\mathbf{B}\times(\nabla\times\mathbf{B}) = \nabla^2\psi\nabla(\nabla^2\psi) - [b,\nabla^2\psi]\mathbf{e}_z + \nabla^2 b\nabla b, \quad \text{(G.5)}$$

$$\nabla\times\Big(\nabla^2\mathbf{B}\times(\nabla\times\mathbf{B})\Big) = -\nabla[b,\nabla^2\psi]\times\mathbf{e}_z + [\nabla^2 b, b]\mathbf{e}_z, \quad \text{(G.6)}$$

And,

$$D\nabla^2\mathbf{B} = D\nabla(\nabla^2\psi)\times\mathbf{e}_z + \nabla^2 b\mathbf{e}_z, \quad \text{(G.7)}$$

Where the Poisson bracket is $[f,g] = \frac{\partial f}{\partial x}\frac{\partial g}{\partial y} - \frac{\partial g}{\partial x}\frac{\partial f}{\partial y}$. Substituting the previous relationships into Eq.(G.1), we obtain the following equations

$$\frac{\partial F}{\partial t} + \frac{1}{\mu_0 en}[b,F] = D\nabla^2\psi, \quad \text{(G.8)}$$

$$\frac{\partial W}{\partial t} + \frac{1}{\mu_0 en}[b,W] = \frac{1}{\mu_0 en}[\nabla^2\psi,\psi] + D\nabla^2 b, \quad \text{(G.9)}$$

Where $W = b - d_e^2\nabla^2 b$, and $F = \psi - d_e^2\nabla^2\psi$. Now, the dimensionless form of the previous system is,

$$\frac{\partial F}{\partial t} + [b,F] = \frac{1}{S_{\text{EMHD}}}\nabla^2\psi, \quad \text{(G.10)}$$

$$\frac{\partial W}{\partial t} + [b,W] = [\nabla^2\psi,\psi] + \frac{1}{S_{\text{EMHD}}}\nabla^2 b, \quad \text{(G.11)}$$

In this regime we normalize times to Whistler time $\tau_w = \frac{L^2}{d_e^2 \omega_{c,e}} = \frac{\tau_A}{d_i}$, with τ_A being the Alfvén time; the spatial scales are normalized to the characteristic length L , which represents the characteristic length of the equilibrium; the the magnetic field is normalized to the guide field B_g. Finally, $D = \frac{\eta}{\mu_0}$. Also, we should be careful about the fact that EMHD Lundquist number is related to RMHD Lundquist number by the following relation

$$S_{\texttt{EMHD}} = d_i S_{\texttt{RMHD}}, \quad \tau_w = \frac{\tau_A}{d_i}, \tag{G.12}$$

H

Linear Analysis of the Full Pressure Tensor

Calculating Different Terms in Equilibrium Pressure Tensor Equation:

The equilibrium full pressure tensor reads,

$$(\nabla\cdot\mathbf{u}_0)\mathcal{P}^0+(\mathbf{u}_0\cdot\nabla)\mathcal{P}^0+\mathcal{P}^0\cdot\nabla\mathbf{u}_0+[\mathcal{P}^0\cdot\nabla\mathbf{u}_0]^T+\frac{e}{m_e}\Big(\mathcal{P}^0\times\mathbf{B}_0+[\mathcal{P}^0\times\mathbf{B}_0]^T\Big)=0, \quad \text{(H.1)}$$

From Eq.(6.36), one has

$$(\nabla\cdot\mathbf{u}_0)\mathcal{P}^0=0, \quad (\mathbf{u}_0\cdot\nabla)\mathcal{P}^0=0, \quad \text{(H.2)}$$

Now using Eq.(B.29), we have

$$[\mathcal{P}^0\cdot\nabla\mathbf{u}_0]=\begin{bmatrix}0 & 0 & \mathcal{P}^0_{xx}\frac{\partial u_{z0}}{\partial x}\\ 0 & 0 & \mathcal{P}^0_{xy}\frac{\partial u_{z0}}{\partial x}\\ 0 & 0 & \mathcal{P}^0_{xz}\frac{\partial u_{z0}}{\partial x}\end{bmatrix} \quad \text{(H.3)}$$

Therefore,

$$[\mathcal{P}^0\cdot\nabla\mathbf{u}_0]+[\mathcal{P}^0\cdot\nabla\mathbf{u}_0]^T=\begin{bmatrix}0 & 0 & \mathcal{P}^0_{xx}\frac{\partial u_{z0}}{\partial x}\\ 0 & 0 & \mathcal{P}^0_{xy}\frac{\partial u_{z0}}{\partial x}\\ 0 & 0 & 2\mathcal{P}^0_{xz}\frac{\partial u_{z0}}{\partial x}\end{bmatrix} \quad \text{(H.4)}$$

The last two terms of equation **??** are given by

$$\frac{e}{m_e}[\mathcal{P}^0\times\mathbf{B}_0]=\frac{e}{m_e}\begin{bmatrix}B_g\mathcal{P}^0_{xy}-B_sf(x)\mathcal{P}^0_{xz} & B_g\mathcal{P}^0_{yy}-B_sf(x)\mathcal{P}^0_{yz} & B_g\mathcal{P}^0_{yz}-B_sf(x)\mathcal{P}^0_{zz}\\ -B_g\mathcal{P}^0_{xx} & -B_g\mathcal{P}^0_{xy} & -B_g\mathcal{P}^0_{xz}\\ B_sf(x)\mathcal{P}^0_{xx} & B_sf(x)\mathcal{P}^0_{xy} & B_sf(x)\mathcal{P}^0_{xz}\end{bmatrix} \quad \text{(H.5)}$$

Then,

$$\frac{e}{m_e}[\mathcal{P}^0\times\mathbf{B}_0]+\frac{e}{m_e}[\mathcal{P}^0\times\mathbf{B}_0]^T=\frac{e}{m_e}\times$$
$$\begin{bmatrix}2B_g\mathcal{P}^0_{xy}-2B_sf(x)\mathcal{P}^0_{xz} & B_g\mathcal{P}^0_{yy}-B_g\mathcal{P}^0_{xx}-B_sf(x)\mathcal{P}^0_{yz} & B_g\mathcal{P}^0_{yz}+B_sf(x)\mathcal{P}^0_{xx}-B_sf(x)\mathcal{P}^0_{zz}\\ B_g\mathcal{P}^0_{yy}-B_g\mathcal{P}^0_{xx}-B_sf(x)\mathcal{P}^0_{yz} & -2B_g\mathcal{P}^0_{xy} & B_sf(x)\mathcal{P}^0_{xy}-B_g\mathcal{P}^0_{xz}\\ B_g\mathcal{P}^0_{yz}+B_sf(x)\mathcal{P}^0_{xx}-B_sf(x)\mathcal{P}^0_{zz} & B_sf(x)\mathcal{P}^0_{xy}-B_g\mathcal{P}^0_{xz} & 2B_sf(x)\mathcal{P}^0_{xz}\end{bmatrix} \quad \text{(H.6)}$$

Now substituting Eqs[H.6, H.4, H.2] into Eq.(**??**), we find the following set of equations

$$\omega_{c,e}\mathcal{P}^0_{xy} - \bar{\omega}_{c,e}f(x)\mathcal{P}^0_{xz} = 0, \tag{H.7}$$

$$\omega_{c,e}\mathcal{P}^0_{yy} - \omega_{c,e}\mathcal{P}^0_{xx} - \bar{\omega}_{c,e}f(x)\mathcal{P}^0_{yz} = 0, \tag{H.8}$$

$$\omega_{c,e}\mathcal{P}^0_{yz} + \bar{\omega}_{c,e}f(x)\mathcal{P}^0_{xx} - \bar{\omega}_{c,e}f(x)\mathcal{P}^0_{zz} + \frac{\partial u_{z0}}{\partial x}\mathcal{P}^0_{xx} = 0, \tag{H.9}$$

$$-2\omega_{c,e}\mathcal{P}^0_{xy} = 0, \tag{H.10}$$

$$\omega_{c,e}\mathcal{P}^0_{xz} - \bar{\omega}_{c,e}f(x)\mathcal{P}^0_{xy} - \frac{\partial u_{z0}}{\partial x}\mathcal{P}^0_{xy} = 0, \tag{H.11}$$

$$\bar{\omega}_{c,e}f(x)\mathcal{P}^0_{xz} + \frac{\partial u_{z0}}{\partial x}\mathcal{P}^0_{xz} = 0, \tag{H.12}$$

where,

$$\omega_{c,e} = \frac{eB_g}{m}, \quad \bar{\omega}_{c,e} = \frac{eB_s}{m} \tag{H.13}$$

Evaluation of Different Terms in Linearized Pressure Tensor Equation with Guide Field:

Linearizing Eq.(6.52) gives

$$\begin{aligned}&\frac{\partial \mathcal{P}^1}{\partial t} + (\nabla\cdot\mathbf{u}_1)\mathcal{P}^0 + (\mathbf{u}_1\cdot\nabla)\mathcal{P}^0 + \mathcal{P}^0\cdot\nabla\mathbf{u}_1 + [\mathcal{P}^0\cdot\nabla\mathbf{u}_1]^T + +\mathcal{P}^1\cdot\nabla\mathbf{u}_0 + [\mathcal{P}^1\cdot\nabla\mathbf{u}_0]^T\\ &+\frac{e}{m}\Big(\mathcal{P}^0\times\mathbf{B}_1 + \mathcal{P}^1\times\mathbf{B}_0 + [\mathcal{P}^0\times\mathbf{B}_1]^T + [\mathcal{P}^1\times\mathbf{B}_0]^T\Big) = 0,\end{aligned} \tag{H.14}$$

Using Eq.(6.51), and the compressibility assumption, $\nabla\cdot\mathbf{u}_1 \neq 0$, the second term becomes

$$(\nabla\cdot\mathbf{u}_1)\mathcal{P}^0 = \begin{bmatrix} (\frac{\partial u_{x1}}{\partial x} + \frac{\partial u_{y1}}{\partial y})\mathcal{P}^0_{\perp} & 0 & 0 \\ 0 & (\frac{\partial u_{x1}}{\partial x} + \frac{\partial u_{y1}}{\partial y})\mathcal{P}^0_{\perp} & (\frac{\partial u_{x1}}{\partial x} + \frac{\partial u_{y1}}{\partial y})\mathcal{P}^0_{yz} \\ 0 & (\frac{\partial u_{x1}}{\partial x} + \frac{\partial u_{y1}}{\partial y})\mathcal{P}^0_{yz} & (\frac{\partial u_{x1}}{\partial x} + \frac{\partial u_{y1}}{\partial y})\mathcal{P}^0_{||} \end{bmatrix} \tag{H.15}$$

The third term is

$$(\mathbf{u}_1\cdot\nabla)\mathcal{P}^0 = \begin{bmatrix} u_{x1}\frac{d\mathcal{P}^0_{\perp}}{dx} & 0 & 0 \\ 0 & u_{x1}\frac{d\mathcal{P}^0_{\perp}}{dx} & u_{x1}\frac{d\mathcal{P}^0_{yz}}{dx} \\ 0 & u_{x1}\frac{d\mathcal{P}^0_{yz}}{dx} & u_{x1}\frac{d\mathcal{P}^0_{||}}{dx} \end{bmatrix} \tag{H.16}$$

The fourth and fifth terms are given by

$$\mathcal{P}^0\cdot\nabla\mathbf{u}_1 = \begin{bmatrix} \mathcal{P}^0_{\perp}\frac{\partial u_{x1}}{\partial x} & \mathcal{P}^0_{\perp}\frac{\partial u_{y1}}{\partial x} & \mathcal{P}^0_{\perp}\frac{\partial u_{z1}}{\partial x} \\ \mathcal{P}^0_{\perp}\frac{\partial u_{x1}}{\partial y} & \mathcal{P}^0_{\perp}\frac{\partial u_{y1}}{\partial y} & \mathcal{P}^0_{\perp}\frac{\partial u_{z1}}{\partial y} \\ \mathcal{P}^0_{yz}\frac{\partial u_{x1}}{\partial y} & \mathcal{P}^0_{yz}\frac{\partial u_{y1}}{\partial y} & \mathcal{P}^0_{yz}\frac{\partial u_{z1}}{\partial y} \end{bmatrix} \tag{H.17}$$

Then,

$$\mathcal{P}^0\cdot\nabla\mathbf{u}_1 + [\mathcal{P}^0\cdot\nabla\mathbf{u}_1]^T = \begin{bmatrix} 2\mathcal{P}^0_{\perp}\frac{\partial u_{x1}}{\partial x} & \mathcal{P}^0_{\perp}(\frac{\partial u_{x1}}{\partial y} + \frac{\partial u_{y1}}{\partial x}) & \mathcal{P}^0_{\perp}\frac{\partial u_{z1}}{\partial x} + \mathcal{P}^0_{yz}\frac{\partial u_{x1}}{\partial y} \\ \mathcal{P}^0_{\perp}(\frac{\partial u_{x1}}{\partial y} + \frac{\partial u_{y1}}{\partial x}) & 2\mathcal{P}^0_{\perp}\frac{\partial u_{y1}}{\partial y} & \mathcal{P}^0_{\perp}\frac{\partial u_{z1}}{\partial y} + \mathcal{P}^0_{yz}\frac{\partial u_{y1}}{\partial y} \\ \mathcal{P}^0_{\perp}\frac{\partial u_{z1}}{\partial x} + \mathcal{P}^0_{yz}\frac{\partial u_{x1}}{\partial y} & \mathcal{P}^0_{\perp}\frac{\partial u_{z1}}{\partial y} + \mathcal{P}^0_{yz}\frac{\partial u_{y1}}{\partial y} & 2\mathcal{P}^0_{yz}\frac{\partial u_{z1}}{\partial y} \end{bmatrix} \tag{H.18}$$

Also,

$$\mathcal{P}^1 \cdot \nabla \mathbf{u}_0 = \begin{bmatrix} 0 & 0 & \mathcal{P}_{xx}\frac{\partial u_{z0}}{\partial x} \\ 0 & 0 & \mathcal{P}_{xy}\frac{\partial u_{z0}}{\partial x} \\ 0 & 0 & \mathcal{P}_{xz}\frac{\partial u_{z0}}{\partial x} \end{bmatrix} \tag{H.19}$$

Then,

$$\mathcal{P}^1 \cdot \nabla \mathbf{u}_0 + [\mathcal{P}^1 \cdot \nabla \mathbf{u}_0]^T = \begin{bmatrix} 0 & 0 & \mathcal{P}_{xx}\frac{\partial u_{z0}}{\partial x} \\ 0 & 0 & \mathcal{P}_{xy}\frac{\partial u_{z0}}{\partial x} \\ 0 & 0 & 2\mathcal{P}_{xz}\frac{\partial u_{z0}}{\partial x} \end{bmatrix} \tag{H.20}$$

and

$$\mathcal{P}^0 \times \mathbf{B}_1 = \begin{bmatrix} 0 & \mathcal{P}^0_{\perp}B_{z1} - \mathcal{P}^0_{yz}B_{y1} & \mathcal{P}^0_{yz}B_{z1} - \mathcal{P}^0_{||}B_{y1} \\ -\mathcal{P}^0_{\perp}B_{z1} & \mathcal{P}^0_{yz}B_{x1} & \mathcal{P}^0_{||}B_{x1} \\ \mathcal{P}^0_{\perp}B_{y1} & -\mathcal{P}^0_{\perp}B_{x1} & -\mathcal{P}^0_{yz}B_{x1} \end{bmatrix} \tag{H.21}$$

$$\mathcal{P}^0 \times \mathbf{B}_1 + [\mathcal{P}^0 \times \mathbf{B}_1]^T = \begin{bmatrix} 0 & -\mathcal{P}^0_{yz}B_{y1} & \mathcal{P}^0_{yz}B_{z1} + (\mathcal{P}^0_{\perp} - \mathcal{P}^0_{||})B_{y1} \\ -\mathcal{P}^0_{yz}B_{y1} & 2\mathcal{P}^0_{yz}B_{x1} & (\mathcal{P}^0_{||} - \mathcal{P}^0_{\perp})B_{x1} \\ \mathcal{P}^0_{yz}B_{z1} + (\mathcal{P}^0_{\perp} - \mathcal{P}^0_{||})B_{y1} & (\mathcal{P}^0_{||} - \mathcal{P}^0_{\perp})B_{x1} & -2\mathcal{P}^0_{yz}B_{x1} \end{bmatrix} \tag{H.22}$$

$$\mathcal{P}^1 \times \mathbf{B}_0 = \begin{bmatrix} B_g\mathcal{P}_{xy} - B_y\mathcal{P}_{xz} & B_g\mathcal{P}_{yy} - B_y\mathcal{P}_{yz} & B_g\mathcal{P}_{yz} - B_y\mathcal{P}_{zz} \\ -B_g\mathcal{P}_{xx} & -B_g\mathcal{P}_{xy} & -B_g\mathcal{P}_{xz} \\ B_y\mathcal{P}_{xx} & B_y\mathcal{P}_{xy} & B_y\mathcal{P}_{xz} \end{bmatrix} \tag{H.23}$$

$$\mathcal{P}^1 \times \mathbf{B}_0 + [\mathcal{P}^1 \times \mathbf{B}_0]^T = \begin{bmatrix} 2B_g\mathcal{P}_{xy} - 2B_y\mathcal{P}_{xz} & B_g\mathcal{P}_{yy} - B_g\mathcal{P}_{xx} - B_y\mathcal{P}_{yz} & B_g\mathcal{P}_{yz} - B_y\mathcal{P}_{zz} + B_y\mathcal{P}_{xx} \\ B_g\mathcal{P}_{yy} - B_g\mathcal{P}_{xx} - B_y\mathcal{P}_{yz} & -2B_g\mathcal{P}_{xy} & B_y\mathcal{P}_{xy} - B_g\mathcal{P}_{xz} \\ B_g\mathcal{P}_{yz} - B_y\mathcal{P}_{zz} + B_y\mathcal{P}_{xx} & B_y\mathcal{P}_{xy} - B_g\mathcal{P}_{xz} & 2B_y\mathcal{P}_{xz} \end{bmatrix} \tag{H.24}$$

Here $B_y = B_y(x) = B_s f(x)$, such that $\mathbf{B}_0 = B_y\mathbf{e}_y + B_g\mathbf{e}_z$. These will help us to identify the importance of each term in the linear equations under different conditions. For example, under the assumption of a strong guide field, $\omega_{c,e} \gg \bar{\omega}_{c,e}$. Substituting the previous equations into Eq.(H.14), we obtain the following system of equations (we omit the "1" superscript)

$$\frac{\partial \mathcal{P}^1_{xx}}{\partial t} + 2\omega_{c,e}\mathcal{P}^1_{xy} - 2\bar{\omega}_{c,e}f(x)\mathcal{P}^1_{xz} = -\mathcal{P}^0_{\perp}(\frac{\partial u_{x1}}{\partial x} + \frac{\partial u_{y1}}{\partial y}) - \frac{d\mathcal{P}^0_{\perp}}{dx}u_{x1} - 2\mathcal{P}^0_{\perp}\frac{\partial u_{x1}}{\partial x}, \tag{H.25}$$

$$\frac{\partial \mathcal{P}^1_{xy}}{\partial t} + \omega_{c,e}\mathcal{P}^1_{yy} - \omega_{c,e}\mathcal{P}^1_{xx} - \bar{\omega}_{c,e}f(x)\mathcal{P}^1_{yz} = \frac{e}{m}\mathcal{P}^0_{yz}B_{y1} - \mathcal{P}^0_{\perp}(\frac{\partial u_{x1}}{\partial y} + \frac{\partial u_{y1}}{\partial x}), \tag{H.26}$$

$$\begin{aligned} \frac{\partial \mathcal{P}^1_{xz}}{\partial t} + \omega_{c,e}\mathcal{P}^1_{yz} - \bar{\omega}_{c,e}f(x)\mathcal{P}^1_{zz} + \bar{\omega}_{c,e}f(x)\mathcal{P}^1_{xx} = &-\frac{e}{m}\mathcal{P}^0_{yz}B_{z1} - \frac{e}{m}(\mathcal{P}^0_{\perp} - \mathcal{P}^0_{||})B_{y1} - \mathcal{P}^0_{\perp}\frac{\partial u_{z1}}{\partial x} \\ &- \mathcal{P}_{xx}\frac{\partial u_{z0}}{\partial x} - \mathcal{P}^0_{yz}\frac{\partial u_{x1}}{\partial y}, \end{aligned} \tag{H.27}$$

$$\frac{\partial \mathcal{P}^1_{yz}}{\partial t} + \bar{\omega}_{c,e} f(x) \mathcal{P}^1_{xy} - \omega_{c,e} \mathcal{P}^1_{xz} = -\frac{e}{m}(\mathcal{P}^0_{||} - \mathcal{P}^0_{\perp}) B_{x1} - \mathcal{P}^0_{\perp} \frac{\partial u_{z1}}{\partial y} - \mathcal{P}^0_{yz} \frac{\partial u_y}{\partial y} - \mathcal{P}_{xy} \frac{\partial u_{z0}}{\partial x} - u_{x1} \frac{d\mathcal{P}^0_{yz}}{dx} - (\frac{\partial u_{x1}}{\partial x} + \frac{\partial u_{y1}}{\partial y}) \mathcal{P}^0_{yz},, \tag{H.28}$$

$$\frac{\partial \mathcal{P}^1_{yy}}{\partial t} - 2\omega_{c,e} \mathcal{P}^1_{xy} = -2\frac{e}{m} \mathcal{P}^0_{yz} B_{x1} - 2\mathcal{P}^0_{\perp} \frac{\partial u_{y1}}{\partial y} - u_{x1} \frac{d\mathcal{P}^0_{\perp}}{dx} - (\frac{\partial u_{x1}}{\partial x} + \frac{\partial u_{y1}}{\partial y}) \mathcal{P}^0_{\perp}, \tag{H.29}$$

$$\frac{\partial \mathcal{P}^1_{zz}}{\partial t} + 2\bar{\omega}_{c,e} f(x) \mathcal{P}^1_{xz} = 2\frac{e}{m} \mathcal{P}^0_{yz} B_{x1} - 2\mathcal{P}^0_{yz} \frac{\partial u_{z1}}{\partial y} - 2\mathcal{P}_{xz} \frac{\partial u_{z0}}{\partial x} - u_{x1} \frac{d\mathcal{P}^0_{||}}{dx} - (\frac{\partial u_{x1}}{\partial x} + \frac{\partial u_{y1}}{\partial y}) \mathcal{P}^0_{||}, \tag{H.30}$$

In `EMHD` model, the electron cyclotron frequency of the shear field ($\bar{\omega}_{c,e}$) and the growth rate of the reconnecting mode (γ) will be much smaller than the frequency of the guide field ($\omega_{c,e}$), that is, $\gamma \ll \bar{\omega}_{c,e} \ll \omega_{c,e}$. Thus, depending on the system under investigation, we can neglect some terms. The previous set of equations becomes

$$\frac{\gamma}{2\omega_{c,e}} \mathcal{P}_{xx} + \mathcal{P}_{xy} - \frac{\bar{\omega}_{c,e}}{\omega_{c,e}} f(x) \mathcal{P}_{xz} = \Lambda_1 \tag{H.31}$$

$$\frac{\gamma}{\omega_{c,e}} \mathcal{P}_{xy} + \mathcal{P}_{yy} - \mathcal{P}_{xx} - \frac{\bar{\omega}_{c,e}}{\omega_{c,e}} f(x) \mathcal{P}_{yz} = \Lambda_2 \tag{H.32}$$

$$\frac{\gamma}{\omega_{c,e}} \mathcal{P}_{xz} + \mathcal{P}_{yz} - \frac{\bar{\omega}_{c,e}}{\omega_{c,e}} f(x) \mathcal{P}_{zz} + \frac{\bar{\omega}_{c,e}}{\omega_{c,e}} f(x) \mathcal{P}_{xx} + \frac{1}{\omega_{c,e}} \frac{\partial u_{z0}}{\partial x} \mathcal{P}_{xx} = \Lambda_3 \tag{H.33}$$

$$\frac{\gamma}{\omega_{c,e}} \mathcal{P}_{yz} + \frac{\bar{\omega}_{c,e}}{\omega_{c,e}} f(x) \mathcal{P}_{xy} - \mathcal{P}_{xz} + \frac{1}{\omega_{c,e}} \frac{\partial u_{z0}}{\partial x} \mathcal{P}_{xy} = \Lambda_4 \tag{H.34}$$

$$\frac{\gamma}{2\omega_{c,e}} \mathcal{P}_{yy} - \mathcal{P}_{xy} = \Lambda_5 \tag{H.35}$$

$$\frac{\gamma}{2\bar{\omega}_{c,e}} \mathcal{P}_{zz} + f(x) \mathcal{P}_{xz} + \frac{1}{\bar{\omega}_{c,e}} \frac{\partial u_{z0}}{\partial x} \mathcal{P}_{xz} = \Lambda_6 \tag{H.36}$$

$$\Lambda_1 = -\frac{1}{2\omega_{c,e}} (\frac{\partial u_{x1}}{\partial x} + \frac{\partial u_{y1}}{\partial y}) \mathcal{P}^0_{\perp} - \frac{1}{2\omega_{c,e}} u_{x1} \frac{d\mathcal{P}^0_{\perp}}{dx} - \frac{1}{\omega_{c,e}} \mathcal{P}^0_{\perp} \frac{\partial u_{x1}}{\partial x}, \tag{H.37}$$

$$\Lambda_2 = \frac{e}{m\omega_{c,e}} \mathcal{P}^0_{yz} B_{y1} - \frac{1}{\omega_{c,e}} \mathcal{P}^0_{\perp} (\frac{\partial u_{x1}}{\partial y} + \frac{\partial u_{y1}}{\partial x}), \tag{H.38}$$

$$\Lambda_3 = -\frac{e}{m\omega_{c,e}} \mathcal{P}^0_{yz} B_{z1} - \frac{e}{m\omega_{c,e}} (\mathcal{P}^0_{\perp} - \mathcal{P}^0_{||}) B_{y1} - \frac{1}{\omega_{c,e}} \mathcal{P}^0_{\perp} \frac{\partial u_{z1}}{\partial x} - \frac{1}{\omega_{c,e}} \mathcal{P}^0_{yz} \frac{\partial u_{x1}}{\partial y}, \tag{H.39}$$

$$\Lambda_4 = -\frac{e}{m\omega_{c,e}} (\mathcal{P}^0_{||} - \mathcal{P}^0_{\perp}) B_{x1} - \frac{1}{\omega_{c,e}} \mathcal{P}^0_{\perp} \frac{\partial u_{z1}}{\partial y} - \frac{1}{\omega_{c,e}} \mathcal{P}^0_{yz} \frac{\partial u_y}{\partial y} - \frac{1}{\omega_{c,e}} u_{x1} \frac{d\mathcal{P}^0_{yz}}{dx} - \frac{1}{\omega_{c,e}} (\frac{\partial u_{x1}}{\partial x} + \frac{\partial u_{y1}}{\partial y}) \mathcal{P}^0_{yz}, \tag{H.40}$$

$$\Lambda_5 = -\frac{e}{m\omega_{c,e}}\mathcal{P}^0_{yz}B_{x1} - \frac{1}{\omega_{c,e}}\mathcal{P}^0_{\perp}\frac{\partial u_{y1}}{\partial y} - \frac{1}{2\omega_{c,e}}u_{x1}\frac{d\mathcal{P}^0_{\perp}}{dx} - \frac{1}{2\omega_{c,e}}(\frac{\partial u_{x1}}{\partial x} + \frac{\partial u_{y1}}{\partial y})\mathcal{P}^0_{\perp}, \tag{H.41}$$

$$\Lambda_6 = \frac{e}{m\bar{\omega}_{c,e}}\mathcal{P}^0_{yz}B_{x1} - \frac{1}{\bar{\omega}_{c,e}}\mathcal{P}^0_{yz}\frac{\partial u_{z1}}{\partial y} - \frac{1}{2\bar{\omega}_{c,e}}u_{x1}\frac{d\mathcal{P}^0_{||}}{dx} - \frac{1}{2\bar{\omega}_{c,e}}(\frac{\partial u_{x1}}{\partial x} + \frac{\partial u_{y1}}{\partial y})\mathcal{P}^0_{||}, \tag{H.42}$$

When, $\mathcal{P}^0_{yz} = 0$, the previous equations read

$$\frac{\gamma}{2\omega_{c,e}}\mathcal{P}^1_{xx} + \mathcal{P}^1_{xy} - \frac{\bar{\omega}_{c,e}}{\omega_{c,e}}f(x)\mathcal{P}^1_{xz} = \Lambda_1 \tag{H.43}$$

$$\frac{\gamma}{\omega_{c,e}}\mathcal{P}^1_{xy} + \mathcal{P}^1_{yy} - \mathcal{P}^1_{xx} - \frac{\bar{\omega}_{c,e}}{\omega_{c,e}}f(x)\mathcal{P}^1_{yz} = \Lambda_2 \tag{H.44}$$

$$\frac{\gamma}{\omega_{c,e}}\mathcal{P}^1_{xz} + \mathcal{P}^1_{yz} - \frac{\bar{\omega}_{c,e}}{\omega_{c,e}}f(x)\mathcal{P}^1_{zz} + \frac{\bar{\omega}_{c,e}}{\omega_{c,e}}f(x)\mathcal{P}^1_{xx} + \frac{1}{\omega_{c,e}}\frac{\partial u_{z0}}{\partial x}\mathcal{P}^1_{xx} = \Lambda_3 \tag{H.45}$$

$$\frac{\gamma}{\omega_{c,e}}\mathcal{P}^1_{yz} + \frac{\bar{\omega}_{c,e}}{\omega_{c,e}}f(x)\mathcal{P}^1_{xy} - \mathcal{P}^1_{xz} + \frac{1}{\omega_{c,e}}\frac{\partial u_{z0}}{\partial x}\mathcal{P}^1_{xy} = \Lambda_4 \tag{H.46}$$

$$\frac{\gamma}{2\omega_{c,e}}\mathcal{P}^1_{yy} - \mathcal{P}^1_{xy} = \Lambda_5 \tag{H.47}$$

$$\frac{\gamma}{2\bar{\omega}_{c,e}}\mathcal{P}^1_{zz} + f(x)\mathcal{P}^1_{xz} + \frac{1}{\bar{\omega}_{c,e}}\frac{\partial u_{z0}}{\partial x}\mathcal{P}^1_{xz} = \Lambda_6 \tag{H.48}$$

where,

$$\Lambda_1 = -\frac{1}{2\omega_{c,e}}\mathcal{P}^0_{\perp}(\frac{\partial u_{x1}}{\partial x} + \frac{\partial u_{y1}}{\partial y}) - \frac{1}{2\omega_{c,e}}\frac{d\mathcal{P}^0_{\perp}}{dx}u_{x1} - \frac{1}{\omega_{c,e}}\mathcal{P}^0_{\perp}\frac{\partial u_{x1}}{\partial x}, \tag{H.49}$$

$$\Lambda_2 = -\frac{1}{\omega_{c,e}}\mathcal{P}^0_{\perp}(\frac{\partial u_{x1}}{\partial y} + \frac{\partial u_{y1}}{\partial x}), \tag{H.50}$$

$$\Lambda_3 = -\frac{1}{\omega_{c,e}}\mathcal{P}^0_{\perp}\frac{\partial u_{z1}}{\partial x} - \frac{e}{m\omega_{c,e}}(\mathcal{P}^0_{\perp} - \mathcal{P}^0_{||})B_{y1}, \tag{H.51}$$

$$\Lambda_4 = -\frac{e}{m\omega_{c,e}}(\mathcal{P}^0_{||} - \mathcal{P}^0_{\perp})B_{x1} - \frac{1}{\omega_{c,e}}\mathcal{P}^0_{\perp}\frac{\partial u_{z1}}{\partial y}, \tag{H.52}$$

$$\Lambda_5 = -\frac{1}{\omega_{c,e}}\mathcal{P}^0_{\perp}\frac{\partial u_{y1}}{\partial y} - \frac{1}{2\omega_{c,e}}\frac{d\mathcal{P}^0_{\perp}}{dx}u_{x1} - \frac{1}{2\omega_{c,e}}\mathcal{P}^0_{\perp}(\frac{\partial u_{x1}}{\partial x} + \frac{\partial u_{y1}}{\partial y}) \tag{H.53}$$

$$\Lambda_6 = -\frac{1}{2\bar{\omega}_{c,e}}\frac{d\mathcal{P}^0_{||}}{dx}u_{x1} - \frac{1}{2\bar{\omega}_{c,e}}\mathcal{P}^0_{||}(\frac{\partial u_{x1}}{\partial x} + \frac{\partial u_{y1}}{\partial y}), \tag{H.54}$$

In the previous equations the terms that contain $\frac{\partial u_{z0}}{\partial x}$ are also of order $\frac{\bar{\omega}_{c,e}}{\omega_{c,e}}$ according to Eq.(6.36). Neglecting these terms is further justified when $d_e \ll L_0$, where L_0 is the characteristic length of equilibrium field.

In the following discussion, we always neglect the off-diagonal terms when multiplied by $\frac{\bar{\omega}_{c,e}}{\omega_{c,e}}$, or $\frac{\gamma}{\omega_{c,e}}$, Eq.(H.46) gives,

$$\mathcal{P}^1_{xz} = -\Lambda_4 = \frac{e}{m\omega_{c,e}}(\mathcal{P}^0_{||} - \mathcal{P}^0_{\perp})B_{x1} + \frac{\mathcal{P}^0_{\perp}}{\omega_{c,e}}\frac{\partial u_{z1}}{\partial y}, \tag{H.55}$$

Eq.(H.44) leads to the following important relation between the perturbed components: $\mathcal{P}^1_{xx}$ and $\mathcal{P}^1_{yy}$.

$$\mathcal{P}^1_{yy} - \mathcal{P}^1_{xx} = \Lambda_2 = -\frac{\mathcal{P}^0_{\perp}}{\omega_{c,e}}(\frac{\partial u_{x1}}{\partial y} + \frac{\partial u_{y1}}{\partial x}), \tag{H.56}$$

Now subtracting Eq.(H.43) from Eq.(H.47), and substituting Eq.(H.56) into the results, one finds

$$\mathcal{P}^1_{xy} = \frac{\Lambda_1 - \Lambda_5}{2} + \frac{\gamma\Lambda_2}{4\omega_{c,e}} = \frac{\mathcal{P}^0_{\perp}}{2\omega_{c,e}}(\frac{\partial u_{y1}}{\partial y} - \frac{\partial u_{x1}}{\partial x}), \tag{H.57}$$

In the previous equation we neglect the second term which is of order of $\frac{\gamma}{\omega_{c,e}}$. Now substituting $\mathcal{P}^1_{xy}$ and $\mathcal{P}^1_{xz}$ into Eq.(H.43) and then into Eq.(H.56) , we obtain

$$\begin{aligned}\mathcal{P}^1_{xx} = \frac{2\omega_{c,e}}{\gamma}\Lambda_1 - \frac{2\omega_{c,e}}{\gamma}\mathcal{P}^1_{xy} + \frac{2\bar{\omega}_{c,e}}{\gamma}\mathcal{P}^1_{xz} = -\frac{2\mathcal{P}^0_{\perp}}{\gamma}(\frac{\partial u_{x1}}{\partial x} + \frac{\partial u_{y1}}{\partial y}) - \frac{1}{\gamma}\frac{d\mathcal{P}^0_{\perp}}{dx}u_{x1} \\ + \frac{2\bar{\omega}_{c,e}}{\gamma}f(x)\Big[\frac{e}{m\omega_{c,e}}(\mathcal{P}^0_{||} - \mathcal{P}^0_{\perp})B_{x1} + \frac{\mathcal{P}^0_{\perp}}{\omega_{c,e}}\frac{\partial u_{z1}}{\partial y}\Big],\end{aligned} \tag{H.58}$$

$$\begin{aligned}\mathcal{P}^1_{yy} = \mathcal{P}^1_{xx} + \Lambda_2 = -\frac{\mathcal{P}^0_{\perp}}{\omega_{c,e}}(\frac{\partial u_{x1}}{\partial y} + \frac{\partial u_{y1}}{\partial x}) - \frac{2\mathcal{P}^0_{\perp}}{\gamma}(\frac{\partial u_{x1}}{\partial x} + \frac{\partial u_{y1}}{\partial y}) - \frac{1}{\gamma}\frac{d\mathcal{P}^0_{\perp}}{dx}u_{x1} \\ + \frac{2\bar{\omega}_{c,e}}{\gamma}f(x)\Big[\frac{e}{m\omega_{c,e}}(\mathcal{P}^0_{||} - \mathcal{P}^0_{\perp})B_{x1} + \frac{\mathcal{P}^0_{\perp}}{\omega_{c,e}}\frac{\partial u_{z1}}{\partial y}\Big],\end{aligned} \tag{H.59}$$

Substituting Eq.(H.55) and Eq. (6.36) into Eq.(H.48), we obtain

$$\begin{aligned}\mathcal{P}^1_{zz} = \frac{2\bar{\omega}_{c,e}}{\gamma}\Lambda_6 - \frac{2\bar{\omega}_{c,e}}{\gamma}\Big[f(x) + \frac{1}{\bar{\omega}_{c,e}}\frac{\partial u_{z0}}{\partial x}\Big]\mathcal{P}^1_{xz} = -\frac{1}{\gamma}\frac{d\mathcal{P}^0_{||}}{dx}u_{x1} - \frac{\mathcal{P}^0_{||}}{\gamma}(\frac{\partial u_{x1}}{\partial x} + \frac{\partial u_{y1}}{\partial y}) \\ - \frac{2\bar{\omega}_{c,e}}{\gamma}\Big[f(x) - d_e^2 f''(x)\Big]\Big[\frac{e}{m\omega_{c,e}}(\mathcal{P}^0_{||} - \mathcal{P}^0_{\perp})B_{x1} + \frac{\mathcal{P}^0_{\perp}}{\omega_{c,e}}\frac{\partial u_{z1}}{\partial y}\Big],\end{aligned} \tag{H.60}$$

Another important relation is the difference $\mathcal{P}^1_{zz} - \mathcal{P}^1_{xx}$ which can be calculated by subtracting Eq.(H.58) from Eq.(H.30), which gives

$$\mathcal{P}^1_{zz} - \mathcal{P}^1_{xx} = \frac{1}{\gamma}\mathbf{u}\cdot\nabla(\mathcal{P}^0_{\perp} - \mathcal{P}^0_{||}) + \frac{1}{\gamma}(2\mathcal{P}^0_{\perp} - \mathcal{P}^0_{||})(\frac{\partial u_{x1}}{\partial x} + \frac{\partial u_{y1}}{\partial y}), \tag{H.61}$$

In the previous equation we neglected terms of order $\frac{\bar{\omega}_{c,e}}{\omega_{c,e}}$, or larger. Now, $\mathcal{P}_{yz}$ can be obtained from Eq.(H.45) after substituting Eq.(H.61) into it, which gives

$$\begin{aligned}\mathcal{P}^1_{yz} = \Lambda_3 + \frac{\bar{\omega}_{c,e}}{\omega_{c,e}}f(x)(\mathcal{P}^1_{zz} - \mathcal{P}^1_{xx}) + \frac{\bar{\omega}_{c,e}}{\omega_{c,e}}d_e^2 f''(x)\mathcal{P}^1_{xx} = -\frac{1}{\omega_{c,e}}\mathcal{P}^0_{\perp}\frac{\partial u_{z1}}{\partial x} - \frac{e}{m\omega_{c,e}}(\mathcal{P}^0_{\perp} - \mathcal{P}^0_{||})B_{y1} \\ + \frac{\bar{\omega}_{c,e}}{\omega_{c,e}}f(x)\Big\{\frac{1}{\gamma}\mathbf{u}\cdot\nabla(\mathcal{P}^0_{\perp} - \mathcal{P}^0_{||}) + \frac{1}{\gamma}(2\mathcal{P}^0_{\perp} - \mathcal{P}^0_{||})(\frac{\partial u_{x1}}{\partial x} + \frac{\partial u_{y1}}{\partial y})\Big\} \\ - \frac{\bar{\omega}_{c,e}}{\omega_{c,e}}d_e^2 f''(x)\Big\{\frac{2\mathcal{P}^0_{\perp}}{\gamma}(\frac{\partial u_{x1}}{\partial x} + \frac{\partial u_{y1}}{\partial y}) + \frac{1}{\gamma}\frac{d\mathcal{P}^0_{\perp}}{dx}u_{x1}\Big\},\end{aligned} \tag{H.62}$$

In the previous derivation of $\mathcal{P}_{yz}$, we ignored terms of order $\frac{\bar{\omega}_{c,e}^2}{\omega_{c,e}^2}$. Now, Eqs[H.58, H.59, H.57, H.55, H.62, H.60] can be used to formulate the eigenvalue problem to study the effect of full pressure tensor on the reconnection.

Estimating the Derivatives of the Full Pressure Tensor Components with Guide Field:

Estimating the derivatives of the perturbed components of the full pressure tensor is important since they appear in the linearized Ohm's law and momentum equation. Therefore, we start by listing some necessary relationships obtained from the equilibrium quantities. They read,

$$\mathcal{P}_{\perp}^{0}-\mathcal{P}_{||}^{0}=\frac{B_s^2 d_e^2}{2\mu_0}f^{''}f,\quad 2\mathcal{P}_{\perp}^{0}-\mathcal{P}_{||}^{0}=\frac{B_s^2}{2\mu_0}[f^2+d_e^2 f^{''}f], \tag{H.63}$$

In terms of these quantities, $\mathcal{P}_{yz}^{1}$ can be written as,

$$\mathcal{P}_{yz}^{1}=\frac{B_s^2}{2\mu_0}\Big\{-\frac{f^2}{\omega_{c,e}}\frac{\partial u_{z1}}{\partial x}-\frac{ed_e^2}{m\omega_{c,e}}f_3 B_{y1}+\frac{\bar{\omega}_{c,e}d_e^2}{\omega_{c,e}\gamma}f_5 u_{x1}+\frac{\bar{\omega}_{c,e}}{\omega_{c,e}\gamma}f_6\frac{\partial u_{x1}}{\partial x}+\frac{\bar{\omega}_{c,e}}{\omega_{c,e}\gamma}f_6\frac{\partial u_{y1}}{\partial y}\Big\}, \tag{H.64}$$

Where,

$$f_1=f^{''}f^2,\quad f_2=f^3+d_e^2 f_1,\quad f_3=f^{''}f,\quad f_4=f^{''}(f^2)^{'},\quad f_5=ff_3^{'}-f_4,\quad f_6=f_2-2d_e^2 f_1, \tag{H.65}$$

Therefore the different derivatives of this component are,

$$\begin{aligned}\frac{\partial\mathcal{P}_{yz}^{1}}{\partial x}&=\frac{B_s^2}{2\mu_0}\Big\{-\frac{1}{\omega_{c,e}}(f^2\frac{\partial^2}{\partial x^2}+2f^{'}f\frac{\partial}{\partial x})u_{z1}-\frac{ed_e^2}{m\omega_{c,e}}(f_3\frac{\partial}{\partial x}+f_3^{'})B_{y1}+\frac{\bar{\omega}_{c,e}d_e^2}{\omega_{c,e}\gamma}(f_5\frac{\partial}{\partial x}+f_5^{'})u_{x1}\\&+\frac{\bar{\omega}_{c,e}}{\omega_{c,e}\gamma}(f_6\frac{\partial^2}{\partial x^2}+f_6^{'}\frac{\partial}{\partial x})u_{x1}+\frac{\bar{\omega}_{c,e}}{\omega_{c,e}\gamma}(f_6\frac{\partial^2}{\partial x\partial y}+f_6^{'}\frac{\partial}{\partial y})u_{y1}\Big\}\\&=\frac{B_s^2}{2\mu_0}\Big\{\frac{\bar{\omega}_{c,e}d_e^2}{\omega_{c,e}\gamma}(f_5\frac{\partial}{\partial x}+f_5^{'})u_{x1}+\frac{\bar{\omega}_{c,e}}{\omega_{c,e}\gamma}(f_6\frac{\partial^2}{\partial x^2}+f_6^{'}\frac{\partial}{\partial x})u_{x1}+\frac{\bar{\omega}_{c,e}}{\omega_{c,e}\gamma}(f_6\frac{\partial^2}{\partial x\partial y}+f_6^{'}\frac{\partial}{\partial y})u_{y1}\\&-\frac{1}{\omega_{c,e}}(f^2\frac{\partial^2}{\partial x^2}+2f^{'}f\frac{\partial}{\partial x})u_{z1}-\frac{ed_e^2}{m\omega_{c,e}}(f_3\frac{\partial}{\partial x}+f_3^{'})B_{y1}\Big\},\end{aligned} \tag{H.66}$$

$$\begin{aligned}\frac{\partial\mathcal{P}_{yz}^{1}}{\partial y}&=\frac{B_s^2}{2\mu_0}\Big\{-\frac{f^2}{\omega_{c,e}}\frac{\partial^2 u_{z1}}{\partial y\partial x}-\frac{ed_e^2}{m\omega_{c,e}}f_3\frac{\partial B_{y1}}{\partial y}+\frac{\bar{\omega}_{c,e}d_e^2}{\omega_{c,e}\gamma}f_5\frac{\partial u_{x1}}{\partial y}+\frac{\bar{\omega}_{c,e}}{\omega_{c,e}\gamma}f_6\frac{\partial^2 u_{x1}}{\partial y\partial x}+\frac{\bar{\omega}_{c,e}}{\omega_{c,e}\gamma}f_6\frac{\partial^2 u_{y1}}{\partial y^2}\Big\}\\&=\frac{B_s^2}{2\mu_0}\Big\{\frac{\bar{\omega}_{c,e}d_e^2}{\omega_{c,e}\gamma}f_5\frac{\partial u_{x1}}{\partial y}+\frac{\bar{\omega}_{c,e}}{\omega_{c,e}\gamma}f_6\frac{\partial^2 u_{x1}}{\partial y\partial x}+\frac{\bar{\omega}_{c,e}}{\omega_{c,e}\gamma}f_6\frac{\partial^2 u_{y1}}{\partial y^2}-\frac{f^2}{\omega_{c,e}}\frac{\partial^2 u_{z1}}{\partial y\partial x}-\frac{ed_e^2}{m\omega_{c,e}}f_3\frac{\partial B_{y1}}{\partial y}\Big\},\end{aligned} \tag{H.67}$$

$$\frac{\partial^2\mathcal{P}_{yz}^{1}}{\partial y^2}=\frac{B_s^2}{2\mu_0}\Big\{\frac{\bar{\omega}_{c,e}d_e^2}{\omega_{c,e}\gamma}f_5\frac{\partial^2 u_{x1}}{\partial y^2}+\frac{\bar{\omega}_{c,e}}{\omega_{c,e}\gamma}f_6\frac{\partial^3 u_{x1}}{\partial y^2\partial x}+\frac{\bar{\omega}_{c,e}}{\omega_{c,e}\gamma}f_6\frac{\partial^3 u_{y1}}{\partial y^3}-\frac{f^2}{\omega_{c,e}}\frac{\partial^3 u_{z1}}{\partial y^2\partial x}-\frac{ed_e^2}{m\omega_{c,e}}f_3\frac{\partial^2 B_{y1}}{\partial y^2}\Big\}, \tag{H.68}$$

$$\begin{aligned}\frac{\partial^2\mathcal{P}_{yz}^{1}}{\partial y\partial x}&=\frac{B_s^2}{2\mu_0}\Big\{\frac{\bar{\omega}_{c,e}d_e^2}{\omega_{c,e}\gamma}\times(f_5\frac{\partial^2}{\partial y\partial x}+f_5^{'}\frac{\partial}{\partial y})u_{x1}+\frac{\bar{\omega}_{c,e}}{\omega_{c,e}\gamma}(f_6\frac{\partial^3}{\partial y\partial x^2}+f_6^{'}\frac{\partial^2}{\partial y\partial x})u_{x1}+\frac{\bar{\omega}_{c,e}}{\omega_{c,e}\gamma}\times\\&(f_6\frac{\partial^3}{\partial x\partial y^2}+f_6^{'}\frac{\partial^2}{\partial y^2})u_{y1}-(\frac{f^2}{\omega_{c,e}}\frac{\partial^3}{\partial y\partial x^2}+\frac{2f^{'}f}{\omega_{c,e}}\frac{\partial^2}{\partial y\partial x})u_{z1}-\frac{ed_e^2}{m\omega_{c,e}}(f_3\frac{\partial^2}{\partial y\partial x}+f_3^{'}\frac{\partial}{\partial y})B_{y1}\Big\},\end{aligned} \tag{H.69}$$

Now we write $\mathcal{P}^1_{xz}$ in terms of equilibrium quantities and lower order perturbed moments:

$$\mathcal{P}^1_{xz} = \frac{B_s}{2\mu_0}\Big\{\frac{f^2}{\omega_{c,e}}\frac{\partial u_{z1}}{\partial y} - \frac{ed_e^2}{m\omega_{c,e}} f_3 B_{x1}\Big\}, \tag{H.70}$$

Therefore, the different derivatives are

$$\frac{\partial \mathcal{P}^1_{xz}}{\partial x} = \frac{B_s^2}{2\mu_0}\Big\{(\frac{f^2}{\omega_{c,e}}\frac{\partial^2}{\partial x\partial y} + \frac{2ff^{'}}{\omega_{c,e}}\frac{\partial}{\partial y})u_{z1} - \frac{ed_e^2}{m\omega_{c,e}}(f_3\frac{\partial}{\partial x} + f_3^{'})B_{x1}\Big\}, \tag{H.71}$$

$$\frac{\partial^2 \mathcal{P}^1_{xz}}{\partial x^2} = \frac{B_s^2}{2\mu_0}\Big\{(\frac{f^2}{\omega_{c,e}}\frac{\partial^3}{\partial x^2\partial y} + \frac{4ff^{'}}{\omega_{c,e}}\frac{\partial^2}{\partial x\partial y} + \frac{2f_3 + 2f^{'2}}{\omega_{c,e}}\frac{\partial}{\partial y})u_{z1} - \frac{ed_e^2}{m\omega_{c,e}}(f_3\frac{\partial^2}{\partial x^2} + 2f_3^{'}\frac{\partial}{\partial x} + f_3^{''})B_{x1}\Big\}, \tag{H.72}$$

$$\frac{\partial \mathcal{P}^1_{xz}}{\partial y} = \frac{B_s^2}{2\mu_0}\Big\{\frac{f^2}{\omega_{c,e}}\frac{\partial^2 u_{z1}}{\partial y^2} - \frac{ed_e^2}{m\omega_{c,e}} f_3\frac{\partial B_{x1}}{\partial y}\Big\}, \tag{H.73}$$

$$\frac{\partial^2 \mathcal{P}^1_{xz}}{\partial y^2} = \frac{B_s^2}{2\mu_0}\Big\{\frac{f^2}{\omega_{c,e}}\frac{\partial^3 u_{z1}}{\partial y^3} - \frac{ed_e^2}{m\omega_{c,e}} f_3\frac{\partial^2 B_{x1}}{\partial y^2}\Big\}, \tag{H.74}$$

and

$$\frac{\partial^2 \mathcal{P}^1_{xz}}{\partial y\partial x} = \frac{B_s^2}{2\mu_0}\Big\{(\frac{f^2}{\omega_{c,e}}\frac{\partial^3}{\partial x\partial y^2} + \frac{2ff^{'}}{\omega_{c,e}}\frac{\partial^2}{\partial y^2})u_{z1} - \frac{ed_e^2}{m\omega_{c,e}}(f_3\frac{\partial^2}{\partial y\partial x} + f_3^{'}\frac{\partial}{\partial y})B_{x1}\Big\}, \tag{H.75}$$

The $\mathcal{P}^1_{xy}$ is given by

$$\mathcal{P}^1_{xy} = \frac{B_s^2}{2\mu_0}\Big\{ - \frac{f^2}{2\omega_{c,e}}\frac{\partial u_{x1}}{\partial x} + \frac{f^2}{2\omega_{c,e}}\frac{\partial u_{y1}}{\partial y}\Big\}, \tag{H.76}$$

$$\frac{\partial \mathcal{P}^1_{xy}}{\partial x} = \frac{B_s^2}{2\mu_0}\Big\{ - (\frac{f^2}{2\omega_{c,e}}\frac{\partial^2}{\partial x^2} + \frac{ff^{'}}{\omega_{c,e}}\frac{\partial}{\partial x})u_{x1} + (\frac{f^2}{2\omega_{c,e}}\frac{\partial^2}{\partial x\partial y} + \frac{ff^{'}}{\omega_{c,e}}\frac{\partial}{\partial y})u_{y1}\Big\}, \tag{H.77}$$

$$\frac{\partial^2 \mathcal{P}^1_{xy}}{\partial x^2} = \frac{B_s^2}{2\mu_0}\Big\{-(\frac{f^2}{2\omega_{c,e}}\frac{\partial^3}{\partial x^3} + \frac{2ff^{'}}{\omega_{c,e}}\frac{\partial^2}{\partial x^2} + \frac{f_3 + f^{'2}}{\omega_{c,e}}\frac{\partial}{\partial x})u_{x1} + (\frac{f^2}{2\omega_{c,e}}\frac{\partial^3}{\partial x^2\partial y} + \frac{2ff^{'}}{\omega_{c,e}}\frac{\partial^2}{\partial x\partial y} + \frac{f_3 + f^{'2}}{\omega_{c,e}}\frac{\partial}{\partial y})u_{y1}\Big\}, \tag{H.78}$$

$$\frac{\partial \mathcal{P}^1_{xy}}{\partial y} = \frac{B_s^2}{2\mu_0}\Big\{ - \frac{f^2}{2\omega_{c,e}}\frac{\partial^2 u_{x1}}{\partial y\partial x} + \frac{f^2}{2\omega_{c,e}}\frac{\partial^2 u_{y1}}{\partial y^2}\Big\}, \tag{H.79}$$

and

$$\frac{\partial^2 \mathcal{P}^1_{xy}}{\partial y^2} = \frac{B_s^2}{2\mu_0}\Big\{ - \frac{f^2}{2\omega_{c,e}}\frac{\partial^3 u_{x1}}{\partial y^2\partial x} + \frac{f^2}{2\omega_{c,e}}\frac{\partial^3 u_{y1}}{\partial y^3}\Big\}, \tag{H.80}$$

Now, we focus on the difference $\mathcal{P}^1_{yy} - \mathcal{P}^1_{xx}$ which occurs in Faraday equations. It reads,

$$\mathcal{P}^1_{yy} - \mathcal{P}^1_{xx} = \frac{B_s^2}{2\mu_0}\Big\{ - \frac{f^2}{\omega_{c,e}}\frac{\partial u_{x1}}{\partial y} - \frac{f^2}{\omega_{c,e}}\frac{\partial u_{y1}}{\partial x}\Big\}, \tag{H.81}$$

$$\frac{\partial}{\partial x}(\mathcal{P}^1_{yy} - \mathcal{P}^1_{xx}) = \frac{B_s^2}{2\mu_0}\Big\{ - (\frac{f^2}{\omega_{c,e}}\frac{\partial^2}{\partial x\partial y} + \frac{2ff^{'}}{\omega_{c,e}}\frac{\partial}{\partial y})u_{x1} - (\frac{f^2}{\omega_{c,e}}\frac{\partial^2}{\partial x^2} + \frac{2ff^{'}}{\omega_{c,e}}\frac{\partial}{\partial x})u_{y1}\Big\}, \tag{H.82}$$

and

$$\frac{\partial^2}{\partial x\partial y}(\mathcal{P}^1_{yy} - \mathcal{P}^1_{xx}) = \frac{B_s^2}{2\mu_0}\Big\{-(\frac{f^2}{\omega_{c,e}}\frac{\partial^3}{\partial x\partial y^2} + \frac{2ff^{'}}{\omega_{c,e}}\frac{\partial^2}{\partial y^2})u_{x1} - (\frac{f^2}{\omega_{c,e}}\frac{\partial^3}{\partial y\partial x^2} + \frac{2ff^{'}}{\omega_{c,e}}\frac{\partial^2}{\partial y\partial x})u_{y1}\Big\}, \tag{H.83}$$

$\mathcal{P}^1_{xx}$ reads,

$$\mathcal{P}^1_{xx} = \frac{B_s^2}{2\mu_0}\Big\{ -\frac{2f^2}{\gamma}\frac{\partial u_{x1}}{\partial x} - \frac{1}{\gamma}\frac{df^2}{dx}u_{x1} - \frac{2f^2}{\gamma}\frac{\partial u_{y1}}{\partial y} + \frac{2\bar{\omega_{c,e}}}{\omega_{c,e}\gamma}f^3\frac{\partial u_{z1}}{\partial y} - \frac{2e\bar{\omega}_{c,e}d_e^2}{m\omega_{c,e}\gamma}f_1 B_{x1}\Big\}, \tag{H.84}$$

The only derivative, as we are going to see later, needed in the calculation is the first derivative with respect to x, which is given by

$$\begin{aligned}\frac{\partial \mathcal{P}^1_{xx}}{\partial x} = \frac{B_s^2}{2\mu_0}\Big\{ &-\frac{1}{\gamma}(2f^2\frac{\partial^2}{\partial x^2} + 4f^{'}f\frac{\partial}{\partial x})u_{x1} - \frac{1}{\gamma}(f^{2'}\frac{\partial}{\partial x} + 2f_3 + 2f^{'2})u_{x1} - \frac{1}{\gamma}(2f^2\frac{\partial^2}{\partial x\partial y} + 4f^{'}f\frac{\partial}{\partial y})u_{y1} \\ &- \frac{2e\bar{\omega}_{c,e}d_e^2}{m\omega_{c,e}\gamma}(f_1\frac{\partial}{\partial x} + f_1^{'})B_{x1} + \frac{2\bar{\omega_{c,e}}}{\omega_{c,e}\gamma}(f^3\frac{\partial^2}{\partial x\partial y} + 3f^{'}f^2\frac{\partial}{\partial y})u_{z1}\Big\},\end{aligned} \tag{H.85}$$

The component $\mathcal{P}^1_{yy}$ reads,

$$\begin{aligned}\mathcal{P}^1_{yy} = \frac{B_s^2}{2\mu_0}\Big\{ &-\frac{f^2}{\omega_{c,e}}\frac{\partial u_{x1}}{\partial y} - \frac{2f^2}{\gamma}\frac{\partial u_{x1}}{\partial x} - \frac{2f^2}{\gamma}\frac{\partial u_{y1}}{\partial y} - \frac{f^2}{\omega_{c,e}}\frac{\partial u_{y1}}{\partial x} - \frac{1}{\gamma}\frac{df^2}{dx}u_{x1} - \frac{2e\bar{\omega}_{c,e}d_e^2}{m\omega_{c,e}\gamma}f_1 B_{x1} \\ &+ \frac{2\bar{\omega_{c,e}}}{\omega_{c,e}\gamma}f^3\frac{\partial u_{z1}}{\partial y}\Big\},\end{aligned} \tag{H.86}$$

The only derivative, as we are going to see later, needed in the calculation is the first derivative with respect to y, which is given by

$$\begin{aligned}\frac{\partial \mathcal{P}^1_{yy}}{\partial y} = \frac{B_s^2}{2\mu_0}\Big\{ &-\frac{f^2}{\omega_{c,e}}\frac{\partial^2 u_{x1}}{\partial y^2} - \frac{1}{\gamma}(f^{2'}\frac{\partial}{\partial y} + 2f^2\frac{\partial^2}{\partial y\partial x})u_{x1} - \frac{2f^2}{\gamma}\frac{\partial^2 u_{y1}}{\partial y^2} - \frac{f^2}{\omega_{c,e}}\frac{\partial^2 u_{y1}}{\partial y\partial x} + \frac{2\bar{\omega_{c,e}}}{\omega_{c,e}\gamma}f^3\frac{\partial^2 u_{z1}}{\partial y^2} \\ &- \frac{2e\bar{\omega}_{c,e}d_e^2}{m\omega_{c,e}\gamma}f_1\frac{\partial B_{x1}}{\partial y}\Big\},\end{aligned} \tag{H.87}$$

With these equations we have all the elements to formulate the eigenvalue problem with a full pressure tensor.

Calculating Different Terms in Linearized Pressure Tensor Equation without Guide Field:

Linearizing Eq.(6.52) gives

$$\begin{aligned}&\frac{\partial \mathcal{P}^1}{\partial t} + (\nabla\cdot\mathbf{u}_1)\mathcal{P}^0 + (\mathbf{u}_1\cdot\nabla)\mathcal{P}^0 + \mathcal{P}^0\cdot\nabla\mathbf{u}_1 + [\mathcal{P}^0\cdot\nabla\mathbf{u}_1]^T + +\mathcal{P}^1\cdot\nabla\mathbf{u}_0 + [\mathcal{P}^1\cdot\nabla\mathbf{u}_0]^T \\ &+ \frac{e}{m}\Big(\mathcal{P}^0\times\mathbf{B}_1 + \mathcal{P}^1\times\mathbf{B}_0 + [\mathcal{P}^0\times\mathbf{B}_1]^T + [\mathcal{P}^1\times\mathbf{B}_0]^T\Big) = 0,\end{aligned} \tag{H.88}$$

Based on Eq.(6.51), and thanks to the compressibility assumption, $\nabla\cdot\mathbf{u}_1 \neq 0$, thus the second term becomes

$$(\nabla\cdot\mathbf{u}_1)\mathcal{P}^0 = \begin{bmatrix} (\frac{\partial u_{x1}}{\partial x} + \frac{\partial u_{y1}}{\partial y})\mathcal{P}^0_{xx} & 0 & 0 \\ 0 & (\frac{\partial u_{x1}}{\partial x} + \frac{\partial u_{y1}}{\partial y})\mathcal{P}^0_{yy} & 0 \\ 0 & 0 & (\frac{\partial u_{x1}}{\partial x} + \frac{\partial u_{y1}}{\partial y})\mathcal{P}^0_{zz} \end{bmatrix} \tag{H.89}$$

The third term is

$$(\mathbf{u}_1 \cdot \nabla)\mathcal{P}^0 = \begin{bmatrix} u_{x1}\frac{d\mathcal{P}^0_{xx}}{dx} & 0 & 0 \\ 0 & u_{x1}\frac{d\mathcal{P}^0_{yy}}{dx} & 0 \\ 0 & 0 & u_{x1}\frac{d\mathcal{P}^0_{zz}}{dx} \end{bmatrix} \tag{H.90}$$

The fourth and fifth terms are given by

$$\mathcal{P}^0 \cdot \nabla \mathbf{u}_1 = \begin{bmatrix} \mathcal{P}^0_{xx}\frac{\partial u_{x1}}{\partial x} & \mathcal{P}^0_{xx}\frac{\partial u_{y1}}{\partial x} & \mathcal{P}^0_{xx}\frac{\partial u_{z1}}{\partial x} \\ \mathcal{P}^0_{yy}\frac{\partial u_{x1}}{\partial y} & \mathcal{P}^0_{yy}\frac{\partial u_{y1}}{\partial y} & \mathcal{P}^0_{yy}\frac{\partial u_{z1}}{\partial y} \\ 0 & 0 & 0 \end{bmatrix} \tag{H.91}$$

Then,

$$\mathcal{P}^0 \cdot \nabla \mathbf{u}_1 + [\mathcal{P}^0 \cdot \nabla \mathbf{u}_1]^T = \begin{bmatrix} 2\mathcal{P}^0_{xx}\frac{\partial u_{x1}}{\partial x} & \mathcal{P}^0_{xx}\frac{\partial u_{y1}}{\partial x} + \mathcal{P}^0_{yy}\frac{\partial u_{x1}}{\partial y} & \mathcal{P}^0_{xx}\frac{\partial u_{z1}}{\partial x} \\ \mathcal{P}^0_{xx}\frac{\partial u_{y1}}{\partial x} + \mathcal{P}^0_{yy}\frac{\partial u_{x1}}{\partial y} & 2\mathcal{P}^0_{yy}\frac{\partial u_{y1}}{\partial y} & \mathcal{P}^0_{yy}\frac{\partial u_{z1}}{\partial y} \\ \mathcal{P}^0_{xx}\frac{\partial u_{z1}}{\partial x} & \mathcal{P}^0_{yy}\frac{\partial u_{z1}}{\partial y} & 0 \end{bmatrix} \tag{H.92}$$

Also,

$$\mathcal{P}^1 \cdot \nabla \mathbf{u}_0 = \begin{bmatrix} 0 & 0 & \mathcal{P}_{xx}\frac{\partial u_{z0}}{\partial x} \\ 0 & 0 & \mathcal{P}_{xy}\frac{\partial u_{z0}}{\partial x} \\ 0 & 0 & \mathcal{P}_{xz}\frac{\partial u_{z0}}{\partial x} \end{bmatrix} \tag{H.93}$$

Then,

$$\mathcal{P}^1 \cdot \nabla \mathbf{u}_0 + [\mathcal{P}^1 \cdot \nabla \mathbf{u}_0]^T = \begin{bmatrix} 0 & 0 & \mathcal{P}_{xx}\frac{\partial u_{z0}}{\partial x} \\ 0 & 0 & \mathcal{P}_{xy}\frac{\partial u_{z0}}{\partial x} \\ 0 & 0 & 2\mathcal{P}_{xz}\frac{\partial u_{z0}}{\partial x} \end{bmatrix} \tag{H.94}$$

and

$$\mathcal{P}^0 \times \mathbf{B}_1 = \begin{bmatrix} 0 & \mathcal{P}^0_{yy}B_{z1} & -\mathcal{P}^0_{zz}B_{y1} \\ -\mathcal{P}^0_{xx}B_{z1} & 0 & \mathcal{P}^0_{zz}B_{x1} \\ \mathcal{P}^0_{xx}B_{y1} & -\mathcal{P}^0_{yy}B_{x1} & 0 \end{bmatrix} \tag{H.95}$$

$$\mathcal{P}^0 \times \mathbf{B}_1 + [\mathcal{P}^0 \times \mathbf{B}_1]^T = \begin{bmatrix} 0 & (\mathcal{P}^0_{yy} - \mathcal{P}^0_{xx})B_{z1} & (\mathcal{P}^0_{xx} - \mathcal{P}^0_{zz})B_{y1} \\ (\mathcal{P}^0_{yy} - \mathcal{P}^0_{xx})B_{z1} & 0 & (\mathcal{P}^0_{zz} - \mathcal{P}^0_{yy})B_{x1} \\ (\mathcal{P}^0_{xx} - \mathcal{P}^0_{zz})B_{y1} & (\mathcal{P}^0_{zz} - \mathcal{P}^0_{yy})B_{x1} & 0 \end{bmatrix} \tag{H.96}$$

$$\mathcal{P}^1 \times \mathbf{B}_0 = \begin{bmatrix} -B_y\mathcal{P}_{xz} & -B_y\mathcal{P}_{yz} & -B_y\mathcal{P}_{zz} \\ 0 & 0 & 0 \\ B_y\mathcal{P}_{xx} & B_y\mathcal{P}_{xy} & B_y\mathcal{P}_{xz} \end{bmatrix} \tag{H.97}$$

$$\mathcal{P}^1 \times \mathbf{B}_0 + [\mathcal{P}^1 \times \mathbf{B}_0]^T = \begin{bmatrix} -2B_y\mathcal{P}_{xz} & -B_y\mathcal{P}_{yz} & B_y\mathcal{P}_{xx} - B_y\mathcal{P}_{zz} \\ -B_y\mathcal{P}_{yz} & 0 & B_y\mathcal{P}_{xy} \\ B_y\mathcal{P}_{xx} - B_y\mathcal{P}_{zz} & B_y\mathcal{P}_{xy} & 2B_y\mathcal{P}_{xz} \end{bmatrix} \tag{H.98}$$

Here $B_y = B_y(x) = B_s f(x)$, such that $\mathbf{B}_0 = B_y\mathbf{e}_y$, which represents the sheared field that leads to reconnection events. Now, substituting the previous equations into Eq.(H.88)

$$\frac{\partial \mathcal{P}_{xx}}{\partial t} - 2\bar{\omega}_{c,e} f(x)\mathcal{P}_{xz} = -(3\frac{\partial u_{x1}}{\partial x} + \frac{\partial u_{y1}}{\partial y})\mathcal{P}^0_{xx} - \frac{d\mathcal{P}^0_{xx}}{dx}u_{x1}, \tag{H.99}$$

$$\frac{\partial \mathcal{P}_{xy}}{\partial t} - \bar{\omega}_{c,e} f(x)\mathcal{P}_{yz} = \frac{e}{m}(\mathcal{P}^0_{xx} - \mathcal{P}^0_{yy})B_{z1} - \mathcal{P}^0_{xx}\frac{\partial u_{y1}}{\partial x} - \mathcal{P}^0_{yy}\frac{\partial u_{x1}}{\partial y}, \tag{H.100}$$

$$\frac{\partial \mathcal{P}_{xz}}{\partial t} + (\bar{\omega}_{c,e} f(x) + \frac{\partial u_{z0}}{\partial x})\mathcal{P}_{xx} - \bar{\omega}_{c,e} f(x)\mathcal{P}_{zz} = \frac{e}{m}(\mathcal{P}^0_{zz} - \mathcal{P}^0_{xx})B_{y1} - \mathcal{P}^0_{xx}\frac{\partial u_{z1}}{\partial x}, \tag{H.101}$$

$$\frac{\partial \mathcal{P}_{yz}}{\partial t} + (\bar{\omega}_{c,e} f(x) + \frac{\partial u_{z0}}{\partial x})\mathcal{P}_{xy} = \frac{e}{m}(\mathcal{P}^0_{yy} - \mathcal{P}^0_{zz})B_{x1} - \mathcal{P}^0_{yy}\frac{\partial u_{z1}}{\partial y}, \tag{H.102}$$

$$\frac{\partial \mathcal{P}_{yy}}{\partial t} = -(\frac{\partial u_{x1}}{\partial x} + 3\frac{\partial u_{y1}}{\partial y})\mathcal{P}^0_{yy} - \frac{d\mathcal{P}^0_{yy}}{dx}u_{x1}, \tag{H.103}$$

$$\frac{\partial \mathcal{P}_{zz}}{\partial t} + 2(\bar{\omega}_{c,e} f(x) + \frac{\partial u_{z0}}{\partial x})\mathcal{P}_{xz} = -(\frac{\partial u_{x1}}{\partial x} + \frac{\partial u_{y1}}{\partial y})\mathcal{P}^0_{zz} - \frac{d\mathcal{P}^0_{zz}}{dx}u_{x1}, \tag{H.104}$$

In the `EMHD` model, the electron cyclotron frequency and the growth rate of reconnecting mode (γ) will be much smaller than that frequency, that is $\gamma \ll \bar{\omega}_{c,e}$. Hence, the previous equations become

$$\gamma\mathcal{P}_{xx} - 2\bar{\omega}_{c,e} f(x)\mathcal{P}_{xz} = \Lambda_1, \tag{H.105}$$

$$\gamma\mathcal{P}_{xy} - \bar{\omega}_{c,e} f(x)\mathcal{P}_{yz} = \Lambda_2, \tag{H.106}$$

$$\gamma\mathcal{P}_{xz} + (\bar{\omega}_{c,e} f(x) + \frac{\partial u_{z0}}{\partial x})\mathcal{P}_{xx} - \bar{\omega}_{c,e} f(x)\mathcal{P}_{zz} = \Lambda_3, \tag{H.107}$$

$$\gamma\mathcal{P}_{yz} + (\bar{\omega}_{c,e} f(x) + \frac{\partial u_{z0}}{\partial x})\mathcal{P}_{xy} = \Lambda_4 \tag{H.108}$$

$$\mathcal{P}_{yy} = \frac{\Lambda_5}{\gamma}, \tag{H.109}$$

$$\gamma\mathcal{P}_{zz} + 2(\bar{\omega}_{c,e} f(x) + \frac{\partial u_{z0}}{\partial x})\mathcal{P}_{xz} = \Lambda_6, \tag{H.110}$$

where,

$$\Lambda_1 = -3\mathcal{P}^0_{xx}\frac{\partial u_{x1}}{\partial x} - \frac{d\mathcal{P}^0_{xx}}{dx}u_{x1} - \mathcal{P}^0_{xx}\frac{\partial u_{y1}}{\partial y}, \tag{H.111}$$

$$\Lambda_2 = -\mathcal{P}^0_{yy}\frac{\partial u_{x1}}{\partial y} - \mathcal{P}^0_{xx}\frac{\partial u_{y1}}{\partial x} + \frac{e}{m}(\mathcal{P}^0_{xx} - \mathcal{P}^0_{yy})B_{z1}, \tag{H.112}$$

$$\Lambda_3 = -\mathcal{P}^0_{xx}\frac{\partial u_{z1}}{\partial x} + \frac{e}{m}(\mathcal{P}^0_{zz} - \mathcal{P}^0_{xx})B_{y1}, \tag{H.113}$$

$$\Lambda_4 = -\mathcal{P}^0_{yy}\frac{\partial u_{z1}}{\partial y} + \frac{e}{m}(\mathcal{P}^0_{yy} - \mathcal{P}^0_{zz})B_{x1}, \tag{H.114}$$

$$\Lambda_5 = -\mathcal{P}^0_{yy}\frac{\partial u_{x1}}{\partial x} - \frac{d\mathcal{P}^0_{yy}}{dx}u_{x1} + 3\mathcal{P}^0_{yy}\frac{\partial u_{y1}}{\partial y}, \tag{H.115}$$

$$\Lambda_6 = -\mathcal{P}^0_{zz}\frac{\partial u_{x1}}{\partial x} - \frac{d\mathcal{P}^0_{zz}}{dx}u_{x1} - \mathcal{P}^0_{zz}\frac{\partial u_{y1}}{\partial y}, \tag{H.116}$$

From Eq.(H.109) and Eq.(H.115), $\mathcal{P}^1_{yy}$ reads

$$\mathcal{P}^1_{yy} = -\frac{\mathcal{P}^0_{yy}}{\gamma}\frac{\partial u_{x1}}{\partial x} - \frac{1}{\gamma}\frac{d\mathcal{P}^0_{yy}}{dx}u_{x1} + \frac{3\mathcal{P}^0_{yy}}{\gamma}\frac{\partial u_{y1}}{\partial y}, \tag{H.117}$$

The equations of $\mathcal{P}^1_{xy}$ and $\mathcal{P}^1_{yz}$ lead to

$$\begin{aligned}\mathcal{P}^1_{xy} = \frac{1}{\bar{\omega}_{c,e}}\frac{f}{l_1}\Lambda_4 + \frac{\gamma}{\bar{\omega}^2_{c,e}}\frac{1}{l_1}\Lambda_2 = &-\frac{\gamma}{\bar{\omega}^2_{c,e}}\frac{1}{l_1}\mathcal{P}^0_{yy}\frac{\partial u_{x1}}{\partial y} - \frac{\gamma}{\bar{\omega}^2_{c,e}}\frac{1}{l_1}\mathcal{P}^0_{xx}\frac{\partial u_{y1}}{\partial x} - \frac{1}{\bar{\omega}_{c,e}}\frac{f}{l_1}\mathcal{P}^0_{yy}\frac{\partial u_{z1}}{\partial y}\\ &+ \frac{e}{m\bar{\omega}_{c,e}}\frac{f}{l_1}(\mathcal{P}^0_{yy} - \mathcal{P}^0_{zz})B_{x1} + \frac{e\gamma}{m\bar{\omega}^2_{c,e}}\frac{1}{l_1}(\mathcal{P}^0_{xx} - \mathcal{P}^0_{yy})B_{z1},\end{aligned} \tag{H.118}$$

$$\begin{aligned}\mathcal{P}^1_{yz} = \frac{\gamma}{\bar{\omega}^2_{c,e}l_1}\Lambda_4 - \frac{l_0}{\bar{\omega}_{c,e}l_1}\Lambda_2 = &\frac{1}{\bar{\omega}_{c,e}}\frac{l_0}{l_1}\mathcal{P}^0_{yy}\frac{\partial u_{x1}}{\partial y} + \frac{1}{\bar{\omega}_{c,e}}\frac{l_0}{l_1}\mathcal{P}^0_{xx}\frac{\partial u_{y1}}{\partial x} - \frac{\gamma}{\bar{\omega}^2_{c,e}}\frac{1}{l_1}\mathcal{P}^0_{yy}\frac{\partial u_{z1}}{\partial y}\\ &+ \frac{e\gamma}{m\bar{\omega}^2_{c,e}}\frac{1}{l_1}(\mathcal{P}^0_{yy} - \mathcal{P}^0_{zz})B_{x1} - \frac{e}{m\bar{\omega}_{c,e}}\frac{l_0}{l_1}(\mathcal{P}^0_{xx} - \mathcal{P}^0_{yy})B_{z1},\end{aligned} \tag{H.119}$$

The remaining equations lead to

$$\begin{aligned}\mathcal{P}^1_{xz} = &\frac{1}{2\bar{\omega}_{c,e}}\frac{1}{l_0}\Lambda_6 - \frac{\gamma}{\bar{\omega}^2_{c,e}}\frac{1}{l_3}\Lambda_3 + \frac{1}{\bar{\omega}_{c,e}}\frac{l_0}{l_3}\Lambda_1 = -\frac{1}{2\bar{\omega}_{c,e}}\frac{1}{l_0}\mathcal{P}^0_{zz}\frac{\partial u_{x1}}{\partial x} - \frac{1}{2\bar{\omega}_{c,e}}\frac{1}{l_0}\frac{d\mathcal{P}^0_{zz}}{dx}u_{x1}\\ &- 3\frac{1}{\bar{\omega}_{c,e}}\frac{l_0}{l_3}\mathcal{P}^0_{xx}\frac{\partial u_{x1}}{\partial x} - \frac{1}{\bar{\omega}_{c,e}}\frac{l_0}{l_3}\frac{d\mathcal{P}^0_{xx}}{dx}u_{x1} - \frac{1}{\bar{\omega}_{c,e}}\frac{l_0}{l_3}\mathcal{P}^0_{xx}\frac{\partial u_{y1}}{\partial y} - \frac{1}{2\bar{\omega}_{c,e}}\frac{1}{l_0}\mathcal{P}^0_{zz}\frac{\partial u_{y1}}{\partial y}\\ &+ \frac{\gamma}{\bar{\omega}^2_{c,e}}\frac{1}{l_3}\mathcal{P}^0_{xx}\frac{\partial u_{z1}}{\partial x} - \frac{e\gamma}{m\bar{\omega}^2_{c,e}}\frac{1}{l_3}(\mathcal{P}^0_{zz} - \mathcal{P}^0_{xx})B_{y1},\end{aligned} \tag{H.120}$$

$$\begin{aligned}\mathcal{P}^1_{xx} = &\frac{1}{\gamma}\frac{f}{l_0}\Lambda_6 - \frac{2}{\bar{\omega}_{c,e}}\frac{f}{l_3}\Lambda_3 + \frac{1}{\gamma}\frac{l_4}{l_3}\Lambda_1 = -\frac{1}{\gamma}\frac{f}{l_0}\mathcal{P}^0_{zz}\frac{\partial u_{x1}}{\partial x} - \frac{1}{\gamma}\frac{f}{l_0}\frac{d\mathcal{P}^0_{zz}}{dx}u_{x1} - 3\frac{1}{\gamma}\frac{l_4}{l_3}\mathcal{P}^0_{xx}\frac{\partial u_{x1}}{\partial x}\\ &- \frac{1}{\gamma}\frac{l_4}{l_3}\frac{d\mathcal{P}^0_{xx}}{dx}u_{x1} - \frac{1}{\gamma}\frac{l_4}{l_3}\mathcal{P}^0_{xx}\frac{\partial u_{y1}}{\partial y} - \frac{1}{\gamma}\frac{f}{l_0}\mathcal{P}^0_{zz}\frac{\partial u_{y1}}{\partial y} + \frac{2}{\bar{\omega}_{c,e}}\frac{f}{l_3}\mathcal{P}^0_{xx}\frac{\partial u_{z1}}{\partial x} - \frac{2e}{m\bar{\omega}_{c,e}}\times\\ &\frac{f}{l_3}(\mathcal{P}^0_{zz} - \mathcal{P}^0_{xx})B_{y1},\end{aligned} \tag{H.121}$$

$$\begin{aligned}\mathcal{P}^1_{zz} = &\frac{2}{\bar{\omega}_{c,e}}\frac{l_0}{l_3}\Lambda_3 - \frac{2}{\gamma}\frac{l_0^2}{l_3}\Lambda_1 = 3\frac{2}{\gamma}\frac{l_0^2}{l_3}\mathcal{P}^0_{xx}\frac{\partial u_{x1}}{\partial x} + \frac{2}{\gamma}\frac{l_0^2}{l_3}\frac{d\mathcal{P}^0_{xx}}{dx}u_{x1} + \frac{2}{\gamma}\frac{l_0^2}{l_3}\mathcal{P}^0_{xx}\frac{\partial u_{y1}}{\partial y} - \frac{2}{\bar{\omega}_{c,e}}\frac{l_0}{l_3}\mathcal{P}^0_{xx}\frac{\partial u_{z1}}{\partial x}\\ &+ \frac{2e}{m\bar{\omega}_{c,e}}\frac{l_0}{l_3}(\mathcal{P}^0_{zz} - \mathcal{P}^0_{xx})B_{y1},\end{aligned} \tag{H.122}$$

where

$$l_0 = f - d_e^2 f'', \quad l_1 = \frac{\gamma^2}{\bar{\omega}^2_{c,e}} + l_0 f, \quad l_2 = \frac{\gamma^2}{\bar{\omega}^2_{c,e}} + 2l_0 f, \quad l_3 = l_2 + 2l_0 f, \quad l_4 = l_2 + 4l_0 f, \tag{H.123}$$

I

Linear Analysis of Faraday-Maxwell Equation Combined with Generalized Ohm's Law

In this appendix we linearize Faraday-Maxwell equation, given by Eq.(6.32). First, from the equation of motion, given by Eq.(6.31), the electric field can be written as

$$n\mathbf{E} = -n(\mathbf{u}\times\mathbf{B}) - \frac{m}{e}n\frac{\partial \mathbf{u}}{\partial t} - \frac{m}{e}n\mathbf{u}\cdot\nabla\mathbf{u} - \frac{\nabla\cdot\mathcal{P}}{e}, \tag{I.1}$$

The linear version of this equation reads

$$\mathbf{E}_1 = -(\mathbf{u}_0\times\mathbf{B}_1)-(\mathbf{u}_1\times\mathbf{B}_0)-(\mathbf{u}_0\times\mathbf{B}_0)\frac{n_1}{n_0}-\frac{m}{e}\frac{\partial \mathbf{u}_1}{\partial t}-\frac{m}{e}\mathbf{u}_0\cdot\nabla\mathbf{u}_1-\frac{m}{e}\mathbf{u}_1\cdot\nabla\mathbf{u}_0-\frac{m}{en_0}n_1\mathbf{u}_0\cdot\nabla\mathbf{u}_0-\frac{\nabla\cdot\mathcal{P}^1}{en_0}, \tag{I.2}$$

Due to the fact that z is the ignorable variable, and the dependence of the equilibrium only on x, we have

$$\mathbf{u}_0\cdot\nabla\mathbf{u}_0 = \mathbf{u}_0\cdot\nabla\mathbf{u}_1 = 0, \quad \nabla\times(\mathbf{u}_0\times\mathbf{B}_0) = 0, \tag{I.3}$$

Thus Eq.(I.2) becomes

$$\mathbf{E}_1 = -(\mathbf{u}_0\times\mathbf{B}_1) - (\mathbf{u}_1\times\mathbf{B}_0) - (\mathbf{u}_0\times\mathbf{B}_0)\frac{n_1}{n_0} - \frac{m}{e}\frac{\partial\mathbf{u}_1}{\partial t} - \frac{m}{e}\mathbf{u}_1\cdot\nabla\mathbf{u}_0 - \frac{\nabla\cdot\mathcal{P}^1}{en_0}, \tag{I.4}$$

Substituting this equation into linear version of Faraday equation, one finds,

$$\begin{aligned}\frac{\partial\mathbf{B}_1}{\partial t} = {}& \nabla\times\left[(\mathbf{u}_0\times\mathbf{B}_0)\frac{n_1}{n_0}\right] + \nabla\times(\mathbf{u}_0\times\mathbf{B}_1) + \nabla\times(\mathbf{u}_1\times\mathbf{B}_0) + \frac{m}{e}\frac{\partial}{\partial t}\nabla\times\mathbf{u}_1 \\ & + \frac{m}{e}\nabla\times(\mathbf{u}_1\cdot\nabla\mathbf{u}_0) + \frac{1}{e}\nabla\times(\frac{\nabla\cdot\mathcal{P}_1}{n_0}),\end{aligned} \tag{I.5}$$

The first term on the right-hand side can be written as

$$\begin{aligned}\nabla\times\left[(\mathbf{u}_0\times\mathbf{B}_0)\frac{n_1}{n_0}\right] &= \frac{n_1}{n_0}\nabla\times(\mathbf{u}_0\times\mathbf{B}_0) + \frac{1}{n_0}\nabla n_1\times(\mathbf{u}_0\times\mathbf{B}_0) + n_1\nabla(\frac{1}{n_0})\times(\mathbf{u}_0\times\mathbf{B}_0) \\ &= -\frac{B_s^2}{\mu_0 e}\frac{ff'}{n_0^2}\frac{\partial n_1}{\partial y}\mathbf{e}_z,\end{aligned} \tag{I.6}$$

In the previous equation, due to Eq.(I.3), the first and last terms on the right-hand side are obviously equal to zero. Now we calculate terms one by one. Using Eq.(6.35) and Eq.(6.36), we have

$$\mathbf{u}_0 \times \mathbf{B}_1 = -\frac{B_s f^{'}(x)}{\mu_0 e n_0} \begin{cases} -B_{y1} \\ B_{x1} \\ 0, \end{cases} \tag{I.7}$$

We find

$$\nabla \times (\mathbf{u}_0 \times \mathbf{B}_1) = -\frac{B_s}{\mu_0 e n_0} \begin{cases} 0 \\ 0 \\ f^{''}(x) B_{x1} - \frac{n_0^{'} f^{'}(x)}{n_0} B_{x1}, \end{cases} \tag{I.8}$$

In the derivation of the previous equation we made use of Thomson-Maxwell equation. Now, we have for non-zero guide field

$$\mathbf{u}_1 \times \mathbf{B}_0 = \begin{cases} B_g u_{y1} - B_s f(x) u_{z1}, \\ -B_g u_{x1}, \\ B_s f(x) u_{x1}, \end{cases} \tag{I.9}$$

While for a null guide field, the previous equation becomes

$$\mathbf{u}_1 \times \mathbf{B}_0 = \begin{cases} -B_s f(x) u_{z1}, \\ 0, \\ B_s f(x) u_{x1}, \end{cases} \tag{I.10}$$

The curl of the case with guide field gives

$$\nabla \times (\mathbf{u}_1 \times \mathbf{B}_0) = \begin{cases} B_s f(x) \frac{\partial u_{x1}}{\partial y}, \\ -B_s f^{'}(x) u_{x1} - B_s f(x) \frac{\partial u_{x1}}{\partial x}, \\ -B_g (\frac{\partial u_{x1}}{\partial x} + \frac{\partial u_{y1}}{\partial y}) + B_s f(x) \frac{\partial u z1}{\partial y}, \end{cases} \tag{I.11}$$

whereas for zero-guide field, one writes

$$\nabla \times (\mathbf{u}_1 \times \mathbf{B}_0) = \begin{cases} B_s f(x) \frac{\partial u_{x1}}{\partial y}, \\ -B_s f^{'}(x) u_{x1} - B_s f(x) \frac{\partial u_{x1}}{\partial x}, \\ B_s f(x) \frac{\partial u z1}{\partial y}, \end{cases} \tag{I.12}$$

The curl of the perturbed velocity is

$$\nabla \times \mathbf{u}_1 = \begin{cases} \frac{\partial u_{z1}}{\partial y}, \\ -\frac{\partial u_{z1}}{\partial x}, \\ \frac{\partial u_{y1}}{\partial x} - \frac{\partial u_{x1}}{\partial y}, \end{cases} \tag{I.13}$$

The convective is given by,

$$\mathbf{u}_1 \cdot \nabla \mathbf{u}_0 = \begin{cases} 0, \\ 0, \\ -\frac{B_s}{\mu_0 e n_0} f^{''}(x) u_{x1} + \frac{B_s}{\mu_0 e n_0^2} f^{'}(x) n_0^{\prime} u_{x1}, \end{cases} \tag{I.14}$$

In the previous derivation the only derivative that matters is $\frac{\partial}{\partial x}$ because the equilibrium quantities are only functions of x. Then,

$$\nabla \times (\mathbf{u}_1 \cdot \nabla \mathbf{u}_0) = \begin{cases} \frac{B_s}{\mu_0 e}\Big[- \frac{f^{''}}{n_0} + \frac{f^{'} n_0^{'}}{n_0^2}\Big] \frac{\partial u_{x1}}{\partial y}, \\ \frac{B_s}{\mu_0 e}\Big[\frac{f^{''}}{n_0} - \frac{f^{'} n_0^{'}}{n_0^2}\Big] \frac{\partial u_{x1}}{\partial x} + \frac{B_s}{\mu_0 e}\Big[\frac{f^{'''}}{n_0} - \frac{2 f^{''} n_0^{'}}{n_0} + \frac{2 f^{'} {n_0^{'}}^2}{n_0^3} - \frac{f^{'} n_0^{''}}{n_0^2}\Big] u_{x1}, \\ 0, \end{cases} \tag{I.15}$$

Now we calculate the terms which include the full pressure tensor. First,

$$\nabla \times [\frac{\nabla \cdot \mathcal{P}^1}{e n_0}] = \frac{1}{e n_0} \nabla \times \nabla \cdot \mathcal{P}^1 - \frac{1}{e n_0^2} \nabla n_0 \times \nabla \cdot \mathcal{P}^1, \tag{I.16}$$

Using Eq.(B.29), we obtain

$$\nabla \times \nabla \cdot \mathcal{P}^1 = \begin{cases} \frac{\partial^2 \mathcal{P}^1_{xz}}{\partial x \partial y} + \frac{\partial^2 \mathcal{P}^1_{yz}}{\partial y^2}, \\ -\frac{\partial^2 \mathcal{P}^1_{xz}}{\partial x^2} - \frac{\partial^2 \mathcal{P}^1_{yz}}{\partial x \partial y}, \\ \frac{\partial^2}{\partial x \partial y}(\mathcal{P}^1_{yy} - \mathcal{P}^1_{xx}) + \frac{\partial^2 \mathcal{P}^1_{xy}}{\partial x^2} - \frac{\partial^2 \mathcal{P}^1_{xy}}{\partial y^2}, \end{cases} \tag{I.17}$$

and

$$\nabla n_0 \times \nabla \cdot \mathcal{P}^1 = \begin{cases} 0, \\ -n_0^{'} \frac{\partial \mathcal{P}^1_{xz}}{\partial x} - n_0^{'} \frac{\partial \mathcal{P}^1_{yz}}{\partial y}, \\ n_0^{'} \frac{\partial \mathcal{P}^1_{xy}}{\partial x} + n_0^{'} \frac{\partial \mathcal{P}^1_{yy}}{\partial y}, \end{cases} \tag{I.18}$$

Thus,

$$\nabla \times [\frac{\nabla \cdot \mathcal{P}^1}{e n_0}] = \frac{1}{e n_0} \begin{cases} \frac{\partial^2 \mathcal{P}^1_{xz}}{\partial x \partial y} + \frac{\partial^2 \mathcal{P}^1_{yz}}{\partial y^2}, \\ -\frac{\partial^2 \mathcal{P}^1_{xz}}{\partial x^2} - \frac{\partial^2 \mathcal{P}^1_{yz}}{\partial x \partial y} + \frac{n_0^{'}}{n_0} \frac{\partial \mathcal{P}^1_{xz}}{\partial x} + \frac{n_0^{'}}{n_0} \frac{\partial \mathcal{P}^1_{yz}}{\partial y}, \\ \frac{\partial^2}{\partial x \partial y}(\mathcal{P}^1_{yy} - \mathcal{P}^1_{xx}) + \frac{\partial^2 \mathcal{P}^1_{xy}}{\partial x^2} - \frac{\partial^2 \mathcal{P}^1_{xy}}{\partial y^2} - \frac{n_0^{'}}{n_0} \frac{\partial \mathcal{P}^1_{xy}}{\partial x} - \frac{n_0^{'}}{n_0} \frac{\partial \mathcal{P}^1_{yy}}{\partial y} \end{cases} \tag{I.19}$$

Substituting the previous equations into Eq.(I.5), we obtain for the linearized components of Faraday-Ohm equation, given by

$$\frac{\partial B_{x1}}{\partial t} = \Big[B_s f + \frac{m B_s}{\mu_0 e^2} (-\frac{f^{''}}{n_0} + \frac{f^{'} n_0^{'}}{n_0^2}) \Big] \frac{\partial u_{x1}}{\partial y} + \frac{m}{e} \frac{\partial}{\partial t} (\frac{\partial u_{z1}}{\partial y}) + \frac{1}{e n_0} \Big(\frac{\partial^2 \mathcal{P}^1_{xz}}{\partial x \partial y} + \frac{\partial^2 \mathcal{P}^1_{yz}}{\partial y^2} \Big), \tag{I.20}$$

$$\begin{aligned} \frac{\partial B_{y1}}{\partial t} = & \Big[- B_s f^{'} + \frac{m B_s}{\mu_0 e^2} \times \Big(\frac{f^{'''}}{n_0} - \frac{2 f^{''} n_0^{'}}{n_0} + \frac{2 f^{'} {n_0^{'}}^2}{n_0^3} - \frac{f^{'} n_0^{''}}{n_0^2} \Big) \Big] u_{x1} - \Big[B_s f - \frac{m B_s}{\mu_0 e^2} \Big(\frac{f^{''}}{n_0} \\ & - \frac{f^{'} n_0^{'}}{n_0^2} \Big) \Big] \frac{\partial u_{x1}}{\partial x} - \frac{m}{e} \frac{\partial}{\partial t} (\frac{\partial u_{z1}}{\partial x}) - \frac{1}{e n_0} \frac{\partial^2 \mathcal{P}^1_{xz}}{\partial x^2} - \frac{1}{e n_0} \frac{\partial^2 \mathcal{P}^1_{yz}}{\partial x \partial y} + \frac{n_0^{'}}{e n_0^2} \frac{\partial \mathcal{P}^1_{xz}}{\partial x} + \frac{n_0^{'}}{e n_0^2} \frac{\partial \mathcal{P}^1_{yz}}{\partial y}, \end{aligned} \tag{I.21}$$

$$\begin{aligned} \frac{\partial B_{z1}}{\partial t} = & - \frac{B_s^2}{\mu_0 e} \frac{f f^{'}}{n_0^2} \frac{\partial n_1}{\partial y} - \Big[\frac{B_s}{\mu_0 e n_0} f^{''}(x) - \frac{B_s}{\mu_0 e} \frac{n_0^{'} f^{'}(x)}{n_0^2} \Big] B_{x1} - B_g (\frac{\partial u_{x1}}{\partial x} + \frac{\partial u_{y1}}{\partial y}) + B_s f(x) \frac{\partial u_{z1}}{\partial y} \\ & + \frac{m}{e} \frac{\partial}{\partial t} (\frac{\partial u_{y1}}{\partial x} - \frac{\partial u_{x1}}{\partial y}) + \frac{1}{e n_0} \frac{\partial^2}{\partial x \partial y} (\mathcal{P}^1_{yy} - \mathcal{P}^1_{xx}) + \frac{1}{e n_0} \frac{\partial^2 \mathcal{P}^1_{xy}}{\partial x^2} - \frac{1}{e n_0} \frac{\partial^2 \mathcal{P}^1_{xy}}{\partial y^2} - \frac{n_0^{'}}{e n_0^2} \frac{\partial \mathcal{P}^1_{xy}}{\partial x} - \frac{n_0^{'}}{e n_0^2} \frac{\partial \mathcal{P}^1_{yy}}{\partial y}, \end{aligned} \tag{I.22}$$

The previous equations are dimensional, and can be applied to regimes with arbitrary equilibrium density profiles, which make them very useful to study realistic cases. Of course, a numerical solution is the best strategy to be used in order to solve them.

J

Generalized Eigenvalue Problem with Full Pressure Tensor: Constant Density

For a constant equilibrium density profile ($n_0 = const$), which is consistent with the chosen equilibrium for the magnetic field and pressure tensor, all the terms containing a derivative of n_0 in linearized Faraddy-Ohm and Ampere-Ohm equations vanish. Setting to zero the derivatives of the density, and taking the Fourier transform, the dimensionless equations become

$$\gamma^2 B_{x1} - \gamma^2 d_e^2 \frac{\partial u_{z1}}{\partial y} - \gamma \frac{\bar{\omega}_{c,e}}{\omega_{c,e}} \Big[f - d_e^2 f'' \Big] \frac{\partial u_{x1}}{\partial y} + \frac{\gamma}{2} (\frac{\bar{\omega}_{c,e}}{\omega_{c,e}})^2 d_e^2 \frac{\partial^3 u_{z1}}{\partial y^2 \partial x} - \frac{\gamma}{2} (\frac{\bar{\omega}_{c,e}}{\omega_{c,e}})^2 d_e^2 (f^2 \frac{\partial^3}{\partial x \partial y^2} + 2 f f' \times \frac{\partial^2}{\partial y^2}) u_{z1} + \frac{\gamma}{2} (\frac{\bar{\omega}_{c,e}}{\omega_{c,e}})^2 d_e^2 (f_3 \frac{\partial^2}{\partial y \partial x} + f_3' \frac{\partial}{\partial y}) B_{x1} + \frac{\gamma}{2} (\frac{\bar{\omega}_{c,e}}{\omega_{c,e}})^2 d_e^2 f_3 \frac{\partial^2 B_{y1}}{\partial y^2} = \frac{1}{2} (\frac{\bar{\omega}_{c,e}}{\omega_{c,e}})^3 d_e^2 f_5 \frac{\partial^2 u_{x1}}{\partial y^2} + \frac{1}{2} \times (\frac{\bar{\omega}_{c,e}}{\omega_{c,e}})^3 f_6 \frac{\partial^3 u_{x1}}{\partial y^2 \partial x} + \frac{1}{2} (\frac{\bar{\omega}_{c,e}}{\omega_{c,e}})^3 f_6 \frac{\partial^3 u_{y1}}{\partial y^3} \tag{J.1}$$

$$\gamma^2 B_{y1} + \gamma^2 d_e^2 \frac{\partial u_{z1}}{\partial x} + \gamma (\frac{\bar{\omega}_{c,e}}{\omega_{c,e}}) \Big[f' - d_e^2 f''' \Big] u_{x1} + \gamma (\frac{\bar{\omega}_{c,e}}{\omega_{c,e}}) \Big[f - d_e^2 f'' \Big] \frac{\partial u_{x1}}{\partial x} + \frac{\gamma}{2} (\frac{\bar{\omega}_{c,e}}{\omega_{c,e}})^2 \Big[f^2 \frac{\partial^3}{\partial x^2 \partial y} + 4 f f' \frac{\partial^2}{\partial x \partial y} + (2 f_3 + 2 f'^2) \frac{\partial}{\partial y} \Big] u_{z1} - \frac{\gamma}{2} (\frac{\bar{\omega}_{c,e}}{\omega_{c,e}})^2 \Big[f^2 \frac{\partial^3}{\partial y \partial x^2} + 2 f' f \frac{\partial^2}{\partial y \partial x} \Big] u_{z1} - \frac{\gamma}{2} (\frac{\bar{\omega}_{c,e}}{\omega_{c,e}})^2 d_e^2 \times \Big[f_3 \frac{\partial^2}{\partial x^2} + 2 f_3' \frac{\partial}{\partial x} + f_3'' \Big] B_{x1} - \frac{\gamma}{2} (\frac{\bar{\omega}_{c,e}}{\omega_{c,e}})^2 d_e^2 \Big[f_3 \frac{\partial^2}{\partial y \partial x} + f_3' \frac{\partial}{\partial y} \Big] B_{y1} = -\frac{1}{2} (\frac{\bar{\omega}_{c,e}}{\omega_{c,e}})^3 d_e^2 \times \Big[f_5 \frac{\partial^2}{\partial y \partial x} + f_5' \frac{\partial}{\partial y} \Big] u_{x1} - \frac{1}{2} (\frac{\bar{\omega}_{c,e}}{\omega_{c,e}})^3 \Big[f_6 \frac{\partial^3}{\partial y \partial x^2} + f_6' \frac{\partial^2}{\partial y \partial x} \Big] u_{x1} - \frac{1}{2} (\frac{\bar{\omega}_{c,e}}{\omega_{c,e}})^3 \Big[f_6 \frac{\partial^3}{\partial x \partial y^2} + f_6' \frac{\partial^2}{\partial y^2} \Big] u_{y1}, \tag{J.2}$$

$$\gamma B_{z1} + \gamma d_e^2 \frac{\partial u_{x1}}{\partial y} - \gamma d_e^2 \frac{\partial u_{y1}}{\partial x} = -(\frac{\bar{\omega}_{c,e}}{\omega_{c,e}})^2 f f' \frac{\partial n_1}{\partial y} - \frac{\partial u_{x1}}{\partial x} - \frac{1}{2} (\frac{\bar{\omega}_{c,e}}{\omega_{c,e}})^2 d_e^2 \Big[\frac{f^2}{2} \frac{\partial^3}{\partial x^3} + 2 f f' \frac{\partial^2}{\partial x^2} + (f_3 + f'^2) \frac{\partial}{\partial x} \Big] u_{x1} - \frac{1}{2} (\frac{\bar{\omega}_{c,e}}{\omega_{c,e}})^2 d_e^2 \Big[f^2 \frac{\partial^3}{\partial x \partial y^2} + 2 f f' \frac{\partial^2}{\partial y^2} \Big] u_{x1} + \frac{1}{4} (\frac{\bar{\omega}_{c,e}}{\omega_{c,e}})^2 d_e^2 f^2 \frac{\partial^3 u_{x1}}{\partial y^2 \partial x} - \frac{\partial u_{y1}}{\partial y} + \frac{1}{2} (\frac{\bar{\omega}_{c,e}}{\omega_{c,e}})^2 d_e^2 \Big[\frac{f^2}{2} \frac{\partial^3}{\partial x^2 \partial y} + 2 f f' \frac{\partial^2}{\partial x \partial y} + (f_3 + f'^2) \frac{\partial}{\partial y} \Big] u_{y1} - \frac{1}{2} (\frac{\bar{\omega}_{c,e}}{\omega_{c,e}})^2 d_e^2 \Big[f^2 \frac{\partial^3}{\partial y \partial x^2} + 2 f f' \frac{\partial^2}{\partial y \partial x} \Big] u_{y1} - \frac{1}{4} (\frac{\bar{\omega}_{c,e}}{\omega_{c,e}})^2 d_e^2 \frac{f^2}{2} \frac{\partial^3 u_{y1}}{\partial y^3} + (\frac{\bar{\omega}_{c,e}}{\omega_{c,e}}) f \frac{\partial u_{z1}}{\partial y} - (\frac{\bar{\omega}_{c,e}}{\omega_{c,e}}) f'' B_{x1}, \tag{J.3}$$

$$\gamma^2 u_{x1} - \frac{\gamma}{4}(\frac{\bar{\omega}_{c,e}}{\omega_{c,e}})^2 f^2 \frac{\partial^2 u_{x1}}{\partial y \partial x} + \frac{\gamma}{d_e^2} u_{y1} + \frac{\gamma}{2}(\frac{\bar{\omega}_{c,e}}{\omega_{c,e}})^2 f^2 \frac{\partial^2 u_{y1}}{\partial y^2} - \frac{\gamma}{d_e^2}(\frac{\bar{\omega}_{c,e}}{\omega_{c,e}}) f u_{z1} + \frac{\gamma}{d_e^2}(\frac{\bar{\omega}_{c,e}}{\omega_{c,e}}) f^{'} B_{y1} =$$
$$- \frac{1}{d_e^4}(\frac{\omega_{p,e}}{\omega_{c,e}})^2 u_{x1} + \frac{1}{2d_e^2}(\frac{\bar{\omega}_{c,e}}{\omega_{c,e}})^2 \Big[2f^2 \frac{\partial^2}{\partial x^2} + 4f^{'} f \frac{\partial}{\partial x} + f^{2'} \frac{\partial}{\partial x} + 2f_3 + 2f^{'2}\Big] u_{x1} + \frac{1}{2d_e^2}(\frac{\bar{\omega}_{c,e}}{\omega_{c,e}})^2 \times$$
$$\Big[2f^2 \frac{\partial^2}{\partial x \partial y} + 4f^{'} f \frac{\partial}{\partial y}\Big] u_{y1} - \frac{1}{d_e^2}(\frac{\bar{\omega}_{c,e}}{\omega_{c,e}})^3 \Big[f^3 \frac{\partial^2}{\partial x \partial y} + 3f^{'} f^2 \frac{\partial}{\partial y}\Big] u_{z1} + \frac{1}{d_e^2}(\frac{\bar{\omega}_{c,e}}{\omega_{c,e}})^3 \Big[f_1 \frac{\partial}{\partial x} + f_1^{'}\Big] B_{x1}$$
$$- \frac{1}{d_e^4}(\frac{\omega_{p,e}}{\omega_{c,e}})^2 \frac{\partial B_{z1}}{\partial y}, \tag{J.4}$$

$$\gamma^2 u_{y1} - \frac{\gamma}{d_e^2} u_{x1} - \frac{\gamma}{2}(\frac{\bar{\omega}_{c,e}}{\omega_{c,e}})^2 \Big[\frac{f^2}{2}\frac{\partial^2}{\partial x^2} + f f^{'} \frac{\partial}{\partial x} - f^2 \frac{\partial^2}{\partial y^2}\Big] u_{x1} + \frac{\gamma}{2}(\frac{\bar{\omega}_{c,e}}{\omega_{c,e}})^2 \Big[\frac{f^2}{2}\frac{\partial^2}{\partial x \partial y} + f f^{'} \frac{\partial}{\partial y} - f^2 \times$$
$$\frac{\partial^2}{\partial y \partial x}\Big] u_{y1} - \frac{\gamma}{d_e^2}(\frac{\bar{\omega}_{c,e}}{\omega_{c,e}}) f^{'} B_{x1} = \frac{1}{2d_e^2}(\frac{\bar{\omega}_{c,e}}{\omega_{c,e}})^2 \Big[f^{2'} \frac{\partial}{\partial y} + 2f^2 \frac{\partial^2}{\partial y \partial x}\Big] u_{x1} - \frac{1}{d_e^4}(\frac{\omega_{p,e}}{\omega_{c,e}})^2 u_{y1} + \frac{1}{d_e^2}(\frac{\bar{\omega}_{c,e}}{\omega_{c,e}})^2 f^2 \times$$
$$\frac{\partial^2 u_{y1}}{\partial y^2} - \frac{1}{d_e^2}(\frac{\bar{\omega}_{c,e}}{\omega_{c,e}})^3 f^3 \frac{\partial^2 u_{z1}}{\partial y^2} + \frac{1}{d_e^2}(\frac{\bar{\omega}_{c,e}}{\omega_{c,e}})^3 f_1 \frac{\partial B_{x1}}{\partial y} + \frac{1}{d_e^4}(\frac{\omega_{p,e}}{\omega_{c,e}})^2 \frac{\partial B_{z1}}{\partial x}, \tag{J.5}$$

$$\gamma^2 u_{z1} + \frac{\gamma}{d_e^2}(\frac{\bar{\omega}_{c,e}}{\omega_{c,e}})\Big[f - d_e^2 f^{''}\Big] u_{x1} + \frac{\gamma}{2}(\frac{\bar{\omega}_{c,e}}{\omega_{c,e}})^2 \Big[f^2 \frac{\partial^2}{\partial x \partial y} + 2 f f^{'} \frac{\partial}{\partial y}\Big] u_{z1} - \frac{\gamma}{2}(\frac{\bar{\omega}_{c,e}}{\omega_{c,e}})^2 f^2 \frac{\partial^2 u_{z1}}{\partial y \partial x} - \frac{\gamma}{2} \times$$
$$(\frac{\bar{\omega}_{c,e}}{\omega_{c,e}})^2 \Big[f_3 \frac{\partial}{\partial x} + f_3^{'}\Big] B_{x1} - \frac{\gamma}{2}(\frac{\bar{\omega}_{c,e}}{\omega_{c,e}})^2 f_3 \frac{\partial B_{y1}}{\partial y} = -\frac{1}{2}(\frac{\bar{\omega}_{c,e}}{\omega_{c,e}})^3 f_5 \frac{\partial u_{x1}}{\partial y} - \frac{1}{2d_e^2}(\frac{\bar{\omega}_{c,e}}{\omega_{c,e}})^3 f_6 \frac{\partial^2 u_{x1}}{\partial y \partial x} - \frac{1}{2d_e^2} \times$$
$$(\frac{\bar{\omega}_{c,e}}{\omega_{c,e}})^3 f_6 \frac{\partial^2 u_{y1}}{\partial y^2} - \frac{1}{d_e^4}(\frac{\bar{\omega}_{c,e}}{\omega_{c,e}})^3 u_{z1} + \frac{1}{d_e^4}(\frac{\omega_{p,e}}{\omega_{c,e}})^2 \frac{\partial B_{x1}}{\partial y} - \frac{1}{d_e^4}(\frac{\omega_{p,e}}{\omega_{c,e}})^2 \frac{\partial B_{y1}}{\partial x} + \frac{1}{d_e^4}\frac{\bar{\omega}_{c,e}\omega_{p,e}^2}{\omega_{c,e}^3} f^{'} n_1, \tag{J.6}$$

In the previous derivations, time, velocity, magnetic field, and length are normalized to whistler time (τ_w), whistler velocity (u_w), the guide field (B_g), the characteristic length (L_0), which must be smaller than the ion-skin depth, respectively. Now, these equations, after Fourier transforming with respect to y, become

$$\gamma^2 B_{x1} + \gamma^2 k d_e^2 u_{z1} + \gamma k \frac{\bar{\omega}_{c,e}}{\omega_{c,e}}\Big[f - d_e^2 f^{''}\Big] u_{x1} - i\frac{\gamma}{2}(\frac{\bar{\omega}_{c,e}}{\omega_{c,e}})^2 k^2 d_e^2 \Big[\frac{\partial}{\partial x} - f^2 \frac{\partial}{\partial x} - 2 f f^{'}\Big] u_{z1} - \frac{\gamma}{2}(\frac{\bar{\omega}_{c,e}}{\omega_{c,e}})^2 \times$$
$$k d_e^2 \Big[f_3 \frac{\partial}{\partial x} + f_3^{'}\Big] B_{x1} - i\frac{\gamma}{2}(\frac{\bar{\omega}_{c,e}}{\omega_{c,e}})^2 k^2 d_e^2 f_3 B_{y1} = -\frac{i}{2}(\frac{\bar{\omega}_{c,e}}{\omega_{c,e}})^3 k^2 \Big[f_6 \frac{\partial}{\partial x} + d_e^2 f_5\Big] u_{x1} + \frac{1}{2}(\frac{\bar{\omega}_{c,e}}{\omega_{c,e}})^3 k^3 f_6 u_{y1}, \tag{J.7}$$

$$\gamma^2 B_{y1} + \gamma^2 d_e^2 \frac{\partial u_{z1}}{\partial x} + \gamma(\frac{\bar{\omega}_{c,e}}{\omega_{c,e}})\Big[f \frac{\partial}{\partial x} - d_e^2 f^{''} \frac{\partial}{\partial x} + f^{'} - d_e^2 f^{'''}\Big] u_{x1} - \frac{\gamma}{2}(\frac{\bar{\omega}_{c,e}}{\omega_{c,e}})^2 k \Big[2 f f^{'} \frac{\partial}{\partial x} + 2f_3 + 2f^{'2}$$
$$\Big] u_{z1} - \frac{\gamma}{2}(\frac{\bar{\omega}_{c,e}}{\omega_{c,e}})^2 d_e^2 \Big[f_3 \frac{\partial^2}{\partial x^2} + 2f_3^{'} \frac{\partial}{\partial x} + f_3^{''}\Big] B_{x1} + \frac{\gamma}{2}(\frac{\bar{\omega}_{c,e}}{\omega_{c,e}})^2 k d_e^2 \Big[f_3 \frac{\partial}{\partial x} + f_3^{'}\Big] B_{y1} = \frac{1}{2}(\frac{\bar{\omega}_{c,e}}{\omega_{c,e}})^3 k \Big[f_6 \frac{\partial^2}{\partial x^2}$$
$$+ (f_6^{'} + d_e^2 f_5)\frac{\partial}{\partial x} + d_e^2 f_5^{'}\Big] u_{x1} + i\frac{1}{2}(\frac{\bar{\omega}_{c,e}}{\omega_{c,e}})^3 k^2 \Big[f_6 \frac{\partial}{\partial x} + f_6^{'}\Big] u_{y1}, \tag{J.8}$$

$$\gamma B_{z1} - \gamma k d_e^2 u_{x1} - \gamma d_e^2 \frac{\partial u_{y1}}{\partial x} = (\frac{\bar{\omega}_{c,e}}{\omega_{c,e}})^2 k f f' \frac{\partial n_1}{\partial y} - \frac{\partial u_{x1}}{\partial x} - \frac{1}{2}(\frac{\bar{\omega}_{c,e}}{\omega_{c,e}})^2 d_e^2 \Big[\frac{f^2}{2}\frac{\partial^3}{\partial x^3} + 2ff'\frac{\partial^2}{\partial x^2} + (f_3 + f'^2)\frac{\partial}{\partial x} - ik^2 f^2 \frac{\partial}{\partial x} - 2ik^2 f f' + \frac{i}{2}k^2 f^2 \frac{\partial}{\partial x}\Big] u_{x1} + k\Big[1 + \frac{1}{4}(\frac{\bar{\omega}_{c,e}}{\omega_{c,e}})^2 d_e^2 \Big(f^2 \frac{\partial^2}{\partial x} - 2f_3 - 2f'^2 - k^2 \frac{f^2}{2}\Big)\Big] \times u_{y1} - (\frac{\bar{\omega}_{c,e}}{\omega_{c,e}}) k f u_{z1} - (\frac{\bar{\omega}_{c,e}}{\omega_{c,e}}) f'' B_{x1}, \tag{J.9}$$

$$\gamma^2 u_{x1} + \frac{\gamma}{4}(\frac{\bar{\omega}_{c,e}}{\omega_{c,e}})^2 k f^2 \frac{\partial u_{x1}}{\partial x} + \frac{\gamma}{d_e^2}\Big[1 - \frac{i}{2}(\frac{\bar{\omega}_{c,e}}{\omega_{c,e}})^2 k^2 d_e^2 f^2\Big] u_{y1} - \frac{\gamma}{d_e^2}(\frac{\bar{\omega}_{c,e}}{\omega_{c,e}}) f u_{z1} + \frac{\gamma}{d_e^2}(\frac{\bar{\omega}_{c,e}}{\omega_{c,e}}) f' B_{y1} = -\frac{1}{d_e^4}\Big[(\frac{\omega_{p,e}}{\omega_{c,e}})^2 - \frac{d_e^2}{2}(\frac{\bar{\omega}_{c,e}}{\omega_{c,e}})^2 \Big(2f^2 \frac{\partial^2}{\partial x^2} + 4f' f \frac{\partial}{\partial x} + f^{2'}\frac{\partial}{\partial x} + 2f_3 + 2f'^2\Big)\Big] u_{x1} - \frac{k}{2d_e^2}(\frac{\bar{\omega}_{c,e}}{\omega_{c,e}})^2 \times \Big[2f^2 \frac{\partial}{\partial x} + 4f' f\Big] u_{y1} + \frac{k}{d_e^2}(\frac{\bar{\omega}_{c,e}}{\omega_{c,e}})^3 \Big[f^3 \frac{\partial}{\partial x} + 3f' f^2\Big] u_{z1} + \frac{1}{d_e^2}(\frac{\bar{\omega}_{c,e}}{\omega_{c,e}})^3 \Big[f_1 \frac{\partial}{\partial x} + f_1'\Big] B_{x1} + \frac{k}{d_e^4}(\frac{\omega_{p,e}}{\omega_{c,e}})^2 B_{z1}, \tag{J.10}$$

$$\gamma^2 u_{y1} - \frac{\gamma}{d_e^2}\Big[1 + \frac{d_e^2}{2}(\frac{\bar{\omega}_{c,e}}{\omega_{c,e}})^2 \Big(\frac{f^2}{2}\frac{\partial^2}{\partial x^2} + ff'\frac{\partial}{\partial x} + if^2 k^2\Big)\Big] u_{x1} - \frac{\gamma}{2}(\frac{\bar{\omega}_{c,e}}{\omega_{c,e}})^2 k \Big[\frac{f^2}{2}\frac{\partial}{\partial x} + ff' - f^2 \times \frac{\partial}{\partial x}\Big] u_{y1} - \frac{\gamma}{d_e^2}(\frac{\bar{\omega}_{c,e}}{\omega_{c,e}}) f' B_{x1} = -\frac{1}{2d_e^2}(\frac{\bar{\omega}_{c,e}}{\omega_{c,e}})^2 k \Big[f^{2'} + 2f^2 \frac{\partial}{\partial x}\Big] u_{x1} - \frac{1}{d_e^4}\Big[(\frac{\omega_{p,e}}{\omega_{c,e}})^2 + i d_e^2 (\frac{\bar{\omega}_{c,e}}{\omega_{c,e}})^2 k^2 f^2 \times \Big] u_{y1} + \frac{i}{d_e^2}(\frac{\bar{\omega}_{c,e}}{\omega_{c,e}})^3 k^2 f^3 u_{z1} - \frac{1}{d_e^2}(\frac{\bar{\omega}_{c,e}}{\omega_{c,e}})^3 k f_1 B_{x1} + \frac{1}{d_e^4}(\frac{\omega_{p,e}}{\omega_{c,e}})^2 \frac{\partial B_{z1}}{\partial x}, \tag{J.11}$$

$$\gamma^2 u_{z1} + \frac{\gamma}{d_e^2}(\frac{\bar{\omega}_{c,e}}{\omega_{c,e}})\Big[f - d_e^2 f''\Big] u_{x1} + \gamma(\frac{\bar{\omega}_{c,e}}{\omega_{c,e}})^2 f f' \frac{\partial u_{z1}}{\partial y} - \frac{\gamma}{2}(\frac{\bar{\omega}_{c,e}}{\omega_{c,e}})^2 \Big[f_3 \frac{\partial}{\partial x} + f_3'\Big] B_{x1} + \frac{\gamma}{2}(\frac{\bar{\omega}_{c,e}}{\omega_{c,e}})^2 k f_3 B_{y1} = \frac{1}{2d_e^2}(\frac{\bar{\omega}_{c,e}}{\omega_{c,e}})^3 k [f_6 \frac{\partial}{\partial x} + d_e^2 f_5\Big] u_{x1} + \frac{i}{2d_e^2}(\frac{\bar{\omega}_{c,e}}{\omega_{c,e}})^3 k^2 f_6 u_{y1} - \frac{1}{d_e^4}(\frac{\bar{\omega}_{c,e}}{\omega_{c,e}})^3 u_{z1} - \frac{1}{d_e^4}(\frac{\omega_{p,e}}{\omega_{c,e}})^2 k B_{x1} - \frac{1}{d_e^4} \times (\frac{\omega_{p,e}}{\omega_{c,e}})^2 \frac{\partial B_{y1}}{\partial x} + \frac{1}{d_e^4}\frac{\bar{\omega}_{c,e}\omega_{p,e}^2}{\omega_{c,e}^3} f' n_1, \tag{J.12}$$

With the continuity equation,

$$\gamma n_1 = -\frac{\partial}{\partial x} u_{x1} - ik u_{y1}, \tag{J.13}$$

the previous seven equations form an eigenvalue problem, where the eigenvalue is the growth rate γ, and the eigenvector is $\mathbf{V}_\gamma = [B_x, B_y, B_z, u_x, u_y, u_z, n]^T$. This eigenvalue problem can be

written as

$$\gamma^2\begin{bmatrix}\mathcal{I}&0&0&0&0&kd_e^2\mathcal{I}&0\\0&\mathcal{I}&0&0&0&\mathcal{S}_{22z}&0\\0&0&0&0&0&0&0\\0&0&0&d_e^4\mathcal{I}&0&0&0\\0&0&0&0&d_e^4\mathcal{I}&0&0\\0&0&0&0&0&d_e^4\mathcal{I}&0\\0&0&0&0&0&0&0\end{bmatrix}\begin{bmatrix}B_x\\B_y\\B_z\\u_x\\u_y\\u_z\\n\end{bmatrix}+\gamma\begin{bmatrix}\mathcal{M}_{11x}&\mathcal{M}_{11y}&0&\mathcal{S}_{11x}&0&\mathcal{S}_{11z}&0\\\mathcal{M}_{21x}&\mathcal{M}_{21y}&0&\mathcal{S}_{21x}&0&\mathcal{S}_{21z}&0\\0&0&\mathcal{I}&-kd_e^2\mathcal{I}&\mathcal{S}_{31y}&0&0\\0&\mathcal{M}_{41y}&0&\mathcal{S}_{41x}&\mathcal{S}_{41y}&\mathcal{S}_{41z}&0\\\mathcal{M}_{51x}&0&0&\mathcal{S}_{51x}&\mathcal{S}_{51y}&0&0\\\mathcal{M}_{61x}&\mathcal{M}_{61y}&0&\mathcal{S}_{61x}&0&\mathcal{S}_{61z}&0\\0&0&0&0&0&0&\mathcal{I}\end{bmatrix}$$
$$\times\begin{bmatrix}B_x\\B_y\\B_z\\u_x\\u_y\\u_z\\n\end{bmatrix}+\begin{bmatrix}0&0&0&\mathcal{S}_{10x}&\mathcal{S}_{10y}&0&0\\0&0&0&\mathcal{S}_{20x}&\mathcal{S}_{20y}&0&0\\\mathcal{M}_{30x}&0&0&\mathcal{S}_{30x}&\mathcal{S}_{30y}&\mathcal{S}_{30z}&\mathcal{N}_{30n}\\\mathcal{M}_{40x}&0&\mathcal{M}_{40z}&\mathcal{S}_{40x}&\mathcal{S}_{40y}&\mathcal{S}_{40z}&0\\\mathcal{M}_{50x}&0&\mathcal{M}_{50z}&\mathcal{S}_{50x}&\mathcal{S}_{50y}&\mathcal{S}_{50z}&0\\\mathcal{M}_{60x}&\mathcal{M}_{60y}&0&\mathcal{S}_{60x}&\mathcal{S}_{60y}&\mathcal{S}_{60z}&\mathcal{N}_{60n}\\0&0&0&\mathcal{S}_{70x}&\mathcal{S}_{70y}&0&0\end{bmatrix}\begin{bmatrix}B_x\\B_y\\B_z\\u_x\\u_y\\u_z\\n\end{bmatrix}=0, \tag{J.14}$$

where,

$$S_{11x}=k\frac{\bar{\omega}_{c,e}}{\omega_{c,e}}\Big[f-d_e^2f^{''}\Big],\quad S_{11z}=-\frac{i}{2}(\frac{\bar{\omega}_{c,e}}{\omega_{c,e}})^2k^2d_e^2\Big[\frac{\partial}{\partial x}-f^2\frac{\partial}{\partial x}-2ff^{'}\Big],\quad M_{11x}=-\frac{1}{2}(\frac{\bar{\omega}_{c,e}}{\omega_{c,e}})^2k\times$$
$$d_e^2\Big[f_3\frac{\partial}{\partial x}+f_3^{'}\Big],M_{11y}=-\frac{i}{2}(\frac{\bar{\omega}_{c,e}}{\omega_{c,e}})^2k^2d_e^2f_3,\quad S_{10x}=\frac{i}{2}(\frac{\bar{\omega}_{c,e}}{\omega_{c,e}})^3k^2\Big[f_6\frac{\partial}{\partial x}+d_e^2f_5\Big],\quad S_{10y}=\frac{i}{2}(\frac{\bar{\omega}_{c,e}}{\omega_{c,e}})^3$$
$$\times k^2\Big[f_6\frac{\partial}{\partial x}+d_e^2f_5\Big],S_{22z}=d_e^2\frac{\partial}{\partial x},\quad S_{21x}=(\frac{\bar{\omega}_{c,e}}{\omega_{c,e}})\Big[f\frac{\partial}{\partial x}-d_e^2f^{''}\frac{\partial}{\partial x}+f^{'}-d_e^2f^{'''}\Big],S_{21z}=-\frac{1}{2}\times$$
$$(\frac{\bar{\omega}_{c,e}}{\omega_{c,e}})^2k\Big[2ff^{'}\frac{\partial}{\partial x}+2f_3+2f^{'2}\Big],M_{21x}=-\frac{1}{2}(\frac{\bar{\omega}_{c,e}}{\omega_{c,e}})^2d_e^2\Big[f_3\frac{\partial^2}{\partial x^2}+2f_3^{'}\frac{\partial}{\partial x}+f_3^{''}\Big],\quad M_{21y}=\frac{1}{2}(\frac{\bar{\omega}_{c,e}}{\omega_{c,e}})^2$$
$$\times kd_e^2\Big[f_3\frac{\partial}{\partial x}+f_3^{'}\Big], \tag{J.15}$$

$$S_{20x}=-\frac{1}{2}(\frac{\bar{\omega}_{c,e}}{\omega_{c,e}})^3k\Big[f_6\frac{\partial^2}{\partial x^2}+(f_6^{'}+d_e^2f_5)\frac{\partial}{\partial x}+d_e^2f_5^{'}\Big],S_{20y}=-i\frac{1}{2}(\frac{\bar{\omega}_{c,e}}{\omega_{c,e}})^3k^2\Big[f_6\frac{\partial}{\partial x}+f_6^{'}\Big],$$
$$S_{31y}=-d_e^2\frac{\partial}{\partial x},S_{30x}=\Big\{\frac{\partial}{\partial x}+\frac{1}{2}(\frac{\bar{\omega}_{c,e}}{\omega_{c,e}})^2d_e^2\Big[\frac{f^2}{2}\frac{\partial^3}{\partial x^3}+2ff^{'}\frac{\partial^2}{\partial x^2}+(f_3+f^{'2})\frac{\partial}{\partial x}-ik^2f^2\frac{\partial}{\partial x}-2ik^2$$
$$\times ff^{'}+\frac{i}{2}k^2f^2\frac{\partial}{\partial x}\Big]\Big\},S_{30y}=-k\Big[1+\frac{1}{4}(\frac{\bar{\omega}_{c,e}}{\omega_{c,e}})^2d_e^2\Big(f^2\frac{\partial^2}{\partial x}-2f_3-2f^{'2}-k^2\frac{f^2}{2}\Big)\Big],N_{30n}=-(\frac{\bar{\omega}_{c,e}}{\omega_{c,e}})^2$$
$$\times kff^{'}\frac{\partial}{\partial y},S_{30z}=(\frac{\bar{\omega}_{c,e}}{\omega_{c,e}})kf,M_{30x}=(\frac{\bar{\omega}_{c,e}}{\omega_{c,e}})f^{''},\quad S_{41x}=\frac{d_e^4}{4}(\frac{\bar{\omega}_{c,e}}{\omega_{c,e}})^2kf^2\frac{\partial}{\partial x},S_{41y}=d_e^2\Big[1-\frac{i}{2}(\frac{\bar{\omega}_{c,e}}{\omega_{c,e}})^2$$
$$\times k^2d_e^2f^2\Big],\quad S_{41z}=-d_e^2(\frac{\bar{\omega}_{c,e}}{\omega_{c,e}})f,M_{41y}=d_e^2(\frac{\bar{\omega}_{c,e}}{\omega_{c,e}})f^{'},\quad S_{40x}=\Big[(\frac{\omega_{p,e}}{\omega_{c,e}})^2-\frac{d_e^2}{2}(\frac{\bar{\omega}_{c,e}}{\omega_{c,e}})^2\times$$
$$\Big(2f^2\frac{\partial^2}{\partial x^2}+4f^{'}f\frac{\partial}{\partial x}+f^{2'}\frac{\partial}{\partial x}+2f_3+2f^{'2}\Big)\Big], \tag{J.16}$$

$$S_{40y} = \frac{kd_e^2}{2}(\frac{\bar{\omega}_{c,e}}{\omega_{c,e}})^2\Big[2f^2\frac{\partial}{\partial x} + 4f^{'}f\Big], S_{40z} = -kd_e^2(\frac{\bar{\omega}_{c,e}}{\omega_{c,e}})^3\Big[f^3\frac{\partial}{\partial x} + 3f^{'}f^2\Big], M_{40x} = -d_e^2(\frac{\bar{\omega}_{c,e}}{\omega_{c,e}})^3\Big[f_1\frac{\partial}{\partial x}$$
$$+ f_1^{'}\Big], \quad M_{40z} = -k(\frac{\omega_{p,e}}{\omega_{c,e}})^2, \quad S_{51x} = -d_e^2\Big[1 + \frac{d_e^2}{2}(\frac{\bar{\omega}_{c,e}}{\omega_{c,e}})^2\Big(\frac{f^2}{2}\frac{\partial^2}{\partial x^2} + ff^{'}\frac{\partial}{\partial x} + if^2k^2\Big)\Big],$$
$$M_{51x} = -d_e^2(\frac{\bar{\omega}_{c,e}}{\omega_{c,e}})f^{'},$$

(J.17)

and

$$S_{51y} = -\frac{d_e^4}{2}(\frac{\bar{\omega}_{c,e}}{\omega_{c,e}})^2k\Big[\frac{f^2}{2}\frac{\partial}{\partial x} + ff^{'} - f^2\frac{\partial}{\partial x}\Big], \quad S_{50x} = \frac{d_e^2}{2}(\frac{\bar{\omega}_{c,e}}{\omega_{c,e}})^2k\Big[f^{2'} + 2f^2\frac{\partial}{\partial x}\Big], \quad S_{50z} = -id_e^2\times$$
$$(\frac{\bar{\omega}_{c,e}}{\omega_{c,e}})^3k^2f^3, S_{50y} = \Big[(\frac{\omega_{p,e}}{\omega_{c,e}})^2 + id_e^2(\frac{\bar{\omega}_{c,e}}{\omega_{c,e}})^2k^2f^2\Big], \quad M_{50x} = d_e^2(\frac{\bar{\omega}_{c,e}}{\omega_{c,e}})^3kf_1, \quad M_{50z} = -(\frac{\omega_{p,e}}{\omega_{c,e}})^2\frac{\partial}{\partial x},$$
$$S_{61x} = d_e^2(\frac{\bar{\omega}_{c,e}}{\omega_{c,e}})\Big[f - d_e^2f^{''}\Big], \quad S_{61z} = d_e^4(\frac{\bar{\omega}_{c,e}}{\omega_{c,e}})^2ff^{'}\frac{\partial}{\partial y}, \quad M_{61x} = -\frac{d_e^4}{2}(\frac{\bar{\omega}_{c,e}}{\omega_{c,e}})^2\Big[f_3\frac{\partial}{\partial x} + f_3^{'}\Big],$$
$$M_{61y} = \frac{d_e^4}{2}(\frac{\bar{\omega}_{c,e}}{\omega_{c,e}})^2kf_3, \quad S_{60x} = -\frac{d_e^2}{2}(\frac{\bar{\omega}_{c,e}}{\omega_{c,e}})^3k[f_6\frac{\partial}{\partial x} + d_e^2f_5\Big], \quad S_{60y} = -\frac{id_e^2}{2}(\frac{\bar{\omega}_{c,e}}{\omega_{c,e}})^3k^2f_6,$$
$$S_{60z} = (\frac{\bar{\omega}_{c,e}}{\omega_{c,e}})^3, \quad M_{60x} = (\frac{\omega_{p,e}}{\omega_{c,e}})^2k, \quad M_{60y} = (\frac{\omega_{p,e}}{\omega_{c,e}})^2\frac{\partial}{\partial x}, \quad N_{60n} = -\frac{\bar{\omega}_{c,e}\omega_{p,e}^2}{\omega_{c,e}^3}f^{'}, \quad S_{70x} = \frac{\partial}{\partial x},$$
$$S_{70y} = ik,$$

(J.18)

Bibliography

[1] J. Derouillat, A. Beck, F. Pérez, T. Vinci, M. Chiaramello, A. Grassi, M. Flé, G. Bouchard, I. Plotnikov, N. Aunai, and C. J. Dargent, "Smilei : A collaborative, open-source, multi-purpose particle-in-cell code for plasma simulation," *Computer Physics Communications*, vol. 222, pp. 351–373, 2018.

[2] M. Sarrat, A. Ghizzo, D. Del Sarto, and L. Serrat, "Parallel implementation of a relativistic semi-lagrangian vlasov–maxwell solver," *The European Physical Journal D*, vol. 71, 2017.

[3] A. Ghizzo, D. Del Sarto, and M. Sarrat, "Low- and high-frequency nature of oblique filamentation modes. i. linear theory," *Physics of Plasmas*, vol. 27, no. 7, p. 072103, 2020.

[4] F. Califano, D. Del Sarto, and F. Pegoraro, "Resonant evolution of the current filamentation (weibel) instability in the relativistic regime," in *In AIP Conference Proceedings*, 04 2006.

[5] F. Califano, D. Del Sarto, and F. Pegoraro, "Three-dimensional magnetic structures generated by the development of the filamentation (weibel) instability in the relativistic regime," *Phys. Rev. Lett.*, vol. 96, p. 105008, Mar 2006.

[6] R. J. Goldston and P. H. Rutherford, *Introduction to plasma physics*. Taylor and Francis, 1997.

[7] E. S. Weibel, "Spontaneously growing transverse waves in a plasma due to an anisotropic velocity distribution," *Phys. Rev. Lett.*, vol. 2, pp. 83–84, Feb 1959.

[8] B. D. Fried, "Mechanism for instability of transverse plasma waves," *The Physics of Fluids*, vol. 2, no. 3, pp. 337–337, 1959.

[9] S. von Goeler, W. Stodiek, and N. Sauthoff, "Studies of internal disruptions and $m = 1$ oscillations in tokamak discharges with soft—x-ray tecniques," *Phys. Rev. Lett.*, vol. 33, pp. 1201–1203, Nov 1974.

[10] V. D. Shafranov *Sov. Phys. Tech. Phys.*, vol. 15, 1970.

[11] D. J. Campbell, D. F. H. Start, J. A. Wesson, D. V. Bartlett, V. P. Bhatnagar, M. Bures, J. G. Cordey, G. A. Cottrell, P. A. Dupperex, A. W. Edwards, C. D. Challis, C. Gormezano, C. W. Gowers, R. S. Granetz, J. H. Hammen, T. Hellsten, J. Jacquinot, E. Lazzaro, P. J. Lomas, N. L. Cardozo, P. Mantica, J. A. Snipes, D. Stork, P. E. Stott, P. R. Thomas, E. Thompson, K. Thomsen, and G. Tonetti, "Stabilization of sawteeth with additional heating in the jet tokamak," *Phys. Rev. Lett.*, vol. 60, pp. 2148–2151, May 1988.

[12] J. A. Van Allen, G. H. Ludwig, E. C. Ray, and C. E. Mcilwain, "Observation of high intensity radiation by satellites 1958 alpha and gamma," *Journal of Jet Propulsion*, vol. 28, no. 9, pp. 588–592, 1958.

[13] P. J. Kellogg, "Van allen radiation of solar origin," *Nature*, vol. 183, 1959.

[14] J. Burch and J. F. Drake, "Reconnecting magnetic fields," *American Scientist*, vol. 97, no. 5, p. 392, 2009.

[15] NASA, "Sdo website."

[16] NASA, "Rhessi website."

[17] NASA, "X marks the spot: Sdo sees reconnection," 2013.

[18] W. Greiner, *Classical Electrodynamics*. Springer-Verlag New York, 1998.

[19] J. W. Dungey, *Cosmic Electrodynamics*. Cambrdige University Press, 1958.

[20] R. G. Giovanelli, "A theory of chromospheric flares," *Nature*, vol. 158, p. 81, 1946.

[21] R. G. Giovanelli, "Magnetic and electric phenomena in the sun's atmosphere associated with sunspots," *Monthly Notices of the Royal Astronomical Society*, vol. 107, pp. 338–355, 11 1947.

[22] R. G. Giovanelli, "Chromospheric flares," *mnras*, vol. 108, p. 163, Jan. 1948.

[23] S. W. H. Cowley, "Hoyle and the magnetosphere," *Astronomy and Geophysics*, vol. 57, pp. 1.12–1.12, 02 2016.

[24] D. Del Sarto, F. Pucci, A. Tenerani, and M. Velli, ""ideal" tearing and the transition to fast reconnection in the weakly collisional MHD and EMHD regimes," *J. Geophys. Res.-Space Phys.*, vol. 121, no. 3, pp. 1857–1873, 2016.

[25] F. Hoyle, *Some recent Researches in Solar Physics*. Cambridge (UK): Cambrdige University Press, 1949.

[26] J. W. Dungey, *Some Researches in Cosmic Magnetism*. PhD thesis, Cambridge University, Cambridge (UK), 1950.

[27] J. Dungey, "Lxxvi. conditions for the occurrence of electrical discharges in astrophysical systems," *The London, Edinburgh, and Dublin Philosophical Magazine and Journal of Science*, vol. 44, no. 354, pp. 725–738, 1953.

[28] J. W. Dungey, "Interplanetary magnetic field and the auroral zones," *Phys. Rev. Lett.*, vol. 6, pp. 47–48, Jan 1961.

[29] M. Lockwood, "Jim dungey, the open magnetosphere, and space weather," *Space Weather*, vol. 14, no. 6, pp. 380–383, 2016.

[30] P. J. Coleman, L. Davis, and C. P. Sonett, "Steady component of the interplanetary magnetic field: Pioneer v," *Phys. Rev. Lett.*, vol. 5, pp. 43–46, Jul 1960.

[31] P. A. SWEET, "Electromagnetic phenomena in cosmical physics," *IAU Symp. 6*, vol. 123, 1958.

[32] E. N. Parker, "The Solar-Flare Phenomenon and the Theory of Reconnection and Annihiliation of Magnetic Fields.," *apjs*, vol. 8, p. 177, July 1963.

[33] D. D. Schnack, *Lectures in Magnetohydrodynamics*. Springer-Verlag Berlin Heidelberg, 2009.

[34] V. M. Vasyliunas, "Theoretical models of magnetic field line merging," *Reviews of Geophysics*, vol. 13, no. 1, pp. 303–336, 1975.

[35] E. G. Zweibel and M. Yamada, "Magnetic reconnection in astrophysical and laboratory plasmas," *Annual Review of Astronomy and Astrophysics*, vol. 47, no. 1, pp. 291–332, 2009.

[36] M. Yamada, R. Kulsrud, and H. Ji, "Magnetic reconnection," *Rev. Mod. Phys.*, vol. 82, pp. 603–664, Mar 2010.

[37] M. Hesse and P. A. Cassak, "Magnetic reconnection in the space sciences: Past, present, and future," *Journal of Geophysical Research: Space Physics*, vol. 125, no. 2, p. e2018JA025935, 2020.

[38] N. F. Ness, "The geomagnetic tail," *Reviews of Geophysics*, vol. 7, no. 1-2, pp. 97–127, 1969.

[39] J. H. Piddington, "Geomagnetic storm theory," *Journal of Geophysical Research (1896-1977)*, vol. 65, no. 1, pp. 93–106, 1960.

[40] F. S. Johnson, "The gross character of the geomagnetic field in the solar wind," *Journal of Geophysical Research (1896-1977)*, vol. 65, no. 10, pp. 3049–3052, 1960.

[41] E. N. Parker, "Dynamics of the Interplanetary Gas and Magnetic Fields.," *apj*, vol. 128, p. 664, Nov. 1958.

[42] E. N. Parker, "Interaction of the solar wind with the geomagnetic field," *The Physics of Fluids*, vol. 1, no. 3, pp. 171–187, 1958.

[43] A. J. Dessler, "Length of magnetospheric tail," *Journal of Geophysical Research (1896-1977)*, vol. 69, no. 19, pp. 3913–3918, 1964.

[44] J. W. Dungey, "The length of the magnetospheric tail," *Journal of Geophysical Research (1896-1977)*, vol. 70, no. 7, pp. 1753–1753, 1965.

[45] J. W. Dungey, "The theory of the quiet magnetosphere," in *Solar-Terrestrial Physics* (N. W. S. King, J. W., ed.), p. 91, 1967.

[46] E. J. Smith, P. J. Coleman, D. L. Judge, and C. P. Sonett, "Characteristics of the extraterrestrial current system: Explorer vi and pioneer v," *Journal of Geophysical Research (1896-1977)*, vol. 65, no. 6, pp. 1858–1861, 1960.

[47] E. J. Smith, P. J. Coleman, D. L. Judge, and C. P. Sonett, "Characteristics of the extraterrestrial current system: Explorer vi and pioneer v," *Journal of Geophysical Research (1896-1977)*, vol. 65, no. 6, pp. 1858–1861, 1960.

[48] C. P. Sonett, E. J. Smith, D. L. Judge, and P. J. Coleman, "Current systems in the vestigial geomagnetic field: Explorer vi," *Phys. Rev. Lett.*, vol. 4, pp. 161–163, Feb 1960.

[49] J. P. Heppner, N. F. Ness, C. S. Scearce, and T. L. Skillman, "Explorer 10 magnetic field measurements," *Journal of Geophysical Research (1896-1977)*, vol. 68, no. 1, pp. 1–46, 1963.

[50] E. J. Smith, "A comparison of explorer vi and explorer x magnetometer data," *Journal of Geophysical Research (1896-1977)*, vol. 67, no. 5, pp. 2045–2049, 1962.

[51] J. W. Freeman Jr., "The morphology of the electron distribution in the outer radiation zone and near the magnetospheric boundary as observed by explorer 12," *Journal of Geophysical Research (1896-1977)*, vol. 69, no. 9, pp. 1691–1723, 1964.

[52] L. J. Cahill, "Inflation of the magnetosphere near 8 earth radii in the dark hemisphere.," 1966.

[53] J. Cahill, Laurence J., *Preliminary Results of Magnetic Field Measurements in the Tail of the Geomagnetic Cavity*, vol. 3, p. 227. 1965.

[54] S. Singer, "The vela satellite program for detection of high-altitude nuclear detonations," *Proceedings of the IEEE*, vol. 53, no. 12, pp. 1935–1948, 1965.

[55] A. Dessler and R. Juday, "Configuration of auroral radiation in space," *Planetary and Space Science*, vol. 13, no. 1, pp. 63 – 72, 1965.

[56] W. I. Axford, "Magnetic storm effects associated with the tail of the magnetosphere," *ssr*, vol. 7, no. 2-3, pp. 149–157, 1967.

[57] H. Furth, J. Killeen, and M. Rosenbluth, "Finite-resistivity instabilities of a sheet pinch," *Phys. Fluids*, vol. 6, no. 4, pp. 459–484, 1963.

[58] M. A. Cross and G. Van Hoven, "Magnetic and gravitational energy release by resistive instabilities," *Phys. Rev. A*, vol. 4, p. 2347, 1971.

[59] G. Van Hoven and M. A. Cross, "Resistive instability of a sheet pinch," *Phys. Fluids*, vol. 14, p. 1141, 1971.

[60] G. Van Hoven and M. A. Cross, "Inertial magnetic field reconnection and magnetospheric substorms," *Phys. Rev. Lett.*, vol. 30, p. 641, 1973.

[61] G. Van Hoven and M. A. Cross, "Energy release by magnetic tearing: the nonlinear limit," *Phys. Rev. A*, vol. 7, p. 1347, 1973.

[62] H. Furth., "Hydromagnetic instabilities due to finite resistivity," in *Propagation and Instabilities in Plasmas – Seventh Lockheed symposium on magnetohydrodynamics* (Walter I. Futtermann , ed.), pp. 87–102 , Stanford University Press, 1963.

[63] B. Coppi, ""inertial" instabilities in plasmas," *Phys. Lett.*, vol. 11, no. 3, pp. 226–228, 1964.

[64] B. Coppi, "Addendum on inertial interchange modes," *Phys. Lett.*, vol. 12, pp. 213–214, 1964.

[65] G. Laval, R. Pellat, and M. Vuillemin, "Instabilites electromagnetiques des plasmas sans collisions," vol. 1, no. 259, 1966.

[66] B. Coppi, G. Laval, and R. Pellat, "Dynamics of the geomagnetic tail," *Phys. Rev. Lett.*, vol. 16, p. 1207, 1966.

[67] J. Drake and Y. Lee, "Kinetic theory of tearing instabilities," *Phys. Fluids B*, vol. 20, p. 1341, 1977.

[68] W. Daughton, "The unstable eigenmodes of a neutral sheet," *Physics of Plasmas*, vol. 6, no. 4, pp. 1329–1343, 1999.

[69] H. E. Petschek, *Magnetic Field Annihilation*, vol. 50, p. 425. 1964.

[70] M. Ugai and T. Tsuda, "Magnetic field-line reconnexion by localized enhancement of resistivity: Part 1. evolution in a compressible mhd fluid," *Journal of Plasma Physics*, vol. 17, no. 3, p. 337–356, 1977.

[71] T. Tsuda and M. Ugai, "Magnetic field-line reconnexion by localized enhancement of resistivity. part 2. quasi-steady process," *Journal of Plasma Physics*, vol. 18, no. 3, p. 451–471, 1977.

[72] T. Sato and T. Hayashi, "Externally driven magnetic reconnection and a powerful magnetic energy converter," *The Physics of Fluids*, vol. 22, no. 6, pp. 1189–1202, 1979.

[73] M. Scholer, "Undriven magnetic reconnection in an isolated current sheet," *Journal of Geophysical Research: Space Physics*, vol. 94, no. A7, pp. 8805–8812, 1989.

[74] D. Biskamp, "Magnetic reconnection via current sheets," *The Physics of Fluids*, vol. 29, no. 5, pp. 1520–1531, 1986.

[75] D. I. Pontin, "Theory of magnetic reconnection in solar and astrophysical plasmas," *Philosophical Transactions of the Royal Society A: Mathematical, Physical and Engineering Sciences*, vol. 370, no. 1970, pp. 3169–3192, 2012.

[76] H. R. Strauss, "Dynamics of high β tokamaks," *The Physics of Fluids*, vol. 20, no. 8, pp. 1354–1360, 1977.

[77] H. R. Strauss, D. A. Monticello, M. N. Rosenbluth, and R. B. White, "Nonlinear helical perturbations of a tokamak," *The Physics of Fluids*, vol. 20, no. 3, pp. 390–395, 1977.

[78] M. N. Rosenbluth, D. A. Monticello, H. R. Strauss, and R. B. White, "Numerical studies of nonlinear evolution of kink modes in tokamaks," *The Physics of Fluids*, vol. 19, no. 12, pp. 1987–1996, 1976.

[79] B. Kadomtsev and O. P. Pogutse, "Nonlinear helical perturbations of a tokamak," *Sov. Phys*, vol. 38, p. 283, 1973.

[80] F. Pegoraro and T. J. Schep, "Low-frequency modes with high toroidal mode numbers: A general formulation," *Phys. Fluids*, vol. 24, no. 4, p. 478, 1981.

[81] F. Pegoraro and T. Schep, "Theory of resistive modes in the ballooning representation," *Plasma Phys. Control. Fusion*, vol. 28, no. 4, pp. 647–667, 1986.

[82] F. Pegoraro, F. Porcelli, and T. Schep, "Internal kink modes in the ion-kinetic regime," *Phys. Fluids B: Plasma Phys.*, vol. 1, no. 2, pp. 364–374, 1989.

[83] T. J. Schep, F. Pegoraro, and B. N. Kuvshinov, "Generalized two-fluid theory of nonlinear magnetic structures," *Physics of Plasmas*, vol. 1, no. 9, pp. 2843–2852, 1994.

[84] R. D. Hazeltine, "Reduced magnetohydrodynamics and the hasegawa–mima equation," *The Physics of Fluids*, vol. 26, no. 11, pp. 3242–3245, 1983.

[85] F. Porcelli, "Collisionless m=1 tearing mode," *Phys. Rev. Lett.*, vol. 66, p. 425, 1991.

[86] B. U. Ö. Sonnerup, *Magnetic field reconnection*, vol. 3, pp. 45–108. 1979.

[87] G. A. Askaryan, S. V. Bulanov, F. Pegoraro, and A. M. Pukhov, "Nonlinear evolution of ultrastrong laser pulses in a plasma. New phenomena of magnetic interaction between strong electromagnetic beams," *Plasma Physics Reports*, vol. 21, pp. 835–846, Oct. 1995.

[88] S. V. Basova, S. A. Varentsova, A. V. Gordeev, A. V. Gulin, and V. Y. Shukaev *Sov. J. Plasma Phys.*, vol. 17, p. 362, 1991.

[89] S. V. Bulanov, F. Pegoraro, and A. S. Sakharov, "Magnetic reconnection in electron magnetohydrodynamics," *Physics of Fluids B: Plasma Physics*, vol. 4, no. 8, pp. 2499–2508, 1992.

[90] K. Avinash, S. V. Bulanov, T. Esirkepov, P. Kaw, F. Pegoraro, P. V. Sasorov, and A. Sen, "Forced magnetic field line reconnection in electron magnetohydrodynamics," *Physics of Plasmas*, vol. 5, no. 8, pp. 2849–2860, 1998.

[91] A. Kingsep, K. Chukbar, and V. Yan'kov, "Electron magnetohydrodynamics," *Reviews of Plasma Physics, edited by Kadomtsev (Consultants Bureau, New York, 1990)*, vol. 16, p. 243, 1990.

[92] M. Erba and F. Pegoraro, "Long-wavelength limit of the EMHD tearing mode," *Nuovo Cimento D Serie*, vol. 15, pp. 739–752, May 1993.

[93] N. Attico, F. Califano, and F. Pegoraro, "Fast collisionless reconnection in the whistler frequency range," *Physics of Plasmas*, vol. 7, no. 6, pp. 2381–2387, 2000.

[94] M. E. Mandt, R. E. Denton, and J. F. Drake, "Transition to whistler mediated magnetic reconnection," *Geophysical Research Letters*, vol. 21, no. 1, pp. 73–76, 1994.

[95] D. Biskamp, "Magnetic Reconnection in Plasmas," *apss*, vol. 242, pp. 165–207, Mar. 1996.

[96] J. Birn, J. Drake, M. Shay, B. Rogers, R. Denton, M. Hesse, M. Kuznetsova, Z. Ma, A. Bhattacharjee, A. Otto, and P. Pritchett, "Geospace environmental modeling (gem) magnetic reconnection challenge," *Journal of Geophysical Research*, vol. 106, pp. 3715–3720, 03 2001.

[97] W. H. Matthaeus and D. Montgomery, "Selective decay hypothesis at high mechanical and magnetic reynolds numbers*," *Annals of the New York Academy of Sciences*, vol. 357, no. 1, pp. 203–222, 1980.

[98] A. Lazarian, L. Vlahos, G. Kowal, H. Yan, A. Beresnyak, and E. de Gouveia Dal Pino, "Turbulence, magnetic reconnection in turbulent fluids and energetic particle acceleration," *Space Science Reviews*, vol. 173, 10 2012.

[99] W. Daughton, V. Roytershteyn, H. Karimabadi, L. Yin, B. J. Albright, B. Bergen, and K. J. Bowers, "Role of electron physics in the development of turbulent magnetic reconnectioncfi in collisionless plasmas," *Nature*, vol. 7, 2011.

[100] S. Servidio, W. Matthaeus, M. Shay, P. Cassak, and P. Dmitruk, "Magnetic reconnection in two-dimensional magnetohydrodynamic turbulence," *Physical review letters*, vol. 102, p. 115003, 04 2009.

[101] S. Servidio, A. Greco, W. Matthaeus, K. Osman, and P. Dmitruk, "Statistical association of discontinuities and reconnection in magnetohydrodynamic turbulence," *Journal of Geophysical Research*, vol. 116, 09 2011.

[102] W. Matthaeus and M. Velli, "Who needs turbulence?," *Space Science Reviews*, vol. 160, pp. 145–168, 10 2011.

[103] A. Schekochihin, "Mhd turbulence: A biased review," *arXiv: Plasma Physics*, 2020.

[104] H. Alfven, *Cosmical electrodynamics*. Oxford, Clarendon Press, 1d ed., 1950.

[105] S. Lundquist, "On the stability of magneto-hydrostatic fields," *Phys. Rev.*, vol. 83, pp. 307–311, Jul 1951.

[106] W. A. Newcomb, "Motion of magnetic lines of force," *Annals of Physics*, vol. 3, no. 4, pp. 347 – 385, 1958.

[107] F. Pegoraro, D. Borgogno, F. Califano, D. Del Sarto, E. Echkina, D. Grasso, T. Liseikina, and F. Porcelli, "Developments in the theory of collisionless reconnection in magnetic configurations with a strong guide field," *Nonlinear Processes in Geophysics*, vol. 11, no. 5/6, pp. 567–577, 2004.

[108] D. DEL SARTO, F. CALIFANO, and F. PEGORARO, "Electron parallel compressibility in the nonlinear development of two-dimensional collisionless magnetohydrodynamic reconnection," *Modern Physics Letters B*, vol. 20, no. 16, pp. 931–961, 2006.

[109] K. Krienes, "C. truesdell, the kinematics of vorticity. (indiana university publications science seres nr. 14.) xvii + 232 s. bloomington 1954. indiana university press. preis geh. 6,— s," *ZAMM - Journal of Applied Mathematics and Mechanics / Zeitschrift für Angewandte Mathematik und Mechanik*, vol. 37, no. 5-6, pp. 239–239, 1957.

[110] J. B. Taylor, "Relaxation of toroidal plasma and generation of reverse magnetic fields," *Phys. Rev. Lett.*, vol. 33, pp. 1139–1141, Nov 1974.

[111] J. B. Taylor, "Relaxation and magnetic reconnection in plasmas," *Rev. Mod. Phys.*, vol. 58, pp. 741–763, Jul 1986.

[112] W. M. Elsasser, "Hydromagnetic dynamo theory," *Rev. Mod. Phys.*, vol. 28, pp. 135–163, Apr 1956.

[113] L. Woltjer, "A theorem on force-free magnetic fields," *Proceedings of the National Academy of Sciences*, vol. 44, no. 6, pp. 489–491, 1958.

[114] H. K. Moffatt, "The degree of knottedness of tangled vortex lines," *Journal of Fluid Mechanics*, vol. 35, no. 1, p. 117–129, 1969.

[115] K. Moffatt, *The Generation of Magnetic Fields in Electrically Conducting Fluids.* 01 1978.

[116] H. K. Moffatt, "Magnetostatic equilibria and analogous euler flows of arbitrarily complex topology. part 1. fundamentals," *Journal of Fluid Mechanics*, vol. 159, p. 359–378, 1985.

[117] C. Mayer, *Topological link invariants of magnetic fields.* PhD thesis, 06 2003.

[118] C. F. Gauss, *Werke*, vol. 5 of *Cambridge Library Collection - Mathematics.* Cambridge University Press, 2011.

[119] P. Tait, *On knots.* Cambridge University Press, 1898.

[120] C. Gauss, "Allgemeine theorie des erdmagnetismus,"

[121] D. Deturck and H. Gluck, "The gauss linking integral on the 3-sphere and in hyperbolic 3-space," 06 2004.

[122] R. L. RICCA and B. NIPOTI, "Gauss' linking number revisited," *Journal of Knot Theory and Its Ramifications*, vol. 20, no. 10, pp. 1325–1343, 2011.

[123] J. C. Maxwell, *A Treatise on Electricity and Magnetism*, vol. 2 of *Cambridge Library Collection - Physical Sciences.* Cambridge University Press, 2010.

[124] M. A. Berger, "Introduction to magnetic helicity," *Plasma Physics and Controlled Fusion*, vol. 41, pp. B167–B175, dec 1999.

[125] V. Arnold, "Proc. summer school in differential equations at dilijan, armenian ssr," 1974. English translation: 1986 Sel. Math. Sov.5,327–45.

[126] V. Arnold and B. Khesin, "Topological methods in hydrodynamics," vol. 24, pp. 145–166, 11 2003.

[127] M. A. Berger and G. B. Field, "The topological properties of magnetic helicity," *Journal of Fluid Mechanics*, vol. 147, p. 133–148, 1984.

[128] T. H. Jensen and M. S. Chu, "Current drive and helicity injection," *The Physics of Fluids*, vol. 27, no. 12, pp. 2881–2885, 1984.

[129] J. Finn and Antonsen, "Magnetic helicity: What is it and what is it good for?," *Comments Plasma Phys. Controlled Fusion*, vol. 9, p. 111, 12 1984.

[130] M. A. Berger, "Rigorous new limits on magnetic helicity dissipation in the solar corona," *Geophysical & Astrophysical Fluid Dynamics*, vol. 30, no. 1-2, pp. 79–104, 1984.

[131] J. H. C. Whitehead, *Knots and Links.* London: Pergamon Press, 1976.

[132] L. Kauffman, *Knots and Physics.* World Scientific, 1991.

[133] H. BRUNN, "Uber verkettung," *S.-B.Math.-Phys.Kl.Bayer Akad.Wiss.*, vol. 22, pp. 77–99, 1892.

[134] D. Rolfsen, *Knots and Links.* American Mathematical Societys, 2003.

[135] A. Ruzmaikin and P. Akhmetiev, "Topological invariants of magnetic fields, and the effect of reconnections," *Physics of Plasmas*, vol. 1, no. 2, pp. 331–336, 1994.

[136] E. N. Parker, "Sweet's mechanism for merging magnetic fields in conducting fluids," *Journal of Geophysical Research (1896-1977)*, vol. 62, no. 4, pp. 509–520, 1957.

[137] R. L. Moore, A. C. Sterling, H. S. Hudson, and J. R. Lemen, "Onset of the magnetic explosion in solar flares and coronal mass ejections," *The Astrophysical Journal*, vol. 552, pp. 833–848, may 2001.

[138] F. Ellerman, "Solar hydrogen "bombs"," *apj*, vol. 46, p. 298, Nov. 1917.

[139] A. Reid, M. Mathioudakis, J. G. Doyle, E. Scullion, C. J. Nelson, V. Henriques, and T. Ray, "MAGNETIC FLUX CANCELLATION IN ELLERMAN BOMBS," *The Astrophysical Journal*, vol. 823, p. 110, may 2016.

[140] E. N. Parker, *Cosmical Magnetic Fields : Their Origin and Their Activity*. Oxford University Press, 01 1979.

[141] R. M. Kulsrud, "Magnetic reconnection in a magnetohydrodynamic plasma," *Physics of Plasmas*, vol. 5, no. 5, pp. 1599–1606, 1998.

[142] E. R. Priest, "Current sheet models of solar flares," *Solar Phys.*, vol. 47, pp. 41–75, 1976.

[143] D. Biskamp, E. Schwarz, and J. F. Drake, "Two-dimensional electron magnetohydrodynamic turbulence," *Phys. Rev. Lett.*, vol. 76, pp. 1264–1267, Feb 1996.

[144] W. H. Matthaeus and S. L. Lamkin, "Turbulent magnetic reconnection," *The Physics of Fluids*, vol. 29, no. 8, pp. 2513–2534, 1986.

[145] S. C. Jardin, "presentation at cemm planning meeting, general atomics," 2002.

[146] D. Schnack, "The internal kink mode and giant sawteeth in tokamaks," 2012.

[147] M. Yamada, "Review of controlled laboratory experiments on physics of magnetic reconnection," *Journal of Geophysical Research: Space Physics*, vol. 104, no. A7, pp. 14529–14541, 1999.

[148] H. P. Furth, "Nonideal magnetohydrodynamic instabilities and toroidal magnetic confinement," *The Physics of Fluids*, vol. 28, no. 6, pp. 1595–1611, 1985.

[149] J. F. Drake and T. M. Antonsen, "Nonlinear reduced fluid equations for toroidal plasmas," *The Physics of Fluids*, vol. 27, no. 4, pp. 898–908, 1984.

[150] G. Ara, B. Basu, B. Coppi, G. Laval, M. Rosenbluth, and B. Waddell, "Magnetic reconnection and m = 1 oscillations in current carrying plasmas," *Annals of Physics*, vol. 112, no. 2, pp. 443–476, 1978.

[151] B. Coppi, R. Galvao, R. Pellat, M. Rosenbluth, and P. Rutherford, "Resistive internal kink modes," *Fizika Plazmy*, vol. 2, pp. 961–966, 1976.

[152] M. Ottaviani and F. Porcelli, "Nonlinear collisionless magnetic reconnection," *Phys. Rev. Lett.*, vol. 71, p. 3802, 1993.

[153] H. Betar, D. Del Sarto, M. Ottaviani, and A. Ghizzo, "Multiparametric study of tearing modes in thin current sheets," *Physics of Plasmas*, vol. 27, no. 10, p. 102106, 2020.

[154] C. A. Bender and S. A. Orszag, *Advanced Mathematical Methods for Scientists and Engineers*. McGraw-Hill., 1978.

[155] D. Del Sarto, M. Ottaviani, F. Pucci, A. Tenerani, and M. Velli, "Spontaneous magnetic reconnection of thin current sheets," in *21e Rencontre du Non Linéaire*, (Paris, France), p. 13, 2018.

[156] E. G. Harris, "On a plasma sheath separating regions of oppositely directed magnetic field," *Il Nuovo Cimento*, vol. 23, no. 1, pp. 115–121, 1962.

[157] M. Velli and A. W. Hood, "Resistive tearing in line-tied magnetic fields: slab geometry," *Solar Phys.*, vol. 119, pp. 107–124, 1988.

[158] L. Comisso, D. Grasso, F. L. Waelbroeck, and D. Borgogno, "Gyro-induced acceleration of magnetic reconnection," *Phys. Plasmas*, vol. 20, no. 9, p. 092118, 2013.

[159] A. Bhattacharjee, Y.-M. Huang, H. Yang, and B. Rogers, "Fast reconnection in high-lundquist-number plasmas due to the plasmoid instability," *Physics of Plasmas*, vol. 16, no. 11, p. 112102, 2009.

[160] D. Del Sarto and M. Ottaviani, "Secondary fast reconnecting instability in the sawtooth crash," *Physics of Plasmas*, vol. 24, no. 1, p. 012102, 2017.

[161] F. Pucci and M. Velli, "RECONNECTION OF QUASI-SINGULAR CURRENT SHEETS: THE "IDEAL" TEARING MODE," *The Astrophysical Journal*, vol. 780, p. L19, dec 2013.

[162] T. Tajima and K. Shibata, *Plasma Astrophysics*. Addison-Wesley, 1997.

[163] N. Loureiro, A. Schekochihin, and S. Cowley, "Instability of current sheets and formation of plasmoid chains," *Phys. Plasmas*, vol. 14, p. 100703, 2007.

[164] F. Pucci, M. Velli, A. Tenerani, and D. Del Sarto, "Onset of fast "ideal" tearing in thin current sheets: Dependence on the equilibrium current profile," *Phys. Plasmas*, vol. 25, no. 3, p. 032113, 2018.

[165] H. Ji and W. Daughton, "Phase diagram for magnetic reconnection in heliophysical, astrophysical, and laboratory plasmas," *Physics of Plasmas*, vol. 18, no. 11, p. 111207, 2011.

[166] Y. Klimontovich, *The Statistical Theory of Non-equilibrium Processes in a Plasma*. The MIT Press, Cambridge, 1967.

[167] N. Krall and A. Trivelpiece, *Principle of Plasma Physics*. McGraw-Hill, 1973.

[168] D. G. Swanson, *Elementary Space Plasma Physics*. Chapman and Hall/CRC, 2008.

[169] L.-H. Lyu, *Elementary Space Plasma Physics*. Airiti Press, 2010.

[170] R. Balescu, *Transport Processes in Plasmas: Classical transport*. North-Holland, 1988.

[171] N. N. Bogolyubov, *Problems of a Dynamical Theory in Statistical Physics*. Moscow, 1946.

[172] M. Born and H. Green, *A General Kinetic Theory of Liquids*. Cambridge University Press, England, 1949.

[173] J. G. Kirkwood, "The statistical mechanical theory of transport processes i. general theory," *The Journal of Chemical Physics*, vol. 14, no. 3, pp. 180–201, 1946.

[174] J. G. Kirkwood, "The statistical mechanical theory of transport processes ii. transport in gases," *The Journal of Chemical Physics*, vol. 15, no. 1, pp. 72–76, 1947.

[175] J. Yvon, *La theorie statistique des fluides et lequation detat*. Hermann and Cie, Paris, 1935.

[176] J. Bittencourt, *Fndamentals of Plasma Physics*. Springer-Verlag, New York, 3d ed., 2004.

[177] P. Bertrand, D. Del Sarto, and A. Ghizzo, *The Vlasov Equation 1: History and General Properties*. wiley, 2019.

[178] S. Chapman and T. G. Cowling, *The Mathematical Theory of Non-Uniform Gases*. Cambridge University Press, Cambridge, 2 ed., 1952.

[179] K. Huang, *Statistical Mechanics*. John Wiley & Sons, 2 ed., 1987.

[180] H. Strauss, "Nonlinear, three-dimensional magnetohydrodynamics of noncircular tokamaks," *Phys. Rev.*, vol. 19, p. 134, 1976.

[181] S. Braginskii, "Transport processes in plasma," *Reviews of Plasma Physics*, vol. 1, p. 205, 1965.

[182] M. Sarrat, D. D. Sarto, and A. Ghizzo, "Fluid description of weibel-type instabilities via full pressure tensor dynamics," *EPL (Europhysics Letters)*, vol. 115, p. 45001, aug 2016.

[183] M. M. Kuznetsova, M. Hesse, and D. Winske, "Collisionless reconnection supported by nongyrotropic pressure effects in hybrid and particle simulations," *Journal of Geophysical Research: Space Physics*, vol. 106, no. A3, pp. 3799–3810, 2001.

[184] L. Yin, D. Winske, S. P. Gary, and J. Birn, "Hybrid and hall-mhd simulations of collisionless reconnection: Dynamics of the electron pressure tensor," *Journal of Geophysical Research: Space Physics*, vol. 106, no. A6, pp. 10761–10775, 2001.

[185] G. F. Chew, M. L. Goldberger, and F. E. Low, "The boltzmann equation an d the one-fluid hydromagnetic equations in the absence of particle collisions," *Proceedings of the Royal Society of London. Series A. Mathematical and Physical Sciences*, vol. 236, no. 1024, pp. 112–118, 1956.

[186] K. V. Roberts and J. B. Taylor, "Magnetohydrodynamic equations for finite larmor radius," *Phys. Rev. Lett.*, vol. 8, pp. 197–198, Mar 1962.

[187] M. N. Rosenbluth, N. A. Krall, and N. Rostoker, "Finite larmor radius stabilization of "weakly" unstable confined plasmas," *Nuclear Fusion, Suppl.*, 1 1962.

[188] M. N. Rosenbluth and A. Simon, "Finite larmor radius equations with nonuniform electric fields and velocities," *The Physics of Fluids*, vol. 8, no. 7, pp. 1300–1322, 1965.

[189] R. K. Chhajlani and S. C. Bhand, "Derivation of cgl theory with finite larmor radius corrections," *Journal of Plasma Physics*, vol. 23, no. 2, p. 205–208, 1980.

[190] D. Del Sarto and F. Pegoraro, "Violation of the gyrotropic pressure closure due to a velocity shear in a magnetised plasma," 03 2018.

[191] H. Barnard, *Modelling of Anisotropic Pressure Tensor Dynamics in a Magnetically Confined Plasma.* PhD thesis, Universitee de Lorraine, 2013.

[192] A. M. Lyapunov, "The general problem of the stability of motion," *International Journal of Control*, vol. 55, no. 3, pp. 531–534, 1992.

[193] J. Sylvester, "Sur l'equations en matrices," *C. R. Acad. Sci. Paris*, vol. 99, no. 2, pp. 67–71, 115–116, 1884.

[194] F. M. White, *Viscous Fluid Flow.* McGraw-Hill, third ed., 2005.

[195] K. Kundu, I. Cohen, and D. Dowling, *Fluid Mechanics.* Academic Press, sixth ed., 2016.

[196] K. Huang, *Statistical Mechanics.* Wiley, 1987.

[197] W. P. Graebel, *Advanced Fluid Mechanics.* Academic Press, 2007.

[198] F. M. White, *Fluid Mechanics.* McGraw Hill, seventh ed., 2011.

[199] D. S. Chandrasekharaiah and L. Debnath, *Continuum Mechanics.* Academic Press, 1994.

[200] R. Aris, *Vectors Tensors and the Basics Equations of Fluid Mechanics.* Dover, 1989.

[201] G. Stokes, "On the theories of the internal frictions in motion, and of the equilibrium and motion of elastic solids," *Trans. Camb. Philos. Soc*, vol. 8, pp. 287–319, 1845.

[202] A. Dukhin and P. J. Goetz, "Bulk viscosity and compressibility measurement using acoustic spectroscopy," *J. Chem. Phys.*, vol. 130, p. 124519, 2009.

[203] G. Billet, V. Giovangigli, and G. de Gassowski, "Impact of volume viscosity on a shock–hydrogen-bubble interaction," *Combustion Theory and Modelling*, vol. 12, no. 2, pp. 221–248, 2008.

[204] C. Truesdell, "On the viscosity of fluids according to the kinetic theory," *Zeitschrift für Physik.*, vol. 131, p. 273–289, 1952.

[205] M. V. Papalexandris, "On the applicability of stokes' hypothesis to low-mach-number flows," *Continuum Mechanics and Thermodynamics.*, pp. 1432–0959, 1952.

[206] G. Buresti, "A note on stokes hypothesis," *Acta Mechanica*, vol. 226, p. 3555–3559, 2015.

[207] J. P. Freidberg, *Plasma Physics and Fusion Energy.* Cambridge University Press, 2007.

[208] J. P. Freidberg, *Ideal MHD.* Cambridge University Press, 2014.

[209] J. O. Hirschfelder, C. F. Curtiss, and R. B. Bird, *The Molecular Theory of Gases and Liquids.* John Wiley and Sons, Chapman and Hall Ltd, 1954.

[210] W. Marshall, "The kinetic theory of an ionized gas i," tech. rep., UK Atomic Energy Authority, 1957.

[211] W. Marshall, "The kinetic theory of an ionized gas ii," tech. rep., UK Atomic Energy Authority, 1957.

[212] R. Balescu, *Transport Processes in Plasmas.* North-Holland, Amsterdam, 1988.

[213] R. Treumann, C. Jaroschek, R. Nakamura, A. Runov, and M. Scholer, "The role of the hall effect in collisionless magnetic reconnection," *Advances in Space Research*, vol. 38, no. 1, pp. 101 – 111, 2006. Dynamical Processes in Critical Regions of the Heliosphere.

[214] B. V. Somov, *Plasma Astrophysics, Part I: Fundamentals and Practice.* Springer, New York, NY, 2006.

[215] B. V. Somov, *Plasma Astrophysics, Part II: Magnetic Reconnection.* Springer, New York, NY, 2013.

[216] K. Yee, "Numerical solution of initial boundary value problems involving maxwell's equations in isotropic media," *IEEE Transactions on Antennas and Propagation*, vol. 14, no. 3, pp. 302–307, 1966.

[217] U. S. Inan and R. A. Marshall, *Numerical Electromagnetics: The FDTD Method.* Cambridge University Press, 2011.

[218] S. Salon and M. Chari, *Numerical Methods in Electromagnetism.* Academic Press, 2000.

[219] J. P. Boris, "Relativistic plasma simulation—optimization of a hybrid code„" in *4th Conference on Numerical Simulation of Plasmas*, pp. 3–67, 1970.

[220] C. K. Birdsall and A. B. Langdon, *Principle of Plasma Physics.* McGraw-Hill, 1985.

[221] D. Kopriva, *Implementing Spectral Methods for Partial Differential Equations.* Springer Netherlands, 2009.

[222] L. N. Trefethen, *Spectral Methods in MATLAB.* Oxford, 2000.

[223] Y. Saad, *Iterative Methods for Sparse Linear Systems.* Oxford, 2003.

[224] P. Wesseling, *An Introduction to Multigrid Methods.* John Wiley, 1992.

[225] W. Hackbusch, *Multi-Grid Methods and Applications.* Springer-Verlag Berlin Heidelberg, 1992.

[226] R. Courant, K. Friedrichs, and H. Lewy, "Uber die partiellen differenzengleichungen der mathematischen physik," *Mathematische Annale*, vol. 100, p. 32–74, 1928.

[227] C. Runge, "Ueber die numerische auflösung von differentialgleichungen," *Mathematische Annalen*, vol. 46, p. 167–178, 1895.

[228] M. Kutta, *Beitrag zur naherungsweisen Integration totaler Differentialgleichungen.* PhD thesis, Technische Hochschule of Munich, 1901.

[229] S. A. Hirstoaga, *Design and performant implementation of numerical methods for multiscale problems in plasma physics.* Habilitation à diriger des recherches, Université de Strasbourg, IRMA UMR 7501, Apr. 2019.

[230] R. Fitzpatrick, *Computational Physics.* CreateSpace Independent Publishing Platform, 2015.

[231] F. Harlow, "A machine calculation method for hydrodynamic problems," tech. rep., Los Alamos Scientific Laboratory report LAMS, 1956.

[232] J. Dawson, "Particle simulation of plasmas," *Reviews of Modern Physics*, vol. 55, p. 403–447, 1983.

[233] A. Ghizzo, P. Bertrand, M. Shoucri, T. Johnston, E. Fualkow, and M. Feix, "A vlasov code for the numerical simulation of stimulated raman scattering," *Journal of Computational Physics*, vol. 90, no. 2, pp. 431 – 457, 1990.

[234] A. Ghizzo, P. Bertrand, M. L. Begue, T. W. Johnston, and M. Shoucri, "A hilbert-vlasov code for the study of high-frequency plasma beatwave accelerator," *IEEE Transactions on Plasma Science*, vol. 24, no. 2, pp. 370–378, 1996.

[235] E. Sonnendrücker, J. Roche, P. Bertrand, and A. Ghizzo, "The semi-lagrangian method for the numerical resolution of the vlasov equation," *Journal of Computational Physics*, vol. 149, no. 2, pp. 201 – 220, 1999.

[236] A. Ghizzo, B. Izrar, P. Bertrand, M. Feix, E. Fijalkow, and M. Shoucri, "Bgk structures as quasi-particles," *Physics Letters A*, vol. 120, no. 4, pp. 191 – 195, 1987.

[237] A. Ghizzo, B. Izrar, P. Bertrand, E. Fijalkow, M. R. Feix, and M. Shoucri, "Stability of bernstein–greene–kruskal plasma equilibria. numerical experiments over a long time," *The Physics of Fluids*, vol. 31, no. 1, pp. 72–82, 1988.

[238] J. R. Bates and A. McDonald, "Multiply-upstream, semi-lagrangian advective schemes: Analysis and application to a multi-level primitive equation model," *Monthly Weather Review*, vol. 110, no. 12, pp. 1831–1842, 1982.

[239] A. Staniforth and J. Cote, "Semi-lagrangian integration schemes for atmospheric models - a review," *Monthly Weather Review*, vol. 119, 9 1991.

[240] R. FJØRTOFT, "On a numerical method of integrating the barotropic vorticity equation," *Tellus*, vol. 4, no. 3, pp. 179–194, 1952.

[241] P. Welander, "Studies on the general development of motion in a two-dimensional, ideal fluid," *Tellus*, vol. 7, no. 2, pp. 141–156, 1955.

[242] A. Wien-Nielsen, "On the application of trajectory methods in numerical forecasting," *Tellus*, vol. 11, no. 2, pp. 180–196, 1959.

[243] J. S. Sawyer, "A semi-lagrangian method of solving the vorticity advection equation," *Tellus*, vol. 15, no. 4, pp. 336–342, 1963.

[244] S. Fletcher, *Semi-Lagrangian Advection Methods and Their Applications in Geoscience*. Elsevier, 1d ed., 2019.

[245] A. Robert, "A stable numerical integration scheme for the primitive meteorological equations," *Atmosphere-Ocean*, vol. 19, no. 1, pp. 35–46, 1981.

[246] S. Gravel, A. Staniforth, and J. Côté, "A stability analysis of a family of baroclinic semi-lagrangian forecast models," *Monthly Weather Review*, vol. 121, no. 3, pp. 815–824, 1993.

[247] J. Pudykiewicz and A. Staniforth, "Some properties and comparative performance of the semi-lagrangian method of robert in the solution of the advection-diffusion equation," *Atmosphere-Ocean*, vol. 22, no. 3, pp. 283–308, 1984.

[248] M. Tanguay, E. Yakimiw, H. Ritchie, and A. Robert, "Advantages of spatial averaging in semi-implicit semi-lagrangian schemes," *Monthly Weather Review - MON WEATHER REV*, vol. 120, 1992.

[249] C. Cheng and G. Knorr, "The integration of the vlasov equation in configuration space," *Journal of Computational Physics*, vol. 22, pp. 330–351, 1976.

[250] G. Strang, "On the construction and comparison of difference schemes," *SIAM Journal on Numerical Analysis*, vol. 5, no. 3, pp. 506–517, 1968.

[251] M. M. Shoucri, "Numerical solution of the two-dimensional vlasov equation," *IEEE Transactions on Plasma Science*, vol. 7, no. 2, pp. 69–72, 1979.

[252] C. Cheng, "The integration of the vlasov equation for a magnetized plasma," *Computer Software*, vol. 24, pp. 348–360, 1977.

[253] T. W. Johnston, P. Bertrand, A. Ghizzo, M. Shoucri, E. Fijalkow, and M. R. Feix, "Stimulated raman scattering: Action evolution and particle trapping via euler–vlasov fluid simulation," *Physics of Fluids B: Plasma Physics*, vol. 4, no. 8, pp. 2523–2537, 1992.

[254] P. Bertrand, A. Ghizzo, S. J. Karttunen, T. J. H. Pättikangas, R. R. E. Salomaa, and M. Shoucri, "Two-stage electron acceleration by simultaneous stimulated raman backward and forward scattering," *Physics of Plasmas*, vol. 2, no. 8, pp. 3115–3129, 1995.

[255] A. Ghizzo, M. Shoucri, P. Bertrand, T. Johnston, and J. LebasGhizzo1993, "Trajectories of trapped particles in the field of a plasma wave excited by a stimulated raman scattering," *Journal of Computational Physics*, vol. 108, pp. 373–376, 1993.

[256] M. Shoucri, "Eulerian codes for the numerical solution of the vlasov equation," *Communications in Nonlinear Science and Numerical Simulation*, vol. 13, pp. 174 – 182, 2008.

[257] M. Palmroth, U. Ganse, Y. Pfau-Kempf, M. Battarbee, L. Turc, T. Brito, M. Grandin, S. Hoilijoki, A. Sandroos, and S. von Alfthan, "Vlasov methods in space physics and astrophysics," *Living Reviews in Computational Astrophysics*, vol. 4, 2018.

[258] R. W. Hockney, "Zsp–ngp method," tech. rep., Stanford University, 1966.

[259] C. K. Birdsall and D. Fuss, "Clouds-in-clouds, clouds-in-cells physics for many-body plasma simulation," *The Physics of Fluids*, vol. 9, no. 5, pp. 842–851, 1969.

[260] F. H. Harlow, "The particle-in-cell method for numerical solution of problems in fluid dynamics," tech. rep., United States, 1964.

[261] R. L. Morse and C. W. Nielson, "One-, two-, and three-dimensional numerical simulation of two-beam plasmas," *Phys. Rev. Lett.*, vol. 23, pp. 1087–1090, Nov 1969.

[262] F. H. Harlow and J. E. Welch, "Numerical study of large-amplitude free-surface motions," *Journal of Computational Physics*, vol. 3, pp. 494–511, 1966.

[263] J.-L. Vay, "Simulation of beams or plasmas crossing at relativistic velocity," *Physics of Plasmas*, vol. 15, no. 5, p. 056701, 2008.

[264] T. Esirkepov, "Exact charge conservation scheme for particle-in-cell simulation with an arbitrary form-factor," *Computer Physics Communications*, vol. 135, no. 2, pp. 144 – 153, 2001.

[265] T. Umeda, Y. Omura, T. Tominaga, and H. Matsumoto, "A new charge conservation method in electromagnetic particle-in-cell simulations," *Computer Physics Communications*, vol. 156, pp. 73–85, 2003.

[266] G. Strang, *Essays in Linear Algebra*. Wellesley-Cambridge Press, 2012.

[267] G. I. Marchuk, "Some application of splitting-up methods to the solution of mathematical physics problems," 1968.

[268] G. I. Marchuk, "Osplitting and alternating direction methods," *Elsevier*, vol. 1, pp. 197–462, 1990.

[269] F. Neri, "Lie algebras and canonical integration," 1987.

[270] F. Etienne, "Canonical integrators as tracking codes (or how to integrate perturbation theory with tracking)," *AIP Conf. Proc.*, vol. 184, pp. 1106–1136, 1987.

[271] E. Forest and R. D. Ruth, "Fourth-order symplectic integration," *Physica D: Nonlinear Phenomena*, vol. 43, pp. 105–117, 1990.

[272] H. Yoshida, "Construction of higher order symplectic integrators," *Physics Letters A*, vol. 150, pp. 262–268, 1990.

[273] V. S. Varadarajan, *Lie Groups Lie Algebras and Their Representations*. Prentice-Hall Inc, 1974.

[274] B. Hall, "Lie groups, lie algebras, and representations," *Graduate Texts in Mathematics*, vol. 222, 2015.

[275] M. Sarrat, *Physique des instabilites de type Weibel*. PhD thesis, Universite de Lorraine, 2017.

[276] X. Garbet, Y. Idomura, L. Villard, and T. Watanabe, "Gyrokinetic simulations of turbulent transport," *Nuclear Fusion*, vol. 50, p. 043002, mar 2010.

[277] V. Grandgirard, M. Brunetti, P. Bertrand, N. Besse, X. Garbet, P. Ghendrih, G. Manfredi, Y. Sarazin, O. Sauter, E. Sonnendrücker, J. Vaclavik, and L. Villard, "A drift-kinetic semi-lagrangian 4d code for ion turbulence simulation," *Journal of Computational Physics*, vol. 217, pp. 395–423, 2006.

[278] M. Shoucri, "Splitting schemes for the numerical solution of a two-dimensional vlasov equation," *Journal of Computational Physics*, vol. 27, pp. 315 – 322, 1978.

[279] R. L. Morse and C. W. Nielson, "Numerical simulation of the weibel instability in one and two dimensions," *Computer Physics Communications*, vol. 69, pp. 306–316, 1992.

[280] J. Villasenor and O. Buneman, "Rigorous charge conservation for local electromagnetic field solvers," *The Physics of Fluids*, vol. 23, p. 87–97, 1997.

[281] V. Vshivkov, M. Kraeva, and V. Malyshkin, "Parallel implementation of the particle-in-cell method, program," *Computer Software*, vol. 14, no. 4, pp. 830–840, 1971.

[282] J. D. Hoffman, *Numerical methods for engineers and scientists*. New York: Marcel Dekker, 2001.

[283] G. Strang, *Introduction to Linear Algebra*. Wellesley, MA: Wellesley-Cambridge Press, fourth ed., 2009.

[284] S. J. Axler, *Linear Algebra Done Right*. New York: Springer, 1997.

[285] S. K. Lele, "Compact finite difference schemes with spectral-like resolution," *J. Comp. Phys.*, vol. 103, no. 1, pp. 16–42, 1992.

[286] D. Biskamp, *Magnetohydrodynamic Turbulence*. Cambridge University Press, 2003.

[287] S. Migliuolo, F. Pegoraro, and F. Porcelli, "Stabilization of collisional drift-tearing modes at the breakdown of the constant-ψ approximation," *Physics of Fluids B: Plasma Physics*, vol. 3, no. 6, pp. 1338–1345, 1991.

[288] S. Briguglio, G. Vlad, F. Zonca, and C. Kar, "Hybrid magnetohydrodynamic-gyrokinetic simulation of toroidal alfvén modes," *Physics of Plasmas*, vol. 2, no. 10, pp. 3711–3723, 1995.

[289] S. Briguglio, F. Zonca, and G. Vlad, "Hybrid magnetohydrodynamic-particle simulation of linear and nonlinear evolution of alfvén modes in tokamaks," *Physics of Plasmas*, vol. 5, no. 9, pp. 3287–3301, 1998.

[290] B. Després and R. Sart, "Reduced resistive mhd in tokamaks with general density," *Mathematical Modelling and Numerical Analysis*, vol. 46, pp. 1081–1106, 2012.

[291] O. Czarny and G. Huysmans, "Bézier surfaces and finite elements for mhd simulations," *Journal of Computational Physics*, vol. 227, no. 16, pp. 7423 – 7445, 2008.

[292] D. Grasso, M. Ottaviani, and F. Porcelli, "Linear stability and mode structure of drift tearing modes," *Physics of Plasmas*, vol. 8, no. 10, pp. 4306–4317, 2001.

[293] R. Fitzpatrick and F. Porcelli, "Collisionless magnetic reconnection with arbitrary guide field," *Physics of Plasmas*, vol. 11, no. 10, pp. 4713–4718, 2004.

[294] R. D. Hazeltine, M. Kotschenreuther, and P. J. Morrison, "A four-field model for tokamak plasma dynamics," *The Physics of Fluids*, vol. 28, no. 8, pp. 2466–2477, 1985.

[295] R. Schmalz, "Reduced, three-dimensional, nonlinear equations for high-β plasmas including toroidal effects," *Physics Letters A*, vol. 82, no. 1, pp. 14 – 17, 1981.

[296] H. Strauss, "Finite-aspect-ratio MHD equations for tokamaks," *Nuclear Fusion*, vol. 23, pp. 649–655, may 1983.

[297] D. Grasso, F. Pegoraro, F. Porcelli, and F. Califano, "Hamiltonian magnetic reconnection," *Plasma Physics and Controlled Fusion*, vol. 41, pp. 1497–1515, dec 1999.

[298] S. E. Kruger, C. C. Hegna, and J. D. Callen, "Generalized reduced magnetohydrodynamic equations," *Physics of Plasmas*, vol. 5, no. 12, pp. 4169–4182, 1998.

[299] R. Fitzpatrick, "Scaling of forced magnetic reconnection in the hall-magnetohydrodynamic taylor problem," *Physics of Plasmas*, vol. 11, no. 3, pp. 937–946, 2004.

[300] R. Fitzpatrick, "Scaling of forced magnetic reconnection in the hall-magnetohydrodynamical taylor problem with arbitrary guide field," *Physics of Plasmas*, vol. 11, no. 8, pp. 3961–3968, 2004.

[301] D. O. Gomez, S. M. Mahajan, and P. Dmitruk, "Hall magnetohydrodynamics in a strong magnetic field," *Physics of Plasmas*, vol. 15, no. 10, p. 102303, 2008.

[302] N. H. Bian and D. Tsiklauri, "Compressible hall magnetohydrodynamics in a strong magnetic field," *Physics of Plasmas*, vol. 16, no. 6, p. 064503, 2009.

[303] T. Terasawa, "Hall current effect on tearing mode instability," *Geophysical Research Letters*, vol. 10, no. 6, pp. 475–478, 1983.

[304] F. Pucci, M. Velli, and A. Tenerani, "Fast magnetic reconnection: "ideal" tearing and the hall effect," *The Astrophysical Journal*, vol. 845, p. 25, aug 2017.

[305] C. Shi, M. Velli, F. Pucci, A. Tenerani, and M. E. Innocenti, "Oblique tearing mode instability: Guide field and hall effect," *The Astrophysical Journal*, vol. 902, p. 142, oct 2020.

[306] C. Shi, A. Tenerani, M. Velli, and S. Lu, "Fast recursive reconnection and the hall effect: Hall-MHD simulations," *The Astrophysical Journal*, vol. 883, p. 172, oct 2019.

[307] J. D. Huba, "Hall magnetohydrodynamics in space and laboratory plasmas," *Physics of Plasmas*, vol. 2, no. 6, pp. 2504–2513, 1995.

[308] H. Betar, D. Del Sarto, M. Ottaviani, and A. Ghizzo, "Microscopic scales of linear tearing instabilities," *(to be) Submitted for publication on JPP.*

[309] D. Del Sarto and E. Deriaz, "A multigrid amr algorithm for the study of magnetic reconnection," *Journal of Computational Physics*, vol. 351, pp. 511 – 533, 2017.

[310] U. Trottenberg and A. Schuller, *Multigrid.* USA: Academic Press, Inc., 2000.

[311] W. Briggs, V. Henson, and S. McCormick, *A Multigrid Tutorial, 2nd Edition.* 01 2000.

[312] G. W. Hammett, W. Dorland, and F. W. Perkins, "Fluid models of phase mixing, landau damping, and nonlinear gyrokinetic dynamics," *Physics of Fluids B: Plasma Physics*, vol. 4, no. 7, pp. 2052–2061, 1992.

[313] B. Kuvshinov, F. Pegoraro, and T. Schep, "Hamiltonian formulation of low-frequency, nonlinear plasma dynamics," *Physics Letters A*, vol. 191, no. 3, pp. 296 – 300, 1994.

[314] D. D. Sarto, C. Marchetto, F. Pegoraro, and F. Califano, "Finite larmor radius effects in the nonlinear dynamics of collisionless magnetic reconnection," *Plasma Physics and Controlled Fusion*, vol. 53, p. 035008, jan 2011.

[315] D. D. Sarto, F. Pegoraro, and A. Tenerani, "'magneto-elastic' waves in an anisotropic magnetised plasma," *Plasma Physics and Controlled Fusion*, vol. 59, p. 045002, feb 2017.

[316] A. Gordeev, A. Kingsep, and L. Rudakov, "Electron magnetohydrodynamics," *Physics Reports*, vol. 243, no. 5, pp. 215 – 315, 1994.

[317] T. M. Abdalla, B. N. Kuvshinov, T. J. Schep, and E. Westerhof, "Electron vortex generation by strong, localized plasma heating," *Physics of Plasmas*, vol. 8, no. 9, pp. 3957–3966, 2001.

[318] J. M. Urrutia, R. L. Stenzel, and M. C. Griskey, "Laboratory studies of magnetic vortices. iii. collisions of electron magnetohydrodynamic vortices," *Physics of Plasmas*, vol. 7, no. 2, pp. 519–528, 2000.

[319] V. Petviashivili and V. Yan'kov *Reviews of Plasma Physics, edited by Kadomtsev (Consultants Bureau, New York, 1990)*, vol. 14, p. 1, 1989.

[320] M. Isichenko and A. Marnachev *Sov. Phys. JETP*, vol. 66, p. 702, 1987.

[321] S. Dastgeer, A. Das, P. Kaw, and P. H. Diamond, "Whistlerization and anisotropy in two-dimensional electron magnetohydrodynamic turbulence," *Physics of Plasmas*, vol. 7, no. 2, pp. 571–579, 2000.

[322] V. Y. Bychenkov and V. Silin *Sov. Phys. JETP*, vol. 71, p. 709, 1990.

[323] N. Attico, F. Califano, and F. Pegoraro, "Charge separation effects in electron-magnetohydrodynamic reconnection," *Physics of Plasmas*, vol. 8, no. 1, pp. 16–22, 2001.

[324] L. Chacón, A. N. Simakov, and A. Zocco, "Steady-state properties of driven magnetic reconnection in 2d electron magnetohydrodynamics," *Phys. Rev. Lett.*, vol. 99, p. 235001, Dec 2007.

[325] H. Cai and D. Li, "Magnetic reconnection with electron viscosity in electron magnetohydrodynamics," *Physics of Plasmas*, vol. 15, no. 3, p. 032301, 2008.

[326] H. Cai and D. Li, "Magnetic reconnection with pressure gradient effect in compressible electron magnetohydrodynamics," *Physics of Plasmas*, vol. 15, no. 4, p. 042101, 2008.

[327] D. Biskamp, *Nonlinear Magnetohydrodynamics.* Cambridge Monographs on Plasma Physics, Cambridge University Press, 1993.

[328] J. Cho and A. Lazarian, "simulations of electron magnetohydrodynamic turbulence," *The Astrophysical Journal*, vol. 701, pp. 236–252, jul 2009.

[329] X. Qian, J. Balbás, A. Bhattacharjee, and H. Yang, "A numerical study of magnetic reconnection : A central scheme for hall mhd," 2008.

[330] D. Del Sarto, *Generation and annihilation of magnetic fields in plasmas.* PhD thesis, Pisa University, 2006.

[331] R. A. Helliwell, "Whistlers and related ionospheric phenomena," *Geophysical Journal of the Royal Astronomical Society*, vol. 11, no. 5, pp. 563–564, 1966.

[332] J. Wesson and D. Campbell, *Tokamaks.* Oxford University Press, 3d ed., 2004.

[333] M. H. Holmes, *Introduction to Perturbation Methods.* Springer Science and Business Media, 2 ed., 2012.

[334] P. Holoborodko, "Advanpix multiprecision computing tool for MATLAB," 2012.

[335] G. H. Golub and C. F. Van Loan, *Matrix Computations*. John Hopkins University Press, 1996.

[336] F. Porcelli, D. Borgogno, F. Califano, D. Grasso, M. Ottaviani, and F. Pegoraro, "Recent advances in collisionless magnetic reconnection," *Plasma Phys. Controll. Fusion*, vol. 44, no. 12B, pp. B389–B405, 2002.

[337] D. Grasso, R. J. Hastie, F. Porcelli, and C. Tebaldi, "Critical Δ' for stability of viscoresistive tearing modes," *Phys. Plasmas*, vol. 15, no. 7, p. 072113, 2008.

[338] J. W. Dungey, "Conditions for the occurrence of electrical discharges in astrophysical systems," *Lond. Edinb. Dubl. Phil. Mag.*, vol. 29, no. 7, pp. 752–738, 1953.

[339] J. H. Piddington, "A theory of auroras and the ring current," *J. Atmos. Sol.-Terr. Phys.*, vol. 29, no. 1, pp. 87–105, 1967.

[340] B. Coppi and A. B. Friedland, "Processes of magnetic-energy conversion and solar flares," *Astrophys. J.*, vol. 169, p. 379, 1971.

[341] K. Shibata and S. Tanuma, "Plasmoid-induced-reconnection and fractal reconnection," *Earth Planets Space*, vol. 53, pp. 473–482, 2001.

[342] A. Ali, J. Li, and Y. Kishimoto, "On the abrupt growth dynamics of nonlinear resistive tearing mode and the viscosity effects," *Physics of Plasmas*, vol. 21, no. 5, p. 052312, 2014.

[343] A. Tenerani, A. F. Rappazzo, M. Velli, and F. Pucci, "The tearing mode instability of thin current sheets: the transition to fast reconnection in presence of viscosity," *Astrophys. J.*, vol. 801, p. 145, mar 2015.

[344] E. Papini, S. Landi, and L. D. Zanna, "Fast magnetic reconnection: Secondary tearing instability and role of the hall term," *The Astrophysical Journal*, vol. 885, p. 56, oct 2019.

[345] F. Porcelli, "Viscous resistive magnetic reconnection," *Phys. Fluids*, vol. 30, no. 6, pp. 1734–1742, 1987.

[346] G. Einaudi and F. Rubini, "Resistive instabilities in a flowing plasma. ii. Effects of viscosity," *Phys. Fluids B*, vol. 61, p. 2224, 1989.

[347] L. Ofman, X. L. Chen, and P. J. Morrison, "Resistive tearing mode instability with shear flow and viscosity," *Phys. Plasmas B*, vol. 3, p. 1346, 1991.

[348] K. Takeda, O. Agullo, S. Benkadda, A. Sen, N. Bian, and X. Garbet, "Nonlinear viscoresistive dynamics of the m=1 tearing instability," *Phys. Plasmas*, vol. 82, no. 5, p. 535820501, 2016.

[349] H. Betar, "Study of reconnecting modes approaching the ideal tearing regime," Master's thesis, Institut Jean Lamour, Universite de Lorraine, 2017.

[350] J. R. Pinzon, "Study of slab reconnection instabilities at single and double resonant surfaces in resistive and inertial regimes," Master's thesis, Institut Jean Lamour, Universite de Lorraine, 2014.

[351] F. L. Waelbroeck, R. D. Hazeltine, and P. J. Morrison, "A hamiltonian electromagnetic gyrofluid model," *Physics of Plasmas*, vol. 16, no. 3, p. 032109, 2009.

[352] E. Tassi, P. J. Morrison, F. L. Waelbroeck, and D. Grasso, "Hamiltonian formulation and analysis of a collisionless fluid reconnection model," *Plasma Phys. Controll. Fusion*, vol. 50, p. 085014, 2008.

[353] A. Zocco and A. A. Schekochihin, "Fast linear growth of collisionless double tearing modes in a cylindrical plasma," *Phys. Plasmas*, vol. 18, p. 102309, 2011.

[354] M. Ottaviani and F. Porcelli, "Fast nonlinear magnetic reconnection," *Phys. Plasmas*, vol. 2, p. 4104, 1995.

[355] F. Pegoraro, D. Borgogno, F. Califano, D. Del Sarto, E. Echkina, D. Grasso, T. Liseikina, and F. Porcelli, "Developments in the theory of collisionless reconnection in magnetic configurations with a strong guide field," *Nonlinear Processes in Geophysics*, vol. 11, no. 5/6, pp. 567–577, 2004.

[356] M. Velli, F. Pucci, F. Rappazzo, and A. Tenerani, "Models of coronal heating, turbulence and fast reconnection," *Philosophical Transactions of the Royal Society A: Mathematical, Physical and Engineering Sciences*, vol. 373, no. 2042, p. 20140262, 2015.

[357] A. Tenerani, M. Velli, A. F. Rappazzo, and F. Pucci, "MAGNETIC RECONNECTION: RECURSIVE CURRENT SHEET COLLAPSE TRIGGERED BY "IDEAL" TEARING," *The Astrophysical Journal*, vol. 813, p. L32, nov 2015.

[358] A. Tenerani, M. Velli, A. Rappazzo, and F. Pucci, "Magnetic reconnection: Self-similar current sheet collapse triggered by "ideal" tearing," *The Astrophysical Journal*, vol. 813, 06 2015.

[359] L. D. Zanna, S. Landi, E. Papini, F. Pucci, and M. Velli, "Theidealtearing mode: theory and resistive MHD simulations," *Journal of Physics: Conference Series*, vol. 719, p. 012016, may 2016.

[360] A. Bhattacharjee, H. Yi-Min, H. Yang, and B. Rogers, "Fast reconnection in high-lundquist-number plasmas due to the plasmoid instability," *Phys. Plasmas*, vol. 16, no. 11, p. 112102, 2009.

[361] L. Comisso and D. Grasso, "Visco-resistive plasmoid instability," *Phys. Plasmas*, vol. 23, no. 3, p. 032111, 2016.

[362] A. Tenerani, M. Velli, A. F. Rappazzo, and F. Pucci, ""Ideally" unstable current sheets and the triggering of fast magnetic reconnection," *J. Plasma Phys.*, vol. 82, no. 5, p. 535820501.

[363] F. Califano, N. Attico, F. Pegoraro, G. Bertin, and S. V. Bulanov, "Fast formation of magnetic islands in a plasma in the presence of counterstreaming electrons," *Phys. Rev. Lett.*, vol. 86, pp. 5293–5296, Jun 2001.

[364] J. D. Scudder, H. Karimabadi, W. Daughton, and V. Roytershteyn, "Frozen flux violation, electron demagnetization and magnetic reconnection," *Physics of Plasmas*, vol. 22, no. 10, p. 101204, 2015.

[365] S. Servidio, F. Valentini, D. Perrone, A. Greco, F. Califano, W. H. Matthaeus, and P. Veltri, "A kinetic model of plasma turbulence," *Journal of Plasma Physics*, vol. 81, no. 1, p. 325810107, 2015.

[366] R. M. Green, "Modes of annihilation and reconnection of magnetic fields," in *Stellar and Solar Magnetic Fields* (R. Lust, ed.), vol. 22, p. 398, Jan. 1965.

[367] A. Ghizzo and D. Del Sarto, "Low- and high-frequency nature of oblique filamentation modes. ii. vlasov–maxwell simulations of collisionless heating process," *Physics of Plasmas*, vol. 27, no. 7, p. 072104, 2020.

[368] J. M. Finn and P. K. Kaw, "Coalescence instability of magnetic islands," *The Physics of Fluids*, vol. 20, no. 1, pp. 72–78, 1977.

[369] T. Tajima and J. Dawson, "Ion cyclotron resonance heating and the alfvén-ion cyclotron instability," *Nuclear Fusion*, vol. 20, pp. 1129–1152, sep 1980.

[370] T. Tajima, F. Brunel, J.-I. Sakai, L. Vlahos, and M. R. Kundu, "The coalescence instability in solar flares," *Symposium - International Astronomical Union*, vol. 107, p. 197–210, 1985.

[371] D. W. Longcope and H. R. Strauss, "The coalescence instability and the development of current sheets in two-dimensional magnetohydrodynamics," *Physics of Fluids B: Plasma Physics*, vol. 5, no. 8, pp. 2858–2869, 1993.

[372] A. Bhattacharjee, F. Brunel, and T. Tajima, "Magnetic reconnection driven by the coalescence instability," *The Physics of Fluids*, vol. 26, no. 11, pp. 3332–3337, 1983.

[373] M. R. Feix and P. Bertrand, "A universal model: The vlasov equation," *Transport Theory and Statistical Physics*, vol. 34, no. 1-2, pp. 7–62, 2005.

[374] P. Bertrand, M. Albrecht-Marc, T. Réveillé, and A. Ghizzo, "Vlasov models for laser-plasma interaction," *Transport Theory and Statistical Physics*, vol. 34, no. 1-2, pp. 103–126, 2005.

[375] A. Ghizzo, P. Bertrand, T. W. Johnston, and N. Besse, "Lecture note ISSS9 The 9 th International School of Space Simulations: Eulerian Vlasov models for plasma simulation: review and advances," in *ISSS9, the 9th International School of Space and Simulations, 3-11 July 2009, Paris, France.*, (PARIS, France), 2009.

[376] G. Arfken, *Mathematical Methods for Physicists.* Academic Press, 2d ed., 1970.

[377] H. Grad and H. Rubin, "Hydromagnetic equilibria and force-free fields," *Proceedings of the 2nd UN Conf. on the Peaceful Uses of Atomic Energy*, vol. 31, p. 190, 1958.

[378] V. D. Shafranov, "The classical thermal conductivity in a toroidal plasma filament," *Journal of Nuclear Energy. Part C, Plasma Physics, Accelerators, Thermonuclear Research*, vol. 8, pp. 314–322, jan 1966.